

Special Issue Reprint

Molecular Spectroscopy and Molecular Structure

Commemorative Issue in Honor of Professor Austin
J. Barnes on Occasion of his 75th Birthday

Edited by
Rui Fausto, Sylvia Turrell and Gulce Ogruc Ildiz

mdpi.com/journal/molecules

**Molecular Spectroscopy
and Molecular Structure:
Commemorative Issue in Honor
of Professor Austin J. Barnes on
Occasion of His 75th Birthday**

Molecular Spectroscopy and Molecular Structure: Commemorative Issue in Honor of Professor Austin J. Barnes on Occasion of His 75th Birthday

Editors

Rui Fausto

Sylvia Turrell

Gulce Ogruc Ildiz



Basel • Beijing • Wuhan • Barcelona • Belgrade • Novi Sad • Cluj • Manchester

Editors

Rui Fausto

Department of Chemistry

University of Coimbra

Coimbra

Portugal

Sylvia Turrell

Department of Chemistry

Université des Sciences et

Technologies de Lille 1

Lille

France

Gulce Ogruc Ildiz

Department of Physics

Istanbul Kultur University

Istanbul

Turkey

Editorial Office

MDPI AG

Grosspeteranlage 5

4052 Basel, Switzerland

This is a reprint of articles from the Special Issue published online in the open access journal *Molecules* (ISSN 1420-3049) (available at: https://www.mdpi.com/journal/molecules/special_issues/moleclar_struc).

For citation purposes, cite each article independently as indicated on the article page online and as indicated below:

Lastname, A.A.; Lastname, B.B. Article Title. <i>Journal Name</i> Year , <i>Volume Number</i> , Page Range.
--

ISBN 978-3-7258-1852-5 (Hbk)

ISBN 978-3-7258-1851-8 (PDF)

doi.org/10.3390/books978-3-7258-1851-8

© 2024 by the authors. Articles in this book are Open Access and distributed under the Creative Commons Attribution (CC BY) license. The book as a whole is distributed by MDPI under the terms and conditions of the Creative Commons Attribution-NonCommercial-NoDerivs (CC BY-NC-ND) license.

Contents

About the Editors	vii
Preface	ix
Barbara Golec, Magdalena Sałdyka and Zofia Mielke Complexes of Formaldehyde and α -Dicarbonyls with Hydroxylamine: FTIR Matrix Isolation and Theoretical Study Reprinted from: <i>Molecules</i> 2021 , <i>26</i> , 1144, doi:10.3390/molecules26041144	1
Gulce Ogruc Ildiz and Rui Fausto Structural Aspects of the <i>Ortho</i> Chloro- and Fluoro- Substituted Benzoic Acids: Implications on Chemical Properties Reprinted from: <i>Molecules</i> 2020 , <i>25</i> , 4908, doi:10.3390/molecules25214908	20
Esther J. Ocola and Jaan Laane Spectroscopic and Theoretical Study of the Intramolecular π -Type Hydrogen Bonding and Conformations of 2-Cyclopenten-1-ol Reprinted from: <i>Molecules</i> 2021 , <i>26</i> , 1106, doi:10.3390/molecules26041106	70
Justyna Krupa, Maria Wierzejewska and Jan Lundell Structure and IR Spectroscopic Properties of HNCO Complexes with SO ₂ Isolated in Solid Argon Reprinted from: <i>Molecules</i> 2021 , <i>26</i> , 6441, doi:10.3390/molecules26216441	80
Thomas A. Ford The Structures, Molecular Orbital Properties and Vibrational Spectra of the Homo- and Heterodimers of Sulphur Dioxide and Ozone. An Ab Initio Study Reprinted from: <i>Molecules</i> 2021 , <i>26</i> , 626, doi:10.3390/molecules26030626	93
T. M. Dung Cao, T. T. Giang Le, Sylvia Turrell, Maurizio Ferrari, Quang Vinh Lam and T. T. Van Tran Luminescent Ink Based on Upconversion of NaYF ₄ :Er,Yb@MA Nanoparticles: Environmental Friendly Synthesis and Structural and Spectroscopic Assessment Reprinted from: <i>Molecules</i> 2021 , <i>26</i> , 1041, doi:10.3390/molecules26041041	113
Gulce Ogruc Ildiz, Ahmet Karadag, Ersin Kaygisiz and Rui Fausto PLS-DA Model for the Evaluation of Attention Deficit and Hyperactivity Disorder in Children and Adolescents through Blood Serum FTIR Spectra Reprinted from: <i>Molecules</i> 2021 , <i>26</i> , 3400, doi:10.3390/molecules26113400	123
Ilya G. Shenderovich and Gleb S. Denisov Modeling of the Response of Hydrogen Bond Properties on an External Electric Field: Geometry, NMR Chemical Shift, Spin-Spin Scalar Coupling Reprinted from: <i>Molecules</i> 2021 , <i>26</i> , 4967, doi:10.3390/molecules26164967	135
Sylwia Zięba, Agata Piotrowska, Adam Mizera, Paweł Ławniczak, Karolina H. Markiewicz, Andrzej Gzella, et al. Spectroscopic and Structural Study of a New Conducting Pyrazolium Salt Reprinted from: <i>Molecules</i> 2021 , <i>26</i> , 4657, doi:10.3390/molecules26154657	150

Dana Ortansa Dorohoi, Dan-Gheorghe Dimitriu, Mihaela Maria Dulcescu-Oprea, Ana Cezarina Morosanu, Nicoleta Puica-Melniciuc, Elena Ardelean, et al. Solvatochromic Study of Two Carbanion Monosubstituted 4-Tolyl-1,2,4-triazol-1-ium Phenacylids in Binary Hydroxyl Solvent Mixtures Reprinted from: <i>Molecules</i> 2021 , <i>26</i> , 3910, doi:10.3390/molecules26133910	167
Lamya H. Al-Wahaibi, Althaf Shaik, Mohammed A. Elmorsy, Mohammed S. M. Abdelbaky, Santiago Garcia-Granda, Subbiah Thamotharan, et al. Structural Insights of Three 2,4-Disubstituted Dihydropyrimidine-5-carbonitriles as Potential Dihydrofolate Reductase Inhibitors Reprinted from: <i>Molecules</i> 2021 , <i>26</i> , 3286, doi:10.3390/molecules26113286	183
Dorota Kowalczyk, Agata Gładysz, Monika Pitucha, Daniel M. Kamiński, Agnieszka Barańska and Bartłomiej Drop Spectroscopic Study of the Molecular Structure of the New Hybrid with a Potential Two-Way Antibacterial Effect Reprinted from: <i>Molecules</i> 2021 , <i>26</i> , 1442, doi:10.3390/molecules26051442	199

About the Editors

Rui Fausto

Rui Fausto is Professor at the Department of Chemistry of the University of Coimbra, Portugal, the Coordinator of the Computational Chemistry, Spectroscopy and Thermodynamics Research Group of the Coimbra Chemistry Centre (CQC), and Head of the Laboratory of Raman Spectroscopy and Materials of CQC. He is also Invited Professor at the Istanbul Culture University (IKU) and the Spectroscopy@IKU ERA Chair Holder. He is a member of the European Academy of Arts, Sciences and Humanities (Paris), and served as the Coordinator of the Directorate for High-Education of the International Observatory of Human Rights (Lisbon). Rui Fausto is President of the permanent Steering Committee of the EUCMOS (European Congress on Molecular Spectroscopy) series of meetings, and is on the editorial boards of several scientific journals. His main scientific interests focus on molecular spectroscopy, quantum chemistry, solid state photochemistry and chemometrics, and he is the author/editor of over 30 books, and the author of over 500 peer-reviewed articles and book chapters. During his career, he has occupied many different positions in administration and scientific management at the University of Coimbra. In 2004 and 2005, he was awarded the Excellence Prize of the Portuguese Science Foundation / Portuguese Ministry of Science.

Sylvia Turrell

Sylvia Turrell is Emeritus Professor of Chemistry of the University of Lille, France. During her career, she has been a professor and researcher at several universities in Zaire, Canada (Montreal and Quebec) and France (Limoges, Lille). Her research focuses on the use of spectroscopic techniques for the characterization of the structure of materials and the elucidation of the mechanisms responsible for specific properties. Specifically, infrared and Raman spectroscopies and force field calculations for crystalline systems, detection and characterization of Alzheimer's disease, development of sol-gel materials, fabrication and studies of planar wave guides, alteration processes in glasses, and the fabrication and characterization of semiconductor nanoparticles for photonics and photovoltaics. She has a wide scientific curriculum and editorial experience. She is Vice-President of the permanent Steering Committee of the EUCMOS (European Congress on Molecular Spectroscopy).

Gulce Ogruc Ildiz

Gulce Ogruc Ildiz was born in Istanbul in 1977. After graduating from Kültür College, she received her undergraduate degree from Istanbul Technical University in Physics Engineering (2001), and her master's degree from the Istanbul Technical University Nuclear Energy Engineering (2004) and Istanbul Kültür University Business Administration (MBA) (2003) departments. She received her doctorate degrees from the Istanbul University Department of Atomic and Molecular Physics (2008) and Istanbul Kültür University Department of Civil Engineering Project Management Program (2009). She was appointed as Assistant Professor (2010) at the Istanbul Kültür University Department of Physics, and as Professor in 2020. Between 2015 and 2022, she was the Executive Secretary of Istanbul Kültür University, Technology and Project Support Unit (TPDB), Scientific Research Projects (BAP) Coordinator, Faculty Administrative Board and Faculty Board Member at IKU Faculty of Engineering, Faculty of Education and Faculty of Arts and Sciences. She is the editor of several international journals in the field of spectroscopy. Ildiz's main scientific interests focus on the investigation of biologically relevant Raman spectroscopy and chemometrics, matrix isolation infrared spectroscopy and computational chemistry. She has been Vice Rector of Istanbul Kültür University since August 2022.

Preface

This Special Issue of *Molecules* is dedicated to Prof. Austin James Barnes by occasion of his 75th birthday, in acknowledgment of his influential scientific contributions in the fields of molecular spectroscopy and molecular structure. The Special Issue comprises 12 articles that span a broad range of interests in the fields of molecular structure, molecular spectroscopy, hydrogen bonding, intermolecular interactions, chemical reactivity, weakly bound species and applied spectroscopy.

Austin J. Barnes was born on 2 June 1945. He was awarded his PhD degree in 1969 at the University College of Swansea for research on infrared spectra of matrix-isolated species. He was appointed as a lecturer at the University of Salford in 1973, where he remained for the rest of his career. He was awarded a DSc degree by the University of Wales in 1986, and in 1991, was promoted to Reader. From 1996 to 1999, he served as Head of the Department of Chemistry and Applied Chemistry. He had a continued association with the University as an Honorary Visiting Professor until the end of 2015. Austin's principal research interests focused on infrared and Raman matrix isolation spectroscopy, particularly applied to the investigation of molecular interactions and conformational isomerism. His investigations of the conformational behavior of molecules trapped in matrices led to a proposed empirical relationship referred to by some authors as 'the Barnes relation'. Austin's interests in strongly hydrogen-bonded systems have also extended to the structural studies of ferroelectric crystals and nonlinear optical materials. He was one of the first to report on the so called 'blue-shifting' hydrogen bonds.

Austin has published around 125 research and review papers, and edited many books and volumes of conference proceedings. He was awarded the Gold Medal of the University of Wroclaw, Poland, in 2008.

Austin served as President of the International Committee of the European Congress on Molecular Spectroscopy (EUCMOS) from 1994 to 2016, and from 1979 to 1993, he served as Assistant Editor for both the *Journal of Molecular Structure* and *THEOCHEM*. In January 1994, he was appointed to act as an Editor of the *Journal of Molecular Structure* and continued in this role until the end of 2009.

Prof. Austin J. Barnes was one of the most influential scientists in the fields of molecular structure and molecular spectroscopy, and his long scientific career has been an example to follow. Austin passed away on 25 June 2021 (Bolton) at the age of 76, just one year after the publication of this Special Issue.

We must thank all our colleagues who contributed to this Special Issue to honor Austin, as well as the diligent reviewers whose meticulous evaluations have elevated the scientific rigor and quality of the submitted articles.

Rui Fausto, Sylvia Turrell, and Gulce Ogruc Ildiz
Editors

Article

Complexes of Formaldehyde and α -Dicarbonyls with Hydroxylamine: FTIR Matrix Isolation and Theoretical Study

Barbara Golec ^{1,*}, Magdalena Sałdyka ² and Zofia Mielke ²¹ Institute of Physical Chemistry, Polish Academy of Sciences, Kasprzaka 44/52, 01-224 Warsaw, Poland² Faculty of Chemistry, University of Wrocław, F. Joliot-Curie 14, 50-383 Wrocław, Poland; magdalena.saldyka@chem.uni.wroc.pl (M.S.); zofia.mielke@chem.uni.wroc.pl (Z.M.)

* Correspondence: bgolec@ichf.edu.pl; Tel.: +48-22-343-3410

Abstract: The interactions of formaldehyde (FA), glyoxal (Gly) and methylglyoxal (MGly) with hydroxylamine (HA) isolated in solid argon and nitrogen were studied using FTIR spectroscopy and ab initio methods. The spectra analysis indicates the formation of two types of hydrogen-bonded complexes between carbonyl and hydroxylamine in the studied matrices. The cyclic planar complexes are stabilized by O–H ··· O(C), and C–H ··· N interactions and the nonplanar complexes are stabilized by O–H ··· O(C) bond. Formaldehyde was found to form with hydroxylamine, the cyclic planar complex and methylglyoxal, the nonplanar one in both argon and nitrogen matrices. In turn, glyoxal forms with hydroxylamine the most stable nonplanar complex in solid argon, whereas in solid nitrogen, both types of the complex are formed.

Keywords: carbonyls; hydroxylamine; hydrogen bond; matrix isolation; vibrational spectroscopy; computational chemistry

Citation: Golec, B.; Sałdyka, M.; Mielke, Z. Complexes of Formaldehyde and α -Dicarbonyls with Hydroxylamine: FTIR Matrix Isolation and Theoretical Study. *Molecules* **2021**, *26*, 1144. <https://doi.org/10.3390/molecules26041144>

Academic Editors: Rui Fausto, Sylvia Turrell and Gulce Ogruc Ildiz

Received: 26 January 2021

Accepted: 18 February 2021

Published: 20 February 2021

Publisher's Note: MDPI stays neutral with regard to jurisdictional claims in published maps and institutional affiliations.



Copyright: © 2021 by the authors. Licensee MDPI, Basel, Switzerland. This article is an open access article distributed under the terms and conditions of the Creative Commons Attribution (CC BY) license (<https://creativecommons.org/licenses/by/4.0/>).

1. Introduction

Chemical and photochemical reactions often proceed through many intermediate stages between the substrates and products. The reactive intermediates formed at the first stages are usually not observed at normal conditions but can be stabilized in an inert environment. The excellent technique for such a purpose is a low-temperature matrix isolation method, which enables the isolation of unstable intermediates in the rare gas matrix [1]. Many reactions begin with the formation of the molecular complexes between the substrates, which also can be isolated in the matrices. Using the FTIR spectroscopy and ab initio methods, we are able to distinguish the nature of interactions and the structures of the isolated complexes [2,3].

In this work, we used the FTIR matrix isolation spectroscopy and MP2 calculations to investigate the structures of the complexes formed between simple carbonyl (formaldehyde) and α -dicarbonyl compounds glyoxal and methylglyoxal, with hydroxylamine in argon and nitrogen environment. Identification and characterization of these complexes is the first step of our study on isolation of highly unstable intermediate, called hemiaminal, that is formed in oxime formation reaction [4,5] and will be the subject of our next paper. Oximes are widely used compounds in synthetic chemistry in biomedical fields, for example, in the coupling reactions of peptides, proteins, oligosaccharides, and oligonucleotides and in bioconjugation reaction [6–11]. On the other hand, to explain the acid-catalyzed reaction of nucleophiles with the carbonyl group, the formation of weak hydrogen bonds between the carbonyl group of aldehydes and ketones with proton donors has been postulated [12]. Therefore, the deep understanding of the hydrogen bond interaction of carbonyl compounds with nucleophilic hydroxylamine is an important issue.

Some binary complexes between formaldehyde or α -dicarbonyls and proton donors have been investigated. The most studied are the complexes of formaldehyde with water [13–31]. Additionally, there are some words about the interaction of formaldehyde with

hydrogen halides and cyanide [32–36], formamide [37,38], nitroxyl [39], ammonia [33], methane [40], and methanol [41]. For α -dicarbonyls, the interactions of glyoxal, methylglyoxal and diacetyl with water [42], methanol [43,44], hydrogen peroxide [45,46], and hydroperoxyl radical [47] have been studied. The results of these investigations show that the water complexes of formaldehyde or α -dicarbonyls trapped in argon matrices are stabilized by the $\text{OH}\cdots\text{O}(\text{C})$ hydrogen bond formed between water and carbonyl oxygen. The most stable structure of the methanol complex with formaldehyde is also predicted to be stabilized by a hydrogen bond. However, for the methanol complexes with α -dicarbonyls, the ab initio calculations predict the non-hydrogen-bonded structures as the most stable ones. Experimental data show that in the Ar matrix, glyoxal forms the non-hydrogen-bonded structure with methanol, but methylglyoxal and diacetyl form the planar cyclic structures stabilized by $\text{O}-\text{H}\cdots\text{O}(\text{C})$ and $\text{C}-\text{H}\cdots\text{O}(\text{C})$ interactions.

Hydroxylamine dimers and their complexes with water and ammonia isolated in argon and nitrogen matrices have been studied by Yao and Ford [48–50]. The dimer $(\text{NH}_2\text{OH})_2$ has a cyclic structure stabilized by two $\text{O}-\text{H}\cdots\text{N}$ hydrogen bonds. In hydroxylamine complexes with H_2O and NH_3 , the OH group of NH_2OH acts as a proton donor to the oxygen or nitrogen atom of water or ammonia, respectively. These complexes are relatively strong; the $\nu(\text{OH})$ band of hydroxylamine shifts by 100 and 300 cm^{-1} to lower wavenumbers in the spectra of the H_2O and NH_3 complexes, respectively. A much weaker complex formed between hydroxylamine and carbon monoxide stabilized by $\text{O}-\text{H}\cdots\text{C}=\text{O}$ interaction has been observed in the Ar matrix. In this complex, the $\nu(\text{OH})$ band shifts 39 cm^{-1} towards lower energies [51]. For the isocyanic acid-hydroxylamine complex, only the hydrogen-bonded structure with the NH group of HNCO attached to the oxygen atom of the NH_2OH molecule was identified in solid argon [52].

2. Results and Discussion

2.1. Formaldehyde–hydroxylamine Complexes

Ab Initio Calculations. The MP2/6-311++G(2d,2p) calculations predict the stability of five different structures of a hydrogen-bonded complex between formaldehyde and hydroxylamine with stoichiometry 1:1. Their structures and binding energies ($\Delta E^{\text{CP}}(\text{ZPE})$ in kJ mol^{-1}) are presented in Figure 1 and Figure S1 in Supplementary Material.

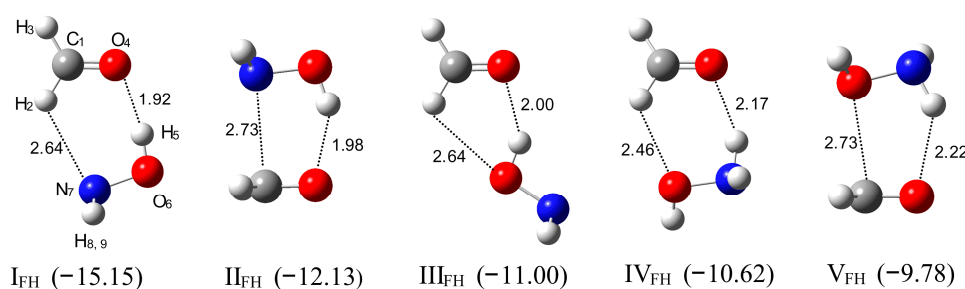


Figure 1. The optimized structures of the $\text{HCHO}-\text{NH}_2\text{OH}$ complexes, $\text{I}_{\text{FH}}-\text{V}_{\text{FH}}$. The $\Delta E_{\text{CP}}(\text{ZPE})$ -binding energies in kJ mol^{-1} are given in parentheses. The intermolecular distances are given in Å.

The most stable complex, I_{FH} , has a cyclic structure in which two subunits are stabilized by two hydrogen bonds: the relatively strong $\text{OH}\cdots\text{O}(\text{C})$ bond ($R(\text{H}\cdots\text{O}) = 1.92\text{ Å}$) and the weak $\text{CH}\cdots\text{N}$ interaction ($R(\text{H}\cdots\text{N}) = 2.64\text{ Å}$). The selected structural parameters of this complex are listed in Table S1 in Supplementary Material. In this complex, the OH group of hydroxylamine acts as a proton donor and the nitrogen atom as a proton acceptor. The two hydrogen bonds are positioned in one plane, which is reflected by the value of the torsion angles $\varphi\text{C1}-\text{O4}-\text{H5}-\text{O6}$ and $\varphi\text{C1}-\text{H2}-\text{N7}-\text{O6}$ equal to 0 degrees. This structure is about 3 kJ mol^{-1} more stable than II_{FH} , which is stabilized by one hydrogen bond, $\text{OH}\cdots\text{O}(\text{C})$, formed between the OH group of hydroxylamine and the oxygen atom of formaldehyde ($R(\text{H}\cdots\text{O}) = 1.98\text{ Å}$). The next three structures, III_{FH} , IV_{FH} and V_{FH} ,

have comparable energies (-11.00 , -10.62 , and -9.78 kJ mol $^{-1}$, respectively). In III_{FH}, the hydroxylamine hydroxyl group interacts with formaldehyde forming OH \cdots O(C) bond ($R\cdots O(C) = 2.0$ Å) weaker than in I_{FH} and II_{FH}. The structures IV_{FH} and V_{FH} are stabilized by NH \cdots O(C) interaction between the NH group of hydroxylamine and an oxygen atom of formaldehyde.

Experimental Spectra. The infrared spectra of the formaldehyde and hydroxylamine molecules isolated in argon and nitrogen matrices agree with those previously reported [25,48,49,53–56]. When both FA and HA are trapped in the matrices, a set of new absorptions appears in the spectra that are not observed in the spectra of parent molecules. The selected regions of experimental spectra of FA/HA/Ar matrix are shown in Figure 2.

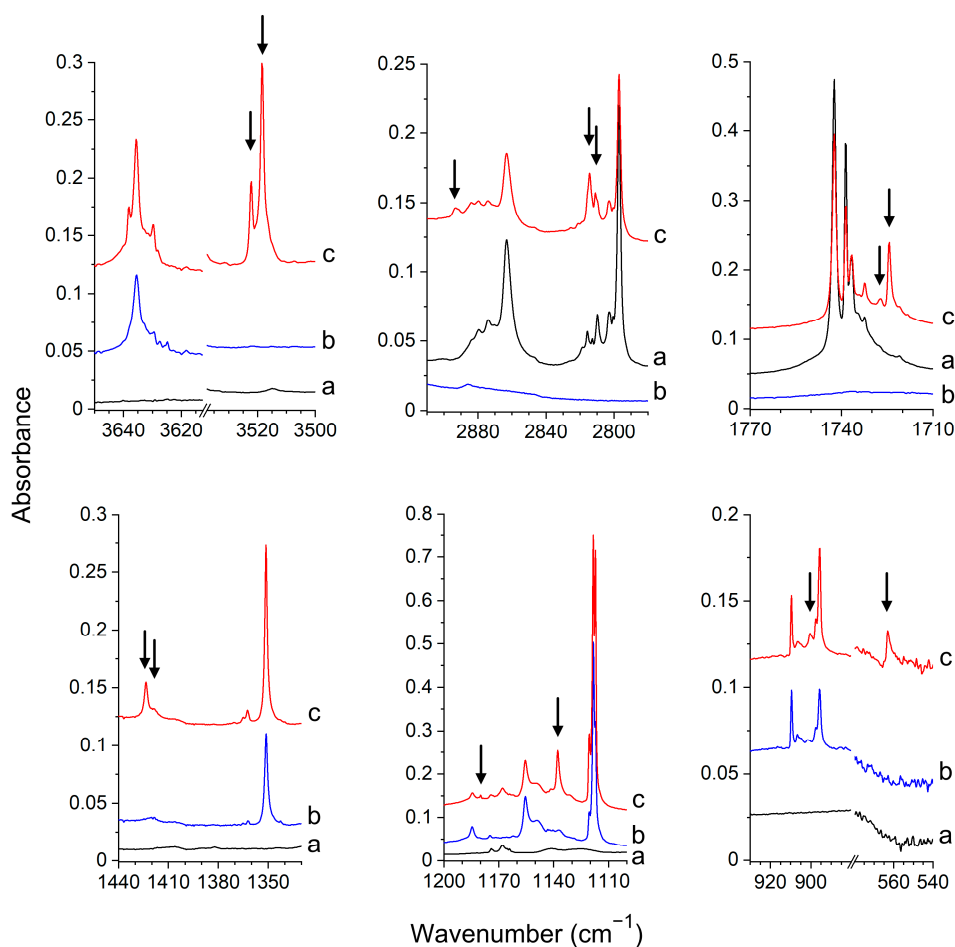


Figure 2. The spectra of the HCHO/Ar (a), NH₂OH/Ar (b) and HCHO/NH₂OH/Ar (c) matrices recorded after matrix deposition at 11 K. The bands of the HCHO–NH₂OH complex are marked by the arrows.

The new absorptions, indicated in the spectra by the arrows, are assigned to the HCHO–NH₂OH complex. The splitting of the bands is assigned to the matrix cage effect as the observed spectral pattern of the complex differs in the spectra of argon and nitrogen matrices. In Table 1, the observed experimental wavenumbers and wavenumbers shifts are compared with the MP2 calculated values predicted for the two most stable forms of the formaldehyde–hydroxylamine complexes (I_{FH} and II_{FH}). The large red-shift of the $\nu(\text{OH})$ band of HA (-115.1 and -124.6 cm $^{-1}$ in Ar and N₂ matrices, respectively) and the red-shift of the $\nu(\text{C}=\text{O})$ band of FA after complex formation (-16.8 and -17.1 cm $^{-1}$) in Ar and N₂ matrices, respectively indicate that the complex has the hydrogen-bonded structure with the NH₂OH molecule attached to the carbonyl group of HCHO. The comparison of the experimental and theoretical spectra clearly shows that in both argon and nitrogen

matrices, one type of complex is formed. The identified complex bands for the OH, C=O groups evidence that the I_{FH} structure is created in both matrices. The calculations indicate that for the structure I_{FH}, the strongest band corresponds to the $\nu(\text{OH})$ stretching vibration (408 km mol^{-1}). It is ca 3.5 times more intense than the other band of the OH group, namely $\tau(\text{OH})$ (115 km mol^{-1}). For the II_{FH} complex, both $\nu(\text{OH})$ and $\tau(\text{OH})$ bands are predicted to have comparable intensities ($117, 122 \text{ km mol}^{-1}$). Moreover, $\tau(\text{OH})$ is distinctly more perturbed in I_{FH} than in II_{FH} ($+238, +106 \text{ cm}^{-1}$, respectively). In experimental spectra, the $\nu(\text{OH})$ band is much more intense than the $\tau(\text{OH})$ one, which indicates that the I_{FH} structure is formed. The observed shift of the $\tau(\text{OH})$ vibration of HA (162.1 cm^{-1} , Ar; 172.5 cm^{-1} , N₂) also corresponds better with the value $+238 \text{ cm}^{-1}$ predicted for the structure I_{FH} than with the value $+106 \text{ cm}^{-1}$ calculated for the complex II_{FH}. The other calculated wavenumber shifts and intensities for the I_{FH} structure also match well the observed ones, as one can see in Table 1.

Table 1. The comparison of the observed wavenumbers (cm^{-1}) and wavenumber shifts ($\Delta\nu = \nu_{\text{FH}} - \nu_{\text{M}}$) for the HCHO–NH₂OH (FH) complexes present in the argon (Ar) and nitrogen (N₂) matrices with the corresponding values calculated for the structures I_{FH} and II_{FH}. In parentheses, the calculated band intensities are given (km mol^{-1}).

Approximate Description	Experimental						Calculated	
	Ar			N ₂			$\Delta\nu$	
	ν_{M}	ν_{FH}	$\Delta\nu^1$	ν_{M}	ν_{FH}	$\Delta\nu^1$	I _{FH}	II _{FH}
Hydroxylamine								
$\nu(\text{OH})$	3635.5	3522.2 3518.5	−115.1	3637.6	3516.0 3510.0	−124.6	−141 (408)	−126 (117)
$\delta(\text{NOH})$	1351.2	1423.4 1418.7	+69.9	1367.4	1427.7	+60.3	+86 (36)	+62 (51)
$\omega(\text{NH}_2)$	1118.3	1137.8	+19.5	1133.0	1156.7	+23.7	+24 (117)	+13 (102)
$\nu(\text{NO})$	895.6	900.5	+4.9	895.3	897.0 901.8	+4.1	+6 (7)	+8 (4)
$\tau(\text{OH})$	402 ²	562.1	+162.1	402 ²	574.5	+172.5	+238 (115)	+106 (122)
Formaldehyde								
$\nu_{\text{as}}(\text{CH})$	2864.1	2893.3 2891.1	+28.1	2866.4	2892.3	+25.9	+56 (34)	+34 (72)
$\nu_{\text{s}}(\text{CH})$	2798.0	2814.2 2811.0	+14.6	2800.1 2798.0			+25 (77)	+29 (56)
$\nu(\text{C=O})$	1742.2	1727.1 1724.4	−16.8	1740.7 1739.7	1723.1	−17.1	−20 (53)	−9 (66)
$\delta(\text{CH}_2)$	1499.1	1493.9	−5.2	1499.6 1496.4			−6 (15)	−3 (14)
$\gamma(\text{CH}_2)$	1168.6	1179.8	+11.2	1170.0 1167.9	1180.0	+11.0	+12 (5)	+8 (20)

¹ In the case when the splitting of the band was observed, the average of the two wavenumbers at which the two peaks appear was taken into account to calculate $\Delta\nu$ value. ² Gas-phase data [56].

Nelander [25] studied the HCHO–H₂O complex and found that the hydrogen-bonded structures stabilized by the O–H...O(C) bond are formed both in argon and nitrogen matrices. The wavenumbers shifts of the H₂O vibrations for the complex isolated in solid argon were found to be $−25.0 \text{ cm}^{-1}$ for the $\nu_{\text{as}}(\text{OH})$ and $−52.9, −57.6 \text{ cm}^{-1}$ for the $\nu_{\text{s}}(\text{OH})$ vibrations, whereas $\nu(\text{C=O})$ of FA was shifted by $−5.2 \text{ cm}^{-1}$ after complex formation. Such shifts pattern indicates that the HCHO–H₂O complex is weaker than the HCHO–NH₂OH one.

2.2. Glyoxal–hydroxylamine Complexes

Ab Initio Calculations. Glyoxal in the standard conditions exists in a *trans* form [57–59], so exclusively, this conformer is considered in our study. The MP2 calculations show the stability of eight different complexes of 1:1 stoichiometry, which can be formed between Gly and HA. The four most stable ones are presented in Figure 3, and all complexes are shown in Figure S2 in Supplementary Material. The selected structural parameters of these complexes are listed in Table S2. The two most stable structures, I_{GH} and II_{GH}, are the nonplanar hydrogen-bonded complexes in which the hydroxylamine moiety is placed above the plane of one of the carbonyl groups of glyoxal moiety. The I_{GH} complex with the binding energy of -18.25 kJ mol⁻¹ is stabilized by the O–H···O(C) bond, as evidenced by the elongation of the O–H and C=O bonds (see Table S2). The intermolecular distance between the oxygen atom of glyoxal and the hydrogen atom of hydroxylamine has a length of 1.988 Å, and the O–H···O angle is equal to 148.2°. In turn, the II_{GH} complex ($\Delta E = -15.35$ kJ mol⁻¹) is stabilized by N–H···O(C) interaction, which leads to elongation of the N–H and C=O bonds (see Table S2). The *ab initio* studies performed earlier for the glyoxal–methanol [43] and methylglyoxal–methanol complexes [44] indicated that the nonplanar non-hydrogen-bonded structures are the most stable ones. Decomposition of the interaction energy performed for the glyoxal–methanol complex [43] showed that the relative stability of the isomeric glyoxal complexes results from the subtle interplay between all energy components. However, the calculations indicated also that the dispersion energy contributed more to the stabilization of the non-hydrogen-bonded complex than to the hydrogen-bonded one.

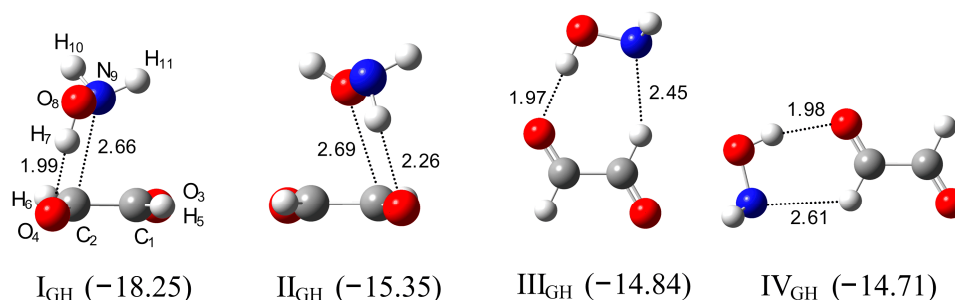


Figure 3. The optimized structures of the CHOCHO–NH₂OH complexes, I_{GH}–IV_{GH}. The ΔE^{CP} (ZPE)-binding energies in kJ mol⁻¹ are given in parentheses. The intermolecular distances are given in Å.

The next six complexes are stabilized by two hydrogen bonds and have planar, cyclic structures. Four of them are sustained by the O–H···O(C) bond and additionally by C–H···N (III_{GH}, IV_{GH}) or C–H···O(N) interaction (V_{GH}). Two complexes are stabilized by the N–H···O(C) and C–H···O(N) bonds (VI_{GH}, VII_{GH}). In III_{GH} and IV_{GH} complexes, the intermolecular distances between the oxygen atom of Gly and hydrogen atom of HA are equal to 1.970 Å, and 1.980 Å and the O–H···O angle values are equal to 176.9° and 163.3°, respectively. The CH···N bond lengths are predicted as 2.458 Å and 2.609 Å and angles as 151.5° and 118.9°.

Experimental Spectra. The infrared spectra of the Gly/Ar(N₂), HA/Ar(N₂) and d-HA/Ar(N₂) matrices agree well with those reported in the literature [48,49,56,59,60]. In the spectra of the matrices doped both with glyoxal and hydroxylamine, a set of new absorptions appeared in the vicinity of Gly and HA or d-HA absorptions that can be assigned to the complexes formed between glyoxal and hydroxylamine. The selected regions of the spectra of Gly/HA/Ar and Gly/HA/N₂ are presented in Figures 4 and 5, respectively. The bands assigned to the glyoxal–hydroxylamine complexes are marked by the arrows. The wavenumbers of all observed complex bands are collected in Table 2 and Table S3 in Supplementary Material. The results obtained in experiments with the deuterated hydroxylamine are presented in Figures S3 and S4 and in Table S4 in Supplementary Material.

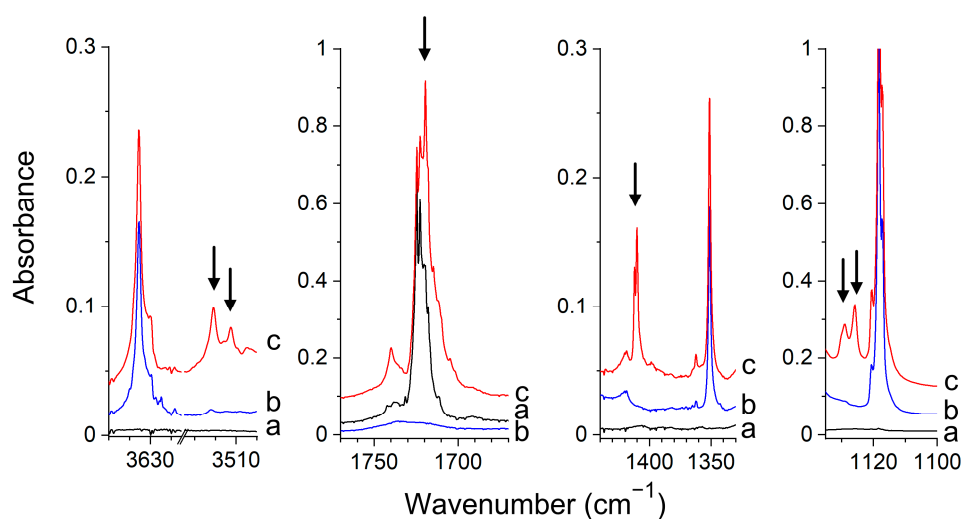


Figure 4. The spectra of the CHOCHO/Ar (a), NH₂OH/Ar (b) and CHOCHO/NH₂OH/Ar (c) matrices recorded after matrix deposition at 11 K. The bands of the CHOCHO–NH₂OH complex are indicated by the arrows.

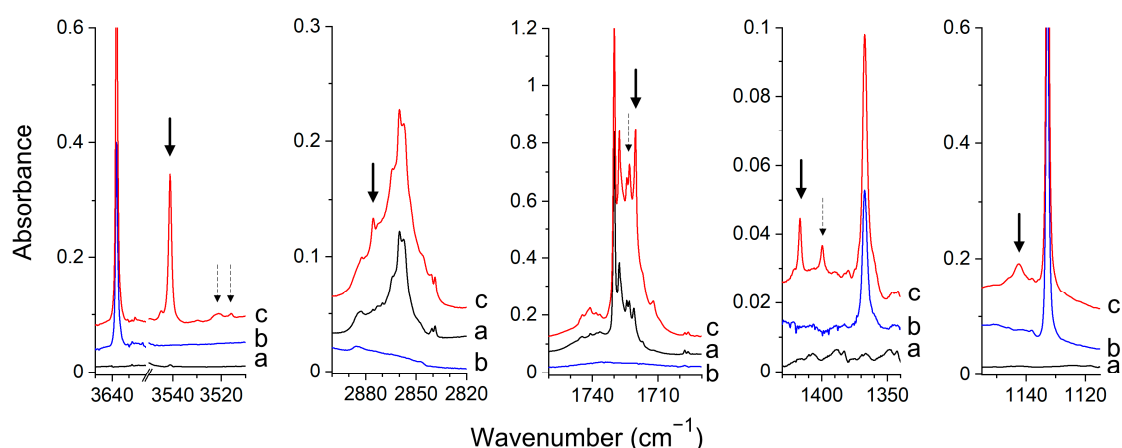


Figure 5. The spectra of the CHOCHO/N₂ (a), NH₂OH/N₂ (b) and CHOCHO/NH₂OH/N₂ (c) matrices recorded after matrix deposition at 11 K. The bands of CHOCHO–NH₂OH complexes are indicated by the arrows. Solid and dashed arrows correspond to the III_{GH} and I_{GH} structures, respectively.

Based on the experimental data and calculated wavenumber shifts, we have assigned the new bands in the spectra of an argon matrix to the nonplanar I_{GH} structure. In the nitrogen matrix, both the doubly hydrogen-bonded cyclic structure corresponding to III_{GH} and the nonplanar I_{GH} complex were found formed, as discussed below. In the spectra of argon matrices, the $\nu(\text{OH})$ band of the complexed hydroxylamine is distinctly shifted to lower wavenumbers, which suggests the formation of the hydrogen-bonded complex. The observed $\Delta\nu(\text{OH})$ value, -118.8 cm^{-1} , matches quite well the predicted value of -145 cm^{-1} for the structure I_{GH}. The intensity of the $\nu(\text{OH})$ band is comparable with the intensities of the other strong bands of the complex as predicted for I_{GH} by calculations. The observed, large shift ($+60.9\text{ cm}^{-1}$) of the $\delta(\text{NOH})$ band of hydroxylamine after complex formation agrees well with the calculated value for I_{GH}, equal to $+61.0\text{ cm}^{-1}$. In an experiment with deuterated hydroxylamine, the wavenumbers shifts for the $\nu(\text{OD})$ and $\delta(\text{NOD})$ modes are equal to -84.1 cm^{-1} and $+33.5\text{ cm}^{-1}$, respectively. These values agree with the calculated ones equal to -106 cm^{-1} and $+38\text{ cm}^{-1}$. The other experimental wavenumber shifts of the identified complex bands also match well those calculated for the I_{GH} structure.

Table 2. The comparison of the observed wavenumbers (cm^{-1}) and wavenumber shifts ($\Delta\nu = \nu_{\text{GH}} - \nu_{\text{M}}$) for the CHOCHO-NH₂OH (GH) complexes present in the Ar and N₂ matrices with the corresponding calculated values for the complexes I_{GH}, III_{GH} and IV_{GH}. In parentheses, the calculated band intensities are given (km mol^{-1}).

Approximate Description	Experimental						Calculated		
	Ar			N ₂			$\Delta\nu$		
	ν_{M}	ν_{GH}	$\Delta\nu^1$	ν_{M}	ν_{GH}^2	$\Delta\nu^1$	I _{GH}	III _{GH}	IV _{GH}
Hydroxylamine									
$\nu(\text{OH})$	3635.5	3521.0 3512.4	−118.8	3637.6	3541.1 3520.9 3515.8	−96.5 −119.2	−145 (7)	−106 (383)	−103 (356)
$\delta(\text{NOH})$	1351.2	1412.1 1410.2	+60.9	1367.4	1416.6 1399.7	+49.2 +32.3	+61 (63)	+72 (29)	+71 (34)
$\omega(\text{NH}_2)$	1118.3	1129.0 1125.8	+9.1	1133.0	1142.6	+9.6	+14 (11)	+24 (112)	+22 (122)
$\nu(\text{NO})$	895.6			895.3	898.8	+3.5	+14 (3)	+9 (8)	+6 (8)
Glyoxal									
$\nu(\text{CH})$	2860.1 2854.9	2857.6	−0.4	2857.1	2875.6	+18.5	−9 (60) +12 (39)	+15 (53) +20 (1)	+1 (52) +51 (8)
$\nu(\text{C=O})$	1724.5	1719.0	−5.5	1730.1	1720.2 1723.1	−9.9 −7.0	−4 (122) +4 (23)	−11 (126) −6 (20)	−13 (89) −6 (33)
$\gamma(\text{CH})$	812.1 807.8			807.4	820.8	+13.4	+37 (0)	+23 (8)	+16 (2)

¹ In the case when the splitting of the band was observed, the average of the two wavenumbers at which the two peaks appeared was taken into account to calculate $\Delta\nu$ value. ² The wavenumbers in italic are due to complex of different structure (see text).

The noticeable difference between the spectra of the complex trapped in solid argon and the one trapped in solid nitrogen is strong $\nu(\text{OH})$ absorption in nitrogen spectra, which is much more intense than the other bands of the complex (see Figure 5). This is not the case for the argon spectra. For example, the estimated experimental intensity ratios $(I_{\nu(\text{OH})}/I_{\delta(\text{NOH})})_{\text{exp}}$, $(I_{\nu(\text{OH})}/I_{\omega(\text{NH}_2)})_{\text{exp}}$ are equal to ca. 0.8, 0.4 for the complex identified in the argon matrix, and they increase to ca. 12, 4, respectively, for the complex trapped in the nitrogen matrix. Such experimental intensity ratios match well the calculated ones for the $\nu(\text{OH})$ absorptions of the nonplanar I_{GH} and cyclic planar III_{GH} (IV_{GH}) complexes. The calculated ratios $(I_{\nu(\text{OH})}/I_{\delta(\text{NOH})})_{\text{calc}}$, $(I_{\nu(\text{OH})}/I_{\omega(\text{NH}_2)})_{\text{calc}}$ are equal to ca. 1.2, 0.7 for I_{GH} and ca. 13, 3.5 for III_{GH} (for IV_{GH} similar intensity ratios are obtained as for III_{GH}). The observed $\nu(\text{OH})$ shift for the complex trapped in nitrogen ($−96.5 \text{ cm}^{-1}$) is slightly less than that for the complex in argon ($−118.8 \text{ cm}^{-1}$), which is in accord with the shifts predicted for III_{GH}, IV_{GH} and I_{GH} ($−106$, $−103$, $−145 \text{ cm}^{-1}$, respectively). The experimental shift of the $\nu(\text{CH})$ vibration ($+18.5 \text{ cm}^{-1}$) suggests that the III_{GH} complex and not the IV_{GH} one is created in the nitrogen matrix. The $+18.5 \text{ cm}^{-1}$ shift matches better with the $+15 \text{ cm}^{-1}$ value predicted for the III_{GH} structure than with the $+1$ value calculated for IV_{GH}. The wavenumber shifts of the other identified vibrations are also in accord with the calculated ones for the III_{GH} structure (see Table 2 and Table S3). The significant red-shift of $\nu(\text{OH})$ of glyoxal accompanied by a noticeable blue shift of $\nu(\text{CH})$ after complex formation indicates that the III_{GH} complex isolated in solid nitrogen is stabilized both by the O–H⋯O(C) hydrogen bond and by blue-shifting C–H⋯N hydrogen bond. The blue shift of the $\nu(\text{X-H})$ stretching wavenumber of the proton donor after complex formation is characteristic of the blue-shifting hydrogen bonding, also called the improper hydrogen bond. These bonds, formed mainly by the CH proton donors, have been a subject of intense theoretical [61–66] and experimental studies [65,66].

All the bands identified for the I_{GH} complex in the spectra of the argon matrices, as well as all the bands assigned to the III_{GH} complex in the spectra of solid nitrogen, exhibited the same intensity ratios in all performed experiments as expected for the bands due to the same species. However, in the spectra of the $CHOCHO/NH_2OH/N_2$ matrices, in addition to the bands attributed to III_{GH} (marked by solid arrows in Figure 5), three additional bands appeared (marked by dashed arrows in Figure 5) whose relative intensities were the same with respect to each other in the performed experiments however differed with respect to the absorptions assigned to III_{GH} . The bands appeared as a very weak doublet at $3520.9, 3515.8\text{ cm}^{-1}$, and as single absorptions at $1723.1, 1399.7\text{ cm}^{-1}$ in the region of the $\nu(OH)$, $\nu(C=O)$ and $\delta(NOH)$ vibrations, respectively. The shifts of these bands with respect to the corresponding absorptions of the parent molecules ($\Delta\nu(OH) = -116.7, -121.8\text{ cm}^{-1}$, $\Delta\nu(C=O) = -7.0\text{ cm}^{-1}$ and $\delta(NOH) = +32.4\text{ cm}^{-1}$) and their relative intensities indicate that they are due to the $CHOCHO-NH_2OH$ complex of the I_{GH} structure. The concentration ratio of the complexes III_{GH}/I_{GH} was estimated on the basis of the $\nu(OH)$ and $\delta(NOH)$ absorptions ($(I_{exp}(III_{GH})/I_{exp}(I_{GH})) \times (I_{calc}(I_{GH})/I_{calc}(III_{GH}))$) and was found to be ca. 3:2. The change of the conditions of matrix deposition (concentration, depositions temperature) slightly affected the mutual concentration of the two structures.

Mucha and Mielke studied the glyoxal complexes with water and hydrogen peroxide in the argon matrices [42,45]. $Gly-H_2O$ and $Gly-H_2O_2$ complexes isolated in solid argon have planar, cyclic structures analogous to the III_{GH} one. The observed shifts of the $\nu(C-H)$, $\nu(C=O)$ wavenumbers of glyoxal are equal to $+2.5, -0.6\text{ cm}^{-1}$, respectively, for the $Gly-H_2O$ complex; and to $+28.9, +3.3\text{ cm}^{-1}$ ($\nu_s(CH), \nu_{as}(CH)$), -5.0 cm^{-1} ($\nu(C=O)$) for the $Gly-H_2O_2$ one as compared to $+18.5, -9.9\text{ cm}^{-1}$, respectively, for $Gly-NH_2OH, III_{GH}$. The observed perturbations of glyoxal vibrations in the above complexes indicate that the glyoxal complex with hydroxylamine is much stronger than that with water, and its strength is comparable to the complex with hydrogen peroxide. This is in accord with the calculated energy values for the above complexes (ca. $-11, -17$ and -18 kJ mol^{-1} for $Gly-H_2O, Gly-NH_2OH$ and $Gly-H_2O_2$, respectively) [42,45].

2.3. Methylglyoxal–Hydroxylamine Complexes

Ab Initio Calculations. Methylglyoxal, like glyoxal, in the standard conditions exists only as of the *trans* isomer [67], so only this conformer is considered in our study. The predicted structures of the complexes formed between methylglyoxal and hydroxylamine are presented in Figure 6 (eight most stable structures) and in Figure S5 in Supplementary Material (all fifteen structures). The geometrical parameters are listed in Table S5.

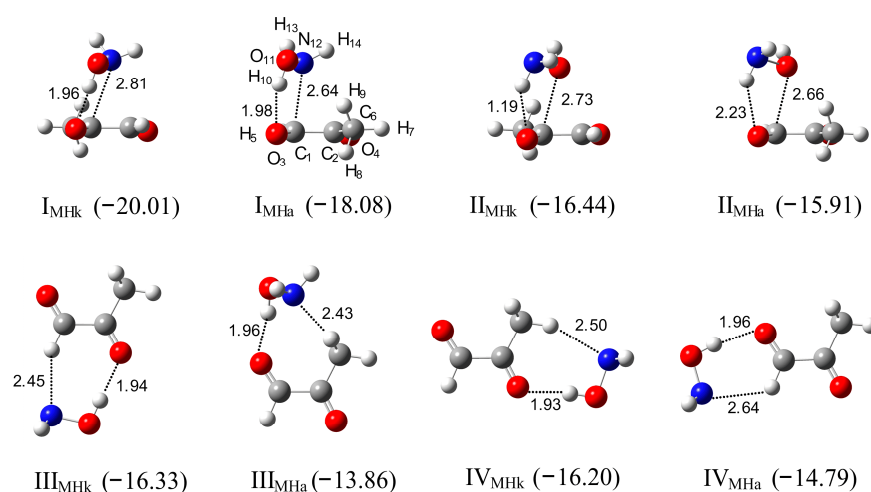


Figure 6. The optimized structures of the $CH_3COCHO-NH_2OH$ complexes, $I_{MHk}-IV_{MHk}$ and $I_{MHa}-IV_{MHa}$. The intermolecular distances are given in Å. The $\Delta E^{CP}(ZPE)$ -binding energies in kJ mol^{-1} are given in parentheses.

The structures of the MGly–HA complexes are analogous to the structures predicted for the Gly–HA ones. The two most stable structures, I_{MHK} and I_{MHa} , with the binding energies of about -20 and -18 kJ mol^{-1} , are nonplanar. In I_{MHK} , the hydroxylamine moiety is placed above the acetyl group and in I_{MHa} above the aldehyde group of methylglyoxal. These complexes are stabilized by the $\text{O–H} \cdots \text{O}(\text{C})$ interaction between the oxygen atom of the aldehyde or acetyl group of methylglyoxal and the OH group of hydroxylamine. The formation of the hydrogen bond is manifested by the elongation of the O–H bond of hydroxylamine from 0.959 \AA to 0.968 \AA . The intermolecular $\text{H} \cdots \text{O}$ distances and $\text{O–H} \cdots \text{O}(\text{C})$ angles are equal to 1.956 \AA , 151.5° for I_{MHK} and 1.980 \AA , 148.6° for I_{MHa} . The nonplanar structures II_{MHK} and II_{MHa} are stabilized by $\text{N–H} \cdots \text{O}(\text{C})$ interaction. The other predicted complexes have cyclic forms stabilized by two hydrogen bonds. Structures III_{MHK} , III_{MHa} , IV_{MHK} , IV_{MHa} , V_{MHK} , V_{MHa} , VI_{MHK} and VI_{MHa} are stabilized by the $\text{O–H} \cdots \text{O}(\text{C})$ and, additionally, by $(\text{O})\text{C–H} \cdots \text{N}$ or $\text{H}_2\text{C–H} \cdots \text{N}$ interactions and the complexes VII_{MHK} , $VIII_{\text{MHK}}$, $VIII_{\text{MHa}}$ by the $\text{N–H} \cdots \text{O}(\text{C})$ hydrogen bond and by $(\text{O})\text{C–H} \cdots \text{O}$ or $\text{H}_2\text{C–H} \cdots \text{N}$ interaction.

Experimental Spectra. In Figure 7 and Figure S6 (Supplementary Material), the infrared spectra of doubly doped MGly/HA/Ar, MGly/d-HA/Ar matrices are compared with the singly doped MGly/Ar, HA/Ar, d-HA/Ar matrices. In Figure 8, the result of the experiment carried in solid nitrogen is presented. The infrared spectra of MGly agree well with those reported earlier [42,60,68]. The new bands that appeared in the spectra of doubly doped matrices are marked by the arrows and are assigned to the MGly–HA, I_{MHa} complex.

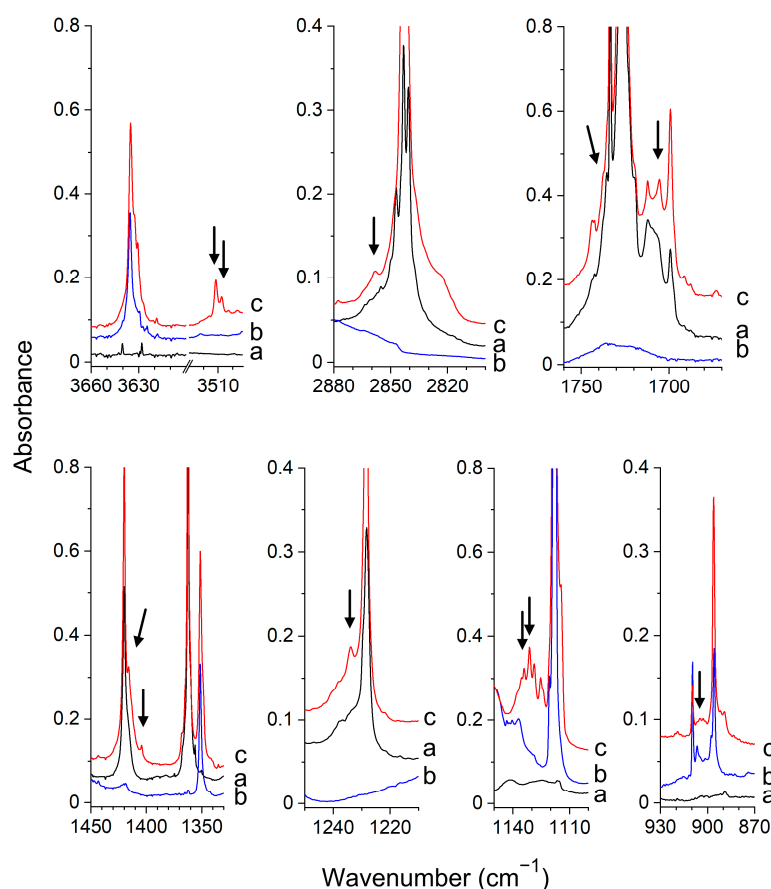


Figure 7. The spectra of the $\text{CH}_3\text{COCHO}/\text{Ar}$ (a), $\text{NH}_2\text{OH}/\text{Ar}$ (b) and $\text{CH}_3\text{COCHO}/\text{NH}_2\text{OH}/\text{Ar}$ (c) matrices recorded after matrix deposition at 11 K. The bands of the $\text{CH}_3\text{COCHO–NH}_2\text{OH}$ complex are indicated by the arrows.

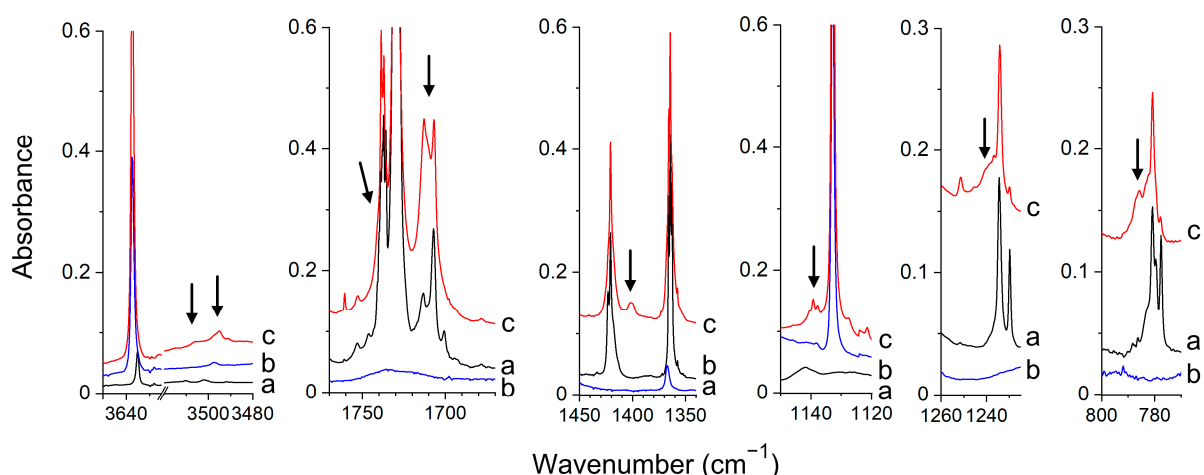


Figure 8. The spectra of the $\text{CH}_3\text{COCHO}/\text{N}_2$ (a), $\text{NH}_2\text{OH}/\text{N}_2$ (b) and $\text{CH}_3\text{COCHO}/\text{NH}_2\text{OH}/\text{N}_2$ (c) matrices recorded after matrix deposition at 11 K. The bands of $\text{CH}_3\text{COCHO}-\text{NH}_2\text{OH}$ complex are indicated by the arrows.

Analysis of the spectra shows that in doubly doped argon and nitrogen matrices, the same type of hydrogen-bonded complex is formed. The comparison of our experimental data with the theoretical ones (see Table 3, Tables S6 and S7 in Supplementary Material) indicates that the isolated complex has a structure I_{MHa} , as discussed below. The new band due to the $\nu(\text{OH})$ vibration of the $\text{MGly}-\text{HA}$ complex is shifted 125.8, 137.1 cm^{-1} towards lower wavenumbers in the spectra of argon and nitrogen matrices, respectively. The red-shift of the $\nu(\text{OH})$ is accompanied by the blue shift of $\delta(\text{NOH})$. The latter vibration is coupled in the complex with the perturbed $\delta(\text{CH}_3)$ vibration. The coupling is supported by the $\text{CH}_3\text{COHCO}-\text{ND}_2\text{OD}$ spectra in which neither of the two bands is observed (when $\delta(\text{NOD})$ is shifted to lower wavenumbers and not coupled with $\delta(\text{CH}_3)$, the latter band may be too weak to be observed). Two bands that are assigned to the coupled $\delta(\text{NOH}) + \delta(\text{CH}_3)$ vibrations appear at 1404.1, 1416.1 cm^{-1} in the spectra of an argon matrix. In the nitrogen matrix, only one new band was identified in the region of the $\delta(\text{NOH})$, which is shifted +34.1 cm^{-1} from the corresponding monomer band. The above facts indicate that the OH group of hydroxylamine interacts with the methylglyoxal molecule forming the $\text{O}-\text{H} \cdots \text{O}(\text{C})$ hydrogen bond and allow to exclude all structures in which this bond is not formed (II_{MHa} , II_{MHk} , VII_{MHk} , $VIII_{\text{MHa}}$, $VIII_{\text{MHk}}$). The intensity of the $\nu(\text{OH})$ band is comparable (or slightly larger) to the intensities of the other most intense bands ($\delta(\text{NOH})$, $\omega(\text{NH}_2)$, $\nu(\text{C}=\text{O})$) of $\text{MGly}-\text{HA}$ complex in the spectra of Ar and N_2 matrices as can be seen in Figures 7 and 8. This is in accord with the predicted intensities for the I_{MHa} , I_{MHk} complexes and allows us to eliminate the cyclic structures III_{MHa} , III_{MHk} , IV_{MHa} , IV_{MHk} for, which the $\nu(\text{OH})$ is predicted to be ca. 3.5–5 times more intense than the second most intense band of the complex (see Table 3 and Table S6). The other spectral features of the recorded spectra point to the presence of I_{MHa} in the matrix. The observed shifts of the $\nu_{\text{ket}}(\text{C}=\text{O})$ and $\nu_{\text{ald}}(\text{C}=\text{O})$ bands of MGly after complexation are equal to +4.2 and -21.0 in Ar (+3.9 and -18.2 cm^{-1} in N_2 matrix, respectively), which suggests that in the complex the OH group of HA is interacting with the oxygen atom of the aldehyde group and not with acetyl one. The corresponding calculated shifts of the $\nu_{\text{ket}}(\text{C}=\text{O})$ and $\nu_{\text{ald}}(\text{C}=\text{O})$ bands are equal to +4, -10 cm^{-1} for I_{MHa} and -5 , +6 cm^{-1} for I_{MHk} , respectively. The observed shift of the CH stretch of the aldehyde group (+16.3 cm^{-1} in Ar) confirms that I_{MHa} is formed and not I_{MHk} . The calculated $\Delta\nu$ shifts for CH stretch vibration are equal to -1 , +24 cm^{-1} for I_{MHk} , I_{MHa} , respectively. The observed shifts of all other bands identified for the complex present in the Ar, N_2 matrices also match well the predicted ones for the I_{MHa} complex.

Table 3. The comparison of the observed wavenumbers (cm^{-1}) and wavenumber shifts ($\Delta\nu = \nu_{\text{MH}} - \nu_{\text{M}}$) for the $\text{CH}_3\text{COCHO-NH}_2\text{OH}$ (MH) complexes present in the Ar and N_2 matrices with the corresponding calculated values for the complexes I_{MHk} and I_{MHa} . In parentheses, the calculated band intensities are given (km mol^{-1}).

Approximate Description	Experimental						Calculated	
	Ar			N_2			$\Delta\nu$	
	ν_{M}	ν_{MH}	$\Delta\nu^1$	ν_{M}	ν_{MH}	$\Delta\nu^1$	I_{MHk}	I_{MHa}
Hydroxylamine								
$\nu(\text{OH})$	3635.5	3511.7 3507.6	-125.8	3637.6	3505.7 3495.2	-137.1	-148 (138)	-156 (73)
$\delta(\text{NOH})^2$	1351.2	1404.1	+52.9	1367.4	1402.7 1400.3	+34.1	+64 (58)	+62 (51)
$\omega(\text{NH}_2)$	1118.3	1134.1 1131.2	+14.4	1133.0	1139.3 1140.6	+7.0	+17 (117)	+11 (109)
$\nu(\text{NO})$	895.6	904.8 902.9	+8.3	895.3			+9 (5)	+13 (6)
Methylglyoxal								
$\nu(\text{CH})$	2843.1 2840.7	2858.2	+16.3	2844.7 2840.2 2835.9			-1 (60)	+24 (51)
$\nu_{\text{ket}}(\text{C=O})$	1733.5	1737.7	+4.2	1739.0 1737.2 1735.9	1741.3	+3.9	-5 (132)	+4 (61)
$\nu_{\text{ald}}(\text{C=O})$	1726.4	1705.4	-21.0	1730.1 1727.9	1710.8	-18.2	+6 (27)	-10 (97)
$\delta(\text{CH}_3)^2$	1420.0	1416.1	-3.9	1423.2 1420.8			0 (8) +3 (24) -3 (36)	+5 (6) +3 (25) -2 (31)
$\nu_{\text{as}}(\text{C-C})$	1228.3	1233.7	+5.4	1234.5 1229.9	1240.5 1237.1	+6.6	+5 (14)	+5 (15)
$\nu_{\text{s}}(\text{C-C})$	777.1	784.7	+7.6	780.9 779.5 777.6	785.8 782.3	+4.8	+6 (15)	+6 (15)

¹ In the case when the splitting of the band was observed, the average of the two wavenumbers at which the two peaks appear was taken into account to calculate $\Delta\nu$ value. ² The 1416.1, 1404.1 cm^{-1} bands observed in the spectra of the complex in Ar matrix are assigned to the coupled $\delta(\text{NOH})+\delta(\text{CH}_3)$ vibrations.

We have found no sign of formation of any cyclic MGly-HA complex. In contrast, the interaction of methylglyoxal with water and methanol forms exclusively the cyclic planar complexes stabilized by the $\text{O-H} \cdots \text{O}(\text{C})$ and $\text{C-H} \cdots \text{O}$ hydrogen bonds between the OH group of H_2O or CH_3OH and the acetyl or aldehyde oxygen atom of CH_3COCHO [42,44]. The presence of the less stable complex I_{MHa} than the more stable I_{MHk} is probably due to the steric effects between the hydroxylamine moiety and methyl group of methylglyoxal.

2.4. AIM Analysis

In Figures S7 and S8 (Supporting Information), the location of the bond critical points (BCP) and ring critical points (RCP) in all optimized structures of the formaldehyde-hydroxylamine and glyoxal-hydroxylamine complexes are presented. The AIM parameters of intermolecular BCPs are collected in Table 4. The general classification of the interaction type can be performed using topological parameters [69,70]. The investigation of Laplacian of electron density ($\nabla^2\rho_{\text{b}}$) indicates if there is a local concentration ($\nabla^2\rho_{\text{b}} < 0$) or a local depletion ($\nabla^2\rho_{\text{b}} > 0$) of charge. Low ρ_{b} and $\nabla^2\rho_{\text{b}}$ values and total electron energy $H \approx 0$ indicate that the complexes are stabilized by weak hydrogen bonds or van der Waals

interaction. The criteria for the presence of hydrogen bond limit the lower values of the electron density, ρ_b , and the Laplacian of the electron density, $\nabla^2\rho_b$, to 0.002, 0.024 a.u., respectively, and the corresponding upper values to 0.034, 0.139 a.u.

Table 4. AIM properties of selected critical points computed at the MP2/6-311++G(2d,2p) level. All data reported in atomic units.

Complex	BCP	ρ_b	$\nabla^2\rho_b$	Complex	BCP	ρ_b	$\nabla^2\rho_b$
Formaldehyde–Hydroxylamine Complexes				Glyoxal–Hydroxylamine Complexes			
I _{FH}	O4-H5 ^a	0.0256	0.0855	I _{GH}	C2-N9	0.0203	0.0626
	H2-N7 ^c	0.0090	0.0268		O4-H7 ^a	0.0213	0.0800
II _{FH}	O4-H5 ^a	0.0207	0.0791	II _{GH}	C1-O8	0.0158	0.0582
	C1-N7	0.0160	0.0514		O3-H10 ^b	0.0129	0.0472
III _{FH}	O4-H5 ^a	0.0226	0.0798	III _{GH}	O4-H7 ^a H5-N9 ^d	0.0225 0.0122	0.0772 0.0342
IV _{FH}	O4-H8 ^b	0.0164	0.0560	IV _{GH}	O4-H7 ^a H6-N9 ^d	0.0227 0.0097	0.0782 0.0290
	H2-O6 ^c	0.0099	0.0337				
V _{FH}	C1-O6	0.0131	0.0478	V _{GH}	O4-H7 ^a H5-O8 ^c	0.0194 0.0107	0.0687 0.0404
	O4-H8 ^b	0.0136	0.0513				
				VI _{GH}	O4-H10 ^b H5-O8 ^c	0.0143 0.0126	0.0494 0.0414
				VII _{GH}	H6-O8 ^c O4-H10 ^b	0.0108 0.0144	0.0370 0.0499
				VIII _{GH}	O4-H7 ^a	0.0186	0.0690

^a OH...O path, ^b NH...O path, ^c CH...O path, ^d CH...N path.

The inspection of the results presented in Figure S7 and Table 4 shows that the HCHO–NH₂OH complexes are stabilized by OH...O, NH...O, CH...O and CH...N interactions. In two complexes, the N...C or O...C interaction occurs (II_{FH}, V_{FH}, respectively). For the OH...O and NH...O interactions, the ρ_b values are in the range $0.0136 < \rho_b < 0.0256$ a.u., and positive Laplacian $\nabla^2\rho_b$, is in the range $0.0513 < \nabla^2\rho_b < 0.0855$ a.u., such values are characteristic of hydrogen bonds. The structures I_{FH}, II_{FH}, IV_{FH} and V_{FH}, are characterized by two intermolecular bond critical points, BCP, and one ring critical point, RCP. The structure III_{FH} involves only one BCP on the bond path corresponding to the interaction between the oxygen atom of formaldehyde and the hydrogen atom of the hydroxyl group of the hydroxylamine molecule. For the bonding in which the hydrogen atom of the CH group is involved (structures I_{FH} and IV_{FH}), the electron densities values fall within the range: $0.009 < \rho_b < 0.01$ a.u., and the Laplacian in the range: $0.0268 < \nabla^2\rho_b < 0.0337$ a.u. These parameters indicate that a very weak hydrogen bond is responsible for the formation of CH...N and CH...O interactions. Data in Table 4 show that the highest values of the discussed parameters occurred for the complex I_{FH}, which is the most stable one according to calculations.

The topological analysis indicates that the structures of the CHOCHO–NH₂OH complex are maintained by similar types of interactions as the configurations of the hydroxylamine complex with formaldehyde. In the glyoxal complexes, like in the formaldehyde ones, one BCP point corresponds to the OH...O or NH...O interaction and the second one to the CH...N or CH...O interaction which involves the hydrogen atom one of the two CH groups. In the nonplanar glyoxal complexes, one BCP corresponds to the OH...O or NH...O hydrogen bonding and the second one to the N...C or O...C interaction (I_{GH}, II_{GH}). The AIM parameters of BCPs along OH...O in the glyoxal complexes (I_{GH}, III_{GH}, IV_{GH}, V_{GH}, VIII_{GH}) have very close values: $\rho_b \approx 0.02$ a.u., $\nabla^2\rho_b \approx 0.07$ a.u. as well as the: $\rho_b \approx 0.013$ a.u., $\nabla^2\rho_b \approx 0.05$ a.u. values calculated for the NH...O bond paths (II_{GH}, VI_{GH}, VII_{GH}). It is interesting to notice that the structures I and II of the CHOCHO–NH₂OH

complexes, like the structures II and V of the HCHO–NH₂OH system, involve one BCP on the bond path corresponding to the interaction between the nitrogen or oxygen atoms of hydroxylamine and the carbon atom of the glyoxal or formaldehyde molecule. The BCPs parameters for the bond paths involving CH···O or CH···N interactions in the CHOCHO–NH₂OH complex have slightly larger values ($\rho_b \approx 0.01$ a.u. and $\nabla^2\rho \approx 0.04$ a.u.) than those characterizing analogous interactions in the HCHO–NH₂OH complex.

The classification of the OH···O, NH···O interactions in all configurations of the HCHO–NH₂OH and CHOCHO–NH₂OH complexes as a hydrogen bonding interaction is strongly confirmed both by experimental and theoretical data and is free from doubt. The electron density and Laplacian values in the BCPs on the O···H and N···H bond paths are within the range characteristic for the hydrogen bonding. The large perturbations of the OH or NH stretching vibrations accompanied by perturbations of the carbonyl group vibrations, as demonstrated in the recorded infrared spectra of the hydroxylamine complexes, provide strong evidence of the formation of the O–H···O or N–H···O bonds. The other important interactions stabilizing the studied complexes are the ones in which the hydrogen atoms of the CH group of the carbonyl molecule are involved.

2.5. Hydrogen Bonding in the Carbonyl-Hydroxylamine Complexes

The results of our experimental and theoretical studies show that all studied carbonyl compounds (formaldehyde, glyoxal and methylglyoxal) form the hydrogen-bonded complexes with hydroxylamine in the argon and nitrogen matrices. The structures attributed to the complexes are gathered in Figures S9 and S10 in Supporting Information. FA was found to form the cyclic planar structure, I_{FH}, and MGly the nonplanar one, I_{MHa}, in both argon and nitrogen matrices. In turn, Gly forms the nonplanar complex, I_{GH}, in the argon matrix, whereas in the nitrogen matrix, both the cyclic planar, III_{GH}, structure and the nonplanar one are created.

The topological analysis indicated the following types of hydrogen bonding in the hydroxylamine complexes with formaldehyde and glyoxal, namely: OH···O, NH···O and CH···O, CH···N. In addition, in two FA complexes and two Gly ones, the analysis indicated the N···C and O···C interactions (II_{FH}, I_{GH} and V_{FH}, II_{GH}, respectively). The most stable HCHO–NH₂OH complex, I_{FH}, observed in the argon and nitrogen matrices, is stabilized by two hydrogen bonds, OH···O and CH···N. In turn, the most stable CHOCHO–NH₂OH complex, I_{GH}, is stabilized by the OH···O hydrogen bond and N···C interaction; this complex is formed both in argon and nitrogen matrix. In the nitrogen matrix, the less stable, cyclic complex, III_{GH}, stabilized by two hydrogen bonds, OH···O and CH···N is also created. Comparison of the predicted structural parameters for the isolated complexes shows that in the cyclic planar complexes, I_{FH}, III_{GH}, the OH···O(C) intermolecular distance is slightly shorter (0.02–0.06 Å) than in the nonplanar structures, I_{GH}, I_{MHa}. The formation of the cyclic structures is accompanied by a strong increase of $\nu(\text{OH})$ intensity in contrast with the nonplanar ones.

In Table 5, the wavenumber shifts of the hydroxylamine vibrations in the complexes with various proton acceptors are compared. It can be observed that in the complexes with formaldehyde, glyoxal and methylglyoxal, the perturbation of hydroxylamine vibrations is quite similar and shows small sensitivity to the carbonyl molecule and to the complex structure. The shifts for carbonyl complexes are comparable with the data reported for the NH₂OH–H₂O complex [49] and are much smaller (two/three times) than the values reported for the hydroxylamine complexes with NH₃ [50] and for the hydroxylamine dimer (NH₂OH)₂ [48] in accord with much stronger interaction in the latter complexes. The smallest perturbation of hydroxylamine vibrations is observed for the NH₂OH–CO complex identified in the argon matrix, which is much weaker than the complexes of hydroxylamine with formaldehyde and α -dicarbonyls [51].

Table 5. The comparison of wavenumber shifts (cm^{-1}) of the vibrational bands of the hydroxylamine moiety in the complexes with formaldehyde, glyoxal, methylglyoxal, hydroxylamine, carbon monoxide and ammonia observed in argon and nitrogen matrices.

Approximate Description	HCHO		CHOCHO		CH ₃ COCHO		NH ₂ OH ¹		CO ²	H ₂ O ³		NH ₃ ⁴	
	Ar (p) ⁵	N ₂ (p) ⁵	Ar (n) ⁵	N ₂ (p,n) ⁵	Ar (n) ⁵	N ₂ (n) ⁵	Ar	N ₂	Ar	Ar	N ₂	Ar	N ₂
$\nu(\text{OH})$	−115	−125	−119	−97 (p) −119 (n)	−126	−137	−294 −345	−289 −333	−39	−93	−139	−297	−345
$\delta(\text{NOH})$	+70	+60	+61	+49 (p) +34 (n)	+53	+34	+119	+105		+10	+54	+121	+108
$\omega(\text{NH}_2)$ $\omega(\text{NH}_2)$	+20	+24	+9	+10 (p)	+14	+7	+34	+31	+4	+19	+18	+12	+13
$\nu(\text{NO})$		+4	+5	+4 (p)	+8		+14	+9		+12	+19	+10	+8
$\tau(\text{OH})$	+162	+173					+362 +32	+340 +28				+422	+350

¹ Data taken from ref [48]. ² Data taken from ref [51]. ³ Data taken from ref [49]. ⁴ Data taken from ref [50]. ⁵ The wavenumbers shifts of the bands identified for the cyclic, planar (p) and nonplanar complexes (n).

Over the many past decades, there have been many attempts to decode from vibrational spectra the information on the electronic structure of a molecule and about the strength of its bonds. Such information can now be obtained from the local vibrational mode analysis that was originally introduced by Konkoli and Cremer and is becoming increasingly popular [71]. The method was successfully applied to various systems, among them to a number of hydrogen-bonded systems, mainly to homo-aggregates [71–74]. It would be very interesting to apply the local vibrational mode analysis to study the heterodimers between hydroxylamine α -dicarbonyls in order to get a deeper insight into the bonding of these systems, and such study is planned to be performed in the future.

3. Materials and Methods

Formaldehyde, HCHO (FA), was prepared by heating paraformaldehyde (95%, Sigma-Aldrich) up to 65–75 °C directly in the deposition line. Glyoxal, CHOCHO (Gly), was prepared by heating the solid trimer dihydrate (98%, Sigma-Aldrich: St. Louis, MO, USA) topped with phosphorus pentoxide (P₄O₁₀) powder under vacuum to 120 °C and collecting the gaseous monomer in a trap at 77 K. Methylglyoxal, CH₃COCHO (MGly), was obtained from 40% aqueous solution of methylglyoxal (Sigma-Aldrich). The major amount of water was distilled off in a vacuum line; then, the sample was depolymerized by heating at about 90 °C. Next, the gaseous monomeric methylglyoxal was passed through P₄O₁₀ and trapped in 77 K. The sample was stored at liquid nitrogen temperature. Hydroxylamine, NH₂OH (HA), was generated by heating (at 50–65 °C) the hydroxylamine phosphate salt (95%, Fluka: Buchs, Switzerland) directly in the deposition line. Deuterated hydroxylamine, ND₂OD (d-HA), was prepared by heating hydroxylamine phosphate salt in D₂O solution and evaporating water in a vacuum. This procedure was repeated several times until the deuteration degree was about 90%.

The carbonyl/hydroxylamine/argon (or nitrogen) matrices were prepared by simultaneous deposition of carbonyl/Ar(N₂) and NH₂OH vapor on a cold gold mirror held at 11–17 K by a closed-cycle helium refrigerator (Displex 202A, Air Products: Allentown, PA, USA). The carbonyl/Ar(N₂) concentration was varied in a range of 1/100–1/2000. The absolute concentration of NH₂OH in the matrices could not be determined, but its concentration was varied by changing the rare gas flow rate and the heating temperature of the hydroxylamine salt. The infrared spectra with a resolution of 0.5 cm^{-1} were recorded in a reflection mode with Bruker 113v FTIR spectrometer using a liquid-nitrogen-cooled MCT detector.

The bands that are assigned to the 1:1 complexes between carbonyl and hydroxylamine were observed already in the spectra of the diluted matrices; their relative intensities with respect to the other species trapped in the matrix decreased after matrix annealing and when the matrix concentration increased. The relative intensities of all bands assigned to one type of the 1:1 complex were constant in all performed experiments. Matrix annealing

increased the concentration of the HA dimers and higher-order complexes and obscured the spectra.

The MP2 method with 6-311++G(2d,2p) basis set was used for geometry optimization of the structures and calculation of harmonic vibrational spectra of the monomers and hydroxylamine (HA- and d-HA-substituted) complexes with FA, Gly and MGly [75,76]. All the presented monomer and complex structures correspond to the real minima on PES as indicated by the positive values of their calculated wavenumbers. Binding energies were corrected by the Boys–Bernardi full counterpoise procedure [77]. The calculations were performed using the Gaussian 03 program [78]. The topological analysis of the electron density was performed with the AIMAll program [79].

4. Conclusions

The FTIR matrix isolation spectroscopy and MP2/6-311++G(2d,2p) calculations were applied to investigate the complexes of formaldehyde and α -dicarbonyls (glyoxal, methylglyoxal) with hydroxylamine in solid argon and nitrogen matrices. The results of the study show that NH_2OH forms with carbonyls two types of hydrogen-bonded complexes. One type involves the nonplanar structures stabilized by the $\text{O}-\text{H}\cdots\text{O}(\text{C})$ interactions in which the hydroxylamine moiety is placed above the carbonyl group of formaldehyde or above one of the two $\text{C}=\text{O}$ groups of α -dicarbonyls. The ab initio calculations predict this structure as the most stable form of the 1:1 complex between α -dicarbonyl and hydroxylamine. The other type includes the planar cyclic structure stabilized by the $\text{O}-\text{H}\cdots\text{O}(\text{C})$ and $\text{C}-\text{H}\cdots\text{N}$ hydrogen bonds. This structure is predicted to be the most stable one for $\text{HCHO}-\text{NH}_2\text{OH}$ and was observed for this complex isolated in both argon and nitrogen matrices. The structure of the glyoxal–hydroxylamine complex is affected by the matrix in which it is isolated. In the argon matrix, the most stable nonplanar complex is formed, whereas in solid nitrogen, both the cyclic planar structure, corresponding to one of the local minima and the most stable nonplanar structure, are created. In turn, the methylglyoxal–hydroxylamine complex forms the most stable nonplanar structure in both argon and nitrogen matrices.

The obtained data confirm that the matrix can influence the nature of the isolated complex and can stabilize the less stable structures as it was observed for the $\text{CHOCHO}-\text{NH}_2\text{OH}$ complex. The formation of the less stable complex in matrices is attributed to the dipole–dipole interactions that dominate at long-range geometries and direct the two approaching submolecules in the matrix to one of the energy minima. It is not excluded that the carbonyl complexes with hydroxylamine are formed in a similar way [80]. This kind of process was observed for the formation of formic acid dimers [81], acetohydroxamic acid [82] and *N*-hydroxyurea dimers [83] or *N,N*-dimethylformamide complexes with water and ammonia in solid argon [84].

Supplementary Materials: The following are available online, Figure S1: The optimized structures of the HCHO–NH₂OH complexes; Figure S2: The optimized structures of the CHOCHO–NH₂OH complexes; Figure S3: The spectra of the CHOCHO/Ar (a), ND₂OD/Ar (b) and CHOCHO/ND₂OD/Ar (c) matrices recorded after matrix deposition at 11 K; Figure S4: The spectra of the CHOCHO/N₂ (a), ND₂OD/N₂ (b) and CHOCHO/ND₂OD/N₂ (c) matrices recorded after matrix deposition at 11 K; Figure S5: The optimized structures of the CH₃COCHO–NH₂OH complexes; Figure S6: The spectra of the CH₃COCHO/Ar (a), ND₂OD/Ar (b) and CH₃COCHO/ND₂OD/Ar (c) matrices recorded after matrix deposition at 11 K; Figure S7: The location of the bond (3,-1) and ring (3,1) critical points in the MP2/6-311++G(2d,2p) optimized structures of the HCHO–NH₂OH complexes; Figure S8: The location of the bond (3,-1) and ring (3,1) critical points in the MP2/6-311++G(2d,2p) optimized structures of the CHOCHO–NH₂OH complexes; Figure S9: The MP2 optimized structures of the formaldehyde, glyoxal and methylglyoxal complexes with hydroxylamine assigned to the structures isolated in argon matrix; Figure S10: The MP2 optimized structures of the formaldehyde, glyoxal and methylglyoxal complexes with hydroxylamine assigned to the structures isolated in nitrogen matrix; Table S1: Selected geometrical parameters of the hydroxylamine and formaldehyde subunits in their binary complexes; Table S2: Selected geometrical parameters of the hydroxylamine and glyoxal subunits in their binary complexes; Table S3: The comparison of the observed wavenumbers (cm⁻¹) and wavenumber shifts ($\Delta\nu = \nu_{GH} - \nu_M$) for the CHOCHO–NH₂OH (GH) complexes present in the Ar and N₂ matrices with the corresponding calculated values for the complexes I_{GH}–IV_{GH}; Table S4: The comparison of the observed wavenumbers (cm⁻¹) and wavenumber shifts ($\Delta\nu = \nu_{GH} - \nu_M$) for the CHOCHO–ND₂OD (GH) complexes present in the Ar and N₂ matrices with the corresponding calculated values for the complexes I_{GH}–IV_{GH}; Table S5: Selected geometrical parameters of the hydroxylamine and methylglyoxal subunits in their binary complexes; Table S6: The comparison of the observed wavenumbers (cm⁻¹) and wavenumber shifts ($\Delta\nu = \nu_{MH} - \nu_M$) for the CH₃COCHO–NH₂OH (MH) complexes present in the Ar and N₂ matrices with the corresponding calculated values for the complexes I_{MHk}–IV_{MHk} and I_{MHa}–IV_{MHa}; Table S7: The comparison of the observed wavenumbers (cm⁻¹) and wavenumber shifts ($\Delta\nu = \nu_{MH} - \nu_M$) for the CH₃COCHO–ND₂OD (MH) complexes present in the Ar and N₂ matrices with the corresponding calculated values for the complexes I_{MHk}–IV_{MHk} and I_{MHa}–IV_{MHa}.

Author Contributions: Conceptualization, B.G. and Z.M.; methodology, B.G. and Z.M.; formal analysis, B.G. and M.S.; investigation, B.G. and M.S.; resources, Z.M.; data curation, B.G.; writing—original draft preparation, B.G.; writing—review and editing, B.G., Z.M. and M.S.; visualization, B.G.; supervision, Z.M.; project administration, B.G. and Z.M.; funding acquisition, Z.M. All authors have read and agreed to the published version of the manuscript.

Funding: This research received no external funding.

Institutional Review Board Statement: Not applicable.

Informed Consent Statement: Not applicable.

Data Availability Statement: The data presented in this study are available in this article.

Acknowledgments: The authors acknowledge the Wrocław Supercomputer Centre (WCSS) for providing computer time and facilities.

Conflicts of Interest: The authors declare no conflict of interest.

Sample Availability: Samples of the compounds are not available from the authors.

References

- Whittle, E.; Dows, D.A.; Pimentel, G.C. Matrix isolation method for the experimental study of unstable species. *J. Chem. Phys.* **1954**, *22*, 1943. [CrossRef]
- Ault, B.S. Matrix isolation studies of reactive intermediate complexes. *Rev. Chem. Intermed.* **1988**, *9*, 233–269. [CrossRef]
- Barnes, A.J. Matrix isolation studies of hydrogen bonding—An historical perspective. *J. Mol. Struct.* **2018**, *1163*, 77–85. [CrossRef]
- Rosenberg, S.; Silver, S.M.; Sayer, J.M.; Jencks, W.P. Evidence for two concurrent mechanisms and a kinetically significant proton transfer process in acid-catalyzed o-methyloxime formation. *J. Am. Chem. Soc.* **1974**, *96*, 7986–7998. [CrossRef]
- Sayer, J.M.; Pinsky, B.; Schonbrunn, A.; Washtien, W. Mechanism of carbinolamine formation. *J. Am. Chem. Soc.* **1974**, *96*, 7998–8009. [CrossRef]

6. Lahann, J. *Click Chemistry for Biotechnology and Materials Science*; John Wiley and Sons Ltd.: Chichester, UK, 2009; ISBN 9780470699706.
7. Gauthier, M.A.; Klok, H.A. Peptide/protein-polymer conjugates: Synthetic strategies and design concepts. *Chem. Commun.* **2008**, 2591–2611. [CrossRef]
8. Venkatesan, N.; Kim, B.H. Peptide conjugates of oligonucleotides: Synthesis and applications. *Chem. Rev.* **2006**, *106*, 3712–3761. [CrossRef]
9. Hermanson, G.T. *Bioconjugate Techniques*, 3rd ed.; Elsevier: Amsterdam, The Netherlands, 2013; ISBN 978-0-12-382239-0.
10. Kubler-Kielb, J. Conjugation of LPS-derived oligosaccharides to proteins using oxime chemistry. *Methods Mol. Biol.* **2011**, *751*, 317–327. [CrossRef] [PubMed]
11. Kölmel, D.K.; Kool, E.T. Oximes and hydrazones in bioconjugation: Mechanism and catalysis. *Chem. Rev.* **2017**, *117*, 10358–10376. [CrossRef]
12. Lowry, T.H.; Schueller Richardson, K. *Mechanism and Theory in Organic Chemistry*, 2nd ed.; HarperCollins Publishers: New York, NY, USA, 1987; ISBN 13-978-0063504288.
13. Morokuma, K. Molecular orbital studies of hydrogen bonds. III. C=O...H-O hydrogen bond in H₂CO...H₂O and H₂CO...2H₂O. *J. Chem. Phys.* **1971**, *55*, 1236–1244. [CrossRef]
14. Del Bene, J.E. Molecular orbital theory of hydrogen bond. VI. Effect of hydrogen bonding on n-π* transitions in dimers ROHOCH₂. *J. Am. Chem. Soc.* **1973**, *2042*, 6517–6522. [CrossRef]
15. Ventura, O.N.; Coitiño, E.L.; Irving, K.; Iglecias, A.; Lledós, A. Comparison of semiempirical and bsse corrected møller-pleeset ab initio calculations on the direct addition of water to formaldehyde. *J. Mol. Struct. Theochem.* **1990**, *210*, 427–440. [CrossRef]
16. Vos, R.J.; Hendriks, R.; Van Duijneveldt, F.B. SCF, MP2 and CEPA-1 calculations on the OH-O hydrogen bonded complexes (H₂O)₂ and (H₂O-H₂CO). *J. Comput. Chem.* **1990**, *11*, 1–18. [CrossRef]
17. Nelander, B. A matrix isolation study of the water-formaldehyde complex. The far-infrared region. *Chem. Phys.* **1992**, *159*, 281–287. [CrossRef]
18. Ventura, O.N.; Coitiño, E.L.; Lledós, A.; Bertran, J. Analysis of the gas-phase addition of water to formaldehyde: A semiempirical and ab initio study of bifunctional catalysis by H₂O. *J. Comput. Chem.* **1992**, *13*, 1037–1046. [CrossRef]
19. Ha, T.K.; Makarewicz, J.; Bauder, A. Ab initio study of the water-formaldehyde complex. *J. Phys. Chem.* **1993**, *97*, 11415–11419. [CrossRef]
20. Dimitrova, Y.; Peyerimhoff, S.D. Theoretical study of the n → π* transitions in hydrogen-bonded formaldehyde complexes. *Chem. Phys. Lett.* **1994**, *227*, 384–389. [CrossRef]
21. Sánchez, M.L.; Aguilar, M.A.; Del Valle, F.J.O. Solvent effects on optical emission and absorption spectra: Theoretical calculation of the ¹(n, π*) transition of formaldehyde in solution. *J. Phys. Chem.* **1995**, *99*, 15758–15764. [CrossRef]
22. Dimitrova, Y. Solvent effects on vibrational spectra of hydrogen-bonded complexes of formaldehyde and water: An ab initio study. *J. Mol. Struct. Theochem.* **1997**, *391*, 251–257. [CrossRef]
23. Galano, A.; Narciso-Lopez, M.; Francisco-Marquez, M. Water complexes of important air pollutants: Geometries, complexation energies, concentrations, infrared spectra, and intrinsic reactivity. *J. Phys. Chem. A* **2010**, *114*, 5796–5809. [CrossRef]
24. Ahlström, M.; Jönsson, B.; Karlström, G. Ab initio molecular orbital calculations on hydrogen- and non-hydrogen-bonded complexes. H₂CO-H₂O and H₂CO-H₂S. *Mol. Phys* **1979**, 1051–1059. [CrossRef]
25. Nelander, B. Infrared spectrum of the water formaldehyde complex in solid argon and solid nitrogen. *J. Chem. Phys.* **1980**, *72*, 77–84. [CrossRef]
26. Butler, L.G.; Brown, T.L. Nuclear quadrupole coupling constants and hydrogen-bonding. A molecular-orbital study of O¹⁷ and deuterium field gradients in formaldehyde-water hydrogen bonding. *J. Am. Chem. Soc.* **1981**, *103*, 6541–6549. [CrossRef]
27. Williams, I.H.; Spangler, D.; Femec, D.A.; Maggiora, G.M.; Schowen, R.L. Theoretical models for solvation and catalysis in carbonyl addition. *J. Am. Chem. Soc.* **1983**, *105*, 31–40. [CrossRef]
28. Lewell, X.Q.; Hillier, I.H.; Field, M.J.; Morris, J.J.; Taylor, P.J. Theoretical studies of vibrational frequency shifts upon hydrogen bonding. The carbonyl stretching mode in complexes of formaldehyde. *J. Chem. Soc. Faraday Trans. 2* **1988**, *84*, 893–898. [CrossRef]
29. Blair, J.T.; Krogh-Jespersen, K.; Levy, R.M. Solvent effects on optical absorption spectra: The ¹A₁—¹A₂ transition of formaldehyde in water. *J. Am. Chem. Soc.* **1989**, *111*, 6948–6956. [CrossRef]
30. Blair, J.T.; Westbrook, J.D.; Levy, R.M.; Kroghjespersen, K. Simple-models for solvation effects on electronic-transition energies. Formaldehyde and water. *Chem. Phys. Lett.* **1989**, *154*, 531–535. [CrossRef]
31. Kumpf, R.A.; Damewood, J.R. Interaction of formaldehyde with water. *J. Phys. Chem.* **1989**, *93*, 4478–4486. [CrossRef]
32. Nelander, B. Infrared spectra of formaldehyde complexes with hydrogen bromide, chlorine and iodine chloride. *J. Mol. Struct.* **1980**, *69*, 59–68. [CrossRef]
33. Nelander, B. Infrared spectra and structure of formaldehyde complexes with ammonia and acetonitrile. *J. Mol. Struct.* **1982**, *81*, 223–228. [CrossRef]
34. Baiocchi, F.A.; Klemperer, W. The rotational and hyperfine spectrum and structure of H₂CO-HF. *J. Chem. Phys.* **1983**, *78*, 3509–3520. [CrossRef]
35. Bach, S.B.H.; Ault, B.S. Infrared matrix isolation study of the hydrogen-bonded complexes between formaldehyde and the hydrogen halides and cyanide. *J. Phys. Chem.* **1984**, *88*, 3600–3604. [CrossRef]
36. Rivelino, R. Lewis acid-base interactions in weakly bound formaldehyde complexes with CO₂, HCN, and FCN: Considerations on the cooperative H-bonding effects. *J. Phys. Chem. A* **2008**, *112*, 161–165. [CrossRef]

37. Mitchell, J.B.O.; Price, S.L. The nature of the N-H O-C hydrogen bond—An intermolecular perturbation theory study of the formamide/formaldehyde complex. *J. Comput. Chem.* **1990**, *11*, 1217–1233. [CrossRef]
38. Tolosa, S.; Hidalgo, A.; Sansón, J.A. Thermodynamic, structural, and dynamic study of the N-H···O=C hydrogen bond association in aqueous solution. *Chem. Phys.* **2000**, *255*, 73–84. [CrossRef]
39. Müller, R.P.; Russegger, P.; Huber, J.R. Hydrogen-bonded complex between HNO and formaldehyde. Photolysis of methyl nitrite in an argon matrix. *Chem. Phys.* **1982**, *70*, 281–290. [CrossRef]
40. Moore, K.B.; Sadeghian, K.; Sherrill, C.D.; Ochsenfeld, C.; Schaefer, H.F. C-H···O Hydrogen bonding. the prototypical methane-formaldehyde system: A critical assessment. *J. Chem. Theory Comput.* **2017**, *13*, 5379–5395. [CrossRef]
41. Brumer, Y.; Shapiro, M.; Brumer, P.; Baldrige, K.K. Controlled alcohol-ketone interconversion by dihydrogen transfer: An ab initio study of the methanol-formaldehyde complex. *J. Phys. Chem. A* **2002**, *106*, 9512–9519. [CrossRef]
42. Mucha, M.; Mielke, Z. Complexes of atmospheric α -dicarbonyls with water: FTIR Matrix isolation and theoretical study. *J. Phys. Chem. A* **2007**, *111*, 2398–2406. [CrossRef]
43. Mielke, Z.; Mucha, M.; Bil, A.; Golec, B.; Coussan, S.; Roubin, P. Photo-induced hydrogen exchange reaction between methanol and glyoxal: Formation of hydroxyketene. *ChemPhysChem* **2008**, *9*, 1774–1780. [CrossRef]
44. Mucha, M.; Mielke, Z. Structure and photochemistry of the methanol complexes with methylglyoxal and diacetyl: FTIR matrix isolation and theoretical study. *Chem. Phys.* **2009**, *361*, 27–34. [CrossRef]
45. Mucha, M.; Mielke, Z. Photochemistry of the glyoxal-hydrogen peroxide complexes in solid argon: Formation of 2-hydroxy-2-hydroperoxyethanal. *Chem. Phys. Lett.* **2009**, *482*, 87–92. [CrossRef]
46. Mucha, M. Faculty of Chemistry. Ph.D. Thesis, University of Wrocław, Wrocław, Poland, 2008.
47. Aloisio, S.; Francisco, J.S. Complexes of hydroperoxyl radical with glyoxal, methylglyoxal, methylvinyl ketone, acrolein, and methacrolein: Possible new sinks for HO₂ in the atmosphere? *J. Phys. Chem. A* **2003**, *107*, 2492–2496. [CrossRef]
48. Yeo, G.A.; Ford, T.A. The infrared spectrum of the hydroxylamine dimer. *J. Mol. Struct.* **1990**, *217*, 307–323. [CrossRef]
49. Yeo, G.A.; Ford, T.A. Matrix isolation infrared spectrum of the water-hydroxylamine complex. *Vib. Spectrosc.* **1991**, *253*, 173–181. [CrossRef]
50. Yeo, G.A.; Ford, T.A. The matrix isolation infrared spectrum of the hydroxylamine-ammonia complex. *Spectrochim. Acta Part A* **1991**, *47*, 919–925. [CrossRef]
51. Sałdyka, M.; Mielke, Z. Photodecomposition of formohydroxamic acid. Matrix isolation FTIR and DFT studies. *Phys. Chem. Chem. Phys.* **2003**, *5*, 4790–4797. [CrossRef]
52. Sałdyka, M. Photodecomposition of N-hydroxyurea in argon matrices. FTIR and theoretical studies. *RSC Adv.* **2013**, *3*, 1922–1932. [CrossRef]
53. Khoshkhoo, H.; Nixon, E.R. Infrared and Raman spectra of formaldehyde in argon and nitrogen matrices. *Spectrochim. Acta Part A* **1973**, *29*, 603–612. [CrossRef]
54. Nelander, B. Infrared spectrum of formaldehyde in solid nitrogen. I. Monomer absorption. *J. Chem. Phys.* **1980**, *73*, 1026–1033. [CrossRef]
55. Nelander, B. Infrared spectrum of formaldehyde in solid nitrogen. II. Dimer spectrum and dimer structure. *J. Chem. Phys.* **1980**, *73*, 1034–1039. [CrossRef]
56. Withnall, R.; Andrews, L. Matrix infrared spectra and normal-coordinate analysis of isotopic hydroxylamine molecules. *J. Phys. Chem.* **1988**, *92*, 2155–2161. [CrossRef]
57. Kuchtsu, K.; Fukuyama, T.; Morino, Y. Average structures of butadiene, acrolein, and glyoxal determined by gas electron diffraction and spectroscopy. *J. Mol. Struct.* **1968**, *1*, 463–479. [CrossRef]
58. Osamura, Y.; Schaefer, H.F. Internal rotation barrier and transition state for glyoxal. *J. Chem. Phys.* **1981**, *74*, 4576–4580. [CrossRef]
59. Diem, M.; MacDonald, B.G.; Lee, E.K.C. Photolysis and laser-excited fluorescence and phosphorescence emission of trans-glyoxal in an argon matrix at 13 K. *J. Phys. Chem.* **1981**, *85*, 2227–2232. [CrossRef]
60. Profeta, L.T.M.; Sams, R.L.; Johnson, T.J.; Williams, S.D. Quantitative infrared intensity studies of vapor-phase glyoxal, methylglyoxal, and 2,3-butanedione (diacetyl) with vibrational assignments. *J. Phys. Chem. A* **2011**, *115*, 9886–9900. [CrossRef]
61. Hobza, P.; Havlas, Z. Blue-shifting hydrogen bonds. *Chem. Rev.* **2000**, *100*, 4253–4264. [CrossRef]
62. Hermansson, K. Blue-shifting hydrogen bonds. *J. Phys. Chem. A* **2002**, *106*, 4695–4702. [CrossRef]
63. Karpfen, A.; Kryachko, E.S. Blue-shifted hydrogen-bonded complexes. II. CH₃F···(HF)_{1≤n≤3} and CH₂F₂···(HF)_{1≤n≤3}. *Chem. Phys.* **2005**, *310*, 77–84. [CrossRef]
64. Rutkowski, K.S.; Rodziewicz, P.; Melikova, S.M.; Koll, A. Theoretical study of Hal₃CH/F₂CD₂ (Hal=F,Cl) and F₃CH/FH heterodimers with blue shifted hydrogen bonds. *Chem. Phys.* **2006**, *327*, 193–201. [CrossRef]
65. Melikova, S.M.; Rutkowski, K.S.; Rodziewicz, P.; Koll, A. Unusual spectroscopic properties of CF₃H dissolved in liquified Ar, N₂, CO and CO₂. *Chem. Phys. Lett.* **2002**, *352*, 301–310. [CrossRef]
66. Asfin, R.E.; Melikova, S.M.; Rutkowski, K.S. The infrared study of fluororoform+methyl fluoride mixtures in argon and nitrogen matrices. Evidence of nonlinear blue-shifting complex formation. *Spectrochim. Acta Part A* **2018**, *208*, 185–194. [CrossRef]
67. Dyllick-Brenzinger, C.E.; Bauder, A. Microwave spectrum, dipole moment and barrier to internal rotation of trans-methyl glyoxal. *Chem. Phys.* **1978**, *30*, 147–153. [CrossRef]
68. Reid, S.A.; Kim, H.L.; McDonald, J.D. A stimulated emission pumping study of jet-cooled methyl glyoxal. *J. Chem. Phys.* **1990**, *92*, 7079–7086. [CrossRef]

69. Grabowski, S.J. What is the covalency of the hydrogen bonding? *Chem. Rev.* **2011**, *111*, 2597–2625. [CrossRef] [PubMed]
70. Koch, U.; Popelier, P.L.A. Characterization of C-H-O hydrogen-bonds on the basis of the charge density. *J. Phys. Chem.* **1995**, *99*, 9747–9754. [CrossRef]
71. Kraka, E.; Zou, W.; Tao, Y. Decoding chemical information from vibrational spectroscopy data: Local vibrational mode theory. *WIREs Comput. Mol. Sci.* **2020**, *10*, e1480. [CrossRef]
72. Kalescky, R.; Zou, W.; Kraka, E.; Cremer, D. Local vibrational modes of the water dimer—Comparison of theory and experiment. *Chem. Phys. Lett.* **2012**, *554*, 243–247. [CrossRef]
73. Tao, Y.; Zou, W.; Jia, J.; Li, W.; Cremer, D. Different ways of hydrogen bonding in water—Why does warm water freeze faster than cold water? *J. Chem. Theory Comput.* **2017**, *13*, 55–76. [CrossRef]
74. Tao, Y.; Zou, W.; Kraka, E. Strengthening of hydrogen bonding with the push-pull effect. *Chem. Phys. Lett.* **2017**, *685*, 251–258. [CrossRef]
75. Frisch, M.J.; Pople, J.A.; Binkley, J.S. Self-consistent molecular orbital methods 25. Supplementary functions for Gaussian basis sets. *J. Chem. Phys.* **1984**, *80*, 3265–3269. [CrossRef]
76. Krishnan, R.; Binkley, J.S.; Seeger, R.; Pople, J.A. Self-consistent molecular orbital methods. XX. A basis set for correlated wave functions. *J. Chem. Phys.* **1980**, *72*, 650–654. [CrossRef]
77. Boys, S.F.; Bernardi, F. Calculation of small molecular interactions by differences of separate total energies—Some procedures with reduced errors. *Mol. Phys.* **1970**, *19*, 553–566. [CrossRef]
78. Frisch, M.J.; Trucks, G.W.; Schlegel, H.B.; Scuseria, G.E.; Robb, M.A.; Cheeseman, J.R.; Montgomery, J.A., Jr.; Vreven, T.; Kudin, K.N.; Burant, J.C.; et al. *Gaussian 03, Revision, C.02*; Gaussian Inc.: Wallingford, CT, USA, 2003.
79. Keith, T.A. AIMAll, Version 12.09.23, Standard, 1997–2012. Available online: <http://aim.tkgristmill.com> (accessed on 19 February 2021).
80. Barnes, A.J.; Mielke, Z. Matrix effects on hydrogen-bonded complexes trapped in low-temperature matrices. *J. Mol. Struct.* **2012**, *1023*, 216–221. [CrossRef]
81. Gantenberg, M.; Halupka, M.; Sander, W. Dimerization of formic acid—an example of a “noncovalent” reaction mechanism. *Chem. Eur. J.* **2000**, *6*, 1865–1869. [CrossRef]
82. Sałdyka, M.; Mielke, Z. Dimerization of the keto tautomer of acetohydroxamic acid—Infrared matrix isolation and theoretical study. *Spectrochim. Acta A Mol. Biomol. Spectrosc.* **2005**, *61*, 1491–1497. [CrossRef] [PubMed]
83. Sałdyka, M. N-Hydroxyurea dimers: A matrix isolation and theoretical study. *Vib. Spectrosc.* **2016**, *85*, 149–156. [CrossRef]
84. Sałdyka, M.; Mielke, Z.; Haupa, K. Structural and spectroscopic characterization of DMF complexes with nitrogen, carbon dioxide, ammonia and water. Infrared matrix isolation and theoretical studies. *Spectrochim. Acta A Mol. Biomol. Spectrosc.* **2018**, *190*, 423–432. [CrossRef]

Article

Structural Aspects of the *Ortho* Chloro- and Fluoro-Substituted Benzoic Acids: Implications on Chemical Properties

Gulce Ogruc Ildiz ^{1,2,*} and Rui Fausto ¹

¹ Department of Chemistry, University of Coimbra, CQC, P 3004–535 Coimbra, Portugal; rfausto@ci.uc.pt

² Department of Physics, Faculty of Sciences and Letters, Atakoy Campus, Istanbul Kultur University, 34156 Bakirkoy, Istanbul, Turkey

* Correspondence: g.ogruc@iku.edu.tr

Academic Editor: Derek J. McPhee

Received: 29 September 2020; Accepted: 18 October 2020; Published: 23 October 2020

Abstract: This article presents a detailed comprehensive investigation of the *ortho* fluoro- and chloro-substituted benzoic acids both, as isolated molecules and in the crystalline phase. Quantum chemical calculations performed within the density functional theory (DFT) formalism are used to investigate the potential energy landscapes of the molecules, taking into special consideration the effects of the interactions between the carboxylic group and the *ortho* halogen substituents, as well as the nature of these later on the structure and properties of the investigated systems. The structures of the relevant conformers of the molecules are discussed in comparative terms, and used to rationalize experimental data obtained for the compounds in the gas phase and isolated in low-temperature inert matrices. The UV-induced photofragmentation reactions of two of the compounds isolated in cryogenic inert matrices were studied as illustrative cases. The structures of the crystals reported previously in the literature are revisited and discussed also in a comparative basis. Particular emphasis is given to the analysis of the intermolecular interactions in the different crystals, using Hirshfeld surface analysis, the CE-B3LYP energy decomposition model and the HOMA index, and to their correlation with thermodynamic data.

Keywords: *ortho* chloro- and fluoro- substituted benzoic acids; structural aspects; conformational landscape; crystal features; quantum chemical calculations; isolated-molecule infrared spectroscopy; photochemistry

1. Introduction

Fluoro- and chloro-substituted benzoic acid derivatives have been shown to exhibit relevant practical applications, namely as precursors of agrochemical and pharmaceutical products, food additives and dyes [1]. The fluoro-substituted compounds are considered to be environmentally acceptable alternatives to chlorinated compounds [2], which makes them presently particularly relevant. They have been also used as artificial tracers to investigate flow dynamics in geothermal, hydrothermal and oil well applications to optimize oil recovery [3–5]. It was also shown that some bacterial strains use fluorobenzoates as the sole source of carbon and energy [6,7], and the metabolic and catabolic processes involving these compounds have been extensively studied [7–12]. Due to its complexing ability, the *ortho*-substituted fluorobenzoic acid (2-fluorobenzoic acid) has been for long used in the quantitative determination of iron in aqueous solution [13]. In its turn, the chloro-substituted benzoic acids are amongst the more versatile precursors or intermediates in the synthesis of pesticides [14]. Diclofenac (2-[2-(2,6-dichloroanilino)phenyl]acetic acid), which is

a widespread non-steroid anti-inflammatory drug, is synthesized from 2-chlorobenzoic acid and 2,6-dichloroaniline [15].

From a structural point of view, the *ortho* substituted derivatives are particularly interesting compounds, due to the expected intramolecular interactions between the carboxylic acid moiety and the substituents. This subject has been explored in recent studies on the *ortho* mono-substituted fluoro- and chloro- benzoic acid derivatives [16,17]. For both compounds, the asymmetric substitution at the *ortho* positions (in one side of the carboxylic substituent there is a hydrogen atom and in the other a halogen atom) results in dissimilar intramolecular interactions in the different conformers of these molecules, which in turn, determine their distinct chemical behavior [16,17]. The two molecules possess two conformers with the carboxylic group in the *trans* configuration (O=C-O-H dihedral $\sim 180^\circ$), which have a considerably higher energy compared to the two related forms having the carboxylic group in the *cis* arrangement (O=C-O-H dihedral $\sim 0^\circ$). The *trans*→*cis* conversion for the pairs of *trans/cis* related conformers was found to take place at very much different rates, as the stabilizing intramolecular interaction between the *ortho* halogen atom and the carboxylic group in one of the *trans* forms leads to a much higher *trans*→*cis* isomerization barrier compared to that existing in the other *trans* conformer, where such interaction is replaced by a destabilizing interaction between the carboxylic group and the *ortho* hydrogen atom. The experimental observation of these effects was achieved using matrix isolation infrared spectroscopy in cryogenic Ar, N₂ or Xe matrices. In situ irradiation either by UV [17] (for 2-chlorobenzoic acid) or IR [16] (for 2-fluorobenzoic acid) allowed conversion of the abundant low-energy *cis* conformers into the higher-energy *trans* forms, and the kinetics of the subsequent *trans*→*cis* decay by quantum mechanical tunneling were then estimated and found to correlate with the size of the *trans*→*cis* isomerization barriers [16,17].

The different intrinsic characteristics of the fluorine versus chlorine substituent atoms have also been shown to be major factors in determining the structures of the conformers of the corresponding isolated molecules of the *ortho*-halogen substituted benzoic acids [16–19]. Likewise, they play a key role in defining other properties of the compounds, as for example relative acidities, cell volumes in crystalline phase, dipole moments, spectroscopic data, and melting points [16–29].

Although, there is a significant amount of information on *ortho* chloro- and fluoro- substituted benzoic acids dispersed in the scientific literature (in particular for the two mono-substituted compounds), no systematic investigation has been reported hitherto that can be used as a comprehensive reference work on this family of compounds. This study aims to fill this gap. Here, a detailed comparative analysis of the potential energy landscapes of the isolated molecules of the *ortho* mono- and di-substituted fluoro- and chloro- benzoic acids, performed by using quantum chemical calculations within the density functional theory (DFT) formalism is presented, taking into special consideration the effects of the interactions between the carboxylic group and the *ortho* halogen substituents, as well as the nature of these later. The structures of the relevant conformers of the molecules are also discussed in comparative terms, and used to rationalize experimental data obtained for the isolated molecules of the compounds, in particular, the compounds in the gas phase and isolated in low-temperature inert matrices. The structures of the crystals reported previously in the literature [20–24,30] are revisited and discussed in a comparative basis. Particular emphasis is given to the analysis of the intermolecular interactions in the different crystals and to their correlation with thermodynamic data.

2. Experimental and Computational Methods

The compounds 2-Fluorobenzoic acid and 2-chloro-6-fluorobenzoic acids were obtained from Sigma-Aldrich Portugal (>98% purity) (Sigma-Aldrich, Saint Louis, MO, USA), and additionally purified using the usual freeze-pump-thaw method to eliminate trace volatile impurities. The low temperature matrices were obtained by co-deposition of the matrix-gas (Ar or Xe; purities: N60, N48, respectively) and vapors of the compounds obtained by their sublimation, using a Knudsen cell connected to the cryostat, onto a CsI substrate assembled at the cold (10–20 K) tip of the cryostat (APD Cryogenics, Allentown, PA, USA, model DE-202A). The matrix/solute ratios were ~ 1000 molar ratio.

Both the nozzle and the Knudsen cell were kept at room temperature, which was controlled using a Scientific Instruments, Model 9650-1 temperature controller (accuracy: ± 0.1 K).

The infrared spectra for the studied matrix-isolated compounds were obtained in a Thermo Nicolet 6700 FTIR spectrometer (Thermo Fisher Scientific, Waltham, MA, USA), with 0.5 cm^{-1} spectral resolution. A DTGS (deuterated triglycine sulphate) detector, a Globar source, and a KBr beam splitter were used. Irradiations were performed using narrowband tunable UV light provided by a Spectra Physics Quanta-Ray optical parametric oscillator (MOPO-SL) (Spectra Physics, Santa Clara, CA, USA) pumped by a Nd:YAG Spectra Physics Quanta-Ray PRO-230-10 pulsed (10 Hz, 10 ns) laser (Spectra Physics, Santa Clara, CA, USA). The UV beam was introduced into the cryostat through a KBr window. Gas phase infrared spectra were taken from the Coblenz Society infrared spectra database [31].

The DFT/B3LYP [32–34] calculations for the isolated molecules were undertaken using Gaussian 09 [35], with the 6-311++G(d,p) basis set [36–38]. Potential energy profiles were obtained by scanning the conformationally relevant torsional coordinates and optimizing all remaining structural parameters. The calculated vibrational wavenumbers were scaled by 0.978 (our standard scaling factor for this combination of method and basis set [39–41]), mainly to account for the effects of basis set limitations, neglected part of electron correlation and anharmonicity. In the spectra simulation, the bands were represented by convoluting each peak (calculated scaled wavenumber and infrared intensity) with a Lorentzian function with a full-width-at-half-maximum (FWHM) of 2 cm^{-1} .

Lattice energies of the crystals (E_{lat}) of the studied compounds were computed using the CE-B3LYP model (with the 6-31G(d,p) basis set) [42] using CrystalExplorer17 [43], and related with sublimation enthalpies $\Delta H_{\text{sub}}(T)$,

$$\begin{aligned} \Delta H_{\text{sub}}(T) &= (E_{\text{el}}^{\text{g}} + E_{\text{trans}}^{\text{g}} + E_{\text{rot}}^{\text{g}} + E_{\text{vib}}^{\text{g}}) - (E_{\text{el}}^{\text{s}} + E_{\text{vib}}^{\text{s}}) + pV = \\ &= (E_{\text{el}}^{\text{g}} - E_{\text{el}}^{\text{s}}) + (E_{\text{vib}}^{\text{g}} - E_{\text{vib}}^{\text{s}}) + 4RT = \Delta E_{\text{el}} + \Delta E_{\text{vib}} + 4RT = -E_{\text{lat}} + \Delta E_{\text{vib}} + 4RT \end{aligned} \quad (1)$$

where ideal gas behavior is assumed, and the superscripts g and s refer to the gas and solid crystalline states. Several approaches have been used to obtain “experimental” benchmark lattice energies by estimating the thermal effects, $\Delta E_{\text{vib}} + 4RT$, at different levels of sophistication. The most common approximates these two terms by $-2RT$, a result that assumes no difference between gas and crystal intramolecular vibrations, and the intermolecular vibrational energy is at the high-temperature limit of $6RT$. These and other assumptions underlying this approximation are discussed in detail in several places [44–48]. In the CE-B3LYP calculations, molecules within a radius of 20 \AA were considered.

3. Results and Discussion

3.1. Conformers and Barriers to Internal Rotation

A throughout conformational search on the B3LYP/6-311++G(d,p) potential energy surfaces of the studied molecules (the mono- and di- *ortho* fluoro- or/and chloro- substituted benzoic acids, plus the parent benzoic acid, for completeness) was undertaken. The identified conformers are presented in Figures 1 and 2.

All studied molecules have two conformationally relevant degrees of freedom, corresponding to the internal rotations around the exocyclic C-C and C-O bonds. For the last, two minimum energy structures exist, which maximize the π -electron delocalization within the carboxylic moiety: the intrinsically most stable *cis* configuration (O=C-O-H dihedral equal to $\sim 0^\circ$), and the higher-energy *trans* arrangement (O=C-O-H dihedral equal to $\sim 180^\circ$). The reasons for the usual higher stability of the *cis* carboxylic acid structure have been discussed in details elsewhere [49–51]. The major reason is the existence of more favorable bond-dipole/bond-dipole interactions in the *cis* structure, where the dipoles associated to the C=O and O-H bonds are nearly anti-parallelly aligned, compared to those existing in the *trans* structure, where these bond-dipoles are approximately parallel. For each carboxylic acid stable configuration (*cis* or *trans*), the number and type of the minimum energy structures differing in the orientation of the carboxylic acid moiety relatively to the aromatic ring (i.e., differing from

each other by internal rotation about the exocyclic C-C bond) could be anticipated to be very much dependent on the substitution pattern in the aromatic ring. The obtained results plently confirmed these expectations, and stressed the structural relevance of the intramolecular interactions between the *ortho* substituents and the carboxylic group as well as of the nature of the substituents (H vs. F vs. Cl).

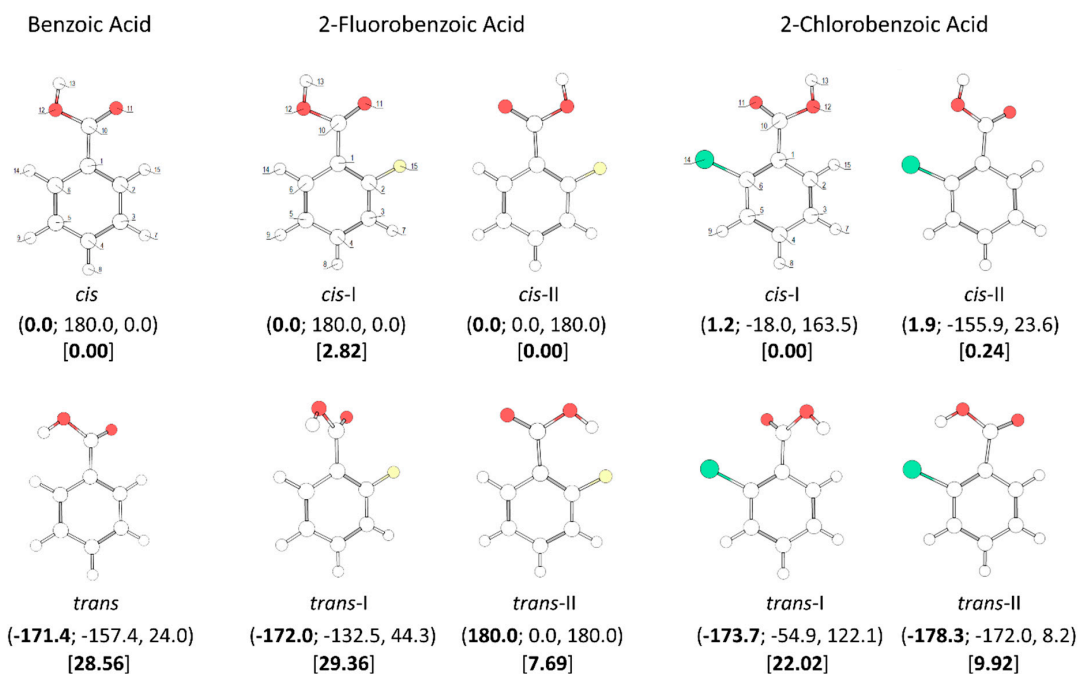


Figure 1. B3LYP/6-311++G(d,p) calculated minimum energy structures of benzoic acid, 2-fluorobenzoic acid and 2-chlorobenzoic acid, with adopted atom numbering. The values of the O=C-O-H, C6-C-C=O and C2-C-C=O dihedral angles (in °) are given in parentheses by this order (the first using bold style). Relative energies are given in square parentheses (in bold), in $\text{kJ}\cdot\text{mol}^{-1}$. Each depicted non-planar structure has a symmetry-related form. The *cis* benzoic acid conformer is also two-fold degenerate, while the *trans* conformer 4-fold symmetry degenerate.

In the case of the parent compound, **benzoic acid** (BA), two conformers exist (Figure 1). The lower-energy *cis* conformer is planar and has two equivalent-by-symmetry forms, corresponding to the experimentally observed species [52–56]. On the other hand, the *trans* conformer has a non-planar structure and has a predicted energy $28.56 \text{ kJ}\cdot\text{mol}^{-1}$ above that of the *cis* conformer. In the *cis* conformer, the *ortho* hydrogen atoms participate in stabilizing attractive interactions with the oxygen atoms of the carboxylic group (carbonyl, O=, and acid, OH), which favor the planarity of the molecule, while in the *trans* conformer the repulsion between the carboxylic hydrogen atom and the nearby located ring *ortho* hydrogen atom leads to the observed tilt of the carboxylic moiety out of the plane of the ring. Due to its non-planarity and the symmetric substitution in the ring, the *trans* BA conformer has four symmetry equivalent forms. The calculated O=C-O-H angle in this conformer is -171.4° (taking as reference the structure shown in Figure 1) and the two C-C-C=O dihedrals are -157.4° and 24.0° . To the best of our knowledge, *trans* BA has never been experimentally observed (we will return to this point later on in this article).

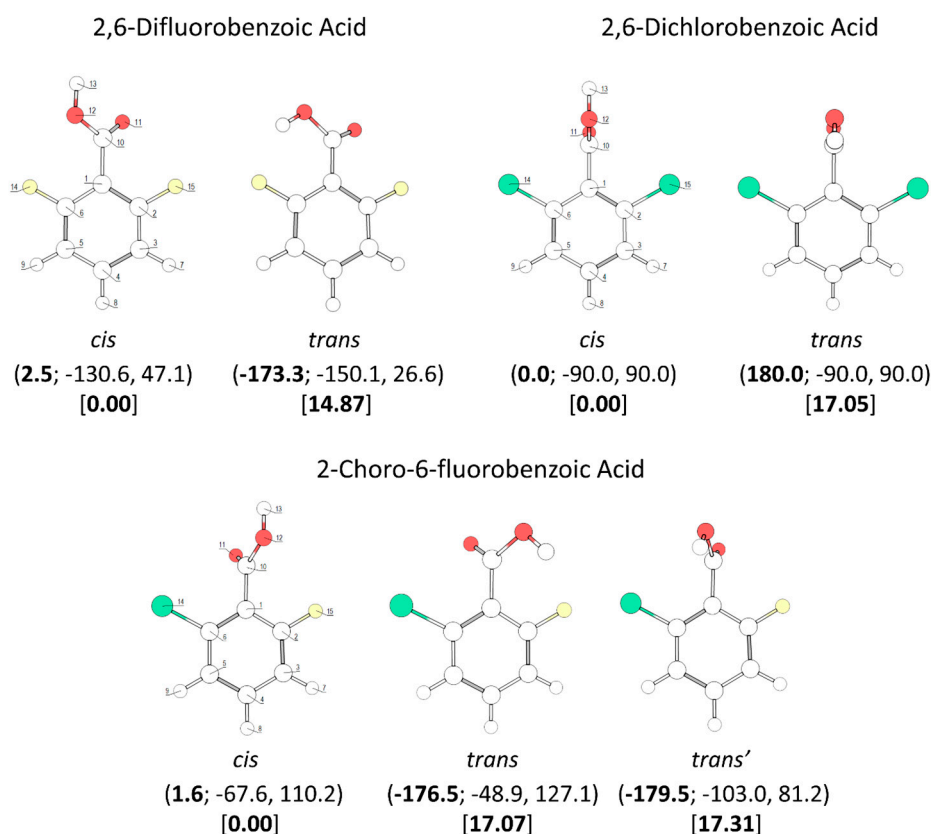


Figure 2. B3LYP/6-311++G(d,p) calculated minimum energy structures of 2,6-difluorobenzoic acid, 2,6-dichlorobenzoic acid and 2-chloro-6-fluorobenzoic acid, with adopted atom numbering. The values of the O=C-O-H, C6-C-C=O and C2-C-C=O dihedral angles (in °) are given in parentheses by this order (the first in bold style). Relative energies are given in square parentheses (in bold), in $\text{kJ}\cdot\text{mol}^{-1}$. Each conformer of 2,6-dichlorobenzoic acid and 2-chloro-6-fluorobenzoic acid has a symmetry-related identical form; the conformers of 2,6-difluorobenzoic acid have 4 symmetry-equivalent structures.

The calculated potential energy profiles for interconversion between the two conformers of BA (internal rotation around the C-O bond) and for internal rotation about the exocyclic C-C bond in the *cis* and *trans* conformers are shown in Figure 3. The *trans*→*cis* barrier is predicted as $23.4\text{ kJ}\cdot\text{mol}^{-1}$ ($52.0\text{ kJ}\cdot\text{mol}^{-1}$ in the reverse direction), with the transition state corresponding to a structure where the carboxylic hydrogen atom is nearly perpendicular to the molecular plane. At the geometry of the transition state, conjugation in the carboxylic fragment is minimal, justifying its high energy.

The profiles for internal rotation around the exocyclic C-C bond are considerably different for the two arrangements of the carboxylic group. For the *cis* arrangement, the energy barrier ($28.2\text{ kJ}\cdot\text{mol}^{-1}$) is more than twice larger than for the *trans* arrangement ($13.4\text{ kJ}\cdot\text{mol}^{-1}$). In the *cis* form, the high energy of the transition state for rotation around the C-C bond is a consequence of the break down of the abovementioned stabilizing interactions between the ring *ortho* hydrogen atoms and the oxygen atoms of the carboxylic acid substituent (that operate in the minimum energy structure), as well as the lack of conjugation between the carboxylic substituent and the aromatic ring. This latter effect can be noticed, for example, by looking to the exocyclic C-C bond lengths in the *cis* conformer and in the transition state, respectively 1.486 and 1.500 \AA . In the equivalent transition state for the *trans* carboxylic group geometry, there is a favorable interaction between the π -system of the aromatic ring and the O-H carboxylic group ($\text{O-H}\cdots\pi$), which considerably lowers the energy barrier for rotation about the C-C bond. This type of $\text{O-H}\cdots\pi$ stabilizing interactions (and similars) has been described for other, structurally related systems [57].

The four symmetry-equivalent *trans* forms can be grouped in two pairs, whose members are separated from each other by a small energy barrier (1.1 kJ·mol⁻¹) at the planar transition state geometry (see Figure 3, top panel). Although low, this barrier is still above the zero-point level for the $\tau_{\text{C-O}}$ torsion in the *trans* conformer (calculated as 0.4 kJ·mol⁻¹), so that the non-planar structures do indeed correspond to potentially experimentally observable minima.

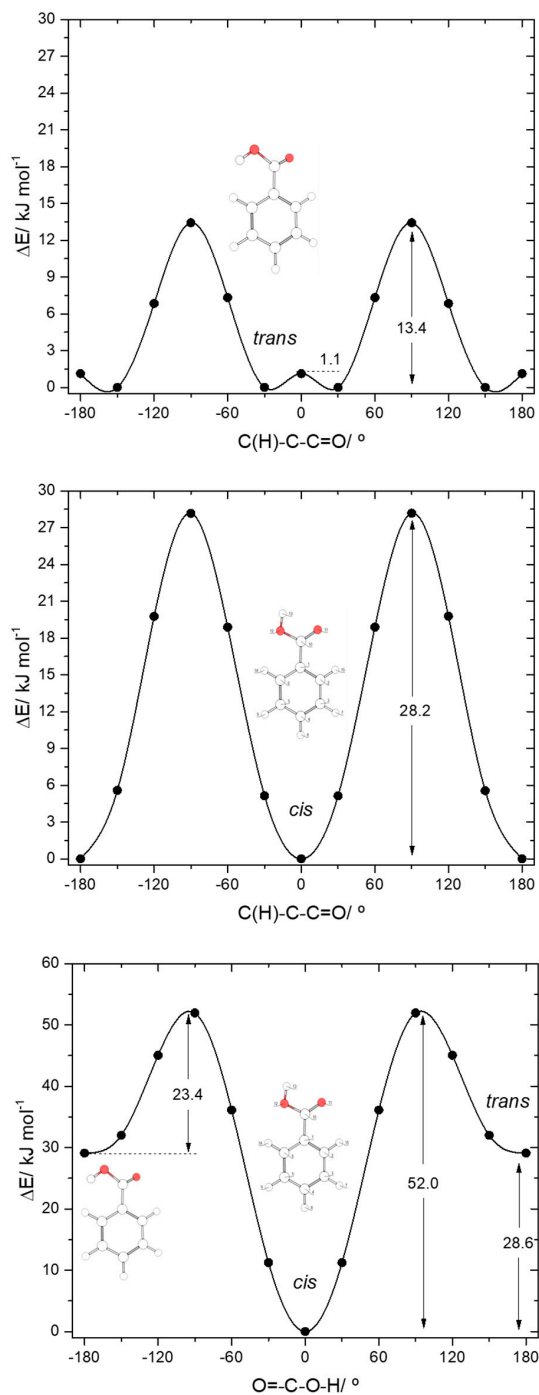


Figure 3. B3LYP/6-311++G(d,p) calculated potential energy profiles for internal rotation about the exocyclic C-C (for *cis* and *trans* arrangement of the carboxylic group) (*top and middle panels*) and about the C-O bond (*bottom panel*) for benzoic acid.

Both **2-fluorobenzoic acid** (2FBA) and **2-chlorobenzoic acid** (2CBA) have two low-energy *cis* conformers and two higher-energy *trans* conformers (see Figure 1). In the fluoro-substituted compound, three conformers are planar, the two *cis* conformers (*cis*-I and *cis*-II) and one *trans* conformer (*trans*-II), all being unique structures. The additional *trans* conformer (*trans*-I) is non planar, being two-fold degenerate by symmetry. The two *cis* conformers have rather similar energies, with *cis*-II (where the fluoro-substituent stays the same side of the molecule as the acid oxygen atom and a C-H \cdots O= stabilizing interaction exists), being the most stable form. The *cis*-I conformer has a relative energy of 2.82 kJ \cdot mol $^{-1}$. In this conformer, the C-H \cdots O= interaction present in *cis*-II is replaced by a weaker stabilizing C-H \cdots OH interaction. The C-H \cdots O= interaction is more efficient in stabilizing *cis*-II than the C-H \cdots OH interaction in stabilizing *cis*-I due to the more favorable localization of the interacting carbonyl oxygen lone electron pair, which stays in the molecular plane, whereas in *cis*-I both lone electron pairs of the acid oxygen atom are out of the molecular plane. On the other hand, the interactions between the fluoro-substituent and the oxygen atoms, which are of repulsive nature, also favor a lower energy for *cis*-II compared to *cis*-I. This can be rationalized in similar terms as for the interactions involving the *ortho* hydrogen atom discussed above. In *cis*-I, the F \cdots O= repulsion is stronger than the F \cdots OH repulsion in *cis*-II because the interacting lone electron pair of the carbonyl oxygen atom is in the same plane as the fluorine atom in the former conformer, while the lone electron pairs of the acid oxygen atom in *cis*-II are both out of the plane in relation to the fluoro-substituent. The calculated atomic charges (Mulliken charges) for the two oxygen atoms, and for the *ortho* fluorine and hydrogen atoms also point to a stronger repulsive F \cdots O interaction in *cis*-I and to a stronger attractive H \cdots O interaction in *cis*-II. The charges (in units of *e*) of the interacting pairs of atoms are: +0.213(H)/−0.193(OH) and −0.133(F)/−0.293(O=) in *cis*-I, and +0.206(H)/−0.295(O=) and −0.139(F)/−0.196(OH) in the most stable *cis*-II conformer.

The planar *trans* 2FBA conformer (*trans*-II) is stabilized by a O-H \cdots F intramolecular hydrogen bond, and has a relative energy of 7.69 kJ \cdot mol $^{-1}$. This energy can be compared with that of the second *trans* 2FBA conformer (*trans*-I), where no such stabilizing interaction exists, which amounts to 29.36 kJ \cdot mol $^{-1}$, very similar to the energy difference between the *trans* and *cis* conformers of benzoic acid (28.56 kJ \cdot mol $^{-1}$; see above). Like for the *trans* BA conformer, in the *trans*-I conformer of 2FBA the OH \cdots H repulsive interaction dominates, being the main factor determining the high relative energy and the non-planarity of the conformer (the C(F)-C-C=O and C(H)-C-C=O angles in *trans*-I are 44.3° and −132.5°, respectively, for the structure shown in Figure 1, which has a symmetry equivalent form where these angles are −44.3° and 132.5°).

The potential energy profiles for conversion between the pairs of related *cis* and *trans* 2FBA conformers (*cis*-I and *trans*-I; *cis*-II and *trans*-II) and those for internal rotation about the exocyclic C-C bond in keeping the conformation of the carboxylic acid fragment as *cis* or *trans* are represented in Figure 4. The *trans*-II \rightarrow *cis*-II conversion takes place over a barrier of 40.4 kJ \cdot mol $^{-1}$ (48.1 kJ \cdot mol $^{-1}$ in the reverse direction), which is more than 3 times higher than that converting *trans*-I into *cis*-I (13.9 kJ \cdot mol $^{-1}$; 50.6 kJ \cdot mol $^{-1}$ in the reverse direction) due to the strong stabilization of *trans*-II originated by the O-H \cdots F hydrogen bond.

The internal rotation about the C-C bond for the *cis* carboxylic acid conformation interconverts *cis*-I and *cis*-II and has an associated energy barrier of 13.1 kJ \cdot mol $^{-1}$ in the *cis*-I \rightarrow *cis*-II direction (15.9 kJ \cdot mol $^{-1}$ in the reverse direction). Interestingly, this barrier is considerably lower than the equivalent one in benzoic acid (28.2 kJ \cdot mol $^{-1}$). Since the intramolecular interactions at the transition states for the C-C internal rotation of both molecules can be expected to be very similar when the carboxylic acid group is in the *cis* conformation, the lower barrier observed in 2FBA compared to BA demonstrates that, globally, the *cis* conformers of 2FBA are destabilized compared to the *cis* form of BA, i.e., F \cdots O repulsions dominate over H \cdots O attractions.

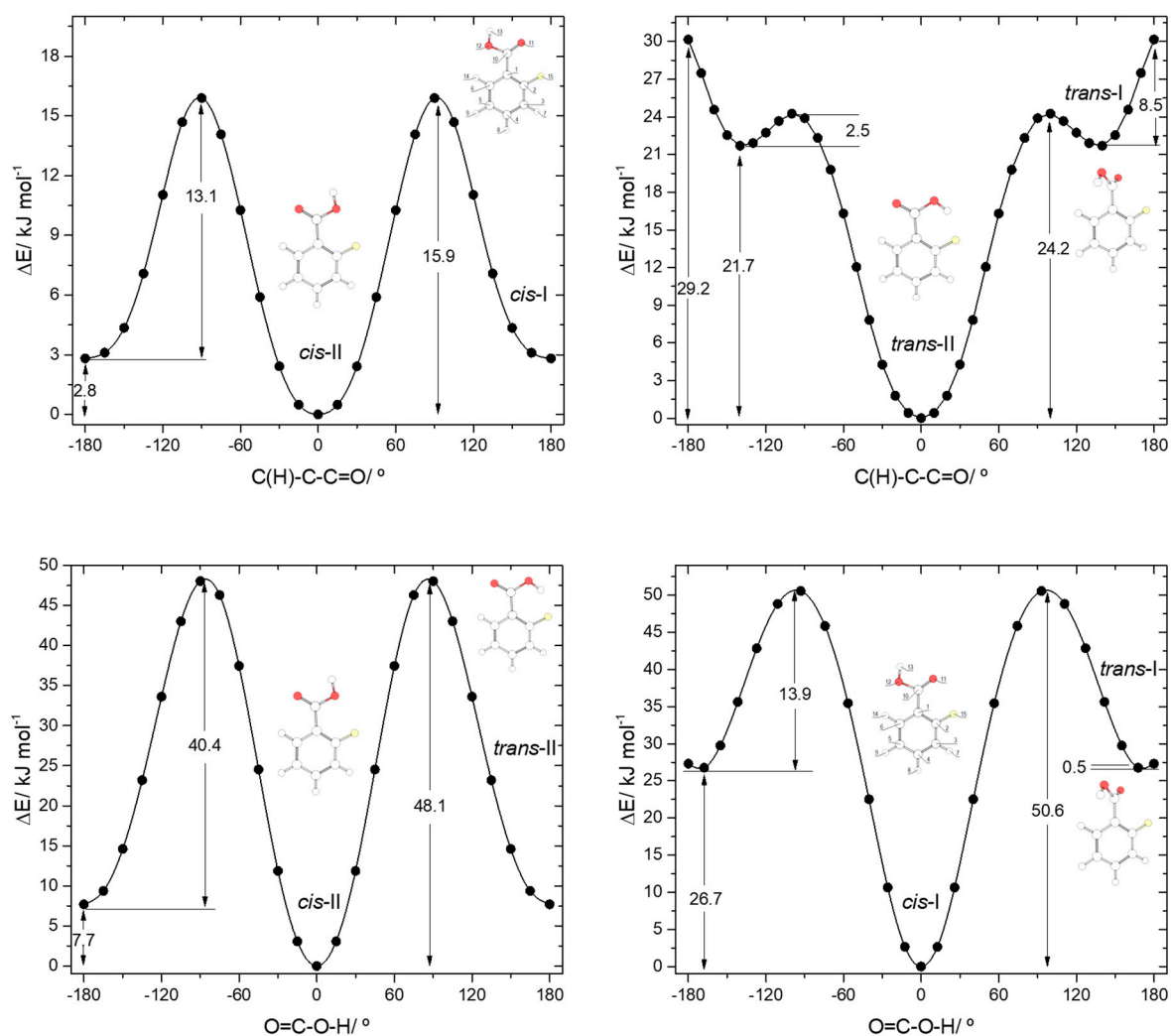


Figure 4. B3LYP/6-311++G(d,p) calculated potential energy profiles for internal rotation about the exocyclic C-C (for *cis* and *trans* arrangement of the carboxylic group) (top left and top right panels) and about the C-O bond (connecting the two pairs of conformers, *cis-II/trans-II* and *cis-I/trans-I*; bottom left and bottom right panels) for 2-fluorobenzoic acid.

The interconversion pathway between the two *trans* 2FBA is strikingly affected by the presence of the $O-H \cdots F$ hydrogen bond in *trans-II*. Indeed, when the conformation of the carboxylic group is *trans*, the potential energy profile for internal rotation about the C-C bond in 2FBA strongly differs from that of benzoic acid (compare Figure 3, top panel, with Figure 4, top-right panel). The stabilization of *trans-II*, due to the intramolecular H-bond makes the energy barrier for its conversion into the *trans-I* form (24.2 kJ mol^{-1}) to be almost twice the equivalent barrier in *trans* BA (13.4 kJ mol^{-1}), while the barrier for the reverse reaction reflects the dominance of strong repulsive interactions in *trans-I* 2FBA, amounting only to 2.5 kJ mol^{-1} . The conversion between the two symmetry-equivalent *trans-I* forms has an associated barrier of 8.5 kJ mol^{-1} , at the planar transition state. Note, also that the *trans-I* \rightarrow *trans-II* barrier is small, but still considerably above the zero-point energy level of the τ_{C-C} torsional vibration in *trans-I*, so that the non-planar *trans-I* conformer should in principle be observable experimentally. We will return to this point later on in this article.

In the case of 2-chlorobenzoic acid, all minimum energy structures are predicted by the calculations as being non-planar. Compared to 2FBA, the order of energy of the two *cis* conformers is predicted by the calculations to be the opposite, with *cis-I* being the most stable conformer. In spite of the small energy difference between the two *cis* conformers predicted by the calculations (0.24 kJ mol^{-1}), their

relative order of stability is predicted correctly. In fact, previously reported infrared spectroscopy experiments for the compound isolated in a low temperature argon matrix [17] have unequivocally demonstrated that the *cis*-I form is the lowest energy conformer of 2CBA. The different order of stability of the two *cis* conformers in 2FBA and 2CBA can be rationalized taking into account that the Cl \cdots O repulsions are considerably stronger in 2CBA than in 2FBA and that, contrarily to what happens for this latter molecule (see above), in 2CBA, due to the large volume of the chlorine atom, the repulsive Cl \cdots O interactions are not significantly affected by the spatial location of the interacting lone electron pair(s) of the oxygen atoms, i.e., the Cl \cdots O interaction is as much effective when involving the “in-plane” lone electron pair of the carbonyl O= atom or the “out-of-plane” lone electron pairs of the acid oxygen atom. In fact, under these assumptions it can even be expected the repulsion to be slightly more important when involving the acid oxygen atom than the carbonyl one (in agreement with the predicted and experimentally observed order of energies of the two conformers of 2CBA), since it is well-known that an acid oxygen atom has a larger effective volume than a carbonyl oxygen [49–51].

It should also be noticed that the analysis of the potential energy profile for rotation around the exocyclic C-C bond for the *cis* conformation of the carboxylic group in 2CBA (see Figure 5, top-left panel) reveals that the two-equivalent-by-symmetry *cis*-I forms and the two symmetry-equivalent *cis*-II forms are separated by low energy barriers, at planar transition states. For *cis*-I, the energy barrier (0.9 kJ \cdot mol $^{-1}$) is above the zero-point energy associated with the torsion around the C-C bond (0.2 kJ \cdot mol $^{-1}$), showing that the non-planar structures correspond to experimentally observable species. On the contrary, the energy barrier separating the two *cis*-II minima (0.1 kJ \cdot mol $^{-1}$) is below their zero-point torsional level (0.2 kJ \cdot mol $^{-1}$), so that the experimentally relevant structure of conformer *cis*-II shall be the planar form. According to these conclusions, the gas phase population of the *cis*-I conformer could be expected to be approximately twice that of the *cis*-II conformer. Such result is confirmed by the experimental data reported in [17]. The ratio of the intensities of the infrared bands assigned to these two conformers (*cis*-I:*cis*-II) measured immediately after deposition of an argon matrix of 2CBA was indeed found to be \sim 2:1.

The main structural characteristics of the *trans* conformers of 2CBA generically follow those described above for the *trans* conformers of 2FBA. Although, two symmetry equivalent minima, corresponding to non-planar geometries, were predicted for the lower energy *trans*-II conformer, the energy barrier separating these minima is lower than 0.1 kJ \cdot mol $^{-1}$ (see Figure 5, top-right panel) and stays below the τ C-C zero point level of this conformer (slightly above 0.1 kJ \cdot mol $^{-1}$), so that the planar structure is the experimentally relevant species. Then, like for 2FBA, the lower energy *trans* conformer in 2CBA is a planar unique structure. Moreover, it is also stabilized by an intramolecular hydrogen bond (O-H \cdots Cl, in this case). The stabilization of *trans*-II by this interaction is, as it could be anticipated considering the relative strengths of typical O-H \cdots Cl and O-H \cdots F hydrogen bonds, not as large as in the case of the equivalent conformer of 2FBA: the relative energy of *trans*-II in 2FBA is 7.69 kJ \cdot mol $^{-1}$; in 2CBA, *trans*-II has a relative energy of 9.7 kJ \cdot mol $^{-1}$. The higher-energy *trans*-I conformer has a relative energy of 22.02 kJ \cdot mol $^{-1}$ and is structurally similar to its counterpart in 2FBA (the angles between the planes of the ring and of the carboxylic group are 44.3 $^\circ$, in 2CBA, and 54.9 $^\circ$, in 2FBA). This conformer can be converted into conformer *trans*-II by rotation around the exocyclic C-C bond (Figure 5, top-right panel), the energy barrier for this process being only 0.6 kJ \cdot mol $^{-1}$, but still above the τ C-C zero-point level of *trans*-I (\sim 0.3 kJ \cdot mol $^{-1}$). The barrier for the reverse transformation (*trans*-II \rightarrow *trans*-I) is 12.7 kJ \cdot mol $^{-1}$, which is about half of the equivalent one in 2FBA (21.7 kJ \cdot mol $^{-1}$) and is consistent with the relative strengths of the distinct intramolecular hydrogen bonds present in the *trans*-II conformers of the two molecules.

The potential energy profiles for interconversion between the *cis* and *trans* conformers (Figure 5, bottom panels) follow the trends, already mentioned above, when comparing the *cis* \leftrightarrow *trans* potential energy profiles of 2FBA with the *cis* \leftrightarrow *trans* one in benzoic acid. The *cis*-II \rightarrow *trans*-II and *cis*-I \rightarrow *trans*-I transformations all have similar energy barriers (52.0 kJ \cdot mol $^{-1}$ in BA, 48.1 and 50.6 kJ \cdot mol $^{-1}$ in 2FBA, 46.3 and 49.5 kJ \cdot mol $^{-1}$ in 2CBA), but the barriers for the reverse reactions involving the hydrogen

bonded conformers (*trans*-II) in 2FBA and 2CBA show the stabilization effect of this intramolecular interaction, increasing along the series BA > 2CBA > 2FBA (23.4, 36.6, 40.4 kJ·mol⁻¹, respectively).

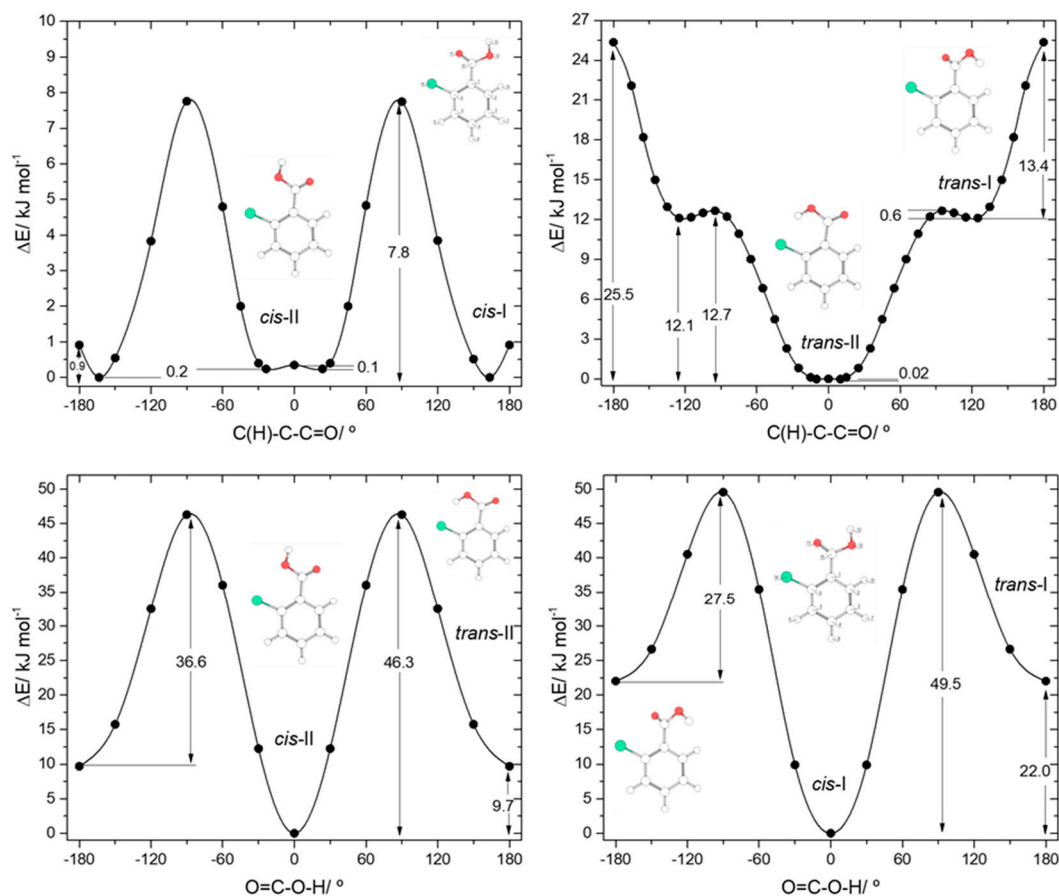


Figure 5. B3LYP/6-311++G(d,p) calculated potential energy profiles for internal rotation about the exocyclic C-C (for *cis* and *trans* arrangement of the carboxylic group) (top left and top right panels) and about the C-O bond (connecting the two pairs of conformers, *cis*-II/*trans*-II and *cis*-I/*trans*-I; bottom left and bottom right panels) for 2-chlorobenzoic acid.

It is interesting to examine the available experimental data on benzoic acid, 2FBA and 2CBA in relation to conformational isomerization at light of the above discussed potential energy landscapes. For the three compounds, only the lower energy *cis* conformers were observed in low temperature infrared matrix isolation experiments [16,17,54,55]. The *cis* conformer of BA was also observed in the gas phase both by electron diffraction experiments and microwave spectroscopy [52,53], and the gas phase infrared spectrum of this species has also been reported [56]. On the other hand, the *trans* conformer of BA has never been observed experimentally. In the case of 2FBA, the intramolecularly hydrogen bonded conformer of 2FBA (*trans*-II) was detected in gas phase (together with the two *cis* conformers) by microwave spectroscopy [18], and it has been produced in argon and N₂ cryomatrices as result of vibrational excitation of the *cis* conformers (using infrared narrowband in situ irradiation) [16]. The existence of the highest energy *trans*-I conformer of 2FBA was inferred indirectly in the matrix isolation conformational studies reported in Ref. [16], but it could not be directly observed due to its fast spontaneous conversion to the lowest-energy *cis* conformers. For 2CBA, in situ UV irradiation of the matrix-isolated *cis* conformers was shown to lead to their conversion into their *trans* counterparts, which were then found to decay by quantum mechanical tunneling back to the *cis* forms [17]. In Ref. [17], the intramolecularly hydrogen bonded *trans*-II conformer was directly observed, while the highest-energy

trans-I conformer was only possible to observe experimentally upon OH→OD isotopic substitution, in order to make its tunneling conversion into the *cis* form slow enough.

The experimental observation of the *cis* forms was expected for all molecules, considering their low energies (see Figure 1) and the fact that they correspond to deep minima in the potential energy surfaces. The intramolecularly hydrogen bonded *trans*-II conformer of 2FBA is also a well-defined minimum with a high energy barrier ($40.4 \text{ kJ}\cdot\text{mol}^{-1}$) of conversion into *cis*-II (see Figure 4, bottom-left panel), and has an expected population in the gas phase at room temperature of ca. 2% [16], justifying its experimental observation in the microwave experiment [18]. *Trans*-II was not detected in the deposited cryogenic matrices [16] most probably because its expected population in the matrix is below the sensitivity of the technique (the infrared spectra is complex, showing the vibrational signatures of the two *cis* conformers and the spectra of *trans*-II conformer is not much different from those of the *cis* forms, which complicates its experimental detection by this technique). However, once *trans*-II is produced in situ by vibrational excitation (upon infrared irradiation) of the matrix-isolated conformer *cis*-II, the high energy barrier for the *trans*-II→*cis*-II conversion precludes this transformation to take place (the over the barrier thermal process is not possible at all, and the experiments showed that quantum mechanical tunneling is also inefficient in this case). It can then be concluded that the *trans*-II conformer of 2FBA is a stable species. In its turn, the higher-energy *trans*-I conformer of 2FBA is unstable, decaying fastly into *cis*-I by tunneling (through a low barrier of only $13.9 \text{ kJ}\cdot\text{mol}^{-1}$; see Figure 4, bottom right panel) or into *trans*-II both via thermal over-the-barrier and tunneling (through a barrier of only $2.5 \text{ kJ}\cdot\text{mol}^{-1}$). The occurrence of these decay processes justify the experimental results described in [16], and are in agreement with the fact that this conformer was not observed in the microwave study (in any case, considering the relative energy of *trans*-I, even in the absence of the spontaneous tunneling decay reactions its population in the room temperature gas phase could be expected to be negligible).

In the case of 2CBA, the highest energy *trans*-I conformer could only be detected [17] upon deuteration of the carboxylic group, which reduces its tunneling decay rate substantially allowing its experimental detection under cryogenic conditions. The barrier for the *trans*-I→*cis*-I conversion is, for 2CBA, of $27.5 \text{ kJ}\cdot\text{mol}^{-1}$, which is still low enough to allow fast tunneling. On the other hand, the 2CBA intramolecularly hydrogen bonded conformer *trans*-II could be experimentally detected after its in situ photoproduction in a cryogenic matrix [17], but found to decay slowly by quantum mechanical tunneling into *cis*-II (half-live of ~10–30 min, at 9–45 K in a Xe matrix). The *trans*-II→*cis*-II energy barrier in 2CBA is $36.6 \text{ kJ}\cdot\text{mol}^{-1}$, i.e., intermediate between that of *trans*-II in 2FBA, which is a stable species (barrier: $40.4 \text{ kJ}\cdot\text{mol}^{-1}$) and the barriers for all other *trans*→*cis* isomerizations in BA, 2FBA and 2CBA (between 27.5 and $13.9 \text{ kJ}\cdot\text{mol}^{-1}$) that lead to fast tunneling and unstable *trans* conformers.

Taking into account the discussion above for 2FBA and 2CBA, the reasons why the *trans* conformer of benzoic acid was not experimentally detected both in the gas phase experiments [52,53,56] and in the matrix isolation studies [54,55] also became clear: the barrier for its conversion into the *cis* form is only $23.4 \text{ kJ}\cdot\text{mol}^{-1}$, intermediate between those for conversion of *trans*-I into *cis*-I forms in 2FCB and 2CBA, and lying within the range of values, which enables fast tunneling; the *trans* conformer of BA is then also unstable, even at cryogenic temperatures.

The conformational spaces of the three investigated di-substituted compounds, **2,6-difluoro-, 2-6-dichloro-, and 2-chloro-6-fluoro- benzoic acids** (abbreviated here as 26DFBA, 26DCBA and 2C6FBA, respectively; see also Figure 2) are relatively more simple than those of the mono-substituted compounds. In practical terms, all these compounds have only one *cis* and one *trans* conformer, though in the case of 2C6FBA three non-equivalent minima exist on the potential energy surface (one *cis* and two *trans*). No structural experimental data has been reported for the isolated molecules of these compounds.

The two conformers of 26DCBA have the carboxylic moiety exactly perpendicular to the plane of the ring, in order to minimize the repulsion between the chlorine *ortho* substituents and the oxygen atoms of the carboxylic group. Each form is two-fold degenerate, the *trans* conformer being higher in

energy than the *cis* by $17.05 \text{ kJ}\cdot\text{mol}^{-1}$. On the contrary, for 26DFBA the conformers are 4-fold degenerate and the planes of the carboxylic group and the aromatic ring make angles of 47.1 and 26.6° , respectively for the *cis* and *trans* conformer. The *trans* conformer is $14.87 \text{ kJ}\cdot\text{mol}^{-1}$ higher in energy than the *cis* form. No intramolecularly hydrogen bonded conformers exist for these two molecules, as the required geometries would also imply strong repulsions between the ring halogen atoms and the oxygen atoms of the carboxylic moiety.

The potential energy profiles for internal rotations about the C-O and exocyclic C-C bonds in these two molecules are shown in Figures 6 and 7.

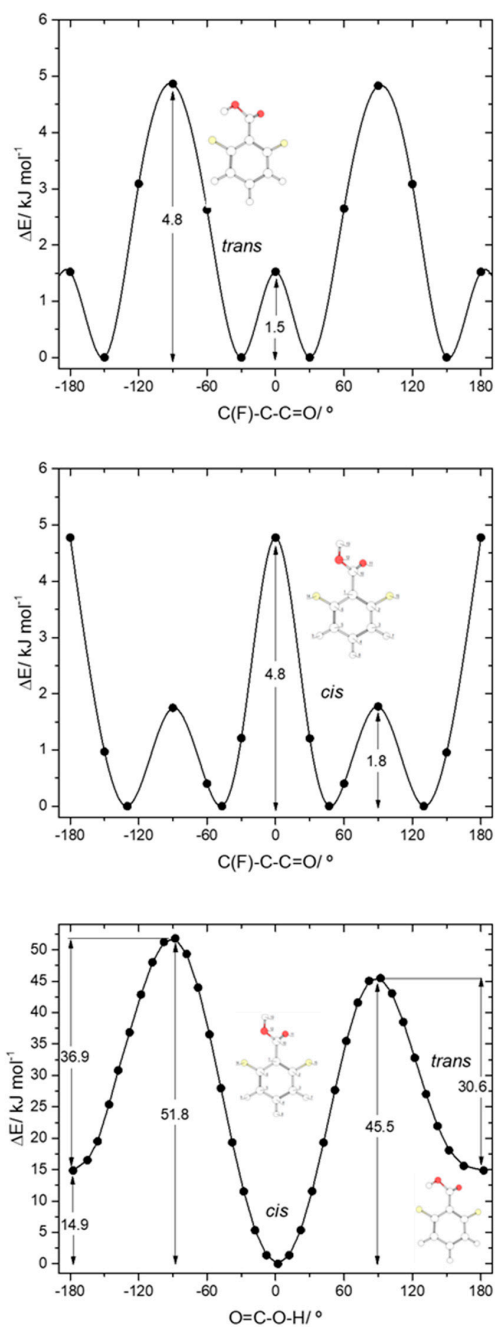


Figure 6. B3LYP/6-311++G(d,p) calculated potential energy profiles for internal rotation about the exocyclic C-C (for *cis* and *trans* arrangement of the carboxylic group) (top and middle panels) and about the C-O bond (connecting the *cis* and *trans* conformers; bottom panel) for 2,6-difluorobenzoic acid.

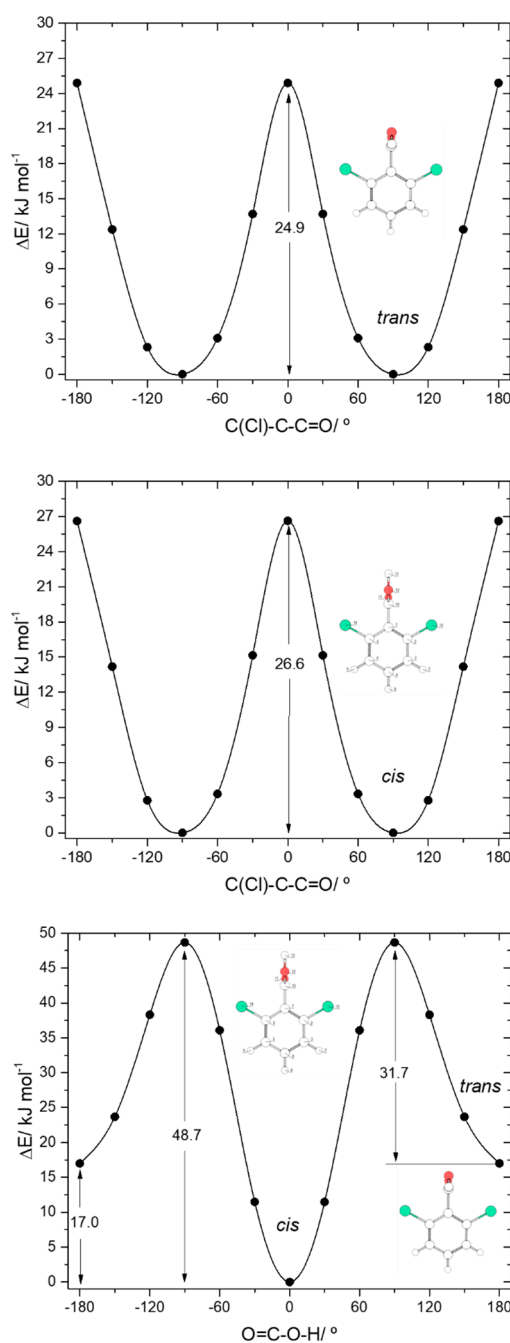


Figure 7. B3LYP/6-311++G(d,p) calculated potential energy profiles for internal rotation about the exocyclic C-C (for *cis* and *trans* arrangement of the carboxylic group) (top and middle panels) and about the C-O bond (connecting the *cis* and *trans* conformers; bottom panel) for 2,6-dichlorobenzoic acid.

The *trans*→*cis* energy barrier in 26DCBA is predicted as being 31.7 kJ·mol⁻¹, which is intermediate between those associated with the *trans*-I→*cis*-I and *trans*-II→*cis*-II transformations in 2CBA (27.5 and 36.6 kJ·mol⁻¹, respectively; see above). This result suggests that *trans* 26DCBA is unstable, decaying spontaneously to the *cis* form via tunnelling if produced in some way. The barrier for the reverse *cis*→*trans* transformation (48.7 kJ·mol⁻¹) is identical to those predicted for BA, 2FBA and 2CBA. The barriers of internal rotation about the C-C bond in 26DCBA are similar for both *cis* and *trans* carboxylic acid group conformations (26.6 and 24.9 kJ·mol⁻¹, for *cis* and *trans* respectively), stressing the dominance of the Cl⋯O repulsive interactions at the planar transition states. These barriers are also similar to the overall energy barrier for internal rotation about the C-C bond in *trans* 2DCBA

(25.5 kJ·mol⁻¹; see Figure 5, top-right panel), which is also dominated by the repulsive Cl···O (and OH···H) interactions, but more than 3-times higher than in *cis* 2DCBA (7.8 kJ·mol⁻¹; Figure 5, top-left panel), where the Cl···O repulsive interaction at the transition state is partially compensated by a stabilizing C-H···O= interaction.

Due to the asymmetrical position of the minimum energy conformations along the C-C internal rotation in both *cis* and *trans* 26DFBA relatively to the two fluoro-*ortho* substituents, the *trans*↔*cis* interconversion in this molecule can take place through two different transition states, depending on the direction of the rotation of the moving carboxylic hydrogen atom along the transformation (see Figure 6, bottom panel). The two barriers are, nevertheless, not much different, amounting to 30.6 and 36.9 kJ·mol⁻¹ in the *trans*→*cis* direction and to 45.5 and 51.8 kJ·mol⁻¹ in the reverse direction. The latter barriers are similar to *cis*→*trans* barriers found for the remaining studied molecules (including 2C6FBA; see below), allowing us to conclude that a barrier in the 45–52 kJ·mol⁻¹ range is characteristic for the carboxylic group *cis*→*trans* transformation in this type of molecules. In the reverse (*trans*→*cis*) direction, the barriers found for 26DFBA are similar to those predicted for both 26DCBA and 2CBA (see above), being of intermediate size within the set of values for these barriers in the whole set of studied molecules, but they are significantly different from those observed for the *trans*-I→*cis*-I and *trans*-II→*cis*-II transformations in 2FBA (13.9 and 40.4 kJ·mol⁻¹, respectively). As for the *trans* conformer of 26DCBA, the *trans* 26DFBA conformer shall be unstable and convert to the *cis* form spontaneously by tunneling.

The potential energy profiles for internal rotation about the exocyclic C-C bond in 26DFBA, for *cis* and *trans* arrangements of the carboxylic group (Figure 6, top and middle panels), reveal the 4 symmetry-equivalent minima in both cases, which can be grouped in two pairs, separated by a transition state where the carboxylic group and the aromatic ring are nearly perpendicular. Within each group, the two forms are connected by a planar transition state. For the *cis* arrangement of the carboxylic group, the first transition state is the lowest energy one (1.8 kJ·mol⁻¹), while the planar transition state separating the members of each pair of symmetry-equivalent forms has an energy of 4.8 kJ·mol⁻¹. This result highlights the dominance of the F···O repulsions at the planar *cis* transition state. On the other hand, for the *trans* arrangement of the carboxylic group the planar transition state has a lower energy (1.5 kJ·mol⁻¹) than the perpendicular one (4.8 kJ·mol⁻¹), a result that indicates that the O-H···F interaction established with one of the F *ortho* atoms partially compensates the effect of the repulsive interaction between the carbonyl oxygen atom and the second *ortho* fluoro-substituent. Compared with the C-C barriers in 26DCBA, the barriers in 26DFBA are much lower, mostly because of the much smaller size of the fluorine atom compared with the chlorine atom, which reduce the strength of the repulsive halogen-oxygen interactions in the fluorinated compound.

The asymmetrically substituted 2-chloro-6-fluorobenzoic acid has one *cis* conformer, which, as for the remaining molecules studied, is the lowest energy conformer, and is lower in energy than the *trans* conformer by 17.07 kJ·mol⁻¹. As already mentioned, the *cis*→*trans* barrier (47.5 kJ·mol⁻¹; see Figure 8) is similar to those in the other compounds, while the barrier for the reverse transformation amounts to 30.4 kJ·mol⁻¹, similar to those found for 26DFBA, 26DCBA and 2CBA, and thus, as for these molecules, the *trans* conformer of 2C6FBA can also be expected to decay spontaneously by tunneling to the *cis* conformer. 2C6FBA has been investigated in a Xe matrix before [58] and, in consonance with these results, only the *cis* conformer was observed in the matrix. In the present study, we attempted to produce the *trans* conformer by using both UV and IR irradiation of the *cis* 2C6FBA conformer isolated in a Xe matrix (see Section 3.4), but we were unable to detect this form (as expected).

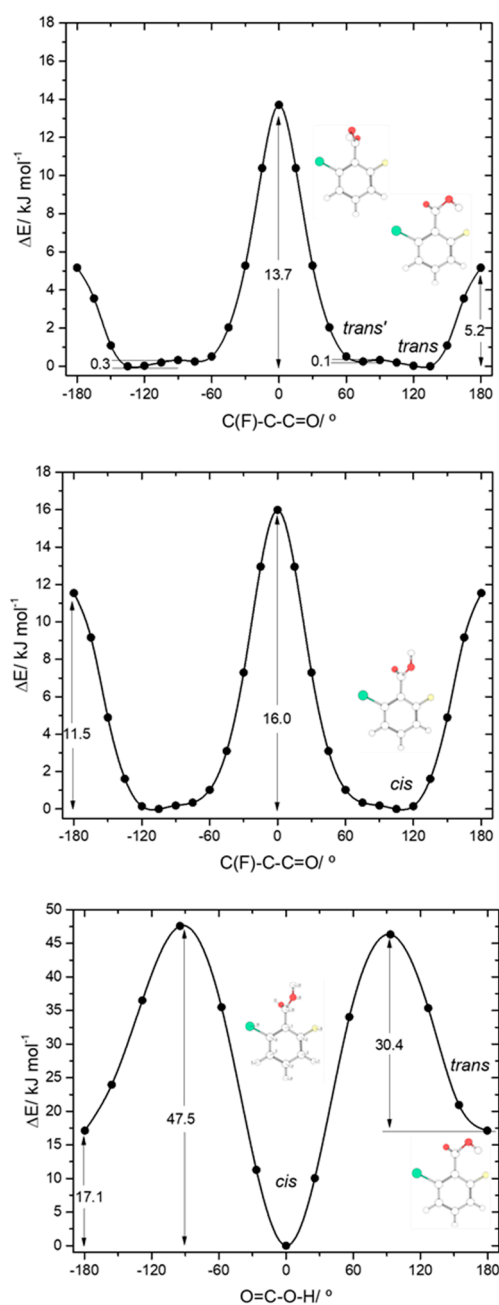


Figure 8. B3LYP/6-311++G(d,p) calculated potential energy profiles for internal rotation about the exocyclic C-C (for *cis* and *trans* arrangement of the carboxylic group) (top and middle panels) and about the C-O bond (connecting the *cis* and *trans* conformers; bottom panel) for 2-chloro-6-fluorobenzoic acid.

The *cis* and *trans* potential energy profiles for internal rotation about the exocyclic C-C bond in 2C6FBA are similar (see Figure 8, top and middle panels), with shallow wells at the position of the conformers. In the case of the *cis* conformer, the two symmetry-equivalent forms are separated by barriers of 16.0 and 11.5 $\text{kJ}\cdot\text{mol}^{-1}$, for the planar transition states with the carbonyl oxygen atom positioned close to the fluorine and chlorine atoms respectively (and the acid oxygen atom positioned close to the second halogen atom). This result indicates that the sum of the energies associated with the $\text{F}\cdots\text{O}=\text{C}$ and $\text{Cl}\cdots\text{OH}$ repulsions is larger than the sum of the $\text{Cl}\cdots\text{O}=\text{C}$ and $\text{F}\cdots\text{OH}$ interactions, as expected taking into account the conclusions from the discussion made above for the mono-substituted compounds. In the case of the *trans* arrangement of the carboxylic group, rotation about the C-C bond reveals two non-equivalent 2-fold degenerated minima (named as *trans* and *trans'* in Figure 2

and also in Figure 8, top panel). However, the barrier separating *trans'* from *trans* ($0.1 \text{ kJ}\cdot\text{mol}^{-1}$) stays below the zero-point energy for the $\tau_{\text{C-C}}$ torsional vibration of *trans'* ($0.2 \text{ kJ}\cdot\text{mol}^{-1}$) so that this structure is better described as a vibrationally excited state of *trans*, resulting that 2C6FBA has a single 2-fold degenerate by symmetry *trans* conformer with experimental significance. The barriers separating the two symmetry equivalent *trans* forms of 2C6FBA amount to 13.7 and $5.2 \text{ kJ}\cdot\text{mol}^{-1}$, for the planar transitions states with the OH carboxylic group pointing to the chlorine and fluorine atoms, respectively. This result can be directly correlated with the relative strengths of the stabilizing $\text{O-H}\cdots\text{F}$ and $\text{O-H}\cdots\text{Cl}$ stabilizing interactions.

3.2. Other Molecular Properties: Internal Strain, Acidity, and Dipole Moment

As detailed in the previous section, the nature of the *ortho* substituents (H, F, Cl), and the relative amount of internal strain they introduce in the studied molecules, play an important role in determining their conformational preferences. Internal strain is also of fundamental importance in determining structural features like bond lengths, and in particular, within the carboxylic moiety, and, together with the relative inductive and resonance abilities of the substituents, also in defining the acidity and the dipole moment of the studied compounds.

The relative internal strain in the experimentally relevant *cis* conformers of the investigated molecules can be promptly estimated by considering the relative lengths of the exocyclic C-C bond connecting their carboxylic acid group to the aromatic ring. As seen in Figure 9, the C-C bond length increases in the order $\text{BA} < 2\text{FBA} < 2\text{CBA} < 26\text{DFBA} < 2\text{C6FCA} < 26\text{DCBA}$, as it could be anticipated (in the plot shown in Figure 9, the average of the C-C bond lengths in the two *cis* conformers for both 2FBA and 2CBA is used). As pointed in the previous section, from the practical point of view the *cis* conformers of benzoic acid and of the two mono-substituted compounds are planar, while those of the three di-substituted compounds are toughly non-planar. This fact influences decisively the properties of the carboxylic acid group, making the two sets of molecules intrinsically different regarding its characteristics.

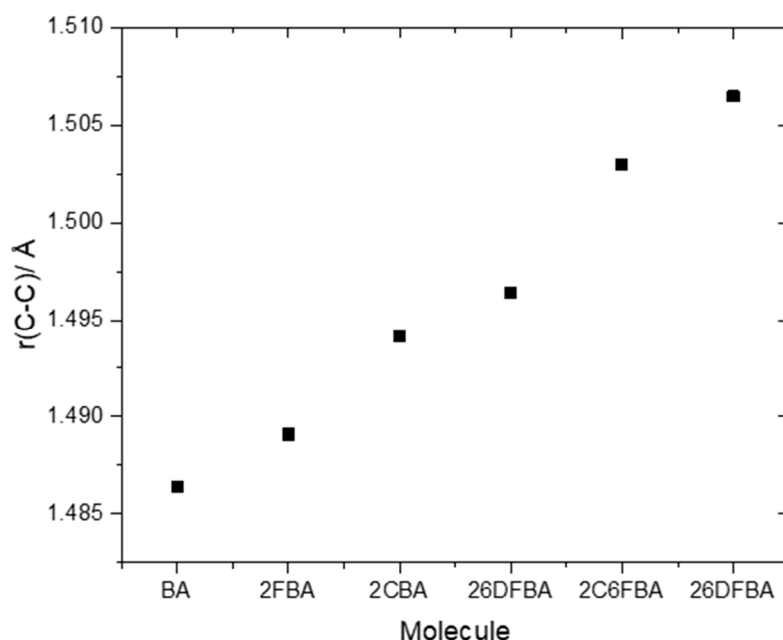
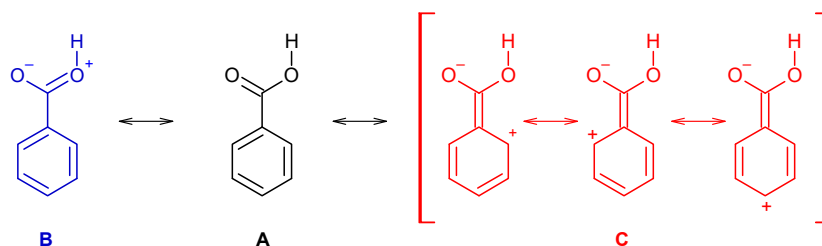


Figure 9. B3LYP/6-311++G(d,p) calculated bond lengths of the exocyclic C-C bond in the studied molecules.

Indeed, the resonance stabilization within the carboxylic group (represented in Scheme 1 by the structure **B**) is weak in benzoic acid and in the two mono-substituted compounds, due to the cross

conjugation with the aromatic ring (C, in Scheme 1), which competes with the first effect. On the other hand, because of the non-planarity due to the stronger steric effects in the di-substituted derivatives, the cross conjugation is diminished in these compounds, so that the resonance stabilization within the carboxylic group becomes considerably more important. This has relevant structural implications, and it also plays a major role in determining the relative acidity of the two groups of molecules (for this latter property, one has also to count with the strain induced by the *ortho* substituents in the ionized carboxylate group of the conjugated bases of the acids, but for these species the effect can even be expected to be more relevant, due to the larger effective volume of the carboxylate moiety when compared with the non-ionized carboxylic acid group [49–51]).



Scheme 1. Mesomeric structures representing the resonance stabilization within the carboxylic group (B) and the competing cross conjugation with the aromatic ring (C). Structure A corresponds to the molecule canonical form.

Figure 10 shows plots of the calculated C-O, C=O and O-H bond lengths, as well as of vibrational frequencies associated of these bonds in the studied molecules [the localized $\nu(\text{O-H})$ and $\nu(\text{C=O})$ stretching and the $\tau(\text{C-O})$ torsion modes; $\nu(\text{C-O})$ is extensively coupled with the $\delta(\text{C-O-H})$ in-plane bending], as a function of their acidity, as expressed by the corresponding pK_a values in water at room temperature (25°) [25–29,59]. To fully understand the plots, one shall recall that both F and Cl have negative (electron withdrawing) inductive effect (–I), which is more important for fluorine than for chlorine (in view of the corresponding relative electronegativities), and positive (electron donating) mesomeric effect (+M), which is also stronger in fluorine compared to chlorine (due to the better orbital interactions of the $2p$ C or O orbitals with the closest in energy $2p$ orbitals of the fluorine atom, compared to the chlorine $3p$ orbitals). Noteworthy, when both +M and –I effects are operating simultaneously, both fluorine and chlorine are globally electron attractors (i.e., the –I effect dominates), but the much stronger +M effect of fluorine compared to chlorine reduces its total electron attractor power substantially compared to the later, so that fluorine becomes a total weaker electron attractor than chlorine. One consequence of this is that 2-fluorobenzoic acid has a lower acidity compared to 2-chlorobenzoic acid (the experimental pK_a values for 2FBA and 2CBA at 25 °C in water are respectively 3.27 and 2.94 [25,27]). Of course, both compounds are considerably more acidic than the unsubstituted benzoic acid ($\text{pK}_a = 4.20$ [59]).

The pK_a values for the difluoro- and dichloro- *ortho* substituted benzoic acids are 2.34 and 1.69, respectively [26,28], with 2-chloro-6-fluorobenzoic acid having an intermediate pK_a (2.04 [29]). In these compounds, besides the inductive and mesomeric effects of the substituents, the internal strain leading to non-planarity between the carboxylic group and the aromatic ring has also to be taken into account. The last, as shown in Figure 9, follows the order 26DFBA < 2C6FBA < 26DCBA (which is also the order of the degree of non-planarity of the *cis* conformers of the three molecules, whose angles made by the planes of the carboxylic group and the aromatic ring are 47.1°, 67.6°, and 90.0°, respectively, see Figure 2).

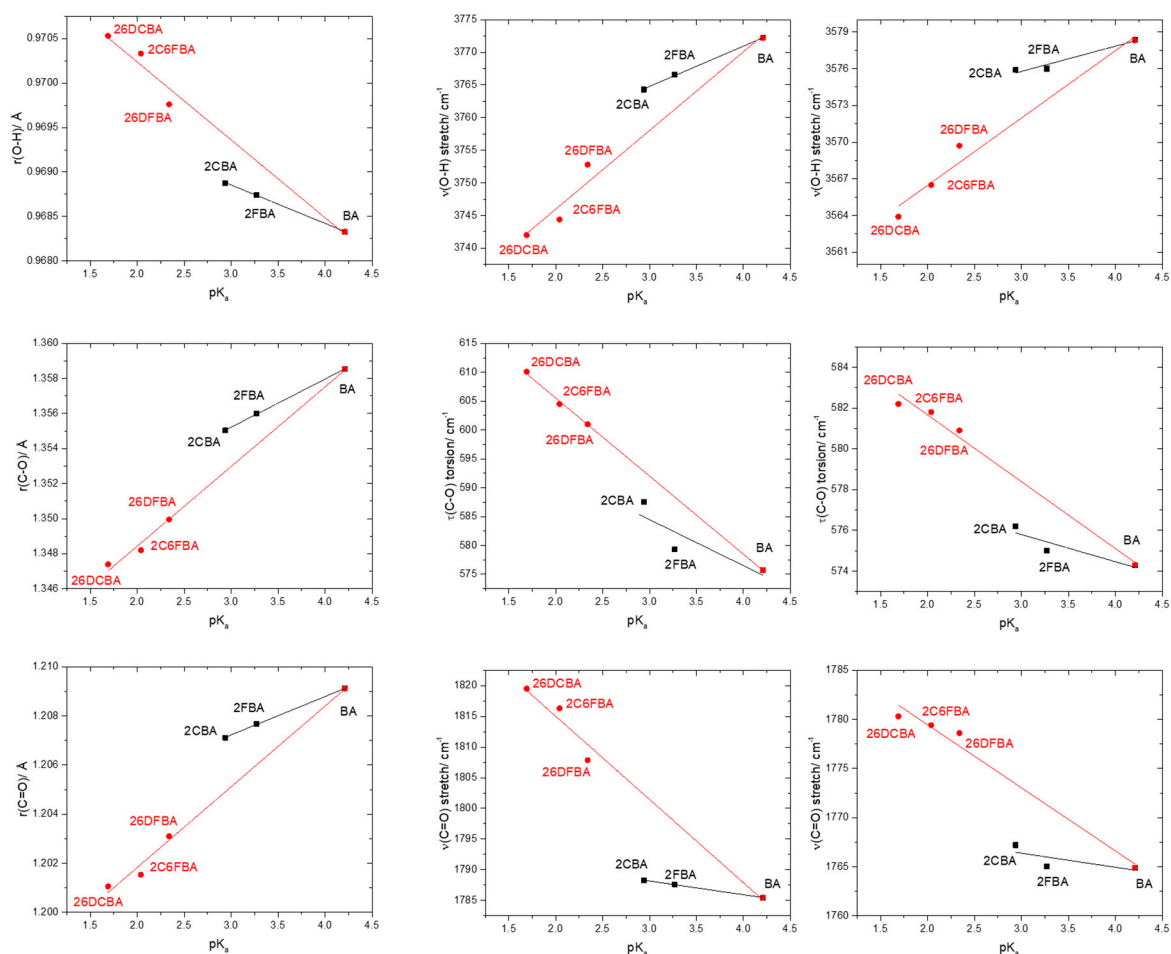


Figure 10. Correlation between the O-H, C-O and C=O bond lengths and of the $\nu(\text{O-H})$, $\tau(\text{C-O})$, and $\nu(\text{C=O})$ vibrational frequencies of the experimentally relevant *cis* conformers and pK_a values (water; 25 °C) for the studied molecules. From *top-left* to *bottom-right* panels (descending by columns), the slopes, intercepts of the fitted lines and the R^2 parameters of the adjustments are: $(-4.318 \times 10^{-4}, 0.970, 0.99897; -8.755 \times 10^{-4}, 0.972, 0.97477)$, $(2.750 \times 10^{-3}, 1.347, 0.99982; 4.550 \times 10^{-3}, 1.339, 0.99409)$, $(1.560 \times 10^{-3}, 1.202, 0.99852; 3.290 \times 10^{-3}, 1.195, 0.99014)$, $(6.162, 3746.3, 0.99771; 12.052, 3721.9, 0.96834)$, $(-7.968, 608.4, 0.60329; -13.522, 632.6, 0.99916)$, $(-2.217, 1794.8, 0.99791; -13.544, 1842.1, 0.97844)$, $(2.063, 3569.6, 0.90715; 3.504, 3555.4, 0.96512)$, $(-1.331, 579.8, 0.66553; -3.277, 588.2, 0.98402)$, $(-1.436, 1770.7, 0.65948; -6.422, 1792.3, 0.96951)$. For both 2-fluorobenzoic acid and 2-chlorobenzoic acid, calculated bond lengths and vibrational frequencies are the means of the values obtained for the two *cis* conformers.

It is clear from the data plotted in Figure 10 that for the two groups of molecules (BA, 2FBA and 2CBA, in one side, and 26DFBA, 2C6FBA and 26DCBA in the other) the correlations between the O-H, C-O and C=O bond lengths within the carboxylic group as well as between the characteristic vibrational frequencies associated to these moieties ($\nu(\text{O-H})$, $\tau(\text{C-O})$, and $\nu(\text{C=O})$) and the pK_a s follow different linear trends. As expected, the trend lines for all the correlations have a larger slope for the di-substituted molecules, where the number of halogen substituents is higher and the internal strain is large enough to make the molecules non-planar, thereby, increasing the importance of the stabilizing resonance effect within the carboxylic acid group (which directly correlates with the lability of the acid hydrogen). Interestingly, with a single exception the slopes of the trend lines for the di-substituted compounds in the plots shown in Figure 10 are approximately twice those for the mono-substituted compounds.

An increase in the acidity of the compounds correlates with a longer O-H, as well as with a shorter C-O bond (as expressed by the resonance structure **B** in Scheme 1). Alongside, the $\nu(\text{O-H})$ stretching

frequency decreases (since the bond becomes weaker), while the frequency of the $\tau(\text{C-O})$ torsion increases (because the C-O bond increases its double bond character, implying a higher force constant for the torsional vibration). The results show also that the C=O bond length decreases with the acidity and, concomitantly, $\nu(\text{C=O})$ increases. Since the electronic charge in the carbonyl π -bond shall reduce (see Scheme 1), these results indicate that the carbonyl σ -bond has to become stronger. In fact, this is in consonance with previous investigations on the behavior of the π and σ electronic systems in the carbonyl moiety [50,60], which have shown that the changes in the strengths of the two components of the carbonyl double bond in general take place in opposite directions, i.e., a weakening of the π -bond leads to strengthen the σ -bond, and vice-versa. It shall also be noticed that the correlations between pK_a and the vibrational frequencies do also verify if instead of the calculated frequencies one considers the experimentally measured ones in the gas phase (Figure 10, right-side panels), although the complex band profiles and band overlappings, observed in the experimental spectra introduce, in some cases, some uncertainty in the experimental frequencies.

Contrary to what happens in the case of acidity, the relative polarity of the different studied molecules, as measured by their total dipole moments, is mostly determined by the intrinsic polarity of the substituents, despite the dipole moment orientation reflects also their degree of planarity. Figure 11 shows the absolute value and the direction of the dipole moments for the experimentally relevant *cis* conformers of the various studied compounds. For benzoic acid and the mono-substituted compounds, the dipole moment is located in the molecular plane. In BA and in the *cis*-I conformers of 2FBA and 2CBA, it has approximately the same orientation, pointing from the C-H *meta* bond opposed to the carbonyl bond towards between this bond and the nearly located C-X ($X = \text{H, F, Cl}$) *ortho* bond, and increases along the series $\text{BA} > 2\text{CBA} < 2\text{FBA}$ (2.12, 3.30, 3.50 D), while in the *cis*-II conformers of 2FBA and 2CBA the dipole moment points from the *para* C-H bond to the middle of the O=C-O angle of the carboxylic acid group, being also larger in the fluoro-substituted compound than in the chloro-substituted one (2.16 vs. 1.99 D). On the other hand, in the di-substituted compounds the dipole moment stays in the plane of the carboxylic acid and makes an angle of approximately 25° with the plane of the aromatic ring. In both 2F6CBA and 26DCBA the dipole moment points from below the *para* C-H bond up towards the carbonyl oxygen atom, while in the difluoro-substituted molecule it points from below the middle of the ring C-C bond connecting the *para* carbon atom to the *meta* one opposing to the carbonyl atom up towards this latter atom (see Figure 11). In the di-substituted molecules the order of increasing dipole moment is $26\text{DCBA} < 2\text{C6FBA} < 26\text{DFBA}$, the magnitude of the dipole moments (2.63, 2.70, 2.94 D, respectively) being in between those of the *cis*-I and of the *cis*-II conformers of the mono-substituted molecules. If we consider the average values of the dipole moments of the two *cis* conformers in these latter molecules (2.83 and 2.64 D, respectively for 2FBA and 2CBA), the absolute values of the calculated dipole moments in the whole series of investigated substituted benzoic acids stay in the rather narrow range of values 2.63–2.94 D.

Unfortunately, to the best of our knowledge no gas phase experimental data on dipole moments for the studied molecules have been reported. For benzoic acid, values in the range 1.7–2.1 D have been reported in dioxane and CCl_4 solution [61], and for 2FBA a value of 2.46 D has been reported [62], but without specification of the experimental conditions. These values seem to indicate that the dipole moments obtained in our calculations are probably within 10% accuracy, but a definitive conclusion on this matter must await for experimental confirmation.

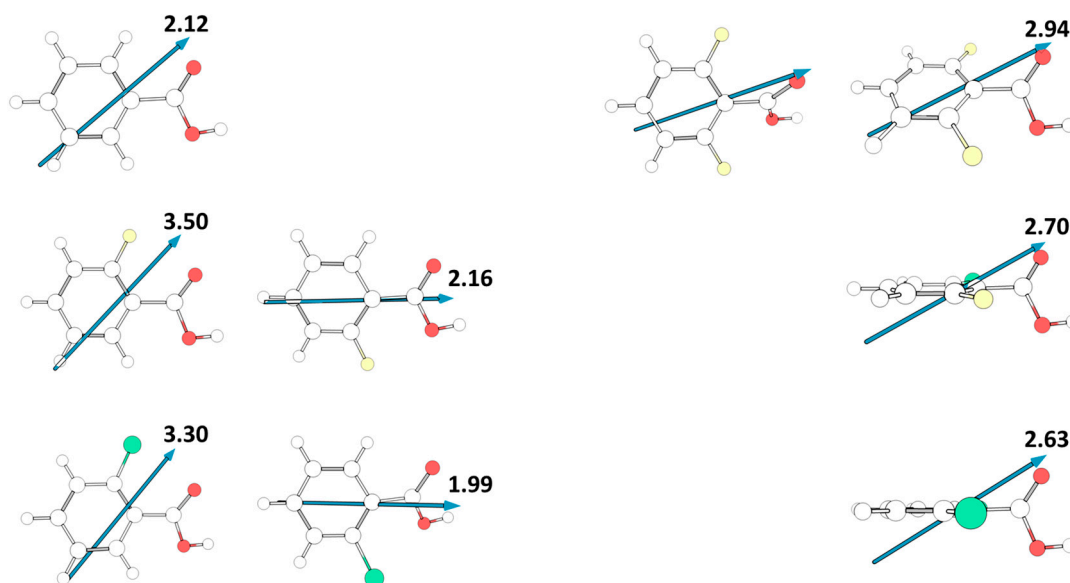


Figure 11. Calculated dipole moments (in Debyes; 1 Debye = $\approx 3.33564 \times 10^{-30}$ C·m) for the studied molecules. For 2,6-difluorobenzoic acid, two representations are provided, one with the aromatic ring in the plane, and the other with the carboxylic acid substituent in the plane. In the case of the mono-substituted compounds (2FBA, 2CBA) the two *cis* conformers are shown.

3.3. Gas Phase IR Spectra

All the molecules studied are asymmetric tops, with 39 fundamental vibrations, all active in infrared. The experimentally relevant *cis* conformers of benzoic acid, 2FBA and 26DBA are C_s symmetry. The symmetry plane for the first two molecules corresponds to the molecular plane and the vibrations spawn the irreducible representations $27A' + 12A''$, while in 26DCBA the plane of symmetry is perpendicular to the aromatic ring and contains the carboxylic group, the vibrations spawning the irreducible representations $23A' + 16A''$. The *cis* conformers of 26DFBA and 2C6FBA, as well as the most stable conformer of 2CBA (*cis*-I), are C_1 symmetry. On the other hand, as discussed in Section 3.1, from the practical point of view the *cis*-II conformer of 2CBA is planar, thus belonging to the symmetry point group C_s and, as in 2FBA, its vibrations spawn the irreducible representations $27A' + 12A''$.

In the gas phase, infrared spectra are complicated by rotational contributions to the vibrational bands, which, together with the symmetry of the vibration, determine the band contours. For asymmetric top molecules of the size of those studied here, a detailed analysis of the band contours is a cumbersome task unless the molecule is approximately a symmetric top (either prolate, or oblate). In this case, band contour analysis may help to perform the assignment of bands that are not extensively overlapped or complicated by other effects (e.g., Fermi resonances and isotopic contributions, the latter being particularly relevant for the chloro-substituted molecules, since chlorine has two isotopes of large natural abundance).

The extent to which an asymmetric top molecule resembles a symmetric top is usually quantified by means of the Ray's parameter κ , which can be estimated from the rotational constants, A , B , C (which directly relate with the moments of inertia, I_A , I_B , I_C):

$$\kappa = \frac{2B - A - C}{A - C} \quad (2)$$

$\kappa = -1$ for a prolate top ($A > B = C$), and $\kappa = 1$ for an oblate top ($A = B > C$).

Table 1 shows the calculated rotational constants and the value of the κ parameter for the relevant conformers of the studied molecules. As it can be seen, only benzoic acid approaches the condition of being an approximate symmetric top (prolate; with $\kappa = -0.80$), with all the other molecules having

$|\kappa| < 0.50$ with the exception of 2C6FBA, where $\kappa = 0.73$ (i.e., 2C6FBA has still a relatively significant oblate character). Considering these results, in the following discussion of the gas phase infrared spectra of the compounds, band contour analysis is only attempted for benzoic acid. In order to do this, it is relevant to know that the orientation of the principal inertial axes, which are depicted in Figure 12 for all the studied molecules.

Table 1. Calculated rotational constants (GHz) and Ray's parameter for the experimentally relevant conformers of the studied molecules.

Molecule	A	B	C	κ
BA	3.8809001	1.2246207	0.9308807	−0.80
2FBA (<i>cis</i> -II)	2.2877050	1.2087660	0.7908917	−0.44
2FBA (<i>cis</i> -I)	2.2641140	1.2114724	0.7891939	−0.43
26DFBA	1.5243775	1.1493339	0.6953489	0.10
2CBA (<i>cis</i> -II)	1.4673930	1.1808936	0.6676423	0.28
2CBA (<i>cis</i> -I)	1.4469943	1.1976874	0.6621492	0.36
2C6FBA	1.1257278	1.0541388	0.5898361	0.73
26DCBA	1.0938018	0.7895163	0.4960684	−0.02

For benzoic acid and the mono- and difluoro- substituted compounds, the A and B axes are nearly in the plane of the aromatic ring, the A axis being almost coincident with the *para* C-H bond and bisecting the O=C-O angle. In the case of benzoic acid, this means that all in-plane vibrations (A' symmetry) shall show A, B or mixed AB band contours, while all out-of-the-plane vibrations (A'' symmetry) shall exhibit C contour profiles. The orientation of the principal inertial axes in the remaining molecules can be seen in Figure 12, the striking case being 26DCBA, where the A axis (of lower momentum of inertia) stays in the plane of the aromatic ring, but aligned perpendicularly to the plane of symmetry of the molecule and passing through the two *ortho* chlorine atoms. In this regard, this molecule substantially differs from all the others being studied, which have the A axis located approximately in the plane of the aromatic ring and roughly oriented (or almost precisely oriented, as in benzoic acid) in a direction defined by the *para* C-H bond and the exocyclic C-C bond connecting the carboxylic acid substituent to the aromatic ring.

The gas phase infrared spectra for all the six studied compounds are shown in Figure 13, together with the B3LYP/6-311++G(d,p) calculated spectra. For simplicity, only the calculated spectra of the most stable conformers of 2FBA (*cis*-II) and 2CBA (*cis*-I) are shown in the figure, since the spectra of the second populated conformers of these molecules in the gas phase (*cis*-I for 2FBA and *cis*-II for 2CBA) are very much similar to those of the corresponding dominant conformers [16,17].

The agreement between the calculated and experimental data is excellent, allowing the assignment of the spectra to be carried out straightforwardly. In Tables 2–7, which show the proposed assignments, previously reported data obtained for jet-cooled gaseous benzoic acid [56] and for the monomer of this compound as well as of 2FBA, 2CBA and 2C6FBA isolated in low-temperature noble gas (Ar or Xe) matrices [16,17,54,55,58] are also presented. As described below, the present assignments agree with the general ones previously proposed for those molecules, but expand them providing assignment of additional bands and more evidence justifying the undertaken assignments (in particular for the unsubstituted compound). No vibrational studies have been reported on both 26DFBA and 26DCBA monomers hitherto.

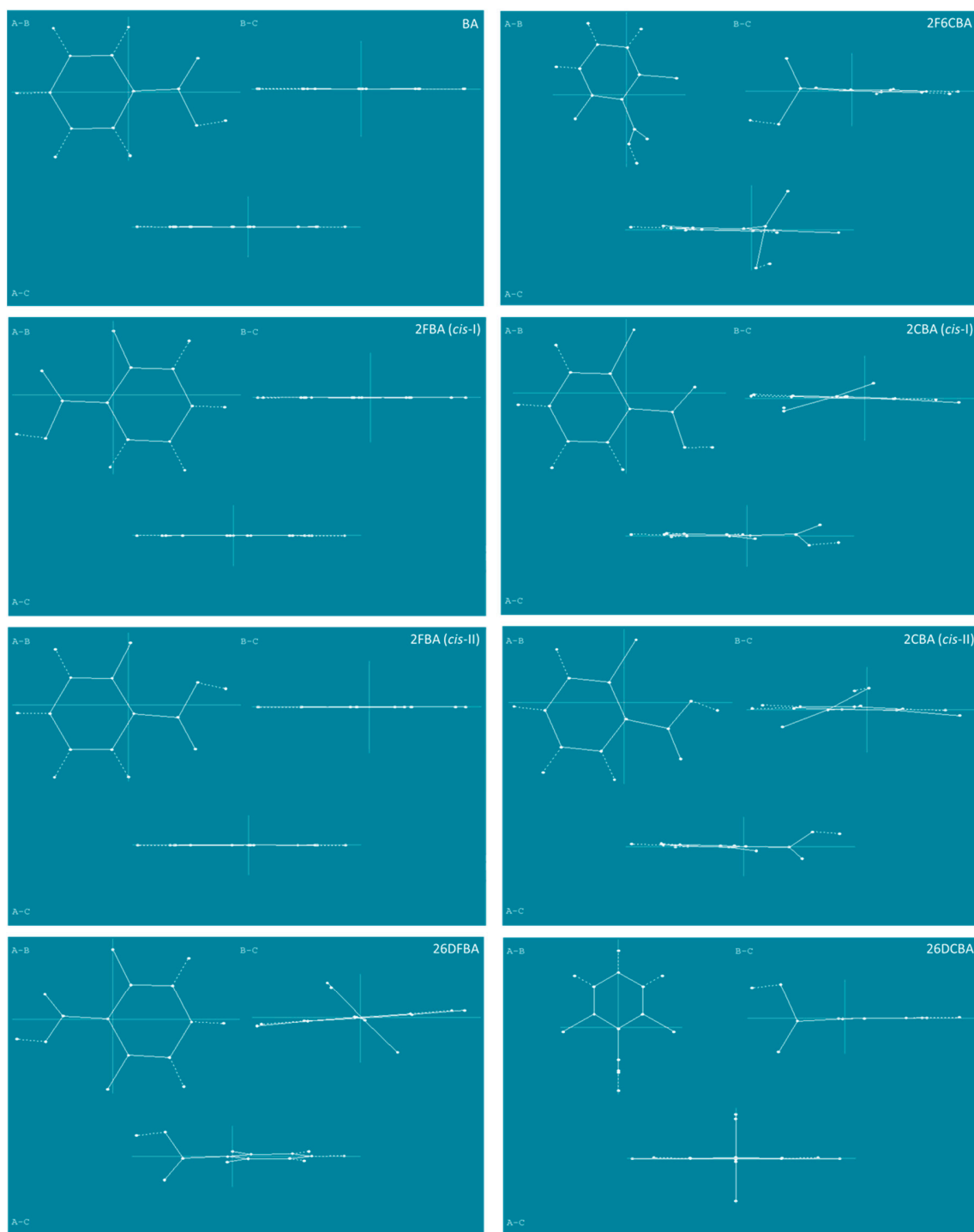


Figure 12. Projection of the experimentally relevant *cis* conformers of the studied molecules in the planes defined by the principal inertial axes, which are also represented in the figure, with lengths proportional to their associated rotational constants, A, B, C.

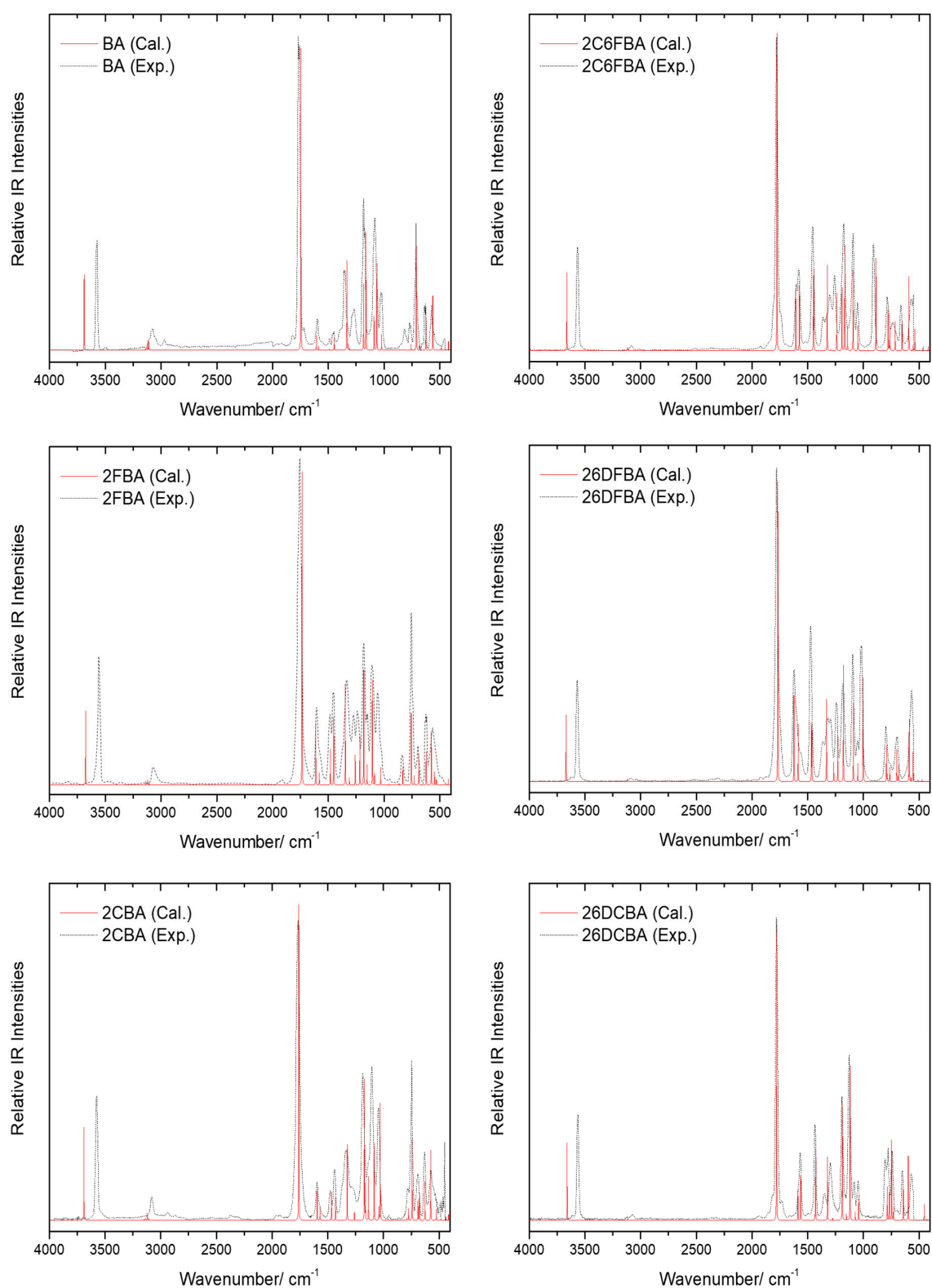


Figure 13. Gas phase infrared spectra of the studied compounds (black dashed traces) and B3LYP/6-311++G(d,p) calculated infrared spectra for their experimentally relevant conformers (red traces), in the 4000–450 cm⁻¹ region. Calculated frequencies are scaled by 0.978. For simplicity, only the calculated spectra for the most stable conformers of 2FBA (*cis*-II) and 2CBA (*cis*-I) are shown in the figure (see also text).

Table 2. Experimental (Exp.) and B3LYP/6-311++G(d,p) calculated (Calc.) infrared spectra of monomeric benzoic acid, and band assignments ^a.

Exp. Gas Phase ν	Exp. [56] Cooled-jet ν	Exp. [54,55] Ar Matrix, 12 K ν	Calc. B3LYP ν	ν_{IR}	Approximate Description ^b	Symmetry	Contour Type ^c
3578	n.i.	3567	3689	99.4	$\nu(O-H)$	A'	A
3124	n.i.	3098	3138	2.5	$\nu(CH) 0000+$	A'	AB
3104	n.i.	3079	3132	4.6	$\nu(CH) +0000$	A'	AB
3083	n.i.	3068	3118	12.7	$\nu(CH) 0+++0$	A'	A
3060	n.i.	3041	3109	10.7	$\nu(CH) 0+0-0$	A'	B
3031	n.i.	3012	3097	0.4	$\nu(CH) 0+-+0$	A'	A
1765	1752	1755/1752/1751 /1743	1746	395.8	$\nu(C=O)$	A'	AB
1599	1609	1606	1606	19.2	$\nu(CC) +---++$	A'	A
1585	1591	1590	1586	5.3	$\nu(CC) 0+-+0-$	A'	AB
1481	n.obs.	1496/1493	1489	1.8	$\nu(CC) 0+-0+, \delta(CH) ++0--$	A'	B
1451	1455	1456	1448	15.7	$\nu(CC) 0+0-0, \delta(CH) 0+++0$	A'	AB
1388/1354 ^d	1387	1383/1380	1333	117.2	$\nu(C-O), \delta(COH)$ $\nu(CC) +---+-, \delta(CH)$	A'	AB
1328	1347	1347	1321	8.1	$+++++$	A'	AB
1284/1269 ^e	1278/1255 ^f	1278/1275/1271/ /1255/1251/1248 ^e	1310	2.1	$\nu(CC) 0+--0-$	A'	A
1184	1187	1185	1184	86.7	$\delta(COH), \delta(CH) 0+0-0$	A'	AB
1177	1173	1169	1163	153.8	$\delta(COH), \delta(CH) +-0-+$	A'	AB
n.obs.	1099	1110/1100	1158	0.6	$\delta(CH) 0+-+0$	A'	AB
1095	1084	1086	1090	44.6	$\nu(C-O), \nu(CC) --0++0,$ $\delta(CH) 0000+$	A'	AB
1078	1063	1066/1063	1065	114.6	$\nu(C-O), \nu(CC) 0000+0,$ $\delta(CH) +0000$	A'	AB
1026	1026	1027	1023	20.7	$\delta(ring)_1$	A'	AB
n.obs.	n.obs.	n.obs.	995	0.4	$\delta(ring)_2$	A'	A
n.obs.	n.obs.	n.obs.	987	0.1	$\nu(CH) +-+-+$	A''	C
n.obs.	n.obs.	n.obs.	976	0.1	$\nu(CH) +-0+-$	A''	C
947	n.obs.	937	939	1.7	$\nu(CH) +0-0+$	A''	C
n.obs.	n.obs.	n.obs.	845	0.1	$\nu(CH) +-0--$	A''	C
n.obs.	n.obs.	n.obs.	806	0.1	$\nu(C=O)$	A''	C
770	767	767/759	758	8.1	$\nu(C-C)$	A'	A
714	710	713/711	711	136.8	$\nu(CH) ++++++, \nu(C=O)$	A''	C
688	688	687	684	5.8	$\tau(ring)_1$	A''	C

Table 2. Cont.

Exp. Gas Phase	Exp. [56] Cooled-jet	Exp. [54,55] Ar Matrix, 12 K	Calc. B3LYP	ν	ν	ν	IR	Approximate Description ^b	Symmetry	Contour Type ^c
631	631	628	626	626	626	626	48.9	$\delta(\text{OCO})$	A'	AB
n.obs.	587	568	618	618	618	618	0.2	$\delta(\text{ring})_3$	A'	AB
574	571	565	563	563	563	563	71.5	$\tau(\text{C-O})$	A''	C
504	n.i.	491	486	486	486	486	6.1	$\gamma(\text{C-[CCC]})$	A'	B
n.i.	n.i.	421	423	423	423	423	12.1	$\tau(\text{ring})_2$	A''	C
n.i.	n.i.	n.obs.	404	404	404	404	0.5	$\tau(\text{ring})_3$	A''	C
n.i.	n.i.	n.i.	375	375	375	375	4.8	$\delta(\text{ring})_4$	A'	AB
n.i.	n.i.	n.i.	212	212	212	212	1.5	$\gamma(\text{COOH})$	A'	AB
n.i.	n.i.	n.i.	155	155	155	155	0.8	w(COOH)	A''	C
n.i.	n.i.	n.i.	64	64	64	64	0.9	$\tau(\text{C-C})$	A''	C

^a Wavenumbers (ν) in cm^{-1} , calculated infrared intensities (ν IR) in $\text{km}\cdot\text{mol}^{-1}$; n.obs., not observed; n.i., not investigated. ^b Approximate description was obtained using the vibrations animation module of Chemcraft [63]; ν , stretching; δ , bending; w, wagging; γ , rocking; τ , torsion; the symbols +, - and 0 placed in front of the $\nu(\text{CC})$, $\nu(\text{CH})$, $\delta(\text{CH})$ and $\gamma(\text{CH})$ ring coordinates indicate the movement (distending, compressing, staying, respectively) of the related bonds, starting from that located *ortho* to the C=O bond of the carboxylic group and proceeding anti-clockwise through the ring. ^c Band contours in gas phase spectra predicted according to the calculated transition dipole moment vector orientation. ^d Fermi interaction with $2 \times \tau(\text{ring})_1$. ^e Fermi interaction with $2 \times \delta(\text{OCO})$.

Table 3. Experimental (Exp.) and B3LYP/6-311++G(d,p) calculated (Calc.; *cis*-II conformer) infrared spectra of monomeric 2-fluorobenzoic acid, and band assignments ^a.

Exp. Gas Phase ν	Exp. (This Work; Also [16]) Ar Matrix, 10 K ν	Cal. B3LYP ν	I_{IR}	Approximate Description ^b	Symmetry
3576	3558/3555	3676	96.4	$\nu(O-H)$	$A\tau$
3100	3069	3137	4.9	$\nu(CH) +++++$	A'
n.obs.	n.obs.	3132	1.1	$\nu(CH) +0--$	A'
3087	3026	3121	6.7	$\nu(CH) +- --+$	A'
3060	n.obs.	3107	2.8	$\nu(CH) 0+--+$	A'
1765/(1778) ^c	1748/1747/1745/1744	1736	407.6	$\nu(C=O)$	A'
1611	1619/1618/1617	1613	79.9	$\nu(CC) ++++++$	A'
1582	1593/1591/1590/1588	1581	16.0	$\nu(CC) +0--0-$	A'
1490	1506/1504/1493/1489/1487	1482	46.6	$\nu(CC) 00+00-, \delta(CH) +++--$	A'
1458	1464/1463/1461	1452	88.5	$\nu(CC) 00+00-, \delta(CH) 0++0$	A'
1340	1395/1390/1388/1361/1360	1348	131.3	$\nu(C-O), \delta(COH)$	A'
n.obs.	1346/1344/1343	1312	9.6	$\nu(CC) +--+-$	A'
1278	1284/1283/1282/1280	1259	38.9	$\delta(COH), \delta(CH) +0++$	A'
1238/(1245) ^c	1240/1239/1235	1217	63.0	$\nu(CF)$	A'
1184/(1162) ^c	1193/1192/1191/1188	1182	149.7	$\nu(C-O), \delta(COH)$	A'
1155/1149 ^d	1158/1155	1152	26.4	$\delta(CH) +-+-$	A'
1111/1105 ^e	1116/1115/1113/1110/1106/1103	1105	137.0	$\nu(C-O), \delta(CH) 0++-$	A'
n.obs.	1093/1091	1086	14.1	$\nu(C-O), \nu(CC) 0+00-0$	A'
1030/(1059) ^c	1032/1031	1031	22.7	$\delta(ring)_1$	A'
973	n.obs.	974	0.6	$\gamma(CH) +-+0$	A''
952	960	958	1.8	$\gamma(CH) +0--$	A''
865	869	865	2.3	$\gamma(CH) ++0-$	A''
835/(845) ^c	841	832	23.6	$\delta(ring)_2$	A'
n.obs.	n.obs.	788	0.002	$\gamma(C=O)$	A''
755	762/761/760/759/758	756	93.8	$\gamma(CH) +++++$	A''
744	741/740/739/738/734/733	730	12.2	$\nu(C-C), \delta(ring)_3$	A'
696	698/697/696	689	40.8	$\tau(ring)_1$	A''
625	626	623	44.1	$\delta(OCO)$	A'
575	587/586/585	576	69.7	$\tau(C-O)$	A''
552	538	548	17.3	$\delta(ring)_3$	A'
525	528	531	6.8	$\delta(ring)_3, \delta(CF)$	A'
n.obs.	517	516	0.3	$\tau(ring)_2, \gamma(CF)$	A''
n.i.	429 (?)	425	7.6	$\gamma(C-[CCC]), \tau(ring)_3$	A''
n.i.	n.i.	369	2.9	$\delta(ring)_4$	A'
n.i.	n.i.	344	0.03	$\delta(CF)$	A'
n.i.	n.i.	244	0.7	$\gamma(CF)$	A''
n.i.	n.i.	208	3.5	$\gamma(COOH)$	A'
n.i.	n.i.	127	0.8	$w(COOH)$	A''
n.i.	n.i.	28	2.4	$\tau(C-C)$	A''

^a Wavenumbers (ν) in cm^{-1} , calculated infrared intensities (I_{IR}) in $km \cdot mol^{-1}$; n.obs., not observed; n.i., not investigated; ?, uncertain. ^b Approximate description was obtained using the vibrations animation module of Chemcraft [63]; ν , stretching; δ , bending; w , wagging; γ , rocking; τ , torsion; the symbols +, - and 0 placed in front of the $\nu(CC)$, $\nu(CH)$, $\delta(CH)$ and $\gamma(CH)$ ring coordinates indicate the movement (distending, compressing, staying, respectively) of the related bonds, starting from that located *ortho* to the $C=O$ bond of the carboxylic group and proceeding anti-clockwise through the ring. ^c Band due to conformer *cis*-I. ^d Fermi interaction with $2 \times \tau(C-O)$. ^e Fermi interaction with $2 \times \tau(ring)_3$.

Table 4. Experimental (Exp.) and B3LYP/6-311++G(d,p) calculated (Calc.; *cis*-I conformer) infrared spectra of monomeric 2-chlorobenzoic acid, and band assignments ^a.

Exp. Gas Phase	Exp. [17] Ar Matrix, 9 K	Calculated		Approximate Description ^b	Sym- metry
		B3LYP	I IR		
ν	ν	ν	I IR		
3576	3574/3565	3689	103.6	$\nu(\text{O-H})$	A
n.obs.	n.i.	3147	1.7	$\nu(\text{CH})$ 00++	A
3144	n.i.	3134	2.3	$\nu(\text{CH})$ ++00	A
3082	n.i.	3121	8.5	$\nu(\text{CH})$ +- -+	A
3036 (?)	n.i.	3106	2.4	$\nu(\text{CH})$ 0+-0	A
1767	1766	1760	353.6	$\nu(\text{C=O})$	A
1595	1597	1595	33.3	$\nu(\text{CC})$ +--+--	A
1571	n.obs.	1569	14.4	$\nu(\text{CC})$ +0-+0-	A
1477	1481	1467	31.0	$\nu(\text{CC})$ +0- -0+, $\delta(\text{CH})$ +++--	A
1438	1438	1431	25.4	$\nu(\text{CC})$ 0+00-0, $\delta(\text{CH})$ ++++0	A
1334/(1371) ^c	1341	1325	85.0	$\nu(\text{C-O})$, $\delta(\text{COH})$	A
n.obs.	n.obs.	1292	0.2	$\nu(\text{CC})$ +--+--	A
1274	n.obs.	1261	8.8	$\delta(\text{CH})$ +00+	A
1185	1179/1176	1171	156.9	$\delta(\text{COH})$, $\nu(\text{C-C})$, $\delta(\text{CH})$ 00+0	A
~1167	1162	1162	39.8	$\delta(\text{CH})$ +--+	A
1134	1143	1134	48.5	$\delta(\text{CH})$ 0+--	A
1103	1103/1101/1098	1083	85.6	$\nu(\text{C-Cl})$, $\nu(\text{C-O})$	A
n.obs.	n.obs.	1041	14.4	$\delta(\text{ring})_1$	A
1045	1048	1029	130.8	$\delta(\text{ring})_2$	A
n.obs.	n.obs.	984	0.2	$\gamma(\text{CH})$ +--+	A
952	n.obs.	958	2.1	$\gamma(\text{CH})$ +- -+	A
864	n.obs.	867	0.6	$\gamma(\text{CH})$ +--+	A
800	n.obs.	792	2.2	$\gamma(\text{C=O})$	A
782/775 ^d	n.obs.	775	13.2	$\nu(\text{C-C})$, $\delta(\text{ring})_3$, $\delta(\text{OCO})$	A
746	749/747	743	89.6	$\gamma(\text{CH})$ +++++	A
707	686	690	21.8	$\tau(\text{ring})_1$	A
690	n.obs.	677	30.4	$\nu(\text{C-Cl})$, $\delta(\text{OCO})$, $\delta(\text{ring})_3$	A
630	631	627	43.7	$\delta(\text{OCO})$	A
576	n.obs.	575	78.3	$\tau(\text{C-O})$	A
n.i.	n.obs.	526	12.2	$\gamma(\text{C-[CCC]})$	A
n.i.	n.i.	483	2.3	$\tau(\text{ring})_2$	A
n.i.	n.i.	440	3.9	$\delta(\text{ring})_3$	A
n.i.	n.i.	416	6.9	$\tau(\text{ring})_3$	A
n.i.	n.i.	350	1.7	$\delta(\text{ring})_4$	A
n.i.	n.i.	293	0.6	$\delta(\text{C-Cl})$	A
n.i.	n.i.	205	1.8	$\gamma(\text{C-Cl})$	A
n.i.	n.i.	192	0.7	$\gamma(\text{COOH})$	A
n.i.	n.i.	114	0.2	w(COOH)	A
n.i.	n.i.	28	0.8	$\tau(\text{C-C})$	A

^a Wavenumbers (ν) in cm^{-1} , calculated infrared intensities (I^{IR}) in $\text{km}\cdot\text{mol}^{-1}$; n.obs., not observed; n.i., not investigated; ?, uncertain. ^b Approximate description was obtained using the vibrations animation module of Chemcraft [63]; ν , stretching; δ , bending; w, wagging; γ , rocking; τ , torsion; the symbols +, - and 0 placed in front of the $\nu(\text{CC})$, $\nu(\text{CH})$, $\delta(\text{CH})$ and $\gamma(\text{CH})$ ring coordinates indicate the movement (distending, compressing, staying, respectively) of the related bonds, starting from that located *ortho* to the C=O bond of the carboxylic group and proceeding anti-clockwise through the ring. ^c Band due to conformer *cis*-II. ^d Fermi interaction with $\tau(\text{C-O})$ + $\gamma(\text{C-Cl})$.

Table 5. Experimental (Exp.) and B3LYP/6-311++G(d,p) calculated (Calc.) infrared spectra of monomeric 2,6-difluorobenzoic acid, and band assignments ^a.

Exp. Gas Phase ν	Calculated B3LYP ν	I^{IR}	Approximate Description ^b	Sym- metry
3570	3670	93.6	$\nu(O-H)$	A
n.obs.	3143	0.1	$\nu(CH) +++$	A
n.obs.	3138	0.7	$\nu(CH) +0-$	A
3082	3118	3.5	$\nu(CH) +-+$	A
1779	1768	421.1	$\nu(C=O)$	A
1621	1623	121.0	$\nu(CC) +-+-+$	A
1597/1563 ^c	1585	80.2	$\nu(CC) +0-+0-$	A
1472	1466	80.1	$\nu(CC) 0++0- -, \delta(CH) 0++$	A
1472	1461	68.7	$\nu(CC) ++0- -0, \delta(CH) ++0$	A
1363/1320 ^d	1331	115.2	$\nu(C-O), \delta(COH)$	A
n.obs.	1304	0.3	$\nu(CC) +-+-+$	A
1295	1266	27.4	$\nu(CF_2) sym$	A
1244/1238 ^e	1230	65.5	$\delta(CH) +++$	A
1182	1179	163.4	$\delta(COH), \nu(C-O)$	A
1150	1153	0.9	$\delta(CH) +-+$	A
1094	1090	109.6	$\nu(C-O), \delta(CH) +0-$	A
1054	1050	24.9	$\delta(ring)_1$	A
1020	1002	146.0	$\nu(CF_2) asym$	A
964	956	0.5	$\gamma(CH) +-+$	A
n.obs.	874	0.1	$\gamma(CH) +0-$	A
798	793	51.2	$\gamma(CH) +++, \gamma(C=O)$	A
786	784	10.3	$\nu(C-C), \delta(ring)_2$	A
763	763	19.6	$\gamma(C=O), \gamma(CH) +++$	A
697	700	44.55	$\tau(ring)_1$	A
683	684	21.7	$\delta(OCO)$	A
611 (?)	594	7.0	$\tau(ring)_3, \gamma(CF_2) asym$	A
581	588	86.9	$\tau(C-O)$	A
n.obs.	573	5.2	$\tau(ring)_2$	A
566	554	41.0	$\delta(OCO), \delta(ring)_3$	A
n.i.	509	2.4	$\delta(CF_2) asym$	A
n.i.	473	3.0	$\tau(ring)_3$	A
n.i.	400	2.1	$\delta(ring)_4$	A
n.i.	385	1.9	$\gamma(C-[CCC])$	A
n.i.	283	0.8	$\delta(CF_2) sym$	A
n.i.	236	0.02	$\gamma(CF_2) asym$	A
n.i.	218	0.9	$\gamma(CF_2) sym$	A
n.i.	165	1.4	w(COOH)	A
n.i.	94	2.3	$\gamma(COOH)$	A
n.i.	44	1.9	$\tau(C-C)$	A

^a Wavenumbers (ν) in cm^{-1} , calculated infrared intensities (I^{IR}) in $km\cdot mol^{-1}$; n.obs., not observed; n.i., not investigated; ?, uncertain. ^b Approximate description was obtained using the vibrations animation module of Chemcraft [63]; ν , stretching; δ , bending; w, wagging; γ , rocking; τ , torsion; the symbols +, - and 0 placed in front of the $\nu(CC)$, $\nu(CH)$, $\delta(CH)$ and $\gamma(CH)$ ring coordinates indicate the movement (distending, compressing, staying, respectively) of the related bonds, starting from that located *ortho* to the C=O bond of the carboxylic group and proceeding anti-clockwise through the ring. ^c Fermi interaction with $2 \times \{\gamma(CH) +++, \gamma(C=O)\}$. ^d Fermi interaction with $2 \times \delta(OCO)$. ^e Fermi interaction with $2 \times \{\tau(ring)_3, \gamma(CF_2) asym\}$.

Table 6. Experimental (Exp.) and B3LYP/6-311++G(d,p) calculated (Calc.) infrared spectra of monomeric 2-chloro-6-fluorobenzoic acid, and band assignments ^a.

Exp. Gas Phase ν	Exp. (This Work; Also [58]) Xe Matrix, 20 K ν	Calc. B3LYP. ν	I_{IR}	Approximate Description ^b	Sym- metry
3566	3542/3522/3519/3512/3507	3662	87.5	$\nu(O-H)$	A
n.obs.	n.obs.	3141	0.5	$\nu(CH) +++$	A
n.obs.	n.obs.	3137	0.4	$\nu(CH) +0-$	A
3083	2976	3116	3.6	$\nu(CH) +++$	A
1779	1770	1776	356.3	$\nu(C=O)$	A
1602	1611	1607	67.0	$\nu(CC) +++++$	A
1580	1581/1579	1575	72.6	$\nu(CC) +0+0-$	A
1455	1464	1450	35.2	$\nu(CC) +0- -0+, \delta(CH) +- -$	A
1455	1457/1454	1446	88.1	$\nu(CC) ++0- -0, \delta(CH) ++0$	A
1362/1331 ^c	1376/1371/1364/1356/1332/1327	1324	96.3	$\nu(C-O), \delta(COH)$	A
1300	1301/1291	1291	1.5	$\nu(CC) +-+--$	A
1258	1258/1255	1239	64.7	$\nu(CF), \delta(CH) +++$	A
1195	1203/1198/1194	1192	70.9	$\delta(COH), \delta(CH) +00$	A
1175	1178/1173/1172/1169	1167	117.9	$\nu(C-O), \delta(COH), \delta(CH) +++$	A
1151	1149	1142	26.9	$\nu(CCl), \delta(CH) 0+0$	A
1093	1101/1098/1096/1094	1093	90.3	$\nu(C-O), \delta(ring)_1, \delta(CH) +0+$	A
1052	1055/1054/1052	1049	27.7	$\delta(ring)_2$	A
964	n.obs.	956	0.9	$\gamma(CH) +++$	A
909	912/910/908/907	887	103.8	$\nu(CCl), \nu(CF)$	A
n.obs.	n.obs.	880	0.4	$\gamma(CH) +0-$	A
786	792/791/788/785	778	46.1	$\gamma(CH) +++, \gamma(C=O)$	A
779	777	768	11.2	$\nu(C-C), \delta(OCO)$	A
779	767	760	26.0	$\gamma(C=O), \gamma(CH) +++,$	A
737	735	715	32.5	$\tau(ring)_1$	A
662	661/659	653	34.0	$\delta(OCO)$	A
582	583/580/575/572	591	82.9	$\tau(C-O)$	A
n.obs.	n.obs.	565	0.6	$\tau(ring)_2$	A
n.i.	569/567	554	5.2	$\tau(ring)_3$	A
n.i.	545/543/542	538	23.7	$\delta(ring)_3$	A
n.i.	469	463	4.8	$\delta(ring)_4, \tau(C-O)$	A
n.i.	n.i.	418	4.4	$\delta(CFCl) asym$	A
n.i.	n.i.	388	0.3	$\gamma(C-[CCC])$	A
n.i.	n.i.	343	1.2	$\delta(ring)_4$	A
n.i.	n.i.	230	0.5	$\delta(CFCl) sym$	A
n.i.	n.i.	225	0.3	$\gamma(CF)$	A
n.i.	n.i.	174	2.0	$\gamma(CCl)$	A
n.i.	n.i.	141	0.4	$w(COOH)$	A
n.i.	n.i.	85	1.6	$\gamma(COOH)$	A
n.i.	n.i.	24	2.3	$\tau(C-C)$	A

^a Wavenumbers (ν) in cm^{-1} , calculated infrared intensities (I_{IR}) in $km\cdot mol^{-1}$; n.obs., not observed; n.i., not investigated; ?, uncertain. ^b Approximate description was obtained using the vibrations animation module of Chemcraft [63]; ν , stretching; δ , bending; w , wagging; γ , rocking; τ , torsion; the symbols +, - and 0 placed in front of the $\nu(CC)$, $\nu(CH)$, $\delta(CH)$ and $\gamma(CH)$ ring coordinates indicate the movement (distending, compressing, staying, respectively) of the related bonds, starting from that located *ortho* to the C=O bond of the carboxylic group and proceeding anti-clockwise through the ring. ^c Fermi interaction with $2 \times \delta(OCO)$.

Table 7. Experimental (Exp.) and B3LYP/6-311++G(d,p) calculated (Calc.) infrared spectra of monomeric 2,6-dichlorobenzoic acid, and band assignments ^a.

Exp. Gas Phase ν	Calculated B3LYP		Approximate Description ^b	Sym- metry
	ν	I IR		
3564	3660	86.1	$\nu(\text{O-H})$	A'
3130	3141	1.0	$\nu(\text{CH})$ +++	A'
n.obs.	3137	0.1	$\nu(\text{CH})$ +0-	A''
3073	3114	3.7	$\nu(\text{CH})$ +-+	A'
1780	1779	330.5	$\nu(\text{C=O})$	A'
1587	1587	33.6	$\nu(\text{CC})$ +---+	A'
1567	1563	49.7	$\nu(\text{CC})$ +0+0-	A''
1455 (?)	1436	5.2	$\nu(\text{CC})$ +0- -0+, $\delta(\text{CH})$ +0-	A'
1434	1429	79.6	$\nu(\text{CC})$ 0+00-, $\delta(\text{CH})$ +++	A''
1349/1297 ^c	1322	70.9	$\nu(\text{C-O})$, $\delta(\text{COH})$	A'
1266	1277	2.4	$\nu(\text{CC})$ +-+--	A''
1192	1193	25.0	$\delta(\text{CH})$ +0+	A''
1192	1189	130.9	$\delta(\text{COH})$, $\delta(\text{ring})$ ₁	A'
1159	1153	7.3	$\delta(\text{CH})$ 0+0	A''
1127	1120	172.4	$\nu(\text{C-O})$, $\delta(\text{COH})$, $\nu(\text{CCl}_2)$ sym, $\delta(\text{CH})$ +0-	A'
1090/1083 ^d	1073	9.1	$\nu(\text{CCl}_2)$ sym	A'
1047	1043	24.0	$\delta(\text{ring})$ ₂	A'
n.obs.	967	1.0	$\gamma(\text{CH})$ +-+	A'
n.obs.	886	0.002	$\gamma(\text{CH})$ +0-	A''
804	785	37.6	$\nu(\text{CCl}_2)$ asym, $\gamma(\text{C=O})$	A''
786	768	26.5	$\nu(\text{C-C})$, $\gamma(\text{CH})$ +++	A'
777	766	25.5	$\gamma(\text{CH})$ +++	A'
747/740 ^e	746	89.6	$\gamma(\text{C=O})$, $\nu(\text{CCl}_2)$ asym	A''
727	729	15.4	$\tau(\text{ring})$ ₁	A'
650	641	35.8	$\delta(\text{OCO})$	A'
582	597	71.7	$\tau(\text{C-O})$	A''
n.obs.	567	0.3	$\tau(\text{ring})$ ₂	A
n.i.	518	0.3	$\tau(\text{ring})$ ₃	A''
n.i.	454	18.2	$\nu(\text{C-C})$, $\nu(\text{CCl}_2)$ sym	A'
n.i.	432	1.6	$\delta(\text{ring})$ ₃	A''
n.i.	382	0.3	$\gamma(\text{CCl}_2)$ sym	A'
n.i.	376	2.9	$\delta(\text{CCl}_2)$ asym	A''
n.i.	313	0.5	$\delta(\text{ring})$ ₄	A'
n.i.	195	0.001	$\gamma(\text{CCl}_2)$ asym	A''
n.i.	185	0.01	$\delta(\text{CCl}_2)$ sym	A'
n.i.	164	2.9	$\gamma(\text{C-[CCC]})$	A'
n.i.	135	0.2	w(COOH)	A''
n.i.	74	0.8	$\gamma(\text{COOH})$	A'
n.i.	38	2.1	$\tau(\text{C-C})$	A''

^a Wavenumbers (ν) in cm^{-1} , calculated infrared intensities (I^{IR}) in $\text{km}\cdot\text{mol}^{-1}$; n.obs., not observed; n.i., not investigated; ?, uncertain. ^b Approximate description was obtained using the vibrations animation module of Chemcraft [63]; ν , stretching; δ , bending; w, wagging; γ , rocking; τ , torsion; the symbols +, - and 0 placed in front of the $\nu(\text{CC})$, $\nu(\text{CH})$, $\delta(\text{CH})$ and $\gamma(\text{CH})$ ring coordinates indicate the movement (distending, compressing, staying, respectively) of the related bonds, starting from that located *ortho* to the C=O bond of the carboxylic group and proceeding anti-clockwise through the ring. ^c Fermi interaction with $2 \times \delta(\text{OCO})$. ^d Fermi interaction with $\tau(\text{ring})_2 + \tau(\text{ring})_3$. ^e Fermi interaction with $2 \times \delta(\text{CCl}_2)$ asym.

According to the performed calculations, **benzoic acid** has 33 vibrations with frequencies lying in the studied spectral region ($4000\text{--}450\text{ cm}^{-1}$), from which 26 are assigned in the present study. The 7 non-assigned vibrations have very low intensity ($\leq 0.6\text{ km}\cdot\text{mol}^{-1}$; see Table 2) and have never been observed experimentally with exception of the $\delta(\text{CH})$ 0+-+0 mode (for the adopted notation of the vibrational modes see footnote *b* of Table 2) that has been tentatively assigned to a band at 1099 cm^{-1} in the IR spectrum of jet-cooled benzoic acid [56] ($1110/1100\text{ cm}^{-1}$ in the Ar matrix spectrum of the compound [54,55]). In the gas phase spectrum of BA investigated in the present study (where

the band profiles are, as expected, considerably broader than those recorded for the jet-cooled or matrix-isolated compound), the band ascribable to this vibration is hidden by the more intense band due to an essentially delocalized vibration with a significant contribution of the $\nu(\text{C-O})$ stretching coordinate (1095 cm^{-1} ; predicted at 1090 cm^{-1} with an intensity of $44.6\text{ km}\cdot\text{mol}^{-1}$). In the work on jet-cooled benzoic acid [56] only 19 modes of the molecule were assigned; moreover, the description of the modes was given in a very general way. In the matrix isolation investigations [54,55], the number of modes assigned within the $4000\text{--}450\text{ cm}^{-1}$ region is equal to the one achieved in the present work (plus the above mentioned $\delta(\text{CH})\ 0+\text{--}+0$ mode), and the observed frequencies in the two studies are within the expected agreement. However, the assignments done in the matrix isolation studies were in large amount based on low-level AM1 semi-empirical calculated spectral data. Therefore, the present study strongly improves the description of the infrared spectrum of gaseous benzoic acid.

The spectrum of BA is dominated by 6 intense bands which are ascribable to vibrations whose major contributors are associated with the polar carboxylic group, $\nu(\text{O-H})$ (3578 cm^{-1}), $\nu(\text{C=O})$ (1765 cm^{-1}), $\nu(\text{C-O})$ ($1354, 1078\text{ cm}^{-1}$) and $\delta(\text{COH})$ ($1354, 1184/1177\text{ cm}^{-1}$), as it could be anticipated. The band at 714 cm^{-1} is assigned to the $\gamma(\text{CH})$ all-in-phase out-of-the-plane bending mode ($\gamma(\text{CH})\ +++++$, according to the notation adopted in the present study), having also a smaller contribution from the $\gamma(\text{C=O})$ coordinate. The calculated frequencies and relative intensities for these modes agree very well with the experimentally observed values (see Figure 13 and Table 2). The remaining two vibrations belonging to the carboxylic acid group which are expected to absorb in the studied spectral region give also rise to bands of considerable intensity, at 631 ($\delta(\text{OCO})$) and 574 ($\tau(\text{C-O})$) cm^{-1} . The aromatic ring modes are also well-described by the calculations both, in terms of frequencies and intensities (see Figure 13 and Table 2), so that their assignment could also be made in a straightforward manner.

There are a few bands in the experimental spectra shown in Figure 13 that deserve here an additional comment. The first is observed at 1388 cm^{-1} , and is probably due to the $2 \times \tau(\text{ring})_1$ overtone enhanced by Fermi interaction with the fundamental mode assigned to the mixed $\{\nu(\text{C-O}), \delta(\text{COH})\}$ mode. The second is observed at 560 cm^{-1} and can be tentatively attributed to the combination tone $\tau(\text{ring})_3 + \omega(\text{COOH})$ (calculated value: $404 + 155 = 559\text{ cm}^{-1}$). The last band is observed at 817 cm^{-1} , and shall be ascribed to an unknown impurity, since it is absent in the spectra of both the jet-cooled and matrix-isolated monomer of benzoic acid and it is also not present in the spectrum of gaseous benzoic acid available in the Wiley Spectral Database [64].

The band contour analysis proved to be particularly interesting in the $800\text{--}450\text{ cm}^{-1}$ range, where bands predicted to exhibit different profiles (A, AB, B and C) are observed. As shown in Figure 14, the profiles of the experimental bands fit nicely the predicted contour types, giving additional support to the proposed assignments.

In the case of **2-fluorobenzoic acid**, from the 32 vibrations predicted by the calculations to absorb in the investigated spectral region ($4000\text{--}450\text{ cm}^{-1}$), 27 were assigned to bands observed in the experimental spectra (see Table 3). Three of the 5 modes not assigned have very low predicted IR intensities (less than $\sim 1\text{ km}\cdot\text{mol}^{-1}$), while the remaining two are expected to give rise to bands of small intensity at about the positions of the very intense bands of the $\{\nu(\text{C-O}), \delta(\text{COH})\}$ (1340 cm^{-1}) and $\{\nu(\text{C-O}), \delta(\text{CH})\ 0++\text{--}\}$ ($1111/1105\text{ cm}^{-1}$) modes, and are then buried underneath those bands.

Like for benzoic acid, the infrared spectrum of 2FBA is dominated by intense bands originated in the carboxylic acid substituent, e.g., $\nu(\text{O-H})$ (3576 cm^{-1}), $\nu(\text{C=O})$ (1765 cm^{-1}), $\nu(\text{C-O})$ ($1340, 1184, 1111/1105\text{ cm}^{-1}$), $\delta(\text{COH})$ ($1340, 1184\text{ cm}^{-1}$), and $\tau(\text{C-O})$ (575 cm^{-1}). Also, as with BA, the $\gamma(\text{CH})$ all-in-phase out-of-the-plane bending mode ($\gamma(\text{CH})\ +++++$) in 2FBA gives rise to an intense band at 755 cm^{-1} . All these bands are well predicted by the calculations (see Figure 13 and Table 3).

The $\nu(\text{CF})$ stretching mode is assigned to the band at 1238 cm^{-1} , in fairly good agreement with the predicted value (1217 cm^{-1}). As suggested in [16], the in-plane ($\delta(\text{CF})$) and out-of-the-plane ($\gamma(\text{CF})$) bending modes give some contribution to the vibrations predicted at 531 cm^{-1} (observed at 525 cm^{-1}) and 516 cm^{-1} (with a very low predicted intensity and not observed experimentally), respectively, which are, however, better described as skeletal ring deformation modes, due to major

contributions from the ring coordinates. The $\delta(\text{CF})$ and $\gamma(\text{CF})$ modes have been reassigned to the calculated vibrations with frequencies at 344, and 244 cm^{-1} , respectively, rectifying the approximate description given previously for these modes as ring skeletal deformations [16].

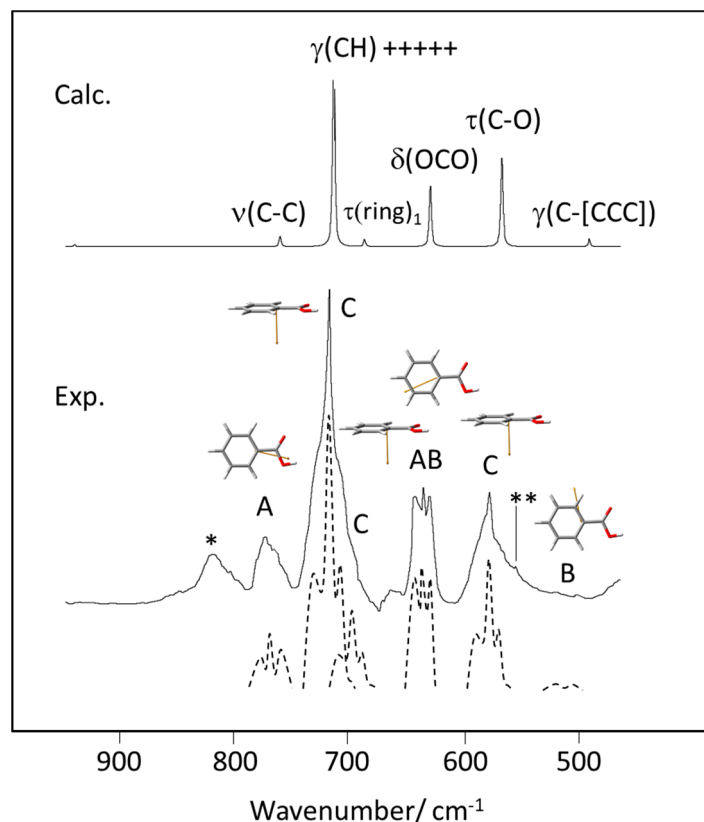


Figure 14. 900–450 cm^{-1} spectral region of the experimental (Exp.) gas phase infrared spectrum of benzoic acid, with indication of the band contour type (A, B, AB, C). The dashed figures are approximate deconvolutions of the experimental bands, drawn with increased resolution to highlight the characteristic bands profiles. The calculated (Calc.) spectrum is shown at the top of the figure, with indication of the band assignments. The drawings of the molecule show the the transition dipole moments (in orange color) for the different vibrations (see Figure 12 for orientation of the principal axes of inertia of the molecule). *-band due to an unknown impurity; **-band due to the combination tone $\tau(\text{ring})_3 + \nu(\text{COOH})$ (calculated values: $404 + 155 = 559 \text{ cm}^{-1}$ (see Table 2).

For 2FBA, besides the lowest energy *cis*-II conformer, the higher energy *cis*-I conformer shall also contribute to the spectrum. As mentioned before, the infrared spectra of the two conformers are predicted to be very similar and in the gas phase spectrum the evidence of *cis*-I can only be clearly noticed in a few spectral regions, where this conformer gives rise to intense bands at positions sufficiently distinct from the corresponding bands of the dominant *cis*-II conformer. The bands of *cis*-I predicted to have a large intensity and obeying the condition of not being too close in frequency to those of *cis*-II are calculated at 3691 ($\nu(\text{O-H})$), 1760 ($\nu(\text{C=O})$), 1226 ($\nu(\text{CF})$), 1175 ($\{\nu(\text{C-O}), \delta(\text{COH})\}$), 1048 ($\delta(\text{ring})_1$), 841 ($\delta(\text{ring})_2$) and 557 ($\tau(\text{C-O})$) cm^{-1} . In the case of the $\nu(\text{O-H})$ and $\tau(\text{C-O})$ modes, no clear bands due to *cis*-I could be identified, though the bands assigned to these modes are considerably asymmetric, with a more extended wing in the side where the bands due to *cis*-I are expected (respectively for higher and lower frequencies). In all the other cases, the bands due to the *cis*-I conformer are clearly seen in the experimental spectrum, at frequencies matching well the predicted values (1778, 1245, 1162, 1059 and 845 cm^{-1} ; see also Figure 13 and Table 3).

The presence of two conformers at equilibrium in the gas phase occurs also for **2-chlorobenzoic acid**. Being nearly degenerate, the expected relative population of the two conformers is determined

by their symmetry. As mentioned in Section 3.1, these considerations lead to an expected population of the slightly more stable *cis*-I conformer of 2CBA that is approximately twice that of the less stable *cis*-II conformer. However, compared to 2FBA, the spectra of the two *cis* conformers of 2CBA are considerably more similar, so that in this case the band overlapping is more extensive. In fact, only one band in the experimental gas phase IR spectrum of 2CBA could be clearly assigned to the *cis*-II conformer. This band is observed at 1371 cm^{-1} , and is ascribable to the $\{\nu(\text{C-O}), \delta(\text{COH})\}$ mode, in fairly good agreement with the calculated frequency (1344 cm^{-1}).

As for BA and 2FBA, the most intense bands in the infrared spectrum of 2CBA are due to vibrations mostly localized in the carboxylic acid fragment, $\nu(\text{O-H})$ (3576 cm^{-1}), $\nu(\text{C=O})$ (1767 cm^{-1}), $\nu(\text{C-O})$ ($1334, 1103, 1083\text{ cm}^{-1}$), $\delta(\text{COH})$ ($1334, 1185\text{ cm}^{-1}$) and $\tau(\text{C-O})$ (576 cm^{-1}), plus the $\gamma(\text{CH})$ all-in-phase out-of-the-plane bending mode ($\gamma(\text{CH})$ +++) (746 cm^{-1}). The stretching of the *ortho* C-Cl bond contributes significantly to two bands, being strongly mixed with the $\nu(\text{C-O})$ coordinate in the vibration giving rise to the intense band at 1103 cm^{-1} (predicted at 1083 cm^{-1}), and with both the $\delta(\text{OCO})$ and $\delta(\text{ring})_3$ coordinates in the vibration giving rise to the band observed at 690 cm^{-1} (predicted at 677 cm^{-1}). The in-plane and out-of-the-plane bending CCl vibrations are predicted to originate bands of low intensity outside the investigated spectral region (respectively at 293 and 205 cm^{-1} ; see Table 4).

As a whole, 25 from the 27 fundamental vibrations of 2CBA predicted to absorb above 450 cm^{-1} with an intensity larger than $2.5\text{ km}\cdot\text{mol}^{-1}$ have been assigned in the present investigation, the two non-assigned modes corresponding to low-intensity vibrations whose bands are hidden by intense bands due to other closely located in frequency modes, specifically $\{\nu(\text{C-O}), \delta(\text{COH})\}$ and $\tau(\text{C-O})$ (see Figure 13 and Table 4). In the matrix isolation study of 2CBA [17] only 14 modes were assigned.

The general spectroscopic pattern described above for BA, 2FBA and 2CBA in relation to the dominance of the bands originated in the carboxylic group regarding intensities is also observed for the studied **di-substituted compounds**. For both 26DFBA and 26DCBA no previous vibrational data have been reported. In here, 24 from 25 fundamental vibrations with intensities over $1\text{ km}\cdot\text{mol}^{-1}$ predicted to occur in the studied spectral region ($4000\text{--}550\text{ cm}^{-1}$) were assigned in the spectrum of 26DFBA, while for 26DCBA all 23 vibrations matching these criteria were ascribed to bands in the experimental spectrum (Tables 5 and 7). The symmetric stretching vibration of the *ortho* fluorine substituents in 26DFBA is observed at 1295 cm^{-1} as a mid intensity band (predicted at 1266 cm^{-1}), while the anti-symmetric mode gives rise to an intense band at 1020 cm^{-1} (predicted at 1002 cm^{-1}). As for the mono-fluoro-substituted compound, the CF stretching frequencies in 26DFBA are underestimated by ca. 20 cm^{-1} by the calculations upon scaling. Interestingly, the unscaled calculated frequencies almost exactly match the experimental ones in both molecules ($1294, 1024$ versus $1295, 1020\text{ cm}^{-1}$ for 26DFBA, and 1244 vs. 1238 cm^{-1} for 2FBA), and the same trends are also observed for 2C6FBA (1266 cm^{-1} , calculated unscaled versus 1258^{-1} , observed versus 1239 cm^{-1} , calculated scaled; see Table 6). The in-plane and out-of-the-plane CF_2 bending vibrations in 26DFBA as well as the CCl_2 bending modes in 26DCBA are predicted to absorb below 550 cm^{-1} , i.e., outside the studied spectral region. All bands associated to these vibrations are predicted to have very low intensity ($< 3\text{ km}\cdot\text{mol}^{-1}$; see Tables 5 and 7).

The infrared spectrum of 2F6CBA isolated in a cryogenic Xe matrix has been reported before [58] and assigned with help of calculated data obtained at the B3LYP/6-311++G(d,p) level of theory. The interpretation of the gas phase spectrum of the compound closely follows that made in the matrix isolation study, though a few bands are reassigned, in particular the stretching of the exocyclic C-C bond, now assigned to the band at 779 cm^{-1} (which has also contributions from the $\delta(\text{OCO})$, $\gamma(\text{C=O})$ and $\gamma(\text{CH})$ +++ coordinates; see Table 6). This band was previously mis-assigned to the stretching vibration of the CF bond, which is now reassigned to the band at 1258 cm^{-1} that appears at approximately the same frequency as the identical vibration in 2FBA (1238 cm^{-1}). The νCCl stretching (not assigned in the matrix isolation study) is ascribed to the experimentally observed band at 1151 cm^{-1} , in good agreement with the calculated data (1149 cm^{-1}) and also not very much different from the frequency of the νCCl mode in 2CBA (1103 cm^{-1} ; calculated: 1083 cm^{-1} ; see Table 4). Both νCF and νCCl coordinates also

contribute (in opposition of phase) to the intense band observed at 909 cm^{-1} . Another way to describe the vibrations of the CF and CCl bonds is to state that the two stretchings combine anti-symmetrically to give rise to the band at 909 cm^{-1} , while the putative symmetric combination is replaced by vibrations where each one of the coordinates combine with $\delta(\text{CH})$ ring bending modes (see Table 6). According to the calculations, the in-plane bending associated with the CF and CCl bonds also combine to give rise to symmetric (predicted at 230 cm^{-1}) and anti-symmetric vibrations (predicted at 418 cm^{-1}). Interestingly, the out-of-plane deformations are predicted to be independent from each other. For 2C6FBA, all 23 vibrations predicted to absorb in the studied spectral region with an intensity $>1\text{ km}\cdot\text{mol}^{-1}$ are here assigned to experimental bands in the gas phase spectrum of the compound.

3.4. Photochemistry under Matrix Isolation Conditions

Two of the compounds were selected as targets for photochemical experiments, 2FBA and 2C6FBA. In these experiments, monomers of the compounds were isolated in cryogenic Ar (2FBA) or Xe (2C6FBA) matrices and subjected to narrowband UV ($\lambda \geq 235\text{ nm}$) irradiation. The spectra of the as-deposited matrices are identical to those reported before [16,58]. Upon irradiation, new bands appeared in the infrared spectra, which are due to the formed photoproducts, while concomitantly the bands of the reactant decrease of intensity. Figure 15 summarizes the results obtained for 2FBA, and Figures 16 and 17 those found for 2C6FBA.

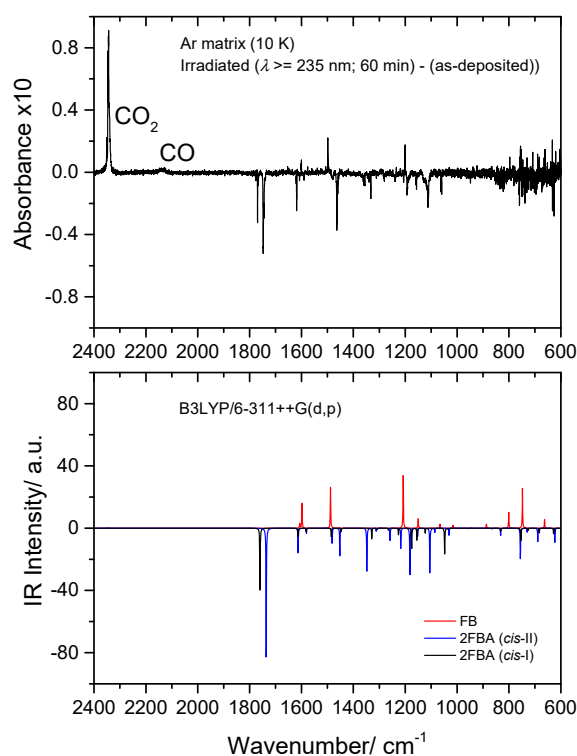


Figure 15. *Top:* $2400\text{--}600\text{ cm}^{-1}$ region of the difference IR spectrum: irradiated Ar matrix of 2-fluorobenzoic acid (2FBA) minus as-deposited matrix. *Bottom:* Simulated difference spectrum based on the B3LYP/6-311++G(d,p) calculated IR spectra of 2FBA (*cis-I* and *cis-II* conformers; bands pointing down) and the observed photoproducts: CO_2 , CO, and fluorobenzene (FB) (bands pointing up). The calculated wavenumbers were scaled by 0.978, and the calculated intensities were multiplied by arbitrary factors in order to fit better the observed spectrum (in a ratio of $\sim 2:1:3$, 2FBA *cis-II*:2FBA *cis-I*:FB).

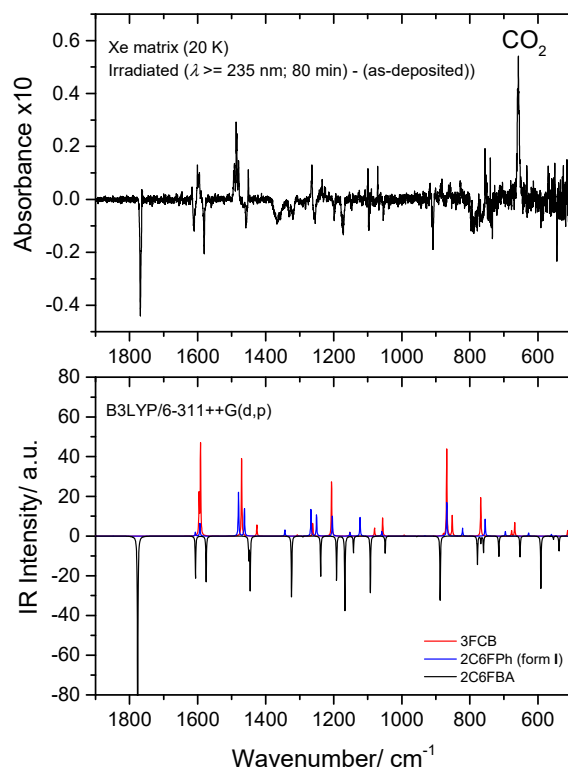


Figure 16. Top: Low frequency region of the difference IR spectrum: irradiated Xe matrix of 2-chloro-6-fluorobenzoic acid (2C6FBA) *minus* as-deposited matrix. Bottom: Simulated difference spectrum based on the B3LYP/6-311++G(d,p) calculated IR spectra of 2C6FBA (*cis* conformer; bands pointing down) and the observed photoproducts: CO₂, 2-chloro-6-fluorophenol (2C6FPh) and 3-fluoro-chlorobenzene (3FCB) (bands pointing up). The calculated wavenumbers were scaled by 0.978, and the calculated intensities of the reactant and of the different photoproducts were multiplied by arbitrary factors in order to fit better the observed spectrum (in a ratio of ~3:2:1, 2C6FBA:3FCB:2C6FPh).

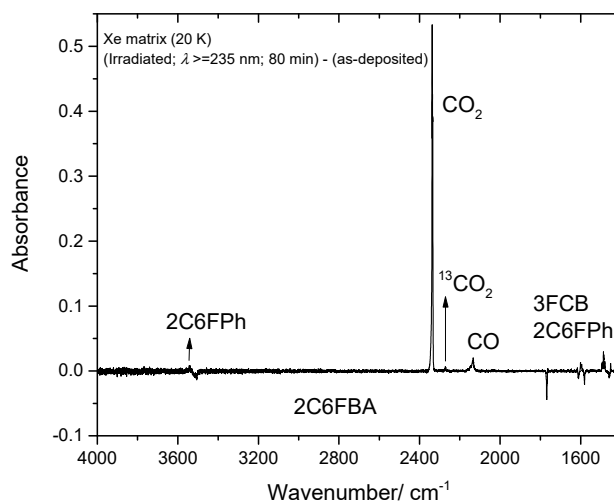


Figure 17. High frequency region of the difference IR spectrum: irradiated Xe matrix of 2-chloro-6-fluorobenzoic acid (2C6FBA) *minus* as-deposited matrix. Bands that arise due to the photoproducted CO₂ (including its ¹³C isotopologue), CO, 2-chloro-6-fluorophenol (2C6FPh) and 3-fluoro-chlorobenzene (3FCB) are pointing up, while bands due to the reactant (*cis* conformer) are pointing down. The lower frequency region shown in this figure (<2000 cm⁻¹) was included to allow a faster comparison of the intensities of the bands with those presented in Figure 16.

For both compounds characteristic bands of CO₂ and CO were observed in the spectra of the photolysed matrices, indicating that decarboxylation and decarbonylation reactions take place upon UV irradiation, decarboxylation being the major process. In the case of 2C6FBA, the decarboxylation:decarbonylation reaction branch is estimated to be ~2:1, based on the relative intensities of the bands due to the two photoproducts. For this compound, both photoproducts accompanying CO₂ and CO, i.e., 3-fluoro-chlorobenzene and 2-chloro-6-fluorophenol (2C6FPh), respectively, were observed. The photoreactions in the case of 2FBA appear to be less effective, and the decarboxylation strongly dominates, precluding experimental detection of 2-fluorophenol, the product that is expected to be formed together with CO. It is also interesting to note that 2-chloro-6-fluorophenol, which has two conformers differing in orientation of the phenolic OH group, is produced in the lowest energy conformer I, where the OH group is intramolecularly H-bonded to the fluorine *ortho* substituent. Also, it is worth noticing that in the case of 2FBA the two conformers trapped in the cryogenic matrix (*cis*-I and *cis*-II) seem to react at nearly equal rates.

Both photodecarboxylation and photodecarbonylation are commonly observed reactions of carboxylic acids, and have been described for this type of compounds isolated in cryogenic matrices and subjected to UV irradiation [65,66]. General mechanistic insights on these processes escape the scope of the present article and can be found in [65–69]. Nevertheless, one shall point out that the recombination of radical species produced in the excited states after UV irradiation, which have been described as the primary photoproducts of UV-photolysis of carboxylic acids as a result of the cleavage of the C-O or C-C bond alpha to the carbonyl, is particularly easy in the solid matrix media, due to the cage-confined nature of the processes. Under these conditions, stable species like CO₂ and CO shall be promptly formed, as observed. In addition, quantum chemical calculations (performed at the CASSCF level of theory) on benzoic acid [69] have shown that the transition states for cleavage of those bonds have the carboxylic group and the aromatic ring perpendicular to each other. This may explain, at least partially, the observed larger efficiency of the photoreactions observed for 2C6FBA (whose molecules have these two groups almost perpendicular in the starting geometry) compared to 2FBA (where the two groups are in the same plane).

It shall also be noticed that a previous photochemical investigation of matrix-isolated 2CBA has been reported [17]. In that study, monomeric 2CBA isolated in a low-temperature (9 K) argon matrix was subjected to irradiation using a super-high-pressure mercury broad-band source assembled with a short-wavelength filter ($\lambda > 240$ nm). The authors were able to induce conversion of the initially deposited *cis* conformers into the high-energy *trans* conformers, which were then found to spontaneously convert back to the initial forms by quantum mechanical tunneling (as it has already been mentioned in this article; see Section 3.1). However, no information about simultaneous occurrence of any photolysis reaction has been provided.

3.5. Structural Characteristics of the Crystalline Materials

The crystal structures for all the compounds investigated here have been previously reported [20–24,30]. Table 8 summarizes the crystal data, while Figures 18–20 depict the crystal packing schemes observed for the different compounds. All compounds except 26DCBA crystallize in the monoclinic system, the crystals belonging to the P2₁/c (or P2₁/n) space group N° 14 (BA, and all fluoro-containing compounds) or to the closely related C2/c space group N° 15 (2CBA). The crystals of the dichloro-substituted compound are triclinic, space group P1, and also differs in the number of non-equivalent molecules in the unit cell (*Z'*), which is 2, instead of 1 as for all other compounds. The fundamental dissimilarity of the crystal of 26DCBA compared to those of the remaining compounds can be ascribed to the different packing constraints imposed by the favored nearly perpendicular arrangement of the carboxylic acid substituent and the aromatic ring in the 26DCBA molecules (see Section 3.1). The average value of the angle between the planes of the carboxylic acid substituent and the aromatic ring (φ) in 26DCBA is ~85°, slightly smaller than in the isolated molecule (90.0°), but much larger than in the remaining studied compounds. For all compounds, the monomeric units

exist in a carboxylic acid *cis* conformation and are associated in centrosymmetric dimers connected by two O-H...O intermolecular hydrogen bonds. In the BA crystal, the molecules are planar, as for the isolated molecule. The crystals of the two mono-substituted compounds (2FBA and 2CBA) show molecules slightly non-planar: for 2CBA, the angle between the carboxylic acid substituent and the aromatic ring is $\sim 14^\circ$, very much similar to that predicted for the most stable conformer of the molecule, *cis*-I (18.0° ; see Figure 1); for 2FBA, this angle is $\sim 10^\circ$, while the minimum energy *cis* structures of the isolated molecule are planar. Interestingly, 2FBA is the only compound among all those studied here where the conformer selected to form the crystal (*cis*-I) is not the most stable conformer found for the isolated molecule (*cis*-II, as discussed in Section 3.1). Both 26DFBA and 2C6FBA crystals are constituted by non-planar molecules where the φ angle is somewhat smaller than in the corresponding minimum energy structures of the isolated molecules ($\sim 34^\circ$ vs. 47.1° in the case of 26DFBA, and $\sim 46^\circ$ vs. 67.6° , for 2C6FBA). In practical terms, the trends described above lead to geometries adopted by the different *ortho* halogeno-substituted benzoic acids molecules in crystalline phase that are more similar to each other than for the isolated molecules, this being particularly noticeable for the compounds crystallizing in the monoclinic system.

Table 8. Summary of the data for the crystals of the studied compounds ^a.

	BA	2FBA	26DFBA	2CBA	26DCBA	2C6FBA
	[30]	[20]	[22]	[21]	[23]	[24]
Crystal system	Monoclinic	Monoclinic	Monoclinic	Monoclinic	Triclinic	Monoclinic
Space group	P2 ₁ /c	P2 ₁ /n	P2 ₁ /c	C2/c	P $\bar{1}$	P2 ₁ /c
Z	4	4	4	8	4	4
Z'	1	1	1	1	2	1
a/Å	5.4996(5)	6.5523(13)	3.6517(4)	14.6382(16)	7.2678(9)	3.7655(2)
b/Å	5.1283(5)	3.7524(8)	14.1214(15)	3.8142(6)	9.8543(8)	13.9660(7)
c/Å	21.950(2)	25.021(5)	12.2850(13)	23.812(3)	11.8290(11)	13.2300(7)
$\alpha/^\circ$	90	90	90	90	95.000(7)	90
$\beta/^\circ$	97.37(1)	92.82(3)	95.651(3)	101.146(11)	104.262(10)	98.034(3)
$\gamma/^\circ$	90	90	90	90	102.128(8)	90
Cell volume/Å ³	614(1)	614.5(2)	630.42(12)	1304.4(3)	794.07(14)	688.92(6)
Density	1.322	1.515	1.666	1.544	1.598	1.683
Conformer	<i>cis</i>	<i>cis</i> -I	<i>cis</i>	<i>cis</i> -I	<i>cis</i>	<i>cis</i>
$\varphi/^\circ$	0.0	10.4(3)	33.7(14)	13.7(2)	88.1//82.2	46.4(2)
Temperature/K	RT	100(2)	100.0(1)	150(2)	198(2)	200(1)

^a Uncertainties are given in parentheses in units of the last digit. RT, room temperature. φ , represents the angle between the planes of the aromatic ring and the carboxylic acid substituent; for 26DCBA the two values presented correspond to the value of this angle in the two non-equivalent molecules in the crystal.

It is interesting to note the similarity of the cell parameters for the pairs BA/2FBA and 26DFBA/2C6FBA (see Table 8), which follows the general pattern of greater structural similarity between these pairs of molecules already pointed out in the previous sections of this article. In this regard, the two chloro-substituted compounds, 2CBA and 26DCBA, have unique characteristics, though in the case of the mono-substituted compound this is mostly due to the different number of molecules in the unit cell, which is twice those of the remaining compounds (indeed, the cell parameters for 2CBA can also be made in close correspondence with those of the pair 26DFBA and 2C6FBA if one takes $\frac{1}{2}$ of the value of the *c* axis and interchanges the *a* and *b* axes; see Table 8).

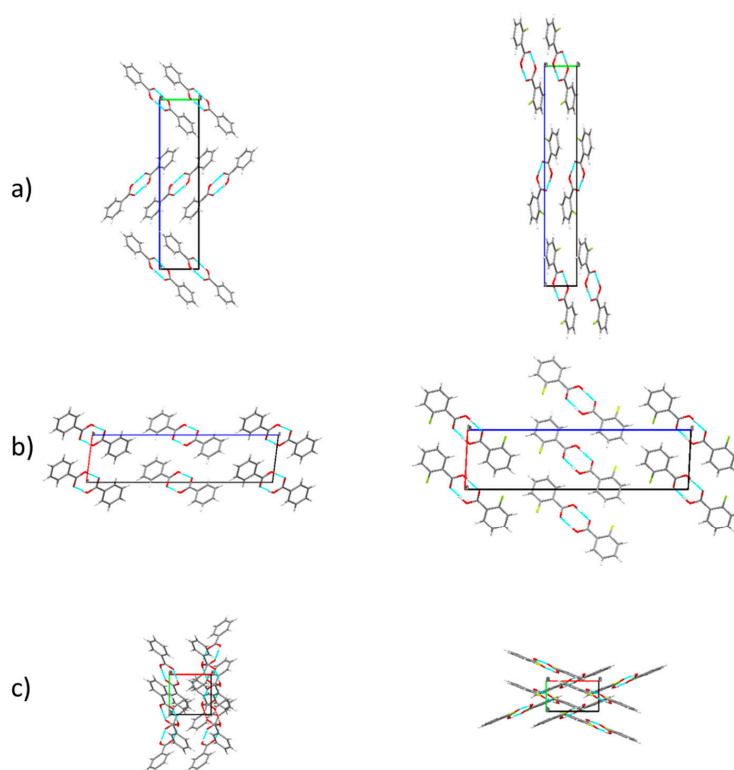


Figure 18. Crystal packing for BA (*left*) and 2FBA (*right*) as viewed from the (a) (*top*), (b) (*middle*) and (c) (*bottom*) crystallographic axes. Data from Refs. [20,30], respectively.

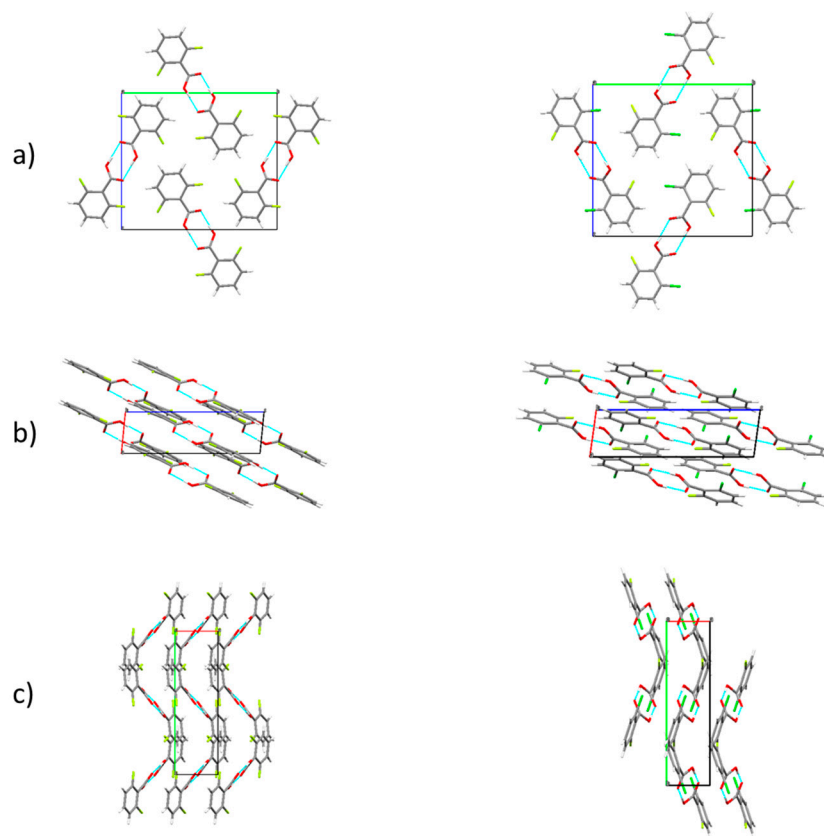


Figure 19. Crystal packing for 26DFBA (*left*) and 2C6FBA (*right*) as viewed from the (a) (*top*), (b) (*middle*) and (c) (*bottom*) crystallographic axes. Data from [22], and [24], respectively.

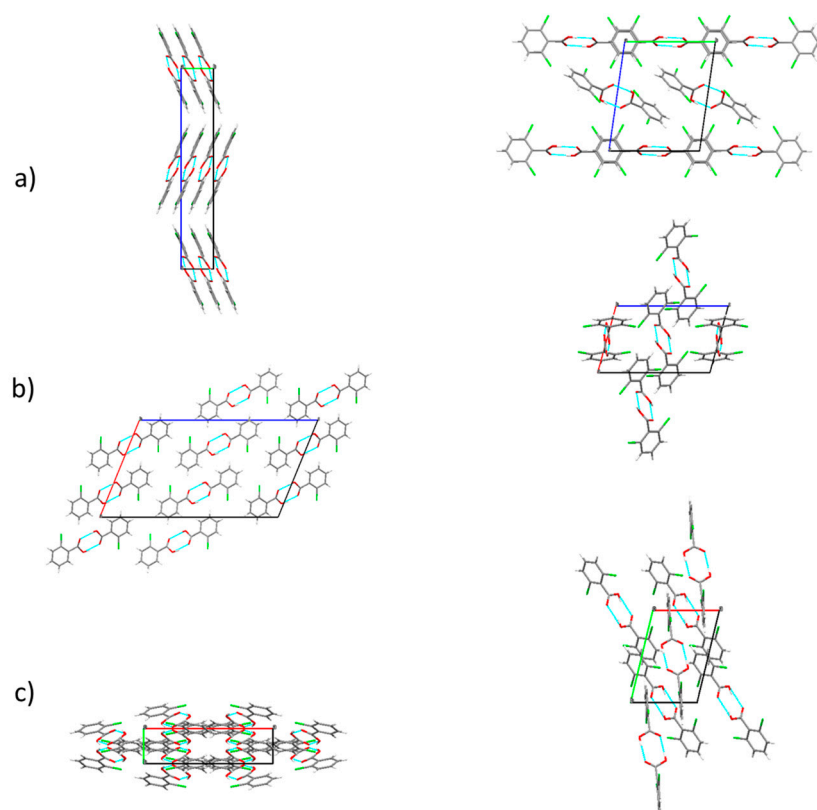


Figure 20. Crystal packing for 2CBA (*left*) and 26DCBA (*right*) as viewed from the (a) (*top*), (b) (*middle*) and (c) (*bottom*) crystallographic axes. Data from [21], and [23], respectively.

The cell volumes for the crystals of the different compounds shown in Table 7 follow the expected order, tacking into account the size of the respective molecules, i.e., $BA < 2FBA < 26DFBA < \frac{1}{2}2CBA < 2C6FBA < 26DCBA$, though the cell volume of the crystal of the unsubstituted compound (BA) given in Table 8 is comparatively larger. However, this is in a large amount due to the higher temperature used in the X-ray structure determination measurements, since neutron diffraction studies performed at 130 K [30] render a cell volume for BA crystal of only 589 \AA^3 .

Intermolecular interactions in the studied crystals are here characterized in details using the Hirshfeld surface analysis approach [43,70,71] and the CE-B3LYP method [42,43].

Hirshfeld surfaces are obtained from electron distributions that are calculated as sums of spherical atomic electron densities [43,70,71]. The Hirshfeld surface of a molecule in a crystal defines the region where the electron distribution given by the sum of the electron densities of the spherical atoms of a given molecule (the *promolecule*) exceeds that from all other promolecules in the crystal. Structure-related properties can then be mapped on the Hirshfeld surface. The normalized contact distance (d_{norm}) is calculated from the distances of a given point of the surface to the nearest atom outside (d_e) and inside (d_i) of the surface (normalized by the corresponding van der Waals radii, r_i^{vdw} and r_e^{vdw} , respectively), as defined by Equation (3), and allows the identification of the regions of the molecule where intermolecular interactions are more important [71,72]. Additionally, the combination of d_e and d_i in the form of a two-dimensional (2D)-fingerprint plot allows to condense information about the intermolecular contacts present in the crystal [71,73–75]. The 2D-fingerprint plots provide a visual summary of the frequency of each combination of d_e and d_i across the surface of a molecule, thus indicating not just which intermolecular interactions are present, but also the relative area of the

surface corresponding to each kind of interaction, which is a measure of the relative amount of each interaction in the crystal:

$$d_{\text{norm}} = \frac{d_i - r_i^{\text{vdw}}}{r_i^{\text{vdw}}} + \frac{d_e - r_e^{\text{vdw}}}{r_e^{\text{vdw}}} \quad (3)$$

The CE-B3LYP method has been described in details in refs. [42,43], and allows the partition of the interaction energies in a crystal in components which are of electrostatic, polarization, dispersion and exchange-repulsion nature. As described in Section 2 of this article, this method enables the computation of lattice energies (E_{lat}), which can be then related with sublimation enthalpies $\Delta H_{\text{sub}}(T)$.

Table 9 summarizes the results of the Hirshfeld analysis performed on the crystals of the studied compounds regarding the relative importance of the different intermolecular interactions, expressed as atom \cdots atom interactions according to the d_{norm} signatures. The total and atom \cdots atom d_{norm} plots and 2D-fingerprint plots (d_e , d_i) are shown in Figures 21 and 22. It can be seen that, as expected, the O \cdots H interactions are of fundamental importance in all crystals, since they are mostly related with the intermolecular H-bond interactions joining individual molecules in the centrosymmetric dimers present in the crystals. The O \cdots H interactions percent contribution is in the short range of 23.1–24.9% in the series of compounds studied, testifying the similar nature of this type of interaction in all of them. It is interesting to point out that the strengths of the intermolecular O-H \cdots O interactions in the dimers present in the crystals, as measured by the O \cdots O distances (the shorter the distance, the stronger the H-bonding) correlate approximately in an inverse way with the pK_a of the compounds (grouping the mono-substituted and di-substituted compounds; Figure 23), once again 26DCBA being a notorious exception to this trend.

Table 9. Atom \cdots atom interactions (%) in the crystals of the studied compounds, according to the Hirshfeld method (d_{norm} signatures).

Interaction	BA	2FBA	26DFBA	2CBA	26DCBA	2C6FBA
O \cdots H	24.9	24.7	23.7	23.9	26.8	23.1
C \cdots H	21.1	8.7	5.7	11.1	8.1	6.0
H \cdots H	43.0	26.4	12.1	21.7	12.6	13.0
O \cdots O	0.9	1.4	0.7	1.1	0.0	1.4
O \cdots C	6.4	4.3	4.6	4.3	2.5	3.9
C \cdots C	3.6	10.8	11.8	9.4	7.2	10.7
F \cdots O		0.0	2.2			1.9
F \cdots H		20.0	31.1			11.1
F \cdots F		0.2	5.4			1.0
F \cdots C		3.4	2.8			0.7
Cl \cdots O				0.1	5.9	0.8
Cl \cdots H				24.0	24.2	15.8
Cl \cdots Cl				1.8	7.3	1.1
Cl \cdots C				2.7	5.2	3.4
F \cdots Cl						6.3

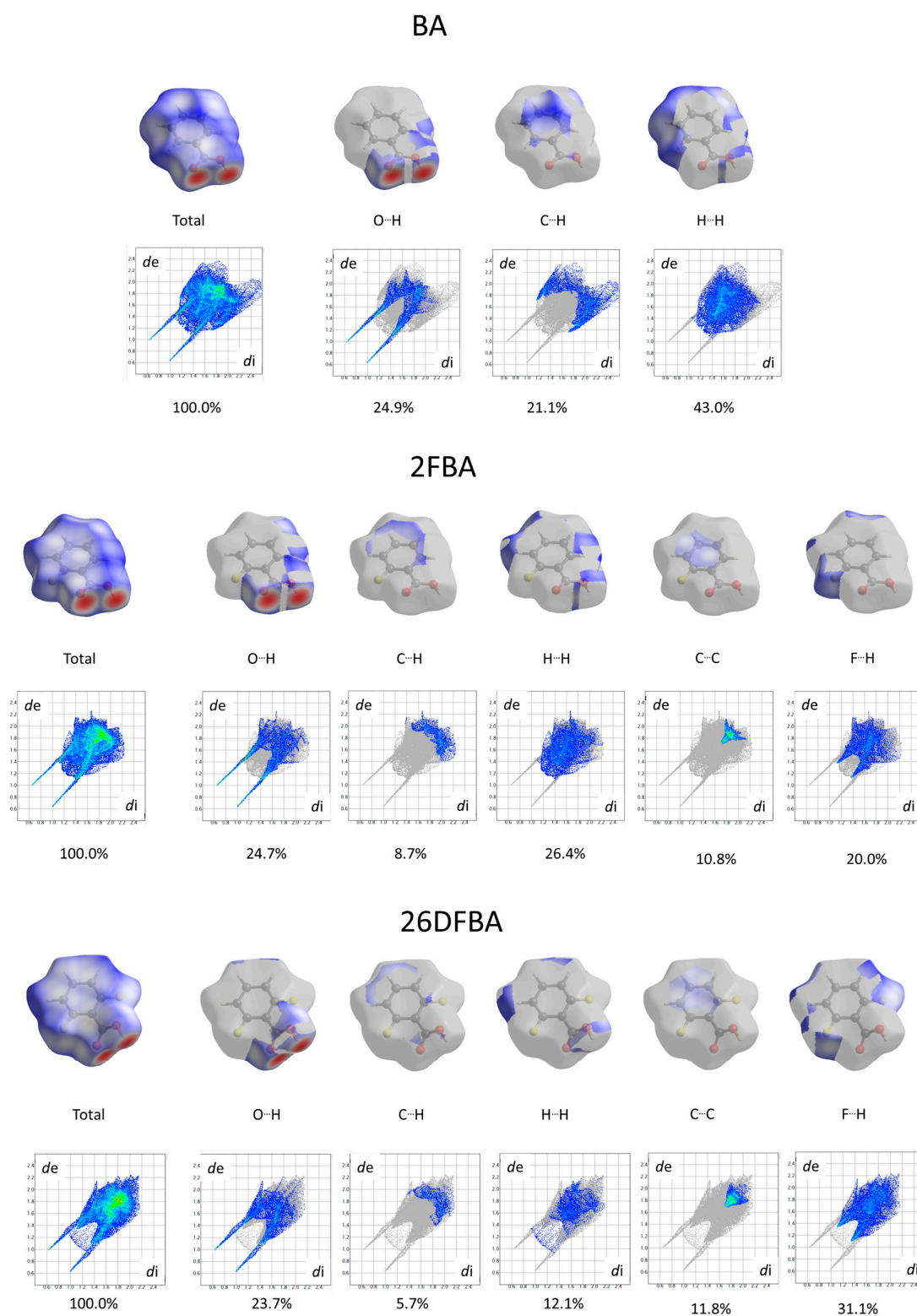


Figure 21. Total and atom···atom d_{norm} Hirshfeld plots and 2D-fingerprint plots (d_e , d_i) for BA, 2FBA and 26DFBA. Grey, colors means no interaction, blue-to-red colors mean increasing strength of interaction (in the d_{norm} Hirshfeld plots) or increased number of interactions (in the 2D fingerprint plots).

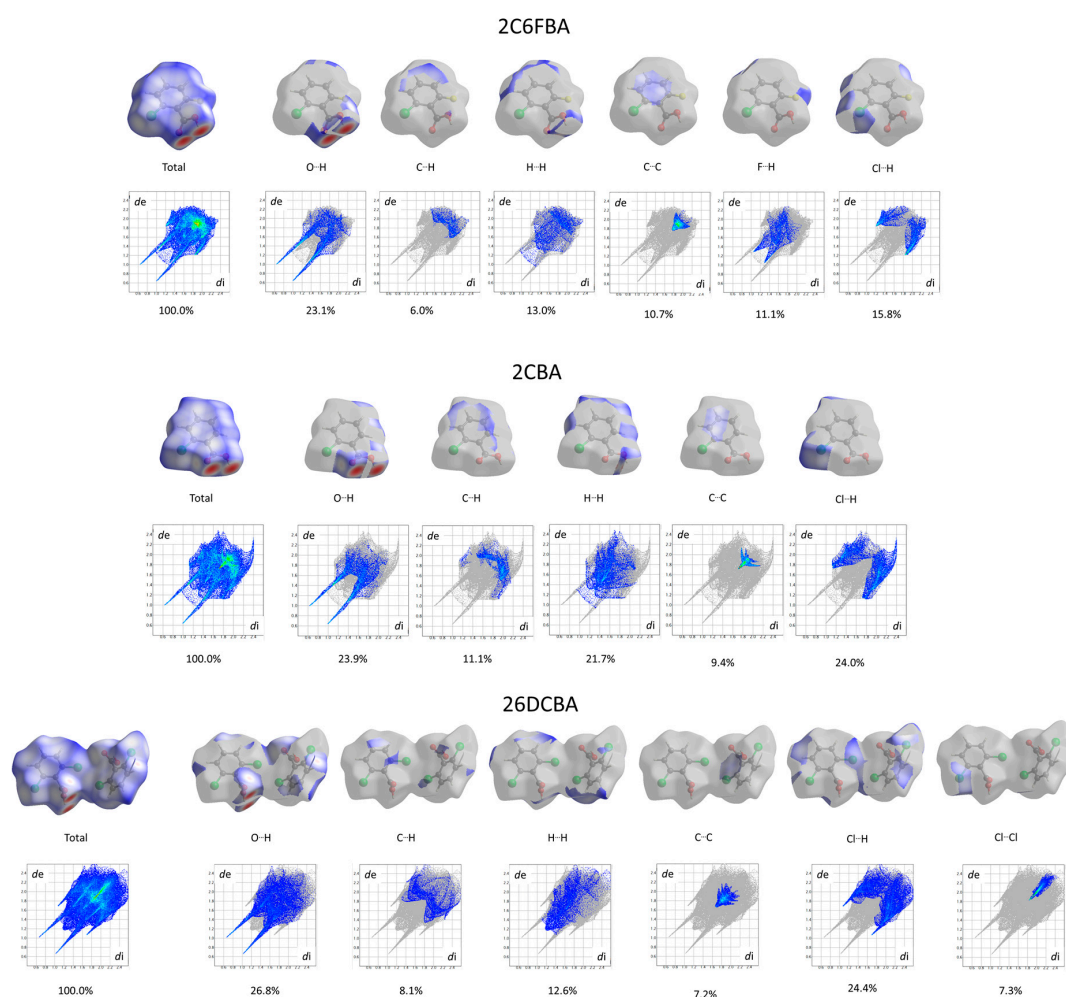


Figure 22. Total and atom \cdots atom d_{norm} Hirshfeld plots and 2D-fingerprint plots (d_e , d_i) for 2C6FBA, 2CBA and 26DCBA. Grey colors mean no interaction, blue-to-red colors mean increasing strength of interaction (in the d_{norm} Hirshfeld plots) or increased number of interactions (in the 2D fingerprint plots).

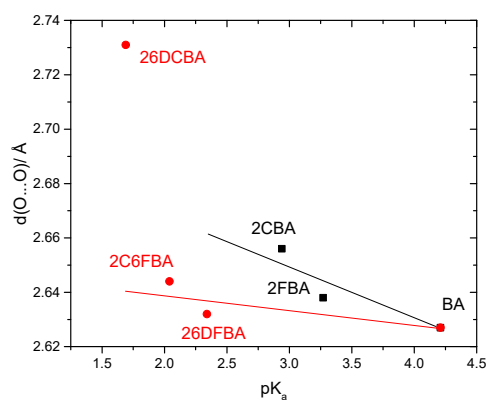


Figure 23. Intramolecular $d(\text{O} \cdots \text{O})$ distances in the dimers existing in the crystals of the studied compounds [20–24,30] vs. pK_a values (water; 25 °C).

Besides the $\text{O} \cdots \text{H}$ interactions, in the BA crystal the other two most relevant types of interactions are the $\text{H} \cdots \text{H}$ and $\text{C} \cdots \text{H}$ contacts, accounting for 43.0 and 21.1% of the Hirshfeld surface d_{norm} values, respectively. As shown in Figure 21, the $\text{H} \cdots \text{H}$ interactions are mapped on the Hirshfeld

surface around all ring hydrogen atoms and are related with the dispersion interactions involving these atoms, which occur both parallelly and perpendicularly to the aromatic ring plane, as seen in Figure 18. On the other hand, the C \cdots H interactions are a measure of the C-H \cdots π interactions involving the π system of the aromatic ring and the *meta* and *para* hydrogens of neighboring molecules, as shown in Figure 18. Note that in the crystal of BA the π - π stacking between the aromatic rings is limited, since the rings of neighbor dimers are dephased (see Figure 18), what justifies the small importance of the C \cdots C interactions in the crystal (only 3.6%; Table 9). This strongly contrasts with what happens in the case of 2FBA, where the π - π stacking between adjacent rings is perfect and, consequently, the C \cdots C interactions increase of importance (10.8%) at cost of the C \cdots H interactions (which account only for 8.7% of the Hirshfeld d_{norm} surface area), and are mapped, as expected, above the aromatic ring carbon atoms (see Figures 18 and 21). In the crystal of 2FBA, besides the O \cdots H and C \cdots C interactions, the most important interactions are the H \cdots H and H \cdots F ones, accounting respectively for 26.4 and 20.0% of the Hirshfeld d_{norm} surface area and representing mostly H \cdots H dispersive and C-H \cdots F-C bond-polar interactions. Interestingly, the F \cdots F interactions are practically inexistent (0.2%), in consonance with the fact that in the crystal the atoms close to the fluorine atoms are essentially hydrogen atoms.

A similar picture can be traced for the difluoro-substituted compound, whose percentual assignment of the Hirshfeld d_{norm} surface area to the different atom \cdots atom interactions is very much identical to that of 2FBA (see Table 9 and also Figures 18, 19 and 21). The major difference is the increase of percentage allocated to the F \cdots H interactions and the reduction of that assigned to the H \cdots H interactions, as expecting considering the replacement of one H atom by a F atom in going from 2FBA to 26DFBA.

The patterns of atom \cdots atom interactions in the crystals of 2CBA and 26DCBA generally follow those discussed above for the two fluoro-substituted compounds, as it can be noticed by the percentual values for the different interactions shown in Table 9, and also by comparing the plots depicted in Figures 21 and 22 for these molecules. It shall, however, be emphasised that the specific geometry adopted by the molecules of 26DCBA, with the planes of the aromatic ring and of the carboxylic group nearly perpendicular to each other, leads to a reduction of the π - π staking between the aromatic rings (as measured by the C \cdots C interaction, which has the lowest percent value among all these four molecules; see also Figure 20 for 26DCBA crystal packing), and also to an increase of the relevance of the Cl \cdots O interactions (which are by far more important in 26DCBA than in 2CBA, and also much more important than the F \cdots O interactions in both 2FBA and 16DFBA; see Table 9).

Finally, in the crystal of 2C6FBA, whose structural organization resembles that of 26DFBA (Figure 19), the intermolecular atom \cdots atom interactions do also resemble those operating in the difluoro-substituted compound, with the relevant O \cdots H, H \cdots H and C \cdots C interactions having identical percentual contributions to the Hirshfeld d_{norm} surface area (Table 9 and Figures 21 and 22). Naturally, the percentage assigned to the F \cdots H interactions in 26DFBA (31.1%) are split in 2C6FBA among the F \cdots H (11.1%), Cl \cdots H (15.8%) and F \cdots Cl (6.3%) interactions. Additionally, the Hirshfeld d_{norm} surface maps for 2C6FBA clearly reveal that the F \cdots H interactions occur predominantly with the *para* hydrogen atom, while the Cl \cdots H interactions involve essentially the *meta* hydrogen atoms (Figure 22), in consonance with its characteristic crystal packing, shown in Figure 19. For 26DFBA, the F \cdots H interactions extend to both *para* and *meta* hydrogen atoms (Figures 19 and 21).

The results obtained using the CE-B3LYP interaction energy decomposition model [42,43] are summarized in Table 10. A comparative analysis of the data for the 6 studied crystals was done by using the Ward's clustering method [77] with squared Euclidian distances, and is presented in Figure 24. The clustering analysis clearly shows the similarity of the pairs of crystals BA/2FBA and 26DFBA/2C6FBA already pointed out above, with the latter pair being that whose components show the highest degree of similarity. The crystals of the chlorosubstituted compounds (2CBA and 26DCBA) are also grouped together in the clustering analysis, but their degree of similarity is considerably

smaller than those exhibited by the remaining pairs of crystals, as seen by the relative distances of the branching points of the dendrogram for the different groups.

Table 10. CE-B3LYP intreraction energies partition results for the crystals of the studied compounds ^a.

Molecule	E_ele	E_pol	E_dis	E_rep	E_tot
BA	−84.4	−25.0	−75.7	110.8	−106.3
2FBA	−81.3	−24.0	−85.6	116.4	−107.0
26DFBA	−87.1	−25.6	−91.9	125.9	−113.8
2CBA	−69.7	−18.6	−87.8	106.6	−98.8
26DCBA	−65.2	−15.3	−75.8	96.8	−87.4
2C6FBA	−82.3	−21.4	−91.4	124.5	−107.0

^a E_ele, E_pol, E_dis, E_rep and E_tot represent the electrostatic, polarization, dispersion, exchange-repulsion, and total interaction energies (in kJ·mol^{−1}). E_tot corresponds to the crystal lattice energy (E_{lat}) and has been scaled for benchmarked energy models, according to the recommendations [42,43].

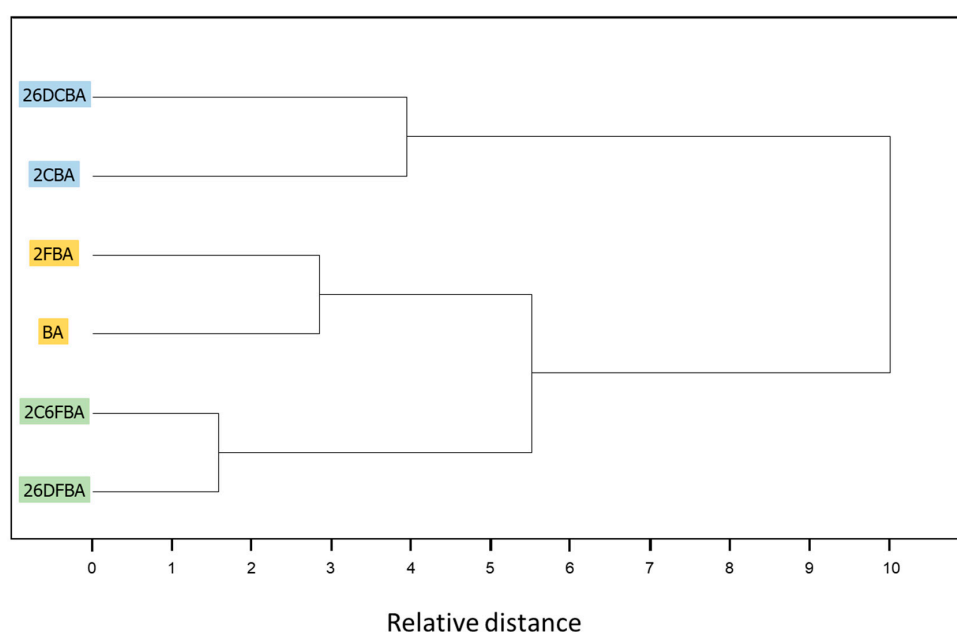


Figure 24. Results of clustering analysis (Ward's method with squared Euclidean distance) of the CE-B3LYP data for the crystals of the studied compounds. For this analysis, the UnscramblerTM CAMO software (Version 10.5) [76] was used.

The electrostatic and polarization components of the intermolecular interactions (E_{ele}; E_{pol}) are larger for all fluoro-containing compounds (including 2C6FBA), compared to the chloro-substituted ones (see Table 10), as it could be expected taking into account the relative electronegativities of the two halogen atoms. The maximum value of these terms are observed for 26DFBA, and are ca. 30%, and ~70% higher, respectively, than for 26DCBA. Interestingly, the results indicate that these terms are also large for the unsubstituted BA.

The dispersion component of the intermolecular interactions (E_{dis}) is, as expected, smaller in BA, compared with all halogenated benzoic acids (with the notorious exception of 26DCBA), and in these latter, also as it could be anticipated that it is larger in the di-substituted compounds than in the mono-substituted ones. The fact that the crystal of 26DCBA appears (again) as an outlier shall be ascribed to its significant structural differences compared to the remaining crystals, which were already pointed out above.

In its turn, the exchange-repulsion component (E_{rep}) of BA has an intermediate value, being larger than those found for 2CBA and 26DCBA and smaller than those calculated for all the fluoro-containing derivatives. Assuming a similar compactness of the crystals, these results can be correlated with the

relative hardness of the halogen atoms, fluorine being a harder atom than hydrogen and chlorine being considerably softer [78,79].

The CE-B3LYP calculated lattice energies of the crystals $E_{\text{lat}} = E_{\text{tot}}$ (see Table 10) appear in the following order: 26DFBA < 2C6FBA = 2FBA \approx BA < 2CBA < 26DCBA. From the obtained values of E_{lat} , the sublimation enthalpies were estimated as described in Section 2 as being 109 (26DFBA), 102 (2C6FBA and 2FBA), 101 (BA), 94 (2CBA) and 82 (26DCBA) $\text{kJ}\cdot\text{mol}^{-1}$. The estimated values are expected to have an absolute error within 8 $\text{kJ}\cdot\text{mol}^{-1}$ [42], so that the obtained results compare fairly well with the available experimental data: 94.4 ± 0.8 , 93.3 ± 1.2 and 79 ± 2 $\text{kJ}\cdot\text{mol}^{-1}$, for 2FBA, BA and 2CBA, respectively [80–82] (no experimental data is available for the remaining compounds).

We have also looked to the influence of the crystal environment on the properties of the aromatic ring. Aromaticity can be estimated using the harmonic oscillator model of aromaticity (HOMA) index [83–85], which is defined as,

$$\text{HOMA} = 1 - \frac{257.7}{6} \sum_{i=1}^6 (1.388 - r_i)^2 \quad (4)$$

where r_i are the C-C bond lengths.

Table 11 presents the values of the ring C-C bond lengths for the isolated molecule, as calculated in the present study, and those obtained experimentally for the crystals [20–24,30]. For both situations, the less aromatic rings are present in the mono-substituted compounds due to pronouncedly different nature of the *ortho* substituents, with 2CBA being the compound exhibiting the smaller HOMA index. Interestingly, the aromaticity index in the di-substituted compounds assumes higher values than in BA, both in the crystalline state and for the isolated molecules. It is also worth noticing that, with no exceptions, the intermolecular interactions present in the crystals lead to a reduction of the aromaticity degree of the aromatic moiety (from a reduction of $\sim 0.15\%$ in the HOMA index, in both 26DFBA and 26DCBA, to $\sim 5\%$ in 2CBA).

Table 11. Aromatic ring C-C bond lengths (Å) and HOMA index for the studied molecules (in the crystals and as isolated molecules) ^a.

Crystal							
	BA	2FBA	2CBA	26DFBA	26DCBA	26DCBA	2C6FBA
				Mol. 1	Mol. 2		
	1.384	1.401	1.406	1.398	1.388	1.389	1.396
	1.377	1.391	1.385	1.381	1.386	1.381	1.382
	1.380	1.397	1.387	1.387	1.382	1.380	1.377
	1.366	1.394	1.362	1.389	1.378	1.375	1.377
	1.383	1.392	1.408	1.381	1.382	1.387	1.367
	1.386	1.416	1.366	1.396	1.387	1.387	1.389
HOMA:	0.969	0.953	0.919	0.989	0.992	0.988	0.966
				Average:0.990			
Isolated Molecule							
	BA	2FBA	2CBA	26DFBA	26DCBA		2C6FBA
	1.400	1.402	1.407	1.398	1.397		1.399
	1.390	1.388	1.394	1.385	1.391		1.392
	1.396	1.391	1.390	1.392	1.391		1.392
	1.395	1.395	1.393	1.392	1.391		1.392
	1.392	1.388	1.388	1.385	1.391		1.384
	1.400	1.405	1.405	1.397	1.397		1.393
HOMA:	0.982	0.977	0.969	0.990	0.991		0.991

^a C-C bond lengths are presented starting from that connecting the ring carbon atom where the carboxylic acid substituent is bound to the *ortho* carbon atom staying closest to the carbonyl oxygen atom and rotating through the ring. Experimental data for the crystals was taken from Refs. [20–24,30]. Calculated data are from this study and for both 2FBA and 2CBA correspond to the geometrical parameters of the *cis*-I conformer.

4. Conclusions

In this article, the structure and properties of the *ortho* mono- and di-substituted fluoro- and chloro- benzoic acids were investigated in a comparative basis. First, the potential energy landscape of the isolated molecules of the compounds were characterized using DFT calculations performed with the B3LYP functional and the 6-311++G(d,p) basis set. Special attention was given to the influence of the interactions between the carboxylic group and the *ortho* halogen substituents as well as the nature of these later on the structures and properties of the studied series of compounds. The structures of the relevant conformers of the molecules were rationalized and used to interpret the experimental data obtained for the isolated molecules of the compounds, and in particular, their vibrational spectra in the gas phase and isolated in low-temperature inert matrices, and the photochemistry of selected illustrative compounds in the latter experimental conditions. The stability of the higher-energy *trans* carboxylic conformers regarding their spontaneous conversion by quantum mechanical tunneling to the most stable *cis* forms was evaluated. The conclusions derived from the analysis of the potential energy landscapes of the molecules regarding this matter were found to duly explain previously reported experimental data [16,17,58] and were used to make predictions regarding the stability of the *trans* conformers of the molecules not yet experimentally investigated (BA, 26DFBA and 26DCBA). The structures of the crystals reported previously in the literature [20–24,30] were revisited and discussed, also in a comparative basis. Intermolecular interactions in the different crystals and their effects on the properties of the compounds were evaluated through Hirshfeld surface analysis, the CE-B3LYP energy decomposition model and HOMA index. The structural characteristics of the crystals were correlated with thermodynamic data. On the whole, this article presents a detailed comprehensive investigation of the *ortho* fluoro- and chloro- substituted benzoic acids both as isolated molecules and in the crystalline phase.

Author Contributions: Conceptualization, R.F.; Data curation, G.O.I.; Formal analysis, G.O.I.; Funding acquisition, R.F.; Investigation, G.O.I.; Methodology, R.F.; Resources, R.F.; Writing—original draft, R.F. All authors have read and agreed to the published version of the manuscript.

Funding: The authors acknowledge financial support from the Portuguese Science Foundation (“Fundação para a Ciência e a Tecnologia”—FCT)—Projects CQC UIDB/00313/2020 and UIDP/00313/2020, also co-funded by FEDER/COMPETE 2020-EU.

Acknowledgments: Access to instruments from Laser-Lab Coimbra and TAIL-UC facilities funded under QREN-Mais Centro is gratefully acknowledged.

Conflicts of Interest: The authors declare no conflict of interest. The funders had no role in the design of the study; in the collection, analyses, or interpretation of data; in the writing of the manuscript, or in the decision to publish the results.

References

1. Maki, T.; Takeda, K. Benzoic Acid and Derivatives. In *Ullmann's Encyclopedia of Industrial Chemistry*; Wiley-VCH: Weinheim, Germany, 2002.
2. Key, B.D.; Howell, R.D.; Criddle, C.S. Fluorinated Organics in the Biosphere. *Environ. Sci. Technol.* **1997**, *31*, 2445–2454. [CrossRef]
3. Holder, B.R.; Reuter, W.M. *Perkin Elmer Application Note “Analysis of Fluorobenzoic Acids via UHPLC-MS/MS for Water Tracer Studies”*; PerkinElmer, Inc.: Waltham, MA, USA, 2018.
4. Serres-Piole, C.; Preud'homme, H.; Morandi-Tehrani, N.; Allanic, C.; Jullia, H.; Lobinski, R. Water Tracers in Oilfield Applications: Guidelines. *J. Petrol. Sci. Eng.* **2012**, *98–99*, 22–39. [CrossRef]
5. Serres-Piole, C.; Moradi-Tehrani, N.; Lobinski, R.; Preud'homme, H. Direct Sensitive Simultaneous Determination of Fluorinated Benzoic Acids in Oil Reservoir Waters by Ultra High-performance Liquid Chromatography-tandem Mass Spectrometry. *J. Chromatogr. A* **2011**, *1218*, 5872–5877. [CrossRef] [PubMed]
6. Goldman, P.; Milne, G.W.A.; Pignataro, M.T. Fluorine Containing Metabolites Formed from 2-Fluorobenzoic Acid by *Pseudomonas* Species. *Arch. Biochem. Biophys.* **1967**, *118*, 178–184. [CrossRef]

7. MCarvalho, F.; Alves, C.C.T.; Ferreira, M.I.M.; de Marco, P.; Castro, P.M.L. Isolation and Properties of a Pure Bacterial Strain Capable of Fluorobenzene Degradation as Sole Carbon and Energy Source. *Appl. Environ. Microbiol.* **2002**, *68*, 102–105.
8. Milne, G.W.A.; Goldman, P.; Holtzman, J.L. The Metabolism of 2-Fluorobenzoic acid. *J. Biol. Chem.* **1968**, *243*, 5374–5376.
9. Engesser, K.H.; Schmidt, E.; Knackmuss, H.-J. Adaptation of *Alcaligenes eutrophus* B9 and *Pseudomonas* sp. B13 to 2-Fluorobenzoate as Growth Substrate. *Appl. Environ. Microbiol.* **1980**, *39*, 68–73. [CrossRef]
10. Vora, K.A.; Singh, C.; Modi, V.V. Degradation of 2-Fluorobenzoate by a *Pseudomonas*. *Curr. Microbiol.* **1988**, *17*, 249–254. [CrossRef]
11. Drzyzga, O.; Jannsen, S.; Blotevogel, K.H. Mineralization of Monofluorobenzoate by a Diculture under Sulfate-reducing Conditions. *FEMS Microbiol. Lett.* **1994**, *116*, 215–220. [CrossRef]
12. Engesser, K.H.; Schulte, P. Degradation of 2-Bromo-, 2-Chloro- and 2-Fluorobenzoate by *Pseudomonas putida* CLB 250. *FEMS Microbiol. Lett.* **1989**, *60*, 143–148. [CrossRef]
13. Buchanan, E.B., Jr.; Wagner, W. Spectrophotometric Determination of Iron with 2-Fluorobenzoic Acid. *Anal. Chem.* **1957**, *29*, 754–756. [CrossRef]
14. Gohier, F.; Castanet, A.-S.; Mortier, J. Ortholithiation of Unprotected Benzoic Acids: Application for Novel 2-Chloro-6-Substituted Benzoic Acid Syntheses. *Synth. Commun.* **2005**, *35*, 799–806. [CrossRef]
15. Vardanyan, R.S.; Hruby, V.J. Local Anesthetics. In *Synthesis of Essential Drugs*; Elsevier Science: Amsterdam, The Netherlands, 2006; Chapter 2.
16. Kuş, N.; Fausto, R. Effects of the Matrix and Intramolecular Interactions on the Stability of the Higher-energy Conformers of 2-Fluorobenzoic Acid. *J. Chem. Phys.* **2017**, *146*, 124305. [CrossRef] [PubMed]
17. Nishino, S.; Nakata, M. Intramolecular Hydrogen Atom Tunneling in 2-Chlorobenzoic Acid Studied by Low-Temperature Matrix-Isolation Infrared Spectroscopy. *J. Phys. Chem. A* **2007**, *111*, 7041–7047. [CrossRef] [PubMed]
18. Daly, A.M.; Carey, S.J.; Pejlovas, A.M.; Li, K.; Kukolich, S.G. Gas Phase Measurements of Mono-fluoro-benzoic Acids and the Dimer of 3-Fluoro-benzoic Acid. *J. Chem. Phys.* **2015**, *142*, 144303. [CrossRef] [PubMed]
19. Kumar, J.S.; Arivazhagan, M.; Thangaraju, P. Vibrational Spectra, NLO Analysis, and HOMO–LUMO Studies of 2-Chloro-6-Fluorobenzoic Acid and 3,4-Dichlorobenzoic Acid by Density Functional Method. *Spectrochim. Acta Part A Mol. Biomol. Spectrosc.* **2015**, *147*, 235–244. [CrossRef] [PubMed]
20. Hathwar, V.R.; Thakur, T.S.; Dubey, R.; Pavan, M.S.; Row, T.N.G.; Desiraju, G.R. Extending the Supramolecular Synthons Based Fragment Approach (SBFA) for Transferability of Multipole Charge Density Parameters to Monofluorobenzoic Acids and their Cocrystals with Isonicotinamide: Importance of C–H \cdots O, C–H \cdots F, and F \cdots F Intermolecular Regions. *J. Phys. Chem. A* **2011**, *115*, 12852–12863. [CrossRef]
21. Polito, M.; D’Oria, E.; Maini, L.; Karamertzanis, P.G.; Grepioni, F.; Braga, D.; Price, S.L. The Crystal Structures of Chloro and Methyl *ortho*-benzoic Acids and their Co-crystal: Rationalizing Similarities and Differences. *CrystEngComm* **2008**, *10*, 1848–1854. [CrossRef]
22. Al-Dajani, M.T.M.; Wahab, H.A.; Mohamed, N.; Yeap, C.S.; Fun, H.-K. 2,6-Difluorobenzoic Acid. *Acta Cryst. E* **2010**, *66*, o2109. [CrossRef]
23. Pinkus, A.G.; Kautz, J.A.; Ahobila-Vajjula, P. Crystal Structures of 2,6- and 3,5-Dichlorobenzoic acids: Nonbonded Cl \cdots Cl Contacts. *J. Chem. Crystall.* **2003**, *33*, 181–186. [CrossRef]
24. Betz, R.; Gerber, T. 2-Chloro-6-fluorobenzoic Acid. *Acta Cryst. E* **2011**, *67*, o1329. [CrossRef] [PubMed]
25. 2-Fluorobenzoic Acid. Wikipedia. Available online: https://en.wikipedia.org/wiki/2-Fluorobenzoic_acid (accessed on 25 August 2020).
26. 2,6-Difluorobenzoic Acid. Chemical Book. Available online: https://www.chemicalbook.com/ProductList_En.aspx?kwd=2,6-difluorobenzoic%20acid (accessed on 25 August 2020).
27. Davis, M.M.; Hetzer, H.B. Relative Strengths of Forty Aromatic Carboxylic Acids in Benzene at 25 °C. *J. Res. Natl. Bur. Stand.* **1958**, *60*, 569–592. [CrossRef]
28. 2,6-Dichlorobenzoic Acid. Chemical Book. Available online: https://www.chemicalbook.com/ProductMSDSDetailCB1673902_EN.htm#2 (accessed on 25 August 2020).
29. 2-Chloro-6-Fluorobenzoic Acid. Chemical Book. Available online: https://www.chemicalbook.com/ChemicalProductProperty_EN_CB1688854.htm (accessed on 25 August 2020).

30. Feld, R.; Lehmann, M.S.; Muir, K.W.; Speakman, J.C. The Crystal Structure of Benzoic Acid: A Redetermination with X-rays at Room Temperature; a Summary of Neutron-diffraction Work at Temperatures Down to 5 K. *Zeitsch. Kristall.* **1981**, *157*, 215–231.
31. Smith, A.L. The Coblenz Society Desk Book of Infrared Spectra. In *The Coblenz Society Desk Book of Infrared Spectra*, 2nd ed.; Carver, C.D., Ed.; The Coblenz Society: Kirkwood, MO, USA, 1982; pp. 1–24.
32. Becke, A.D. Density-functional Exchange-energy Approximation with Correct Asymptotic Behavior. *Phys. Rev. A* **1988**, *38*, 3098–3100. [CrossRef]
33. Lee, C.; Yang, W.; Parr, R.G. Development of the Colle-Salvetti Correlation-energy Formula into a Functional of the Electron Density. *Phys. Rev. B* **1988**, *37*, 785–789. [CrossRef] [PubMed]
34. Vosko, S.H.; Wilk, L.; Nusair, M. Accurate Spin-dependent Electron Liquid Correlation Energies for Local Spin Density Calculations: A Critical Analysis. *Can. J. Phys.* **1980**, *58*, 1200–1211. [CrossRef]
35. Frisch, M.J.; Trucks, G.W.; Schlegel, H.B.; Scuseria, G.E.; Robb, M.A.; Cheeseman, J.R.; Scalmani, G.; Barone, V.; Mennucci, B.; Petersson, G.A.; et al. *Gaussian 09, Revision A.02*; Gaussian, Inc.: Wallingford, CT, USA, 2009.
36. McLean, A.D.; Chandler, G.S. Contracted Gaussian Basis Sets for Molecular Calculations. I. Second Row Atoms, Z=11–18. *J. Chem. Phys.* **1980**, *72*, 5639–5648. [CrossRef]
37. Raghavachari, K.; Binkley, J.S.; Seeger, R.; Pople, J.A. Self-consistent Molecular Orbital Methods. XX. A Basis Set for Correlated Wave Functions. *J. Chem. Phys.* **1980**, *72*, 650–654.
38. Frisch, M.J.; Pople, J.A.; Binkley, J.S. Self-consistent Molecular Orbital Methods 25. Supplementary Functions for Gaussian Basis Sets. *J. Chem. Phys.* **1984**, *80*, 3265–3269. [CrossRef]
39. Ildiz, G.O.; Konarska, J.; Fausto, R. UV-Induced Conformational Isomerization and Photochemistry of 3-Chloro-4-methoxybenzaldehyde in Cryogenic Inert Matrices. *J. Chem. Phys.* **2019**, *151*, 104303. [CrossRef]
40. Cluyts, L.; Sharma, A.; Kuş, N.; Schoone, K.; Fausto, R. Matrix Isolation Infrared Spectroscopic Study of 4-Pyridinecarboxaldehyde and of its UV-induced Photochemistry. *Spectrochim. Acta Part A Mol. Biomol. Spectrosc.* **2017**, *171*, 207–212. [CrossRef] [PubMed]
41. Kuş, N.; Sharma, A.; Fausto, R. First Observation of Methane Photochemical Generation from an *N,N*-dimethylamino-substituted Arene: The case of 4-(*N,N*-dimethylamino) benzaldehyde (DMABA). *Tetrahedron* **2016**, *72*, 5914–5922. [CrossRef]
42. Thomas, S.P.; Spackman, P.R.; Jayatilaka, D.; Spackman, M.A. Accurate Lattice Energies for Molecular Crystals from Experimental Crystal Structures. *J. Chem. Theory Comput.* **2018**, *14*, 1614–1623. [CrossRef]
43. Turner, M.J.; McKinnon, J.J.; Wolff, S.K.; Grimwood, D.J.; Spackman, P.R.; Jayatilaka, D.; Spackman, M.A.; University of Western Australia. CrystalExplorer17. 2017. Available online: <http://hirshfeldsurface.net> (accessed on 22 October 2020).
44. De la Roza, A.O.; Johnson, E.J. A Benchmark for Non-Covalent Interactions in Solids. *J. Chem. Phys.* **2012**, *137*, 054103. [CrossRef]
45. Reilly, A.M.; Tkatchenko, A. Understanding the Role of Vibrations, Exact Exchange, and Many-body van der Waals Interactions in the Cohesive Properties of Molecular Crystals. *J. Chem. Phys.* **2013**, *139*, 024705. [CrossRef] [PubMed]
46. Cutini, M.; Civalleri, B.; Corno, M.; Orlando, R.; Brandenburg, J.C.; Maschio, L.; Ugliengo, P. Assessment of Different Quantum Mechanical Methods for the Prediction of Structure and Cohesive Energy of Molecular Crystals. *J. Chem. Theory Comput.* **2016**, *12*, 3340–3352. [CrossRef]
47. Gavezzotti, A.; Filippini, G. *Theoretical Aspects and Computer Modeling of the Molecular Solid State*; Gavezzotti, A., Ed.; Wiley: Chichester, UK, 1997; pp. 61–97.
48. Buchholz, H.K.; Hylton, R.K.; Brandenburg, J.G.; Seidel-Morgenstern, A.; Lorenz, H.; Stein, M.; Price, S.L. Thermochemistry of Racemic and Enantiopure Organic Crystals for Predicting Enantiomer Separation. *Cryst. Growth Des.* **2017**, *17*, 4676–4686. [CrossRef]
49. Fausto, R.; de Carvalho, L.A.E.B.; Teixeira-Dias, J.J.C.; Ramos, M.N. *S-cis* and *S-trans* Conformers of Formic, Thioformic and Dithioformic Acids. An Ab Initio Study. *J. Chem. Soc. Faraday Trans.* **1989**, *85*, 1945–1962. [CrossRef]
50. Fausto, R. Bonding in Carbonyl and Thiocarbonyl Compounds: An Ab Initio Charge Density Study of $H_2C=X$ and $HC(=X)YH$ ($X, Y = O$ or S). *J. Mol. Struct. (Theochem.)* **1994**, *315*, 123–136. [CrossRef]
51. Teixeira-Dias, J.J.C.; Fausto, R. A Molecular Mechanics Force Field for Conformational Analysis of Simple Acyl Chlorides, Carboxylic Acids and Esters. *J. Mol. Struct.* **1986**, *144*, 199–213. [CrossRef]

52. Aarset, K.; Page, E.M.; Rice, D.A. Molecular Structures of Benzoic Acid and 2-Hydroxybenzoic Acid, Obtained by Gas-Phase Electron Diffraction and Theoretical Calculations. *J. Phys. Chem. A* **2006**, *110*, 9014–9019. [CrossRef]
53. Onda, M.; Asai, M.; Takise, K.; Kuwae, K.; Hayami, K.; Kuroe, A.; Mori, M.; Miyazaki, H.; Suzuki, N.; Yamaguchi, I. Microwave Spectrum of Benzoic Acid. *J. Mol. Struct.* **1999**, *482–483*, 301–303. [CrossRef]
54. Stepanian, S.G.; Reva, I.D.; Radchenko, E.D.; Sheina, G.G. Infrared Spectra of Benzoic Acid Monomers and Dimers in Argon Matrix. *Vibrat. Spectrosc.* **1996**, *11*, 123–133. [CrossRef]
55. Reva, I.D.; Stepanian, S.G. An Infrared Study on Matrix-Isolated Benzoic Acid. *J. Mol. Struct.* **1995**, *349*, 337–340. [CrossRef]
56. Bakker, J.M.; Aleese, L.M.; von Helden, G.; Meijer, G. The Infrared Absorption Spectrum of the Gas Phase Neutral Benzoic Acid Monomer and Dimer. *J. Chem. Phys.* **2003**, *119*, 11180. [CrossRef]
57. Arendorf, J.R.T. A Study of Some Non-Covalent Functional Group Interactions. Ph.D. Thesis, University College, London, UK, 2011.
58. Kuş, N. Structural Characterization and Photochemistry of 2-Chloro-6-fluorobenzoic Acid Isolated in a Xenon Matrix. *Anadolu Univ. J. Sci. Techn. A Appl. Sci. Eng.* **2017**, *18*, 315–322. [CrossRef]
59. Harris, D. *Quantitative Chemical Analysis*, 8th ed.; W. H. Freeman and Company: New York, NY, USA, 2010; p. AP12.
60. Nogueira, B.A.; Ildiz, G.O.; Canotilho, J.; Eusebio, M.E.S.; Fausto, R. Molecular Structure, Infrared Spectra, Photochemistry, and Thermal Properties of 1-Methylhydantoin. *J. Phys. Chem. A* **2014**, *118*, 5994–6008. [CrossRef]
61. Timosheva, A.P.; Abdullina, S.G.; Kondrashina, Y.G.; Vul'fson, S.G. Kerr Constants and Structure of Benzoic Acid in Dioxane and CCl₄. *Russ. Chem. Bull.* **1994**, *43*, 803–805. [CrossRef]
62. 2-Fluorobenzoic Acid, Home Page of R. Stenutz. Available online: <http://www.stenutz.eu/chem/solv6.php?name=2-fluorobenzoic%20acid>. (accessed on 25 August 2020).
63. ChemCraft (Version 1.8)—Graphical Software for Visualization of Quantum Chemistry Computations. Available online: <https://www.chemcraftprog.com> (accessed on 22 October 2020).
64. Wiley Spectrabase. Available online: <https://spectrabase.com/spectrum/pk7U3jDypt> (accessed on 9 September 2020).
65. Maçôas, E.M.S.; Kriachtchev, L.; Fausto, R.; Räsänen, M. Photochemistry and Vibrational Spectroscopy of the *trans* and *cis* Conformers of Acetic Acid in Solid Argon. *J. Phys. Chem. A* **2004**, *108*, 3380. [CrossRef]
66. Fausto, R.; Khriachtchev, L.; Hamm, P. Conformational Changes in Cryogenic Matrices. In *Physics and Chemistry at Low Temperatures*; Khriachtchev, L., Ed.; World Scientific: New York, NY, USA, 2011; Chapter 3; pp. 51–84.
67. Chang, X.-P.; Fang, Q.; Cui, G. Mechanistic Photodecarboxylation of Pyruvic Acid: Excited-state Proton Transfer and Three-state Intersection. *J. Chem. Phys.* **2014**, *141*, 154311. [CrossRef]
68. Singleton, D.L.; Paraskevopoulos, G.; Irwin, R.S. Laser Photolysis of Carboxylic Acids in the Gas Phase. Direct Determination of the OH Quantum Yield at 222 nm. *J. Phys. Chem.* **1990**, *94*, 695–699. [CrossRef]
69. Li, J.; Zhang, F.; Fang, W.-H. Probing Photophysical and Photochemical Processes of Benzoic Acid from *ab Initio* Calculations. *J. Phys. Chem. A* **2005**, *109*, 7718–7772. [CrossRef] [PubMed]
70. Spackman, M.A.; Byrom, P.G. A Novel Definition of a Molecule in a Crystal. *Chem. Phys. Lett.* **1997**, *267*, 215–220. [CrossRef]
71. Spackman, M.A.; Jayatilaka, D. Hirshfeld Surface Analysis. *CrystEngComm* **2009**, *11*, 19–32. [CrossRef]
72. McKinnon, J.J.; Mitchell, A.S.; Spackman, M.A. Hirshfeld Surfaces: A New Tool for Visualising and Exploring Molecular Crystals. *Chem. Eur. J.* **1998**, *4*, 2136–2141. [CrossRef]
73. Spackman, M.A.; McKinnon, J.J. Fingerprinting Intermolecular Interactions in Molecular Crystals. *CrystEngComm* **2002**, *4*, 378–392. [CrossRef]
74. Rohl, A.L.; Moret, M.; Kaminsky, W.; Claborn, K.; McKinnon, J.J.; Kahr, B. Hirshfeld Surfaces Identify Inadequacies in Computations of Intermolecular Interactions in Crystals: Pentamorphic 1,8-Dihydroxyanthraquinone. *Cryst. Growth Des.* **2008**, *8*, 4517–4525. [CrossRef]
75. Parkin, A.; Barr, G.; Dong, W.; Gilmore, C.J.; Jayatilaka, D.; McKinnon, J.J.; Spackman, M.A.; Wilson, C.C. Comparing Entire Crystal Structures: Structural Genetic Fingerprinting. *CrystEngComm* **2007**, *9*, 648–652. [CrossRef]
76. *The Unscrambler*TM, Version 10.5; CAMO A/S: Trondheim, Norway, 2018.

77. Ward, J.H.J. Hierarchical Grouping to Optimize an Objective Function. *J. Am. Stat. Assoc.* **1963**, *58*, 236–244. [CrossRef]
78. Pearson, R.G. Hard and Soft Acids and Bases. *J. Am. Chem. Soc.* **1963**, *85*, 3533–3539. [CrossRef]
79. Toufar, H.; Nulens, K.; Janssens, G.O.A.; Mortier, W.J.; Schoonheydt, R.A.; de Proft, F.; Geerlings, P. Dependence of the Hardness of Atoms in Molecules on the Local Environment: An ab Initio Study. *J. Phys. Chem.* **1996**, *100*, 15383–15387. [CrossRef]
80. Freedman, A.; Keabian, P.L.; Li, Z.; Robinson, W.A.; Wormhoudt, J.C. Apparatus for Determination of Vapor Pressures at Ambient Temperatures Employing a Knudsen Effusion Cell and Quartz Crystal Microbalance. *Meas. Sci. Technol.* **2008**, *19*, 125102. [CrossRef]
81. Monte, M.J.S.; Hillesheim, D.M. Thermodynamic Study on the Sublimation of the Three Iodobenzoic Acids and of 2-Fluoro- and 3-Fluorobenzoic Acids. *J. Chem. Thermodyn.* **2000**, *32*, 1727–1735. [CrossRef]
82. Wolf, K.L.; Weghofer, H. Uber Sublimationswarmen. *Z. Phys. Chem.* **1938**, *39*, 194–208. [CrossRef]
83. Kruszewski, J.; Krygowski, T.M. Definition of aromaticity basing on the harmonic oscillator model. *Tetrahedron Lett.* **1972**, *13*, 3839–3842. [CrossRef]
84. Krygowski, T.M.; Cyrański, M. Structural Aspects of Aromaticity. *Chem. Rev.* **2001**, *101*, 1385–1410. [CrossRef]
85. Cyrański, M. Energetic Aspects of Cyclic Pi-Electron Delocalization: Evaluation of the Methods of Estimating Aromatic Stabilization Energies. *Chem. Rev.* **2005**, *105*, 3773–3811. [CrossRef] [PubMed]

Sample Availability: Samples of the compounds are not available from the authors.

Publisher's Note: MDPI stays neutral with regard to jurisdictional claims in published maps and institutional affiliations.



© 2020 by the authors. Licensee MDPI, Basel, Switzerland. This article is an open access article distributed under the terms and conditions of the Creative Commons Attribution (CC BY) license (<http://creativecommons.org/licenses/by/4.0/>).

Article

Spectroscopic and Theoretical Study of the Intramolecular π -Type Hydrogen Bonding and Conformations of 2-Cyclopenten-1-ol

 Esther J. Ocola ^{1,2} and Jaan Laane ^{1,2,*}
¹ Department of Chemistry, Texas A&M University, College Station, TX 77843-3255, USA; eocola@chem.tamu.edu

² Institute for Quantum Science and Engineering, Texas A&M University, College Station, TX 77843-4242, USA

* Correspondence: laane@chem.tamu.edu; Tel.: +1-979-845-3352

Abstract: The conformations of 2-cyclopenten-1-ol (2CPOL) have been investigated by high-level theoretical computations and infrared spectroscopy. The six conformational minima correspond to specific values of the ring-puckering and OH internal rotation coordinates. The conformation with the lowest energy possesses intramolecular π -type hydrogen bonding. A second conformer with weaker hydrogen bonding has somewhat higher energy. Ab initio coupled-cluster theory with single and double excitations (CCSD) was used with the cc-pVTZ (triple- ζ) basis set to calculate the two-dimensional potential energy surface (PES) governing the conformational dynamics along the ring-puckering and internal rotation coordinates. The two conformers with the hydrogen bonding lie about 300 cm^{-1} (0.8 kcal/mole) lower in energy than the other four conformers. The lowest energy conformation has a calculated distance of 2.68 \AA from the hydrogen atom on the OH group to the middle of the C=C double bond. For the other conformers, this distance is at least 0.3 \AA longer. The infrared spectrum in the O-H stretching region agrees well with the predicted frequency differences between the conformers and shows the conformers with the hydrogen bonding to have the lowest values. The infrared spectra in other regions arise mostly from the two hydrogen-bonded species.

Keywords: 2-cyclopenten-1-ol; π -type intramolecular hydrogen bonding; infrared spectroscopy; conformations; potential energy surface; theoretical calculations

Citation: Ocola, E.J.; Laane, J. Spectroscopic and Theoretical Study of the Intramolecular π -Type Hydrogen Bonding and Conformations of 2-Cyclopenten-1-ol. *Molecules* **2021**, *26*, 1106. <https://doi.org/10.3390/molecules26041106>

Academic Editors: Rui Fausto, Sylvia Turrell and Gulce Ogruc Ildiz

Received: 28 January 2021

Accepted: 13 February 2021

Published: 19 February 2021

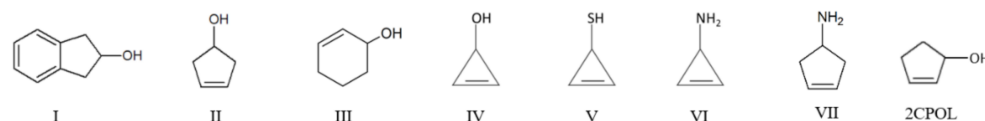
Publisher's Note: MDPI stays neutral with regard to jurisdictional claims in published maps and institutional affiliations.



Copyright: © 2021 by the authors. Licensee MDPI, Basel, Switzerland. This article is an open access article distributed under the terms and conditions of the Creative Commons Attribution (CC BY) license (<https://creativecommons.org/licenses/by/4.0/>).

1. Introduction

For many years, our research group has focused on utilizing both experiment and theory to develop a more comprehensive understanding of one-dimensional vibrational potential energy functions (PEFs) and two-dimensional potential energy surfaces (PESs) [1–7]. In particular, we have investigated the PEFs and PESs which govern the conformational dynamics of small ring molecules as well as those governing internal rotations. In recent years, we have applied our expertise to investigating cyclic molecules that possess intramolecular π -type hydrogen bonding. Among the molecules which we studied are 2-indanol (I) [8], 3-cyclopenten-1-ol (II) [9,10], 2-cyclohexen-1-ol (III) [11], 2-cyclopropen-1-ol (IV) [12], 2-cyclopropen-1-thiol (V) [12], 2-cyclopropen-1-amine (VI) [12], and 3-cyclopenten-1-amine (VII) [13]. These molecules are shown in Scheme 1.



Scheme 1. Molecules with intramolecular π -type hydrogen bonding.

Each of these molecules can exist as several different conformers which are determined by specific coordinate values of the internal rotations of the OH groups and/or the out-of-

plane ring bending modes (ring-puckering or ring-twisting). For each of these molecules, the conformer with the intramolecular π -type hydrogen bonding has the lowest energy, and the π bonding stabilizations range from about 2 to 10 kJ/mol. In our present study, we focus our attention on the π -type hydrogen bonding of the OH group to the C=C double bonds of 2-cyclopenten-1-ol (2CPOL).

Other researchers have also reported previous experimental evidence of intramolecular π -type hydrogen bonding between OH groups and C=C double bonds in molecules such as 2-allylphenol [14], 3-buten-2-ol [15], allyl alcohol [16], 1,4-pentadien-3-ol [17], 2-cyclopropylideneethanol [18], 3-buten-1-ol [19], 1-ethenylcyclopropan-1-ol [20], 4-substituted 2-allylphenols [21], allyl-carbinol [22,23], and methallyl-carbinol [23].

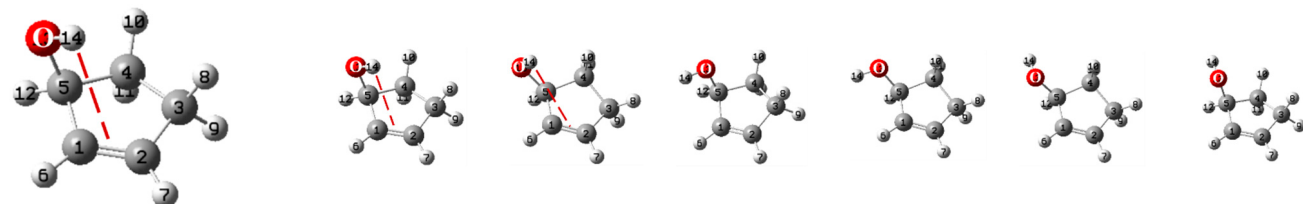
In this paper, we report our experimental infrared spectra and computational results for 2CPOL. The focus of the work was to investigate the different conformations of this molecule and to understand the nature of the π -type hydrogen bond involving the OH group. In addition, we wished to investigate the two-dimensional potential energy surface (PES) that governs the conformational changes.

2. Results and Discussion

2.1. Calculated Molecular Conformations

The six conformers of 2CPOL with energy minima on the PES result from different values of the ring-puckering coordinate and the internal rotation angle of the OH group. Table 1 presents the key features of these conformations. Figure 1 shows the atomic numbering and the geometrical parameters calculated for the two lowest energy conformers. The lowest energy conformation A clearly possesses π -type hydrogen bonding as the calculated distance from the hydrogen atom on the OH group to the middle of the C=C double bond is 2.68 Å. This is very similar to the distance of 2.75 Å for 3-cyclopenten-1-ol (II) and for other cyclic alcohols with this type of π bonding as shown in Table 2. The conformers A and B differ by having carbon atom 4 puckered in opposite directions. According to the CCSD/cc-pVTZ computations, B is only 9 cm⁻¹ higher in energy from A, whereas the other conformers are 293 to 361 cm⁻¹ higher in energy. MP2/cc-pVTZ computations predict B to be 89 cm⁻¹ higher in energy. For B, the calculated distance from the hydrogen atom on the OH group to the middle of the C=C double bond is 3.00 Å, and this is considerably longer than that in the other molecules shown in Table 2, suggesting that the π type hydrogen bonding, if present, is quite small. On the other hand, as discussed below, the calculated and observed O-H stretching frequencies for A and B are both considerably lower than for the other conformers, and this would result from the hydrogen bonding. Figure 2 shows all six calculated structures for the conformational minima. Table 1 presents the ring-puckering angles and OH internal rotation angles, the calculated energy differences, and the calculated relative populations of the six conformers of 2CPOL at 25 °C. Supplementary Table S1 presents the calculated structural parameters for all six conformers from our CCSD/cc-pVTZ computations. Table 1 and Table S1 also show the calculated distances from the hydrogen atoms of the OH group to the center of the C=C bond.

As can be seen in Table 1, the absolute value of the ring-puckering angle is $22^\circ \pm 2^\circ$ for each of the conformers. Thus, the conformational energy differences arise primarily from the internal rotation of the OH group. Conformers A and B differ by about 14° of the OH internal rotational angle, and both may allow the intramolecular hydrogen bonding to occur. However, the A conformer is lower in energy and has a stronger hydrogen bond as reflected by the shorter distance from the OH hydrogen to the center of the C=C bond. For conformer A, this distance is 2.682 Å, whereas for the conformers without hydrogen bonding, the distances are at least 0.3 Å longer.

Table 1. Selected characteristics from CCSD/cc-pVTZ computations for all of the six 2CPOL conformers.


	2CPOL Conformers					
	A	B	C	D	E	F
Energy						
Energy (cm ⁻¹)	0	9	293	304	308	361
Energy (kJ/mol)	0	0.11	3.51	3.64	3.68	4.32
Energy (kcal/mol)	0	0.03	0.84	0.87	0.88	1.03
Relative population (%)						
At 25°	35%	34%	9%	8%	8%	6%
Angles (degrees)						
Ring-puckering angle	−21.1°	22.5°	−23.1°	22.8°	23.7°	−22.8°
OH internal rotation angle, ϕ	24.8°	39.2°	−75.7°	−91.0°	172.3°	166.9°
Distance (Å)						
O–H ₁₄	0.960	0.960	0.958	0.958	0.958	0.958
dH ₁₄ ^a	2.682	3.001	3.019	3.335	3.680	3.554

^a Distance between H₁₄ of the OH group to the midpoint of the double C=C bond.

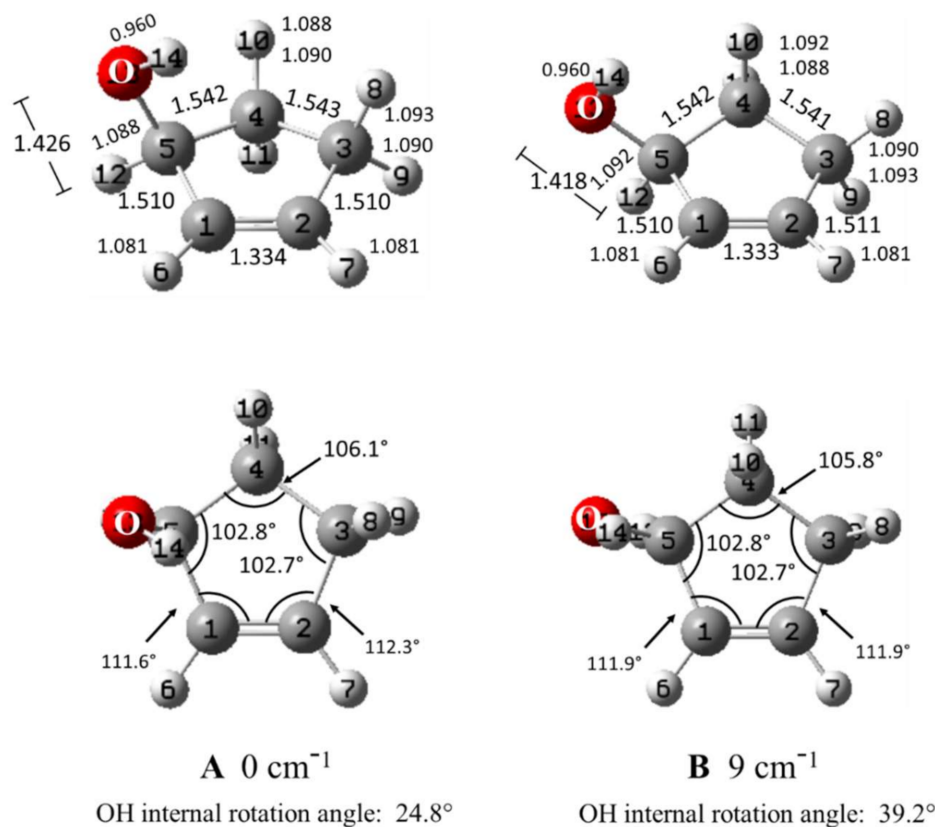
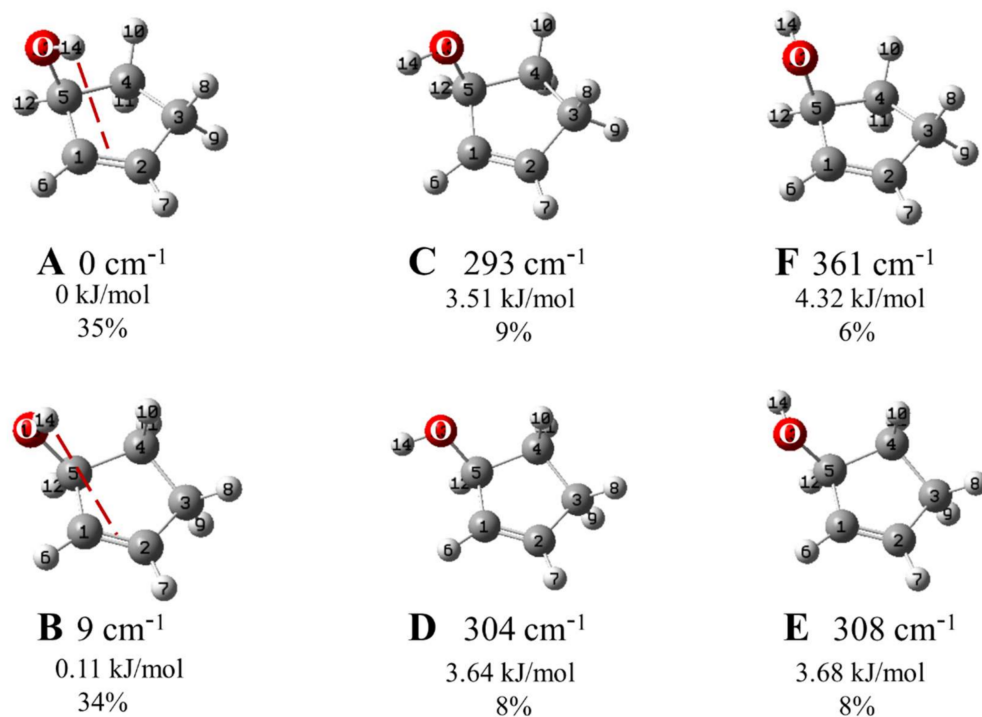
**Figure 1.** Calculated structures of the lowest energy conformers of 2CPOL from coupled-cluster theory with single and double excitations (CCSD)-pVTZ computations.

Table 2. Calculated H- π (C=C) bonding distances in cyclic molecules.

Molecule	H \cdots π (C=C) Distance, Å	Method	Reference
2-indanol (I)	2.650	CCSD/cc-pVTZ	This work
	2.580	MP2/cc-pVTZ	This work
3-cyclopenten-1-ol (II)	2.744	CCSD/cc-pVTZ	This work
	2.673	MP2/cc-pVTZ	This work
2-cyclohexen-1-ol (III)	2.756	CCSD/cc-pVTZ	This work
	2.737	MP2/cc-pVTZ	[11]
2-cyclopropen-1-ol (IV)	2.488	CCSD/cc-pVTZ	[12]
	2.478	MP2/cc-pVTZ	[12]
2-cyclopropen-1-thiol (V)	2.774	CCSD/cc-pVTZ	[12]
	2.740	MP2/cc-pVTZ	[12]
2-cyclopropen-1-amine (VI)	2.583	CCSD/cc-pVTZ	[12]
	2.571	MP2/cc-pVTZ	[12]
3-cyclopenten-1-amine (VII)	2.850	CCSD/cc-pVTZ	[13]
	2.773	MP2/cc-pVTZ	This work
2-cyclopenten-1-ol (2CPOL)	2.682	CCSD/cc-pVTZ	This work
	2.632	MP2/cc-pVTZ	This work

**Figure 2.** Calculated conformational minima, relative energies, and calculated abundances at 25 °C of 2CPOL from CCSD/cc-pVTZ computations. Conformers A, C, and F are puckered down, whereas conformers B, D, and E are puckered up.

2.2. Vibrational Spectra

Figure 3 shows a comparison of the experimental liquid phase and vapor-phase infrared spectra. Since intermolecular hydrogen bonding will be much stronger in the liquid phase than the intramolecular hydrogen bonding, bands corresponding to the specific A, B, C, D, E, and F conformers will not be present in the liquid spectra. Table 3 shows the observed vapor-phase and calculated frequencies for selected vibrations of the A conformer of 2CPOL compared to those observed for the related molecules 3-cyclopentenol (II) [9], 3-cyclopenten-1-amine (VII) [13], and cyclopentene [24].

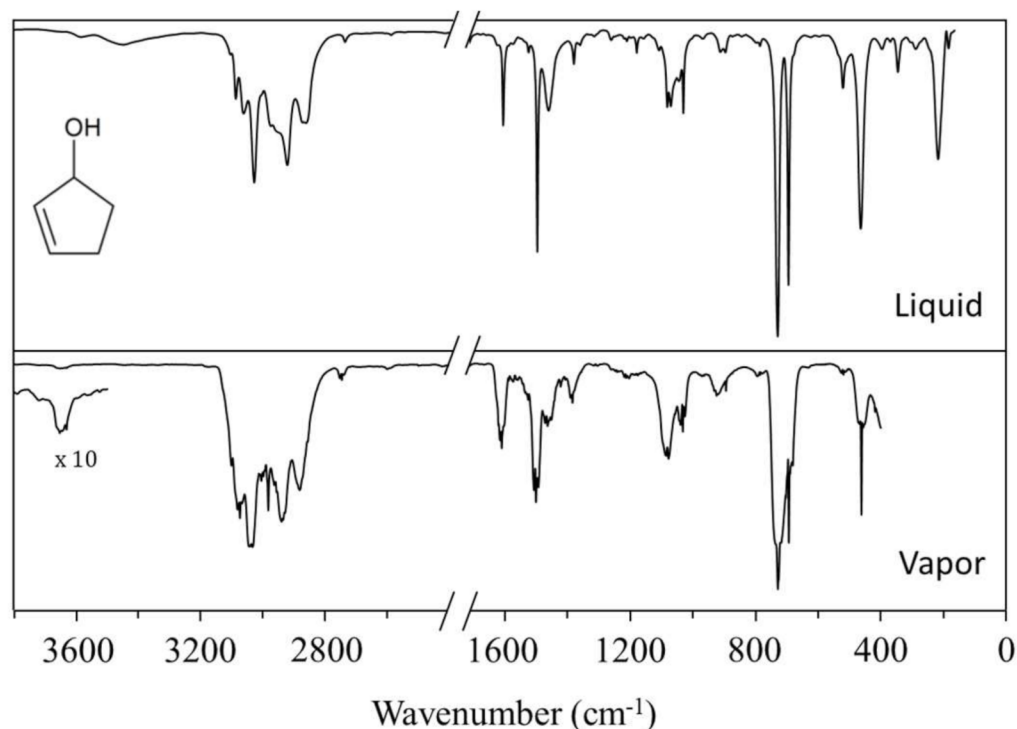


Figure 3. Observed infrared spectra of 2CPOL.

Table 3. Observed and calculated frequency differences for selected vibrations conformer A of 2CPOL compared to those observed for other five-membered ring molecules.

	2-Cyclopenten-1-ol		3-Cyclopenten-1-ol		3-Cyclopenten-1-amine		Cyclopentene				
	Observed		Calculated		Observed		Puckered, C _s				
	A	A	A	A	A	A	A	A			
<u>Ring-Pseudo C_{2v}</u>	Freq.	IR ^a	Freq.	(IR, R) ^b	Freq. ^c	(IR, R) ^{d,e}	Freq. ^f	(IR, R) ^{d,f}	Freq. ^e	(IR, R) ^{b,e}	
A1											
<i>v</i> ₃	C=C stretch	1609	m	1609	(3, 80)	1607	(2, 46)	1613	(m, 88)	1623	(m, 91)
<i>v</i> ₄	CH ₂ deformation	1500	s	1459	(8, 67)	1446 ^f	(3, 19)	1452	(m, 17)	1471 ^f	(vw, 16)
<i>v</i> ₆	=C-H in plane wag	1077	m	1095	(10, 100)	1108 ^f	(4, 95)	1109	(w, 58)	1101	(w, 66)
<i>v</i> ₈	Ring stretch	894	m	869	(13, 60)	832	(5, 3)	804	(s, 43)	900	(m, 100)
<i>v</i> ₉	Ring angle bend	694	s	692	(6, 9)	745	(51, 77)	735	(w, 9)	796 ^g	(vw, 1)
B1											
<i>v</i> ₁₇	CH ₂ deformation	1463	m	1436	(7, 77)	1446 ^f	(17, 19)	1437	(m, 4)	1445 ^f	(m, 23)
B2											
<i>v</i> ₂₅	CH ₂ rock	924	m	971	(14, 36)	948 ^f	(29, 17)	934	(m, 4)	1047	(s, 1)
<i>v</i> ₂₆	=C-H out-of-plane wag	726	s	719	(20, 15)	674	(97, 12)	671	(s, 11)	695	(s, 1)
<i>v</i> ₂₇	Ring puckering	—	—	119	(2, 11)	—	(—, —)	—	(—, —)	—	(—, —)
<u>Other vibrations</u>											
<i>v</i> _{OH}	OH stretch	3632	w	3632	(32, 26)	3623	(41, 9)	N. A.	N. A.	N. A.	N. A.
<i>ω</i> _{CH}	C-H wag (up and down)	1385	m	1386	(80, 53)	1395	(38, 13)	1379	(m, 7)	N. A.	N. A.
<i>ω</i> _{OH}	COH wag	1212	w	1224	(13, 14)	1275	(9, 3)	N. A.	N. A.	N. A.	N. A.
<i>ω</i> _{CO}	C-O wag (up and down)	462	s	487	(5, 21)	—	—	N. A.	N. A.	N. A.	N. A.
<i>ω</i> ' _{CO}	C-O wag (sideways)	346 (L)	w	388	(12, 7)	444	(0.5, 2)	N. A.	N. A.	N. A.	N. A.
<i>v</i> _{CO}	C-O stretch	1032	m	1045	(75, 21)	1048	(54, 0.7)	N. A.	N. A.	N. A.	N. A.
<i>τ</i> _{OH}	OH torsion	217 (L)	m	313	(100, 21)	397 ^h	(—, 8)	N. A.	N. A.	N. A.	N. A.

^a IR intensities. s-strong, m-medium, w-weak. ^b Relative IR and Raman intensities. ^c From Reference [9], unless indicated. ^d From Reference [13], unless indicated. ^e From Reference [24], unless indicated. ^f Reassigned according to MP2/cc-pVTZ computations.

Figure 4 shows the observed infrared band for the conformers of 2CPOL for the O-H stretch region. Based on the calculated frequency differences for the different conformers, the observed IR band at 3632 cm^{-1} is assigned to both A and B; 3654 cm^{-1} is assigned to C; 3664 cm^{-1} is assigned to D; 3664 cm^{-1} is assigned to E; and 3644 cm^{-1} is assigned to F. Table 4 shows the observed O-H stretching frequencies for the six conformers of 2CPOL compared to the calculated values. As expected, the weak hydrogen bonding lowers the O-H stretching frequency so that conformers A and B have the lowest value. The weakening of the O-H bond due to its interaction with the C=C double bond is supported by our CCSD/cc-pVTZ computations. The good agreement between observed and calculated frequencies strongly supports the presence of the six expected conformers. Figure 5 shows the vibrational spectra and assignments of 2CPOL in the $400\text{--}1700\text{ cm}^{-1}$ region. Due to the relatively low molecular populations of the other conformers, all of the bands have been assigned to A and B, which make up 69% of the molecular population. The A and B frequencies are predicted to differ very little in this region so each of the bands seen in Figure 5 arises mainly from both conformers.

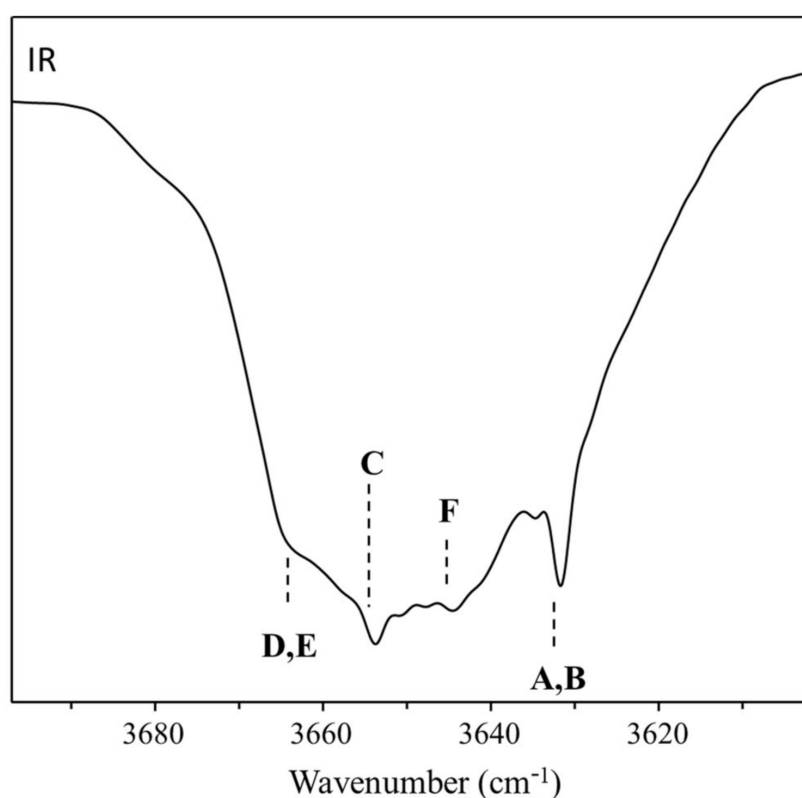


Figure 4. Observed vapor-phase infrared of 2CPOL for the O-H stretch region.

Table 4. O-H stretching frequencies (cm^{-1}) for the six conformers of 2CPOL.

Conformer	Observed		Calculated	
	Frequency	Shift	Frequency	Shift
A	3632	0	3632	0
B	3632	0	3634	2
C	3654	22	3648	16
D	3664	32	3658	26
E	3664	32	3656	24
F	3644	12	3644	12

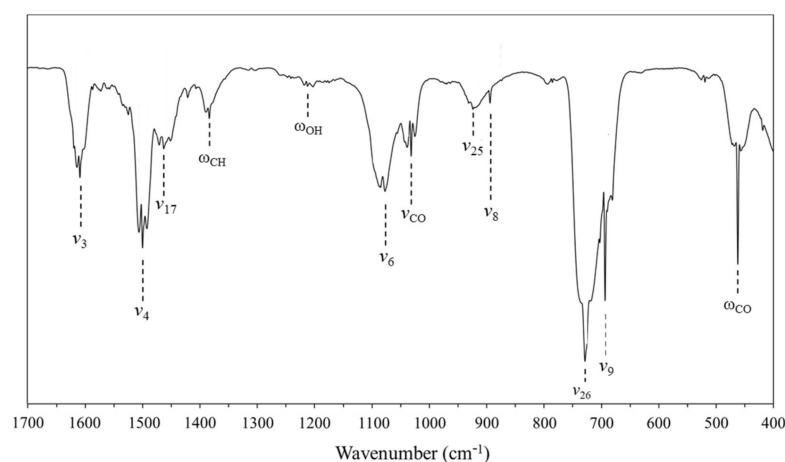


Figure 5. Observed vapor-phase infrared of 2CPOL for the 400–1700 cm^{-1} region.

2.3. Potential Energy Surface

Figure 6 shows the calculated potential energy surface (PES) for 2CPOL in terms of its ring-puckering and OH internal rotation coordinates. This PES was generated by individually computing the energies of more than 150 conformations of 2CPOL using MP2/cc-pVTZ calculations. CCSD/cc-pVTZ calculations for so many conformations would have taken an inordinate amount of computer time. The zero value of the OH internal rotation angle is defined at the position where the hydrogen atom of the hydroxyl group OH points toward the center of the C=C double bond. The PES clearly shows the presence of the six different minima which reside at six different conformational energies. The mathematical function that best satisfies the fit of the calculated data has the form:

$$V = \sum_{i=1}^6 a_i x^i + \sum_{n=1}^6 b_n \sin(n\phi) + \sum_{n=1}^6 c_n \sin(n\phi) \cos(n\phi) + \sum_{n=1}^3 d_n \cos(n\phi) + x \left(\sum_{n=1}^6 e_n \sin(n\phi) + \sum_{n=1}^6 f_n \cos(n\phi) \right) \quad (1)$$

where x and ϕ refer to the puckering and internal rotation coordinates. This equation consists of a polynomial component dependent on the x term to describe the ring-puckering motion, three sums of trigonometric functions to define the periodicity of the OH internal rotation, and a final set of cross terms, which describe the interaction between the ring-puckering and the internal rotation. Equation (1) is complex due to the lack of symmetry in the 2CPOL molecule. Figure 6 also shows the contour map of the PES calculated for 2CPOL. The calculated interconversion barriers from the MP2/cc-pVTZ computations are also indicated. Table 5 shows a comparison of the calculated results for 2CPOL from CCSD/cc-pVTZ computations to those from MP2/cc-pVTZ computations. We expect the CCSD calculations to be more reliable, but it is gratifying to see that the differences are relatively small.

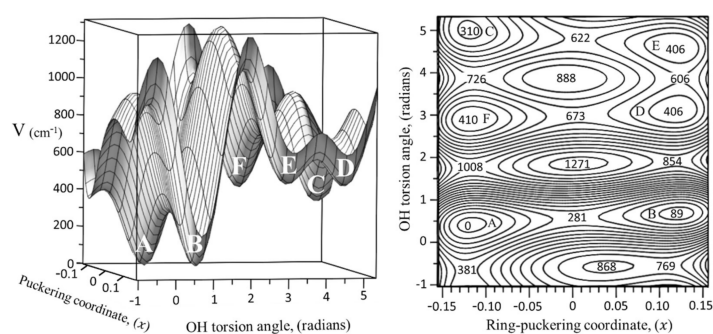


Figure 6. Potential energy surface (PES) and contour map of 2CPOL in terms of its ring-puckering and the OH internal rotation coordinates.

Table 5. Comparison of calculated conformational energies and geometrical parameters for 2CPOL from CCSD/cc-pVTZ and MP2/cc-pVTZ computations.

	2CPOL Conformers					
	A	B	C	D	E	F
Energy, (cm ⁻¹)						
CCSD/cc-pVTZ	0	9	293	304	308	361
MP2/cc-pVTZ	0	89	308	406	406	409
Ring-puckering coordinate, (Å)						
CCSD/cc-pVTZ	-0.102	0.109	-0.112	0.110	0.115	-0.110
MP2/cc-pVTZ	-0.114	0.118	-0.124	0.118	0.124	-0.122
Ring-puckering angle, (degrees)						
CCSD/cc-pVTZ	-21.1°	22.5°	-23.1°	22.8°	23.7°	-22.8°
MP2/cc-pVTZ	-23.6°	24.3°	-25.7°	24.4°	25.6°	-25.3°
OH internal rotation angle, (degrees)						
CCSD/cc-pVTZ	24.8°	39.2°	284.3°	269.0°	172.3°	166.9°
MP2/cc-pVTZ	22.6°	38.7°	286.4°	268.6°	172.3°	166.6°

The PES shows the barrier to ring planarity to be 281 cm⁻¹ and the internal rotation barriers between energy minima to be in the 300 to 1000 cm⁻¹ range.

3. Materials and Methods

2CPOL (95% purity) was purchased from CHEMSAMPCo and was purified by trap-to-trap distillation. Infrared spectra with a spectral resolution of 0.5 cm⁻¹ were recorded using a Bruker Vertex 70 instrument, which was purged by a stream of dry nitrogen gas. The mid-infrared vapor-phase spectrum of 2CPOL was obtained at its vapor pressure at room temperature in a 10 cm cell. 2CPOL has a boiling point of 137 °C and vapor pressure of 3.1 Torr at 25 °C. KBr windows were used for the infrared cell. Spectra of liquid samples were recorded by placing a drop between either KBr plates for the mid-infrared or between CsI plates for the far-infrared. We were not able to record the vapor-phase Raman spectrum of this molecule at the higher temperatures required to obtain sufficient vapor pressure.

3.1. Computations

3.1.1. Structure and Frequency Calculations

The ab initio coupled-cluster theory with single and double excitations (CCSD) method was used with the cc-pVTZ (triple- ζ) basis set to calculate the conformational energies and to compute the geometries for each of the six conformers of 2CPOL. The GAUSSIAN 16 program [25] was used for the computations, and the GaussView 6 program [26] was used to visualize the structures.

Vibrational frequencies were calculated using MP2/cc-pVTZ computations. The scaling factors used for the MP2/cc-pVTZ calculations were 0.970 for frequencies below 1600 cm⁻¹, 0.976 for 1600–2000 cm⁻¹, 0.976 for 1600–2000 cm⁻¹, and 0.948 for higher frequencies except for the O-H stretching region [13]. For the O-H region, 3520–3680 cm⁻¹ the scaling factor of 0.950 was chosen to match the observed value for the lowest energy hydrogen-bonded conformer so that the predicted frequency shifts could readily be calculated.

3.1.2. Potential Energy Surface

The data points required for determining the theoretical PES of 2CPOL and its contour map were obtained from MP2/cc-pVTZ computations. The MAPLE 2015.1 computing environment [27] was used to perform the mathematical fit and plot the data. The PES was generated in terms of the ring-puckering coordinate (x), which is defined in Figure 7a, and the OH internal rotational angle. This angle is defined as the dihedral angle between the OH bond and the black dotted line that connects atom 5 to the mid-point of the C=C double bond as shown in Figure 7b.

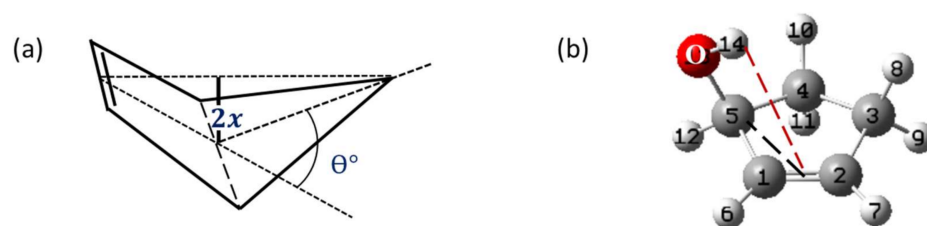


Figure 7. (a) Definition of the ring-puckering coordinate (x), where $2x$ is the distance between the two dotted lines and θ is the ring puckering angle. (b) 2-cyclopenten-1-ol (2CPOL).

4. Conclusions

2CPOL can exist in six different conformers and the one with the lowest energy shows π -type hydrogen bonding. This conformation has an OH hydrogen to the center of the C=C bond distance of 2.68 Å. This value is similar to those we found previously for the related molecules II to IV. The PES for 2CPOL derived in this work shows how the six conformers of this molecule can interconvert from one to another and what are the magnitudes of the barriers that must be overcome. It also shows that the intramolecular π -type hydrogen bonding lowers the conformational energy by approximately 300 cm^{-1} (0.8 kcal/mole). The experimental infrared spectrum in the O-H stretching region shows evidence for the presence of the predicted conformers.

Supplementary Materials: The following is available online, Table S1: Structural parameters for the six conformers of 2CPOL from CCSD/cc-pVTZ computations.

Author Contributions: E.J.O. and J.L. contributed equally. Both authors have read and agreed to the published version of the manuscript.

Funding: This research was funded by Welch Foundation, grant number A-0396. The APC was funded by MDPI.

Data Availability Statement: The data presented in this study are available in this article.

Acknowledgments: The authors wish to thank the Welch Foundation (Grant A-0396) for financial support and the Laboratory for Molecular Simulation at Texas A&M University, College Station for computational resources. This paper is dedicated to Austin Barnes for his many contributions to the fields of spectroscopy and molecular structure.

Conflicts of Interest: The authors declare no conflict of interest. The funders had no role in the design of the study; in the collection, analyses, or interpretation of data; in the writing of the manuscript, or in the decision to publish the results.

Sample Availability: Not available.

References

1. Laane, J.; Ocola, E.J.; Chun, H.J. Vibrational Potential Energy Surfaces in Ground and Electronic Excited States. In *Frontiers and Advances in Molecular Spectroscopy*; Laane, J., Ed.; Elsevier: Amsterdam, The Netherlands, 2017; pp. 101–142. [CrossRef]
2. Laane, J. Vibrational Potential Energy Surfaces in Electronic Excited States. In *Frontiers of Molecular Spectroscopy*; Laane, J., Ed.; Elsevier: Amsterdam, The Netherlands, 2009; pp. 63–132. [CrossRef]
3. Laane, J. Experimental Determination of Vibrational Potential Energy Surfaces and Molecular Structures in Electronic Excited States. *J. Chem. Phys. A* **2000**, *104*, 7715–7733. [CrossRef]
4. Laane, J. Spectroscopic Determination of Ground and Excited State Vibrational Potential Energy Surfaces. *Int. Rev. Phys. Chem.* **1999**, *18*, 301–341. [CrossRef]
5. Laane, J. Vibrational Potential Energy Surfaces and Conformations of Molecules in Ground and Excited Electronic States. *Annu. Rev. Phys. Chem.* **1994**, *45*, 179–211. [CrossRef]
6. Laane, J. Vibrational Potential Energy Surfaces of Non-Rigid Molecules in Ground and Excited Electronic States. In *Structures and Conformations of Non-Rigid Molecules*; Laane, J., Dakkouri, M., Eds.; Kluwer Publishing: Amsterdam, The Netherlands, 1993; pp. 65–98. [CrossRef]
7. Laane, J. Determination of Vibrational Potential Energy Surfaces from Raman and Infrared Spectra. *J. Pure Appl. Chem.* **1987**, *59*, 1307–1326. [CrossRef]

8. Al-Saadi, A.A.; Wagner, M.; Laane, J. Spectroscopic and Computational Studies of the Intramolecular Hydrogen Bonding of 2-Indanol. *J. Phys. Chem. A* **2006**, *110*, 12292–12297. [CrossRef]
9. Ocola, E.J.; Al-Saadi, A.A.; Mlynek, C.; Hopf, H.; Laane, J. Intramolecular π -Type Hydrogen Bonding and Conformations of 3-Cyclopenten-1-ol. 2. Infrared and Raman Spectral Studies at High Temperatures. *J. Phys. Chem. A* **2010**, *114*, 7457–7461. [CrossRef]
10. Al-Saadi, A.A.; Ocola, E.J.; Laane, J. Intramolecular π -Type Hydrogen Bonding and Conformations of 3-Cyclopenten-1-ol. 1. Theoretical Calculations. *J. Phys. Chem. A* **2010**, *114*, 7453–7456. [CrossRef] [PubMed]
11. Ocola, E.J.; Laane, J. Spectroscopic and Theoretical Study of the Intramolecular π -Type Hydrogen Bonding and Conformations of 2-Cyclohexen-1-ol. *J. Phys. Chem. A* **2016**, *120*, 74–80. [CrossRef] [PubMed]
12. Ocola, E.J.; Laane, J. Theoretical Investigation of Intramolecular π -Type Hydrogen Bonding and Internal Rotation of 2-Cyclopropen-1-ol, 2-Cyclopropen-1-thiol and 2-Cyclopropen-1-amine. *Mol. Phys.* **2019**, *17*, 1404–1412. [CrossRef]
13. Ocola, E.J.; Laane, J. Spectroscopic and Theoretical Study of the Intramolecular π -type Hydrogen Bonding and Conformations of 3-Cyclopentene-1-amine. *J. Phys. Chem.* **2020**, *124*, 5907–5916. [CrossRef] [PubMed]
14. Baker, A.W.; Shulgin, A.T. Intramolecular Hydrogen Bonds to π -Electrons and Other Weakly Basic Groups. *J. Am. Chem. Soc.* **1958**, *80*, 5358–5363. [CrossRef]
15. Smith, Z.; Carballo, N.; Wilson, E.B.; Marstokk, K.-M.; Møllendal, H. Conformations, Possible H Bonding, and Microwave Spectrum of 3-Buten-2-ol. *J. Am. Chem. Soc.* **1951**, *107*, 1951–1957. [CrossRef]
16. Murty, A.N.; Curl, R.F., Jr. Microwave Spectrum of Allyl Alcohol. *J. Chem. Phys.* **1967**, *46*, 4176–4180. [CrossRef]
17. Marstokk, K.-M.; Møllendal, H. Microwave Spectrum, Conformation and Intramolecular Hydrogen Bonding of 1,4-Pentadien-3-ol. *Acta Chem. Scand.* **1990**, *44*, 18–22. [CrossRef]
18. Bråse, S.; Klæboe, P.; Marstokk, K.-M.; de Meijere, A.; Møllendal, H.; Nielsen, C.J. Conformational Properties of 2-Cyclopropylideneethanol as Studied by Microwave, Infrared and Raman Spectroscopy and by Ab Initio Computations. *Acta Chem. Scand.* **1998**, *52*, 1122–1136. [CrossRef]
19. Bakke, J.M.; Bjerkeseth, L.H. The Conformational Composition of 3-Buten-1-ol, the Importance of Intramolecular Hydrogen Bonding. *J. Mol. Struct.* **1998**, *470*, 247–263. [CrossRef]
20. Leonov, A.; Marstokk, K.-M.; de Meijere, A.; Møllendal, H. Microwave Spectrum, Conformational Equilibrium, Intramolecular Hydrogen Bonding, Tunneling, and Quantum Chemical Calculations for 1-Ethenylcyclopropan-1-ol. *J. Phys. Chem. A* **2000**, *104*, 4421–4428. [CrossRef]
21. Rademacher, P.; Khelashvili, L.; Kowski, K. Spectroscopic and Theoretical Studies on Intramolecular OH– π Hydrogen Bonding in 4-Substituted 2-Allylphenols. *Org. Biomol. Chem.* **2005**, *3*, 2620–2625. [CrossRef]
22. Miller, B.J.; Lane, J.R.; Kjaergaard, H.G. Intramolecular OH \cdots π Interactions in Alkenols and Alkynols. *Phys. Chem. Chem. Phys.* **2011**, *13*, 14183–14193. [CrossRef]
23. Mackeprang, K.; Schröder, S.D.; Kjaergaard, H.G. Weak Intramolecular OH– π Hydrogen Bonding in Methallyl- and Allyl-Carbinol. *Chem. Phys. Lett.* **2013**, *582*, 31–37. [CrossRef]
24. Al-Saadi, A.A.; Laane, J. Ab Initio and DFT Calculations for the Structure and Vibrational Spectra of Cyclopentene and its Isotopomers. *J. Mol. Struct.* **2007**, *830*, 46–57. [CrossRef]
25. Frisch, M.J.; Trucks, G.W.; Schlegel, H.B.; Scuseria, G.E.; Robb, M.A.; Cheeseman, J.R.; Scalmani, G.; Barone, V.; Mennucci, B.; Petersson, G.A.; et al. *Gaussian 09, Revision A.02*; Gaussian, Inc: Wallingford, CT, USA, 2009.
26. Dennington, R.D.; Keith, T.A.; Millam, J.M. *GaussView 6.1.1, Graphical Interface*; Semichem Inc.: Shawnee, KS, USA, 2000–2019.
27. Waterloo Maple. *Maple 2015*; Waterloo Maple Inc.: Waterloo, ON, Canada, 2015.

Article

Structure and IR Spectroscopic Properties of HNCO Complexes with SO₂ Isolated in Solid Argon

Justyna Krupa ^{1,*}, Maria Wierzejewska ¹ and Jan Lundell ^{2,*}

¹ Faculty of Chemistry, University of Wrocław, Joliot-Curie 14, 50-383 Wrocław, Poland; maria.wierzejewska@chem.uni.wroc.pl

² Department of Chemistry, University of Jyväskylä, P.O. Box 35, FI-40014 Jyväskylä, Finland

* Correspondence: justyna.krupa@chem.uni.wroc.pl (J.K.); jan.c.lundell@ju.fi (J.L.); Tel.: +358-40-744-5270 (J.L.)

Abstract: FTIR spectroscopy was combined with the matrix isolation technique and quantum chemical calculations with the aim of studying complexes of isocyanic acid with sulfur dioxide. The structures of the HNCO ··· SO₂ complexes of 1:1, 1:2 and 2:1 stoichiometry were optimized at the MP2, B3LYPD3, B2PLYPD3 levels of theory with the 6-311++G(3df,3pd) basis set. Five stable 1:1 HNCO ··· SO₂ complexes were found. Three of them contain a weak N-H ··· O hydrogen bond, whereas two other structures are stabilized by van der Waals interactions. The analysis of the HNCO/SO₂/Ar spectra after deposition indicates that mostly the 1:1 hydrogen-bonded complexes are present in argon matrices, with a small amount of the van der Waals structures. Upon annealing, complexes of the 1:2 stoichiometry were detected, as well.

Keywords: hydrogen bond; van der Waals interaction; Matrix isolation; vibrational spectroscopy; computational chemistry

Citation: Krupa, J.; Wierzejewska, M.; Lundell, J. Structure and IR Spectroscopic Properties of HNCO Complexes with SO₂ Isolated in Solid Argon. *Molecules* **2021**, *26*, 6441. <https://doi.org/10.3390/molecules26216441>

Academic Editor: Zhiwu Yu

Received: 29 September 2021

Accepted: 22 October 2021

Published: 25 October 2021

Publisher's Note: MDPI stays neutral with regard to jurisdictional claims in published maps and institutional affiliations.



Copyright: © 2021 by the authors. Licensee MDPI, Basel, Switzerland. This article is an open access article distributed under the terms and conditions of the Creative Commons Attribution (CC BY) license (<https://creativecommons.org/licenses/by/4.0/>).

1. Introduction

Isocyanic acid (HNCO) is an intriguing molecule that has been widely studied both experimentally and theoretically [1–19]. It is one of the simplest molecules containing all four important biogenic elements (C, N, O, and H). There are four open-chain isomers identified for CHNO species: fulminic acid (HCNO), isofulminic acid (HONC), cyanic acid (HOCN) and isocyanic acid (HNCO), with the latter being the most stable. Shapley and Bacskay [18] have shown by various theoretical methods that in addition to these open-chain structures, several cyclic and branched HNCO isomers of much higher energies can exist. Experimentally, structure of HCNO isomers was determined by microwave and infrared spectroscopies. Bondybey et al. [6] characterized HNCO and HCNO molecules isolated in low temperature matrices, as well as their photoproducts upon UV photolysis. Infrared spectra of all four HCNO isomers and their isotopomers isolated in argon matrices were reported Teles et al. [8]. Furthermore, Pettersson et al. [12,13] used infrared and LIF spectroscopies as detection methods to follow the UV photolysis of HNCO isolated in xenon matrices, and identified plethora of interesting photoproducts. Among them were H₂NCO radical, HCO, HXeNCO, HXeCN, HXeNC, and HXeH. It was also found that irradiation of formamide in solid Xe at 193 nm led to HNCO+H₂ binary system as a product specific for the xenon matrix [20]. Some papers on properties of less stable isomers of HNCO have been published as well [21,22].

Isocyanic acid can be found in urban environments and biomass-burning-affected regions [23]. It plays an important role in combustion reactions as for instance RapreNO_x processes in which HNCO reduces NO and other toxic nitrogen oxides via a complex chain reaction [24–27]. HNCO was also detected in 1973 in the interstellar medium [28], and has been considered in several astrophysical surrounds as well [29].

Although the properties of HNCO and its isomers are now relatively well recognized, only a small number of HNCO complexes have been studied so far. Raunier et al. [30] investigated thermal reactivity of HNCO with water ice and presented also infrared spectra of the 1:1 HNCO complex with H₂O isolated in an argon matrix. The complex was found to present shifts of the ν_{NH} and ν_{asNCO} vibrational modes to be -215 and $+13$ cm^{-1} , respectively, relative to the HNCO monomer modes. Based on the data, it was concluded, in agreement with the performed MP2/6-31G(d,p) calculations, that HNCO interacts with H₂O via NH...O hydrogen bond. Sałdyka and Mielke [31] studied photodecomposition of formohydroxamic acid isolated in solid argon and detected formation of two different structures of the 1:1 HNCO complex with water. One of them corresponds to the structure reported by Raunier et al. [30], in which the NH group of isocyanic acid acts as a proton donor toward the oxygen atom of water molecule. For the second structure identified the water molecule acts as a proton donor toward the nitrogen atom of HNCO. Similarly, photodecomposition of N-hydroxyurea and acetohydroxamic acid in argon matrices led to the formation of HNCO complexes with NH₂OH and CH₃OH, respectively [32,33]. Very recently, a report on the photolysis of 1,2,5- and 1,3,4-oxadiazoles was published [34]. Here, laser photolysis of 1,3,4-oxadiazole at 220 nm generated HCN...HNCO and HCN...HOCN complexes, whereas upon a secondary photolysis by a hydrogen lamp, three isocyanide complexes HCNO...HNC, HNCO...HNC and HNC...HOCN were detected and characterized.

Sulfur dioxide is also a very important atmospheric component. It is emitted to the atmosphere from a variety of sources [35,36]. Weak molecular complexes containing SO₂ have received considerable attention since they are considered to affect the mechanism of its oxidation [37–42]. Due to the negative impact of sulfur dioxide on human health, various methods have been developed for its capture [43].

In this paper, we present results of our studies of complexes formed between isocyanic acid (HNCO) and sulfur dioxide. The study relies on low-temperature matrix isolation infrared spectroscopy (MI-FTIR) and computational chemistry as the tools of investigation. MI-FTIR is a successful technique for studying both van der Waals and hydrogen bonded complexes, providing valuable information on the studied molecular systems. One of the most prominent scientists in the field of matrix isolation infrared spectroscopy was Dr. Austin Barnes, who made a great contribution to the development of this method and enriched the subject with many interesting publications and reviews [44–54]. Dr. Barnes used the MI-FTIR method to unravel the secrets of many molecules and their complexes, and here we follow in his footsteps to gain experimental and computational insight into a molecular complex that could have atmospheric or astrochemical interest.

2. Results and Discussion

2.1. Computational Results

2.1.1. Structure and Energetics of the 1:1 HNCO...SO₂ Complexes

At all levels of theory, five minima were found for the 1:1 HNCO...SO₂ complex. Figure 1 shows the MP2 optimized geometries of these molecular complexes. Their MP2 calculated values of intermolecular distances and angles are presented in Table 1. Cartesian coordinates of the optimized species are provided in Table S1 in Supplementary Material. The values of two important topological AIM [55] parameters: the electron density $\rho(\mathbf{r})$ and its Laplacian $\nabla^2\rho(\mathbf{r})$ at the critical points are also shown in Table 1. Additionally, the positions of the bond (3,-1) critical points derived from AIM calculations are depicted in Figure 1. These data provide valuable information on different kinds of non-covalent bonds and intermolecular interactions in the studied complexes.

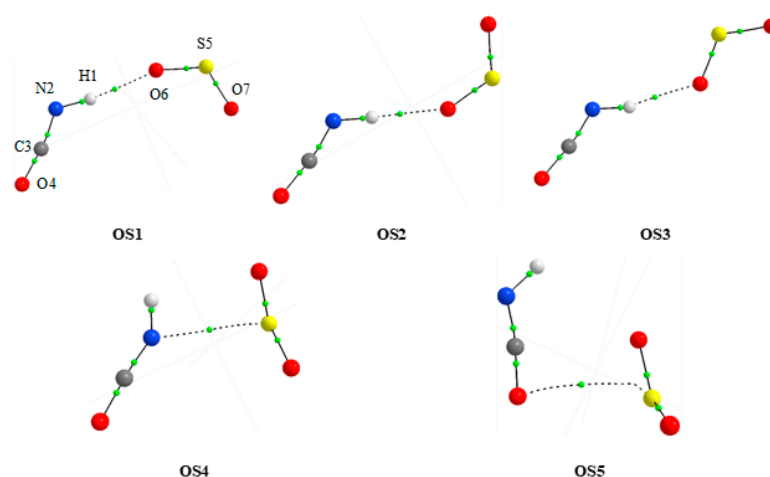


Figure 1. The MP2 optimized structures of the 1:1 complexes of HNCO with SO₂.

Table 1. Interatomic distances (Å), angles (degree) and electron density parameters of the intermolecular bond critical points (au) of the HNCO complexes with SO₂ (1:1) computed at the MP2/6-311++G(3df,3pd) level.

Complex	Intermolecular Parameters ^a			AIM Parameters		
	Interatomic Distances		Angle	BCP	$\rho(r)$	$\nabla^2\rho(r)$
	H...Y	X...Y	X-H...Y			
OS1	2.115	3.121	175.4	H1...O6	0.0167	0.0615
OS2	2.115	3.123	178.9	H1...O6	0.0172	0.0685
OS3	2.115	3.103	166.0	H1...O6	0.0176	0.0694
OS4		3.135		S5...N2	0.0110	0.0367
OS5		3.274		S5...O4	0.0080	0.0289

^a X: N or S; Y: O or N.

Out of five stable 1:1 species, three structures (OS1, OS2 and OS3) are characterized, as supported by AIM parameters, by the presence of a weak N-H...O hydrogen bond. These complexes are planar and differ by the arrangement of the SO₂ moiety with respect to the HNCO molecule. Two other 1:1 complexes are of the van der Waals (vdW) type. The S...N and S...O contacts were found for the OS4 and OS5 species, respectively. It is worth mentioning that the attempts undertaken to optimize the structure in which the N-H group interacts with the sulfur atom of the sulfur dioxide were unsuccessful.

Table 2 presents energetic parameters together with the abundance and dipole moment values obtained for HNCO...SO₂ complexes (1:1) using MP2, B3LYPD3 and B2PLYPD3 methods. These data reveal that the order of the interaction energies in the case of B3LYPD3 calculations differs slightly from those obtained by the MP2 and B2PLYPD3 methods. The same is true for the stability order (ΔE). All three hydrogen bonded complexes are, according to MP2 and B2PLYPD3, more stable than those containing vdW bonds, whereas at B3LYPD3, two structures with hydrogen bonds (OS1, OS2) and one with the vdW interaction (OS5) are the three most stable species. In general, the interaction energies calculated for all five 1:1 complexes are similar in magnitude, and fall within the range of 11.1–12.7, 13.5–14.9 and 12.3–13.8 kJ mol⁻¹, for the MP2, B3LYPD3 and B2PLYPD3 methods, respectively. It is worth noting that the relative Gibbs free energy values favor, at all three levels of theory, the hydrogen-bonded species and, in consequence, their estimated gas phase abundance is much higher than those of the van der Waals complexes. It is also worth noting that the optimized structures of the HNCO...SO₂ complex with three hydrogen-bonded and two van der Waals species are very similar to those reported for HNCS...SO₂ interaction [38].

Table 2. BSSE-corrected interaction energies E_{int} , relative energies ΔE , relative Gibbs free energies ΔG (kJ mol^{-1}), abundance A (%) and dipole moments μ (Debye) of the $\text{HNCO} \cdots \text{SO}_2$ complexes of the 1:1 stoichiometry calculated at MP2, B3LYPD3 and B2PLYPD3 levels.

Complex 1:1	E_{int}	ΔE	ΔG	A	μ
MP2					
OS1	−12.68	0.00	0.00	34	4.3
OS2	−12.59	0.11	0.22	32	4.2
OS3	−12.18	0.54	0.88	24	2.8
OS4	−11.13	1.46	4.45	6	1.6
OS5	−11.13	1.53	5.09	4	1.8
B3LYPD3					
OS1	−14.90	0.00	0.00	38	4.5
OS2	−14.77	0.18	0.33	34	4.5
OS3	−14.35	0.60	1.92	18	2.6
OS4	−13.47	1.31	4.46	6	1.7
OS5	−14.48	0.52	5.55	4	1.9
B2PLYPD3					
OS1	−13.77	0.00	0.00	42	4.5
OS2	−13.68	0.08	0.69	31	4.4
OS3	−13.26	0.49	1.97	19	2.8
OS4	−12.30	1.37	5.54	4	1.8
OS5	−12.80	0.95	5.60	4	1.8

2.1.2. Structure and Energetics of the 1:2 and 2:1 $\text{HNCO} \cdots \text{SO}_2$ Complexes

According to the calculation methods used, six and ten minima are present for 1:2 and 2:1 complexes, respectively. Figure 2 shows the optimized geometries of 1:2 complexes and those of the 2:1 composition are presented in Figure S1 in the Supplementary Materials. Cartesian coordinates of all optimized species are gathered in Table S1. The analogous information as for 1:1 species (Table 1) derived from AIM calculations for 1:2 and 2:1 complexes is presented in Tables S2 and S3 in Supplementary Material.

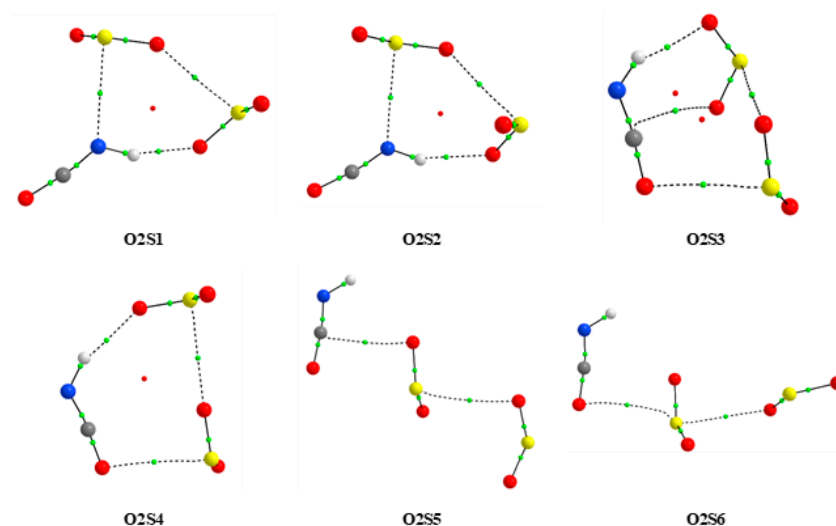


Figure 2. The MP2 optimized structures of the 1:2 complexes of HNCO with SO_2 .

The analysis of the optimized structures of the HNCO complexes with SO_2 of the 1:2 stoichiometry (see Figure 2) reveals that, similarly to the 1:1 species, the $\text{N-H} \cdots \text{O}$ hydrogen bond and different types of van der Waals interaction contribute to the stability of these complexes. The obtained values of the AIM parameters presented in Table S2 confirmed existence of such non-covalent interactions between particular moieties of the

aggregates. Table 3 gathers their interaction energy values which fall into the range of 20.5–34.1 (MP2), 26.2–41.7 (B3LYPD3) and 23.9–38.8 kJ mol⁻¹ (B2PLYPD3). Both types of interactions within the aggregates were found for the 2:1 complexes; however, a higher contribution of the NH...N and NH...O hydrogen bonds was observed. Slightly higher interaction energy values for these forms were estimated in the range of 22.6–41.0 (MP2), 29.2–47.2 (B3LYPD3) and 25.9–44.1 kJ mol⁻¹ (B2PLYPD3). The results obtained for these 2:1 species are presented in Figure S1 and Tables S3 and S4 in the Supplementary Materials.

Table 3. BSSE-corrected interaction energies E_{int} , relative energies ΔE , relative Gibbs free energies ΔG (kJ mol⁻¹) and dipole moments μ (Debye) of the HNCO...SO₂ complexes of the 1:2 stoichiometry calculated at MP2, B3LYPD3 and B2PLYPD3 levels.

Complex 1:2	E_{int}	ΔE	ΔG	μ
MP2				
O2S1	-34.10	0.00	1.71	2.2
O2S2	-33.93	0.17	4.00	2.9
O2S3	-32.22	2.17	8.08	2.3
O2S4	-32.09	2.29	3.28	2.2
O2S5	-20.63	13.38	1.27	2.7
O2S6	-20.50	13.49	0.00	0.7
B3LYPD3				
O2S1	-41.67	0.03	0.00	2.6
O2S2	-41.67	0.00	2.30	2.9
O2S3	-40.17	1.77	5.22	2.2
O2S4	-39.41	2.57	1.05	2.0
O2S5	-26.23	15.15	2.48	2.8
O2S6	-26.15	15.24	1.36	0.8
B2PLYPD3				
O2S1	-38.79	0.00	0.00	2.3
O2S2	-38.62	0.17	2.82	2.9
O2S3	-37.03	2.09	5.91	2.3
O2S4	-36.74	2.39	1.74	2.0
O2S5	-23.93	14.58	2.02	2.8
O2S6	-24.02	14.52	0.59	0.8

2.2. Matrix Isolation Infrared Spectra

First, separate experiments were conducted for HNCO/Ar and SO₂/Ar matrices, and the spectra of monomeric species obtained agreed with those published in the literature, [8,56–58]. As explained by Cugley and Pullin [58] and Teles et al. [8], the ν_{NH} stretching region (ν_1) of HNCO is characterized by three bands of the split rotational $0 \leftarrow 1$ transition and two components of the absorption due to the $0 \leftarrow 0$ transition which originate from Fermi resonance. The values of the unperturbed ν_{NH} fundamental were estimated, on the basis of the positions of the Fermi resonance doublet, at 3511.3 cm⁻¹ [8]. In turn, for the SO₂ monomer isolated in argon matrices doublets were observed in each fundamental vibrational mode region. Upon annealing, the intensity of the low wavenumber component of the doublets decreased whereas the high wavenumber band was nearly temperature insensitive. Such a behavior arises from two types of site at which SO₂ molecules reside: stable sites (cubic close packing) and metastable sites (hexagonal close packing) [56].

Of the six infrared active vibrations of HNCO, two ν_{sNCO} stretching and γ_{NCO} deformation are very low in intensity. Two other vibrations, namely δ_{NH} and δ_{NCO} are strongly coupled and their behavior upon complexation is expected to be ambiguous and difficult to follow. The two remaining bands of ν_{NH} and ν_{asNCO} stretching modes are characterized by relatively high intensity, and they should be good markers for providing information about the structure of the studied complexes.

2.2.1. HNCO ··· SO₂ Complexes of the 1:1 Stoichiometry

When both HNCO/Ar and SO₂/Ar gas mixtures were co-deposited at 15 K (10 K for measurements), several new bands appeared when compared to the spectra of the parent molecules in solid argon. Table 4 summarizes the selected wavenumber shifts calculated for the 1:1 complexes using the three computational methods compared to the experimental results. In addition, theoretical infrared wavenumbers and intensities obtained for the monomers and the 1:1 complexes are presented in Table S5 in the Supplementary Material. It is known that the intermolecular vibrational modes of weak hydrogen bonded and van der Waals complexes are strongly anharmonic [52,59,60]. Therefore, for the experimental data analysis and discussion, the wavenumber shifts were mostly used.

Table 4. Selected wavenumber shifts calculated for the 1:1 complexes using the MP2, B3LYPD3 and B2PLYPD3 methods with basis set 6-311++G(3df,3pd) compared to the experimental results.

MP2					B3LYPD3					B2PLYPD3					Mode	Exp. ^a
OS1	OS2	OS3	OS4	OS5	OS1	OS2	OS3	OS4	OS5	OS1	OS2	OS3	OS4	OS5		
-67	-67	-63	-14	-33	-74	-81	-76	-16	-32	-74	-74	-72	-12	-28	ν NH	-24.0, -39.5, <u>-49.5</u> , -51.5sh, -66.5
+2	+2	+1	0	-3	0	+1	+1	-3	-2	+1	+1	+1	-1	-3	ν_{as} NCO	+1.5, +6.0
-4	-3	-4	-3	-1	-8	-5	-5	-7	-7	-5	-4	-4	-5	-4	ν_{asym} SO ₂	-5.5

^a The experimental shifts were calculated relative to the corresponding monomer band positions at 3511.5, 1355.0 and 2259.0 cm⁻¹, respectively. The underlined value corresponds to the most intense band of the complex in the ν NH region.

Figure 3 shows the ν NH, ν_{as} NCO and ν_{as} SO₂ stretching vibration regions of the spectra of the HNCO/SO₂/Ar matrices at two different HNCO/SO₂ ratios obtained directly after deposition and one of them obtained upon annealing at 30 K/10 K. The corresponding fragments of the HNCO/Ar and SO₂/Ar spectra are also shown for comparison purposes. The respective ranges of the difference spectrum are presented at the top of Figure 3 showing changes upon complexation and annealing the matrix at 30 K/10 K. Directly after deposition of the HNCO/SO₂/Ar mixtures (traces b and c in Figure 3), a new, relatively intense band at 3462.0 cm⁻¹ with a shoulder at 3460.0 cm⁻¹ appeared in the ν NH stretching mode region, as well as three much weaker bands at 3487.5, 3472.0 and 3445.0 cm⁻¹. The intensity ratio of all these bands is the same at both concentrations applied, indicating that they originate from the 1:1 HNCO ··· SO₂ complexes. These bands are accompanied by absorptions in the ν_{as} NCO stretching region at 2265.0 and 2260.5 cm⁻¹.

According to the performed calculations, there should be two other modes of relatively high intensity for 1:1 complexes, namely asymmetric stretching ν_{as} SO₂ and in-plane deformation δ NH (coupled with δ NCO bending). As shown in Figure 3, a new band appeared upon complexation in the ν_{as} SO₂ region at 1349.5 cm⁻¹ with the red shift of 5.5 cm⁻¹ compared to the ν_{as} SO₂ band of the sulfur dioxide monomer isolated in a stable site. This absorption is hardly seen upon deposition because it is close to one of those assigned to the SO₂ dimer [57]. However, it is apparent upon annealing at 30 K. Our calculations predicted a red shift in the range 1 and 8 cm⁻¹ for all five 1:1 HNCO ··· SO₂ complexes. Therefore, the ν_{as} SO₂ mode may not be considered to be a good indicator of the structure of the studied species.

In turn, as it comes to the δ NH deformation mode, it has been suggested to give rise to a very broad absorption and was not observed in the spectra of HNCS ··· SO₂ in solid argon [38]. It is probably that a similar situation is true for the HNCO ··· SO₂ complex, since the δ NH mode could not be localized in the present spectra.

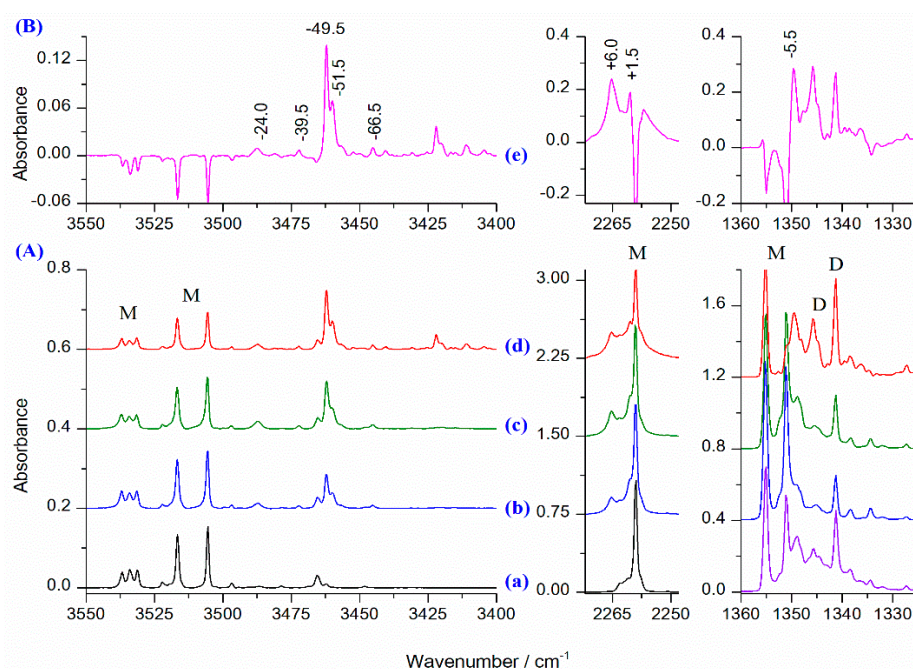


Figure 3. (A) The ν_{NH} , ν_{asNCO} and ν_{asSO_2} regions in the spectra of matrices: HNCO/Ar = 1/6000 or SO₂/Ar = 1/1400 (after 5 min at 30 K/10 K) (a), HNCO/SO₂/Ar = 1/2/5600 (b), HNCO/SO₂/Ar = 1/4/5600 (c), and matrix (c) after 10 min at 30 K/10 K (d). (B) The difference spectrum (e) obtained by subtracting the spectrum (a) from the spectrum (d) (pink trace). The letters M and D denote HNCO and SO₂ monomers and dimer bands, respectively.

Structure determination of the complexes formed between HNCO and SO₂ seems to be a difficult task. As can be seen from Table 2, the differences between the interaction energies (E_{int}) of the five 1:1 HNCO \cdots SO₂ complexes are less than 1.55 kJ mol⁻¹ and the same is true for the relative energy ΔE . Larger differences are predicted for the relative Gibbs free energies. For the hydrogen bonded species, the differences are less than 2 kJ mol⁻¹ whereas for the OS4 and OS5 complexes the ΔG values are, depending on the method used, between 4.45 and 5.60 kJ mol⁻¹. These values determine the population which are clearly higher for the OS1, OS2 and OS3 complexes compared to the OS4 and OS5. Therefore, it can be expected, assuming that the gas equilibrium is frozen in the low temperature matrices upon deposition, that the hydrogen bonded systems will predominate in the studied matrices.

As is evident from Table 4, where the calculated wavenumber shifts for the key modes for different 1:1 HNCO \cdots SO₂ complexes are gathered, none of the three computational methods gives fully satisfactory agreement between theoretical and experimental values. However, taking into account both the presented spectroscopic data and the population estimated for the 1:1 complexes, tentative conclusions can be drawn regarding their structure in the studied argon matrices. Thus, the most intense band of the HNCO \cdots SO₂ complex at 3462.0 cm⁻¹ ($\Delta\nu = -49.5$ cm⁻¹) with a shoulder at 3460.0 cm⁻¹ ($\Delta\nu = -51.5$ cm⁻¹), as well as a weak band at 3445.0 cm⁻¹ ($\Delta\nu = -66.5$ cm⁻¹), may be assigned to the ν_{NH} mode in the hydrogen bonded structures (OS1–OS3). The calculated red shift for this vibration is overestimated, even though values of two other shifts presented in Table 4 fit relatively well to the experimental values. In turn, two weak absorptions at 3472.0 and 3487.5 cm⁻¹ characterized with smaller ν_{NH} shifts ($\Delta\nu = -39.5$ and -24.0 cm⁻¹, respectively) may originate from the van der Waals structures (OS4–OS5). The intensity of all these bands increased in a similar way when the matrix was annealed at 30 K.

The ν_{NH} bands are accompanied by two new bands in the ν_{asNCO} region at 2260.5 and 2265.0 cm⁻¹ characterized by similar behavior upon annealing. These bands are blue shifted by 1.5 and 6.0 cm⁻¹ as compared with the HNCO monomer band and the direction of these changes agrees well with those predicted theoretically for the hydrogen

bonded HNCO \cdots SO₂ (1:1) complexes however the latter shift is slightly higher than those predicted to fall in the range of 0–2 cm⁻¹ (see Table 4).

2.2.2. HNCO Complexes with SO₂ of the 1:2 and 2:1 Stoichiometry

As follows from the computational data shown in Table 3, the four 1:2 complexes containing the N-H \cdots O hydrogen bond and van der Waals interactions (O2S1–O2S4) are generally more stable than two remaining species with exclusively van der Waals contacts. The O2S1–O2S4 structures are characterized by very similar values of the interaction energy with a maximum difference of 2.26 kJ mol⁻¹. Their relative energies are also quite close to each other.

When HNCO/SO₂/Ar matrices were subjected to 10 min annealing at 30 K, bands of the monomeric HNCO in the resultant spectra (taken at 10 K) decreased, absorptions assigned to the 1:1 complexes increased slightly, and new bands situated at 3440.0, 3422.0 with the 3420.0 shoulder, 3411.0 and 3404.0 cm⁻¹ appeared (Figure 3). These absorptions are assigned to the HNCO complexes with SO₂ of the 1:2 stoichiometry. The wavenumber red shifts of these bands relative to the monomeric ν NH are equal to 71.5, 89.5/91.5, 100.5 and 107.5 cm⁻¹, respectively. Table 5 presents selected shifts calculated for the six 1:2 complexes. In addition, computed infrared wavenumbers and intensities obtained for the 1:2 complexes (not observed in the present study) are presented in Table S6 in Supplementary material.

Table 5. Selected wavenumber shifts calculated for the 1:2 complexes using the MP2, B3LYPD3 and B2PLYPD3 methods with basis set 6-311++G(3df,3pd).

MP2						B3LYPD3						B2PLYPD3						Mode
O2S1	O2S2	O2S3	O2S4	O2S5	O2S6	O2S1	O2S2	O2S3	O2S4	O2S5	O2S6	O2S1	O2S2	O2S3	O2S4	O2S5	O2S6	
-118	-123	-74	-82	-19	-15	-143	-145	-68	-91	-21	-18	-132	-137	-74	-88	-17	-14	ν NH
-2	-3	-1	1	-1	0	-2	-3	-3	-3	-4	-3	-2	-3	-1	-1	-2	-1	ν_{as} NCO
-2	-3	-7	-3	-2	-2	-11	-12	-12	-10	-6	-7	-7	-8	-7	-7	-5	-6	ν_{asym} SO ₂
-4	-5	-9	-6	-5	-6	-17	-17	-17	-14	-11	-12	-11	-11	-9	-10	-9	-9	ν_{asym} SO ₂

Similar to the 1:1 complexes case, none of the three computational methods used reproduces the experimental shift values very well. However, the values presented in Table 5 clearly point to the presence of such 1:2 structures which contain HNCO unit hydrogen bonded to the oxygen atom of one the SO₂ moiety. Two such structures, i.e., O2S3 and O2S4, show ν NH to be red shifted, and the values are close to the experimental values (74 and 82, 68 and 91, 74 and 88 cm⁻¹ at MP2, B3LYPD3, B2PLYPD3, respectively). These forms are probably present in the studied matrices, but the two complexes exhibiting larger shifts, O2S1 and O2S2, cannot fully be excluded based on the data available here. The vibrational shifts of the ν_{as} NCO mode predicted for the hydrogen bonded 1:2 species are, with one exception, small negative values in the 2–4 cm⁻¹ range and are not observed experimentally.

Theoretical infrared wavenumbers and intensities obtained for the HNCO complexes with SO₂ of the 2:1 stoichiometry are presented in Table S7 in the Supplementary Material. At the experimental conditions applied in these studies bands originating from such species were not identified.

3. Computational and Experimental Details

3.1. Computational Methods

To support the analysis of the experimental data, computational studies for the 1:1, 1:2 and 2:1 complexes formed between HNCO and SO₂ were carried out using the Gaussian16 program package [61]. The initial geometry of the 1:1 complexes was based on that found for the HNCS \cdots SO₂ structures [38]. The 1:2 and 2:1 complexes were obtained from the geometry optimized for the 1:1 HNCO \cdots SO₂ species by adding the HNCO or SO₂ subunit. Structures of the complexes were optimized at the MP2, [62–65] B3LYPD3 [66–70]

and B2PLYPD3 [71–73] levels of theory using the 6–311++G(3df,3pd) [74,75] basis set. Optimization of the complexes was performed with the Boys-Bernardi full counterpoise method by Dannenberg [76,77]. The interaction energies were estimated by subtracting the energies of the isolated monomers with the frozen geometry from the energy of the 1:1, 1:2 or 2:1 complexes. The relative energy ΔE and relative Gibbs free energy ΔG for a given structure were obtained by subtracting the E or G values of the most stable complex from the values calculated for the given species. The relative abundance of the complexes was estimated based on the calculated Gibbs free energy values using equation: $\Delta G = -RT \ln K$, where ΔG is the difference between Gibbs free energy for two given isomeric forms (at $T = 298$ K) and K is the equilibrium constant for these species.

The topological analysis of the electron density (AIM) [55] was performed at the MP2/6–311++G(3df,3pd) level using AIM studio program (Version 19.10.12, Professional [78]). Generally, the applied methods predicted very much similar geometries for the complexes. There are no significant differences in the values of the bond distances and bond angles computed at various levels. The values of dihedral angles were also fairly independent of the method used.

The harmonic vibrational wavenumbers and infrared intensities were calculated at MP2, B3LYPD3 and B2PLYPD3 levels for all optimized complexes in order to support the analysis of the experimentally obtained vibrational spectra. Spectral shifts upon complexation were obtained as the difference between the complex and monomer vibrational wavenumbers.

3.2. Matrix Isolation FTIR Studies

Isocyanic acid was obtained by strongly heating cyanuric acid powder in an evacuated quartz vessel. Generated HNCO vapor passed several times through P_2O_5 to remove water and HCN and was condensed in a liquid-nitrogen trap and stored in a 250 mL glass bulb. The gaseous mixtures were prepared by mixing of HNCO and SO_2 with argon (Messer, 5.0) in two containers in a vacuum system. Matrices were deposited through two jets containing mixtures of molecular subunits with argon onto a CsI window kept at 15 K. Pressure of the gas mixtures and the deposition rates were controlled by piezotransducers (model 902B, MKS Instruments) installed in both deposition lines. Low temperature was attained using a closed cycle helium refrigerator (APD-Cryogenics) and measured directly at the sample holder by a silicon diode sensor coupled with the digital controller (Scientific Instruments). Infrared spectra were taken at 10 K in a transmission mode with 0.5 cm^{-1} resolution by means of a Bruker IFS 66 Fourier Transform spectrometer equipped with a liquid cooled MCT detector.

4. Conclusions

For the first time, theoretical and matrix isolation FTIR studies of molecular complexes formed between isocyanic acid and sulfur dioxide are reported. All three computational methods used (MP2, B3LYPD3 and B2PLYPD3) revealed five stable 1:1 complexes in which the two subunits are bonded either by the N–H \cdots O hydrogen bond or by van der Waals forces of different type. The differences between the interaction energy (E_{int}) and the relative energy (ΔE) values calculated for the 1:1 HNCO \cdots SO $_2$ complexes are less than 1.55 kJ mol^{-1} . Larger differences are predicted for relative Gibbs free energies which is higher by 4–5 kJ mol^{-1} for the two van der Waals species. These predictions were confirmed by the experimental infrared spectra which showed that complexes with hydrogen bonding were more abundant than those with van der Waals interaction. The performed calculations also revealed several stable structures for the HNCO complexes with SO_2 of the 1:2 stoichiometry. It appeared that the more stable are those containing a N–H \cdots O hydrogen bond in addition to the S \cdots N and S \cdots O van der Waals interactions. These structures give rise to weak bands appearing in the ν_{NH} stretching region upon annealing of the matrix.

Supplementary Materials: The following are available online. Figure S1: The MP2 optimized structures of the 2:1 complexes of HNCO with SO₂. Red dots are the RCP's., Table S1: The MP2 cartesian coordinates of all 1:1, 1:2 and 2:1 optimized species of HNCO with SO₂, Table S2. Interatomic distances (Å), angles (degree) and electron density parameters of the intermolecular bond critical points BCP (au) and ring critical points RCP(au) of the HNCO complexes with SO₂ (1:2) computed at the MP2/6-311++G(3df,3pd) level, Table S3: Interatomic distances (Å), angles (degree) and electron density parameters of the intermolecular bond critical points (au) of the HNCO complexes with SO₂ (2:1) computed at the MP2/6-311++G(3df,3pd) level, Table S4: BSSE-corrected interaction energies E_{int} , relative energies ΔE , relative Gibbs free energies ΔG (kJ mol⁻¹) and dipole moments μ (Debye) of the HNCO-SO₂ complexes of the 2:1 stoichiometry calculated at MP2, B3LYPD3 and B2PLYPD3 levels, Table S5: Theoretical infrared wavenumbers ($\bar{\nu}$, cm⁻¹) and intensities (I, km mol⁻¹) for monomers and 1:1 complexes using the MP2, B3LYPD3 and B2PLYPD3 methods with basis set 6-311++G(3df,3pd), Table S6: Theoretical infrared wavenumbers ($\bar{\nu}$, cm⁻¹) and intensities (I, km mol⁻¹) for 1:2 complexes using the MP2, B3LYPD3 and B2PLYPD3 methods with basis set 6-311++G(3df,3pd), Table S7: Theoretical infrared wavenumbers ($\bar{\nu}$, cm⁻¹) and intensities (I, km mol⁻¹) for 2:1 complexes using the MP2, B3LYPD3 and B2PLYPD3 methods with basis set 6-311++G(3df,3pd).

Author Contributions: Conceptualization, J.K. and M.W.; methodology, J.K. and M.W.; software, J.K. and J.L.; validation, J.K., M.W. and J.L.; formal analysis, J.K. and M.W.; investigation, J.K.; resources, M.W. and J.L.; data curation, M.W.; writing—original draft preparation, J.K. and M.W.; writing—review and editing, M.W. and J.L.; visualization, J.K.; supervision, M.W.; project administration, M.W.; funding acquisition, M.W. and J.L. All authors have read and agreed to the published version of the manuscript.

Funding: This research was funded by the Academy of Finland, grant number 332023, for the work performed at the University of Jyväskylä.

Institutional Review Board Statement: Not applicable.

Informed Consent Statement: Not applicable.

Data Availability Statement: Not applicable.

Acknowledgments: Allocation of computer time at the Wrocław Centre for Networking and Supercomputing (Wrocław, Poland) is gratefully acknowledged.

Conflicts of Interest: The authors declare no conflict of interest. The funders had no role in the design of the study; in the collection, analyses, or interpretation of data; in the writing of the manuscript, or in the decision to publish the results.

Sample Availability: Samples of the compounds are not available from the authors.

References

- Kewley, R.; Sastry, K.V.N.; Winnewisser, M. The Millimeter wave spectra of isocyanic and isothiocyanic acids. *J. Mol. Spectrosc.* **1963**, *10*, 418–441. [CrossRef]
- Jacox, M.E.; Milligan, D.E. Low-temperature infrared study of intermediates in the photolysis of HNCO. *J. Chem. Phys.* **1964**, *40*, 2457–2460. [CrossRef]
- Steiner, D.A.; Wishah, K.A.; Polo, S.R.; McCubbin, T.K. Infrared spectrum of isocyanic acid between 465 and 1100 cm⁻¹. *J. Mol. Spectrosc.* **1979**, *76*, 341–373. [CrossRef]
- Drozdowski, W.S.; Baronavski, A.P.; McDonald, J.R. Photodissociation of HNCO at 193 nm. NH(a₁Δ) internal energy distribution and reaction rate with O₂. *Chem. Phys. Lett.* **1979**, *64*, 421–425. [CrossRef]
- Yamada, K. Molecular structure and centrifugal distortion constants of isocyanic acid from the microwave, millimeter wave, and far-infrared spectra. *J. Mol. Spectrosc.* **1980**, *79*, 323–344. [CrossRef]
- Bondybey, V.E.; English, J.H. Infrared spectra and isomerization of CHNO species in rare gas matrices. *J. Mol. Spectrosc.* **1982**, *92*, 431–442. [CrossRef]
- Fujimoto, G.T.; Umstead, M.E.; Lin, M.C. Dynamics of CO formation in the photodissociation of HNCO and CH₂CO at 193 nm. *Chem. Phys.* **1982**, *65*, 197–203. [CrossRef]
- Teles, J.H.; Maier, G.; Hess, B.A., Jr.; Schaad, L.J.; Winnewisser, M.; Winnewisser, B.P. The CHNO isomers. *Chem. Ber.* **1989**, *122*, 753–766. [CrossRef]
- Ruscic, B.; Berkowitz, J. The H–NCO bond energy and ΔH^0_f (NCO) from photoionization mass spectrometric studies of HNCO and NCO. *J. Chem. Phys.* **1994**, *100*, 4498. [CrossRef]

10. Boyce, C.W.; Gillies, C.W.; Warner, H.; Gillies, J.Z.; Lovas, F.J.; Suenram, R.D. Microwave spectra, structure, and electric dipole moment of the Ar-isocyanic acid van der Waals complex. *J. Mol. Spectrosc.* **1995**, *171*, 533–545. [CrossRef]
11. Droz-Georget, T.; Zyrianov, M.; Sanov, A.; Reisler, H. Photodissociation of HNCO: Three competing pathways. *Ber. Bunsenges. Phys. Chem.* **1997**, *101*, 469–477. [CrossRef]
12. Pettersson, M.; Khriachtchev, L.; Jolkkonen, S.; Räsänen, M. Photochemistry of HNCO in solid Xe: Channels of UV photolysis and creation of H₂NCO radicals. *J. Phys. Chem. A* **1999**, *103*, 9154–9162. [CrossRef]
13. Pettersson, M.; Khriachtchev, L.; Lundell, J.; Jolkkonen, S.; Räsänen, M. Photochemistry of HNCO in solid Xenon: Photoinduced and thermally activated formation of HXeNCO. *J. Phys. Chem. A* **2000**, *104*, 3579–3583. [CrossRef]
14. Yu, S.; Su, S.; Dai, D.; Yuan, K.; Yang, X. Vacuum ultraviolet photodissociation dynamics of isocyanic acid: The hydrogen elimination channel. *J. Phys. Chem. A* **2013**, *117*, 13564–13571. [CrossRef] [PubMed]
15. Yu, S.; Su, S.; Dorenkamp, Y.; Wodtke, A.M.; Dai, D.; Yuan, K.; Yang, X. Competition between direct and indirect dissociation pathways in ultraviolet photodissociation of HNCO. *J. Phys. Chem. A* **2013**, *117*, 11673–11678. [CrossRef]
16. Zhang, Z.; Chen, Z.; Huang, C.; Chen, Y.; Dai, D.; Parker, D.H.; Yang, X. Imaging the pair-correlated HNCO photodissociation: The NH(a¹Δ) + CO(X¹Σ⁺) channel. *J. Phys. Chem. A* **2014**, *118*, 2413–2418. [CrossRef] [PubMed]
17. Holzmeier, F.; Wolf, T.J.A.; Gienger, C.; Wagner, I.; Bozek, J.; Nandi, S.; Nicolas, C.; Fischer, I.; Guhr, M.; Fink, R.F. Normal and resonant Auger spectroscopy of isocyanic acid, HNCO. *J. Chem. Phys.* **2018**, *149*, 034308. [CrossRef]
18. Shapley, W.A.; Bacskay, G.B. A Gaussian-2 quantum chemical study of CHNO: Isomerization and molecular dissociation reactions. *J. Phys. Chem. A* **1999**, *103*, 6624–6631. [CrossRef]
19. Mladenović, M.; Elhiyani, M.; Lewerenz, M. Electric and magnetic properties of the four most stable CHNO isomers from ab initio CCSD(T) studies. *J. Chem. Phys.* **2009**, *131*, 034302. [CrossRef]
20. Lundell, J.; Krajewska, M.; Räsänen, M. Matrix isolation Fourier transform infrared and ab initio studies of the 193-nm-induced photodecomposition of formamide. *J. Phys. Chem. A* **1998**, *102*, 6643–6650. [CrossRef]
21. Maier, G.; Teles, J.H.; Hess, B.A., Jr.; Schaad, L.J. Carboxime (isofulminic acid). *Angew. Chem. Int. Ed. Engl.* **1988**, *27*, 938–939. [CrossRef]
22. Mladenovic, M.; Lewerenz, M.; Mccarthy, M.C.; Thaddeus, P. Isofulminic acid, HONC: Ab initio theory and microwave spectroscopy. *J. Chem. Phys.* **2009**, *131*, 174308. [CrossRef] [PubMed]
23. Jathar, S.H.; Heppding, C.; Link, M.F.; Farmer, D.K.; Akherati, A.; Kleeman, M.J.; de Gouw, J.A.; Veres, P.R.; Roberts, J.M. Investigating diesel engines as an atmospheric source of isocyanic acid in urban areas. *Atmos. Chem. Phys.* **2017**, *17*, 8959–8970. [CrossRef]
24. Perry, R.A.; Siebers, D.L. Rapid reduction of nitrogen oxides in exhaust gas streams. *Nature* **1986**, *324*, 657–658. [CrossRef]
25. Wicke, B.G.; Grady, K.A.; Ratcliffe, J.W. Limitations on the rapid reduction of nitrogen oxides in exhaust gas streams. *Nature* **1989**, *338*, 492–493. [CrossRef]
26. Lyon, R.K.; Cole, J.A. A reexamination of the RapreNO_x process. *Combust. Flame* **1990**, *82*, 435–443. [CrossRef]
27. Miller, J.A.; Bowman, C.T. Kinetic modeling of the reduction of nitric oxide in combustion products by isocyanic acid. *Int. J. Chem. Kinet.* **1991**, *23*, 289–313. [CrossRef]
28. Buhl, D.; Snyder, L.E.; Schwartz, P.R.; Edrich, J. HNCO in the galactic centre. *Nature* **1973**, *243*, 513–514. [CrossRef]
29. Hernandez-Gómez, A.; Sahnoun, E.; Caux, E.; Wiesenfeld, L.; Loinard, L.; Bottinelli, S.; Hammami, K.; Menten, K.M. Modelling the abundance structure of isocyanic acid (HNCO) towards the low-mass solar type protostar IRAS 16293–2422. *Mon. Not. R. Astron. Soc.* **2019**, *483*, 2014–2030. [CrossRef]
30. Raunier, S.; Chiavassa, T.; Allouche, A.; Marinelli, F.; Aycard, J.-P. Thermal reactivity of HNCO with water ice: An infrared and theoretical study. *Chem. Phys.* **2003**, *288*, 197–210. [CrossRef]
31. Sałdyka, M.; Mielke, Z. Photodecomposition of formohydroxamic acid. Matrix isolation FTIR and DFT studies. *Phys. Chem. Chem. Phys.* **2003**, *5*, 4790–4797. [CrossRef]
32. Sałdyka, M. Photodecomposition of N-hydroxyurea in argon matrices. FTIR and theoretical studies. *RSC Adv.* **2013**, *3*, 1922–1932. [CrossRef]
33. Sałdyka, M.; Mielke, Z. Photochemistry of acetohydroxamic acid in solid argon. FTIR and theoretical studies. *J. Phys. Chem. A* **2018**, *122*, 60–71. [CrossRef] [PubMed]
34. Keresztes, B.; Pál Csonka, I.; Lajgút, G.G.; Bazsó, G.; Tarczay, G. Matrix isolation study on the 1:1 hydrogen-bonded complexes [H,C,N] ··· [H,C,N,O]. *J. Mol. Struct.* **2020**, *1219*, 128535. [CrossRef]
35. Seinfeld, J.H.; Pandis, S.N. *Atmospheric Chemistry and Physics: From Air Pollution to Climate Change*; John Wiley & Sons: Hoboken, NJ, USA, 2016.
36. Finlayson-Pitts, B.; Pitts, N.R., Jr. *Atmospheric Chemistry: Fundamentals and Experimental Techniques*; J. Wiley and Sons: New York, NY, USA, 1986.
37. Wierzejewska, M.; Olbert-Majkut, A. Photolysis of Matrix Isolated HONO/SO₂ System. Identification and Infrared Spectra of Nitrososulfonic Acid HO(NO)SO₂ and Hydroxysulfonyl HOSO₂ Radical. *J. Phys. Chem. A* **2003**, *107*, 10944–10952. [CrossRef]
38. Krupa, J.; Wierzejewska, M. Structural and spectroscopic properties of complexes formed between HNCS and SO₂ in low temperature argon matrices. *Spectrochim. Acta A* **2017**, *183*, 144–149. [CrossRef]
39. Biczysko, M.; Krupa, J.; Wierzejewska, M. Theoretical studies of atmospheric molecular complexes interacting with NIR to UV light. *Faraday Discuss.* **2018**, *212*, 421–441. [CrossRef]

40. Hirabayashia, S.; Ito, F.; Yamada, K.M.T. Infrared spectra of the $(\text{H}_2\text{O})_n\text{-SO}_2$ complexes in argon matrices. *J. Chem. Phys.* **2006**, *125*, 034508. [CrossRef] [PubMed]
41. Osthoff, H.D.; Jäger, W. Mid-infrared spectrum of the weakly bound complex $\text{CO}_2\text{-SO}_2$. *Mol. Phys.* **2006**, *104*, 2861–2869. [CrossRef]
42. Ford, T.A. The Structures, Molecular Orbital Properties and Vibrational Spectra of the Homo- and Heterodimers of Sulphur Dioxide and Ozone. An Ab Initio Study. *Molecules* **2021**, *26*, 626. [CrossRef]
43. Sahoo, D.K.; Mundlapati, V.R.; Gagrai, A.A.; Biswal, H.S. Efficient SO_2 Capture through Multiple Chalcogen Bonds, Sulfur-Centered Hydrogen Bonds and $\text{S} \cdots \pi$ Interactions: A Computational Study. *ChemistrySelect* **2016**, *1*, 1688–1694. [CrossRef]
44. Barnes, A.J.; Orville-Thomas, W.J.; Szczepaniak, K. Studies of intermolecular interactions by matrix isolation vibrational spectroscopy. *J. Mol. Struct.* **1978**, *45*, 75–87. [CrossRef]
45. Bentwood, R.M.; Barnes, A.J. Orville-Thomas, W.J. Studies of intermolecular interactions by matrix isolation vibrational spectroscopy. Self-association of water. *J. Mol. Struct.* **1980**, *84*, 391–404. [CrossRef]
46. Barnes, A.J. Matrix isolation vibrational spectroscopy as a tool for studying conformational isomerism. *J. Mol. Struct.* **1984**, *113*, 161–174. [CrossRef]
47. Barnes, A.J. Infrared photochemistry of hydrogen-bonded complexes trapped in low temperature matrices. *Faraday Discuss. Chem. Soc.* **1988**, *86*, 45–53. [CrossRef]
48. Barnes, A.J.; Lasson, E.; Nielsen, C.J. Molecular complexes of nitric acid with N_2 , CO and NO studied by matrix isolation IR spectroscopy. *J. Chem. Soc. Faraday Trans.* **1995**, *91*, 3111–3116. [CrossRef]
49. Barnes, A.J.; Legon, A.C. Proton transfer in amine-hydrogen halide complexes: Comparison of low temperature matrices with the gas phase. *J. Mol. Struct.* **1998**, *448*, 101–106. [CrossRef]
50. Barnes, A.J.; Latajka, Z.; Biczysko, M. Proton transfer in strongly hydrogen-bonded molecular complexes: Matrix effects. *J. Mol. Struct.* **2002**, *614*, 11–21. [CrossRef]
51. Barnes, A.J.; Mielke, Z. Matrix effects on hydrogen-bonded complexes trapped in low-temperature matrices. *J. Mol. Struct.* **2012**, *1023*, 216–221. [CrossRef]
52. Haupa, K.; Bil, A.; Barnes, A.; Mielke, Z. Isomers of the acetic acid–water complex trapped in an argon matrix. *J. Phys. Chem. A* **2015**, *119*, 2522–2531. [CrossRef]
53. Wierzejewska, M.; Yaremko, A.M.; Virko, S.V.; Barnes, A.J.; Ratajczak, H. On the unusual IR spectra of the pentachlorophenol–trimethylamine complex in low temperature matrices. *Chem. Phys. Lett.* **2016**, *660*, 102–106. [CrossRef]
54. Barnes, A.J. Matrix isolation studies of hydrogen bonding. An historical perspective. *J. Mol. Struct.* **2018**, *1163*, 77–85. [CrossRef]
55. Bader, R.F.W. *Atoms in Molecules, A Quantum Theory*; Oxford University Press: Oxford, UK, 1990.
56. Maillard, D.; Allavena, M.; Perchard, J.P. Spectres vibrationnels du dioxyde de soufre dans une matrice d'argon, d'azote et de xenon. *Spectrochim. Acta A* **1975**, *31*, 1523–1531. [CrossRef]
57. Schriver-Mazzuoli, L.; Schriver, A.; Wierzejewska-Hnat, M. Fourier transform infrared study of sulfur dioxide dimer II. Argon matrix. *Chem. Phys.* **1995**, *199*, 227–243. [CrossRef]
58. Cugley, P.A.; Pullin, A.D.E. Matrix isolated spectra of HNCO and HNCS in the far infrared. *Chem. Phys. Lett.* **1973**, *19*, 203–208. [CrossRef]
59. Biswal, H.S.; Bhattacharyya, S.; Bhattacharjee, A.; Wategaonkar, S. Nature and strength of sulfur-centred hydrogen bonds: Laser spectroscopic investigations in the gas phase and quantum-chemical calculations. *Int. Rev. Phys. Chem.* **2015**, *34*, 99–160. [CrossRef]
60. Bhattacharyya, S.; Bhattacharjee, A.; Shirhatti, P.R.; Wategaonkar, S. $\text{O-H} \cdots \text{S}$ Hydrogen Bonds Conform to the Acid–Base Formalism. *J. Phys. Chem. A* **2013**, *117*, 8238–8250. [CrossRef] [PubMed]
61. *Gaussian 16, Revision C.01*; Frisch, M.J.; Trucks, G.W.; Schlegel, H.B.; Scuseria, G.E.; Robb, M.A.; Cheeseman, J.R.; Scalmani, G.; Barone, V.; Petersson, G.A.; Nakatsuji, H.; et al. (Eds.) Gaussian, Inc.: Wallingford, CT, USA, 2016.
62. Head-Gordon, M.; Pople, J.A.; Frisch, M.J. MP2 energy evaluation by direct methods. *Chem. Phys. Lett.* **1988**, *153*, 503–506. [CrossRef]
63. Head-Gordon, M.; Head-Gordon, T. Analytic MP2 frequencies without fifth order storage: Theory and application to bifurcated hydrogen bonds in the water hexamer. *Chem. Phys. Lett.* **1994**, *220*, 122–128. [CrossRef]
64. Frisch, M.J.; Head-Gordon, M.; Pople, J.A. Semi-direct algorithms for the MP2 energy and gradient. *Chem. Phys. Lett.* **1990**, *166*, 281–289. [CrossRef]
65. Sæbø, S.; Almlöf, J. Avoiding the integral storage bottleneck in LCAO calculations of electron correlation. *Chem. Phys. Lett.* **1989**, *154*, 83–89. [CrossRef]
66. Becke, A.D. Density-functional exchange-energy approximation with correct asymptotic-behavior. *Phys. Rev. A* **1988**, *38*, 3098–3100. [CrossRef] [PubMed]
67. Becke, A.D. Density-functional thermochemistry. III. The role of exact exchange. *J. Chem. Phys.* **1993**, *98*, 5648–5652. [CrossRef]
68. Lee, C.; Yang, W.; Parr, R.G. Development of the Colle-Salvetti correlation-energy formula into a functional of the electron density. *Phys. Rev. B* **1988**, *37*, 785–789. [CrossRef] [PubMed]
69. Grimme, S.; Antony, J.; Ehrlich, S.; Krieg, H. A consistent and accurate ab initio parameterization of density functional dispersion correction (DFT-D) for the 94 elements H-Pu. *J. Chem. Phys.* **2010**, *132*, 154104. [CrossRef] [PubMed]

70. Grimme, S.; Ehrlich, S.; Goerigk, L. Effect of the damping function in dispersion corrected density functional theory. *J. Comp. Chem.* **2011**, *32*, 1456–1465. [CrossRef]
71. Grimme, S. Semiempirical hybrid density functional with perturbative second-order correlation. *J. Chem. Phys.* **2006**, *124*, 034108. [CrossRef] [PubMed]
72. Schwabe, T.; Grimme, S. Double-hybrid density functionals with long-range dispersion corrections: Higher accuracy and extended applicability. *Phys. Chem. Chem. Phys.* **2007**, *9*, 3397–3406. [CrossRef]
73. Biczysko, M.; Panek, P.; Scalmani, G.; Bloino, J.; Barone, V. Harmonic and anharmonic vibrational frequency calculations with the double-hybrid B2PLYP method: Analytic second derivatives and benchmark studies. *J. Chem. Theory Comput.* **2010**, *6*, 2115–2125. [CrossRef]
74. McLean, A.D.; Chandler, G.S. Contracted Gaussian-basis sets for molecular calculations. I. Second row atoms, $Z=11-18$. *J. Chem. Phys.* **1980**, *72*, 5639. [CrossRef]
75. Raghavachari, K.; Binkley, J.S.; Seeger, R.; Pople, J.A. Self-consistent molecular orbital methods. XX. Basis set for correlated wave functions. *J. Chem. Phys.* **1980**, *72*, 650. [CrossRef]
76. Boys, S.F.; Bernardi, F. Calculation of small molecular interactions by differences of separate total energies. Some procedures with reduced errors. *Mol. Phys.* **1970**, *19*, 553–566. [CrossRef]
77. Simon, S.; Duran, M.; Dannenberg, J.J. How does basis set superposition error change the potential surfaces for hydrogen-bonded dimers? *J. Chem. Phys.* **1996**, *105*, 11024. [CrossRef]
78. Keith, T.A. *AIMAll (Version 19.10.12)*, TK Gristmill Software; Overland Park, KS, USA, 2019. Available online: aim.tkgristmill.com (accessed on 5 January 2021).

Article

The Structures, Molecular Orbital Properties and Vibrational Spectra of the Homo- and Heterodimers of Sulphur Dioxide and Ozone. An Ab Initio Study

Thomas A. Ford

School of Chemistry and Physics, University of KwaZulu-Natal, Westville Campus, Private Bag X54001, Durban 4000, South Africa; ford@ukzn.ac.za

Abstract: The structures of a number of dimers of sulphur dioxide and ozone were optimized by means of a series of ab initio calculations. The dimer species were classified as either genuine energy minima or transition states of first or higher order, and the most probable structures consistent with the experimental data were confirmed. The molecular orbitals engaged in the interactions resulting in adduct formation were identified and relations between the orbitals of the dimers of the valence isoelectronic monomer species were examined. The vibrational spectra of the most probable structures were computed and compared with those reported in the literature, particularly with spectra observed in cryogenic matrices. The calculations were extended to predict the properties of a number of possible heterodimers formed between sulphur dioxide and ozone.

Keywords: ab initio; sulphur dioxide; ozone; dimers; complexes; structures; vibrational spectra

Citation: Ford, T.A. The Structures, Molecular Orbital Properties and Vibrational Spectra of the Homo- and Heterodimers of Sulphur Dioxide and Ozone. An Ab Initio Study. *Molecules* **2021**, *26*, 626. <https://doi.org/10.3390/molecules26030626>

Academic Editor: Cecilia Coletti

Received: 1 January 2021

Accepted: 20 January 2021

Published: 25 January 2021

Publisher's Note: MDPI stays neutral with regard to jurisdictional claims in published maps and institutional affiliations.



Copyright: © 2021 by the author. Licensee MDPI, Basel, Switzerland. This article is an open access article distributed under the terms and conditions of the Creative Commons Attribution (CC BY) license (<https://creativecommons.org/licenses/by/4.0/>).

1. Introduction

Among the family of non-covalent interactions [1], the chalcogen bond has enjoyed much prominence in recent years. The definition of a chalcogen bond is a “net attractive interaction between an electrophilic region associated with a chalcogen atom in a molecular entity and a nucleophilic region in another, or the same, molecular entity” [2]. Interest in non-covalent bonding in species containing oxygen and sulphur atoms has prompted us to revisit our theoretical study of the sulphur dioxide dimer [3], with particular emphasis on its vibrational spectrum, and to extend our computations to the dimer of the valence isoelectronic analogue ozone. The weakly-bound sulphur dioxide homodimer has been the subject of a number of theoretical investigations [3–9]; in most of these studies the authors considered a number of potential candidates for the global minimum structure, using a variety of medium-sized basis sets. Gas phase studies have been carried out on the dimer by microwave and radiofrequency spectroscopy [9–12], while the infrared spectrum of sulphur dioxide has been extensively investigated in cryogenic matrices [13–23]. In many of these vibrational studies the SO₂ dimer has been specifically identified. Sulphur dioxide also forms binary complexes with a variety of atoms and other small molecules; theoretical studies have included those with H₂S and HCN [5], H₂O [5,11], Ar [6], BF₃ [24], C₂H₂ [25], CHCl₃ [26], NH₃ and (CH₃)₃N [27], CO₂, OCS, CS₂ and N₂O [28], NH₃, H₂O, HF, PH₃, H₂S and HCl [29], and CH₃CN [30]. Many of these, and other, binary complexes have been observed in the gas phase, including those with H₂O [11], BF₃ [24], CH₃CN [30], HF and HCN [31], C₂H₂ [32], C₅H₅N [33], (CH₃)₂O [34], CO₂ [35], OCS [36], CS₂ [37], N₂O [38], and CHCl₃ [39]. As was the case for the SO₂ dimer, matrix isolation vibrational spectroscopy has also proved a fruitful source of data on binary complexes of sulphur dioxide. In this way, complexes of SO₂ with CH₃CN [30], Cl₂, HBr, H₂O, NH₃ and C₂H₄ [40], NH₃ and (CH₃)₃N [41], HF [42], H₂O [43], C₆H₆ [44], and BF₃ [45] in cryogenic matrices have been characterized.

Far less work has been reported on the analogous ozone dimer, indeed, only one theoretical study has apparently been carried out on this species [46]. The vibrational spec-

trum of ozone in cryogenic matrices has been investigated [16,47–59]. However, most of these studies have been more concerned with isotopic analysis [47,48,54,55], the geometry of the monomer [50], with fluorescence [53], or photochemical [55–59] reactions in the matrices. Only in one case was the ozone dimer mentioned [59], and in another example the appearance of additional absorptions was attributed to the existence of multiple trapping sites [51]. A number of binary complexes containing ozone have been observed in low-temperature matrices, including olefins [60], HBr, H₂O, NH₃, H₂CO and C₂H₄ [61], PH₃ [62,63], HF [42,64], H₂O [65], H₂O and SO₂ [66], CH₂F₂ [67], CO [68], and O atoms [69]. In addition to the formation of binary complexes, ozone has been found to be a fairly reactive species in cryogenic matrices, and reactions between O₃ and a range of small molecules and atoms have been analysed. These include reactions with CS₂ and OCS [70], C₂H₄ [71], NO [72–74], NO₂ [75], N₂H₄ [76], AsH₃ [77], SbH₃ [78], P₂ and P₄ [79–81], HCN [82], Cl₂ and Br₂ [83], Cl [84,85], and Ne atoms [86].

The SO₂-O₃ heterodimer has so far eluded investigation, either theoretically or experimentally.

2. Results and Discussion

2.1. Molecular Structures

A number of trial structures were investigated for each adduct. We used as a template the publication of Hargittai [87], which examined a set of seven likely structural models for the metal dihalides, which we considered candidates as potential structures for the sulphur dioxide dimer. This trial set included three cyclic, two “linear”, and two bifurcated models, most of which were also investigated by other workers [3–6,8,9]. Along with the seven Hargittai structures, we also included two species that involved a S . . . S interaction, with no expectation that they would be strong candidates for the preferred SO₂ dimer structure, but simply for completeness. Our nine possible dimer structures are illustrated in Figure 1 and their symmetries, energies, and Hessian indices are given in Table 1. Figure 2 shows their relative energies, separated according to their classification as genuine minima or transition states. We conclude, in agreement with the previous works [3–6,9] and with most of the experimental data [9,10,12,13,15,19,20,22,23], that our dimer **5** is the global minimum and is a non-symmetric species of C_s symmetry. The centrosymmetric dimer **2** is also a genuine minimum, being less than 1 kJ mol^{−1} higher in energy. Dimer **2**, however, being centrosymmetric, would not be observable by microwave spectroscopy, therefore, there is no possibility of identifying this structure in the gas phase. Table 2 reports the computed geometrical parameters of each dimer and their deviations from the corresponding monomer values. The perturbations of the bond lengths and bond angles from their monomer values are small (less than 0.3 pm and 0.6°, respectively), indicating a weak interaction in each case.

Table 1. Properties of some dimers of sulphur dioxide.

Dimer	Symmetry	E/H	Hessian Index	Relative Energy/ kJ mol ^{−1}
5	C _s	−1095.9350 3678 41	0	0
2	C _i	−1095.9347 9649 54	0	0.63
3	C ₂	−1095.9343 3272 07	1	1.85
7	C _s	−1095.9341 4356 32	1	2.35
1	C _{2h}	−1095.9339 0229 81	2	2.98
4	C _{2v}	−1095.9326 6035 55	2	6.24
6	C _{2v}	−1095.9322 8723 09	2	7.22
9	D _{2d}	−1095.9300 0351 25	2	13.32
8	D _{2h}	−1095.9298 6160 93	4	13.59

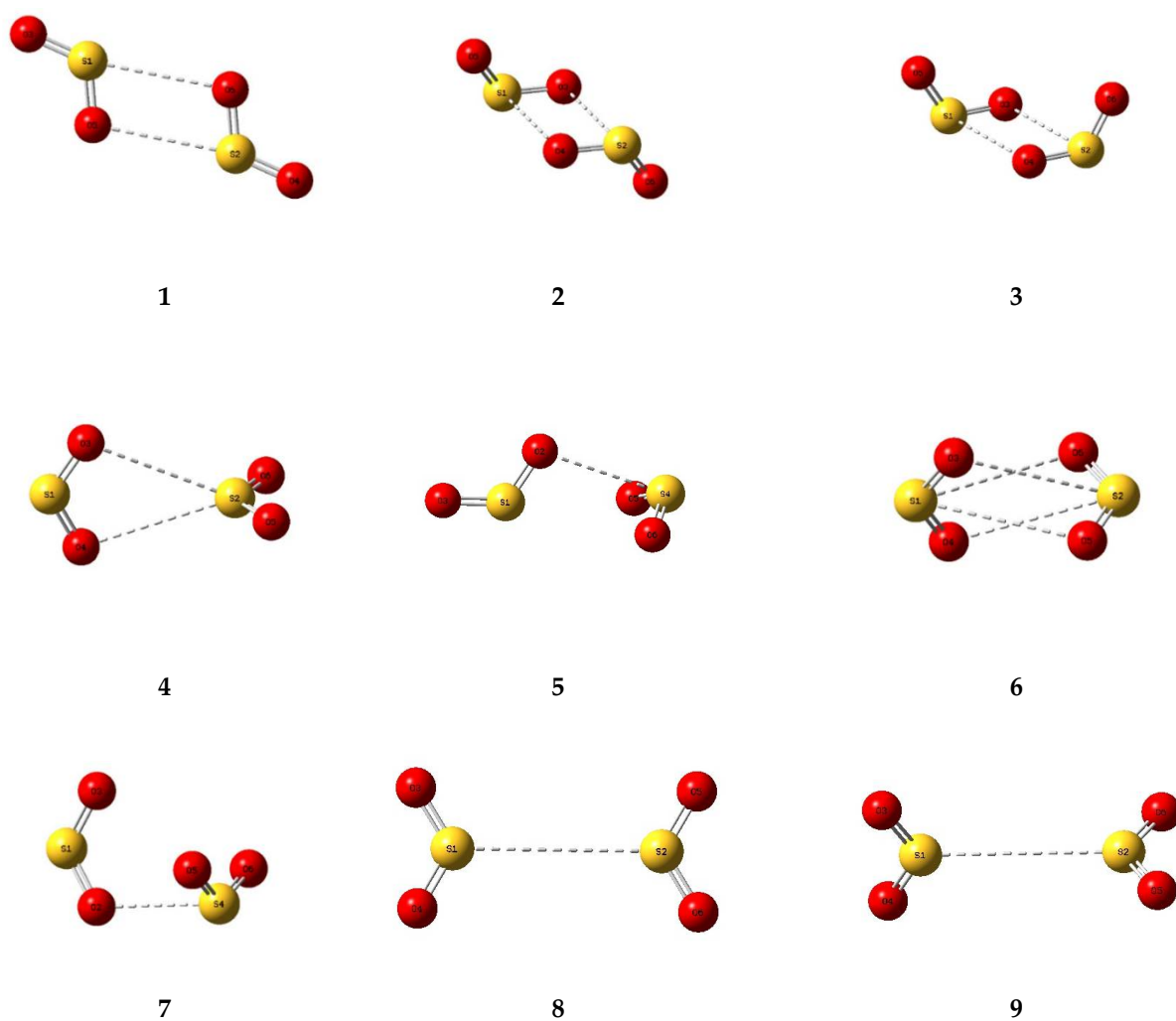


Figure 1. Optimized structures of some dimers of sulphur dioxide.

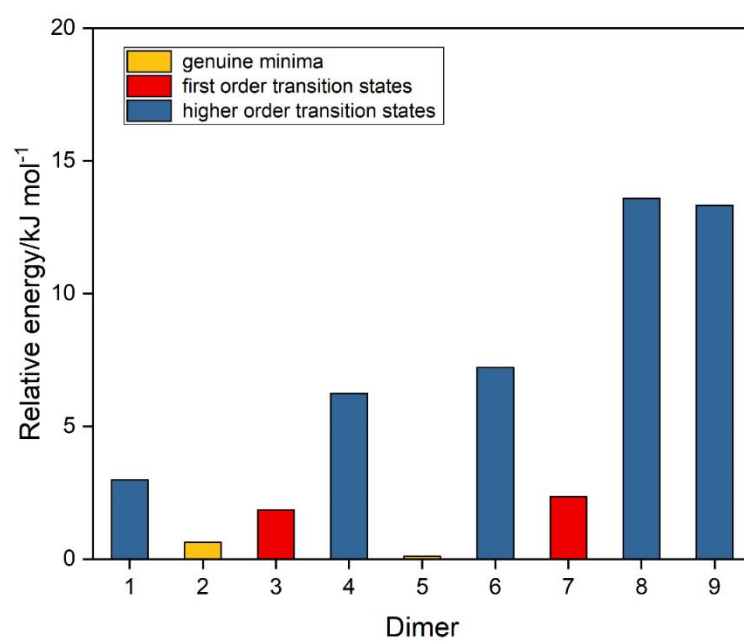


Figure 2. Relative energies of the sulphur dioxide dimers.

Table 2. Optimized geometrical parameters of sulphur dioxide dimers **5** and **2**, and their changes relative to the sulphur dioxide monomer. See Figure 1 for numbering of the atoms.

Dimer 5			Dimer 2		
Parameter	Dimer Value	Difference from Monomer Value	Parameter	Dimer Value	Difference from Monomer Value
r(S1O2)/pm	146.57	0.21	r(S1O3,S2O4)/pm	146.51	0.15
r(S1O3)/pm	146.32	−0.03	r(S1O5,S2O6)/pm	146.30	−0.05
r(S4O5,S4O6)/pm	146.41	0.06	∠O3S1O5,O4S2O6/deg	118.40	−0.39
∠O2S1O3/deg	118.21	−0.58	r(S1 ... O4,S2 ... O3)/pm	322.37	-
∠O5S4O6/deg	118.21	−0.58	∠O5S1 ... O4,O6S2 ... O3/deg	83.85	-
r(O2 ... S4)/pm	318.79	-	∠S1O3 ... S2,S2O4 ... S1/deg	106.60	-
∠S1O2 ... S4/deg	100.27	-	∠O5S1O3 ... S2/deg ^a	73.23	-
∠O2 ... S4O5,O2 ... S4O6/deg	79.37	-	∠O6S2O4 ... S1/deg ^a	−73.23	-
∠O5S4 ... O2S1/deg ^a	−60.82	-			
∠O6S4 ... O2S1/deg ^a	60.82	-			

^a Dihedral angle.

The corresponding set of nine potential dimer structures for ozone are illustrated in Figure 3 and their properties are collected in Table 3. Their relative energies are presented in Figure 4. Only one of our ozone dimers (dimer **2**) was found to be a true minimum. This adduct corresponds with the second lowest energy sulphur dioxide dimer, while the counterpart of the C_s global minimum of $(SO_2)_2$ (ozone dimer **5**) is about 5 kJ mol^{-1} higher in energy. Our result is in contrast to that of Slanina and Adamowicz [46], who found the C_s counterpart of our dimer **5** to be the global minimum species. Part of the difference may be attributed to the use of different basis sets, but it has long been realized that the ozone monomer presents particularly formidable challenges for computation [88,89], and this is even more apparent for its dimer. The parameters of our ozone dimer **2** species are shown in Table 4. Again, the perturbations are minimal (less than 0.25 pm and 0.2°).

Table 3. Properties of some dimers of ozone.

Dimer	Symmetry	E/H	Hessian Index	Relative Energy/ kJ mol^{-1}
2	C_i	−450.2841 9179 490	0	0
3	C_2	−450.2826 9146 051	1	3.94
7	C_s	−450.2824 3399 654	2	4.61
5	C_s	−450.2823 7307 965	1	4.77
1	C_{2h}	−450.2805 4781 872	2	9.57
4	C_{2v}	−450.2802 0490 636	4	10.47
9	D_{2d}	−450.2799 8305 709	4	11.05
8	D_{2h}	−450.2799 1140 084	5	11.24
6	C_{2v}	−450.2793 6382 300	2	12.68

Based on the genuine minimum structures we found for the sulphur dioxide and ozone homodimers, and the C_s first order transition state of $(O_3)_2$, we examined eight structures for the sulphur dioxide-ozone heterodimer, two each corresponding with dimers **2**, **3**, **5**, and **7**, with sulphur dioxide and ozone acting as electron donor or electron acceptor in turn (a or b). These eight structures are illustrated in Figure 5 and their properties in Table 5. Structures **2a**, **2b**, **3a**, and **3b** were found to be virtually identical; these four

structures and complex **5b** are all true minima. The relative energies are presented in Figure 6 and the bond lengths and angles and their changes in Table 6. Again, the pattern of very small perturbations is observed; only the free O2O6 bond of the ozone sub-unit in complex **2a** shows a substantial increase on complexation.

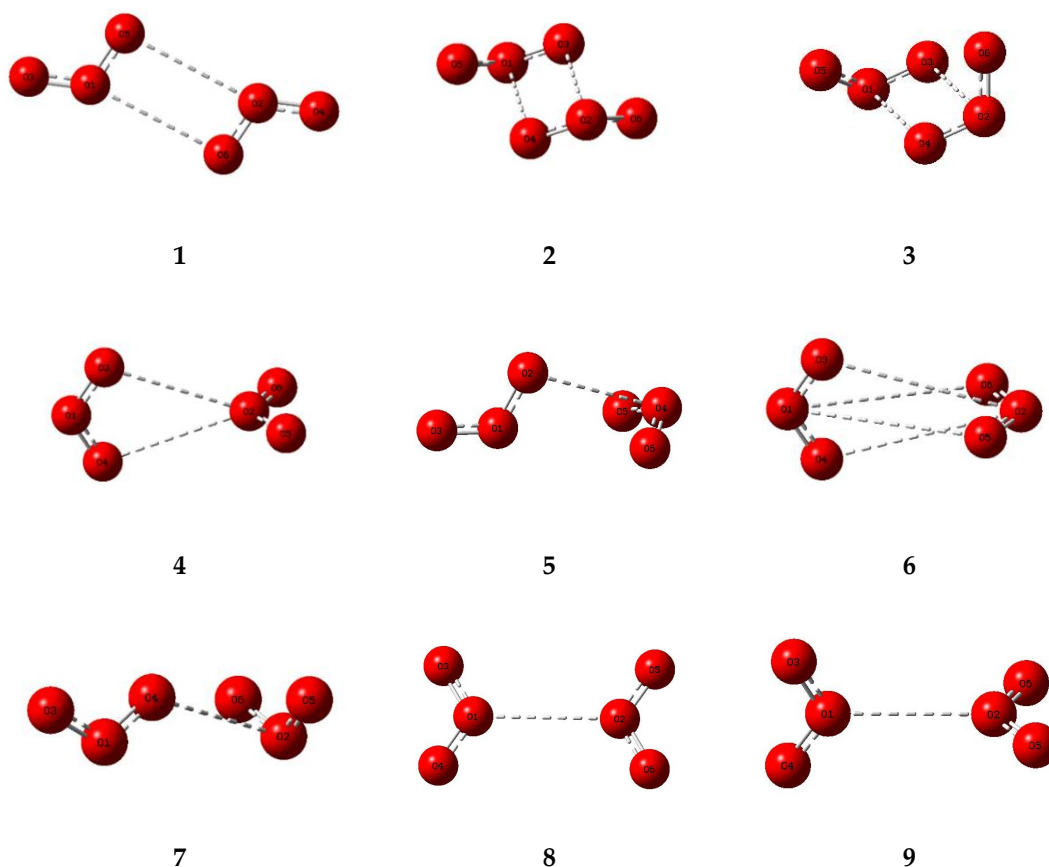


Figure 3. Optimized structures of some dimers of ozone.

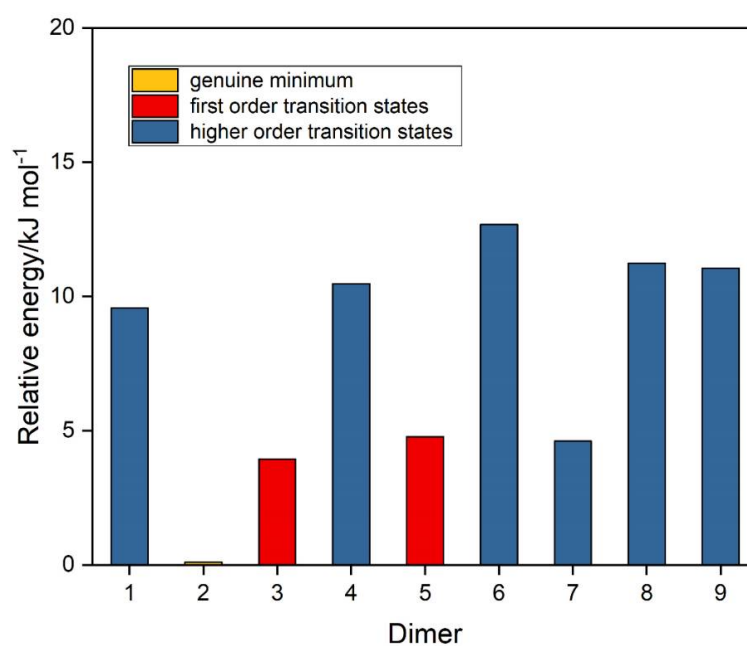
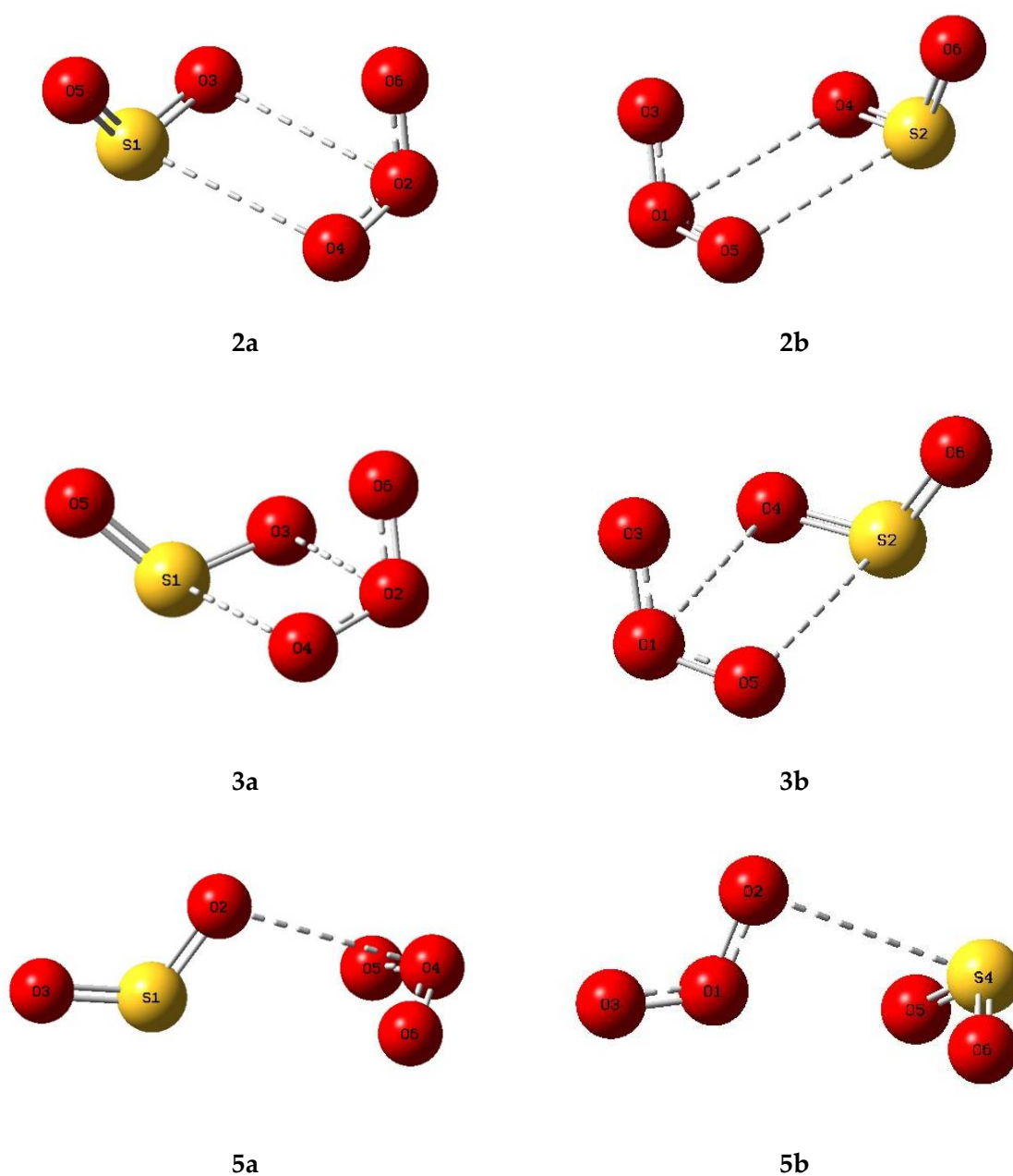


Figure 4. Relative energies of the ozone dimers.

Table 4. Optimized geometrical parameters of ozone dimer 2 and their changes relative to the ozone monomer. See Figure 3 for numbering of the atoms.

Parameter	Dimer Value	Difference from Monomer Value
$r(\text{O1O3}, \text{O2O4})/\text{pm}$	128.58	0.20
$r(\text{O1O5}, \text{O2O6})/\text{pm}$	128.53	0.15
$\angle \text{O3O1O5}, \text{O4O2O6}/\text{deg}$	116.49	-0.17
$r(\text{O1} \dots \text{O4}, \text{O2} \dots \text{O3})/\text{pm}$	299.07	-
$\angle \text{O5O1} \dots \text{O4}, \text{O6} \dots \text{O2O3}/\text{deg}$	65.08	-
$\angle \text{O1O3} \dots \text{O2}, \text{O2O4} \dots \text{O1}/\text{deg}$	108.32	-
$\angle \text{O5O1} \dots \text{O4O2}/\text{deg}^{\text{a}}$	-43.17	-
$\angle \text{O6O2} \dots \text{O3O1}/\text{deg}^{\text{a}}$	43.17	-

^a Dihedral angle.**Figure 5.** *Cont.*

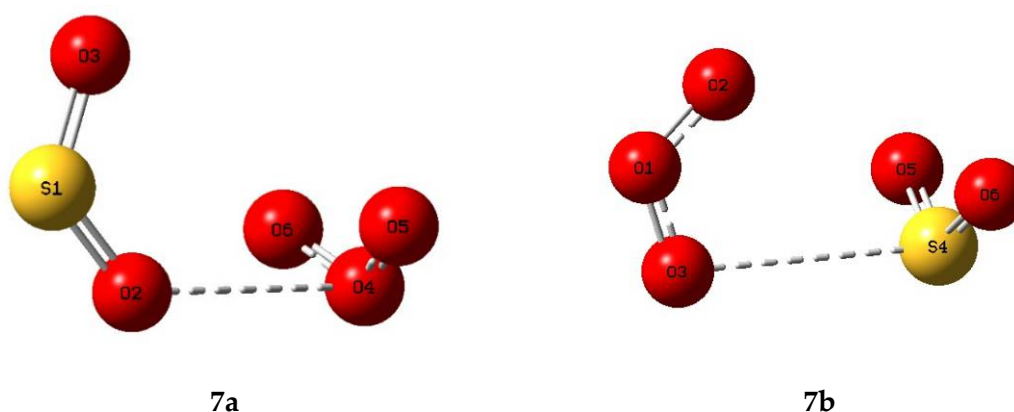


Figure 5. Optimized structures of some complexes of sulphur dioxide and ozone.

Table 5. Properties of some complexes of sulphur dioxide and ozone.

Complex	Symmetry	E/H	Hessian Index	Relative Energy/ kJ mol ⁻¹
2a	C ₁	-773.1098 0096 467	0	0
3a	C ₁	-773.1098 0095 885	0	0
2b	C ₁	-773.1098 0095 755	0	0
3b	C ₁	-773.1098 0095 165	0	0
5a	C _s	-773.1092 1061 632	1	1.55
7b	C _s	-773.1081 7161 056	1	4.28
7a	C _s	-773.1081 3721 831	1	4.37
5b	C _s	-773.1080 7683 409	0	4.53

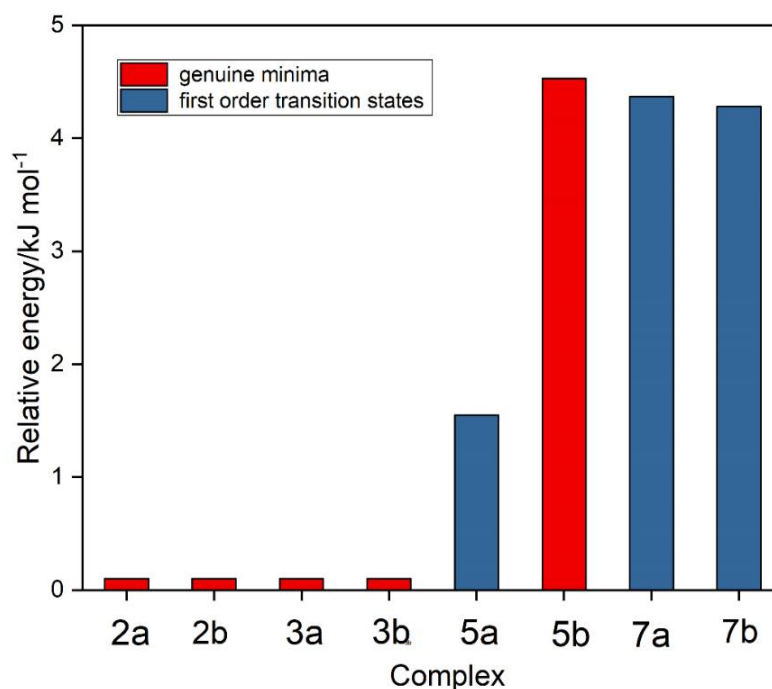


Figure 6. Relative energies of the sulphur dioxide-ozone complexes.

2.2. Interaction Energies

The interaction energies of the five genuine minimum energy structures are given in Table 7, corrected in each case for BSSE [90] and for zero-point energy differences. Consistent with the relatively insignificant intramolecular structural perturbations discussed

above, the interaction energies are all less than 10 kJ mol^{-1} ; the two SO_2 dimers and the **2a** heterodimer all have similar energies, while heterodimer **5b** is barely bound at all.

Table 6. Optimized geometrical parameters of sulphur dioxide–ozone complexes **2a** and **5b**, and their changes relative to the sulphur dioxide and ozone monomers. See Figure 5 for numbering of the atoms.

Complex 2a			Complex 5b		
Parameter	Dimer Value	Difference from Monomer Value	Parameter	Dimer Value	Difference from Monomer Value
r(S1O3)/pm	146.72	0.36	r(O1O2)/pm	128.03	−0.35
r(S1O5)/pm	146.21	−0.15	r(O1O3)/pm	128.69	0.31
r(O2O4)/pm	127.85	−0.53	r(S4O5,S4O6)/pm	146.37	0.02
r(O2O6)/pm	129.76	1.39	∠O2O1O3/deg	116.50	−0.16
∠O3S1O5/deg	118.50	−0.29	∠O5S4O6/deg	118.51	−0.28
∠O4O2O6/deg	116.08	−0.58	r(O2 ... S4)/pm	313.42	-
r(S1 ... O4)/pm	291.71	-	∠O1O2 ... S4/deg	90.03	-
r(O2 ... O3)/pm	291.42	-	∠O2 ... S4O5,O2 ... S4O6/deg	83.45	-
∠O5S1 ... O4/deg	113.06	-	∠O5S4 ... O2O1/deg ^a	59.89	-
∠O6O2 ... O3/deg	66.12	-	∠O6S4 ... O2O1/deg ^a	−59.89	-
∠O5S1O3 ... O2/deg ^a	107.94	-			
∠O6O2O4 ... S1/deg ^a	55.56	-			

^a Dihedral angle.

Table 7. Interaction energies of some dimers and complexes of sulphur dioxide and ozone.

Species	Interaction Energy/kJ mol ^{−1}				
	Raw	BSSE	Corrected	ΔE _o	Net
SO ₂ dimer 5	13.26	2.38	10.88	1.93	8.95
SO ₂ dimer 2	12.59	2.26	10.33	1.86	8.47
O ₃ dimer 2	14.39	3.18	11.21	4.21	7.00
SO ₂ –O ₃ complex 2a	15.52	3.34	12.18	3.67	8.51
SO ₂ –O ₃ complex 5b	9.87	2.17	7.70	1.91	5.79

2.3. Molecular Orbital Properties

The valence molecular orbitals of the sulphur dioxide and ozone monomers are illustrated in Figures 7 and 8, and their descriptions are listed in Tables 8 and 9. The energy ordering of the orbitals follows the conventional sequence, $\sigma < \text{lp}(\text{O}) \approx \text{lp}(\text{S}) < \pi < \pi^* < \sigma^*$. One sulphur and four oxygen lone pairs are expected for the SO_2 monomer, and four terminal and one central oxygen lone pair in the case of O_3 . For both SO_2 and O_3 the π orbitals separate into a bonding orbital delocalized over all three atoms, a non-bonding orbital involving only the out-of-plane p orbitals of the peripheral oxygen atoms, and an antibonding orbital with contributions from the p orbitals of all three atoms. The σ^* orbitals, being more diffuse and involving more excited atomic orbitals, are less easy to visualize and to assign.

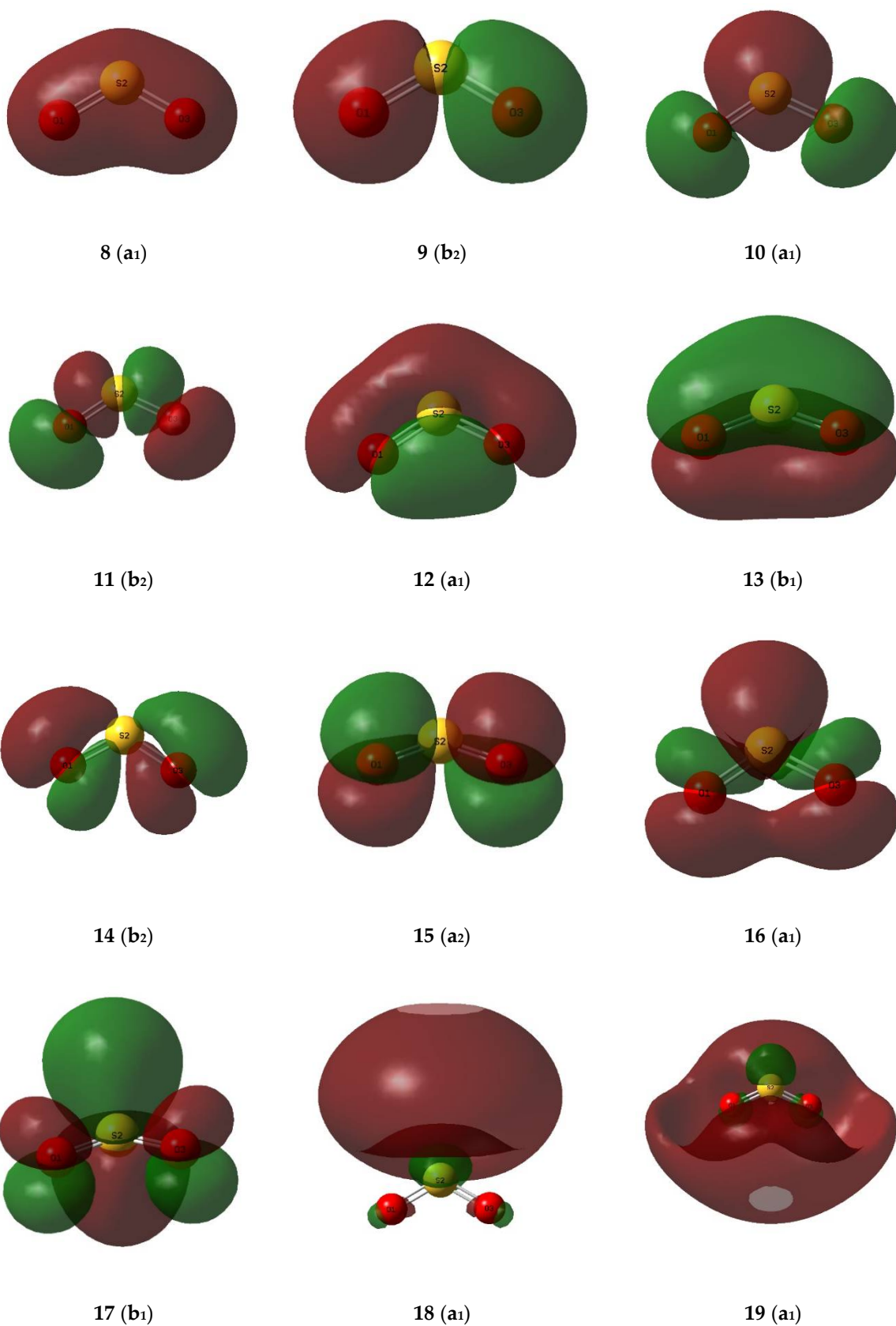


Figure 7. Valence molecular orbitals of the sulphur dioxide monomer.

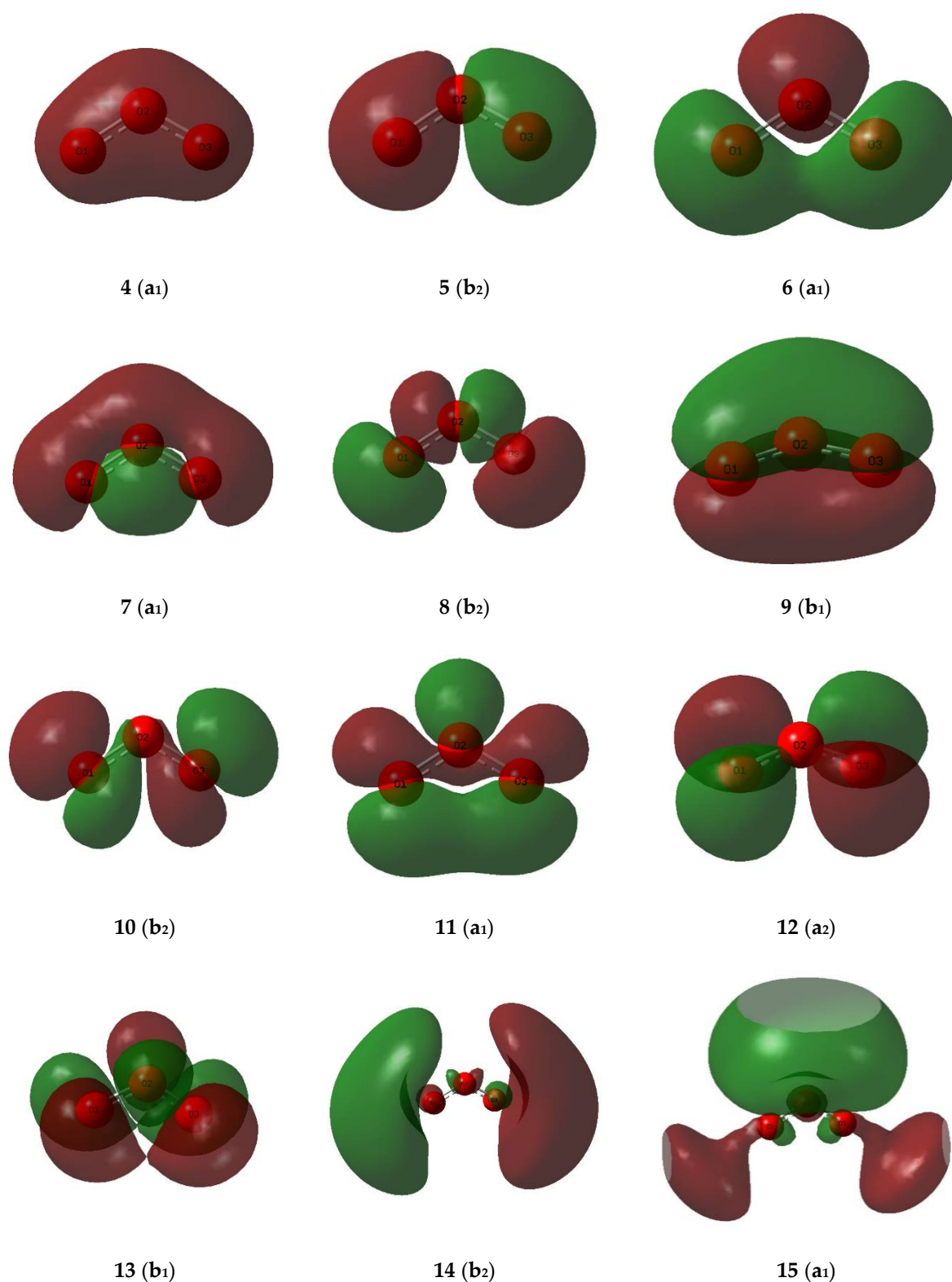


Figure 8. Valence molecular orbitals of the ozone monomer.

These monomer orbitals transform readily into those of the dimer and complex species, and the orbitals of the five genuine minima are shown in the Supplementary Material as Figures S1–S5. The corresponding descriptions of the orbitals of the adducts are given in Supplementary Material Tables S1–S5. The major changes in the characters of the orbitals on complexation are that some of the lone pair orbitals of the monomers transform into σ

bonding orbitals associated with the intermolecular bonding interactions. Thus, for SO₂ dimers **5** and **2**, for example, four oxygen and one sulphur monomer lone pair orbitals go over into six oxygen and two sulphur lone pair orbitals, with two new $\sigma(\text{S} \dots \text{O})$ orbitals.

Table 8. Properties of the valence molecular orbitals of the sulphur dioxide monomer.

No.	Symmetry	Energy/H	Approximate Description ^a
1–7			core
8	a ₁	−1.48513	$\sigma(\text{OSO})$
9	b ₂	−1.38753	$\sigma(\text{OSO})$
10	a ₁	−0.88026	lp(S)
11	b ₂	−0.69488	lp(O)
12	a ₁	−0.68513	lp(O)
13	b ₁	−0.65353	$\pi(\text{OSO})$
14	b ₂	−0.54142	lp(O)
15	a ₂	−0.51405	$\pi(\text{nb})(\text{OSO})$
16 (HOMO)	a ₁	−0.49779	lp(O)
17 (LUMO)	b ₁	−0.00680	$\pi^*(\text{OSO})$
18	a ₁	0.06607	$\sigma^*(\text{OSO})$
19	a ₁	0.07129	$\sigma^*(\text{OSO})$

^a lp—lone pair; nb—non-bonding.

Table 9. Properties of the valence molecular orbitals of the ozone monomer.

No.	Symmetry	Energy/H	Approximate Description ^{a,b}
1–3			core
4	a ₁	−1.74257	$\sigma(\text{OOO})$
5	b ₂	−1.42739	$\sigma(\text{OOO})$
6	a ₁	−1.09905	lp(O2)
7	a ₁	−0.82911	lp(O1) + lp(O3)
8	b ₂	−0.79824	lp(O1) − lp(O3)
9	b ₁	−0.77653	$\pi(\text{OOO})$
10	b ₂	−0.56576	lp(O1) − lp(O3)
11	a ₁	−0.55546	lp(O1) + lp(O3)
12 (HOMO)	a ₂	−0.48829	$\pi(\text{nb})(\text{O1} - \text{O3})$
13 (LUMO)	b ₁	−0.05229	$\pi^*(\text{OOO})$
14	b ₂	0.10144	$\sigma^*(\text{OOO})$
15	a ₁	0.10566	$\sigma^*(\text{OOO})$

^a O1 and O3—terminal atoms; O2—central atom. ^b lp—lone pair; nb—non-bonding.

Further insights into the electronic rearrangements accompanying dimer or complex formation are provided by a consideration of the molecular electrostatic potential maps of the adducts. These plots are shown in Figure 9 for the five associated species. The diagrams indicate the regions of high electron density, shown in red, shading to more electropositive zones, shown in blue, with the peripheral oxygen atoms having the greatest negative potentials and the more positive potentials associated with the sulphur atoms and the central oxygen atoms of the ozone moieties. The potentials cover a range from about −240 to 240 kJ mol^{−1}.

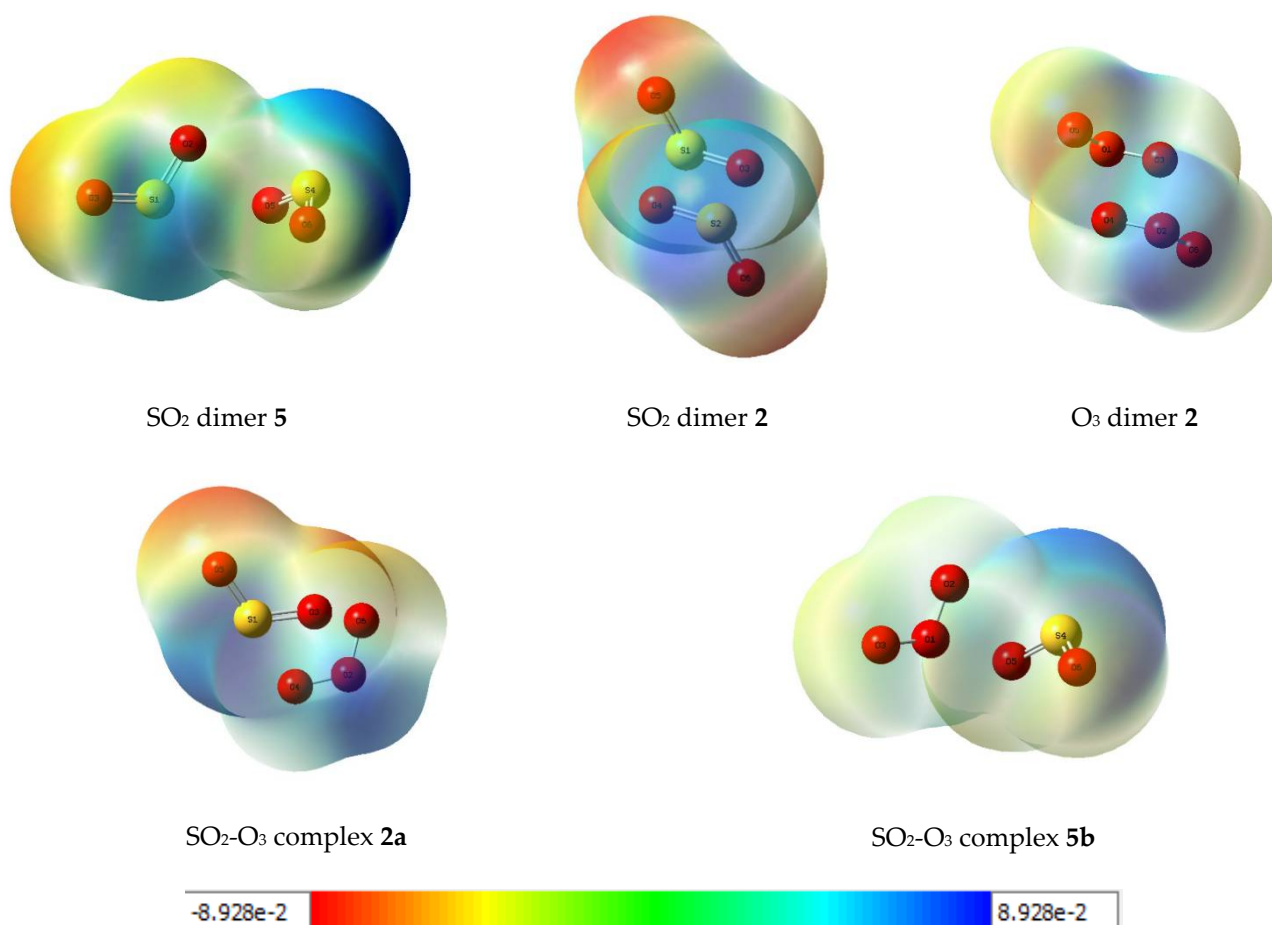


Figure 9. Molecular electrostatic potential plots of some dimers and complexes of sulphur dioxide and ozone. Units: hartree ($1 H = 2625.346583 \text{ kJ mol}^{-1}$).

2.4. Vibrational Spectra

The computed wavenumbers of the five associated species, and their shifts relative to the uncomplexed monomers, are shown in Table 10. For the two sulphur dioxide dimers, the antisymmetric SO₂ stretching modes tend to be displaced to the red and the symmetric stretching and the SO₂ bending to the blue. These shifts are all less than 10 cm^{-1} in either direction, however, consistent with the very low interaction energies (see Table 7). The comparisons of our calculated intramolecular wavenumbers with experimental values derived from matrix isolation infrared spectroscopic studies [13,15,19–23] are given in Table 11. As a measure of the level of agreement between the calculated and experimental wavenumbers of SO₂ dimer 5, the calculated/experimental ratios derived from the data in Table 11 are found to vary between 1.029 for ν_1 (relative to ref. [23]) to 1.060 for ν_5 (ref. [22]).

The vibrational data are all in agreement that the observed spectra are compatible with the C_s dimer 5 structure, except for the argon matrix results of Schriver-Mazzuoli et al. [21] and Ito and Hirabayashi [23], who proposed that the C_i isomer 2 more closely fits the experimental data. Indeed, Schriver-Mazzuoli and co-workers were able to assign only one band in each of the fundamental monomer regions with confidence, consistent with only one mode in each of the monomer regions being infrared-active [21]. There are some minor mismatches among the assignments of the stretching modes [20,23], but definitive assignments to the bands of the electron donor and acceptor based on the experimental spectra alone are difficult to achieve.

Table 10. Wavenumbers and wavenumber shifts of some dimers and complexes of sulphur dioxide and ozone.

Species	SO ₂				O ₃				
	Symmetry	Mode ^a	Wavenumber /cm ⁻¹	Shift /cm ⁻¹	Symmetry	Mode	Wavenumber /cm ⁻¹	Shift /cm ⁻¹	
SO ₂ dimer 5	a'	ν ₁ (ED)	1300.5	-5.0	ag	ν ₁ (OP)	2419.3	175.0	
		ν ₂ (EA)	1102.5	3.3			ν ₂ (IP)	1150.2	-7.7
	ν ₃ (ED)	1099.1	-0.1	ν ₃ (IP)			743.1	1.6	
	ν ₄ (OP)	500.0	6.7	ν ₇ (IP)			2172.0	-72.3	
	ν ₅ (IP)	494.6	1.3	ν ₈ (OP)			1151.6	-6.3	
SO ₂ dimer 2	a''	ν ₉ (EA)	1303.9	-1.6	a	ν ₉ (OP)	742.8	1.3	
	ag	ν ₁ (OP)	1303.2	-2.3			ν ₁	2270.1	25.8
		ν ₂ (IP)	1101.4	2.2			ν ₃	1132.1	-25.8
	au	ν ₃ (IP)	494.9	1.6			ν ₅	740.4	-1.1
ν ₇ (IP)		1304.9	-0.6	ν ₁	2243.8	-0.5			
ν ₈ (OP)		1101.5	2.3	ν ₂	1159.2	1.3			
O ₃ dimer 2	au	ν ₉ (OP)	495.8	2.5	a	ν ₄	744.7	3.2	
SO ₂ -O ₃ complex 2a	a	ν ₂	1301.3	-4.2					
SO ₂ -O ₃ complex 5b	a'	ν ₄	1096.5	-2.7	a'	ν ₁	2243.8	-0.5	
		ν ₆	494.2	0.9			ν ₂	1159.2	1.3
	ν ₃	1102.4	3.2	ν ₄			744.7	3.2	
	ν ₅	495.3	2.0						
	ν ₉	1306.2	0.7						

^a ED—electron donor; EA—electron acceptor; IP—in-phase; OP—out-of-phase.

Table 11. Calculated and experimental intramolecular wavenumbers of sulphur dioxide dimer 5.

Reference	Wavenumber/cm ⁻¹ a					
	$\nu_1(a')$ $\nu_a(\text{SO}_2)(\text{ED})$	$\nu_2(a')$ $\nu_s(\text{SO}_2)(\text{EA})$	$\nu_3(a')$ $\nu_s(\text{SO}_2)(\text{ED})$	$\nu_4(a')$ $\delta(\text{SO}_2)(\text{OP})$	$\nu_5(a')$ $\delta(\text{SO}_2)(\text{IP})$	$\nu_9(a'')$ $\nu_a(\text{SO}_2)(\text{EA})$
This work ^b	1300.5	1102.5	1099.1	500.0	494.6	1303.9
Ref. [13] ^c	1343.1, 1345.2	-	-	-	-	1341.1
Ref. [15] ^d	1348.2	1155.8	1153.7	524.0	521.7	1345.6
Ref. [19] ^d	1349.2	1155.2	1153.9	526.1	524.0	1346.6
Ref. [20] ^d	1346.6	1151.8	1154.2	524.3	522.4	1349.1
Ref. [21] ^c	1341.3	1146.6	-	519.5	-	-
Ref. [22] ^c	1345.1	1155.4	1153.3	527.2	521.8	1341.1
Ref. [22] ^d	1349.4	1156.1	1154.3	526.5	524.3	1346.5
Ref. [23] ^c	1345.8, 1346.5	1154.8, 1155.5	1152.1, 1152.8	-	-	1348.2, 1348.9
Ref. [23] ^e	1344.4, 1345.2	1152.9, 1153.6	1149.9, 1150.5	-	-	1346.3, 1347.0
Ref. [23] ^f	1338.8, 1339.6	1149.0, 1149.8	1145.7, 1146.3	-	-	1341.1, 1342.0

^a EA—electron acceptor; ED—electron donor; OP—out-of-phase; IP—in-phase. ^b Calculated. ^c In argon. ^d In nitrogen. ^e In krypton.

^f In xenon.

Table 10 includes the calculated data for ozone dimer 2. The shifts of the antisymmetric O₃ stretching modes are spectacularly large, given the low interaction energy of this dimer, and are of opposite sign. This result must be viewed in the context of the computed wavenumbers of the ozone monomer, 1157.9, 741.5, and 2244.3 cm⁻¹ for ν_1 , ν_2 , and ν_3 , respectively, which may be compared with the experimental values of 1134.9, 716.0, and 1089.2 cm⁻¹, reported by Barbe et al. [91]. This assignment admits a most unusual ordering of the stretching vibrations, with $\nu_1 > \nu_3$, which has been confirmed by Lee et al. [88,89]. Slanina and Adamowicz [46] report values of 1135, 726, and 2391 cm⁻¹ for the monomer wavenumbers, in much closer agreement with our results. The antisymmetric stretching mode shifts indicate a significant separation of the two (in-phase and out-of-phase) vibrations of 247.3 cm⁻¹, compared with separations of only 3.4 cm⁻¹ and 1.7 cm⁻¹ for SO₂ dimers 5 and 2, respectively, and of 17 cm⁻¹ calculated for the C_s isomer of (O₃)₂ by Slanina and Adamowicz [46]. The anomalous position of the antisymmetric stretching wavenumber confirms the notoriously difficult task of accurately reproducing the experimental wavenumber of the ozone monomer theoretically [88,89,92,93]. These authors pointed out the multiconfigurational nature of the ground state of the ozone monomer, confirmed by a series of high-level computations, including at the CASSCF, MRCI, CCSD, and CCSD(T) levels of theory. In order to examine whether our treatment of the spectra of ozone and its dimer at the MP2/aug-cc-pVTZ level was sufficiently reliable, we repeated those calculations for the monomer at the CASSCF level. We selected the monomer for this test, since the experimental geometry [94] and vibrational spectrum [91] are well-established and are available for comparison. The comparisons of our geometrical parameters and vibrational wavenumbers at the MP2 and CASSCF levels with their experimental counterparts and with the parallel computations of Lee and Scuseria [89] are given in Tables 12 and 13. While the computed bond length and angle are rather insensitive to the level of theory employed, and show fairly similar calculated and experimental differences (see Table 12), the estimation of the antisymmetric OO stretching mode exhibits a large scatter; only the theoretical treatment of Lee and Scuseria using CCSD/TZ+2Pf methodology [89] correctly reproduces the experimental ordering of the ν_1 and ν_3 vibrations (see Table 13). These uncertainties are responsible for the large, computed shifts associated with the monomer

ν_3 mode. Our shifts of the symmetric stretching and bending modes of the ozone dimer are much more in line with those of the SO_2 dimers (less than 10 cm^{-1}).

Table 12. Calculated and experimental bond length and bond angle of the ozone monomer.

	r(OO)/pm	$\angle\text{OOO}/\text{deg}$
Experimental (ref. [94])	127.2	116.8
MP2 (this work)	128.38	116.62
Difference	1.18	−0.18
CASSCF (this work)	125.51	115.82
Difference	−1.69	−0.98
CCSD/TZ+2Pf (ref. [89])	125.2	117.5
Difference	−1.97	0.7

Table 13. Calculated and experimental wavenumbers (cm^{-1}) of the ozone monomer.

	ν_1 (\mathbf{a}_1)	ν_2 (\mathbf{a}_1)	ν_3 (\mathbf{b}_2)
Experimental (ref. [91])	1135	716	1089
MP2 (this work)	1157.9	741.5	2244.3
Ratio	1.02	1.04	2.06
CASSCF (this work)	1092.3	770.2	1358.4
Ratio	0.96	1.08	1.25
CCSD/TZ+2Pf (ref. [89])	1280	758	1261
Ratio	1.13	1.06	1.16

The computed wavenumber shifts of the SO_2 moieties of $\text{SO}_2\text{-O}_3$ complexes **2a** and **5b** are quite consistent with those of the SO_2 dimers (less than 5 cm^{-1} , see Table 10). Similarly, the O_3 shifts of heterodimer **5b** are insignificant, but those of the symmetric and antisymmetric O_3 stretching modes of complex **2a** are quite substantial and of opposite sign, yielding a separation of 51.6 cm^{-1} . While this separation is not as dramatic as the corresponding result for the C_i ozone dimer, it is quite apparent that the antisymmetric stretching vibrations of ozone molecules in these homo- and heterodimers are extremely sensitive to complexation.

3. Computational Methodology

The calculations were carried out using Gaussian-16 [95], at the second order level of the Møller–Plesset perturbation theory (MP2) [96] with Dunning’s augmented correlation-consistent polarized valence triple-zeta basis sets (aug-cc-pVTZ) [97,98]. Structures were optimized using the verytight keyword, where practicable, and stationary points were identified as genuine minima or transition states by vibrational analysis. The wavenumbers and infrared intensities of the resulting species were determined at the harmonic level. Interaction energies were computed and corrected for basis set superposition error (BSSE) [90], using the Boys–Bernardi full counterpoise procedure [99] and the counterpoise = 2 keyword and for zero-point energy differences. Molecular orbital properties and molecular electrostatic potentials were examined using the Gaussian input keywords pop = full, density = current, and cube(full,orbitals) [95]. The model chemistry employed here is consistent with those represented in a number of similar calculations [4–8] in terms of its ability to yield credible results.

4. Conclusions

A series of nine structures each of the sulphur dioxide and ozone homodimers and of eight of their heterodimers were investigated. Of these structures, two sulphur dioxide and one ozone dimer and two sulphur dioxide-ozone complexes were found to be genuine minima on their potential surfaces. These five species were all found to be very weakly bound (less than 10 kJ mol^{-1}). These low interaction energies resulted in very small

perturbations of the bond lengths and bond angles of the monomers (less than 0.36 and 1.39 pm for the SO and OO bond lengths and 0.29° and 0.58° for the OSO and OOO angles, respectively). The minimal perturbations of the intramolecular geometries are matched by the small, computed wavenumber shifts (less than 7 cm⁻¹ for the SO₂ dimers and the SO₂ sub-units of the heterodimers, and less than 10 cm⁻¹ for the symmetric stretching and bending of the O₃ moieties of the ozone dimers and the heterodimers). The exceptions to this statement are ozone dimer 2, where the shifts of the antisymmetric O₃ stretching mode are 175.0 and -72.3 cm⁻¹, and SO₂-O₃ complex **2a**, where the O₃ stretching vibrations undergo shifts of 25.8 cm⁻¹ to the blue (antisymmetric) and the red (symmetric). The ozone moiety appears to be much more sensitive than sulphur dioxide to perturbations of their vibrational spectra due to complexation, but the conclusions regarding the magnitudes of the shifts have to be tempered by recognition of the well-known susceptibility of ozone to the level of theoretical treatment [88,89,92,93]. Miliordos and Xantheas presented evidence that, while the bonding in SO₂ consists of two σ and two π bonds, that in O₃ is better described as a mixture of a closed shell structure featuring two O-O bonds having bond orders of 1.5 (a delocalized 3-centre-4-electron bond) (82%) and a diradical structure with two σ bonds, a lone pair on the central oxygen atom, and a single electron in a p orbital on each of the terminal atoms (18%) [92]. Takeshita et al. concurred with respect to the description of the SO₂ bonding arrangement (recoupled pair bonds), and the fact that O₃ “has significantly more diradical character than SO₂” [93]. These fundamental differences are certainly partly responsible for the marked variations in the ability of sulphur dioxide and ozone to form stable dimers, and hence in the differences in the computed vibrational spectra of the dimers. Neither Miliordos and Xantheas [92] nor Takeshita and co-workers [93] offered any insights into the spectra of the monomers, nor into the properties of the dimers.

We acknowledge the limitations of our methodology as they apply to the ozone species, but in the interests of consistency with our other results, we stand by the conclusions presented in this work.

Supplementary Materials: The following are available online, Figures S1–S5 and Tables S1–S5: titles as indicated in Table of Contents.

Funding: This research was funded by the National Research Foundation of South Africa, grant number 2053648, and by the University of KwaZulu-Natal Research Fund.

Data Availability Statement: The data presented in this study are available from the author and in the Supplementary Material.

Acknowledgments: This material is based upon work supported by the National Research Foundation of South Africa. Any opinion, findings, and conclusions or recommendations expressed in this material are those of the author and do not necessarily reflect the views of the National Research Foundation. The author acknowledges the Centre for High Performance Computing (South Africa) for the use of computing facilities, and Anton Lopis for invaluable technical assistance. The author is also grateful to a reviewer for bringing references 92 and 93 to his attention. He looks back with pleasure on a number of valuable detailed technical discussions and convivial social interactions with Austin Barnes in several countries over many years.

Conflicts of Interest: The author declares no conflict of interest.

Sample Availability: No physical samples of the compounds are available.

References

- Hobza, P.; Müller-Dethlefs, K. *Non-Covalent Interactions. Theory and Experiment*; RSC Publishing: Cambridge, UK, 2010.
- Aakeroy, C.B.; Bryce, D.L.; Desiraju, G.R.; Frontera, A.; Legon, A.C.; Nicotra, F.; Rissanen, K.; Terraneo, S.S.G.; Metrangolo, P.; Resnati, G. Definition of the chalcogen bond (IUPAC recommendations 2019). *Pure Appl. Chem.* **2019**, *91*, 1889–1892. [CrossRef]
- Nxumalo, L.M.; Ford, T.A. Ab initio calculations of the structural, energetic and vibrational properties of some hydrogen-bonded and van der Waals dimers. Part 2. Sulphur dioxide. *Spectrochim. Acta Part A* **1995**, *51*, 1847–1860. [CrossRef]
- Bone, R.G.A.; le Sueur, C.R.; Amos, R.D.; Stone, A.J. Stationary points on the potential energy surfaces of (SO₂)₂ and (SO₂)₃. *J. Chem. Phys.* **1992**, *96*, 8390–8410. [CrossRef]

5. Plummer, P.L.M. Quantum mechanical studies of weakly-bound molecular clusters. *J. Mol. Struct. (Theochem)* **1994**, *307*, 119–133. [CrossRef]
6. Bone, R.G.A.; Bader, R.F.W. Identifying and analyzing intermolecular bonding interactions in van der Waals molecules. *J. Phys. Chem.* **1996**, *100*, 10892–10911. [CrossRef]
7. McKee, M.L. Computational study of the mono- and dianions of SO₂, SO₃, SO₄, S₂O₃, S₂O₄, S₂O₆ and S₂O₈. *J. Phys. Chem.* **1996**, *100*, 3473–3481. [CrossRef]
8. Groves, C.; Lewars, E. Dimers, trimers and oligomers of sulfur oxides: An ab initio and density functional study. *J. Mol. Struct. (Theochem)* **2000**, *530*, 265–279. [CrossRef]
9. Ito, F. Gas phase infrared spectra of SO₂ clusters and quantum chemical calculations of some stable isomers. *Chem. Phys. Letters* **2007**, *436*, 335–340. [CrossRef]
10. Nelson, D.D.; Fraser, G.T.; Klemperer, W. The microwave and radiofrequency rotation-inversion spectrum of (SO₂)₂. *J. Chem. Phys.* **1985**, *83*, 945–949. [CrossRef]
11. Matsumura, K.; Lovas, F.J.; Suenram, R.D. The microwave spectrum and structure of the H₂O-SO₂ complex. *J. Chem. Phys.* **1989**, *91*, 5887–5894. [CrossRef]
12. Taleb-Bendiab, A.; Hillig, K.W., II; Kuczkowski, R.L. The microwave spectrum, structure and tunneling motion of the sulfur dioxide dimer. *J. Chem. Phys.* **1991**, *94*, 6956–6963. [CrossRef]
13. Hastie, J.W.; Hauge, R.; Margrave, J.L. Infrared spectra and geometry of SO₂ and SeO₂ in rare gas matrices. *J. Inorg. Nucl. Chem.* **1969**, *31*, 281–289. [CrossRef]
14. Allavena, M.; Rysnik, R.; White, D.; Calder, V.; Mann, D.E. Infrared spectra and geometry of SO₂ isotopes in solid krypton matrices. *J. Chem. Phys.* **1969**, *50*, 3399–3409. [CrossRef]
15. Fredin, L. An exploratory study of weak molecular complexes in low temperature matrices. *Chem. Scripta* **1973**, *4*, 97–102.
16. Spoliti, M.; Grosso, V.; Nunziante-Cesaro, S. Infrared matrix isolation of, and bonding in, the oxides of group VIB elements: O₃, SO₂, SeO₂ and TeO₂. *J. Mol. Struct.* **1974**, *21*, 7–15. [CrossRef]
17. Maillard, D.; Allavena, M.; Perchard, J.P. Spectres vibrationnels du dioxyde de soufre dans une matrice d'argon, d'azote et de neon. *Spectrochim. Acta Part A* **1975**, *31*, 1523–1531. [CrossRef]
18. Sodeau, J.R.; Lee, E.K.C. Photo-oxidation of sulfur dioxide in low temperature matrices. *J. Phys. Chem.* **1980**, *84*, 3358–3362. [CrossRef]
19. Nord, L. On the sulphur dioxide dimer in solid nitrogen. *J. Mol. Struct.* **1982**, *96*, 19–25. [CrossRef]
20. Wierzejewka-Hnat, M.; Schriver, A.; Schriver-Mazzuoli, L. FT infrared study of sulfur dioxide dimer. I. Nitrogen matrix. *Chem. Phys.* **1994**, *183*, 117–126. [CrossRef]
21. Schriver-Mazzuoli, L.; Schriver, A.; Wierzejewka-Hnat, M. Fourier transform infrared study of sulfur dioxide dimer. II. Argon matrix. *Chem. Phys.* **1995**, *199*, 227–243. [CrossRef]
22. Nxumalo, L.M.; Ford, T.A. The sulphur dioxide dimer. A matrix isolation infrared spectroscopic study. *J. Mol. Struct.* **1995**, *347*, 495–508. [CrossRef]
23. Ito, F.; Hirabayashi, S. Infrared spectroscopy of SO₂ clusters in rare gas matrices revisited. Assignment of species in Ar matrices. *Chem. Phys.* **2009**, *358*, 209–218. [CrossRef]
24. Peebles, S.A.; Sun, L.; Kuczkowski, R.L.; Nxumalo, L.M.; Ford, T.A. The structure of the boron trifluoride-sulphur dioxide complex. *J. Mol. Struct.* **1998**, *471*, 235–242. [CrossRef]
25. Rayon, V.M.; Sordo, J.A. Acetylene-sulfur dioxide van der Waals complexes. A theoretical study. *Chem. Phys. Lett.* **2001**, *341*, 575–584. [CrossRef]
26. Hippler, M. Quantum chemical study of CHCl₃-SO₂ association. *J. Chem. Phys.* **2005**, *123*, 204311. [CrossRef]
27. Studel, R.; Studel, Y. Charge-transfer complexes between the sulfur molecules SO₂, S₂O, S₃, SONH and SOCl₂ and the amine donors NH₃ and NMe₃—A theoretical study. *Eur. J. Inorg. Chem.* **2007**, *2007*, 4385–4392. [CrossRef]
28. Venayagamoorthy, M.; Ford, T.A. Ab initio molecular orbital studies of the vibrational spectra of some van der Waals complexes. Part 4. Complexes of sulphur dioxide with carbon dioxide, carbonyl sulphide, carbon disulphide and nitrous oxide. *S. Afr. J. Chem.* **2009**, *62*, 149–155.
29. Ford, T.A. Ab initio molecular orbital calculations of the structures and vibrational spectra of some molecular complexes containing sulphur dioxide. *J. Mol. Struct.* **2009**, *924–926*, 466–472. [CrossRef]
30. Eigner, A.A.; Wrass, J.P.; Smith, E.L.; Knutson, C.C.; Phillips, J.A. Structural properties of CH₃CN-SO₂ in the gas phase and condensed-phase media via density functional theory and infrared spectroscopy. *J. Mol. Struct.* **2009**, *919*, 312–320. [CrossRef]
31. Dayton, D.C.; Miller, R.E. Infrared spectroscopy of the sulfur dioxide-hydrogen fluoride and hydrogen cyanide-sulfur dioxide binary complexes. *J. Phys. Chem.* **1990**, *94*, 6641–6646. [CrossRef]
32. Andrews, A.M.; Hillig, K.W., II; Kuczkowski, R.L.; Legon, A.C.; Howard, N.W. Microwave spectrum, structure, dipole moment and deuterium nuclear quadrupole coupling constants of the acetylene-sulfur dioxide van der Waals complex. *J. Chem. Phys.* **1991**, *94*, 6947–6955. [CrossRef]
33. Oh, J.J.; Hillig, K.W.; Kuczkowski, R.L. Microwave spectrum and structure of the pyridine-sulfur dioxide complex. *J. Am. Chem. Soc.* **1991**, *113*, 7480–7484. [CrossRef]
34. Oh, J.J.; Hillig, K.W.; Kuczkowski, R.L. Structure of the dimethyl ether-sulfur dioxide complex. *Inorg. Chem.* **1991**, *30*, 4583–4588. [CrossRef]

35. Sun, L.; Ioannou, I.I.; Kuczkowski, R.L. The microwave spectrum and structure of the carbon dioxide-sulphur dioxide complex. *Mol. Phys.* **1996**, *88*, 255–268. [CrossRef]
36. Peebles, S.A.; Sun, L.H.; Ioannou, I.I.; Kuczkowski, R.L. Rotational spectrum, structure and modeling of the SO₂-OCS complex. *J. Mol. Struct.* **1999**, *485–486*, 211–223. [CrossRef]
37. Peebles, S.A.; Sun, L.; Kuczkowski, R.L. Rotational spectrum, structure and modeling of the SO₂-CS₂ complex. *J. Chem. Phys.* **1999**, *110*, 6804–6811. [CrossRef]
38. Peebles, R.A.; Kuczkowski, R.L. Microwave spectrum of the N₂O-SO₂ dimer: Evidence for tunneling and an asymmetric structure. *J. Phys. Chem. A* **2000**, *104*, 4968–4975. [CrossRef]
39. Chung, S.; Hippler, M. Infrared spectroscopy of hydrogen-bonded CHCl₃-SO₂ in the gas phase. *J. Chem. Phys.* **2006**, *124*, 214316–214322. [CrossRef]
40. Nord, L. Some sulphur dioxide complexes in solid nitrogen. *J. Mol. Struct.* **1982**, *96*, 27–35. [CrossRef]
41. Sass, C.S.; Ault, B.S. Matrix isolation infrared spectroscopic study of sulfur dioxide-amine complexes. *J. Phys. Chem.* **1984**, *88*, 432–440. [CrossRef]
42. Andrews, L.; Withnall, R.; Hunt, R.D. Infrared spectra of the ozone . . . hydrogen fluoride and sulfur dioxide . . . hydrogen fluoride complexes in solid argon. *J. Phys. Chem.* **1988**, *92*, 78–81. [CrossRef]
43. Schriver, A.; Schriver, L.; Perchard, J.P. Infrared matrix isolation studies of complexes between water and sulfur dioxide: Identification and structures of the 1:1, 1:2 and 2:1 species. *J. Mol. Spectrosc.* **1988**, *127*, 125–142. [CrossRef]
44. Ault, B.S. Infrared spectroscopic characterization of 1:1 molecular complexes of SO₂ with benzene and related conjugated π electron donors in argon matrices. *J. Mol. Struct.* **1990**, *238*, 111–117. [CrossRef]
45. Nxumalo, L.M.; Ford, T.A. The Fourier transform infrared spectrum of the boron trifluoride-sulphur dioxide van der Waals complex. *J. Mol. Struct.* **2003**, *661–662*, 153–159. [CrossRef]
46. Slanina, Z.; Adamowicz, L. A computational study of the ozone dimer. *J. Atmos. Chem.* **1993**, *16*, 41–46. [CrossRef]
47. Andrews, L.; Spiker, R.C. Argon matrix Raman and infrared spectrum and vibrational analysis of ozone and the oxygen-18 substituted ozone molecules. *J. Phys. Chem.* **1972**, *76*, 3208–3213. [CrossRef]
48. Brewer, L.; Wang, J.L. Infrared absorption spectra of isotopic ozone isolated in rare-gas matrices. *J. Chem. Phys.* **1972**, *56*, 759–761. [CrossRef]
49. Hopkins, A.G.; Brown, D.W. Raman spectrum of matrix isolated ozone. *J. Chem. Phys.* **1973**, *58*, 1776–1777. [CrossRef]
50. Spoliti, M.; Nunziante-Cesaro, S.; Mariti, B. Infrared spectrum and geometry of ozone isolated in inert gas matrices at 20.4 K. *J. Chem. Phys.* **1973**, *59*, 985–986. [CrossRef]
51. Brosset, P.; Dahoo, R.; Gauthier-Roy, B.; Abouaf-Marguin, L. Analysis of IR absorption spectrum of O₃ in inert matrices: Spectroscopic evidence for two trapping sites. *Chem. Phys.* **1993**, *172*, 315–324. [CrossRef]
52. Lakhlifi, A.; Girardet, C.; Dahoo, R.; Brosset, P.; Gauthier-Roy, B.; Abouaf-Marguin, L. Interpretation of the infrared spectrum of ozone trapped in inert matrices. *Chem. Phys.* **1993**, *177*, 31–44. [CrossRef]
53. Jasmin, D.; Brosset, P.; Dahoo, R.; Raducu, V.; Gauthier-Roy, B.; Abouaf-Marguin, L. Laser-induced infrared fluorescence of O₃ trapped in xenon matrices. *J. Chem. Phys.* **1994**, *101*, 7337–7341. [CrossRef]
54. Schriver-Mazzuoli, L.; Schriver, A.; Lugez, C.; Perrin, A.; Camy-Peyret, C.; Flaud, J.M. Vibrational spectra of the ¹⁶O/¹⁷O/¹⁸O substituted ozone molecule isolated in matrices. *J. Mol. Spectrosc.* **1996**, *176*, 85–94. [CrossRef]
55. Bahou, M.; Schriver-Mazzuoli, L.; Camy-Peyret, C.; Schriver, A. Photolysis of ozone at 693 nm in solid oxygen. Isotope effects in ozone reformation. *Chem. Phys. Lett.* **1997**, *273*, 31–36. [CrossRef]
56. Bahou, M.; Schriver-Mazzuoli, L.; Camy-Peyret, C.; Schriver, A. New information on the ozone monomer photochemistry at 266 nm in nitrogen matrices. *J. Chem. Phys.* **1998**, *108*, 6884–6891. [CrossRef]
57. Flaud, J.M.; Bacis, R. The ozone molecule: Infrared and microwave spectroscopy. *Spectrochim. Acta Part A* **1998**, *54*, 3–16. [CrossRef]
58. Bahou, M.; Schriver-Mazzuoli, L.; Schriver, A. Photolysis at 266 nm of argon matrix isolated ozone monomer. *J. Chem. Phys.* **1999**, *110*, 8636–8642. [CrossRef]
59. Bahou, M.; Schriver-Mazzuoli, L.; Schriver, A. Infrared spectroscopy and photochemistry at 266 nm of the ozone dimer trapped in an argon matrix. *J. Chem. Phys.* **2001**, *114*, 4045–4052. [CrossRef]
60. Nelander, B.; Nord, L. Do ozone-olefin complexes really exist? *J. Am. Chem. Soc.* **1979**, *101*, 3769–3770. [CrossRef]
61. Nord, L. Ozone complexes in solid nitrogen. *J. Mol. Struct.* **1983**, *96*, 37–44. [CrossRef]
62. Withnall, R.; Hawkins, M.; Andrews, L. Infrared spectrum of a symmetrical phosphine-ozone complex in solid argon. *J. Phys. Chem.* **1986**, *90*, 575–579. [CrossRef]
63. Withnall, R.; Andrews, L. FTIR spectra of the photolysis products of the phosphine ozone complex in solid argon. *J. Phys. Chem.* **1987**, *91*, 784–797. [CrossRef]
64. Andrews, L. FTIR spectra of base-HF complexes in noble gas matrices. *J. Mol. Struct.* **1988**, *173*, 103–110. [CrossRef]
65. Schriver, L.; Barreau, C.; Schriver, A. Infrared spectroscopic and photochemical study of water-ozone complexes in solid argon. *Chem. Phys.* **1990**, *140*, 429–438. [CrossRef]
66. Schriver, L.; Carrere, D.; Schriver, A.; Jaeger, K. Matrix isolation photolysis of SO₂, O₃ and H₂O: Evidence for the H₂O:SO₃ complex. *Chem. Phys. Lett.* **1991**, *181*, 505–511. [CrossRef]

67. Davis, S.R.; Liu, L. Matrix isolation IR spectroscopy, photochemistry and ab initio calculations of the difluoromethane-ozone complex. *J. Phys. Chem.* **1993**, *97*, 3690–3696. [CrossRef]
68. Raducu, V.; Jasmin, D.; Dahoo, R.; Brosset, P.; Gauthier-Roy, B.; Abouaf-Marguin, L. Experimental study of the CO:O₃ complex in argon matrices: Irradiation at 266 nm. *J. Chem. Phys.* **1994**, *101*, 1878–1884. [CrossRef]
69. Schriver-Mazzuoli, L.; de Saxce, A.; Lugez, C.; Camy-Peyret, C.; Schriver, A. Ozone generation through photolysis of an oxygen matrix at 11 K: Fourier transform infrared spectroscopy identification of the O . . . O₃ complex and isotopic studies. *J. Chem. Phys.* **1995**, *102*, 690–701. [CrossRef]
70. Jones, P.R.; Taube, H. Photochemical studies on ozone with carbon disulfide and with carbonyl sulfide in low-temperature matrixes. *J. Phys. Chem.* **1973**, *77*, 1007–1011. [CrossRef]
71. Nelander, B.; Nord, L. The reaction between ethylene and ozone. A matrix study. *Tetrahedron Lett.* **1977**, *18*, 2821–2822. [CrossRef]
72. Lucas, D.; Pimentel, G.C. Reaction between nitric oxide and ozone in solid nitrogen. *J. Phys. Chem.* **1979**, *83*, 2311–2316. [CrossRef]
73. Bhatia, S.C.; Hall, J.H., Jr. A matrix isolation infrared spectroscopic study of the reactions of nitric oxide with oxygen and ozone. *J. Phys. Chem.* **1980**, *84*, 3255–3259. [CrossRef]
74. Frei, H.; Pimentel, G.C. Reaction of nitric oxide and ozone in cryogenic matrices: Quantum-mechanical tunneling and vibrational enhancement. *J. Phys. Chem.* **1981**, *85*, 3355–3360. [CrossRef]
75. Morris, V.R.; Bhatia, S.C.; Hall, J.H. A study of the gas-phase reaction of nitrogen dioxide with ozone by matrix isolation infrared spectroscopy. *J. Phys. Chem.* **1987**, *91*, 3359–3361. [CrossRef]
76. Lascola, R.; Withnall, R.; Andrews, L. Infrared spectra of hydrazine and products of its reactions with HF, F₂ and O₃ in solid argon. *Inorg. Chem.* **1988**, *27*, 642–648. [CrossRef]
77. Andrews, L.; Withnall, R.; Moores, B.W. Infrared spectra of arsine-ozone complexes, reaction products and photolysis products in solid argon. *J. Phys. Chem.* **1989**, *93*, 1279–1285. [CrossRef]
78. Andrews, L.; Moores, B.W.; Fonda, K.K. Matrix infrared spectra of reaction and photolysis products of stibine and ozone. *Inorg. Chem.* **1989**, *28*, 290–297. [CrossRef]
79. Andrews, L.; McCluskey, M.; Mielke, Z.; Withnall, R. Matrix reactions of P₄ and P₂ with O₃ molecules. *J. Mol. Struct.* **1990**, *222*, 95–108. [CrossRef]
80. Mielke, Z.; McCluskey, M.; Andrews, L. Matrix reactions of P₂ and O₃ molecules. *Chem. Phys. Lett.* **1990**, *165*, 146–154. [CrossRef]
81. Mielke, Z.; Andrews, L. Matrix infrared spectra of the products from photochemical reactions of P₄ with O₃ and decomposition of P₄O₆. *Inorg. Chem.* **1990**, *29*, 2773–2779. [CrossRef]
82. Mielke, Z.; Andrews, L. Matrix infrared studies of the hydrogen cyanide + ozone and hydrogen cyanide + oxygen atom systems. *J. Phys. Chem.* **1990**, *94*, 3519–3525. [CrossRef]
83. Schriver-Mazzuoli, L.; Abdeloui, O.; Lugez, C.; Schriver, A. Matrix reaction of ozone with Cl₂ and Br₂. FTIR identification of BrClO and ClBrO species. *Chem. Phys. Lett.* **1993**, *214*, 519–526. [CrossRef]
84. Bhatia, S.C.; Hall, J.H., Jr. Matrix isolation infrared and laser Raman spectroscopic study of the gas-phase reactions of chlorine atoms and ozone. *J. Phys. Chem.* **1981**, *85*, 2055–2060. [CrossRef]
85. Carter, R.O., III; Andrews, L. Matrix spectroscopic studies of chlorine atom-ozone reaction products. *J. Phys. Chem.* **1981**, *85*, 2351–2354. [CrossRef]
86. Lugez, C.L.; Thompson, W.E.; Jacox, M.E. Matrix-isolated study of the interaction of excited neon atoms with O₃: Infrared spectrum of O₃⁻ and evidence for the stabilization of O₂ . . . O₄⁺. *J. Chem. Phys.* **1996**, *105*, 2153–2160. [CrossRef]
87. Hargittai, M. Molecular structure of metal halides. *Chem. Rev.* **2000**, *100*, 2233–2302. [CrossRef]
88. Lee, T.J.; Allen, W.D.; Schaefer, H.F., III. The analytical evaluation of energy first derivatives for two-configuration self-consistent-field configuration interaction (TCSCF-CI) wave functions. Application to ozone and ethylene. *J. Chem. Phys.* **1987**, *87*, 7062–7075. [CrossRef]
89. Lee, T.J.; Scuseria, G.E. The vibrational frequencies of ozone. *J. Chem. Phys.* **1990**, *93*, 489–494. [CrossRef]
90. Liu, B.; McLean, A.D. Accurate calculations of the attractive interactions of two ground state helium atoms. *J. Chem. Phys.* **1973**, *59*, 4557–4558. [CrossRef]
91. Barbe, A.; Secroun, C.; Jouve, P. Infrared spectra of ¹⁶O₃ and ¹⁸O₃; Darling and Dennison resonance and anharmonic potential function of ozone. *J. Mol. Spectrosc.* **1974**, *49*, 171–182. [CrossRef]
92. Miliordos, E.; Xantheas, S.S. On the bonding nature of ozone (O₃) and its sulphur-substituted analogues SO₂, OS₂ and S₃: Correlation between their diradical character and molecular properties. *J. Am. Chem. Soc.* **2014**, *136*, 2808–2817. [CrossRef]
93. Takeshita, T.Y.; Lindquist, B.A.; Dunning, T.H., Jr. Insights into the electronic structure of ozone and sulphur dioxide from generalized valence bond theory: Bonding in O₃ and SO₂. *J. Phys. Chem. A* **2015**, *119*, 7683–7694. [CrossRef]
94. Tanaka, T.; Morino, Y. Coriolis interaction and anharmonic potential function of ozone from the microwave spectra in the excited vibrational states. *J. Mol. Spectrosc.* **1970**, *33*, 538–551. [CrossRef]
95. Frisch, M.J.; Trucks, G.W.; Schlegel, H.B.; Scuseria, G.E.; Robb, M.A.; Cheeseman, J.R.; Scalmani, G.; Barone, V.; Petersson, G.A.; Nakatsuji, H.; et al. *Gaussian 16, Revision A.03*; Gaussian, Inc.: Wallingford, CT, USA, 2016.
96. Møller, C.; Plesset, M.S. Notes on an approximation treatment for many-electron systems. *Phys. Rev.* **1934**, *46*, 618–622. [CrossRef]
97. Dunning, T.H., Jr. Gaussian basis sets for use in correlated molecular calculations. I. The atoms boron through neon and hydrogen. *J. Chem. Phys.* **1989**, *90*, 1007–1023. [CrossRef]

98. Kendall, R.A.; Dunning, T.H., Jr.; Harrison, R.J. Electron affinities of the first-row atoms revisited. Systematic basis sets and wavefunctions. *J. Chem. Phys.* **1992**, *96*, 6796–6806. [CrossRef]
99. Boys, S.F.; Bernardi, F. The calculation of small molecular interactions by the differences of separate total energies. Some procedures with reduced errors. *Mol. Phys.* **1970**, *19*, 553–556. [CrossRef]

Article

Luminescent Ink Based on Upconversion of NaYF₄:Er,Yb@MA Nanoparticles: Environmental Friendly Synthesis and Structural and Spectroscopic Assessment

T. M. Dung Cao^{1,2}, T. T. Giang Le^{2,3}, Sylvia Turrell⁴, Maurizio Ferrari⁵, Quang Vinh Lam² and T. T. Van Tran^{1,2,*}

¹ Faculty of Materials Science and Technology, University of Science, Ho Chi Minh City 700000, Vietnam; ctmdung@hcmus.edu.vn

² Vietnam National University, Ho Chi Minh City 700000, Vietnam; ltgiang@hcmus.edu.vn (T.T.G.L.); lqvinh@vnuhcm.edu.vn (Q.V.L.)

³ Faculty of Physics and Engineering Physics, University of Science, Ho Chi Minh City 700000, Vietnam

⁴ CNRS, UMR 8516-LASIRE–Laboratoire Avancé de Spectroscopie pour les Interactions la Réactivité et l’Environnement, Université de Lille, F-59000 Lille, France; sylvia.turrelljones@gmail.com

⁵ IFN-CNR CSMFO Lab. and FBK Photonics Unit, Via Alla Cascata 56/C, 38123 Povo, Italy; maurizio.ferrari@unitn.it

* Correspondence: tttvan@hcmus.edu.vn; Tel.: +84-914-396-939

Abstract: NaYF₄:Er,Yb upconversion luminescent nanoparticles (UCNPs) were prepared by hydrothermal methods at 180 °C for 24 h. The X-ray diffraction (XRD) and TEM (transmission electron microscopy) images show that the resulting 60 nm UCNPs possess a hexagonal structure. In this work, maleic anhydride (MA) was grafted on the surface of UCNPs to induce hydrophilic properties. The photoluminescence spectra (PL) show upconversion emissions centered around 545 nm and 660 nm under excitation at 980 nm. The luminescent inks, including UCNPs@MA, polyvinyl alcohol (PVA), deionized water (DI), and ethylene glycol (EG), exhibit suitable properties for screen printing, such as high stability, emission intensity, and tunable dynamic viscosity. The printed patterns with a height of 5 mm and a width of 1.5 mm were clearly observed under the irradiation of a 980 nm laser. Our strategy provides a new route for the controlled synthesis of hydrophilic UCNPs, and shows that the UCNPs@MAs have great potential in applications of anti-counterfeiting packing.

Keywords: NaYF₄:Er,Yb; upconversion emission; surface modification; hydrophilic; screen printing

Citation: Cao, T.M.D.; Le, T.T.G.; Turrell, S.; Ferrari, M.; Lam, Q.V.; Tran, T.T.V. Luminescent Ink Based on Upconversion of NaYF₄:Er,Yb@MA Nanoparticles: Environmental Friendly Synthesis and Structural and Spectroscopic Assessment. *Molecules* **2021**, *26*, 1041. <https://doi.org/10.3390/molecules26041041>

Academic Editor: Rita Cortesi

Received: 24 January 2021

Accepted: 12 February 2021

Published: 17 February 2021

Publisher’s Note: MDPI stays neutral with regard to jurisdictional claims in published maps and institutional affiliations.



Copyright: © 2021 by the authors. Licensee MDPI, Basel, Switzerland. This article is an open access article distributed under the terms and conditions of the Creative Commons Attribution (CC BY) license (<https://creativecommons.org/licenses/by/4.0/>).

1. Introduction

Over the past few years, luminescent inks have been used to detect counterfeiting. Outstanding applications of these inks include banknotes, quick response codes (QR codes), barcodes, security documents, drug packaging, and food security [1–5]. The security ink is invisible under visible light; but, upon ultraviolet radiations, printed information can be read. These security inks are mostly based on the down-conversion effect, and primary materials, such as quantum dots (QDs), are used [6–8]. In fact, due to their wide band gaps, they easily absorb ultraviolet light.

CdS and CdSe are commonly used for syntheses, but they are toxic. Moreover, UV radiation is harmful to our health under specific conditions. In addition, the substrates are also sensitive to UV excitations, which leads to a reduction of the contrast between the substrate and the printed sample. Last but not least, UV to visible down-conversion materials and UV excitation sources have become more accessible, making them much easier to duplicate.

For these reasons, luminescent inks using near-infrared (NIR) excitation are now studied as alternatives. The resulting materials are non-toxic, and the ink can easily glow even on highly luminescent substrates, such as paper and textiles. Near infrared to visible luminescent materials based on the so-called upconversion luminescence are more difficult

to duplicate compared to UV to visible materials. Nowadays, rare earth ion (RE) doped luminescent materials are being studied to replace QDs. This direction is due to the abundance of excitation and luminescence wavelengths depending on the type of REs selected [9–12]. For materials using infrared excitation, Yb³⁺ ions are chosen as sensitizers to absorb 980 nm radiation, while the Er³⁺ ions are activators for visible emissions [13–15].

In another approach, the luminescent host material is constituted by NaYF₄ nanoparticles, synthesized by hydrothermal methods with oleic acid (OA) and used as surfactants [16–19]. The UCNP_s produced using this approach are inherently capped with hydrophobic ligands because OA is a fatty acid, which contains an alkenyl group (–HC = CH–). However, applications require nanocrystals to be dispersed and stabilized in the aqueous phase. Thus, the transfer of these hydrophobic nanocrystals into aqueous media becomes a critical issue.

To synthesize high-quality, water-dispersible nanocrystals, there are many polymers being studied, such as poly(methyl methacrylate) PMMA [20,21], poly(acrylic acid) PAA [22,23], and polyethylene glycol PEG [24]. In our study, maleic anhydride (MA) was chosen for hydrophilic properties [25,26], because it can react with oleic acid capped on the surface of nanoparticles. The resulting UCNP_s will exhibit dispersibility in water.

In the maleinization process, MA can be grafted onto hydrophobic ligands bearing alkenyl functional groups to yield succinic anhydride functional groups. There are a few advantages of this new strategy, such as retaining nanocrystalline characteristics, using a simple hydrolysis treatment and reaction conditions for the maleinization of oleic acid, and providing carboxylic acid functional groups that provide good anchors. The UCNP_s with hydrophilic bonding on the surface can be successfully applied in many fields. One of them is ink printing, due to the stabilities of UCNP_s in water and solvents [27]. Compared to various methods, such as radio frequency identification (RFID) tags [28], inkjet printing [29], and laser holograms [30,31], all of which require high-cost equipment, clean room facilities, and a complex preparation procedure, the screen printing process reveals some outstanding advantages. This method produces images of higher quality than inkjet prints, can be printed on a variety of materials, including glass, wood, textiles, signs, and banners, and can easily be printed on a specific or large area [32,33].

There are many formulas for inks, running from complicated to simple in nature [4,9,27,34]. Ink formulations consist of a solution containing the UCNP_s, a solvent system, and a polymer that can be dissolved in the solvent system. The solvent system must produce a solution with optimal physical properties (viscosity, evaporation rate, surface tension) suitable for printing. The poly(vinyl alcohol) (PVA) was chosen as the polymer matrix for the preparation of screen printing. Among the various solvents evaluated, ethylene glycol produced stable oxide inks and satisfied the printing conditions. With its simple formula, it was deemed suitable for applications.

2. Results and Discussion

2.1. Vibrational Characterization of UCNP_s

The existence of organic bonds on the surface of UCNP_s can be demonstrated by the observation of the FT-IR spectra shown in Figure 1.

Fourier transform infrared spectra of OA, UCNP_s, MA, and UCNP_s@MA nanoparticles are shown in Figure 1. The FT-IR spectra of OA show the ν_{as} (–CH₂–) and ν_s (–CH₂–) stretching vibrations of long alkyl chains at 2931 cm^{–1} and 2854 cm^{–1}, respectively. The O–H vibrational stretching modes of carboxylic acid groups (–COOH) are observed around 3500–2500 cm^{–1}, the C = O stretching of a carboxyl group at 1712 cm^{–1}, the vibrational modes of carboxylate group (COO[–]) around 1650–1360 cm^{–1}, the out-of-plane O–H deformation mode at 941 cm^{–1}, and the rocking mode of CH₂ at 721 cm^{–1}. In the spectrum of OA, there is also the appearance of the peak at 3003 cm^{–1}, attributed to the olefinic (C–H) vibrational mode in (C = C–H) [35,36].

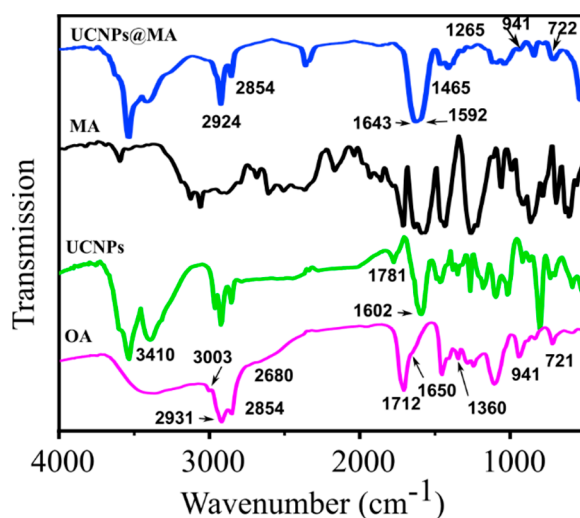


Figure 1. FT-IR spectra of OA, UCNPs, MA, and UCNPs@MA.

For the prepared NaYF_4 sample (UCNPs), the appearance of bands at 2931–2680 cm^{-1} confirms the presence of oleate ligand on the nanoparticle surfaces. Moreover, the broad bands located at 3410 cm^{-1} and 1602 cm^{-1} correspond to the O–H stretching and bending vibrations, respectively, of residual molecular water in the samples. It is worthy to note a redshift in the frequency of the C = O and (COO^-) stretching modes in doped samples, which is the result of the electrostatic attraction and chemical adsorption between the Ln^{3+} ions of nanoparticles and the COO^- group of OA in UCNPs [19].

The UCNPs@MA spectrum presents the characteristic bands of oleic-maleic anhydride copolymer at 722 cm^{-1} , 941 cm^{-1} , 1265 cm^{-1} , and 1465 cm^{-1} , which may be attributed to $(\text{CH}_2)_n$, O–H out of plane bending vibrations, C–O anhydride, and CH_2 vibrational modes, respectively [37]. The broad band around 1643–1592 cm^{-1} is related to the O–H bending and the C = C vibrations of MA. This result confirms the presence of MA bonds on the UCNPs surface. Moreover, the spectra show absorption bands at 2854 cm^{-1} and 2924 cm^{-1} , which may be related to C–H symmetric and asymmetric stretching modes, respectively.

2.2. Structural Characterization of UCNPs

Figure 2 shows XRD patterns of NaYF_4 un-doped, co-doped $\text{NaYF}_4:\text{Er},\text{Yb}$ (UCNPs), and polymer ligand $\text{NaYF}_4:\text{Er},\text{Yb}@\text{MA}$ (UCNPs@MA). The systems have a hexagonal structure, with diffraction peaks at positions $2\theta = 17.26^\circ, 29.95^\circ, 30.86^\circ, 34.73^\circ, 36.69^\circ, 43.47^\circ, 46.39^\circ, 52.16^\circ, 53.09^\circ, 53.61^\circ, \text{ and } 55.24^\circ$, corresponding to the lattice faces (100), (100), (101), (200), (111), (201), (210), (002), (300), (211), and (102) of the hexagonal structure of $\beta\text{-NaYF}_4$, according to the JCPDS 16-0334 standard.

XRD patterns of NaYF_4 crystals show no peaks of an α phase cubic structure, as well as no presence of intermediate or doped phases. Thus, the role of REs has had an insignificant effect on the hexagonal structure of $\beta\text{-NaYF}_4$. However, the diffraction peaks of the doped samples shift to larger angles. This implies that the dopants lead to a decrease in the lattice parameters. The substitution of doping ions in the Y^{3+} sites causes a compressive strain, because the ionic radii of Er^{3+} (89 pm) and Yb^{3+} (87 pm) are smaller than the radius of Y^{3+} ions (90 pm).

The XRD pattern of UCNPs with MA shows the same hexagonal structure of NaYF_4 , and there is no peak characteristic of MA. This result shows that the MA bond is formed on the surface of NaYF_4 and that it does not exist independently in the sample.

The calculated crystal size of UCNPs@MA is 60 ± 1 nm, and the crystal lattice parameters are 0.59 nm and 0.35 nm, corresponding to a and c, respectively.

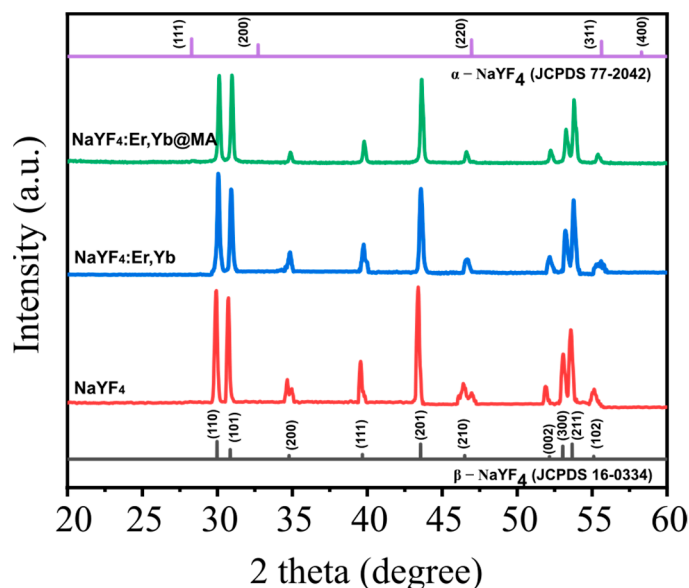


Figure 2. XRD patterns of NaYF₄ un-doped, co-doped NaYF₄:Er,Yb, and polymer ligand NaYF₄:Er,Yb@MA.

2.3. Optical Characterization

Figure 3a shows the photoluminescence spectra of UCNP and UCNP@MA nanoparticles obtained under an excitation of 980 nm. The PL spectra show visible emission of NaYF₄ co-doped with Er³⁺ and Yb³⁺ ions, with green emission (512 and 560 nm) and red emission (640 and 680 nm) corresponding to the characteristic transition of Er³⁺ ion activators from ⁴H_{11/2}, ⁴S_{3/2}, and ⁴F_{9/2} levels to the ⁴I_{15/2} ground state, respectively. The effect of hydrophilic polymer bonds on the luminescent intensity of UCNP is evidenced in Figure 3a. The existence of polymer binding on the surface of the UCNP results in a reduction of the emission intensity by a factor of about three. The CIE chromaticity coordinates ($x = 0.349$, $y = 0.612$) taken from PL data of the UC emission spectra using Origin software show the color of materials to be green, as shown in Figure 3b.

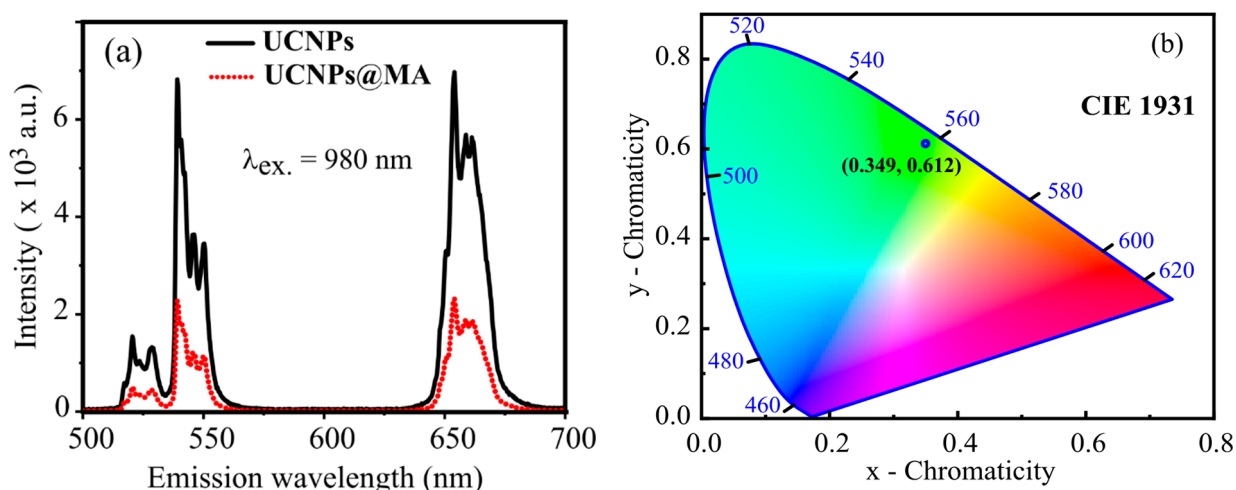


Figure 3. (a) UC photoluminescence spectra of UCNP and UCNP@MA obtained upon 980 nm excitation; (b) the CIE 1931 chromaticity coordinates of the UCNP@MA.

To reconfirm the UC emission occurring in UCNP@MA, the integrated PL intensities (I_{UC}) of UCNP@MA were investigated as a function of excitation power P using the relation $I_{UC} \sim P^n$, where n is the number of photons [38]. Figure 4 shows the UCNP@MA

upconversion photoluminescence intensity at 545 nm (green) and 660 nm (red) as a function of the excitation power. The fitting curves indicate the value of n as 1.71 ± 0.20 and 1.40 ± 0.16 for green and red luminescence, respectively.

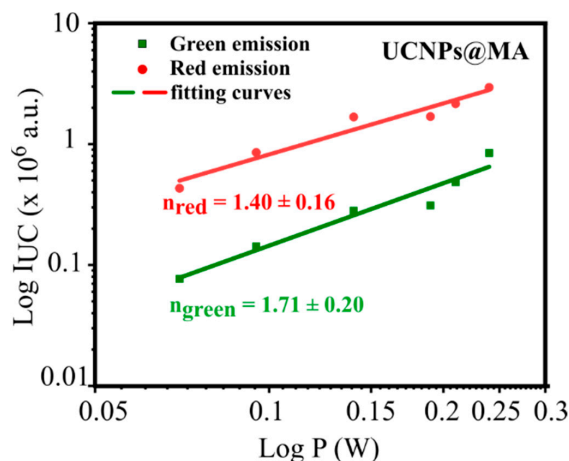


Figure 4. UCNPs@MA upconversion photoluminescence intensity at 545 nm (green) and 660 nm (red) as a function of the excitation power. The excitation wavelength was 980 nm. The solid lines are the curves of a power-law function fitted to the data, which gives the indicated slopes.

The green luminescence is assigned to a two-photon process. The main two-photon upconversion mechanism is described in Figure 5, where the ground state absorption (GSA), subsequent excited-state absorption process (ESA), energy transfer (ET), and cross-relaxation (CR) in the population of the excited states are indicated. The $^4S_{3/2}$ level of Figure 5 is populated by two near-infrared photons. We observe a slope less than two due to competitive processes, such as co-operative energy transfer and cross-relaxation, which are well-described in the literature [39,40]. The slope of 1.4, i.e., close to 1.5, can be explained by a process involving three absorbed photons, which give two emitted photons. The process has been discussed by R.R. Gonçalves et al. [41]. In this process, two infrared photons excite the Er^{3+} ions to the $^4F_{7/2}$ state, and one infrared photon promotes another Er^{3+} ion into the $^4I_{11/2}$ excited state. After a cross-relaxation process between them, the two ions relax into the $^4F_{9/2}$ state, and a red emission occurs [41].

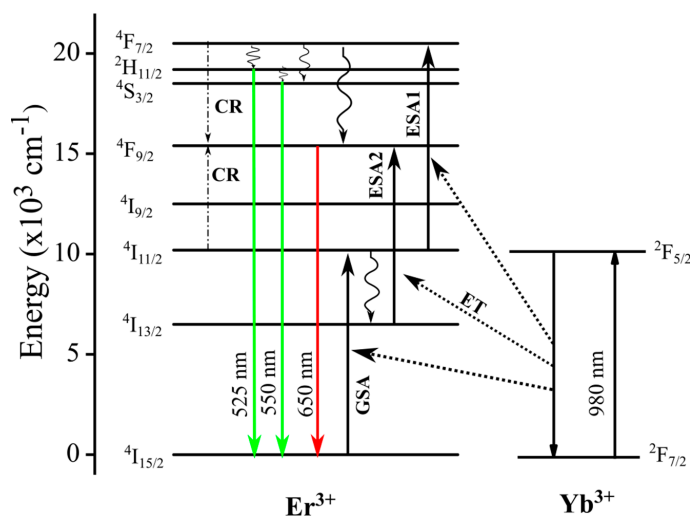


Figure 5. Schematic energy level diagram of co-doped Er^{3+} and Yb^{3+} ions and possible transition processes.

2.4. Screen Printing of UCNPs@MA for Anti-Counterfeiting Applications

Due to the outstanding properties of UCNPs@MA, which include hydrophilic surfaces as well as spherical nanoparticles with an average size of 60 nm, which have strong and tunable upconversion fluorescence, this system was used to fabricate environmentally-friendly inks, which could be screen-printed on paper substrates for anti-counterfeiting.

The UCNPs@MA was dispersed in a solvent mixture of PVA, water, and EG to obtain luminescent ink with a proper dynamic viscosity. By fixing the weight ratio of UCNPs@MA to 0.2 g/mL, a series of UCNPs@MA inks with different solvent compositions were prepared.

The ink viscosities and the surface tensions with different weights of PVA were measured, and are presented in Table 1. These results show a significant increase in viscosity with the weight of PVA, while the surface tension maintains a value around 60 mN/m for these PVA weights.

Table 1. Viscosity and surface tension of ink solutions with different weights of PVA.

Weight of PVA (g)	Viscosity (cP)	Surface Tension (mN/m)
1	7.8	59
2	68.5	58.6
3	392.5	62

An optimized weight ratio of PVA, water, and EG was kept at PVA:EG = 5:1, with a PVA weight of 2 g. These values provided a luminescent ink with the viscosity and surface tension of 68.5 cP and 58.6 mN/m, respectively. This solution was pushed easily through the screen, and displayed clearer images on paper than other PVA weights. The ink solution was scanned through the mesh screen onto the paper, forming 10 layers. The ink patterns were dried under normal ambient conditions for 2–3 min. After screen printing, the designed patterns were invisible under daylight, but clearly observable under the irradiation of a 980 nm LED lamp. This pattern is shown in Figure 6.

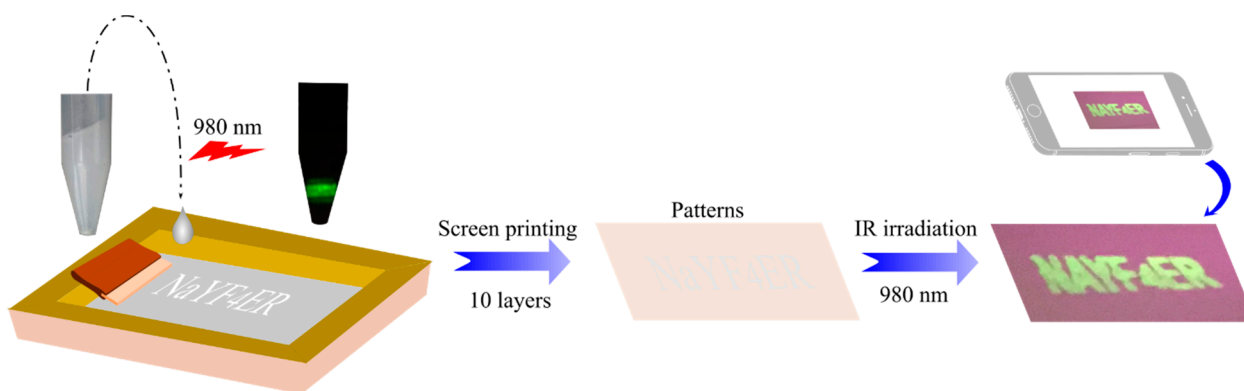


Figure 6. The procedure of screen printing.

3. Materials and Methods

3.1. Synthesis of NaYF₄:Er,Yb Upconversion Nanoparticles with Maleic Anhydride on the Surface

UCNPs materials were synthesized by solvothermal methods at 180 °C for 24 h. This process is the same as that presented in our previous report [42]. The ratio of rare earth stearate and oleic acid (OA) was RES:OA = 1:24, and doping concentrations of 1% Er³⁺ and 20% Yb³⁺ were chosen for this study. Maleic anhydride (MA, China) was chosen as a polymer to form hydrophilic bonds on the UCNPs surface. Figure 7a describes the surface modification schematic of UCNPs.

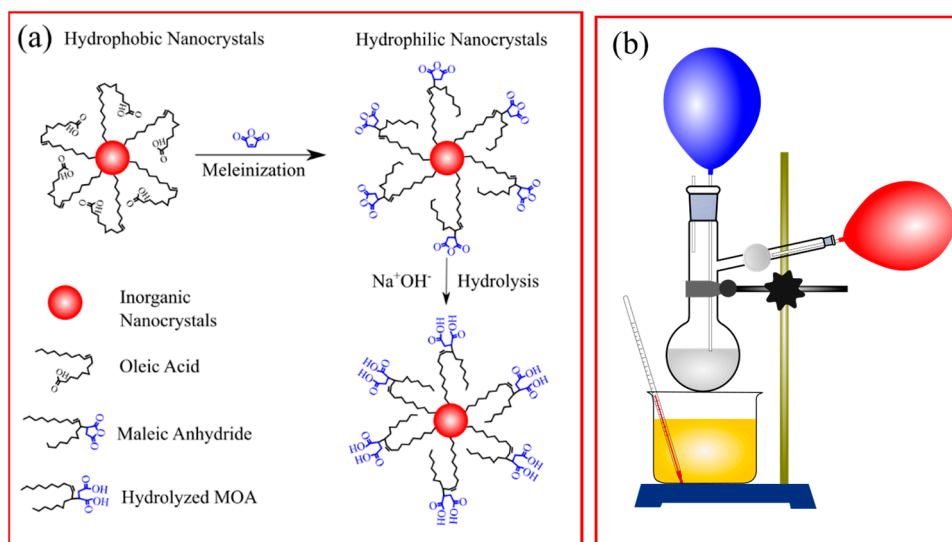


Figure 7. (a) Scheme of surface modification of UCNPs by maleic anhydride (MA); (b) the experimental apparatus is also sketched.

The precursors used for this process were maleic anhydride (MA), benzoyl peroxide (BPO), and toluene (Tol). A weight ratio of UCNPs:MA:BPO = 1:2:5 was employed, and an appropriate volume of Tol was moved into a fixed two-neck flask. Two balloons containing N_2 gas were used for giving gas out from the surface and inside the solution. An oil container worked as a thermal transfer, as shown in Figure 7b. The modification time was 4 h at 90 °C, with a stirring speed of 300 rpm. After being cooled to room temperature, the $\text{NaYF}_4:\text{Er},\text{Yb}$ with MA bonding on the surface (UCNPs@MA) was collected by centrifugation, washed three times with ethanol, and dried at 100 °C for 12 h.

3.2. Ink Manufacturing Process

The precursors used for ink preparation included polyvinyl alcohol (PVA), deionized water (DI), and ethylene glycol (EG). The luminescent inks were synthesized in two steps. The first step was to make a mixture of PVA glue using different weights of PVA (1, 2, and 3 g) and 20 mL of DI, stirring vigorously at room temperature for 15 min. The mixture was then heated to 50 °C for 15 min under ultrasonic treatment until a clear solution was obtained.

The second step was to prepare an ink solution with a ratio of PVA glue and EG as PVA:EG = 5:1. For this procedure, the mixture was vigorously stirred for 15 min at room temperature. At this point, UCNPs@MA was added to the solution and treated ultrasonically for 30 min at 50 °C, in order to ensure that the nanoparticles were well-dispersed in the ink solution. Fluorescent ink solutions exhibited optimal surface tension and viscosity.

The screen-printing frame was used in this work with desirable patterns containing characters with 2 mm width and 5 mm height. An A4 photocopy sheet was used as a substrate for the UCNPs@MA ink deposition during screen printing. No visible images appeared on the paper under normal light, but, under the exposure to a 980 nm excitation, there was the appearance of clear green characters.

3.3. Characterization

Studies of the structural phases were carried out through X-ray diffraction (XRD) patterns under $\text{CuK}\alpha_1$ radiation ($\lambda = 1.5406 \text{ \AA}$), voltage 40 kV, current 40 mA, and tunable

$2\theta = 20\text{--}60^\circ$ of a D2- PHASER diffractometer (Bruker, Germany). The average crystal diameter D was extracted from XRD data using the Halder–Wagner–Langford method [43]:

$$\left(\frac{\beta^*}{d^*}\right)^2 = D^{-1} \frac{\beta^*}{(d^*)^2} + \left(\frac{\varepsilon}{2}\right)^2 \quad (1)$$

$$\beta^* = \frac{\beta \cdot \cos \theta}{\lambda} \quad (2)$$

$$d^* = \frac{2 \cdot \sin \theta}{\lambda} \quad (3)$$

$$\beta = \sqrt{\beta_{\text{exp}}^2 - \beta_{\text{inst}}^2} \quad (4)$$

where β_{exp} is the experimental value of the full width at half maximum (FWHM) of the most intense peak of the sample, and β_{inst} is the instrumental FWHM of a diffraction pattern. Line-broadening β was obtained from Gaussian profile fitting, and a linear fit with terms $(\beta^*/d^*)^2$ and $\beta^*/(d^*)^2$ was performed, where the slope for the straight line provided the average size D . NaYF_4 nanocrystals have a hexagonal structure, with lattice constants a and c calculated as:

$$\frac{1}{d^2} = \frac{4}{3} \left(\frac{h^2 + hk + k^2}{a^2} \right) + \frac{l^2}{c^2} \quad (5)$$

The morphology of UCNPs was observed under transmission electron microscopy (TEM) of JEM-400 (JEOL, Tokyo, Japan), with a voltage of 100 kV. For these measurements, the samples were grounded and dispersed in ethanol. A droplet of the resulting fine-powder suspension was placed on a copper microscope grid. Fourier transform infrared spectra (FT-IR) were obtained in the range of 4000 to 500 cm^{-1} with a Vertex70 spectrometer (Bruker, Germany). Photoluminescence (PL) spectra were collected under 980 nm diode laser excitation using an iHR 320 instrument (Horiba, Kyoto, Japan). All measurements were performed under the same conditions at room temperature.

4. Conclusions

Using hydrothermal methods at 180 °C for 24 h, $\text{NaYF}_4\text{:Er,Yb}$ nanoparticles with an average size of 60 nm were obtained. The surface modification of $\text{NaYF}_4\text{:Er,Yb}$ by maleic anhydride (MA) makes it become a hydrophilic nanoparticle. The visible emissions of these materials can be observed directly with the eyes. A novel and easy ink operating in an upconversion condition has been developed and characterized by its optical, spectroscopic, and structural properties. The core shell structure enables the system to be stable in water and a solvent, thus allowing the use of printing applications.

Finally, the developed ink based on UCNPs@MA emits upconverted green luminescence. This property makes it detectable by human eyes, making this material very competitive for anti-counterfeiting packing.

Author Contributions: Conceptualization, T.T.V.T.; Formal analysis, T.M.D.C.; Investigation, T.M.D.C.; Methodology, T.T.G.L. and Q.V.L.; Writing—original draft, T.T.G.L. and T.T.V.T.; Writing—review & editing, S.T., M.F., and T.T.V.T. All authors have read and agreed to the published version of the manuscript.

Funding: This research is funded by the Vietnam National Foundation for Science and Technology Development (NAFOSTED) under grant number 103.03-2018.326.

Institutional Review Board Statement: Not applicable.

Informed Consent Statement: Not applicable.

Data Availability Statement: The data presented in this study are available on request from the corresponding author. The data are not publicly available due to the rules of research group.

Conflicts of Interest: The authors declare no competing financial interest.

Sample Availability: Samples of the compounds NaYF₄:Er,Yb and their inks are available from the authors.

References

- Cui, Y.; Ling, X.Y. Encoding molecular information in plasmonic nanostructures for anti-counterfeiting applications. *Nanoscale* **2014**, *6*, 282–288. [CrossRef]
- Han, S.; Park, W. Lithographically encoded polymer microtaggant using high-capacity and error-correctable QR code for anti-counterfeiting of drugs. *Adv. Mater.* **2012**, *24*, 5924–5929. [CrossRef] [PubMed]
- Liu, Y.; Ai, K.; Lu, L. Designing lanthanide-doped nanocrystals with both up-and down-conversion luminescence for anti-counterfeiting. *Nanoscale* **2011**, *3*, 4804–4810. [CrossRef]
- Meruga, J.M.; Kellar, J.J. Security printing of covert quick response codes using upconverting nanoparticle inks. *Nanotechnology* **2012**, *23*, 395201. [CrossRef]
- Yoon, B.; Kim, J.M. Recent functional material based approaches to prevent and detect counterfeiting. *J. Mater. Chem. C* **2013**, *1*, 2388–2403. [CrossRef]
- Liu, Y.; Guo, T. Inkjet-printed unclonable quantum dot fluorescent anti-counterfeiting labels with artificial intelligence authentication. *Nat. Commun.* **2019**, *10*, 1–9. [CrossRef]
- Wei, W.; Zheng, G. Preparation of quantum dot luminescent materials through the ink approach. *Mater. Des.* **2016**, *91*, 165–170. [CrossRef]
- Ingrosso, C.; Brugger, J. Drop-on-demand inkjet printing of highly luminescent CdS and CdSe@ZnS nanocrystal based nanocomposites. *Microelectron. Eng.* **2009**, *86*, 1124–1126. [CrossRef]
- Blumenthal, T.; Meruga, J.; Luu, Q.A.N. Patterned direct-write and screen-printing of NIR-to-visible upconverting inks for security applications. *Nanotechnology* **2012**, *23*, 185305. [CrossRef] [PubMed]
- You, M.; Xu, F. Inkjet printing of upconversion nanoparticles for anti-counterfeit applications. *Nanoscale* **2015**, *7*, 4423–4431. [CrossRef]
- Meruga, J.M.; May, P.S. Red-green-blue printing using luminescence-upconversion inks. *J. Mater. Chem. C* **2014**, *2*, 2221–2227. [CrossRef]
- Yao, W.; Wu, W. Dual upconversion nanophotoswitch for security encoding. *Sci. China Mater.* **2019**, *62*, 368–378. [CrossRef]
- Kumar, A.; Tiwari, S.P.; Kumar, K. Security writing application of thermal decomposition assisted NaYF₄:Er³⁺/Yb³⁺ upconversion phosphor. *Laser Phys. Lett.* **2018**, *15*, 075901. [CrossRef]
- Xie, S.; Zhang, C. Hydrothermal synthesis and inkjet printing of hexagonal-phase NaYF₄:Ln³⁺ upconversion hollow microtubes for smart anti-counterfeiting encryption. *Mater. Chem. Front.* **2018**, *2*, 1997–2005. [CrossRef]
- Gong, G.; Zheng, J. Design of core/active-shell NaYF₄: Ln³⁺@NaYF₄:Yb³⁺ nanophosphors with enhanced red-green-blue upconversion luminescence for anti-counterfeiting printing. *Compos. B Eng.* **2019**, *179*, 107504. [CrossRef]
- Himmelstoß, S.F.; Hirsch, T. Long-Term Colloidal and Chemical Stability in Aqueous Media of NaYF₄-Type Upconversion Nanoparticles Modified by Ligand-Exchange. *Part. Part. Syst. Charact.* **2019**, *36*, 1900235. [CrossRef]
- Huang, J.; Chen, N. Growth of β-NaYF₄:Eu³⁺ Crystals by the Solvothermal Method with the Aid of Oleic Acid and Their Photoluminescence Properties. *Materials* **2019**, *12*, 3711. [CrossRef]
- Li, H.; Liu, X.; Li, X. Solvothermal synthesis and modification of NaYF₄:Yb/Er@ NaLuF₄:Yb for enhanced up-conversion luminescence for bioimaging. *RSC Adv.* **2019**, *9*, 42163–42171. [CrossRef]
- Li, Z.; Tang, B. Fabrication of NaYF₄:Yb,Er Nanoprobes for Cell Imaging Directly by Using the Method of Hydrion Rivalry Aided by Ultrasonic. *Nanoscale Res. Lett.* **2016**, *11*, 1–10. [CrossRef]
- Boyer, J.C.; Johnson, N.J.J.; Van Veggel, F.C.J.M. Upconverting lanthanide-doped NaYF₄-PMMA polymer composites prepared by in situ polymerization. *Chem. Mater.* **2009**, *21*, 2010–2012. [CrossRef]
- Chai, R.; Lin, J. Preparation and characterization of upconversion luminescent NaYF₄:Yb³⁺,Er³⁺(Tm³⁺)/PMMA bulk transparent nanocomposites through in situ photopolymerization. *J. Phys. Chem. C* **2010**, *114*, 610–616. [CrossRef]
- Liu, C.H.; Li, Z.P. Surface modification of hydrophobic NaYF₄:Yb,Er upconversion nanophosphors and their applications for immunoassay. *Sci. China Chem.* **2011**, *54*, 1292. [CrossRef]
- Song, Y.; Xu, L. Synthesis and Inkjet Printing of NaYF₄:Ln³⁺@NaYF₄ Core-Shell Nanoparticles with Enhanced Upconversion Fluorescence for Anti-Counterfeiting Applications. *J. Nanosci. Nanotechnol.* **2020**, *20*, 1511–1519. [CrossRef] [PubMed]
- Chen, Z.; Hu, J. PEG-mediated solvothermal synthesis of NaYF₄:Yb/Er superstructures with efficient upconversion luminescence. *J. Alloys Compd.* **2010**, *506*, L17–L21. [CrossRef]
- Peng, E.; Ding, J.; Xue, J.M. Succinic anhydride functionalized alkenoic ligands: A facile route to synthesize water dispersible nanocrystals. *J. Mater. Chem.* **2012**, *22*, 13832–13840. [CrossRef]
- Stefanoiu, F.; Borredon, E. Kinetics and mechanism of the reaction between maleic anhydride and fatty acid esters and the structure of the products. *Eur. J. Lipid Sci. Technol.* **2008**, *110*, 441–447. [CrossRef]
- Kellar, J.; Blumenthal, T. Systems and Methods for Printing Patterns Using Near Infrared Upconverting Inks. U.S. Patent US10358569B2, 23 July 2019.
- Cheng, Z.Y.; Chang, S.C. Authenticated RFID security mechanism based on chaotic maps. *Secur. Commun. Netw.* **2013**, *6*, 247–256. [CrossRef]

29. You, M.; Xu, F. Three-dimensional quick response code based on inkjet printing of upconversion fluorescent nanoparticles for drug anti-counterfeiting. *Nanoscale* **2016**, *8*, 10096–10104. [CrossRef]
30. Peng, H.; Bowman, C.N. Monochromatic visible light “photoinitiator”: Janus-faced initiation and inhibition for storage of colored 3D images. *J. Am. Chem. Soc.* **2014**, *136*, 8855–8858. [CrossRef]
31. Ni, M.; Xie, X. 3D image storage in photopolymer/ZnS nanocomposites tailored by “photoinitiator”. *Macromolecules* **2015**, *48*, 2958–2966. [CrossRef]
32. Yao, W.; Wu, W. Large-scale synthesis and screen printing of upconversion hexagonal-phase NaYF₄:Yb³⁺,Tm³⁺/Er³⁺/Eu³⁺ plates for security applications. *J. Mater. Chem. C* **2016**, *4*, 6327–6335. [CrossRef]
33. Li, D.; She, J. Screen printing of upconversion NaYF₄:Yb³⁺/Eu³⁺ with Li⁺ doped for anti-counterfeiting application. *Chin. Opt. Lett.* **2020**, *18*, 110501. [CrossRef]
34. Attia, M.S.; Abdel-Mottaleb, M.S.A. Inkjet Printable Luminescent Eu³⁺-TiO₂ Doped in Sol Gel Matrix for Paper Tagging. *J. Fluoresc.* **2015**, *25*, 119–125. [CrossRef] [PubMed]
35. Labidi, N.S.; Iddou, A. Adsorption of oleic acid on quartz/water interface. *J. Saudi Chem. Soc.* **2007**, *11*, 221–234.
36. Premaratne, W.A.P.J.; De Alwis, A.A.P. Synthesis of nanosilica from paddy husk ash and their surface functionalization. *J. Sci. Univ. Kelaniya* **2014**, *8*, 33–48. [CrossRef]
37. Soliman, E.A.; Ibrahim, H.S. Synthesis and performance of maleic anhydride copolymers with alkyl linoleate or tetra-esters as pour point depressants for waxy crude oil. *Fuel* **2018**, *211*, 535–547. [CrossRef]
38. Zhang, F. Photon Upconversion Nanomaterials. In *Nanostructure Science and Technology*; Lockwood, D.J., Ed.; Springer: Berlin/Heidelberg, Germany, 2015; ISBN 978-3-662-45596-8.
39. Catunda, T.; Aegerter, M.A. Spectroscopic properties and upconversion mechanisms in Er³⁺ doped fluoroindate glasses. *Phys. Rev. B* **1996**, *53*, 6065–6070. [CrossRef]
40. Reddy, B.R.; Venkateswarlu, P. Infrared to visible energy upconversion in Er³⁺ doped oxide glass. *Appl. Phys. Lett.* **1994**, *64*, 1327–1329. [CrossRef]
41. Gonçalves, R.R.; Messaddeq, Y. Infrared-to-visible CW frequency upconversion in erbium activated silica–hafnia waveguides prepared by sol–gel route. *J. Non-Cryst. Solids* **2003**, *322*, 306–310. [CrossRef]
42. Cao, T.M.D.; Le, T.T.G.; Tran, T.T.V. Investigating the effect of Yb³⁺ and Er³⁺ concentration on red/green luminescent ratio in β-NaYF₄:Er,Yb nanocrystals using spectroscopic techniques. *J. Mol. Struct.* **2020**, *1210*, 128014. [CrossRef]
43. Daly, R.; Njah, N. The studies of crystallite size and microstrains in aluminum powder prepared by mechanical milling. *Phys. Stat. Sol. (C)* **2006**, *3*, 3325–3331. [CrossRef]

Article

PLS-DA Model for the Evaluation of Attention Deficit and Hyperactivity Disorder in Children and Adolescents through Blood Serum FTIR Spectra

Gulce Ogruc Ildiz ^{1,2,*}, Ahmet Karadag ¹, Ersin Kaygisiz ³

¹ Department of Physics, Faculty of Sciences and Letters, Istanbul Kultur University, 34158 Istanbul, Turkey; karadagahmet23@gmail.com

² Department of Chemistry, CQC, University of Coimbra, P-3004-535 Coimbra, Portugal; rfausto@ci.uc.pt

³ Department of Geological Engineering, Istanbul University-Cerrahpasa, 34320 Istanbul, Turkey; ersinkygsz@gmail.com

* Correspondence: g.ogruc@iku.edu.tr; Tel.: +90-(212)-498-4319

Abstract: Attention deficit and hyperactivity disorder (ADHD) is one of the most common neurodevelopmental disorders of childhood. It affects ~10% of the world's population of children, and about 30–50% of those diagnosed in childhood continue to show ADHD symptoms later, with 2–5% of adults having the condition. Current diagnosis of ADHD is based on the clinical evaluation of the patient, and on interviews performed by clinicians with parents and teachers of the children, which, together with the fact that it shares common symptoms and frequent comorbidities with other neurodevelopmental disorders, makes the accurate and timely diagnosis of the disorder a difficult task. Despite the large effort to identify reliable biomarkers that can be used in a clinical environment to support clinical diagnosis, this goal has never been achieved hitherto. In the present study, infrared spectroscopy was used together with multivariate statistical methods (hierarchical clustering and partial least-squares discriminant analysis) to develop a model based on the spectra of blood serum samples that is able to distinguish ADHD patients from healthy individuals. The developed model used an approach where the whole infrared spectrum (in the 3700–900 cm⁻¹ range) was taken as a holistic imprint of the biochemical blood serum environment (spectroscopic biomarker), overcoming the need for the search of any particular chemical substance associated with the disorder (molecular biomarker). The developed model is based on a sensitive and reliable technique, which is cheap and fast, thus appearing promising to use as a complementary diagnostic tool in the clinical environment.

Citation: Ogruc Ildiz, G.; Karadag, A.; Kaygisiz, E.; Fausto, R. PLS-DA Model for the Evaluation of Attention Deficit and Hyperactivity Disorder in Children and Adolescents through Blood Serum FTIR Spectra. *Molecules* **2021**, *26*, 3400. <https://doi.org/10.3390/molecules26113400>

Academic Editor: Zhiwu Yu

Received: 21 April 2021

Accepted: 1 June 2021

Published: 3 June 2021

Keywords: attention deficit and hyperactivity disorder (ADHD); FTIR spectroscopy; chemometrics; PLS-DA

Publisher's Note: MDPI stays neutral with regard to jurisdictional claims in published maps and institutional affiliations.



Copyright: © 2021 by the authors. Licensee MDPI, Basel, Switzerland. This article is an open access article distributed under the terms and conditions of the Creative Commons Attribution (CC BY) license (<https://creativecommons.org/licenses/by/4.0/>).

1. Introduction

Attention deficit and hyperactivity disorder (ADHD) is one of the most common neurodevelopmental disorders of childhood. In general it starts at an early age and may persist throughout the adult life.

ADHD is characterized by a series of symptoms, such as difficulty in sustaining attention, focusing and completing tasks, impulsive behavior and excessive activity [1–3]. According to the diversity of the symptoms, ADHD is classified into three main types [4–6]: predominantly inattentive, predominantly hyperactive-impulsive and the combined type. In the first presentation, individuals find it difficult to organize or finish a task, to pay attention to details and to follow instructions or dialogues, being easily distracted and frequently forgetting details of daily routines. In the second, the person fidgets and talks a lot, expressing difficulty to sit for a long duration to perform an activity, and has problems with control impulsivity. Younger children may run, jump or climb constantly and usually have more accidents and injuries than others. Although ADHD causes trouble

in relationships and difficulties in school life for children and adolescents, no cure has been developed yet for the disorder, and its treatment usually involves the combination of medications, psychotherapy, counseling and lifestyle changes [7].

ADHD is estimated to affect ~10% of the world's population of children, with rates that are similar between countries. It is diagnosed approximately twice more often in boys than in girls, though it is frequently unnoticed in girls because their symptoms are, in general, less disruptive. Interestingly, it does not appear to be related to the style of parenting or discipline. About 30–50% of those diagnosed in childhood continue to have characteristic ADHD symptoms later, and 2–5% of adults have the condition [8–10].

Many studies pointed to genetic, environmental and social factors as possible causes of ADHD, but its precise underlying etiology remains uncertain and appears to vary from case to case [1–3,11,12]. Current diagnosis of ADHD follows the Diagnostic and Statistical Manual of Mental Disorders (Fifth Edition; DSM-5) diagnosis criteria [4] and is based on the clinical evaluation of the patient, including interviews performed by clinicians with parents and teachers of the children, which makes it relatively subjective. The fact that ADHD shares common symptoms and frequent comorbidities with other neurodevelopmental disorders (e.g., autism spectrum disorder, bipolar disorder) [13,14] also contributes to making an accurate and timely diagnosis of the disorder a difficult task. However, early diagnosis facilitates the proper treatment of the symptoms and may considerably improve the life conditions of the young individuals suffering with ADHD.

A large number of studies using several different approaches (e.g., neuroimaging, metabolic and genetic investigations) have been carried out with relative success, in order to find the underlying causes of ADHD and correlate them with specific biomarkers. Unfortunately, so far, none of those approaches has been able to find reliable biomarkers that can be used in a clinical environment to support a clinical diagnosis [15–25]. Schmidt et al. [26] defined a biomarker as a characteristic that can be objectively measured and evaluated as an indicator of a normal biological process, a pathogenic process or a response to a therapeutic intervention. Most biomarker studies compare case patients and control subjects to determine the sensitivity and specificity of the biomarker for detecting the disorder. As stressed by Scassellati and coworkers [15], the mechanistic status of the biomarkers is typically not elucidated by such studies, as the biomarkers can be a measure of vulnerability to the disorder, of processes taking place with the onset of the disorder or leading to chronicity or to epiphenomena of the disorder. Biomarkers can also reflect effects of treatment or physiological responses to the stress of living with a chronic disorder. Nevertheless, the identification of appropriate biomarkers may still provide important clues to the understanding of the causes and mechanisms of the action of the diseases, stimulating studies in this area. In addition, the identification of peripheral biochemical markers, measurable with reliable, fast and non-invasive methods, may help the diagnosis of a given disorder in the clinical environment.

Body fluids are easily accessible, and their use for medical diagnostics is a common practice. The analysis of body fluids using vibrational spectroscopy (either Raman or infrared) has progressively gained the respect of clinicians as a complementary diagnostic tool, with advantages over other techniques, such as being a sensitive and reliable approach, but also cheap, fast and easily adaptable to the clinical environment [27,28]. When used together with modern chemometric methods, Raman and infrared spectroscopies are powerful analytical instruments, which can efficiently probe the biochemical environment of a given biological sample [27–39]. As they are very sensitive to molecular structure and intermolecular interactions, Raman and infrared spectra provide signatures of a biological sample, such as imprints of its molecular constitution and chemical environment. An additional advantage offered by this approach is that one does not need to look for spectroscopic evidence of a specific molecular biomarker, rather the whole spectrum of the sample represents a holistic view of its biochemical environment, i.e., the full spectral data may be used as a biomarker without the need to search for any particular chemical substance. Such a holistic approach does not allow for the extraction of information on the

specific metabolic mechanisms associated with the disease or the precise chemical species involved. However, it is more reliable for the general characterization of the samples and for their differentiation from the controls since no information is ignored and the whole biochemical environments are subjected to scrutiny.

Recently, this approach has been successfully applied to the development of analytical models for evaluation of neurodevelopmental diseases, using principal component analysis (PCA) or partial least-squares discriminant analysis (PLS-DA) applied to Raman infrared spectroscopic data obtained from blood samples [27,29,30]. Autism spectrum disorder, bipolar disorder (including identification of its different characteristic phases) and schizophrenia are recent cases of the successful application of this strategy to neurodevelopmental disorders [27,29,30].

In the present study, infrared spectroscopy was used together with hierarchical clustering analysis and PLS-DA to develop a model based on the spectra of blood serum samples that can distinguish ADHD patients from healthy individuals. The obtained results indicate that the used approach may receive application as a complementary diagnostic tool in the clinical environment.

2. Materials and Methods

2.1. Clinical Stage

Thirty children and adolescent outpatients with diagnosed ADHD according to DSM-5 [4] criteria were included in this study. The patients were chosen from individuals admitted to the Child and Adolescent Psychiatry Clinic of Pamukkale University (Denizli, Turkey) during a time period of 3 months, their ages being 6–14 years (23 boys and 7 girls). Individuals with other psychiatric disorders and those having a chronic medical comorbid condition were excluded. Subjects were chosen from the patients that were not under medication. The blood samples of the controls were obtained during the same period of time as the ADHD patients, with the subjects being chosen to match the patients' cohort regarding sex and age. The control group consisted of 29 healthy children and adolescents, 22 boys and 7 girls, with ages between 6 and 14 years, who did not have any psychiatric history and were not on medication. All parents approved their children's participation in this study by giving written consent. The study was approved by the Ethics Committee of the Pamukkale University, Faculty of Medicine (date: 12 May 2015).

Five milliliters of blood were collected from each participant and placed in Vacutainer plastic SST (Serum Separator Tube) gel tubes in order to separate their serum from cellular material. The gel in the tubes creates a physical barrier between the serum and blood cells after centrifugation and accelerates the serum coagulation by means of silica particles on the tube wall. Without shaking, the tubes were gently inverted 4–5 times so that the blood made good contact with the silica particles. After 30 min, the blood coagulated spontaneously. Following clotting, the samples were centrifuged at 10,000 rpm for 15 min to separate the serum from the cellular material. The obtained serum samples were placed in Eppendorf tubes and frozen at $-20\text{ }^{\circ}\text{C}$. This protocol was applied for all samples.

2.2. Spectroscopic Stage

One microliter of an unfrozen blood sample was placed on the attenuated total reflectance (ATR) unit and allowed to air-dry at room temperature (~ 10 min). ATR Fourier transform infrared (FTIR) spectra, within the $400\text{--}4000\text{ cm}^{-1}$ spectral range, were recorded with 4 cm^{-1} spectral resolution on a Perkin Elmer Spectrum One spectrometer, equipped with a KBr beam splitter and a deuterated triglycine sulfate (DTGS) detector, combined with a diamond Gladi ATR accessory (Pike Technologies). The samples for both ADHD and controls were ordered randomly for spectra recording. For each blood serum sample, 5 spectra (replicates) were obtained, each one being the average of 64 scans. Background was collected immediately prior to each sample measurement.

For the statistical analysis, the $3700\text{--}900\text{ cm}^{-1}$ spectral range was chosen. The spectra were processed by baseline correction using a linear function and area normalization.

For outliers' deletion, all spectra of each group (Control group (C) and ADHD group (A)) were subjected to principal component analysis (PCA) [40–43], using the Nonlinear Iterative Partial Least-Squares (NIPALS) algorithm [44], which allowed facile detection of the outliers by simple inspection of the score plots. After the exclusion of outliers (1 sample of the Control group), the average spectra of each sample and of each group were obtained. All data pre-processing was undertaken with the Unscrambler™ CAMO software (Version 10.5) [45].

2.3. Statistical Stage

As an *a priori* test, the overall similarity of the samples within each group and the dissimilarity between the two groups were investigated by applying unsupervised hierarchical clustering analysis to all samples (30 ADHD, 28 Control) using the Ward's algorithm with squared Euclidean distances [46,47].

For the development of the classification model, 20 samples belonging to the ADHD group and 18 samples belonging to the Control group were randomly chosen as the calibration set. To test the classification model (prediction), the remaining 10 samples from each group were used as the test set.

The classification model was established by using the PLS-DA method [48–51], with internal full cross-validation being applied during calibration [52]. The PLS-DA method consists in a classical PLS regression [50], but in this case the response variable Y is a categorical one, expressing the class membership of the samples. PLS-DA then encompasses two main procedures: PLS component construction (i.e., dimension reduction) and prediction model construction (discriminant analysis). A few underlying or latent factors related to the response (Y) and the observable (X) variables accounting for most of their variances can be found through this method. In practical terms, the latent factors played a similar role as the principal components in PCA, but a better discrimination between the different classes can, in general, be achieved because in PLS, the directions that are associated with high variation in the data are sought in the factor space, while the search is biased toward directions leading to accurate class prediction for the samples in the training set.

Interestingly, while formally in PLS-DA the response matrix is a column vector (strictly speaking, in PLS1-DA [51]) and is categorical (for a two classes experiment, Y values can be simply 0 and 1), it is internally recoded via an indicator variable, which allows the PLS regression to run as if Y is a continuous variable. This PLS classification trick works well in practice, as demonstrated by the success of the method.

The linear regression is expressed by Equation (1), where B is the regression coefficients vector to be determined, and F is the residuals vector, which is to be minimized (in fact, the sum of the squares of the residuals, $\sum_{i=1}^N f^2 = F^T F$, is the effective quantity to minimize):

$$Y = \bar{X}B + F \quad (1)$$

$$B = \left(\begin{array}{c} \bar{X}^T \bar{X} \\ \bar{X} \end{array} \right)^{-1} \bar{X}^T Y \quad (2)$$

The coefficients B can be obtained from Equation (2) if the matrix \bar{X} is full ranked, i.e., if its columns are linearly independent. However, this least-squares solution is ill-conditioned if the data matrix does not have full rank, which happens most often when the number of variables p exceeds the number of samples N . The solution is to project each measurement into a lower-dimensional subspace spanned by the data, which corresponds to define a reduced number of k latent variables (factors), each being a linear combination of the original set of variables. In practice, this is achieved by decomposing \bar{X} and Y as in

Equations (3) and (4), and then solving Equation (5), where \bar{W} is a weight matrix, which during the regression is iteratively determined, being initialized as $\bar{X}^T \bar{Y}$.

$$\bar{X} = \bar{U}\bar{V}^T + \bar{E} \quad (3)$$

$$\bar{Y} = \bar{P}\bar{Q} + \bar{F} \quad (4)$$

$$\bar{B} = \bar{W} \left(\bar{V}^T \bar{W} \right)^{-1} \bar{Q}^T \quad (5)$$

In Equations (3–5), \bar{U} and \bar{P} are the X and Y score matrices and \bar{V} and \bar{Q} the corresponding X and Y loadings. \bar{E} and \bar{F} are the residuals in X and Y , respectively.

Once the coefficients of the regression are obtained, they can be used for subsequent classification (prediction) purposes. First, the unknown samples are reduced into the new low-dimensional space (the one defined by the k PLS latent factors) using \bar{B} , to produce the predicted values (y_{pred}). Given a set of training data that contains G classes, the PLS-DA model produces G predicted values ($y_{\text{pred}}^{(1)}, y_{\text{pred}}^{(2)} \dots y_{\text{pred}}^{(G)}$) for each sample to classify. Ideally, the perfect class membership should be '1' or '0' to indicate that the sample belongs to that class or not. However, as noted above, in practice the resulting predicted values are between 0 and 1, instead of an integer. For that reason, a decision rule (DR) has to be applied in order to translate the predicted value into a meaningful class membership. Many different decision rules can be used, and an interesting discussion on this subject can be found in Reference [51]. A commonly used DR classifies a sample as belonging to class A if the predicted value for that class $y_{\text{pred}}^{(A)}$ differs from the Y (integer) value of that class by less than $\pm Y/2$. For example, using this DR, for a two-classes model with $Y = 1, 0$ (belong, not-belong) values for both classes, classification of the sample in a given class requires that the predicted y_{pred} value for that class stays in the range 1 ± 0.5 .

All chemometric analyses were accomplished using the Unscrambler™ CAMO software (Version 10.5) [45]. The prediction performance of the model was evaluated by calculating its sensitivity, specificity, precision, accuracy and efficiency statistical parameters [53,54].

3. Results and Discussion

3.1. Preliminary Data Analysis

The pre-processed data (as described above) were initially inspected using the heat map, average spectra difference profile and hierarchical cluster analysis.

The heat map is a graphical method for visualizing attribute values by class in a two-way matrix [55]. The values (IR intensities) are represented by colors, the X and Y axes relating to variables and samples, respectively. The latter were grouped according to their class (A or C) membership. The heat map (Figure 1) revealed distinct patterns for the spectra of ADHD patients compared to those of the control healthy individuals, in both the high- and low-frequency regions. By comparing the heat map with the average IR spectrum the blood serum of the ADHD Group and the difference spectrum obtained by subtracting the average spectrum of the Control Group to the average spectrum of the ADHD Group, which are shown in Figure 2, it can be concluded that the data seems to indicate that the blood serum of the ADHD patients has an increase of protein total contents (as shown by the higher relative intensity of the protein characteristic amide A, I and II bands in the ranges 3640–3100, 1700–1590 and 1590–1480 cm^{-1} , respectively) [38,39,56–58] and a slight decrease of tyrosine (as shown by the lower intensity in the region of the tyrosine characteristic bands at ~1350 and 1250 cm^{-1} bands) [59] compared to the control group. These results shall be considered only as indicative; however, a deficiency in the trace amine phenylethylamine, from which tyrosine is a precursor, was reported for ADHD

patients [15,60,61]. This result, as well as the increased level of the total protein contents in the blood serum of children with ADHD, is also in consonance with similar observations for children affected by other neurodevelopmental disorders, such as autism [27,29,62–64].

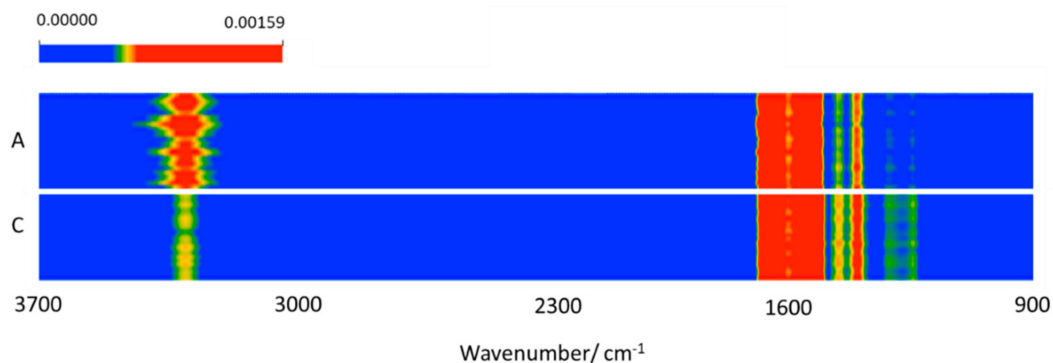


Figure 1. Heat map for the samples belonging to the two groups (A, ADHD; C, control).

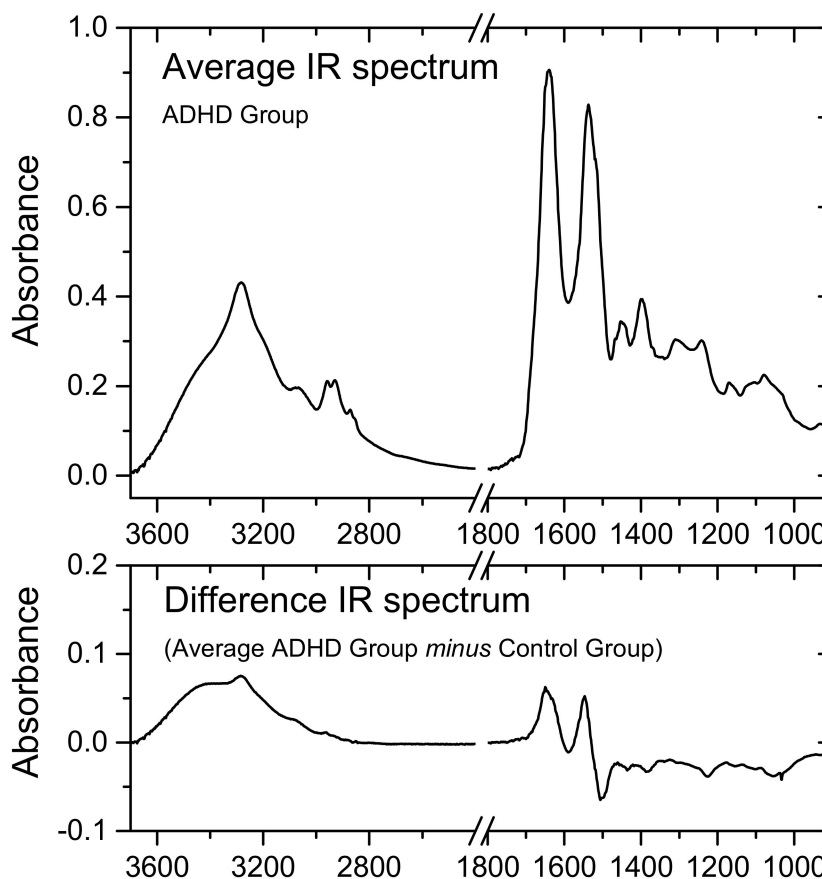


Figure 2. Average IR spectrum of ADHD group blood serum samples (3700–2400 and 1800–900 cm^{-1} regions; top panel), and difference spectrum obtained by subtracting the average spectrum of the Control group to the average spectrum of the ADHD group (bottom). The average IR spectrum of the Control group is provided in Figure S1 (Supplementary Materials).

The dendrogram obtained from the hierarchical clustering analysis conducted on all samples (Figure 3) showed a clear discrimination of the samples belonging to the ADHD group from the Control group. It is worth mentioning that the samples belonging to the Control group appeared as more homogenous in comparison to those belonging to the

ADHD group. This could be expected, taking into account the illness variability, which may result in a range of slightly different blood serum biochemistry.

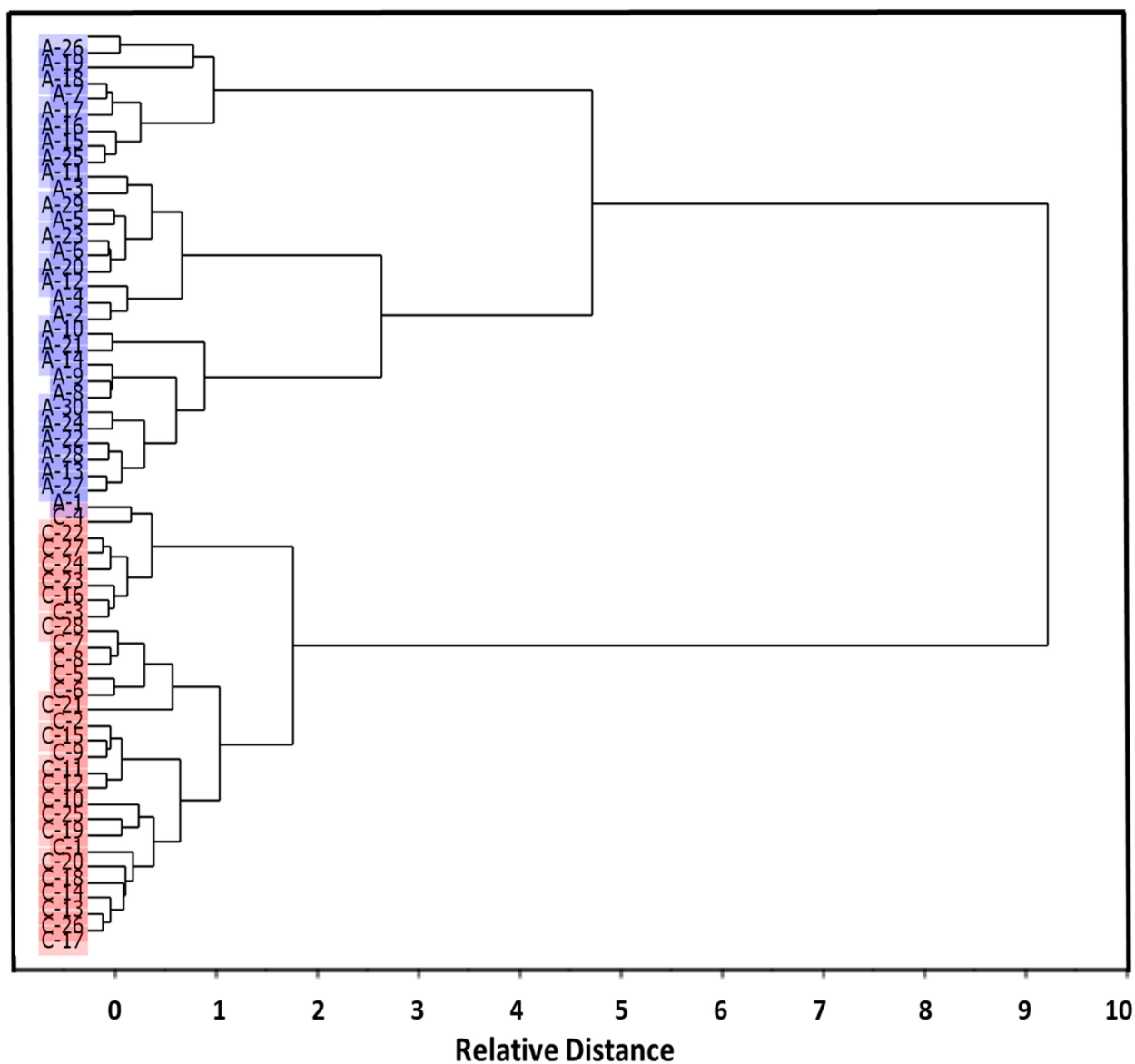


Figure 3. Hierarchical cluster analysis of ADHD (A; highlighted in blue) and control (C; highlighted in red) groups' blood serum IR spectra, according to the Ward's method, using squared Euclidean distances.

3.2. Development of Classification Model

A classification model was built using the PLS-DA method, as explained in Section 2.3. The model was developed using five latent variables (Factors), but it was seen that the first three Factors accounted for over 98% of the variance in both X and Y variables. The root-mean-square errors (RMSEs) for training and validation were calculated as 0.08 and 0.10, respectively, indicating the excellent quality of the regression.

Figure 4 shows the 2D (Factor-2 vs. Factor-1) scores plot for the developed model (including the 95% confidence ellipses), where a clear discrimination between the ADHD and Control groups can be observed along Factor-1. Factor-1 explained 89 and 74% of the total variance in the X and Y variables, respectively, in the training set (Factor-2 and Factor-3 explained 7 and 2% variance in X , and 20 and 4% variance in Y , respectively), the numbers being identical for validation. As it could be anticipated, the loadings for

the discriminative Factor-1 (see Figure S2, in the Supplementary Materials) were found to essentially reproduce the difference IR spectrum obtained by subtracting the average spectrum of the Control Group from the average spectrum of the ADHD Group shown in Figure 2.

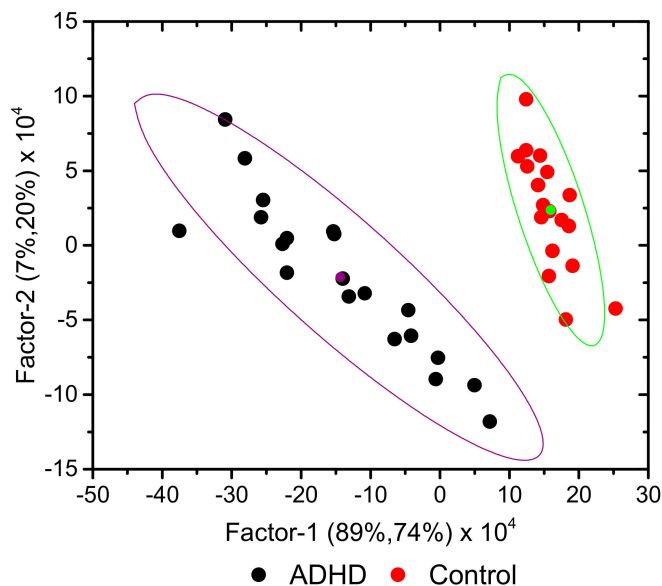


Figure 4. A 2D scores plot (Factor-1 vs. Factor-2) for the developed PLS-DA model, showing the 95% confidence ellipses. The points with the same color of the ellipses correspond to their centers and are the average point of the associated distribution.

Similarly to what was seen in the cluster analysis dendrogram (Figure 3), and by the same reasons, the samples belonging to ADHD Group appeared more dispersed in the PLS-DA scores plots than those belonging to the Control Group.

3.3. Predictions

The prediction accuracy of the developed PLS-DA model was tested using 10 samples from each group (ADHD and Control groups) that were kept out of the calibration set. All spectra belonging to the test set were pre-processed using the same methodology used for calibration set samples.

The results of the model predictions are summarized in Figures 5 and 6. The criterion used to classify the samples as belonging to a given group was that the corresponding predicted Y value falls within ± 0.5 relative to the corresponding Y reference values (0 for control samples, and 1 for ADHD samples). All predicted Y values for the tested samples were found to stay within the range of values established by the used classification criterion for assignment of the samples to their proper class (both for Control and ADHD tested samples; see Figure 5). In other words, the model was able to correctly classify all samples, corresponding to the superlative case where maximal values for the model performance statistical indicators (sensitivity, specificity, precision, accuracy and efficiency performance parameters [53,54]) were obtained.

The projections of the test samples on the 2D Factor-2 vs. Factor-1 scores plot of the model are shown in Figure 6, which provides a simple visual illustration of the classification ability of the model. As it is shown in the figure, with a single exception, all projected predicted points remained within the 95% confidence ellipses of the corresponding class for the calibrating set.

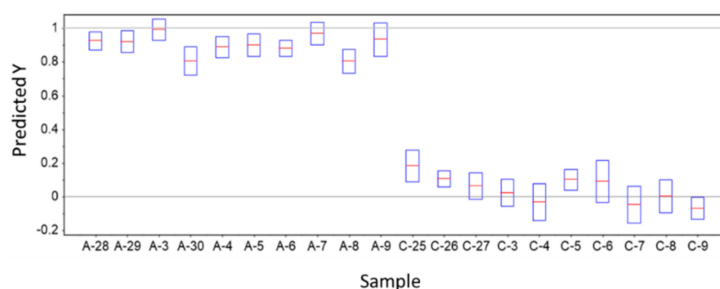


Figure 5. PLS-DA model predicted Y values for ADHD (A) and Control (C) test samples. The predicted values are indicated by the horizontal red lines and the deviations by the blue boxes. In the model, samples belonging to the Control Group define a class with reference Y value equal to 0, and those belonging to ADHD patients define a class with reference Y value equal to 1.

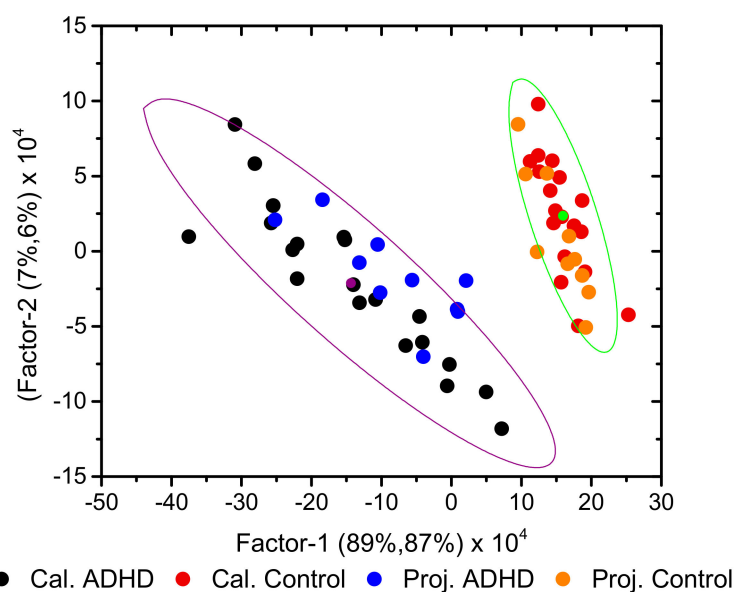


Figure 6. 2D scores plot (Factor-2 vs. Factor-1) of the developed PLS-DA model, showing the calibration (Cal.) and projected test set (Proj.) samples. The 95% confidence ellipses for the calibration set are shown. The points with the same color of the ellipses correspond to their centers and are the average point of the associated distribution.

4. Conclusions

In this study, infrared spectroscopy and multivariate statistical methods (hierarchical clustering and partial least-squares discriminant analysis (PLS-DA)) were used to develop a prediction model based on the spectra of blood serum samples. The model was able to distinguish ADHD patients from healthy individuals with an accuracy of 100% (for the tested samples). The approach used to develop the model considered the whole infrared spectrum (in the $3700\text{--}900\text{ cm}^{-1}$ range) as a holistic imprint of the biochemical blood serum environment (spectroscopic biomarker), overcoming the need for the search of any particular chemical substance associated with the disorder (molecular biomarker). The model relied on a sensitive and reliable spectroscopic technique that is also cheap and fast, which facilitates its practical applications. Overall, the obtained results indicated that the applied approach is promising when used as a complementary diagnostic tool for ADHD in the clinical environment.

Supplementary Materials: The following are available online, Figure S1: Average IR spectrum of Control Group blood serum samples ($3700\text{--}2400$ and $1800\text{--}900\text{ cm}^{-1}$ regions). The average spectrum of the ADHD Group is also depicted (thin line) for comparison, Figure S2: Loadings of Factor-1 and Factor-2 of the developed PLS-DA classification model. The loadings are plotted multiplied by

the factor-10 for a better comparison between the loadings of Factor-1 and the difference spectrum between the average IR spectra of the ADHD and the Control groups shown in Figure 2 of the article.

Author Contributions: Conceptualization: G.O.I.; Spectroscopic and chemometric analyses, manuscript writing and fund raising: G.O.I. and R.F.; FTIR spectroscopy measurements: A.K. and E.K. All authors have read and agreed to the published version of the manuscript.

Funding: This research was funded by the Scientific and Technological Research Council of Turkey-TUBITAK 1001 Project, grant number 116Z294. R.F. thanks the Portuguese Science Foundation (Fundação para a Ciência e a Tecnologia; FCT—Lisbon) for financial support to the Coimbra Chemistry Centre (CQC) through the projects UIDB/EQU/00102/2020 and UIDP/EQU/00102/2020 (national funds), also funded by COMPETE-EU.

Institutional Review Board Statement: The study was conducted according to the guidelines of the Declaration of Helsinki, and approved by the Ethics Committee of the Pamukkale University, Faculty of Medicine (date: 12 May 2015).

Informed Consent Statement: Informed consent was obtained from all subjects involved in the study.

Data Availability Statement: Not Applicable.

Acknowledgments: The authors thank Ahmet Buber (Pamukkale University, Faculty of Medicine, Child and Adolescent Psychiatry Department, Denizli, Turkey) and Omer Faruk Tuncer (Bursa Dörtcelik Pediatric Hospital, Bursa, Turkey) for their contribution in the clinical stage of the study.

Conflicts of Interest: The authors declare no conflict of interest.

References

1. Sroubek, A.; Kelly, M.; Li, X. Inattentiveness in Attention-Deficit/Hyperactivity Disorder. *Neurosci. Bull.* **2013**, *29*, 103–110. [CrossRef] [PubMed]
2. Faraone, S.V.; Rostain, A.L.; Blader, J.; Busch, B.; Childress, A.C.; Connor, D.F.; Newcorn, J.H. Practitioner Review: Emotional Dysregulation in Attention-Deficit/Hyperactivity Disorder—Implications for Clinical Recognition and Intervention. *J. Child Psychol. Psychiatry Allied Discip.* **2019**, *60*, 133–150. [CrossRef] [PubMed]
3. Tenenbaum, R.B.; Musser, E.D.; Morris, S.; Ward, A.R.; Raiker, J.S.; Coles, E.K.; Pelham, W.E. Response Inhibition, Response Execution, and Emotion Regulation among Children with Attention-Deficit/Hyperactivity Disorder. *J. Abnorm. Child Psychol.* **2019**, *47*, 589–603. [CrossRef]
4. American Psychiatric Association. *Diagnostic and Statistical Manual of Mental Disorders*, 5th ed.; American Psychiatric Association: Arlington, VA, USA, 2013.
5. Ramsay, J.R. *Cognitive Behavioral Therapy for Adult ADHD*; Routledge: Abingdon-on-Thames, UK, 2007; pp. 25–26.
6. Steinau, S. Diagnostic Criteria in Attention Deficit Hyperactivity Disorder—Changes in DSM 5. *Front. Psychiatry* **2013**, *4*, 49. [CrossRef] [PubMed]
7. National Institute for Health and Care Excellence. *Attention Deficit Hyperactivity Disorder: Diagnosis and Management*; National Guideline Centre: London, UK, 2019.
8. Kooij, S.J.; Bejerot, S.; Blackwell, A.; Caci, H.; Casas-Brugué, M.; Carpentier, P.J.; Edvinsson, D.; Fayyad, J.; Foeken, K.; Fitzgerald, M.; et al. European Consensus Statement on Diagnosis and Treatment of Adult ADHD: The European Network Adult ADHD. *BMC Psychiatry* **2010**, *10*, 67. [CrossRef] [PubMed]
9. Bálint, S.; Czobor, P.; Mészáros, A.; Simon, V.; Bitter, I. Neuropsychological Impairments in Adult Attention Deficit Hyperactivity Disorder: A Literature Review. *Psychiatr. Hung.* **2008**, *23*, 324–335. [PubMed]
10. Ginsberg, Y.; Quintero, J.; Anand, E.; Casillas, M.; Upadhyaya, H.P. Underdiagnosis of Attention-Deficit/Hyperactivity Disorder in Adult Patients: A Review of the Literature. *Prim. Care Companion CNS Disord.* **2014**, *16*. [CrossRef] [PubMed]
11. Millichap, J.G. Chapter 2: Causative Factors. In *Attention Deficit Hyperactivity Disorder Handbook: A Physician's Guide to ADHD*, 2nd ed.; Springer Science: New York, NY, USA, 2010.
12. Thapar, A.; Cooper, M.; Eyre, O.; Langley, K. What have we learnt about the causes of ADHD? *J. Child Psychol. Psychiatry Allied Discip.* **2013**, *54*, 3–16. [CrossRef] [PubMed]
13. Walitza, S.; Drechsler, R.; Ball, J. The School Child with ADHD. *Ther. Umsch.* **2012**, *69*, 467–473. [CrossRef]
14. Wilens, T.E.; Spencer, T.J. Understanding Attention-Deficit/Hyperactivity Disorder from Childhood to Adulthood. *Postgrad. Med.* **2010**, *122*, 97–109. [CrossRef] [PubMed]
15. Scassellati, C.; Bonvicini, C.; Faraone, S.V.; Gennarelli, M. Biomarkers and Attention-Deficit/Hyperactivity Disorder: A Systematic Review and Meta-Analyses. *J. Am. Acad. Child Adolesc. Psychiatry* **2012**, *51*, 1003–1019. [CrossRef]
16. Cheuk, D.K.L.; Wong, V. Attention-Deficit Hyperactivity Disorder and Blood Mercury Level: A Case-Control Study in Chinese Children. *Neuropediatrics* **2006**, *37*, 234–240. [CrossRef] [PubMed]

17. Jiamei, L.; Yunbo, M.; Min, L. Blood and Hair Zinc Levels in Children with Attention Deficit Hyperactivity Disorder: A Meta-Analysis. *Asian J. Psychiatry* **2020**, *47*, 101805.
18. Yang, R.; Zhan, Y.; Gao, W.; Lin, N.; Li, R.; Zhao, Z. Blood Levels of Trace Elements in Children with Attention-Deficit Hyperactivity Disorder: Results from a Case-Control Study. *Biol. Trace Elem. Res.* **2006**, *187*, 376–382. [CrossRef] [PubMed]
19. Wang, H.; Chen, X.; Yang, B.; Ma, F.; Wang, S.; Tang, M.; Hao, M. Case-Control Study of Blood Lead Levels and Attention Deficit Hyperactivity Disorder in Chinese Children. *Environ. Health Perspect.* **2008**, *116*, 1401–1406. [CrossRef] [PubMed]
20. Viktorinova, A.; Ursinyova, M.; Trebaticka, J.; Uhnakova, I.; Durackova, Z.; Masanova, V. Changed Plasma Levels of Zinc and Copper to Zinc Ratio and Their Possible Associations with Parent and Teacher Rated Symptoms in Children with Attention Deficit Hyperactivity Disorder. *Biol. Trace Elem. Res.* **2016**, *169*, 1–7. [CrossRef] [PubMed]
21. Chen, J.R.; Hsu, S.F.; Hsu, C.D.; Hwang, L.H.; Yang, S.C. Dietary Patterns and Blood Fatty Acid Composition in Children with Attention-Deficit Hyperactivity Disorder in Taiwan. *J. Nutr. Biochem.* **2004**, *15*, 467–472. [CrossRef]
22. Wang, M.; Hu, Z.; Liu, L.; Li, H.; Qian, Q.; Niu, H. Disrupted Functional Brain Connectivity Networks in Children with Attention-Deficit/Hyperactivity Disorder: Evidence from Resting-State Functional Near-Infrared Spectroscopy. *Neurophotonics* **2020**, *7*, 015012. [CrossRef] [PubMed]
23. Güven, A.; Altinkaynak, M.; Dolu, N. Combining Functional Near-Infrared Spectroscopy and EEG Measurements for the Diagnosis of Attention-Deficit Hyperactivity Disorder. *Neural Comput. Appl.* **2020**, *32*, 8367–8380. [CrossRef]
24. Chen, H.; Chen, W.; Song, Y.; Sun, L.; Li, X. EEG Characteristics of Children with Attention-Deficit/Hyperactivity Disorder. *Neuroscience* **2019**, *406*, 444–456. [CrossRef] [PubMed]
25. Nigg, J.T.; Knottnerus, G.M.; Martel, M.M.; Nikolas, M.; Cavanagh, K.; Karmaus, W.; Rappley, M.D. Low Blood Lead Levels Associated with Clinically Diagnosed Attention-Deficit/Hyperactivity Disorder and Mediated by Weak Cognitive Control. *Biol. Psychiatry* **2008**, *63*, 325–331. [CrossRef] [PubMed]
26. Schmidt, H.D.; Shelton, R.C.; Duman, R.S. Functional Biomarkers of Depression: Diagnosis, Treatment, and Pathophysiology. *Neuropsychopharmacology* **2011**, *36*, 2375–2394. [CrossRef] [PubMed]
27. Ogruc Ildiz, G.; Bayari, S.; Yorguner, N.; Fausto, R. Blood Serum Infrared Spectra Based Chemometric Models for Auxiliary Diagnosis of Autism Spectrum Disorder. In *Autism Spectrum Disorder: Diagnosis and Treatment*; El-Bazm, A.S., Mahmoud, A., Eds.; Elsevier: Amsterdam, The Netherlands, 2020; in the press.
28. Shaw, R.A.; Mantsch, H.H. Infrared Spectroscopy of Biological Fluids in Clinical and Diagnostic Analysis. In *Encyclopedia of Analytical Chemistry*; John Wiley & Sons, Ltd.: Hoboken, NJ, USA, 2006; Volume 2, pp. 1–24.
29. Ogruc Ildiz, G.; Bayari, S.; Karadag, A.; Kaygisiz, E.; Fausto, R. Fourier Transform Infrared Spectroscopy Based Complementary Diagnosis Tool for Autism Spectrum Disorder in Children and Adolescents. *Molecules* **2020**, *25*, 2079. [CrossRef] [PubMed]
30. Ogruc Ildiz, G.; Bayari, S.; Aksoy, U.M.; Yorguner, N.; Bulut, H.; Yilmaz, S.S.; Halimoglu, G.; Nur Kabuk, H.; Yavuz, G.; Fausto, R. Auxiliary Differential Diagnosis of Schizophrenia and Phases of Bipolar Disorder Based on the Blood Serum Raman Spectra. *J. Raman Spectrosc.* **2020**, *51*, 2233–2244. [CrossRef]
31. Ahmed, S.S.S.J.; Santosh, W.; Kumar, S.; Christlet, T.H.T. Neural Network Algorithm for the Early Detection of Parkinson's Disease from Blood Plasma by FTIR Micro-Spectroscopy. *Vib. Spectrosc.* **2010**, *53*, 181–188. [CrossRef]
32. Deleris, G.; Petibois, C. Applications of FT-IR Spectrometry to Plasma Contents Analysis and Monitoring. *Vib. Spectrosc.* **2003**, *32*, 129–136. [CrossRef]
33. Khanmohammadi, M.; Ghasemi, K.; Garmarudi, A.B.; Ramin, M. Diagnostic Prediction of Renal Failure from Blood Serum Analysis by FTIR Spectrometry and Chemometrics. *Spectrochim. Acta Part A Mol. Biomol. Spectrosc.* **2015**, *136*, 1782–1785. [CrossRef] [PubMed]
34. Mostaco-Guidolin, L.B.; Bachmann, L. Application of FTIR Spectroscopy for Identification of Blood and Leukemia Biomarkers: A Review over the Past 15 Years. *Appl. Spectrosc. Rev.* **2011**, *46*, 388–404. [CrossRef]
35. Erukhimovitch, V.; Talyshinsky, M.; Souprun, Y.; Huleihel, M. FTIR Spectroscopy Examination of Leukemia Patients Plasma. *Vibrat. Spectrosc.* **2006**, *40*, 40–46. [CrossRef]
36. Lewis, P.D.; Lewis, K.E.; Ghosal, R.; Bayliss, S.; Lloyd, A.J.; Wills, J.; Godfrey, R.; Kloer, P.; Mur, L.A.J. Evaluation of FTIR Spectroscopy as a Diagnostic Tool for Lung Cancer Using Sputum. *BMC Cancer* **2010**, *10*, 640. [CrossRef] [PubMed]
37. Mordechai, S.; Shufan, E.; Katz Porat, B.S.; Salman, A. Early Diagnosis of Alzheimer's Disease Using Infrared Spectroscopy of Isolated Blood Samples Followed by Multivariate Analyses. *Analyst* **2017**, *142*, 1276–1284. [CrossRef]
38. Krimm, S.; Bandekar, J. Vibrational Spectroscopy and Conformation of Peptides, Polypeptides and Proteins. *Adv. Protein Chem.* **1986**, *38*, 181–364. [PubMed]
39. Liu, K.Z.; Shi, M.H.; Mantsch, H.H. Molecular and Chemical Characterization of Blood Cells by Infrared Spectroscopy: A New Optical Tool in Hematology. *Blood Cells Mol. Dis.* **2005**, *35*, 404–412. [CrossRef] [PubMed]
40. Pearson, K. On Lines and Planes of Closest Fit to Systems of Points in Space. *Philos. Mag.* **1901**, *2*, 559–572. [CrossRef]
41. Hotelling, H. Analysis of a Complex of Statistical Variables into Principal Components. *J. Educ. Psychol.* **1933**, *24*, 417–441. [CrossRef]
42. Hotelling, H. Analysis of a Complex of Statistical Variables into Principal Components. *J. Educ. Psychol.* **1933**, *24*, 498–520. [CrossRef]
43. Hotelling, H. Relations Between Two Sets of Variates. *Biometrika* **1936**, *28*, 321–377. [CrossRef]

44. Wold, H. *Quantitative Sociology: International Perspectives on Mathematical and Statistical Model Building*; Academic Press: New York, NY, USA, 1975; pp. 307–357.
45. CAMO Software Inc. *The Unscrambler™ Version 10.5*; CAMO A/S: Trondheim, Norway, 2018.
46. Ward, J.H.J. Hierarchical Grouping to Optimize an Objective Function. *J. Am. Stat. Assoc.* **1963**, *58*, 236–244. [CrossRef]
47. Murtagh, F.; Legendre, P. Ward’s Hierarchical Agglomerative Clustering Method: Which Algorithms Implement Ward’s Criterion? *J. Classif.* **2014**, *31*, 274–295. [CrossRef]
48. Wold, S.; Sjöström, M.; Eriksson, L. PLS-Regression: A Basic Tool of Chemometrics. *Chemom. Intell. Lab. Sys.* **2001**, *58*, 109–130. [CrossRef]
49. Wold, H. Estimation of Principal Components and Related Models by Iterative Least Squares. In *Multivariate Analysis*; Krishnaiah, P.R., Ed.; Academic Press: New York, NY, USA, 1966; pp. 391–420.
50. Bair, E.; Hastie, T.; Paul, D.; Tibshirani, R. Prediction by Supervised Principal Components. *J. Am. Stat. Assoc.* **2006**, *101*, 119–137. [CrossRef]
51. Lee, L.C.; Liong, C.-Y.; Jemain, A.A. Partial Least Squares-Discriminant Analysis (PLS-DA) for Classification of High-Dimensional (HD) Data: A Review of Contemporary Practice Strategies and Knowledge Gaps. *Analyst* **2018**, *143*, 3526–3539. [CrossRef] [PubMed]
52. Barker, M.; Rayens, W. Partial Least Squares for Discrimination. *J. Chemom.* **2003**, *17*, 166–173. [CrossRef]
53. Wiest, M.M.; German, J.B.; Harvey, D.J.; Watkins, S.M.; Hertz-Picciotto, I. Plasma Fatty Acid Profiles in Autism: A Case-Control Study. *Prostaglandins Leukot. Essent. Fat. Acids* **2009**, *80*, 221–227. [CrossRef]
54. Levy, S.E.; Souders, M.C.; Ittenbach, R.F.; Giarelli, E.; Mulberg, A.E.; Pinto-Martin, J.A. Relationship of Dietary Intake to Gastrointestinal Symptoms in Children with Autistic Spectrum Disorders. *Biol. Psychiatry* **2007**, *61*, 492–497. [CrossRef]
55. Wilkinson, L.; Friendly, M. The History of the Cluster Heat Map. *Am. Stat.* **2009**, *63*, 179–184. [CrossRef]
56. Krilov, D.; Balarin, M.; Kosovic, M.; Gamulin, O.; Brnjac-Kralkevic, J. FT-IR Spectroscopy of Lipoproteins—A Comparative Study. *Spectrochim. Acta Part A Mol. Biomol. Spectrosc.* **2009**, *73*, 701–706. [CrossRef] [PubMed]
57. Paraskevaidi, M.; Morais, C.L.M.; Lima, K.M.G.; Snowden, J.S.; Saxon, J.A.; Richardson, A.M.T.; Jones, M.; Mann, D.M.A.; Allsop, D.; Martin-Hirsch, P.L.; et al. Differential Diagnosis of Alzheimer’s Disease Using Spectrochemical Analysis of Blood. *Proc. Natl. Acad. Sci. USA* **2017**, E7929–E7938. [CrossRef]
58. Sheng, D.; Liu, X.; Li, W.; Yang, Y.; Chen, X.; Wang, X. Distinction of Leukemia Patients’ and Healthy Persons’ Serum Using FTIR Spectroscopy. *Spectrochim. Acta Part A Mol. Biomol. Spectrosc.* **2013**, *101*, 228–232. [CrossRef] [PubMed]
59. Infrared Spectrum of Tyrosine, Coblentz Society Collection, Copyright 2018 by the U.S. Secretary of Commerce on Behalf of the United States of America, Ref 3614. Available online: <https://webbook.nist.gov/cgi/cbook.cgi?ID=C60184&Mask=80#IR-Spec> (accessed on 5 April 2021).
60. Berry, M.D. The Potential of Trace Amines and Their Receptors for Treating Neurological and Psychiatric Diseases. *Rev. Recent Clin. Trials* **2007**, *2*, 3–19. [CrossRef] [PubMed]
61. Zametkin, A.J.; Karoum, F.; Rapoport, J.L.; Brown, G.L.; Wyatt, R.J. Phenylethylamine Excretion in Attention Deficit Disorder. *J. Am. Acad. Child Psychiatry* **1984**, *23*, 310–314. [CrossRef]
62. El Baz, F.M.; Zaki, M.M.; Youssef, A.M.; El Dorry, G.F.; Elalfy, D.Y. Study of Plasma Amino Acid Levels in Children with Autism: An Egyptian Sample. *Egypt. J. Med. Hum. Genet.* **2014**, *15*, 181–186. [CrossRef]
63. Tu, W.J.; Chen, H.; He, J. Application of LC-MS/M Analysis of Plasma Amino Acids Profiles in Children with Autism. *J. Clin. Biochem. Nutr.* **2012**, *5*, 1248–1249. [CrossRef] [PubMed]
64. Tirouvanziam, R.; Obukhanych, T.V.; Laval, J.; Aronov, P.A.; Libove, R.; Banerjee, A.G.; Parker, K.J.; Ohara, R.; Herzenberg, L.A.; Herzenberg, L.A.; et al. Distinct Plasma Profile of Polar Neutral Amino Acids, Leucine, and Glutamate in Children with Autism Spectrum Disorders. *J. Autism Dev. Disord.* **2011**, *42*, 827–836. [CrossRef] [PubMed]

Article

Modeling of the Response of Hydrogen Bond Properties on an External Electric Field: Geometry, NMR Chemical Shift, Spin-Spin Scalar Coupling

Ilya G. Shenderovich ^{1,2,*} and Gleb S. Denisov ²¹ Institute of Organic Chemistry, University of Regensburg, Universitaetstrasse 31, 93053 Regensburg, Germany² Department of Physics, St. Petersburg State University, 198504 St. Petersburg, Russia; gldenisov@yandex.ru

* Correspondence: Ilya.Shenderovich@ur.de

Abstract: The response of the geometric and NMR properties of molecular systems to an external electric field has been studied theoretically in a wide field range. It has been shown that this adduct under field approach can be used to model the geometric and spectral changes experienced by molecular systems in polar media if the system in question has one and only one bond, the polarizability of which significantly exceeds the polarizability of other bonds. If this requirement is met, then it becomes possible to model even extreme cases, for example, proton dissociation in hydrogen halides. This requirement is fulfilled for many complexes with one hydrogen bond. For such complexes, this approach can be used to facilitate a detailed analysis of spectral changes associated with geometric changes in the hydrogen bond. For example, in hydrogen-bonded complexes of isocyanide $C\equiv^{15}N-^1H\cdots X$, $^1J(^{15}N^1H)$ depends exclusively on the N-H distance, while $\delta(^{15}N)$ is also slightly influenced by the nature of X.

Citation: Shenderovich, I.G.; Denisov, G.S. Modeling of the Response of Hydrogen Bond Properties on an External Electric Field: Geometry, NMR Chemical Shift, Spin-Spin Scalar Coupling. *Molecules* **2021**, *26*, 4967. <https://doi.org/10.3390/molecules26164967>

Academic Editors: Rui Fausto, Sylvia Turrell and Gulce Ogruc Ildiz

Received: 13 July 2021

Accepted: 16 August 2021

Published: 18 August 2021

Publisher's Note: MDPI stays neutral with regard to jurisdictional claims in published maps and institutional affiliations.



Copyright: © 2021 by the authors. Licensee MDPI, Basel, Switzerland. This article is an open access article distributed under the terms and conditions of the Creative Commons Attribution (CC BY) license (<https://creativecommons.org/licenses/by/4.0/>).

Keywords: cyanide; hydrogen bonding; non-covalent interactions; NMR; dissociation; scalar coupling; DFT; GIAO

1. Introduction

Correlations between spectroscopic parameters and geometric and energy properties of non-covalent interactions are the main tool for the experimental study of these interactions. The variety of such correlations is great. Some of them are general, while most are only applicable to a limited type of molecular systems.

OH, and NH vibrations can be used to characterize inter- and intramolecular hydrogen bonds [1–3]. The intensity of these stretching vibrations correlates strongly to the energy of the corresponding hydrogen bonds [4,5]. This correlation can be proved using the energy of an intermolecular hydrogen bond measured experimentally as the enthalpy of formation [6–8]. The location of hydrogen atoms in X-ray data can be evaluated using Hirshfeld atom refinement [9–11]. For some systems with hydrogen bonds A-H . . . B, accurate correlations are available between the distances A-H and H . . . B [12,13]. Therefore, if one of these distances is known, the other can be estimated. The N . . . H distance in hydrogen-bonded complexes of pyridine derivatives can be obtained from the ¹⁵N nuclear magnetic resonance (NMR) chemical shift of these pyridines [14,15]. Then this correlation was used to establish a correlation between the N . . . H distance and the ¹H NMR chemical shift of the binding proton for such complexes [16,17]. The dependences of ¹H and ¹³C chemical shifts on hydrogen bonding have been extensively studied. They agree with dependences obtained for other experimental and empirical parameters [18–22]. More about the application of these and other correlations can be found elsewhere [23–26].

Appropriate theoretical calculations make it possible to fully understand the relationship between different parameters of the system under study and to facilitate the search for optimal correlations [27–31]. Such calculations are often the only method for

studying weak non-covalent interactions [32–36] or molecular systems with competing interactions [37–42]. However, often these calculations require a very careful selection of the systems to be examined. Accurate calculations of spectral quantities generally require large basis sets [43]. This requirement can easily conflict with the size of the systems examined [44]. A correlation requires a large set of model systems in which the studied parameter varies over a wide range. It can be very difficult to find a sufficient number of molecular systems that have the appropriate size, required properties and do not introduce other competing interactions into the system. The latter requirement is important. Only in very special cases, the considered spectral parameter depends exclusively on a certain type of interaction and the observed spectral changes are associated only with changes in one of the parameters of this interaction [45–47]. More often, the influence of different interactions on spectral changes can be distinguished only in the course of special studies [48,49].

In some cases, these problems can be solved using the adduct under field approach [50]. The properties of a molecular system can be gradually changed by applying an external electric field [51–55]. Electric fields are present in molecular systems [56,57]. These fields can cause measurable spectral changes [58–62] and even specific chemical reactions [63–65]. However, a small external electric field can be also used as a tool to exert pressure on the electron density of a non-covalent bound molecular system. In this approach, the field simulates the influence of other unknown factors causing changes in the geometry of the non-covalent interaction in question. The ability of the adduct under field approach to reproduce the experimental geometry of such molecular systems in solutions has been demonstrated for various complexes [50,66–68]. Nevertheless, the question remains about the direct influence of the field on spectral parameters and the geometry of covalent bonds. This issue will be analyzed here.

This work discusses three aspects of the direct effect of external electric fields on molecular systems. First, we will consider the isotropic ^{15}N chemical shift, $\delta_{\text{iso}}(^{15}\text{N})$, and the scalar spin-spin coupling, $^1J(^{15}\text{N}^1\text{H})$, in $\text{C}\equiv^{15}\text{N}\text{-H}\cdots\text{F}^-$ and $\text{C}\equiv^{15}\text{N}\text{-H}\cdots\text{FLi}$ hydrogen-bonded complexes as functions of an external electric field directed along the axis of molecular symmetry. If the functional dependence is the same for both complexes, then the corresponding spectral parameter depends exclusively on the N-H distance and can be used to measure this distance in any $\text{C}\equiv^{15}\text{N}\text{-H}\cdots\text{X}$ complex using the experimental value of the parameter. Otherwise, the value of the spectral parameter depends either on the nature of X or on the field strength. In the former case, this parameter is not suitable for measuring the distance. In the latter case, the adduct under field approach is not suitable for analyzing the dependency in question. Then we will calculate the strength of the external field required for the dissociation of the proton from diatomic hydrogen halides, linear $\text{N}\equiv\text{C}\text{-H}$ and $\text{C}\equiv\text{N}\text{-H}$, and nonlinear $\text{X}_3\text{C}\text{-OH}$ alcohols. If this strength correlates to the $\text{p}K_{\text{a}}$ of the acid, at least within a series of similar molecules, then the effect of the field on the covalent structure of molecules can be neglected in qualitative calculations. Otherwise, the extension of the adduct under field approach to large fields should be justified on a case-by-case basis. Finally, we will analyze the effect of the external field on the geometry of a weakly bound $\text{H}_3\text{P}=\text{O}\cdots(\text{HF})_2$ complex, in which the oxygen atom forms two hydrogen bonds simultaneously. Here, we aim to determine the field range at which the structure of this complex changes insignificantly with the exception of the O...H distance.

2. Results and Discussion

2.1. $\delta_{\text{iso}}(^{15}\text{N})$ and $^1J(^{15}\text{N}^1\text{H})$ as Functions of the N-H Distance in $\text{C}\equiv\text{N}\text{-H}\cdots\text{F}^-$ and $\text{C}\equiv\text{N}\text{-H}\cdots\text{FLi}$

Recently, we reported the NMR parameters of hydrogen-bonded complexes of the $[\text{C}\equiv^{15}\text{N}]^-$ anion [68]. Of special interest is its complex with hydrogen fluoride. This complex was experimentally studied in a $\text{CDF}_3/\text{CDF}_2\text{Cl}$ mixture at 130 K where its structure is $\text{C}\equiv\text{N}\text{-H}\cdots\text{F}^-$ [69]. This study reported ^1H , ^{15}N , and ^{19}F chemical shifts and $^1J(^1\text{H}^{15}\text{N})$, $^{2h}J(^{15}\text{N}^{19}\text{F})$, and $^hJ(^1\text{H}^{19}\text{F})$ coupling constants. These couplings represent rare examples of

spin-spin interactions across hydrogen bonds [70–73]. It is evident that $\delta_{\text{iso}}(^{19}\text{F})$, $^2J(^{15}\text{N}^{19}\text{F})$, and $^1J(^1\text{H}^{19}\text{F})$ depend on interactions between the fluorine atom and solvent molecules [67]. These interactions are difficult to model, so the calculated and experimental values of these parameters will differ. In contrast, it is reasonable to expect that $\delta_{\text{iso}}(^{15}\text{N})$ and $^1J(^1\text{H}^{15}\text{N})$ depend mainly on the N-H distance, while other interactions affect these parameters only indirectly, through their influence on this distance. In this sense, the ^{15}N NMR parameters of $\text{C}\equiv\text{N}-\text{H}$ can resemble those of pyridines [15,74–76].

Figure 1 shows $^1J(^{15}\text{N}^1\text{H})$ as a function of the N-H distance in hydrogen-bonded complexes of $\text{C}\equiv^{15}\text{N}-^1\text{H}$. The geometry of these complexes was optimized at the wB97XD/def2tzvp approximation and $^1J(^{15}\text{N}^1\text{H})$ was calculated at the GIAO wB97XD/pcJ-2 approximations. The composition of selected complexes and the corresponding numerical data are collected in Table 1. Other complexes are reported in [68]. The dependence is linear for the distance shorter than 1.3 Å. Small deviations are observed for the proton-bound homodimer of the cyanide anion. The use of more accurate methods, MP2/def2qzvpp and GIAO wB97XD/pcJ-3, corrects these deviations, Figure 1. Note that the geometry of this homodimer depends critically on the approximation used, Table 1. The error in the determination of the geometry, in turn, leads to the deviation in the $^1J(^{15}\text{N}^1\text{H})$ dependence. Both approaches provide the same functional dependence, where $^1J(^{15}\text{N}^1\text{H})$ is in Hz and $r(\text{NH})$ stands for the N-H distance in Å and must be shorter than 1.3 Å: $^1J(^{15}\text{N}^1\text{H}) = -419 + 297 \cdot r(\text{NH})$.

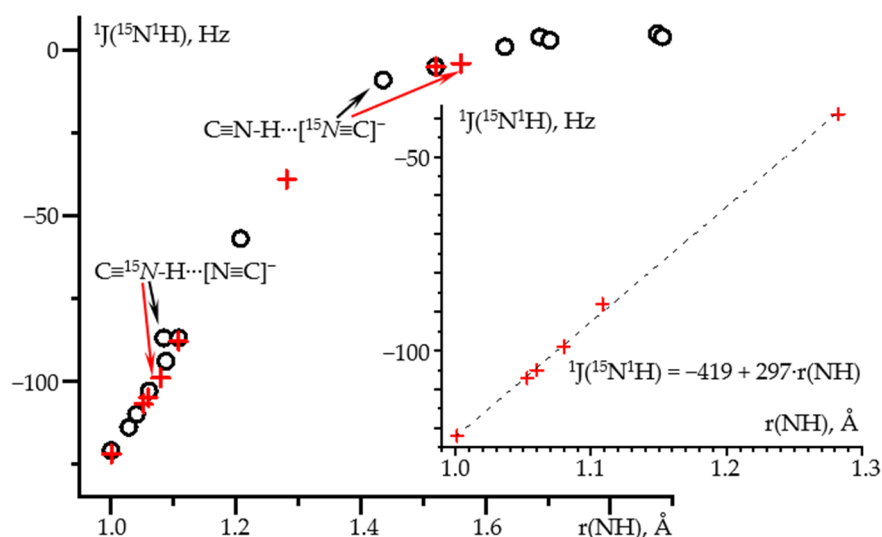


Figure 1. $^1J(^{15}\text{N}^1\text{H})$ as a function of the N-H distance in hydrogen-bonded complexes of $\text{C}\equiv^{15}\text{N}-^1\text{H}$ obtained at different approximations and PCM = water. Geometry optimization at the wB97XD/def2tzvp and NMR at the GIAO wB97XD/pcJ-2 approximations (black circles). Geometry optimization at the MP2/def2qzvpp and NMR at the GIAO wB97XD/pcJ-3 approximations (red crosses). Insert: the distance range at which this dependence is linear.

The dependence of $\delta(^{15}\text{N})$ on the N-H distance in the same complexes is nonlinear, Figure 2 and Table 1. The spread of values is larger than for $^1J(^{15}\text{N}^1\text{H})$ for both approaches used. However, for distances shorter than 1.3 Å the results are similar. Consequently, in this distance range $\delta(^{15}\text{N})$ also depends, almost exclusively, on the N-H distance.

Now we will check whether it is possible to reproduce these dependencies using only one complex, the geometry of which changes when an external electric field is applied. This will be done for two model complexes $\text{C}\equiv^{15}\text{N}-\text{H} \cdots \text{F}^-$ and $\text{C}\equiv^{15}\text{N}-\text{H} \cdots \text{FLi}$. Figure 3 shows the direction of the field and its effect on the geometry of these complexes. Note that the original geometries of these model complexes in the absence of the field are very different. In the first complex the proton is located at the fluorine atom, $[\text{C}\equiv\text{N}]^- \cdots \text{H}-\text{F}$, Figure 3 and Table S2. In the second complex the proton is shared by the fluorine and nitrogen atoms, $[\text{C}\equiv\text{N}]^- \cdots \text{H}^+ \cdots \text{FLi}$, Figure 3 and Table S2. The qualitative changes in the

geometry of these complexes caused by the external electric field are similar. The location of the proton can be changed in both directions by changing the direction of the field. The only principal difference is that in $[\text{C}\equiv\text{N}]^- \cdots \text{H}^+ \cdots \text{FLi}$, this shift occurs smoothly over the entire distance range. In contrast, a transition from $[\text{C}\equiv\text{N}]^- \cdots \text{H}-\text{F}$ to $\text{C}\equiv\text{N}-\text{H} \cdots \text{F}^-$ occurs abruptly when the field changes from 0.0092 to 0.0093 a.u.

Table 1. The ^{15}N isotropic chemical shift, $\delta_{\text{iso}}(^{15}\text{N})$, referenced to free $\text{C}\equiv^{15}\text{N}-^1\text{H}$ at 0 ppm and the $^{15}\text{N}-^1\text{N}$ scalar coupling constant, $^1J(^{15}\text{N}^1\text{H})$, as functions of the N-H distance in hydrogen-bonded complexes of $\text{C}\equiv^{15}\text{N}-^1\text{H}$ obtained at different approximations and PCM = water.

Adduct	¹ Structure: wB97XD/def2tzvp NMR: wB97XD/pcj-2			Structure: MP2/def2qzvpp NMR: wB97XD/pcj-3		
	r(NH), Å	$\delta_{\text{iso}}(^{15}\text{N})$, ppm	$^1J(^{15}\text{N}^1\text{H})$, Hz	r(NH), Å	$\delta_{\text{iso}}(^{15}\text{N})$, ppm	$^1J(^{15}\text{N}^1\text{H})$, Hz
$\text{C}\equiv^{15}\text{N}-^1\text{H}$	1.0007	0 (² 77.6)	-121	1.0010	0 (² 74.3)	-122
$\text{C}\equiv^{15}\text{N}-^1\text{H} \cdots \text{Cl}^-$	-	-	-	1.0528	34	-107
$(\text{C}\equiv^{15}\text{N}-^1\text{H})_3 \cdots \text{F}^-$	1.0612	30	-103	1.0599	32	-105
$\text{C}\equiv^{15}\text{N}-^1\text{H} \cdots [^{15}\text{N}\equiv\text{C}]^-$	1.0847	50	-87	1.0800	44	-99
$(\text{C}\equiv^{15}\text{N}-^1\text{H})_2 \cdots \text{F}^-$	1.1086	43	-87	1.1086	46	-88
$\text{C}\equiv^{15}\text{N}-^1\text{H} \cdots \text{FLi}$	1.2079	62	-57	1.2821	76	-39
$\text{C}\equiv^{15}\text{N}-^1\text{H} \cdots \text{F}^-$	1.5202	95	-5	1.5208	101	-5
$\text{C}\equiv^{15}\text{N}-^1\text{H} \cdots [^{15}\text{N}\equiv\text{C}]^-$	1.4362	100	-9	1.5609	110	-4
$[^{15}\text{N}\equiv\text{C}]^-$	-	124	-	-	129	-

¹ Data from [68]. ² The ^{15}N isotropic chemical shielding, $\sigma_{\text{iso}}(^{15}\text{N})$.

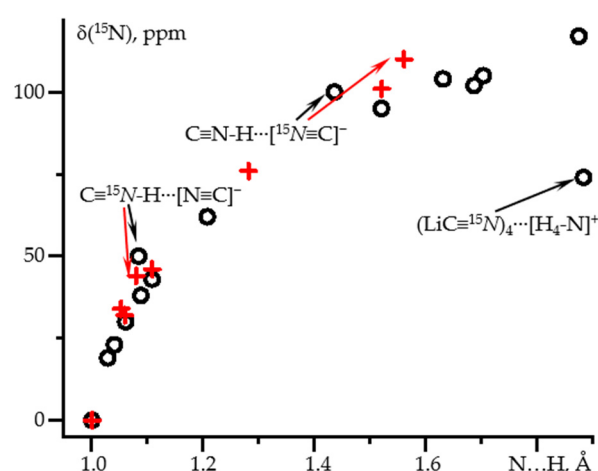


Figure 2. $\delta_{\text{iso}}(^{15}\text{N})$ as a function of the N-H distance in hydrogen-bonded complexes of $\text{C}\equiv^{15}\text{N}-^1\text{H}$ obtained at different approximations and PCM = water. Geometry optimization at the wB97XD/def2tzvp and NMR at the GIAO wB97XD/pcj-2 approximations (black circles). Geometry optimization at the MP2/def2qzvpp and NMR at the GIAO wB97XD/pcj-3 approximations (red crosses).

These geometric changes are illustrated in Figure 4. q_1 stands for the distance of the proton with respect to the center of the $\text{N} \cdots \text{F}$ distance, which is equal to q_2 . The shape of this dependence is the same for all hydrogen bonds [12,77]. Note that for large $\text{N} \cdots \text{H}$ distances, both dependences coincide, while at large $\text{H} \cdots \text{F}$ distances they differ. The reason is that in the former area the proton acceptor is the same, $[\text{C}\equiv\text{N}]^-$, while in the latter they are different, F^- , and FLi . In all of these limiting cases, the distance between the proton and the donating atom changes only slightly.

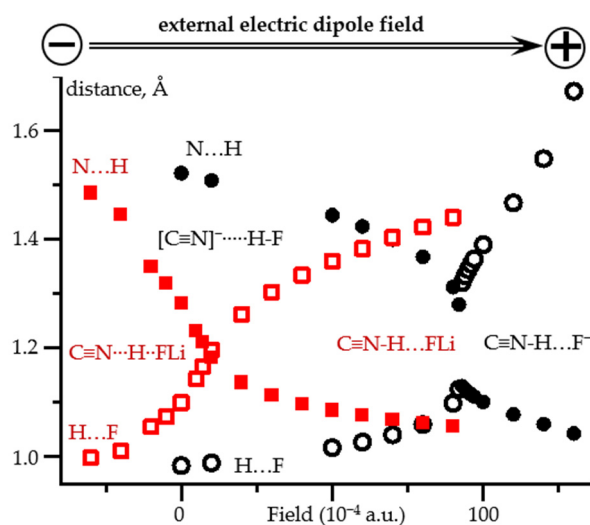


Figure 3. N...H and H...F distances in $C\equiv N-H \dots F^-$ and $C\equiv N-H \dots FLi$ complexes as functions of the applied external electric field at PCM = water. The positive direction of the field corresponds to the direction from the nitrogen to the fluorine atoms. $C\equiv N-H \dots F^-$: N...H (filled black circles) and H...F (open black circles). $C\equiv N-H \dots FLi$: N...H (filled red squares) and H...F (open red squares).

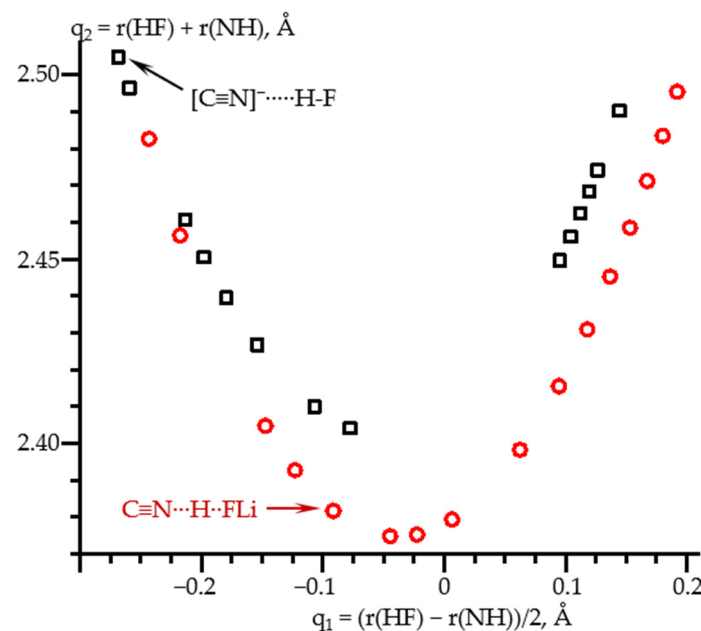


Figure 4. Hydrogen bond correlation q_2 vs. q_1 of the calculated equilibrium geometries of $C\equiv N-H \dots F^-$ (black squares) and $C\equiv N-H \dots FLi$ (red circles) complexes at PCM = water and the effect of the external electric field. $q_2 = r(HF) + r(NH)$ and $q_1 = (r(HF) - r(NH))/2$. The equilibrium geometries in the absence of the field are shown by arrows.

Figure 5 shows $\delta_{iso}^{(15N)}$ as a function of the N-H distance in these two complexes. At the $C\equiv^{15N}-H \dots X$ and $[C\equiv^{15N}]^- \dots H-X$ limits ($X = F^-, FLi$), $\delta_{iso}^{(15N)}$ is the same for both complexes. These limiting cases correspond to weak hydrogen bonds where the effect of the partner is small. For each of the complexes, the corresponding geometry was achieved at different values of the field. Consequently, the effect of the field on $\delta_{iso}^{(15N)}$ in $C\equiv^{15N}-H$ and $[C\equiv^{15N}]^-$ is small and can be neglected. For stronger hydrogen bonds, the area between these limiting cases, $\delta_{iso}^{(15N)}$ depends not only on the N...H distance but also on the partner, Figure 5. Consequently, the spread of $\delta_{iso}^{(15N)}$ values in Figure 2 is not an artifact of the calculations but reflects the difference in the partner. On the other hand,

the effect of the partner is small compared to the dependence on the distance, especially at short distances.

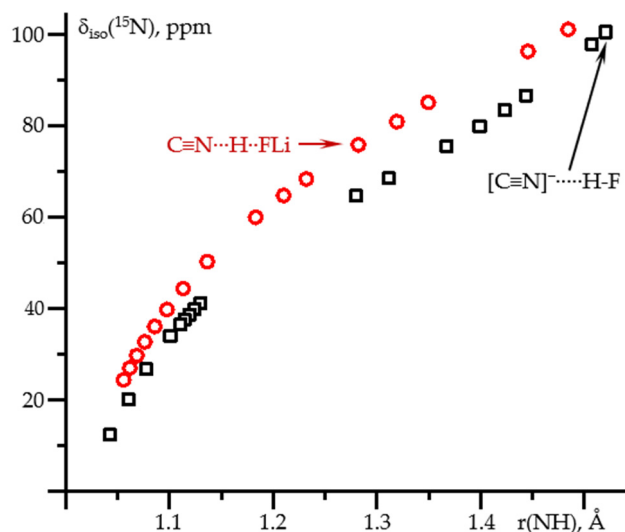


Figure 5. $\delta_{\text{iso}}(^{15}\text{N})$ as a function of the N-H distance in $\text{C}\equiv\text{N}-\text{H} \dots \text{F}^-$ (black squares) and $\text{C}\equiv\text{N}-\text{H} \dots \text{FLi}$ (red circles) complexes at PCM = water and the effect of the external electric field. The values in the absence of the field are shown by arrows.

Figure 6 shows $^1J(^{15}\text{N}^1\text{H})$ as a function of the N-H distance in these two complexes. For both complexes, the dependence is the same over the entire distance range. Consequently, $^1J(^{15}\text{N}^1\text{H})$ depends exclusively on the N...H distance. Again, for each of the complexes, the given N-H distance was achieved at different values of the field. Consequently, the effect of the field on $^1J(^{15}\text{N}^1\text{H})$ in any $\text{C}\equiv^{15}\text{N}-^1\text{H} \dots \text{X}$ complex is small and can be neglected. The experimental value of 92 Hz [69] for a hydrogen-bonded complex of isocyanide with tetrabutylammonium fluoride in $\text{CDF}_3/\text{CDF}_2\text{Cl}$ at 130 K corresponds to the N-H distance of 1.095 ± 0.005 Å, Table S2.

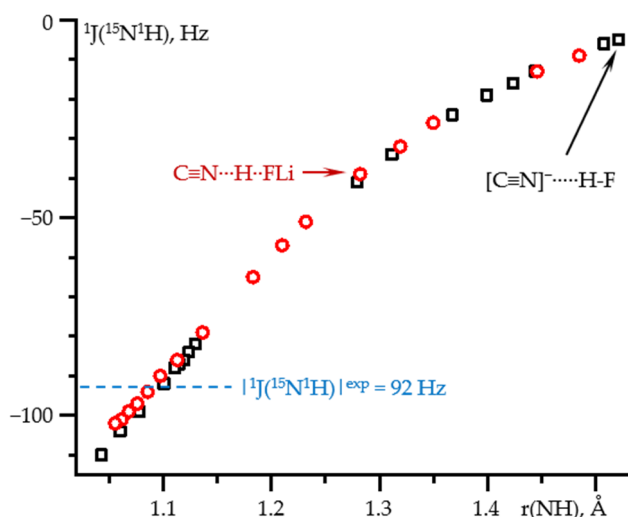


Figure 6. $^1J(^{15}\text{N}^1\text{H})$ as a function of the N-H distance in $\text{C}\equiv\text{N}-\text{H} \dots \text{F}^-$ (black squares) and $\text{C}\equiv\text{N}-\text{H} \dots \text{FLi}$ (red circles) complexes at PCM = water and the effect of the external electric field. The values in the absence of the field are shown by arrows. The experimental value of $^1J(^{15}\text{N}^1\text{H})$ in $\text{CDF}_3/\text{CDF}_2\text{Cl}$ at 130 K is shown by a blue line [69].

2.2. Field-Induced Proton Dissociation

Figure 7 shows the value of the external electric field required for proton dissociation of selected acids as a function of their $\text{p}K_a$. For diatomic hydrogen halides, the correlation

is near linear. The numerical data are reported in Table S3. A noticeable deviation is observed for IH. However, this molecule may require relativistic corrections [78]. Cyanide and isocyanide dissociate at very close field strengths. This, once again, emphasizes the closeness of their properties [68,79,80]. The numerical data are reported in Table S4. For X_3C-OH ($X = H, F, Cl$) alcohols, the result depends on whether the field is directed along the C-O bond or along the O-H bond. The numerical data are reported in Tables S5 and S6. In both cases the correlation is absent. Figure 7 shows the case when the field is directed along the C-O bond. When the field is directed along the O-H bond, the limiting value of the field is smaller for all complexes. However, the magnitude of the change depends greatly on the substitute X. First, the X_3C moieties become asymmetric. This effect is small in H_3C-OH and the resulting field change is also small. In contrast, F_3C-OH and Cl_3C-OH exhibit concerted dissociation of the proton and one of the halogen atoms. Obviously, this behavior has nothing to do with the dissociation of alcohols in water.

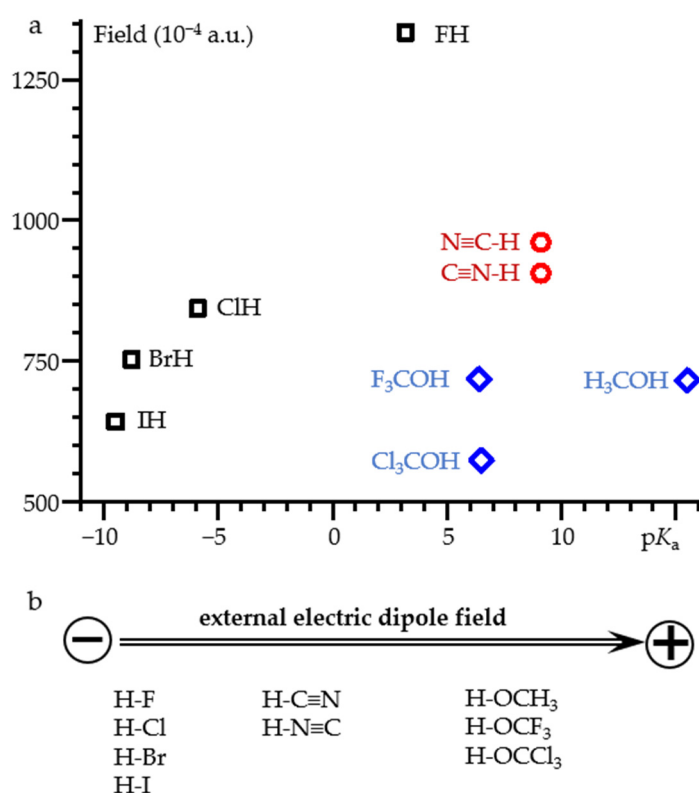


Figure 7. (a) The value of the external electric field required for proton dissociation of selected acids as a function of their pK_a . (b) The orientation of the acids relative to the direction of the field. For $HOCX_3$, the field is directed along the C-O bond.

Note that the field strength required for proton dissociation is about an order of magnitude higher than that required to simulate the real geometry of hydrogen-bonded complexes in solution. Therefore, the influence of the field on the electronic structure of the molecule as a whole is significant. Let us consider the influence of the field on the geometry of molecules.

2.3. Field-Induced Structural Changes

Figure 8 shows how the C-O and O-H distances in X_3COH ($X = H, F, Cl$) alcohols change under the action of the external electric field directed along the C-O bond. The numerical data, including the values of the OCH angle, are reported in Table S5. In the low field range (<0.02 a.u.), only the C-O distance changes noticeably. The changes in the O-H distance and even in the OCH angle are small. In contrast, in the high field range (>0.03 a.u.), the O-H distance increases rapidly and the OCH angle tends to 180° . In the

very high field range (>0.05 a.u.), the changes strongly depend on the chemical composition of the molecule. The results obtained at such fields should be treated with caution [66].

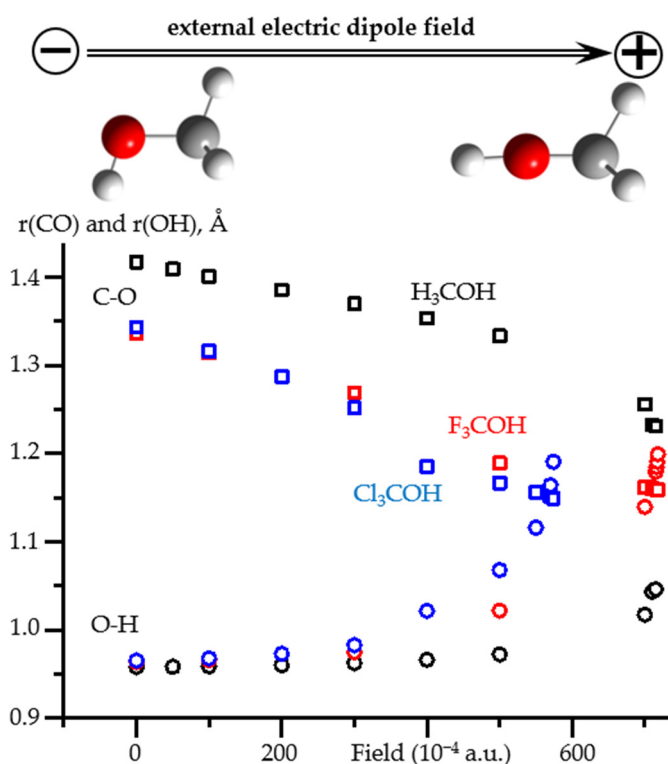


Figure 8. The O-H and C-O distances as functions of an external electric field applied to H₃COH, F₃COH, and Cl₃COH at PCM = water. The O-H distances: H₃COH (black squares), F₃COH (red squares), and Cl₃COH (blue squares). The C-O distances: H₃COH (black circles), F₃COH (red circles), and Cl₃COH (blue circles). The orientation of the acids relative to the direction of the field is shown for H₃COH.

On the other hand, the attempt to simulate the effects of solvation using a very strong fictitious electric field is a very rough approximation. Although this approach somehow works for diatomic hydrogen halides, it is difficult to justify it in other cases. In fact, there is no need to use such strong fields. Proton transfer within a hydrogen bond requires much lower fields. The problem is that it is not clear how to apply this approach to systems in which the non-covalent interaction in question is nonlinear or more than one interaction is present.

Figure 9 shows the changes in the structure of H₃P=O ... (HF)₂ adduct under the action of an external electric field directed along the P=O bond. The numerical values are reported in Table S7. This hydrogen bond pattern is typical for the P=O group [81–83] and anilines [84–86]. The O ... H distances in this complex vary over a wide range in a narrow field window, Figure 9b. In this field range, the H-P distance remains almost constant. The P=O distance varies, but not very much. The same is true for the H-P=O angle, Figure 9c. Consequently, in the range of small fields (<0.01 a.u.), the effect of the field on the covalent structure of H₃P=O is small. The effect on the O ... H distance is not surprising. However, the applied field significantly changes the hydrogen bond pattern, Figure 9a, and the H ... O ... H angle, Figure 9b. The effect is strong even in the range of small fields (<0.01 a.u.). Consequently, the adduct under field approach cannot be applied to such complexes without additional geometric constraints. The need for these restrictions qualitatively reduces the value of this approach.

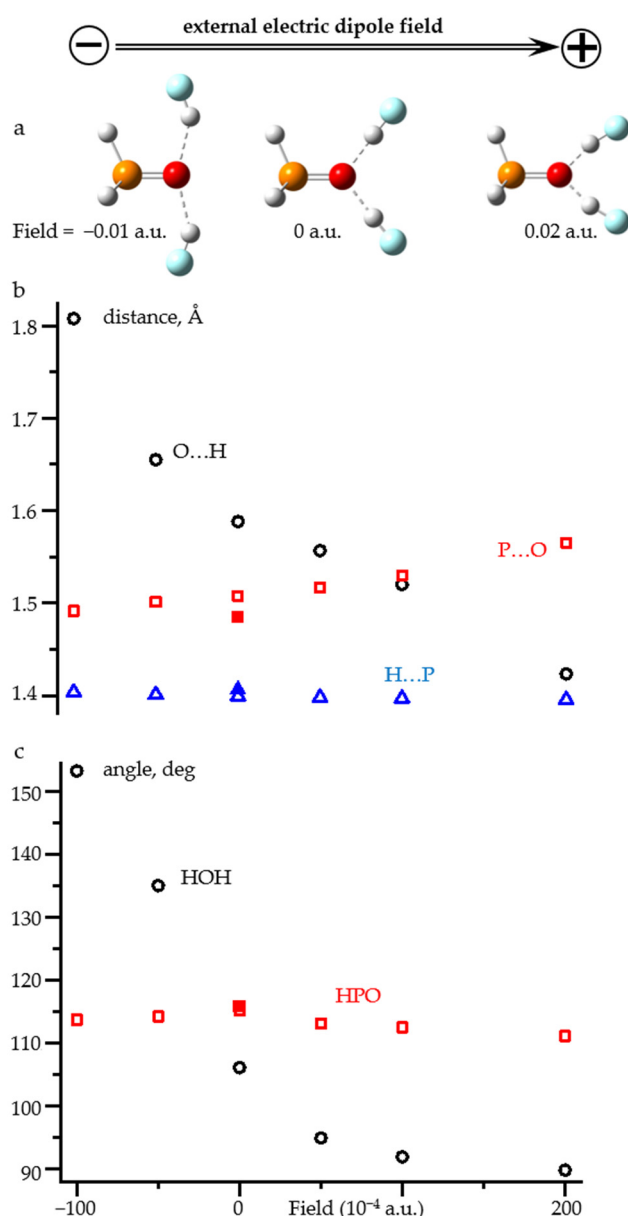


Figure 9. (a) Qualitative changes of the structure of H₃P=O... (H-F)₂ complex under the action of an external electric field directed along the P=O bond. (b) The O...H (open black circles), P=O (open red squares), and H-P (open blue triangles) distances as functions of the field. (c) The HOH (open black circles) and HPO (open red squares) angles as functions of the field. The geometric parameters of free H₃P=O are shown by filled symbols.

3. Materials and Methods

Gaussian 09.D.01 program package (Gaussian, Inc., Wallingford, CT, USA) was used [87]. Geometry optimizations were done in the wB97XD/def2tzvp and MP2/def2qzvpp approximations [88–90]. The NMR parameters were calculated using the Gauge-Independent Atomic Orbital (GIAO) method [91] in the wB97XD/pCJ-2, pCJ-3, and aug-pCJ-3 approximations [92–94]. All calculations were performed using the polarizable continuum model (PCM) with water as a solvent [95–97]. For polar solvents, a change in the values of the dielectric constant has a negligible effect. Therefore, the choice of a specific solvent in the PCM approximation is of no fundamental importance. The default SCRF = PCM method was used to construct the solute cavity.

The wB97XD functional and the pCJ-n basis sets correctly reproduce the experimental values of chemical shielding and scalar spin-spin coupling [43,58,67]. In this work we

have converted the calculated ^{15}N isotropic chemical shieldings, σ_{iso} , to chemical shifts, δ_{iso} , $\delta_{\text{iso}} = \sigma_{\text{ref}} - \sigma_{\text{iso}}$, where σ_{ref} is the isotropic chemical shielding in free $\text{C}\equiv\text{N}-\text{H}$ in the given approximation. More about this issue can be found elsewhere [98–100]. The original $\sigma_{\text{iso}}(^{15}\text{N})$ are reported in Supplementary Materials.

4. Conclusions

This work reports on the response of the geometric and NMR properties of molecular systems to an external electric field. The main issue was the range of field strengths in which this approach can be used to model the geometric and spectral changes experienced by molecular systems in polar media. It has been shown that the main requirement is the presence in the studied molecular system of one and only one bond, the polarizability of which significantly exceeds the polarizability of other bonds. If this requirement is met, then it becomes possible to model even extreme cases. For example, the field required for proton dissociation in hydrogen halides correlates with their $\text{p}K_{\text{a}}$. In contrast, the same correlation is absent for alcohols.

This requirement is met for many complexes with one hydrogen bond. For such complexes, this adduct under field approach can be used to facilitate the analysis of spectral changes associated with geometric changes in the hydrogen bond. This can be conducted in great detail with just two model complexes. For example, in hydrogen-bonded complexes of isocyanide $\text{C}\equiv^{15}\text{N}-\text{H}\cdots\text{X}$, in which the N-H distance $r(\text{NH}) < 1.3 \text{ \AA}$, this distance can be estimated from the experimental value of ${}^1\text{J}(^{15}\text{N}^1\text{H}):r(\text{NH}) = (419 - |{}^1\text{J}(^{15}\text{N}^1\text{H})|)/297 \pm 0.01 \text{ \AA}$. This correlation does not depend on the chemical nature of X. The chemical shift $\delta(^{15}\text{N})$ also correlates with $r(\text{NH})$, but it is also slightly influenced by the nature of X.

When the considered molecular system has several bonds with similar polarizabilities and these bonds are not parallel, the response of the system to an external electric field should be evaluated with caution.

In this study, we did not analyze the effect of an external electric field on the energy of complexes. For molecules, this issue was studied in [101]. Note that an intramolecular basis set superposition error can be important [102].

Supplementary Materials: The following are available online, Table S1: The N-H distance in hydrogen-bonded complexes of $\text{C}\equiv^{15}\text{N}-\text{H}$, the ^{15}N isotropic chemical shielding, $\sigma_{\text{iso}}(^{15}\text{N})$, and the $^{15}\text{N}-^1\text{N}$ scalar coupling constant, ${}^1\text{J}(^{15}\text{N}^1\text{H})$, obtained at different approximations and PCM = water. Table S2: The H...F and N-H distances, the ^{15}N isotropic chemical shielding, $\sigma_{\text{iso}}(^{15}\text{N})$, and the $^{15}\text{N}-^1\text{N}$ scalar coupling constant, ${}^1\text{J}(^{15}\text{N}^1\text{H})$, in $\text{C}\equiv^{15}\text{N}-\text{H}\cdots\text{F}^-$, and $\text{C}\equiv^{15}\text{N}-\text{H}\cdots\text{FLi}$ as functions of the external electric field under the PCM = water approximation. Geometry optimization: MP2/def2qzvpp. NMR calculations: GIAO, wB97XD/pcJ-3. Table S3: The F-H, Cl-H, Br-H, and I-H distances in HF, ClH, BrH, and IH as functions of the external electric field under the PCM = water approximation. Geometry optimization: wB97XD/def2tzvp. Table S4: The C-H and N-H distances in NCH and CNH as functions of the external electric field under the PCM = water approximation. Geometry optimization: wB97XD/def2tzvp. Table S5: The O-H and C-O distances and the COH angle in H_3COH , F_3COH , and Cl_3COH , as functions of the external electric field directed along the C-O bond under the PCM = water approximation. Geometry optimization: wB97XD/def2tzvp. Table S6: The O-H and C-O distances and the COH angle in H_3COH , F_3COH , and Cl_3COH , as functions of the external electric field directed along the O-H bond under the PCM = water approximation. Geometry optimization: wB97XD/def2tzvp. Table S7: The O...H, P=O, and H-P distances and HOH, POH, and HPO angles in $\text{H}_3\text{P}=\text{O}\cdots(\text{HF})_2$ as functions of the external electric field under the PCM = water approximation. Geometry optimization: wB97XD/def2tzvp.

Author Contributions: Conceptualization, I.G.S.; methodology, I.G.S. and G.S.D.; data curation, G.S.D.; writing—original draft preparation, I.G.S.; writing—review and editing, G.S.D.; visualization, I.G.S.; supervision, I.G.S. Both authors have read and agreed to the published version of the manuscript.

Funding: This research was funded by the Russian Foundation of Basic Research (Project 20-03-00231).

Institutional Review Board Statement: Not applicable.

Informed Consent Statement: Not applicable.

Data Availability Statement: The data presented in this study are available in Supplementary Materials.

Acknowledgments: The authors gratefully acknowledge the Gauss Centre for Supercomputing e.V. (www.gauss-centre.eu) for funding this project by providing computing time on the GCS Supercomputer SuperMUC at Leibniz Supercomputing Centre (LRZ, www.lrz.de). G.S.D.: With gratitude, I bring this tribute of respect and memory to Professor A. Barnes. His work on the spectroscopy of hydrogen bonds not only serves as a source of new information but also initiates activity, makes one think, and search. I also owe him the quality of my publications in the Journal of Molecular Structure. I admired the high scientific level and the tact with which they were edited before printing. Much later, I learned that they were edited by Professor Barnes. On a personal acquaintance, I found him to be a charming man of high modesty. His name will remain in molecular spectroscopy for a long time.

Conflicts of Interest: The author declares no conflict of interest.

Sample Availability: Not applicable.

References

- Novak, A. Hydrogen bonding in solids. Correlation of spectroscopic and crystallographic data. *Struct. Bond.* **1974**, *18*, 177–216. [CrossRef]
- Grech, E.; Malarski, Z.; Sobczyk, L. Isotope Effects in NH...N Hydrogen Bonds. *Chem. Phys. Lett.* **1986**, *128*, 259–263. [CrossRef]
- Kong, S.; Borissova, A.O.; Lesnichin, S.B.; Hartl, M.; Daemen, L.L.; Eckert, J.; Antipin, M.Y.; Shenderovich, I.G. Geometry and Spectral Properties of the Protonated Homodimer of Pyridine in the Liquid and Solid States. A Combined NMR, X-ray Diffraction and Inelastic Neutron Scattering Study. *J. Phys. Chem. A* **2011**, *115*, 8041–8048. [CrossRef] [PubMed]
- Iogansen, A.V. Direct proportionality of the hydrogen bonding energy and the intensification of the stretching $\nu(\text{XH})$ vibration in infrared spectra. *Spectrochim. Acta A* **1999**, *55*, 1585–1612. [CrossRef]
- Tupikina, E.Y.; Tolstoy, P.M.; Titova, A.A.; Kostin, M.A.; Denisov, G.S. Estimations of FH...X hydrogen bond energies from IR intensities: Iogansen's rule revisited. *J. Comp. Chem.* **2021**, *42*, 564–571. [CrossRef]
- Asfin, R.E.; Denisov, G.S.; Tokhadze, K.G. The infrared spectra and enthalpies of strongly bound dimers of phosphinic acids in the gas phase. $(\text{CH}_2\text{Cl})_2\text{POOH}$ and $(\text{C}_6\text{H}_5)_2\text{POOH}$. *J. Mol. Struct.* **2002**, *608*, 161–168. [CrossRef]
- Lau, Y.K.; Ikuta, S.; Kebarle, P. Thermodynamics and kinetics of the gas-phase reactions: $\text{H}_3\text{O}^+(\text{H}_2\text{O})_{n-1} + \text{H}_2\text{O} = \text{H}_3\text{O}^+(\text{H}_2\text{O})_n$. *J. Am. Chem. Soc.* **1982**, *104*, 1462–1469. [CrossRef]
- Larson, J.W.; McMahon, T.B. Gas-phase bifluoride ion. An ion cyclotron resonance determination of the hydrogen bond energy in fluoride ion FHF^- from gas-phase fluoride transfer equilibrium measurements. *J. Am. Chem. Soc.* **1982**, *104*, 5848–5849. [CrossRef]
- Malaspina, L.A.; Genoni, A.; Jayatilaka, D.; Turner, M.J.; Sugimoto, K.; Nishibori, E.; Grabowsky, S. The advanced treatment of hydrogen bonding in quantum crystallography. *J. Appl. Crystallogr.* **2021**, *54*, 718–729. [CrossRef] [PubMed]
- Woińska, M.; Grabowski, S.; Dominiak, P.M.; Woźniak, K.; Jayatilaka, D. Hydrogen atoms can be located accurately and precisely by x-ray crystallography. *Sci. Adv.* **2016**, *2*, e1600192. [CrossRef]
- Capelli, S.C.; Bürgi, H.B.; Dittrich, B.; Grabowsky, S.; Jayatilaka, D. Hirshfeld atom refinement. *IUCr* **2014**, *1*, 361–379. [CrossRef] [PubMed]
- Steiner, T. The Hydrogen Bond in the Solid State. *Angew. Chem. Int. Ed.* **2002**, *41*, 48–76. [CrossRef]
- Steiner, T.; Saenger, W. Lengthening of the covalent O–H bond in O–H...O hydrogen bonds re-examined from low-temperature neutron diffraction data of organic compounds. *Acta Crystallogr. Sect. B Struct. Sci.* **1994**, *50*, 348–357. [CrossRef]
- Lesnichin, S.B.; Tolstoy, P.M.; Limbach, H.-H.; Shenderovich, I.G. Counteranion-Dependent Mechanisms of Intramolecular Proton Transfer in Aprotic Solution. *Phys. Chem. Chem. Phys.* **2010**, *12*, 10373–10379. [CrossRef] [PubMed]
- Lorente, P.; Shenderovich, I.G.; Golubev, N.S.; Denisov, G.S.; Buntkowsky, G.; Limbach, H.-H. $^1\text{H}/^{15}\text{N}$ NMR Chemical Shielding, Dipolar $^{15}\text{N}, ^2\text{H}$ Coupling and Hydrogen Bond Geometry Correlations in a Novel Series of Hydrogen-Bonded Acid-Base Complexes of Collidine with Carboxylic Acids. *Magn. Reson. Chem.* **2001**, *39*, S18–S29. [CrossRef]
- Limbach, H.H.; Pietrzak, M.; Sharif, S.; Tolstoy, P.M.; Shenderovich, I.G.; Smirnov, S.N.; Golubev, N.S.; Denisov, G.S. NMR parameters and geometries of OHN and ODN hydrogen bonds of pyridine–acid complexes. *Chem. Eur. J.* **2004**, *10*, 5195–5204. [CrossRef]
- Sharif, S.; Shenderovich, I.G.; González, L.; Denisov, G.S.; Silverman, D.N.; Limbach, H.-H. NMR and Ab initio Studies of Small Complexes Formed between Water and Pyridine Derivatives in Solid and Liquid Phase. *J. Phys. Chem. A* **2007**, *111*, 6084–6093. [CrossRef] [PubMed]
- Hansen, P.E. A Spectroscopic Overview of Intramolecular Hydrogen Bonds of NH...O,S,N Type. *Molecules* **2021**, *26*, 2409. [CrossRef]
- Tupikina, E.Y.; Sigalov, M.; Shenderovich, I.G.; Mulloyarova, V.V.; Denisov, G.S.; Tolstoy, P.M. Correlations of NHN hydrogen bond energy with geometry and ^1H NMR chemical shift difference of NH protons for aniline complexes. *J. Chem. Phys.* **2019**, *150*, 114305. [CrossRef] [PubMed]

20. Afonin, A.V.; Pavlov, D.V.; Albanov, A.I.; Tarasova, O.A.; Nedolya, N.A. Experimental and theoretical study of the intramolecular C–H···N and C–H···S hydrogen bonding effects in the ^1H and ^{13}C NMR spectra of the 2-(alkylsulfanyl)-5-amino-1-vinylpyrroles: A particular state of amine nitrogen. *Magn. Res. Chem.* **2013**, *51*, 414–423. [CrossRef] [PubMed]
21. Kozlecki, T.; Tolstoy, P.M.; Kwocz, A.; Vovk, M.A.; Kochel, A.; Polowczyk, I.; Tretyakov, P.Y.; Filarowski, A. Conformational state of β -hydroxynaphthylamides: Barriers for the rotation of the amide group around CN bond and dynamics of the morpholine ring. *Spectrochim. Acta A* **2015**, *149*, 254–262. [CrossRef]
22. Gorobets, N.Y.; Yermolayev, S.A.; Gurley, T.; Gurinov, A.A.; Tolstoy, P.M.; Shenderovich, I.G.; Leadbeater, N.E. Difference between ^1H NMR signals of primary amide protons as a simple spectral index of the amide intramolecular hydrogen bond strength. *J. Phys. Org. Chem.* **2012**, *25*, 287–295. [CrossRef]
23. Shenderovich, I.G. Actual Symmetry of Symmetric Molecular Adducts in the Gas Phase, Solution and in the Solid State. *Symmetry* **2021**, *13*, 756. [CrossRef]
24. Sobczyk, L.; Obrzud, M.; Filarowski, A. H/D Isotope Effects in Hydrogen Bonded Systems. *Molecules* **2013**, *18*, 4467–4476. [CrossRef] [PubMed]
25. Denisov, G.S.; Mavri, J.; Sobczyk, L. Potential Energy Shape for the Proton Motion in Hydrogen Bonds Reflected in Infrared and NMR Spectra. In *Hydrogen Bonding—New Insights*; Grabowski, S.J., Ed.; Springer: Dordrecht, The Netherlands, 2006. [CrossRef]
26. Denisov, G.S.; Bureiko, S.F.; Kucherov, S.Y.; Tolstoy, P.M. Correlation relationships between the energy and spectroscopic parameters of complexes with F···HF hydrogen bond. *Dokl. Phys. Chem.* **2017**, *475*, 115–118. [CrossRef]
27. Grabowski, S.J. Intramolecular Hydrogen Bond Energy and Its Decomposition—O–H···O Interactions. *Crystals* **2021**, *11*, 5. [CrossRef]
28. Iribarren, Í.; Montero-Campillo, M.M.; Alkorta, I.; Elguero, J.; Quiñonero, D. Cations brought together by hydrogen bonds: The protonated pyridine–boronic acid dimer explained. *Phys. Chem. Chem. Phys.* **2019**, *21*, 5796–5802. [CrossRef]
29. Alkorta, I.; Elguero, J. Theoretical studies of conformational analysis and intramolecular dynamic phenomena. *Struct. Chem.* **2019**, *30*, 2029–2055. [CrossRef]
30. Golubev, N.S.; Melikova, S.M.; Shchepkin, D.N.; Shenderovich, I.G.; Tolstoy, P.M.; Denisov, G.S. Interpretation of H/D Isotope Effects on NMR Chemical Shifts of $[\text{FHF}]^-$ Ion Based on Calculations of Nuclear Magnetic Shielding Tensor Surface. *Z. Phys. Chem.* **2003**, *217*, 1549–1563. [CrossRef]
31. Grabowski, S.J. Study of correlations for dihydrogen bonds by quantum-chemical calculations. *Chem. Phys. Lett.* **1999**, *312*, 542–547. [CrossRef]
32. Kizior, B.; Panek, J.J.; Szyja, B.M.; Jezierska, A. Structure-Property Relationship in Selected Naphtho- and Anthra-Quinone Derivatives on the Basis of Density Functional Theory and Car–Parrinello Molecular Dynamics. *Symmetry* **2021**, *13*, 564. [CrossRef]
33. Alkorta, I.; Walker, N.R.; Legon, A.C. Non-Covalent Interactions of the Lewis Acids Cu–X, Ag–X, and Au–X (X = F and Cl) with Nine Simple Lewis Bases B: A Systematic Investigation of Coinage–Metal Bonds by Ab Initio Calculations. *Inorganics* **2021**, *9*, 13. [CrossRef]
34. Alkorta, I.; Elguero, J.; Frontera, A. Not Only Hydrogen Bonds: Other Noncovalent Interactions. *Crystals* **2020**, *10*, 180. [CrossRef]
35. Grabowski, S.J. Hydrogen Bonds with BF_4^- Anion as a Proton Acceptor. *Crystals* **2020**, *10*, 460. [CrossRef]
36. Shenderovich, I.G. Effect of Noncovalent Interactions on the ^{31}P Chemical Shift Tensor of Phosphine Oxides, Phosphinic, Phosphonic, and Phosphoric Acids, and Their Complexes with Lead(II). *J. Phys. Chem. C* **2013**, *117*, 26689–26702. [CrossRef]
37. Giba, I.S.; Tolstoy, P.M. Self-Assembly of Hydrogen-Bonded Cage Tetramers of Phosphonic Acid. *Symmetry* **2021**, *13*, 258. [CrossRef]
38. Bankiewicz, B.; Palusiak, M. Cooperation/Competition between Halogen Bonds and Hydrogen Bonds in Complexes of 2,6-Diaminopyridines and X-CY₃ (X = Cl, Br; Y = H, F). *Symmetry* **2021**, *13*, 766. [CrossRef]
39. Surov, A.O.; Vasilev, N.A.; Churakov, A.V.; Parashchuk, O.D.; Artobolevskii, S.V.; Alatortsev, O.A.; Makhrov, D.E.; Vener, M.V. Two Faces of Water in the Formation and Stabilization of Multicomponent Crystals of Zwitterionic Drug-Like Compounds. *Symmetry* **2021**, *13*, 425. [CrossRef]
40. Gholami, S.; Aarabi, M.; Grabowski, S.J. Coexistence of Intra- and Intermolecular Hydrogen Bonds: Salicylic Acid and Salicylamide and Their Thiol Counterparts. *J. Phys. Chem. A* **2021**, *125*, 1526–1539. [CrossRef]
41. Shenderovich, I.G. Simplified Calculation Approaches Designed to Reproduce the Geometry of Hydrogen Bonds in Molecular Complexes in Aprotic Solvents. *J. Chem. Phys.* **2018**, *148*, 124313. [CrossRef]
42. Alkorta, I.; Blanco, F.; Solimannejad, M.; Elguero, J. Competition of hydrogen bonds and halogen bonds in complexes of hypohalous acids with nitrogenated bases. *J. Phys. Chem. A* **2008**, *112*, 10856–10863. [CrossRef] [PubMed]
43. Shenderovich, I.G. Experimentally Established Benchmark Calculations of ^{31}P NMR Quantities. *Chem. Methods* **2021**, *1*, 61–70. [CrossRef]
44. Chernyshov, I.Y.; Vener, M.V.; Shenderovich, I.G. Local-structure effects on ^{31}P NMR chemical shift tensors in solid state. *J. Chem. Phys.* **2019**, *150*, 144706. [CrossRef]
45. Shenderovich, I.G. 1,3,5-Triaza-7-Phosphaadamantane (PTA) as a ^{31}P NMR Probe for Organometallic Transition Metal Complexes in Solution. *Molecules* **2021**, *26*, 1390. [CrossRef] [PubMed]
46. Battistin, F.; Balducci, G.; Milani, B.; Alessio, E. Water-Soluble Ruthenium(II) Carbonyls with 1,3,5-Triaza-7-phosphoadamantane. *Inorg. Chem.* **2018**, *57*, 6991–7005. [CrossRef] [PubMed]

47. Battistin, F.; Balducci, G.; Iengo, E.; Demitri, N.; Alessio, E. Neutral 1,3,5-Triaza-7-phosphaadamantane-Ruthenium(II) Complexes as Precursors for the Preparation of Highly Water-Soluble Derivatives. *Eur. J. Inorg. Chem.* **2016**, *2016*, 2850–2860. [CrossRef]
48. Shenderovich, I.G.; Buntkowsky, G.; Schreiber, A.; Gedat, E.; Sharif, S.; Albrecht, J.; Golubev, N.S.; Findenegg, G.H.; Limbach, H.-H. Pyridine-¹⁵N—a Mobile NMR Sensor for Surface Acidity and Surface Defects of Mesoporous Silica. *J. Phys. Chem. B* **2003**, *107*, 11924–11939. [CrossRef]
49. Gurinov, A.A.; Mauder, D.; Akcakayiran, D.; Findenegg, G.H.; Shenderovich, I.G. Does Water Affect the Acidity of Surfaces? The Proton-Donating Ability of Silanol and Carboxylic Acid Groups at Mesoporous Silica. *ChemPhysChem* **2012**, *13*, 2282–2285. [CrossRef] [PubMed]
50. Shenderovich, I.G.; Denisov, G.S. Adduct under Field—A Qualitative Approach to Account for Solvent Effect on Hydrogen Bonding. *Molecules* **2020**, *25*, 436. [CrossRef] [PubMed]
51. Dominikowska, J.; Palusiak, M. Tuning Aromaticity of para-Substituted Benzene Derivatives with an External Electric Field. *ChemPhysChem* **2018**, *19*, 590–595. [CrossRef] [PubMed]
52. Mata, I.; Molins, E.; Alkorta, I.; Espinosa, E. Effect of an external electric field on the dissociation energy and the electron density properties: The case of the hydrogen bonded dimer HF ··· HF. *J. Chem. Phys.* **2009**, *130*, 044104. [CrossRef] [PubMed]
53. Del Bene, J.E.; Jordan, M.J.T. To what extent do external fields and vibrational and isotopic effects influence NMR coupling constants across hydrogen bonds? Two-bond Cl-N spin-spin coupling constants (^{2h}JCl-N) in model ClH:NH₃ complexes. *J. Phys. Chem. A* **2002**, *106*, 5385–5392. [CrossRef]
54. Bevitt, J.; Chapman, K.; Crittenden, D.; Jordan, M.J.T.; Del Bene, J.E. An ab initio study of anharmonicity and field effects in hydrogen-bonded complexes of the deuterated analogues of HCl and HBr with NH₃ and N(CH₃)₃. *J. Phys. Chem. A* **2001**, *105*, 3371–3378. [CrossRef]
55. Ramos, M.; Alkorta, I.; Elguero, J.; Golubev, N.S.; Denisov, G.S.; Benedict, H.; Limbach, H.-H. Theoretical study of the influence of electric fields on hydrogen-bonded acid–base complexes. *J. Phys. Chem. A* **1997**, *101*, 9791–9800. [CrossRef]
56. Suydam, I.T.; Snow, C.D.; Pande, V.S.; Boxer, S.G. Electric fields at the active site of an enzyme: Direct comparison of experiment with theory. *Science* **2006**, *313*, 200–204. [CrossRef]
57. Sellner, B.; Valiev, M.; Kathmann, S.M. Charge and electric field fluctuations in aqueous NaCl electrolytes. *J. Phys. Chem. B* **2013**, *117*, 10869–10882. [CrossRef] [PubMed]
58. Torii, H. Theoretical analysis and modeling of the electrostatic responses of the vibrational and NMR spectroscopic properties of the cyanide anion. *J. Mol. Liq.* **2019**, *284*, 773–779. [CrossRef]
59. Shenderovich, I.G. Electric field effect on ³¹P NMR magnetic shielding. *J. Chem. Phys.* **2020**, *153*, 184501. [CrossRef]
60. Nardo, V.M.; Cassone, G.; Ponterio, R.C.; Saija, F.; Sponer, J.; Tommasini, M.; Trusso, S. Electric-field-induced effects on the dipole moment and vibrational modes of the centrosymmetric indigo molecule. *J. Phys. Chem. A* **2020**, *124*, 10856–10869. [CrossRef] [PubMed]
61. Cassone, G.; Sponer, J.; Trusso, S.; Saija, F. Ab initio spectroscopy of water under electric fields. *Phys. Chem. Chem. Phys.* **2019**, *21*, 21205–21212. [CrossRef]
62. Chranina, O.V.; Czerniakowski, F.P.; Denisov, G.S. UV-vis electrochromism due to proton transfer. *J. Mol. Struct.* **1988**, *177*, 309–315. [CrossRef]
63. Wang, Z.; Danovich, D.; Ramanan, R.; Shaik, S. Oriented-external electric fields create absolute enantioselectivity in Diels–Alder reactions: Importance of the molecular dipole moment. *J. Am. Chem. Soc.* **2018**, *140*, 13350–13359. [CrossRef]
64. Cassone, G. Nuclear quantum effects largely influence molecular dissociation and proton transfer in liquid water under an electric field. *J. Phys. Chem. Lett.* **2020**, *11*, 8983–8988. [CrossRef] [PubMed]
65. Cassone, G.; Sofia, A.; Rinaldi, G.; Sponer, J. Catalyst-free hydrogen synthesis from liquid ethanol: An ab initio molecular dynamics study. *J. Phys. Chem. C* **2019**, *123*, 9202–9208. [CrossRef]
66. Shenderovich, I.G.; Denisov, G.S. Modeling of Solute-Solvent Interactions Using an External Electric Field—From Tautomeric Equilibrium in Nonpolar Solvents to the Dissociation of Alkali Metal Halides. *Molecules* **2021**, *26*, 1283. [CrossRef] [PubMed]
67. Shenderovich, I.G.; Denisov, G.S. Solvent effects on acid-base complexes. What is more important: A macroscopic reaction field or solute-solvent interactions? *J. Chem. Phys.* **2019**, *150*, 204505. [CrossRef] [PubMed]
68. Shenderovich, I.G.; Denisov, G.S. NMR properties of the cyanide anion, a quasisymmetric two-faced hydrogen bonding acceptor. *Symmetry* **2021**, *13*, 1298. [CrossRef]
69. Golubev, N.S.; Detering, C.; Smirnov, S.N.; Shenderovich, I.G.; Denisov, G.S.; Limbach, H.-H.; Tolstoy, P.M. H/D Isotope Effects on NMR Chemical Shifts of Nuclei Involved in a Hydrogen Bridge of Hydrogen Isocyanide Complexes with Fluoride Anion. *Phys. Chem. Chem. Phys.* **2009**, *11*, 5154–5159. [CrossRef] [PubMed]
70. Alkorta, I.; Elguero, J.; Denisov, G.S. A review with comprehensive data on experimental indirect scalar NMR spin–spin coupling constants across hydrogen bonds. *Magn. Res. Chem.* **2008**, *46*, 599–624. [CrossRef]
71. Golubev, N.S.; Shenderovich, I.G.; Smirnov, S.N.; Denisov, G.S.; Limbach, H.-H. Nuclear Scalar Spin-Spin Coupling Reveals Novel Properties of Low-Barrier Hydrogen Bonds in a Polar Environment. *Chem. Eur. J.* **1999**, *5*, 492–497. [CrossRef]
72. Dingley, A.J.; Grzesiek, S. Direct observation of hydrogen bonds in nucleic acid base pairs by internucleotide ²J_{NN} couplings. *J. Am. Chem. Soc.* **1998**, *120*, 8293–8297. [CrossRef]

73. Shenderovich, I.G.; Smirnov, S.N.; Denisov, G.S.; Gindin, V.A.; Golubev, N.S.; Dunger, A.; Reibke, R.; Kirpekar, S.; Malkina, O.L.; Limbach, H.-H. Nuclear Magnetic Resonance of Hydrogen Bonded Clusters between F^- and $(HF)_n$: Experiment and Theory. *Ber. Bunsenges. Phys. Chem. Chem. Phys.* **1998**, *102*, 422–428. [CrossRef]
74. Gurinov, A.A.; Lesnichin, S.B.; Limbach, H.-H.; Shenderovich, I.G. How Short is the Strongest Hydrogen Bond in the Proton-Bound Homodimers of Pyridine Derivatives? *J. Phys. Chem. A* **2014**, *118*, 10804–10812. [CrossRef]
75. Gurinov, A.A.; Denisov, G.S.; Borissova, A.O.; Goloveshkin, A.S.; Greindl, J.; Limbach, H.-H.; Shenderovich, I.G. NMR Study of Solvation Effect on the Geometry of Proton-Bound Homodimers of Increasing Size. *J. Phys. Chem. A* **2017**, *121*, 8697–8705. [CrossRef]
76. Andreeva, D.V.; Ip, B.; Gurinov, A.A.; Tolstoy, P.M.; Denisov, G.S.; Shenderovich, I.G.; Limbach, H.-H. Geometrical Features of Hydrogen Bonded Complexes Involving Sterically Hindered Pyridines. *J. Phys. Chem. A* **2006**, *110*, 10872–10879. [CrossRef] [PubMed]
77. Limbach, H.-H.; Tolstoy, P.M.; Pérez-Hernández, N.; Guo, J.; Shenderovich, I.G.; Denisov, G.S. OHO Hydrogen Bond Geometries and NMR Chemical Shifts: From Equilibrium Structures to Geometric H/D Isotope Effects, with Applications for Water, Protonated Water, and Compressed Ice. *Isr. J. Chem.* **2009**, *49*, 199–216. [CrossRef]
78. Autschbach, J. Perspective: Relativistic effects. *J. Chem. Phys.* **2012**, *136*, 150902. [CrossRef]
79. Ramabhadran, R.O.; Hua, Y.; Flood, A.H.; Raghavachari, K. C vs. N: Which end of the cyanide anion is a better hydrogen bond acceptor? *J. Phys. Chem. A* **2014**, *118*, 7418–7423. [CrossRef] [PubMed]
80. Millar, L.J.; Ford, T.A. Ab initio investigations of some molecular complexes containing hydrogen cyanide: Hydrogen-bonded or donor–acceptor? *J. Mol. Struct.* **2005**, *744*, 195–205. [CrossRef]
81. Tupikina, E.Y.; Bodensteiner, M.; Tolstoy, P.M.; Denisov, G.S.; Shenderovich, I.G. P=O Moiety as an Ambidextrous Hydrogen Bond Acceptor. *J. Phys. Chem. C* **2018**, *122*, 1711–1720. [CrossRef]
82. Arp, F.F.; Bhuvanesh, N.; Blümel, J. Hydrogen peroxide adducts of triarylphosphine oxides. *Dalton Trans.* **2019**, *48*, 14312–14325. [CrossRef] [PubMed]
83. Ahn, S.H.; Lindhardt, D.; Bhuvanesh, N.; Blümel, J. Di(hydroperoxy)cycloalkanes Stabilized via Hydrogen Bonding by Phosphine Oxides: Safe and Efficient Baeyer–Villiger Oxidants. *ACS Sustain. Chem. Eng.* **2018**, *6*, 6829–6840. [CrossRef]
84. Szatyłowicz, H.; Krygowski, T.M.; Panek, J.J.; Jezierska, A. H-bonded complexes of aniline with HF/F^- and anilide with HF in terms of symmetry-adapted perturbation, atoms in molecules, and natural bond orbitals theories. *J. Phys. Chem. A* **2008**, *112*, 9895–9905. [CrossRef]
85. Szatyłowicz, H. Structural aspects of the intermolecular hydrogen bond strength: H-bonded complexes of aniline, phenol and pyridine derivatives. *J. Phys. Org. Chem.* **2008**, *21*, 897–914. [CrossRef]
86. Borisenko, V.E.; Filarovski, A.I. The electrooptical parameters of aniline and its halogen derivatives in hydrogen bonded complexes. *J. Mol. Struct.* **1989**, *196*, 353–370. [CrossRef]
87. Frisch, M.J.; Trucks, G.W.; Schlegel, H.B.; Scuseria, G.E.; Robb, M.A.; Cheeseman, J.R.; Scalmani, G.; Barone, V.; Mennucci, B.; Petersson, G.A.; et al. *Gaussian 09, Revision D.01*; Gaussian Inc.: Wallingford, CT, USA, 2013.
88. Chai, J.-D.; Head-Gordon, M. Long-range corrected hybrid density functionals with damped atom-atom dispersion corrections. *Phys. Chem. Chem. Phys.* **2008**, *10*, 6615–6620. [CrossRef]
89. Weigend, F.; Ahlrichs, R. Balanced basis sets of split valence, triple zeta valence and quadruple zeta valence quality for H to Rn: Design and assessment of accuracy. *Phys. Chem. Chem. Phys.* **2005**, *7*, 3297–3305. [CrossRef]
90. Frisch, M.J.; Head-Gordon, M.; Pople, J.A. Semi-direct algorithms for the MP2 energy and gradient. *Chem. Phys. Lett.* **1990**, *166*, 281–289. [CrossRef]
91. Cheeseman, J.R.; Trucks, G.W.; Keith, T.A.; Frisch, M.J. A Comparison of Models for Calculating Nuclear Magnetic Resonance Shielding Tensors. *J. Chem. Phys.* **1996**, *104*, 5497–5509. [CrossRef]
92. Deng, W.; Cheeseman, J.R.; Frisch, M.J. Calculation of Nuclear Spin-Spin Coupling Constants of Molecules with First and Second Row Atoms in Study of Basis Set Dependence. *J. Chem. Theory Comput.* **2006**, *2*, 1028–1037. [CrossRef]
93. Jensen, F. The optimum contraction of basis sets for calculating spin–spin coupling constants. *Theor. Chem. Acc.* **2010**, *126*, 371–382. [CrossRef]
94. Pritchard, B.P.; Altarawy, D.; Didier, B.; Gibson, T.D.; Windus, T.L. New basis set exchange: An open, up-to-date resource for the molecular sciences community. *J. Chem. Inf. Model.* **2019**, *59*, 4814–4820. [CrossRef]
95. Cossi, M.; Barone, V.; Cammi, R.; Tomasi, J. Ab initio study of solvated molecules: A new implementation of the polarizable continuum model. *Chem. Phys. Lett.* **1996**, *255*, 327–335. [CrossRef]
96. Tomasi, J.; Mennucci, B.; Cammi, R. Quantum Mechanical Continuum Solvation Models. *Chem. Rev.* **2005**, *105*, 2999–3094. [CrossRef]
97. Scalmani, G.; Frisch, M.J. Continuous surface charge polarizable continuum models of solvation. I. General formalism. *J. Chem. Phys.* **2010**, *132*, 114110. [CrossRef]
98. Shenderovich, I.G.; Limbach, H.-H. Solid State NMR for Nonexperts: An Overview of Simple but General Practical Methods. *Solids* **2021**, *2*, 9. [CrossRef]
99. Bryce, D.L.; Bernard, G.M.; Gee, M.; Lumsden, M.D.; Eichele, K.; Wasylshen, R.E. Practical Aspects of Modern Routine Solid-State Multinuclear Magnetic Resonance Spectroscopy: One-Dimensional Experiments. *Can. J. Anal. Sci. Spectrosc.* **2001**, *46*, 46–82. [CrossRef]

100. Duer, M.J. (Ed.) *Solid-State NMR Spectroscopy: Principles and Applications*; Blackwell Science Ltd.: Oxford, UK, 2002.
101. Manzoni, V.; Coutinho, K.; Canuto, S. An insightful approach for understanding solvatochromic reversal. *Chem. Phys. Lett.* **2016**, *655–656*, 30–34. [CrossRef]
102. Vidal, Á.V.; Vicente Poutás, L.C.; Faza, O.N.; López, C.S. On the Use of Popular Basis Sets: Impact of the Intramolecular Basis Set Superposition Error. *Molecules* **2019**, *24*, 3810. [CrossRef]

Article

Spectroscopic and Structural Study of a New Conducting Pyrazolium Salt

Sylvia Zięba¹, Agata Piotrowska², Adam Mizera¹, Paweł Ławniczak¹, Karolina H. Markiewicz³, Andrzej Gzella⁴, Alina T. Dubis³ and Andrzej Łapiński^{1,*}

¹ Institute of Molecular Physics Polish Academy of Sciences, Smoluchowskiego 17, 60-179 Poznań, Poland; zieba@ifmpan.poznan.pl (S.Z.); mizera@ifmpan.poznan.pl (A.M.); lawniczak@ifmpan.poznan.pl (P.Ł.)

² Faculty of Materials Engineering and Technical Physics, Poznań University of Technology, Piotrowo 3, 60-965 Poznań, Poland; agata.m.piotrowska@student.put.poznan.pl

³ Faculty of Chemistry, University of Białystok, Ciołkowskiego 1K, 15-245 Białystok, Poland; k.markiewicz@uwb.edu.pl (K.H.M.); alina@uwb.edu.pl (A.T.D.)

⁴ Department of Organic Chemistry, Poznań University of Medical Sciences, Grunwaldzka 6, 60-780 Poznań, Poland; akgzella@ump.edu.pl

* Correspondence: andrzej.lapinski@ifmpan.poznan.pl; Tel.: +48-618695201

Abstract: The increase in conductivity with temperature in 1*H*-pyrazol-2-ium 2,6-dicarboxybenzoate monohydrate was analyzed, and the influence of the mobility of the water was discussed in this study. The electric properties of the salt were studied using the impedance spectroscopy method. WB97XD/6-311++G(d,p) calculations were performed, and the quantum theory of atoms in molecules (QTAIM) approach and the Hirshfeld surface method were applied to analyze the hydrogen bond interaction. It was found that temperature influences the spectroscopic properties of pyrazolium salt, particularly the carbonyl and hydroxyl frequencies. The influence of water molecules, connected by three-center hydrogen bonds with co-planar tetrameters, on the formation of structural defects is also discussed in this report.

Keywords: proton conductors; X-ray crystallography; IR and Raman spectroscopy; DSC/TGA analysis; impedance spectroscopy; hydrogen bond network; Hirshfeld surface analysis; QTAIM analysis

Citation: Zięba, S.; Piotrowska, A.; Mizera, A.; Ławniczak, P.; Markiewicz, K.H.; Gzella, A.; Dubis, A.T.; Łapiński, A. Spectroscopic and Structural Study of a New Conducting Pyrazolium Salt. *Molecules* **2021**, *26*, 4657. <https://doi.org/10.3390/molecules26154657>

Academic Editors: Rui Fausto, Sylvia Turrell and Gulce Ogruc Ildiz

Received: 25 June 2021

Accepted: 28 July 2021

Published: 31 July 2021

Publisher's Note: MDPI stays neutral with regard to jurisdictional claims in published maps and institutional affiliations.



Copyright: © 2021 by the authors. Licensee MDPI, Basel, Switzerland. This article is an open access article distributed under the terms and conditions of the Creative Commons Attribution (CC BY) license (<https://creativecommons.org/licenses/by/4.0/>).

1. Introduction

Solid proton conductors are attractive materials due to the possibility of their application as an electrolyte in fuel cells for portable electronics and transportation [1]. These solid materials with good proton conductivity and negligible electronic conductivity are often referred to as solid electrolytes. They allow the passage of electrical current through the material by the movement of protons. According to present knowledge, the conductivity of solids by polyatomic protonic species, such as H_3O^+ and NH_4^+ , is relatively low. Therefore, proton conduction based on the movement of H^+ attracts researchers' attention [2]. There are many advantages of facilities using solid electrolytes as compared to liquid electrolytes [3,4]; for example, the only by-products of the reaction occurring in fuel cells based on solid electrolytes are water and heat. This advantage allows the production of pollution-free electrochemical devices, such as the compact power batteries used in mobile and laptops.

Recent studies reveal the numerous requirements for a proton conductor to be used as an electrolyte in a fuel cell [5,6]. For instance, the conduction should be selective to protons, and the electrolyte must be an electrical insulator to prevent the internal short circuit of the cell. Additionally, proton conductors must be thermally stable, which prevents decomposition on heating with the loss of its conductivity. Proton conductors with thermal stability allow the construction of fuel cells with minor corrosion problems.

Some inorganic salts, such as hydrogen sulfates (CsHSO_4), reveal high proton conductivity close to $10^{-1} \text{ S}\cdot\text{cm}^{-1}$ at high temperatures [7,8]. Organic polymers such as Nafion are

also good proton-conducting materials, with conductivity close to $\sim 10^{-1} \text{ S}\cdot\text{cm}^{-1}$ [9], and are currently used in proton exchange membrane fuel cells (PEMFCs) in the USA space program and for transport applications [10,11]. Recently, heteroaromatic triphosphate, 2,4,6-triphosphono-1,3,5-triazine (TPT), was used in the synthesis of novel proton conductors (1-methyl-4-phenyl-1,2,3,6-tetrahydropyridine (MTPT), $M = \text{Ce, Zr, Fe}$) via polymerization with metal ions. Besides TPT, a new class of imidazole-based organic proton conductors has been developed lately [12,13]. Many proton-conducting salts are based on heterocyclic bases and aromatic acids, such as imidazolium salts of benzoic, salicylic, orthophthalic, and terephthalic acids [14,15]. Nevertheless, the hydrogen bonds formed in such solids were weak and medium strength, and their mechanism of conductivity is based on the Grotthuss mechanism. On the other hand, the number and location of the carboxylic group influence the thermal stability and electrical conductivity of the proton conductors [15]. For example, imidazolium orthophthalate and terephthalate revealed high thermal stability with values of 464 and 422 K, respectively, and imidazolium orthophthalate also presented good electrical conductivity ($10^{-1} \text{ S}\cdot\text{m}^{-1}$) [14]. There are many proton-conducting salts with high proton conductivity. They fulfill only a few requirements for application as an electrolyte in a fuel cell. For example, several materials exhibit good conductivities but contain crystal water or hydrated protons. They will lose water and conductivity on heating such as hydrated acid or ion-exchanged ceramics [16,17]. It was shown that the oscillation of hydrogen atoms in hydrogen bonds corresponds to a net transport of charge. The cooperative proton transfer phenomenon, followed by reorientation of donating and accepting groups, is a Grotthuss-type conductivity [18,19]. Thus, the transfer phenomenon is similar to an internal acid–base reaction. Proton transfer needs activation energy. If the proton donating and accepting groups are chemically identical, $\text{X}-\text{H}\cdots\text{X}$, the proton transfer is energetically cost-free. In the case where the proton donating and accepting groups are chemically different $\text{X}-\text{H}\cdots\text{Y}$, the proton-transfer needs extra activation energy, as in the case of transfer of a proton from a NH^+ group to carboxylic group COO^- . Based on our previous studies on conducting materials, we consider a new conducting pyrazolium salt of hydrated 1,2,3-benzene tricarboxylic acid. It was shown previously that due to the presence of water molecules in the crystal lattice of imidazolium selenate dihydrate, the three-dimensional hydrogen bond exists [20]. There are also some inorganic acid hydrates with high proton conductivity stable up to 350 °C. These salts include, for instance, $\text{H}_2\text{Ti}_4\text{O}_9 \times 1.2\text{H}_2\text{O}$ or zirconium sulfate phosphonates [21]. The conductivity of such salts is related to the water content.

The main goal of this study is to extend the knowledge of a conductivity phenomenon within a new hydrated pyrazolium salt. In the first part of this study, we carried out thermal, optical, and structural analyses. In the second part, the geometrical and topological parameters of the salt under investigation were analyzed in terms of the quantum theory of atoms in molecules (QTAIM) and density functional theory (DFT) methods. In proton-conducting systems, intermolecular interactions play a crucial role. Therefore, a study of their role in the real system and theoretical models has outstanding significance. To the best of our knowledge, the QTAIM theoretical calculations and Hirshfeld Surface approach have not been applied so far to analyze the HBs' interactions in pyrazolium hemimellitate hydrate.

2. Results and Discussions

2.1. Crystallographic Investigations

X-ray studies confirmed that the 1*H*-pyrazol-2-ium 2,6-dicarboxybenzoate monohydrate (1:1:1) ($\text{PyrHem} \times \text{H}_2\text{O}$) has the character of salt, and its formula moiety is $\text{C}_9\text{H}_5\text{O}_6^-$, $\text{C}_3\text{H}_5\text{N}_2^+$, H_2O . It was found that the carboxylate group in the anion is in the C-1 position (Figure 1). This is indicated by the found comparable bond lengths $\text{C7a}-\text{O8a}$ (1.2534(18) Å) and $\text{C7a}-\text{O9a}$ (1.2522(18) Å), which are intermediate between the length of the single bond (1.305(2) Å) and double Csp^2-O (1.221(1) Å) in the carboxyl group. In the 2,6-dicarboxybenzoate anion, the carboxyl groups deviate only slightly from the ring

plane C1a—C6a (r.m.s.d.: 0.0022 Å). The dihedral angles (C2a)—COOH/C1a—C6a and (C6a)—COOH/C1a—C6a are 18.87(5)° and 18.14(5)°, respectively. The situation is different for the C-1 carboxylate group, which forms a dihedral angle of 79.57(6)° with the plane of the C1a—C6a ring. The position of the latter is stabilized by the hydrogen bonds N1b—H1b...O8a and N2b—H2b...O9aⁱ, linking the molecules of the 2,6-dicarboxybenzoate anion and the pyrazolinium cation in centrosymmetric tetramers (Figure 1).

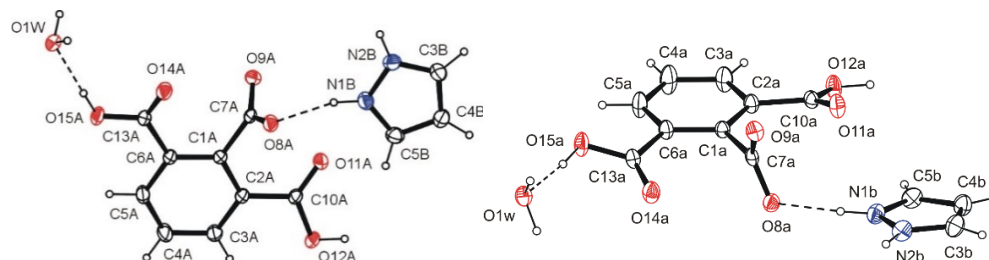


Figure 1. Two views of the molecule of PyrHem × H₂O, showing the atomic labeling scheme. Non-H atoms are drawn as 30% probability displacement ellipsoids, and H atoms are drawn as spheres of arbitrary size.

Co-planar tetramers are further connected by water molecules via three-center hydrogen bonds O12a—H12a...O1wⁱⁱ and O15a—H15a...O1W (or O15a—H15a...O1W...H12a^{ix}—C12a^{ix}; (ix) $x, -1+y, z$) into tapes growing along the *b*-axis (Figure 2). In the latter bifurcated hydrogen bonds, a water oxygen atom acts twice as a proton acceptor. The tapes of molecules arranged antiparallely one above the other are connected via water molecules by hydrogen bonds O1w—H1wB...O8aⁱⁱⁱ and O1W—H1WA...O9a^{iv} into layers parallel to the *bc* plane (Figure 3 and Figure S2, Table 1). In these hydrogen bonds, as can be seen, the oxygen atom of water molecules acts as a proton donor twice in hydrogen bonds. The layered structure (Figure S1) is additionally stabilized by non-classical three-center hydrogen bonds C3b—H3b...O14aⁱ, C3b—H3b...O14a^v and C5b—H5b...O11a, C5b—H5b...O11a^{vi}, as well as interactions of $\pi(\text{Pyr}^{\text{viii}})\cdots\pi(\text{Pyr})\cdots\pi(\text{Pyr}^{\text{vii}})$ stacking (*Pyr* = pyrazolinium cation) type (see Figure S3).

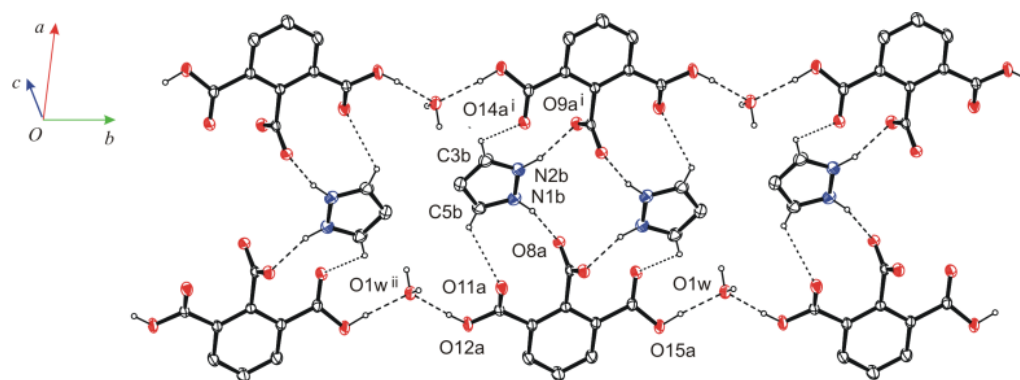


Figure 2. Hydrogen bonds linking molecules into tapes growing along the *b*-axis.

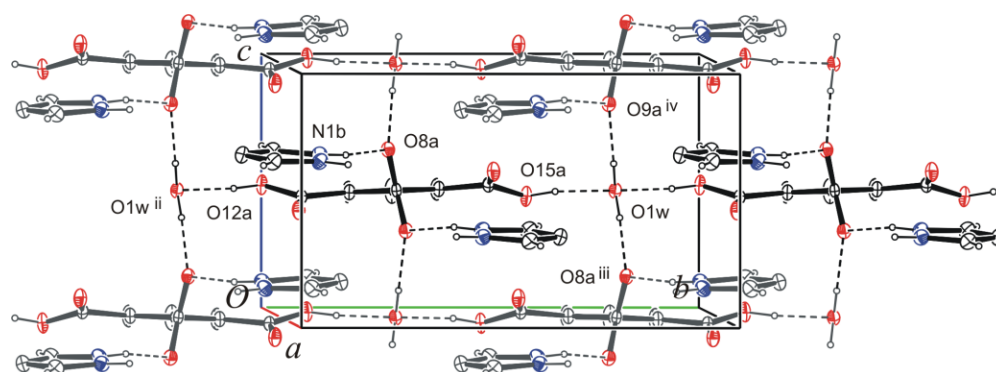


Figure 3. Hydrogen bonds O1w—H1wA...O9a^{iv} and O1w—H1wB...O8aⁱⁱⁱ linking types into layers parallel to the *bc* plane. The symmetry codes are explained in Table 1.

Table 1. Hydrogen-bond geometry (Å, °) for PyrHem×H₂O.

D—H...A	D—H	H...A	D...A	D—H...A
N1b—H1b...O8a	0.89(2)	1.85(2)	2.7137(17)	165(2)
N2b—H2b...O9a ⁱ	0.91(2)	1.87(2)	2.7581(17)	165(2)
O12a—H12a...O1w ⁱⁱ	0.90(2)	1.82(2)	2.7217(15)	175(3)
O15a—H15a...O1w	0.90(3)	1.83(2)	2.7164(15)	172(3)
O1w—H1wA...O9a ^{iv}	0.92(3)	1.86(3)	2.7695(16)	171(3)
O1w—H1wB...O8a ⁱⁱⁱ	0.92(3)	1.86(3)	2.7695(16)	171(3)
C3b—H3b...O14a ⁱ	0.93	2.46	3.057(2)	122
C3b—H3b...O14a ^v	0.93	2.55	3.072(2)	116
C5b—H5b...O11a	0.93	2.56	3.032(2)	112
C5b—H5b...O11a ^{vi}	0.93	2.35	3.071(2)	134

Symmetry codes: (i) $3/2-x, 1/2-y, 1-z$; (ii) $x, -1+y, z$; (iii) $x, 1-y, -1/2+z$; (iv) $x, 1-y, 1/2+z$; (v) $3/2-x, -1/2+y, 3/2-z$; (vi) $x, -y, 1/2+z$.

2.2. Thermal Properties Analysis

Differential scanning calorimetry (DSC) and thermogravimetric analysis (TGA) were used to study the thermal properties of the substrates and the product. The pure hemimelitic acid (Hem×H₂O) decomposes in a broad temperature range from 400 to 650 K (Figure S4). The endothermic peaks observed in the DSC thermogram with the minima at 440, 470, and 600 K represent dehydration, melting, and acid decomposition [22]. Pyrazole (Pyr) decomposes in one stage below 450 K (Figure S5). The DSC thermogram of pyrazole shows two sharp endothermic peaks at 340 and 470 K, attributed to its melting and decomposition. Several overlapping endothermic peaks with the minima at 400, 435, and 600 K can be observed in the DSC thermogram of the PyrHem×H₂O (Figure 4). They are related to the dehydration, melting, and decomposition of the compound. The melting range of PyrHem×H₂O is between 393 and 443 K. The formation of gas bubbles was noted when the sample was heated above 420 K. It seems most likely that decarboxylation of anion moiety proceeds [23]. The salt has a different and more complex decomposition profile compared to pure acid (Hem×H₂O) and pyrazole (Pyr). It decomposes in a few consecutive overlapping stages between 350 and 650 K. These steps may be related to the dehydration, decarboxylation, and decomposition of pyrazole and acid, or its anhydride. However, it is not possible to define these stages precisely, as they overlap.

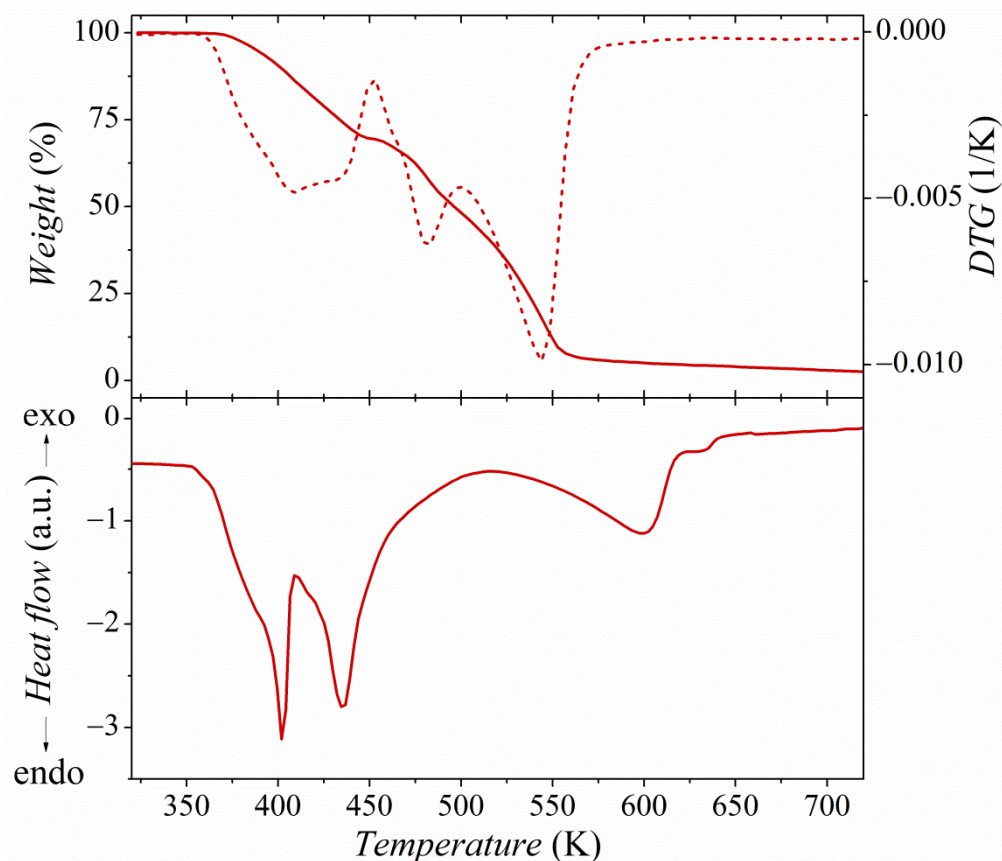


Figure 4. TGA/DTG curves (top panel) and DSC curves (bottom panel) of PyrHem \times H₂O.

2.3. Intermolecular Interactions Analysis

The analysis of intermolecular interactions in the studied hydrated pyrazolium hemimellitate crystal was carried out using the Hirshfeld surface, fingerprint plots, and the quantum theory of atoms in molecules (QTAIM). The Hirshfeld surface of a molecule in a crystal is constructed by partitioning the crystal space into regions in which the electron distribution of the sum of spherical atoms of the molecule dominates the corresponding sum over the crystal. It can be described using the molecular weight-function $w(r)$:

$$w(r) = \frac{\sum_{A \in \text{molecule}} \rho_A(r)}{\sum_{A \in \text{crystal}} \rho_A(r)} = \frac{\rho_{\text{promolecule}}(r)}{\rho_{\text{procrystal}}(r)} \geq 0.5 \quad (1)$$

where $\rho_A(r)$ is a spherically averaged electron density of various atoms centered on the nucleus A . The Hirshfeld surface is defined as the region around a molecule where the weight function ≥ 0.5 . The contribution to electron density from the promolecule to the procrystal exceeds that of all other molecules in this region in the crystal.

The Hirshfeld surfaces and fingerprint plots for the hemimellitic ion, the water molecule, and the pyrazolium ion are shown in Figure 5. The Hirshfeld surfaces are defined by points where the contribution in the electron density of the target molecule equals the contribution of all other molecules. The dominant interaction (H \cdots O and O \cdots H) corresponds to the area presented at Hirshfeld surface: red for the highest contribution through green to blue for points with smaller contribution. Based on the analysis of the Hirshfeld surface and fingerprint plots, the hydrogen bonding patterns can be identified. On the fingerprint plot, each point corresponds to a unique (d_i, d_e) pair. The parameters d_i and d_e present the distance from the Hirshfeld surface to the nearest nucleus outside and inside the surface, respectively [24,25]. All (d_i, d_e) pairs are presented in colors, which correspond to areas presented at the Hirshfeld surface: red for the highest contribution through green to blue for points pointed out the smallest contribution.

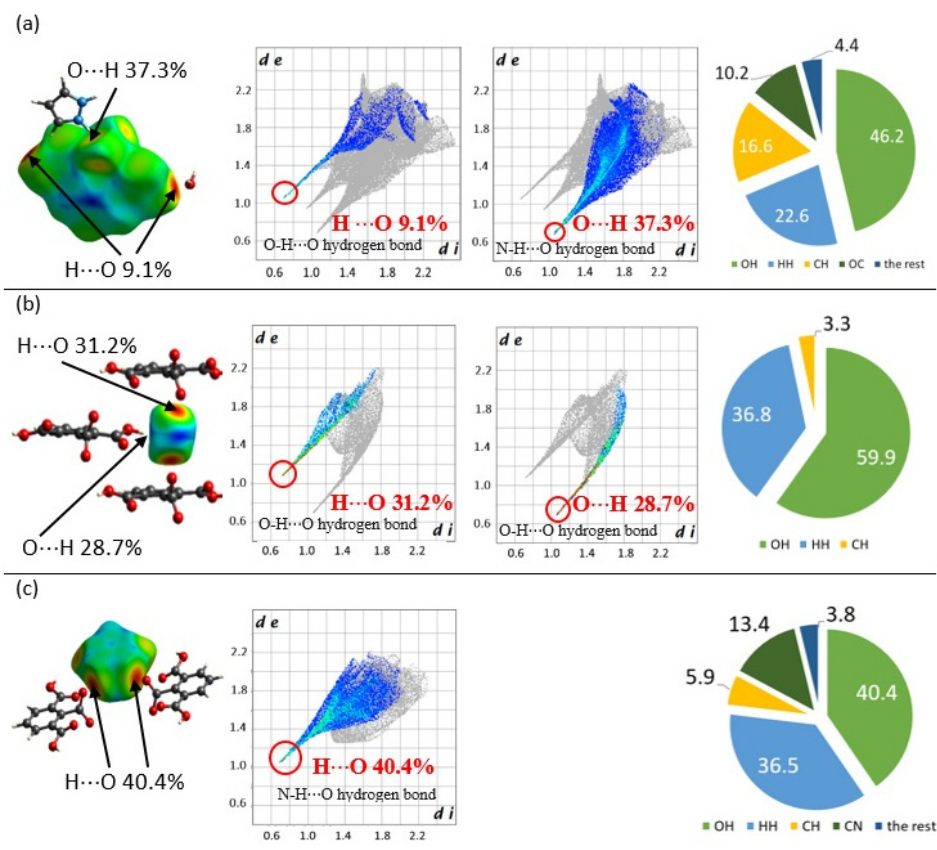


Figure 5. On the left, the Hirshfeld surfaces for the hemimellitate ion (a), the water molecule (b), and the pyrazolium ion (c) mapped with d_i ; mapping range: red (short distance) through green to blue (long-distance). In the middle, fingerprint plots (d_e versus d_i) for these features involving specific pairs of atoms; on the right, histograms showing the percentage of different types of interactions taking place in the studied salt.

The intermolecular H...O and O...H contacts in N—H...O, C—O[−]...H, and O—H...O can be analyzed. For these bonds, the fingerprint plot shows a pair of spikes at the bottom left of the plot, the upper one ($d_i < d_e$) associated with the donor atom, the lower one ($d_i > d_e$) with the acceptor. The carboxylate anion is a proton-accepting center, whereas carboxyl groups are proton-accepting and proton-donating centers. The contribution of N—H...O interaction is 37.3%, whereas O—H...O amounts to 9.1%. The total contribution of O...H interaction is 46.2% of all interactions between the anion and the closest environment. The water molecule plays a role as a proton donor and an acceptor; the total O...H interaction is 59.9%, and this contribution is related to the O—H...O interactions. The pyrazolium ion is connected by N—H...O with two hemimellitate ions, and the O...H interaction is responsible for over 40.4% of all interactions between the pyrazolium ion and the closest environment. The structure is stabilized by N—H...O (36.8%) and C...H (3.3%) interactions. Pyrazolium ions are also stabilized by the C—H...O (5.9%) interaction.

To analyze the hydrogen bond interactions, various descriptors originating from Bader's quantum theory of "Atoms in Molecules" (AIM) are used [26,27]. Koch and Popelier [28] proposed criteria for the description of the D—H...A hydrogen bond (where A is a proton-acceptor center). The electron density at the bond critical point BCP ($\rho_{H...A}$) should be within a range of 0.002–0.040 a.u. The corresponding Laplacian of electron density at the BCPs ($\nabla^2\rho_{BCP}$) should be within a range of 0.024–0.139 a.u. Additionally, there are energetic descriptors of BCPs such as electron energy density at BCP (H_C) and its

components, potential electron energy density (V_C), and kinetic electron energy density (G_C). The equation gives relationships between topological parameters at the critical point:

$$0.25 \nabla^2 \rho_{BCP} = 2G_C + V_C ; H_C = G_C + V_C \quad (2)$$

The Rozas group [29] proposed a classification of hydrogen bonds using the electron energy density and Laplacian of electron density at the BCPs. Weak and moderate H-bonds are characterized by $\nabla^2 \rho_{BCP} > 0$ and $H_C > 0$, which indicates them as closed-shell interactions. Suppose H_C is negative, corresponding to the interaction between the proton and proton acceptor within the hydrogen bridge. In that case, the interaction may be treated as strong hydrogen bonds. The Laplacian of the electron density for interacting pairs of atoms is negative as well. The negative Laplacian for H-bonds indicates their covalent character. If Laplacian is positive and H_C is negative, strong hydrogen bonding is partially covalent [30]. For a very strong hydrogen bond interaction, $\nabla^2 \rho_{BCP}$ and H_C values are both negative. It has been shown that ρ_{BCP} and $\nabla^2 \rho_{BCP}$ correlate with HBs' energy [31,32]. The increase in hydrogen bond strength is related to the growth of electron density at the bond critical points.

For the 1*H*-pyrazol-2-ium 2,6-dicarboxybenzoate monohydrate, geometrical and topological parameters of intermolecular contacts, i.e., O—H...O, N—H...O, and C—H...O (Figure 6) are presented in Table 2. The QTAIM analysis of electron densities at the H...O bond critical points showed that ρ_{BCP} is in a range of 0.0296 to 0.0340 a.u., and Laplacian varies 0.1087 to 0.1268 a.u. A small ρ_{BCP} value indicates the depletion of the electronic charge in the internuclear region. The water molecule plays the role of proton acceptor center (oxygen atom) and proton donator. The most significant electron density at the proton-acceptor O—H...O bond critical point is observed for interaction between the hydroxyl proton of the carboxyl group and water oxygen (—COOH...OH₂). It means that HBs' interaction is more substantial for —COOH...water interaction than for —COO[−]... water interaction. The shortest H...O distances are observed for —COOH...water interaction. There are also —COO[−]... H—N and N—H...OH₂ interactions. The most significant electron density at the bond critical point and the shortest bond length were observed for —COO[−]... H—N interaction. The shortest contact exists connecting the oxygen atom of the water molecule and the hydrogen atom of the carboxylic group. The kinetic and potential electron energy densities at BCP (G_C , V_C) are close to each other for —COO[−]... H—N interaction. The analysis of V_C and G_C shows that G_C is always greater than the modulus of V_C . It means that H_C , the total electron energy density at BCP, is greater than zero. Thus, one can expect that intermolecular interactions are of medium strength.

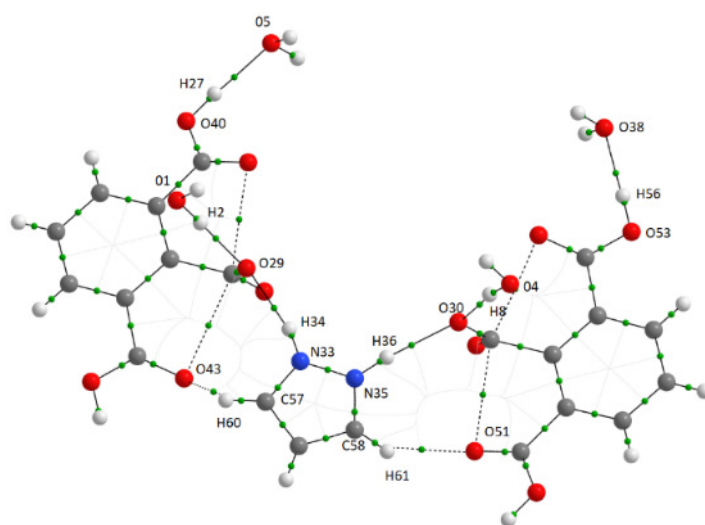


Figure 6. Molecular graphs (representation of bonding interactions according to QTAIM results) of the system analyzed in this study. Green circles correspond to the bond critical point.

Table 2. Geometrical parameters ($d_{H\cdots O}$ in Ångstrom and $\angle D-H\cdots A$ in degrees) corresponding to the D-H \cdots A contacts obtained at the B3LYP/6-311++G(d,p); QTAIM parameters (in atomic unit) corresponding to the H \cdots O bond critical point (BCPs), the electron density at BCP ρ_{BCP} ; Laplacian of electron density at BCP, $\nabla^2\rho_{BCP}$; total electron energy density at BCP, H_C and the components of the H_C : kinetic electron energy density, G_C ; potential electron energy density, V_C . The atomic labeling is presented in Figure 6.

D-H \cdots A	$d_{H\cdots A}$	$\angle D-H\cdots A$	d_{D-H}	ρ_{BCP}	$\nabla^2\rho_{BCP}$	G_C	V_C	H_C
N35—H \cdots O30	1.862	164.8	0.918	0.0305	0.1106	0.0262	−0.0250	0.0014
N33—H \cdots O29	1.851	164.1	0.886	0.0315	0.1202	0.0283	−0.0266	0.0017
O1—H \cdots O29	1.875	175.8	0.900	0.0296	0.1087	0.0258	−0.0243	0.0014
O4—H \cdots O30	1.857	171.1	0.919	0.0307	0.1106	0.0265	−0.0253	0.0012
O40—H \cdots O5	1.804	172.6	0.918	0.0340	0.1262	0.0309	−0.0302	0.0007
O53—H \cdots O38	1.815	174.5	0.911	0.0333	0.1241	0.0302	−0.0293	0.0009
C58—H \cdots O51	2.457	122.3	0.931	0.0099	0.0375	0.0077	−0.0061	0.0016
C57—H \cdots O57	2.556	112.2	0.929	0.0089	0.0346	0.0071	−0.0056	0.0015

2.4. Electrical Properties Analysis

For PyrHem \times H₂O, the temperature dependence (273–393 K) of the electrical conductivity has been investigated from 1 Hz to 10 MHz. The sample was a cylindrical pellet made of powdered crystallites. The frequency dependence of the real part of complex conductivity is presented in Figure 7.

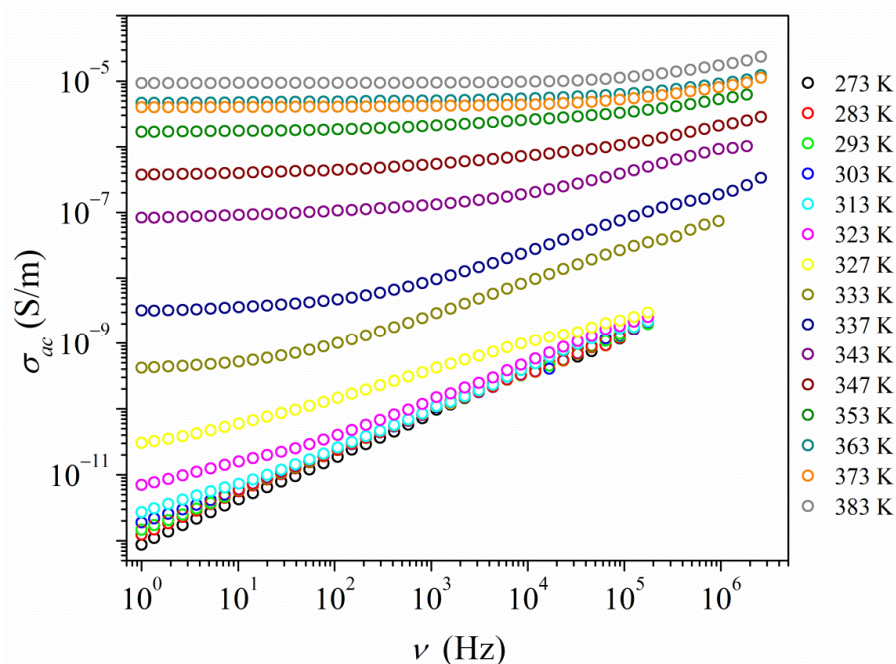


Figure 7. Dependence of the real part of electric conductivity as a function of frequency and temperature obtained for PyrHem \times H₂O.

In the temperature range from 273 to 313 K, the conductivity increases almost linearly with frequency. Measured ac conductivity values are very low and hardly change with temperature changes. Moreover, in a given range of frequency measurements, no plateau was observed to provide information about the value of the dc conductivity. As the temperature rises above 313 K, the frequency relationship of ac conductivity changes, which is typical of the ion conductor response. A plateau appears at the lowest frequencies, corresponding to the dc conductivity.

Figure 8 shows the impedance dependence in the form of Nyquist plots (imaginary part Z'' of total impedance Z^* on the real part Z') collected at temperatures $T = 358$ K and $T = 383$ K for PyrHem \times H₂O. The entire response contains a reply from the two

parts of the sample: grain interior (crystallite) and grain boundaries. They can be easily distinguished from the total measured impedance using the proper fitting procedure. For fitting the experimental data, the Cole–Cole formula for double RC parallel equivalent circuits connected in series was used:

$$Z^*(\omega) = \frac{R_1}{1 + (i\omega R_1 C_1)^{1-\alpha_1}} + \frac{(R_2 - R_1)}{1 + (i\omega(R_2 - R_1)C_2)^{1-\alpha_2}} \quad (3)$$

where R_1 denotes the resistance of the first contribution, R_2 is the resistance of the sum of two contributions (the crystalline and grain boundaries), C_1 and C_2 mean electrical capacities of circuits 1 and 2, α_1 and α_2 are Cole–Cole parameters, and $\omega = 2\pi\nu$ is the angular frequency of the measuring field. Such an approach is commonly used to analyze complex impedance responses in polycrystalline samples and ceramics [33,34]. The two contributions from bulk material (crystallite) and grain boundaries are visible at lower temperatures. As the temperature rises, the shape of the measured response gradually becomes more homogeneous (Figure S6).

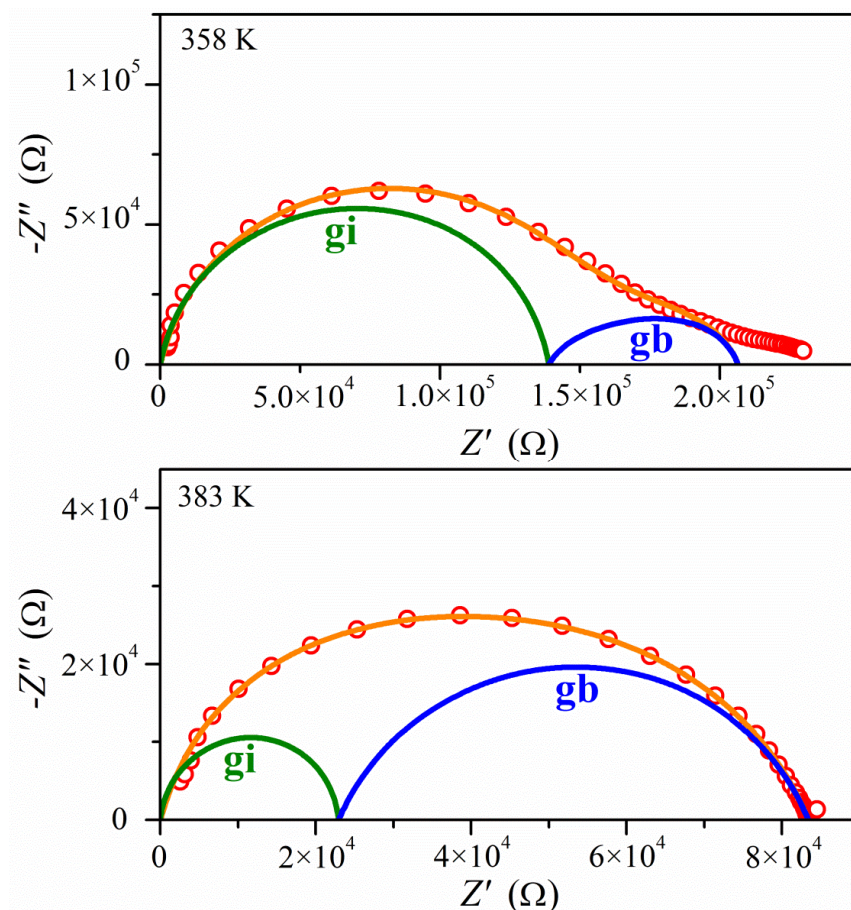


Figure 8. Complex impedance plots $Z''(Z')$ of the impedance for $\text{PyrHem} \times \text{H}_2\text{O}$ for two temperatures 358 and 383 K. Red points are the experimental data, while the lines are obtained from fitting to Equation (3): olive lines denote the contributions from the interior of the crystallites (gi), blue lines are due to the crystallite boundaries (gb), and orange lines represent fitting for all samples.

The fitting procedure values of total impedance were used to calculate the dc conductivity of $\text{PyrHem} \times \text{H}_2\text{O}$. The dc conductivity versus the inverse temperature, in the form of the Arrhenius plot, is presented in Figure 9. The Arrhenius law has described it:

$$\sigma_{dc} = \sigma_0 e^{-\frac{E_a}{kT}} \quad (4)$$

where σ_0 means the pre-exponential factor, E_a is the activation energy, and k is the Boltzmann constant. In the temperature range from 323 to 347 K, the conductivity is characterized by high activation energy $E_{\sigma 1} = 5.05$ eV. Next, at the temperature range $347 \text{ K} \leq T \leq 354 \text{ K}$ and $354 \text{ K} \leq T \leq 360 \text{ K}$, the activation energy decreases to the value of $E_{\sigma 2} = 2.68$ and 1.23 eV, respectively. Above 360 K, dc conductivity is almost temperature-independent. The step decrease of conductivity above 388 K can be related to the degradation of the sample due to melting and the degradation of $\text{PyrHem} \times \text{H}_2\text{O}$. The maximum conductivity amounts to $8.2 \times 10^{-3} \text{ S} \cdot \text{m}^{-1}$ at 388 K for the investigated proton-conducting material. It can be seen that the temperature at which the change in the slope of Arrhenius law is observed is in the temperature region where the dehydration process takes place. TGA measurements (Figure 4) show that the weight loss in the temperature range from 318 to 388 K is 5%. It is in good agreement with the endset temperature (354 K) of the endothermic peak with a minimum of 400 K. Water molecules that have emerged from the crystal lattice cause structural defects. An increase in proton conductivity is then possible.

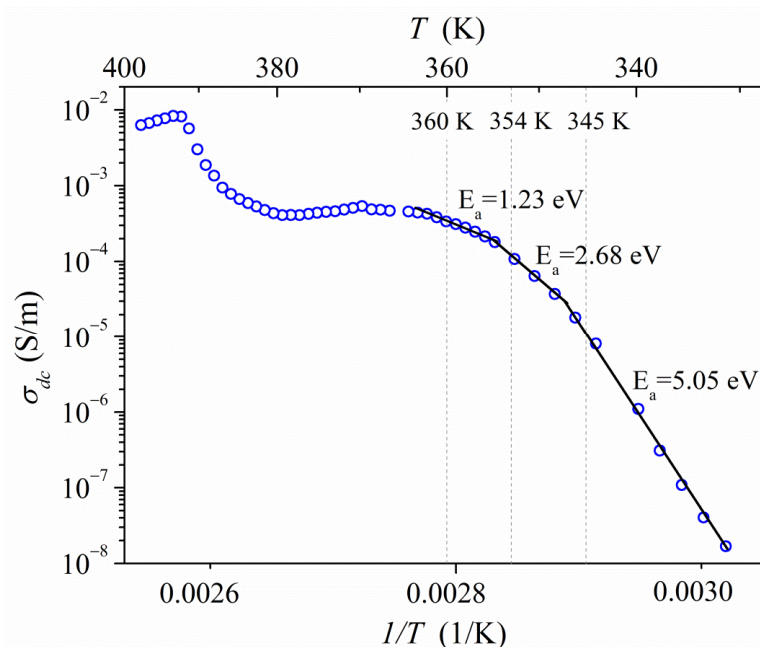


Figure 9. Arrhenius plot of dc conductivity of $\text{PyrHem} \times \text{H}_2\text{O}$.

2.5. Vibrational Analysis

Figure 10 shows the infrared spectra of hemimellitic acid hydrate $\text{Hem} \times \text{H}_2\text{O}$ (a) and $\text{PyrHem} \times \text{H}_2\text{O}$ (b) recorded at room temperature. The most prominent experimental vibrational bands with theoretically calculated frequencies are collected in Table S1. In the spectrum of $\text{Hem} \times \text{H}_2\text{O}$, there is a broad absorption in the range $3200\text{--}2200 \text{ cm}^{-1}$ due to the stretching vibration of the hydrogen-bonded O-H group. Another band characteristic of the acid species is O-H out of plane vibration, which appears as a broad, medium intensity band with a maximum at 898 cm^{-1} . The calculated $\gamma_{\text{O-H}}$ frequency is 889 cm^{-1} . It is worth mentioning that H-bond formation affects the stretching and deformational vibrational modes of the proton donating group as N-H and O-H bond and the modes of the proton accepting center, i.e., the C=O group and O-H of a water molecule. The carbonyl stretching band appears at 1727 and 1701 cm^{-1} . According to theoretically calculated frequencies of vibrational modes, the lower frequency band (1701 cm^{-1}) is due to the C=O stretching vibration of the C=O group, which interacts with a water molecule.

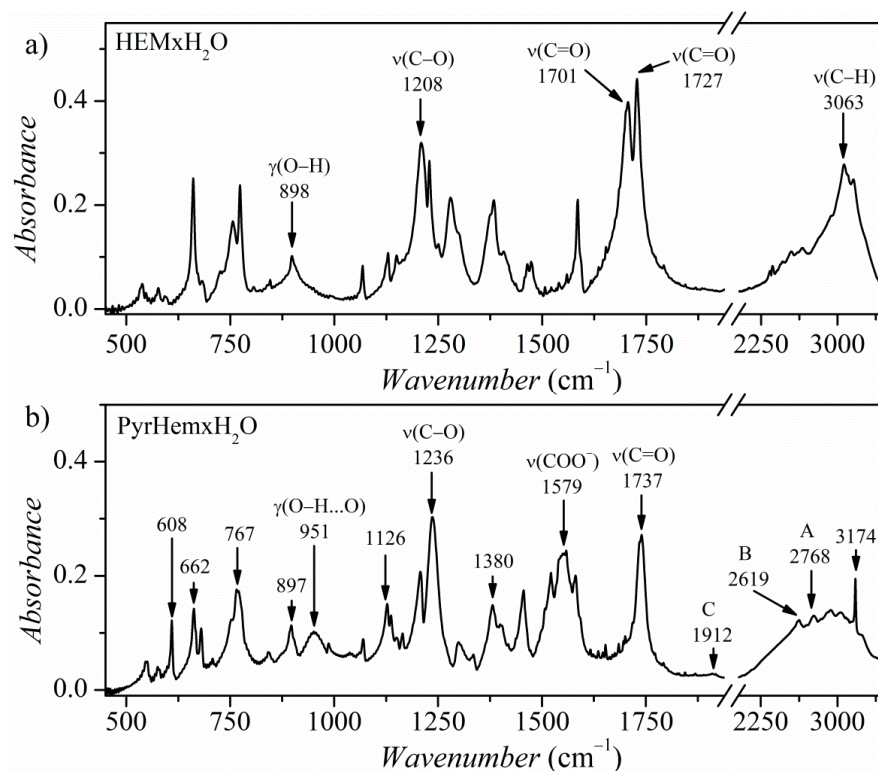


Figure 10. FT-IR absorption spectra of the HemxH₂O (a) and PyrHemxH₂O (b) recorded at 293 K.

For PyrHem×H₂O, in the range 3200–2800 cm⁻¹, there are bands related to the N-H stretching modes of charged amine derivatives (ν_{C=NH⁺}). In the range of 2800–1900 cm⁻¹, multiple combinational bands are present. The bands denoted as A (2768 cm⁻¹), B (2619 cm⁻¹), and C (1912 cm⁻¹) are associated with ν_{OH} stretching vibrations of a hydroxyl group bonded by hydrogen bonds [20,35–37]. The bands A, B, and C are due to Fermi resonance between the ν_{OH} stretching vibration, the overtone of the out-of-plane bending vibrations 2γ_{OH}, and the combination of the out-of-plane γ_{OH} and in-plane δ_{OH} bending modes [38]. The formation of the amine salt results from the transfer phenomenon of a proton from the Lewis acid unit to the Lewis base. Bands at 1579 and 1380 cm⁻¹ are due to the out-of-phase and in-phase COO⁻ stretching vibrations of the carboxylate COO⁻ group, respectively [14,15].

The crystal structure of PyrHem×H₂O revealed that both O—H...OH₂ and C—O⁻...⁺H-N interactions exist (Figure 1). In the spectral range 500–900 cm⁻¹, the HB interaction leads to the formation of bands related to out-of-plane mode γ_{O-H...O} [39]. For PyrHem×H₂O, the hydroxyl O—H moiety of -COOH carboxylic groups interact with water molecules, forming O—H...O hydrogen bonds (Figure 2). The band at 897 cm⁻¹ was ascribed to out-of-plane O—H bending mode based on normal modes' theoretical calculations (see Table S1). A moderately intense, broad IR band at 951 cm⁻¹ is due to the O—H bending of the hydrogen-bonded hydroxyl group of the carboxylic moiety. Decreasing intensity of this γ_{O-H...O} band with temperature in IR spectra of PyrHem×H₂O was observed (Figure 11). At 303 K intensity ratio, I₇₇₀/I₉₅₁ is 4.03, at 343 K it is 5.18, and at 363 K it is 15.87, while at 373 K, the band at 951 cm⁻¹ is almost invisible. It means that the hydrogen bond between the hydroxyl group of the carboxylic moiety and water molecule is broken with increasing temperature.

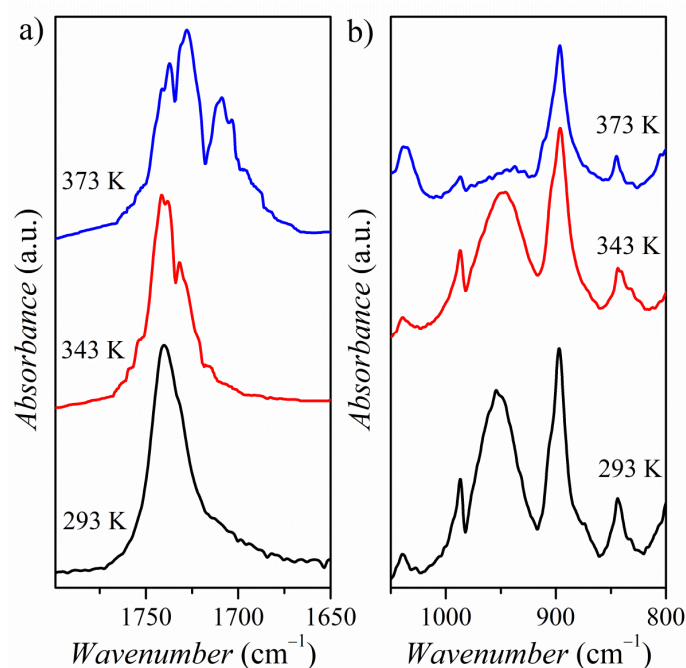


Figure 11. FT-IR absorption spectra of the PyrHem \times H₂O at 293, 343, and 373 K in spectral ranges: 1800–1650 cm⁻¹ (a) and 1100–800 cm⁻¹ (b).

Figure 11 shows the temperature evolution of the carbonyl band. The intense absorption band of the C=O group is present at 1737 cm⁻¹ at 293 K. Under the influence of temperature, the bandwidth broadening and a fine structure of the carbonyl band are revealed. There are two doublets: at 1741, 1737 cm⁻¹ and 1732, 1728 cm⁻¹. The temperature dependence of the positions of the bands 1737 and 1728 cm⁻¹ is presented in Figure 12. This variation in band position correlates very well with changes in activation energy in electrical conductivity measurements (Figure 9).

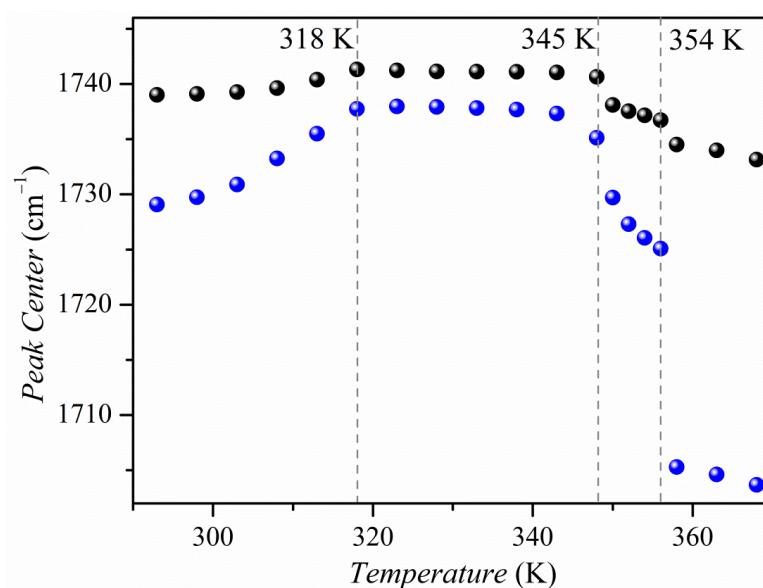


Figure 12. Temperature evolution of the position of the carbonyl bands 1737 (black spheres) and 1728 cm⁻¹ (blue spheres).

Moreover, the position of the band 1702 cm⁻¹ at high temperatures may indicate that carbonyl groups interact with water molecules. The theoretical calculations for Hem \times H₂O showed that the band associated with the C=O stretching vibration of the C=O group, which

interacts with a water molecule, should be observed around 1701 cm^{-1} . The observed splits of the carbonyl band in the IR spectrum of $\text{PyrHem}\times\text{H}_2\text{O}$ can be related to the phenomenon of involvement of the mobile water molecules in the electrical conductivity. Their diffusion process occurs within the dynamic network of hydrogen bonds, which may cause a non-equivalence in the carbonyl groups in the crystal lattice.

Figure 13a presents temperature-dependent Raman spectra of $\text{PyrHem}\times\text{H}_2\text{O}$ in a spectral range of $1800\text{--}1500\text{ cm}^{-1}$. The room temperature spectrum consists of a prominent band at 1760 cm^{-1} ($\nu_{\text{C=O}}$) and 1583 cm^{-1} ($\nu_{\text{C=C}}$). Above the 354 K , a new band at 1640 cm^{-1} arises (Figure 13a). According to theoretical calculations, it is due to the deformational vibration of the water molecule $\delta_{\text{O-H}}$. It may indicate that dynamic water molecules appear in the crystal lattice. This phenomenon influences the band's position and intensity associated with $\text{C}=\text{O}$ vibrations (Figure 13b,c).

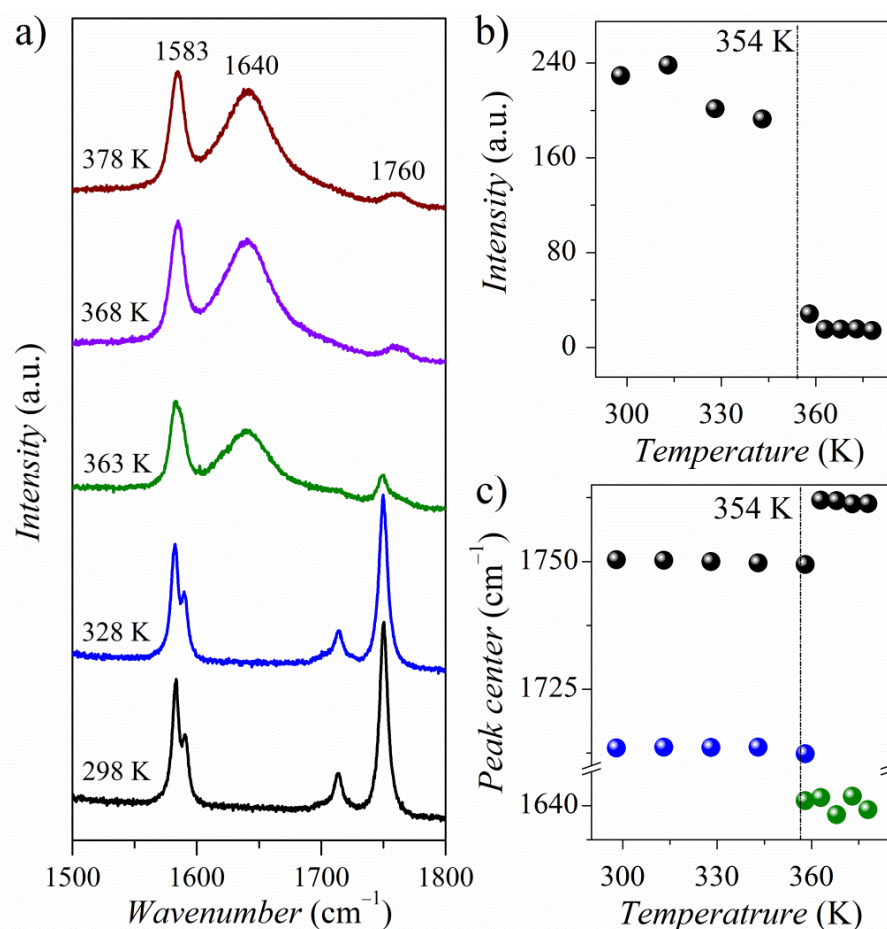


Figure 13. Temperature variation of Raman spectra of the $\text{PyrHem}\times\text{H}_2\text{O}$ (a), the temperature dependence of the intensity of the 1760 cm^{-1} band (b), and the temperature dependence of the positions of the Raman bands (c).

3. Materials and Methods

3.1. Experimental Section

3.1.1. Synthesis

Pyrazole (Pyr) (Sigma-Aldrich, purity 98%) and 1,2,3-benzenetricarboxylic acid hydrate ($\text{Hem}\times\text{H}_2\text{O}$) (Sigma-Aldrich, 98%) are dissolved separately in ethyl acetate (Merck KGaA, 99.8%). The mole ratio of pyrazole to acid amounts 1:1. The solutions were combined and mixed. The precipitate was isolated by filtration, washed out with cold ethyl acetate, and allowed to dry. Crystallization of the salt was carried out in ethyl acetate. The

crystals 1*H*-pyrazol-2-ium 2,6-dicarboxybenzoate monohydrate (1:1:1) (PyrHem×H₂O) formed were transparent plate, 5 mm in length and about 4 mm in thickness.

3.1.2. Crystal Structure Determination

Crystal data. C₁₂H₁₂N₂O₇, Mr = 296.24, monoclinic, space group C2/c, *a* = 31.2067(7), *b* = 11.7802(3), *c* = 6.8118(2) Å, β = 91.381(2)°, *V* = 2503.43(11) Å³, *Z* = 8, *D*_{calc} = 1.572 g/cm³, μ = 1.138 mm⁻¹, *T* = 293(2) K.

Data collection. A colorless pillar crystal (AcOEt) of 0.20×0.16×0.06 mm was used to record 13,154 (Cu *K* α -radiation, θ_{\max} = 76.68°) intensities on a Rigaku SuperNova Dual Atlas diffractometer [40] using mirror-monochromatized Cu *K* α radiation from a high-flux microfocus source (λ = 1.54184 Å). Accurate unit cell parameters were determined by least-squares techniques from the θ values of 5946 reflections, θ range 2.77–76.06°. The data were corrected for Lorentz polarization and for absorption effects [40]. The 2613 total unique reflections (*R*_{int} = 0.033) were used for structure determination.

Structure solution and refinement. The structure was solved by direct methods (SHELXS-97) [41] and refined against *F*² for all data (SHELXL) [42]. The positions of the H atoms bonded to N and O atoms were obtained from the difference Fourier maps and were refined freely. The remaining H atoms were placed geometrically in calculated positions. They were refined with a riding model, with C–H = 0.93 Å (*C*_{ar}H) and *U*_{iso}(H) = 1.2*U*_{eq}(C). Final refinement converged with *R* = 0.0530 (for 2392 data with *F*² > 4σ(*F*²)), *wR* = 0.1569 (on *F*² for all data), and *S* = 1.037 (on *F*² for all data). The largest difference peak and hole was 0.463 and −0.314 eÅ³. The molecular illustrations were drawn using ORTEP-3 for Windows [43]. The software used to prepare material for publication was WINGX [41], OLEX [44], and PLATON [45]. The supplementary crystallographic data are deposited at the Cambridge Crystallographic Data Centre (CCDC), 12 Union ROAD, Cambridge CB2 1EZ (UK) (phone, (+44) 1223/336-408; fax, (+44) 1223/336-033; e-mail, deposit@ccdc.cam.ac.uk; World Wide Web, <http://www.ccdc.cam.ac.uk>, accessed on 18 April 2021 (deposition no. CCDC 2091027)).

3.1.3. DSC/TGA Analysis

Thermogravimetric analyses (TGA) were performed on a Mettler Toledo Star TGA/DSC unit (Greifensee, Switzerland). Samples weighing 2–3 mg were placed in aluminum oxide crucibles and heated from 50 °C (323 K) to 900 °C (1173 K) at a 10 K min⁻¹ under an argon flow rate of 40 mL·min⁻¹. Differential scanning calorimetry (DSC) measurements were performed on a Mettler Toledo Star DSC system (Greifensee, Switzerland). A sample (2–3 mg) was placed in an aluminum crucible, sealed, and then heated from 25 °C (298 K) to 480 °C (753 K) at a heating rate of 10 K min⁻¹ under an argon flow rate of 40 mL·min⁻¹.

3.1.4. FT-IR and Raman Spectroscopy

Bruker Equinox 55 spectrometer connected with FT-IR Hyperion 2000 microscope was used to obtain FT-IR spectra in the spectral range from 450 to 4000 cm⁻¹. The spectral resolution equals 2 cm⁻¹. The spectra were measured using the KBr pellets technique. The Raman spectrum was recorded on a Jobin-Yvon HORIBA LabRAM HR 800 spectrometer equipped with a CCD detector. Raman spectra were recorded from 50 to 3700 cm⁻¹ with the excitation line λ_{ext} = 633 nm and the spectral resolution better than 2 cm⁻¹. The laser power was kept below 1 mW to avoid thermal and photochemical degradation of the sample. A cryostat made by Linkam Corp. was used to investigate the vibrational spectra versus temperature from 278 to 378 K.

3.1.5. Impedance Spectroscopy

The electric properties of the investigated materials were studied using the impedance spectroscopy method. Salt was powdered in the agate mortar. The received powder was pressed at room temperature under 30 MPa to form cylindrical pellets (~0.4 mm thick and ~5 mm in diameter). Next, the electrodes were placed at the proper surface using Hans

Wolbring GmbH silver paste. The real and imaginary parts of the electric impedance of the prepared samples were measured in the frequency range from 1 Hz to 10 MHz using the computer-controlled Alpha A High-Frequency Analyzer (Novocontrol GmbH). The temperature of the sample was stabilized by the Quatro Cryosystem with an accuracy of 0.1 K.

3.2. Computational Methods

The intermolecular interactions were analyzed using the Hirshfeld surface and fingerprint plots analysis. The calculations were carried out using the CrystalExplorer 3.0 program [46]. Normal mode calculations were performed with the Gaussian09 sets of codes [47]. The initial geometry of the pyrazolium hemimellitate was taken from X-ray data, and it was further applied in the geometry optimization. DFT methods with functional WB97XD [48] combined with the 6-311++G(d,p) standard basis set were used. Thus, the calculations were performed at WB97XD/6-311++G(d,p) level of approximation, including the vibrational frequencies. The results of optimizations correspond to energy minima since no imaginary frequencies were found. The method, as mentioned above, overestimates the calculated harmonic frequencies. For this reason, the scaling factors have been proposed in the literature to correct for anharmonicity. The predicted vibrational wavenumbers were scaled down by a single factor of 0.957. Gaussian output wfn files were used as inputs for the QTAIM program to calculate the topological properties of the salt. The bond critical points were located (BCPs and RCPs), and their properties, such as electron densities at critical points (ρ_{BCP} and ρ_{RCP}) and their Laplacians ($\nabla^2\rho_{\text{BCP}}$ and $\nabla^2\rho_{\text{RCP}}$), were calculated. The additional characteristics of BCPs were analyzed, such as total electron energy density at BCP (H_C) and its components, potential electron energy density (V_C), and kinetic electron energy density (G_C) [49].

4. Conclusions

In this paper, we examined the conductive, thermal, and spectroscopic properties of the new proton conductor, 1*H*-pyrazol-2-ium 2,6-dicarboxybenzoate monohydrate with a maximum conductivity of $8.2 \times 10^{-3} \text{ Sm}^{-1}$ at 388 K. The intermolecular interactions analysis shows that the dominant interactions in the investigated salts are hydrogen bonding. The hydrogen bond between the hydroxyl group of the carboxylic moiety and water molecule is broken with increasing temperature. Free water molecules appear in the crystal lattice. The process of proton diffusion takes place in a dynamic network of hydrogen bonds with the participation of water molecules.

Supplementary Materials: The following are available online. Figure S1: The molecular packing in the crystal $\text{PyrHem} \times \text{H}_2\text{O}$, showing sheets (layers) parallel to the *bc* plane. The H atoms not involved in hydrogen bonds have been omitted for clarity, Figure S2: Non-classic C-H...O hydrogen bonds linking types into layers parallel to the *bc* plane. The symmetry codes are explained in Table 1, Figure S3: $\pi \cdots \pi$ interactions between pyrazolium rings. The molecules are shown in two orthogonal projections. Hydrogen atoms have been omitted for clarity, Figure S4: TGA/DTG curves (top panel) and DSC curves (bottom panel) of $\text{Hem} \times \text{H}_2\text{O}$, Figure S5: TGA/DTG curves (top panel) and DSC curves (bottom panel) of Pyr, Figure S6: Scaled complex impedance plots $-Z''(Z')$ plot for the measured pyrazolium hemimellitate, Table S1: Experimental and calculated (WB97XD/6-311++G(d,p)) IR stretching and bending frequencies of the O-H, N-H, and C=O groups.

Author Contributions: Conceptualization, S.Z. and A.T.D.; synthesis, A.T.D.; IR measurements, S.Z. and A.P.; Raman measurements, A.P.; electrical conductivity measurements, P.L.; X-ray measurements, A.G.; DSC/TGA measurements, K.H.M.; intermolecular interaction analysis, S.Z. and A.P.; DFT calculations, A.M.; writing—original draft preparation, S.Z. and A.T.D.; writing—original final preparation, A.L.; supervision, A.L. All authors have read and agreed to the published version of the manuscript.

Funding: This research received no external funding.

Institutional Review Board Statement: Not applicable.

Informed Consent Statement: Not applicable.

Data Availability Statement: The data presented in this study are available on request from the corresponding author.

Acknowledgments: The research was financed from budget funds for science in 2017–2020 as a research project under the “Diamentowy Grant” program (Ministry of Science and Higher Education, DI2016 015846). Calculations were carried out at the Warsaw Supercomputer Center (ICM) (G53-7). Analyses were performed in the Centre of Synthesis and Analysis BioNanoTechno of the University of Białystok. The equipment in the Centre of Synthesis and Analysis BioNano-Techno of the University of Białystok was funded by EU, as a part of the Operational Program Development of Eastern Poland 2007–2013, project: POPW.01.03.00-20-034/09-00 and POPW.01.03.00-004/11.

Conflicts of Interest: The authors declare no conflict of interest.

Sample Availability: Samples of the compound 1*H*-pyrazol-2-ium 2,6-dicarboxybenzoate monohydrate are available from the authors.

References

- Wang, Y.; Chen, K.S.; Mishler, J.; Chan Cho, S.; Adroher, X.C. A review of polymer electrolyte membrane fuel cells: Technology, applications, and needs on fundamental research. *Appl. Energy* **2011**, *88*, 981–1007. [CrossRef]
- Li, Q.; Aili, D.; Savinell, R.F.; Jensen, J.O. Acid–Base Chemistry and Proton Conductivity. In *High-Temperature Polymer Electrolyte Membrane Fuel Cells*; Springer: Cham, Switzerland, 2016; pp. 37–57.
- Haile, S.M. Fuel cell materials and components. *Acta Mater.* **2003**, *51*, 5981–6000. [CrossRef]
- Ma, N.; Kosasang, S.; Yoshida, A.; Horike, S. Proton-conductive coordination polymer glass for solid-state anhydrous proton batteries. *Chem. Sci.* **2021**, *12*, 5818–5824. [CrossRef]
- Sunairi, Y.; Ueda, A.; Yoshida, J.; Suzuki, K.; Mori, H. Anisotropic Proton Conductivity Arising from Hydrogen-Bond Patterns in Anhydrous Organic Single Crystals, Imidazolium Carboxylates. *J. Phys. Chem. C* **2018**, *122*, 11623–11632. [CrossRef]
- Kreuer, K.D.; Fuchs, A.; Ise, M.; Spaeth, M.; Maier, J. Imidazole and pyrazole-based proton conducting polymers and liquids. *J. Electrochim. Acta* **1998**, *43*, 1281–1288. [CrossRef]
- Haile, S.M.; Boysen, D.A.; Chisholm, C.R.I.; Merle, R.B. Solid acids as fuel cell electrolytes. *Nature* **2001**, *410*, 910–913. [CrossRef]
- Chen, X.; Zhang, Y.; Ribeiorinha, P.; Li, H.; Kong, X.; Boaventura, M. A proton conductor electrolyte based on molten CsH₅(PO₄)₂ for intermediate-temperature fuel cells. *RSC Adv.* **2018**, *8*, 5225–5232. [CrossRef]
- Schmidt-Rohr, K.; Chen, Q. Parallel cylindrical water nanochannels in Nafion fuel-cell membranes. *Nat. Mater.* **2008**, *7*, 75–83. [CrossRef]
- Grubb, W.T.; Niedrach, L.W. Batteries with Solid Ion-Exchange Membrane Electrolytes: II. Low-Temperature Hydrogen-Oxygen Fuel Cells. *J. Electrochem. Soc.* **1960**, *107*, 131. [CrossRef]
- Mauritz, K.A.; Moore, R.B. State of Understanding of Nafion. *Chem. Rev.* **2004**, *104*, 4535–4586. [CrossRef]
- Pogorzelec-Glaser, K.; Garbarczyk, J.; Pawlaczyk, C.; Markiewicz, E. Electrical conductivity in new imidazolium salts of dicarboxylic acids. *Mater. Sci. Pol.* **2006**, *24*, 245.
- Higashino, T.; Ueda, A.; Yoshida, J.; Mori, H. Improved stability of a metallic state in benzothienobenzothiophene-based molecular conductors: An effective increase of dimensionality with hydrogen bonds. *Chem. Commun.* **2017**, *53*, 3426–3429. [CrossRef]
- Zięba, S.; Dubis, A.; Ławniczak, P.; Gzella, A.; Pogorzelec-Glaser, K.; Łapiński, A. Effect of counter ions on physical properties of imidazole-based proton conductors. *Electrochim. Acta* **2019**, *306*, 575–589. [CrossRef]
- Zięba, S.; Dubis, A.T.; Gzella, A.K.; Ławniczak, P.; Pogorzelec-Glaser, K.; Łapiński, A. Toward a new type of proton conductor based on imidazole and aromatic acids. *Phys. Chem. Chem. Phys.* **2019**, *21*, 17152–17162. [CrossRef] [PubMed]
- Farrington, G.C.; Briant, J.L. Fast Ionic Transport in Solids. *Science* **1979**, *204*, 1371–1379. [CrossRef] [PubMed]
- Howe, A.T.; Shilton, M.G. Studies of layered uranium(VI) compounds. I. High proton conductivity in polycrystalline hydrogen uranyl phosphate tetrahydrate. *J. Solid State Chem.* **1979**, *28*, 345–361. [CrossRef]
- Krishtalik, L.I. The mechanism of the proton transfer: An outline. *BBA-Bioenerg.* **2000**, *1458*, 6–27. [CrossRef]
- Widelicka, M.; Pogorzelec-Glaser, K.; Pietraszko, A.; Ławniczak, P.; Pankiewicz, R.; Łapiński, A. Order–disorder phase transition in an anhydrous pyrazole-based proton conductor: The enhancement of electrical transport properties. *Phys. Chem. Chem. Phys.* **2017**, *19*, 25653. [CrossRef]
- Zięba, S.; Mizera, A.; Pogorzelec-Glaser, K.; Łapiński, A. Proton conducting system (ImH₂)₂SeO₄·2H₂O investigated with vibrational spectroscopy. *Spectrochim. Acta Part A* **2017**, *180*, 224–233. [CrossRef] [PubMed]
- Phair, J.W.; Badwal, S.P.S. Review of proton conductors for hydrogen separation. *Ionics* **2006**, *12*, 103–115. [CrossRef]
- Vairam, S.; Govindarajan, S. New hydrazinium salts of benzene tricarboxylic and tetracarboxylic acids-preparation and their thermal studies. *Thermochim. Acta* **2004**, *414*, 263–270. [CrossRef]
- Gao, L.; Hu, Y.; Zhang, H.; Liu, Y.; Song, Z.; Dai, Y. DFT computational study on decarboxylation mechanism of salicylic acid and its derivatives in the anionic state. *J. Mol. Struct.* **2016**, *1116*, 56–61. [CrossRef]

24. Spackman, M.A.; McKinnon, J.J. Fingerprinting intermolecular interactions in molecular crystals. *CrystEngComm* **2002**, *4*, 378–392. [CrossRef]
25. Spackman, M.A.; Jayatilaka, D. Hirshfeld surface analysis. *CrystEngComm* **2009**, *11*, 19–32. [CrossRef]
26. Bader, R.F.W. *Atoms in Molecules A Quantum Theory*; Clarendon Press: Oxford, UK, 1994.
27. Matta, C.; Boyd, R.J. *Quantum Theory of Atoms in Molecule: Recent Progress in Theory and Application*; Wiley-VCH: New York, NY, USA, 2007.
28. Koch, U.; Popelier, P.L.A. Characterization of C-H-O Hydrogen Bonds on the Basis of the Charge Density. *J. Phys. Chem.* **1995**, *99*, 9747–9754. [CrossRef]
29. Rozas, I.; Alkorta, I.; Elguero, J. Behavior of ylides containing N, O, and C atoms as hydrogen bond acceptors. *J. Am. Chem. Soc.* **2000**, *122*, 11154–11161. [CrossRef]
30. Cremer, D.; Kraka, E. Chemical Bonds without Bonding Electron Density—Does the Difference Electron-Density Analysis Suffice for a Description of the Chemical Bond? *Angew. Chem. Int. Ed. Engl.* **1984**, *23*, 627. [CrossRef]
31. Jeziorski, B.; Moszynski, R.; Szalewicz, K. Perturbation Theory Approach to Intermolecular Potential Energy Surfaces of van der Waals Complexes. *Chem. Rev.* **1994**, *94*, 1887–1930. [CrossRef]
32. Grabowski, S.J. Hydrogen bonding strength—measures based on geometric and topological parameters. *J. Phys. Org. Chem.* **2004**, *17*, 18–31. [CrossRef]
33. Barsoukov, E.; Macdonald, J.R.J. (Eds.) *Impedance Spectroscopy Theory, Experiment and Applications*; Wiley & Sons: Hoboken, NJ, USA, 2005.
34. Dijk, T.; Burggraaf, A.J. Grain boundary effects on ionic conductivity in ceramic $Gd_xZr_{1-x}O_{2-(x/2)}$ solid solutions. *Phys. Stat. Sol. (A)* **1981**, *63*, 229–240. [CrossRef]
35. Baran, J.; Czaplak, Z.; Ilcyszyn, M.M.; Ratajczak, H. The infrared and polarized Raman spectra of ferroelectric $RbHSeO_4$. *Acta Phys. Pol. A* **1981**, *59*, 753–764.
36. Baran, J.; Czaplak, Z.; Ratajczak, H. Polarized infrared spectra of ferroelectric $RbHSeO_4$ single crystal. *Acta Phys. Pol. A* **1986**, *70*, 389–402.
37. Baran, J.; Barnes, A.J.; Marchewka, M.K.; Pietraszko, A.; Ratajczak, H. Structure and vibrational spectra of the bis(betaine)-selenic acid molecular crystal. *J. Mol. Struct.* **1997**, *416*, 33–42. [CrossRef]
38. Fillaux, F.; Marchon, B.; Novak, A.; Tomkinson, J. Proton dynamics in the hydrogen bond. Inelastic neutron scattering by single crystals of CsH_2PO_4 at 20 K. *Chem. Phys.* **1989**, *130*, 257–270. [CrossRef]
39. Grabowski, S.J. *Hydrogen Bonding—New Insights*; Springer: Dordrecht, The Netherlands, 2006.
40. *CrysAlis PRO, Version 1.171.38.46*; Rigaku Oxford Diffraction: Yarnton, UK, 2015.
41. Sheldrick, G.M. A short history of SHELX. *Acta Cryst.* **2008**, *64*, 112–122. [CrossRef]
42. Sheldrick, G.M. Crystal structure refinement with SHELXL. *Acta Cryst. Sect. C Struct. Chem.* **2015**, *71*, 3–8. [CrossRef]
43. Farrugia, L.J. WinGX and ORTEP for windows: An update. *J. Appl. Cryst.* **2012**, *45*, 849–854. [CrossRef]
44. Dolomanov, O.V.; Bourhis, L.J.; Gildea, R.J.; Howard, J.A.K.; Puschmann, H. OLEX2: A complete structure solution, refinement and analysis program. *J. Appl. Cryst.* **2009**, *42*, 339–341. [CrossRef]
45. Spek, A.L. Structure validation in chemical crystallography. *Acta Cryst. D* **2009**, *65*, 148–155. [CrossRef] [PubMed]
46. Wolff, S.K.; Grimwood, D.J.; McKinnon, J.J.; Turner, M.J.; Jayatilaka, D.; Spackman, M.A. *CrystalExplorer 3.1*; University of Western Australia: Perth, Australia, 2012.
47. Frisch, M.J.; Trucks, G.W.; Schlegel, H.B.; Scuseria, G.E.; Robb, M.A.; Cheeseman, J.R.; Scalmani, G.; Barone, V.; Mennucci, B.; Petersson, G.A.; et al. *Gaussian 09, Revision D.01*; Gaussian, Inc.: Wallingford, CT, USA, 2013.
48. Chai, J.D.; Head-Gordon, M. Systematic optimization of long-range corrected hybrid density functionals. *J. Chem. Phys.* **2008**, *128*, 084106. [CrossRef] [PubMed]
49. Todd, A.; Keith, T.K. *AIMALL, Version 10.05.04*; Gristmill Software: Overland Park, KS, USA, 2017.

Article

Solvatochromic Study of Two Carbanion Monosubstituted 4-Tolyl-1,2,4-triazol-1-ium Phenacylids in Binary Hydroxyl Solvent Mixtures [†]

Dana Ortansa Dorohoi ¹, Dan-Gheorghe Dimitriu ^{1,*}, Mihaela Maria Dulcescu-Oprea ^{1,2}, Ana Cezarina Morosanu ¹, Nicoleta Puica-Melnicuic ³, Elena Ardelean ³, Antonina Gritco-Todirascu ¹ and Corina Cheptea ⁴

¹ Faculty of Physics, Alexandru Ioan Cuza University, 700506 Iasi, Romania; ddorohoi@uaic.ro (D.O.D.); opreamihaelamaria@yahoo.com (M.M.D.-O.); cezarina_morosanu@yahoo.com (A.C.M.); antoninagritco@yahoo.com (A.G.-T.)

² Regional Institute of Oncology, 700483 Iasi, Romania

³ Faculty of Orthodox Theology, Alexandru Ioan Cuza University, 700066 Iasi, Romania; nicoleta.melnicuic@uaic.ro (N.P.-M.); elena.ardelean@uaic.ro (E.A.)

⁴ Department of Biomedical Sciences, Faculty of Biomedical Engineering, “Grigore T. Popa” University of Medicine and Pharmacy, 700454 Iasi, Romania; corina.cheptea@umfiiasi.ro

* Correspondence: dimitriu@uaic.ro; Tel.: +40-232-201183

[†] This work is dedicated to Professor Austin James Barnes, a great scientist and academic teacher, who strongly encouraged the field of molecular structure and molecular spectroscopy, on the occasion of his 75th birthday.

Citation: Dorohoi, D.O.; Dimitriu, D.-G.; Dulcescu-Oprea, M.M.; Morosanu, A.C.; Puica-Melnicuic, N.; Ardelean, E.; Gritco-Todirascu, A.; Cheptea, C. Solvatochromic Study of Two Carbanion Monosubstituted 4-Tolyl-1,2,4-triazol-1-ium Phenacylids in Binary Hydroxyl Solvent Mixtures. *Molecules* **2021**, *26*, 3910. <https://doi.org/10.3390/molecules26133910>

Academic Editors: Rui Fausto, Sylvia Turrell and Gulce Ogruc Ildiz

Received: 20 May 2021

Accepted: 23 June 2021

Published: 26 June 2021

Publisher’s Note: MDPI stays neutral with regard to jurisdictional claims in published maps and institutional affiliations.



Copyright: © 2021 by the authors. Licensee MDPI, Basel, Switzerland. This article is an open access article distributed under the terms and conditions of the Creative Commons Attribution (CC BY) license (<https://creativecommons.org/licenses/by/4.0/>).

Abstract: Two 4-tolyl-1,2,4-triazol-1-ium methylids, namely 4-tolyl-1,2,4-triazol-1-ium-phenacylid and 4-tolyl-1,2,4-triazol-1-ium-4'-nitro-phenacylid, are studied from solvatochromic point of view in binary solvent mixtures of water with ethanol and water with methanol. The contributions (expressed in percent) of the universal and specific interactions are separated from the spectral shifts recorded in the visible range for each composition of the binary solvent mixture. The essential role of the orientation and induction interactions in the studied solutions was demonstrated. Based on the statistic cell model of the binary solvent mixture solutions, the difference between the formation energies of ylid-water and ylid-alcohol complexes is estimated. The composition of the ylid’s first solvation shell was also established using the model of the binary solvent mixture solutions. The results obtained from the statistical cell model were compared with those obtained by using the Suppan’s model, resulting a good agreement.

Keywords: carbanion monosubstituted 4-tolyl-1,2,4-triazol-1-ium phenacylids; solvatochromism; hydroxylic solutions; interaction energy in molecular pairs ylid-water and ylid-alcohol

1. Introduction

Ylids are chemical compounds having a molecule containing a negatively charged carbon atom (called carbanion) directly bonded to a positively charged atom of nitrogen, phosphorus, sulfur, or another element [1,2]. The result can be seen as a structure in which two adjacent atoms are connected by both a covalent and an ionic bond. Thus, the ylids are a subclass of zwitterionic compounds.

Two carbanion monosubstituted triazolium ylids [1,2], namely 4-tolyl-1,2,4-triazol-1-ium phenacylid (TTPY) and 4-tolyl-1,2,4-triazol-1-ium-4'-nitro-phenacylid (TTNPY) are considered in this study as spectrally active molecules. These are dipolar and polarizable molecules with zwitterionic character, having opposite charges separated on one nitrogen of the triazolium cycle and on the negative, monosubstituted carbanion, respectively. Figure 1 shows the chemical structure of the two compounds.

The pharmacological activity and clinical implications of triazolium agents were emphasized in some reviews [3,4]. The chemical and biological applications of triazolium ylids or of their derivatives were also analyzed in numerous publications [5–9].

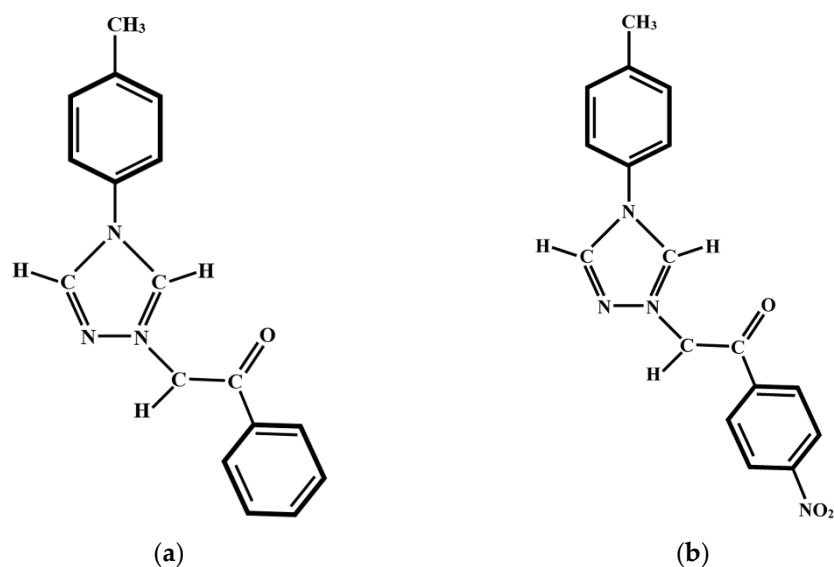


Figure 1. Chemical structure of 4-tolyl-1,2,4-triazol-1-ium phenacylid (TTPY) (a) and 4-tolyl-1,2,4-triazol-1-ium-4'-nitro-phenacylid (TTNPY) (b) molecules.

The knowledge about the interactions of triazolium ylids with different solvents are important because all reactions of these compounds take place in situ. Previous studies revealed the nature of the intermolecular interactions of some cycloimmonium ylids with the liquids in which they are dissolved, based on the solvatochromic analysis of their visible band and very sensitive to the solvent action [10–12].

Taking into account the basic character of cycloimmonium ylids and the solvatochromic analysis, this results in their affinity to form hydrogen bonds with hydroxylic molecules by acceptance of protons. The study of binary solvent mixture solutions of some cycloimmonium ylids can offer the opportunity to characterize the strength of the hydrogen bond between the ylid and hydroxylic solvent molecules, as it was made in previous studies for another ylids [11,12].

1,2,4-Triazolium methylids belong to cycloimmonium class and are basic compounds. They show a visible electronic absorption band [13–17], relatively sensible to the solvent action. As it is known [13,14], triazolium ylids are a few soluble in most of the solvents. Therefore, one solvatochromic study of these molecules in a great number of liquids is practically impossible. They were studied in a few numbers of solvents and in some binary solvent mixtures made by one hydroxylic and one non-hydroxylic liquids [14–17]. 1,2,4-Triazolium methylids are relatively soluble in water and alcohols, and their spectral study in binary solvent mixtures realized from water and one primary alcohol becomes interesting.

The spectral UV-Vis data are very important for understanding the behavior of the ylids in biomedical processes, i.e., for their applications. For example, in quantum mechanics, the biological properties of a substance are correlated with the energy gap $\Delta E = hc\bar{\nu}$ where $\bar{\nu}$ is the wavenumber corresponding to the maximum of the electronic absorption band of the molecule. For small values of ΔE , the substances are more reactive.

In this spectral study, we intend to apply the statistical cell model of binary solvent mixture solutions to the solutions of 1,2,4-Triazolium methylids in mixtures water (1) + ethanol (2), both liquids being of biological interest. For comparison, we added the similar solvatochromic study for the same ylids in binary solvent mixture water (1) + methanol (2).

2. Calculations and Models

The Kamlet–Abboud–Taft (KAT) parameters [18,19] are known for water and the primary alcohols and for their mixtures [20], and can be used in solvatochromic studies. Such study is difficult to achieve because the binary solvent mixtures were made step by step with a 0.05 molar fraction and the solubility of the studied ylid is reduced even in the

mixtures of water and different alcohols, but it can offer information about the structure of the binary solvent mixture solutions of the studied ylids.

The solvatochromic analysis in binary solvent mixture solutions offers information about the nature of the intermolecular interactions between the solute and solvent molecules and about the composition of the first shell of the solute molecules.

Some correlations [21–23] between the wavenumber in the maximum of the electronic absorption band and the solvent parameters, such as the hydrogen bond donor (HBD, noted by α), hydrogen bond acceptor (HBA, noted by β), and polarity/dipolarity number (π^*), known as KAT parameters, were established:

$$\bar{\nu}(\text{cm}^{-1}) = \bar{\nu}_0(\text{cm}^{-1}) + C_1\pi^* + C_2\alpha + C_3\beta \quad (1)$$

The correlation coefficients $\bar{\nu}_0$ and C_1 – C_3 in Equation (1) can be estimated by statistical analysis of the experimental data. They give by their sign and value the sense and the contribution of intermolecular interactions to the electronic absorption band shift in solutions relative to its position in the gaseous phase of the ylid. The contribution of each type of intermolecular interactions to the spectral shift in each binary solvent mixture can also be established based on the values obtained for the regression coefficients C_1 – C_3 and the values of the solvent parameters.

The obtained results in this research can also be judged on the basis of the statistical cell model of the binary solvent mixture solutions [24–29]. In the binary solvent mixture solutions studied by us, the ylid molecules can participate in hydrogen bonds with both solvents, but the formation energies of the complexes differ for the molecules of water, ethanol, or methanol.

In the statistical cell model, the wavenumber $\bar{\nu}$ (cm^{-1}) in the maximum of the absorption band can be computed using the relative statistical average weights p_1 and p_2 , being $p_1 + p_2 = 1$, of the binary solvent mixture (made by water (1) considered the most active solvent and ethanol/methanol (2) considered the less active solvent) [24,25].

$$\bar{\nu}_t = p_1\bar{\nu}_1 + (1 - p_1)\bar{\nu}_2 \quad (2)$$

In relation (2), the indices t , 1, and 2 refer to binary solvent mixtures and binary solutions made in solvent (1) and (2), respectively. Relation (2) shows that the average statistic weights p_1 and p_2 of the two liquids in the first solvation shell of ylid can be computed using the wavenumbers in the maximum of the visible electronic band in binary solvent mixture solution at each molar fractions x_1 and x_2 , being $x_1 + x_2 = 1$, of the binary solvent mixture. Knowing the bulk molar fractions x_1 and x_2 of the two solvents in the mixture, the statistic cell model permits to compute the average statistic weights, p_1 and p_2 , and to establish the following relation between these parameters [24–28]:

$$\ln \frac{p_1}{1 - p_1} = \ln \frac{x_1}{1 - x_1} + n \quad (3)$$

In relation (3) the cut at origin n depends on the difference $w_2 - w_1$ between the interactions in molecular pairs of the type: ylid–water and ylid–alcohol. This dependence is given in relation (4), where k is the Boltzmann constant and T is the absolute temperature:

$$n = \frac{w_2 - w_1}{kT} \quad (4)$$

Based on the cell statistic model of the binary solvent mixture solutions, the difference $w_2 - w_1$ can be estimated using the spectral data [26–28]. This difference is hard to determine with other methods in common laboratories.

The statistical cell model of the binary solvent mixture solutions allows the estimation of the composition of the ylid first shell in the binary solvent mixture solution by the parameter $\delta_1 = p_1 - x_1$, called the excess function of solvent (1) in the first solvation shell,

or by $K_{12} = \frac{p_1 x_2}{p_2 x_1}$, called the preferential solvation constant [29]. When $\delta_1 > 0$, or $K_{12} > 1$, the active solvent noted by (1) is dominant in the first shell of the solute, while the solvent (2) is predominant in the first solvation shell of the solute when the inequalities are inverse.

Similar to the statistical cell model, the model of Suppan [30–32] describes the preferential solvation of solutes in binary solvent mixtures, being frequently approached in the last years [33–36]. The basic idea is that, in a binary solvent mixture, the dipolar solute will be preferentially solvated by the most dipolar solvent. Consequently, the mole fraction in the cybotactic region will be higher for this solvent, i.e., the mole fractions of the two solvents in the cybotactic region differ from those ones in the bulk solution. The ratio of the mole fractions in the cybotactic region (y_2/y_1) is proportional to the ratio of the mole fractions in the bulk solution (x_2/x_1) according to Equation (5):

$$\frac{y_2}{y_1} = \frac{x_2}{x_1} e^{-Z} \quad (5)$$

In the above equation, Z is the so-called index of preferential solvation [37], and it can be estimated from spectrochemical data through the next equation:

$$\frac{1}{\Delta E_{CT}} = -\frac{2a^3}{\mu^2 \Delta \varphi(\varepsilon)_{1-2}} \left(1 + \frac{x_2}{x_1} e^{-Z} \right) \quad (6)$$

where

$$\varphi(\varepsilon) = \frac{2(\varepsilon - 1)}{2\varepsilon + 1} \quad (7)$$

and ε is the dielectric constant, $\Delta E_{CT} = hc(\bar{\nu}_t - \bar{\nu}_2)$ is the inverse peak shift (measured against the peak position corresponding to the solvent 2), and μ and a are the dipole moment and the molecular radius of the solute molecule, respectively.

If the specific solute–solvent interactions have a negligible contribution to the solvatochromism, the graphic representation of $1/\Delta E_{CT}$ versus x_2/x_1 will be a straight line. On the contrary, if the specific interactions are important, the graphical representation will show large deviations from linearity [30–36].

Such studies offer a better understanding of the mechanisms of intermolecular interactions in binary solvent mixtures.

3. Results and Discussion

Figure 2 shows the spectra of TTPY and TTNPY in water, ethanol, methanol, and water + acetic acid, respectively. The quenching of the visible electronic absorption band in the presence of the acetic acid proves that this band appears by $n \rightarrow \pi^*$ transitions of the non-participant electron pair of the carbanion towards the heterocycle or towards the carbanion substituent.

The binary solvent mixtures parameters polarity/polarizability, π^* (characterizing the universal interactions between the solute molecule and all solvent molecules), HBD number α , and HBA number β (characterizing the specific interactions of the hydrogen bond type by donating and receiving proton by a solvent molecule, respectively) determined by Buhvestov et al. [20], as well as the measured wavenumbers in the maximum of the visible bands of TTPY and TTNPY, are listed in Tables 1 and 2 for the binary hydroxylic solvent mixtures: water (1) + ethanol (2) and water (1) + methanol (2), in various water molar concentrations, x_1 .

An increase in the wavenumber of the visible band of the studied ylids (TTPY and TTNPY) is emphasized in Tables 1 and 2 when the water content increases in the binary solvent mixture water (1) + alcohol (2), both for the solvent achieved with ethanol and methanol. The same tendency has been observed in the binary solvent mixture solutions of the carbanion monosubstituted *p*-phenyl-triazol-1-ium ylids [23]. This tendency could be explained by the increase of the electric permittivity of the binary solvent mixture when

its content in water increases, determining the increase of the universal interactions of the orientation–induction type in solutions.

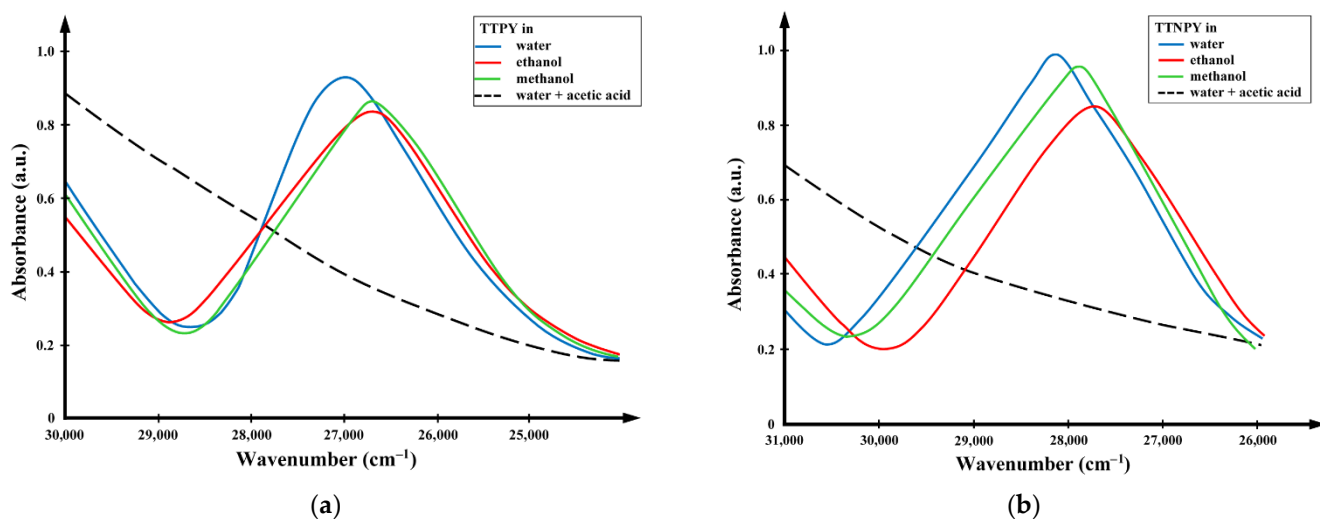


Figure 2. Spectra of 4-tolyl-1,2,4-triazol-1-ium phenacylid (TTPY) (a) and 4-tolyl-1,2,4-triazol-1-ium-4'-nitro-phenacylid (TTNPY) (b) in water, ethanol, methanol, and water + acetic acid, respectively.

Table 1. Molar water composition (x_1), Kamlet–Abboud–Taft parameters (π^* , β , α) of binary solvent mixture water (1) + ethanol (2) [20], and wavenumbers ($\bar{\nu}$ (cm^{-1})) in the maximum of the visible electronic absorption band of 4-tolyl-1,2,4-triazol-1-ium phenacylid (TTPY) and 4-tolyl-1,2,4-triazol-1-ium-4'-nitro-phenacylid (TTNPY), respectively.

x_1	π^*	α	β	$\ln \frac{x_1}{1-x_1}$	$\bar{\nu}$		$\ln \frac{p_1}{1-p_1}$	
					TTPY	TTNPY	TTPY	TTNPY
0.000	0.51	0.98	0.83	-	26,670	27,690	-	-
0.050	0.54	0.97	0.83	-2.94	26,680	27,720	-3.56	-2.56
0.100	0.57	0.96	0.84	-2.20	26,690	27,748	-2.83	-1.83
0.150	0.60	0.94	0.83	-1.73	26,700	27,778	-2.40	-1.33
0.200	0.63	0.93	0.83	-1.39	26,718	27,810	-1.87	-0.92
0.250	0.65	0.93	0.83	-1.10	26,730	27,840	-1.61	-0.59
0.300	0.68	0.92	0.82	-0.85	26,748	27,868	-1.29	-0.31
0.350	0.70	0.91	0.81	-0.62	26,760	27,896	-1.10	-0.04
0.400	0.73	0.91	0.8	-0.41	26,780	27,920	-0.82	0.19
0.450	0.75	0.89	0.79	-0.20	26,800	27,940	-0.57	0.39
0.500	0.77	0.90	0.79	0.00	26,818	27,958	-0.36	0.57
0.550	0.80	0.89	0.78	0.20	26,830	27,980	-0.22	0.80
0.600	0.82	0.89	0.77	0.41	26,850	28,000	0.00	1.04
0.650	0.85	0.89	0.77	0.62	26,877	28,020	0.30	1.30
0.700	0.90	0.88	0.74	0.85	26,898	28,038	0.55	1.58
0.750	0.94	0.86	0.71	1.10	26,920	28,040	0.82	1.61
0.800	1.00	0.87	0.67	1.39	26,940	28,066	1.10	2.15
0.825	1.03	0.87	0.66	1.55	26,950	28,070	1.25	2.25
0.850	1.06	0.90	0.64	1.73	26,964	28,080	1.49	2.56
0.875	1.09	0.92	0.61	1.95	26,978	28,088	1.78	2.90
0.900	1.11	0.97	0.59	2.20	26,988	28,090	2.02	3.00
0.925	1.12	1.03	0.56	2.51	26,995	28,095	2.23	3.30
0.950	1.13	1.11	0.54	2.94	27,008	28,102	2.73	3.94
0.975	1.13	1.18	0.52	3.66	27,012	28,105	2.94	4.42
1.000	1.13	1.26	0.5	-	27,030	28,110	-	-

Table 2. Molar water composition (x_1), Kamlet–Abboud–Taft parameters (π^* , β , α) of binary solvent mixture water (1) + methanol (2) [20], and wavenumbers ($\bar{\nu}$ (cm^{-1})) in the maximum of the visible electronic absorption band of 4-tolyl-1,2,4-triazol-1-ium phenacylid (TTPY) and 4-tolyl-1,2,4-triazol-1-ium-4'-nitro-phenacylid (TTNPY), respectively.

x_1	π^*	α	β	$\ln \frac{x_1}{1-x_1}$	$\bar{\nu}$		$\ln \frac{p_1}{1-p_1}$	
					TTPY	TTNPY	TTPY	TTNPY
0.000	0.58	1.14	0.74	-	26,710	27,890	-	-
0.050	0.61	1.13	0.74	-2.94	26,738	27,908	-2.34	-2.42
0.100	0.64	1.12	0.74	-2.20	26,758	27,922	-1.73	-1.77
0.150	0.66	1.10	0.74	-1.73	26,780	27,938	-1.27	-1.28
0.200	0.70	1.09	0.74	-1.39	26,800	27,950	-0.94	-0.98
0.250	0.73	1.07	0.74	-1.10	26,820	27,962	-0.65	-0.72
0.300	0.76	1.06	0.74	-0.85	26,840	27,979	-0.38	-0.39
0.350	0.78	1.04	0.72	-0.62	26,860	27,986	-0.13	-0.26
0.400	0.82	1.04	0.72	-0.41	26,880	28,000	0.13	0.00
0.450	0.85	1.02	0.71	-0.20	26,898	28,016	0.35	0.29
0.500	0.88	1.03	0.7	0.00	26,910	28,024	0.51	0.44
0.550	0.91	1.02	0.68	0.20	26,928	28,038	0.76	0.72
0.600	0.95	1.01	0.66	0.41	26,940	28,050	0.94	0.98
0.650	0.98	1.01	0.65	0.62	26,952	28,060	1.13	1.22
0.700	1.01	1.01	0.63	0.85	26,968	28,070	1.43	1.50
0.750	1.04	1.02	0.61	1.10	26,982	28,080	1.73	1.85
0.800	1.06	1.06	0.59	1.39	26,996	28,086	2.13	2.10
0.825	1.08	1.07	0.58	1.55	27,000	28,088	2.27	2.20
0.850	1.09	1.09	0.56	1.73	27,008	28,092	2.61	2.42
0.875	1.10	1.12	0.55	1.95	27,012	28,098	2.82	2.85
0.900	1.11	1.13	0.54	2.20	27,016	28,100	3.08	3.04
0.925	1.11	1.17	0.52	2.51	27,022	28,104	3.66	3.57
0.950	1.12	1.19	0.52	2.94	27,024	28,106	3.96	3.99
0.975	1.12	1.22	0.51	3.66	27,026	28,107	4.37	4.28
1.000	1.14	1.23	0.49	-	27,030	28,110	-	-

The experimental data from Tables 1 and 2 were subjected to statistical analysis based on relation (1), and the coefficients multiplying the solvent parameters were estimated (see Table 3) by using the application Multiple Linear Regression from OriginPro 9 software. The coefficients C_j and $j = 1,2,3$, multiplying the solvent parameters π^* , α , and β , are listed in Table 3. They give by their value and sign the magnitude and the sense of the spectral shifts induced by the binary solvent mixture in the visible electronic spectra of the studied ylids. As relation (1) suggests, the sign plus of the correlation coefficients reflects a spectral shift to high wavenumbers (blue shift) in the electronic spectra. All coefficients are positive, showing a hypsochromic effect both of universal interactions (described by the π^* , the polarity/polarizability parameter of the solvent) and of the specific interactions (described by the solvent parameters α and β) [21–23]. This tendency has been observed in other binary hydroxylic solvent mixture solutions of some cycloimmonium ylids [22,38].

Table 3. Regression parameters in relation $\bar{\nu}(\text{cm}^{-1}) = \bar{\nu}_0(\text{cm}^{-1}) + C_1\pi^* + C_2\alpha + C_3\beta$ and the regression coefficient (R) for the binary solvent mixtures solutions of 4-tolyl-1,2,4-triazol-1-ium phenacylid (TTPY) and 4-tolyl-1,2,4-triazol-1-ium-4'-nitro-phenacylid (TTNPY), respectively, with parameters from Tables 1 and 2.

Binary Solvent Mixture	Ylid	$\bar{\nu}_0 \pm \Delta \bar{\nu}_0$	$C_1 \pm \Delta C_1$	$C_2 \pm \Delta C_2$	$C_3 \pm \Delta C_3$	R
Water + Ethanol	TTPY	25,949 \pm 231	696 \pm 72	108 \pm 63	291 \pm 160	0.99178
Water + Ethanol	TTNPY	24,915 \pm 310	1485 \pm 96	450 \pm 84	1880 \pm 214	0.98811
Water + Methanol	TTPY	25,583 \pm 171	804 \pm 47	187 \pm 54	612 \pm 112	0.99179
Water + Methanol	TTNPY	27,279 \pm 99	511 \pm 27	79 \pm 31	309 \pm 65	0.99806

Based on relation (1), the values of the regression coefficients from Table 3, and the binary solvent mixture parameters from Tables 1 and 2, the contribution (expressed in percent) of each type of intermolecular interaction to the spectral shift can be estimated. The results of computations are listed in Tables 4 and 5.

Table 4. Contribution of each type of interaction in solutions of 4-tolyl-1,2,4-triazol-1-ium phenacylid (TPPY) in the binary hydroxylic solvents mixtures.

x_1	Water + Ethanol			Water + Methanol		
	$C_1\pi^*$ (%)	$C_2\alpha$ (%)	$C_3\beta$ (%)	$C_1\pi^*$ (%)	$C_2\alpha$ (%)	$C_3\beta$ (%)
0.000	50.54	15.07	34.39	41.18	18.85	39.96
0.050	52.04	14.51	33.45	42.48	18.33	39.19
0.100	53.26	13.92	32.82	43.72	17.82	38.45
0.150	54.90	13.35	31.76	44.62	17.32	38.06
0.200	56.18	12.87	30.95	46.15	16.74	37.11
0.250	56.95	12.64	30.41	47.34	16.16	36.50
0.300	58.34	12.25	29.41	48.42	15.73	35.86
0.350	59.33	11.97	28.71	49.69	15.43	34.88
0.400	60.54	11.71	27.75	50.94	15.05	34.02
0.450	61.55	11.33	27.11	52.22	14.60	33.18
0.500	62.10	11.26	26.64	53.26	14.52	32.22
0.550	63.28	10.92	25.80	54.66	14.27	31.07
0.600	64.06	10.79	25.15	56.30	13.94	29.75
0.650	64.88	10.54	24.58	57.32	13.76	28.92
0.700	66.86	10.15	22.99	58.57	13.64	27.79
0.750	68.60	9.74	21.67	59.72	13.64	26.64
0.800	70.66	9.54	19.80	60.38	14.06	25.56
0.825	71.48	9.37	19.15	61.00	14.08	24.92
0.850	72.24	9.52	18.24	61.59	14.34	24.07
0.875	73.26	9.60	17.14	61.83	14.66	23.51
0.900	73.64	9.99	16.37	62.22	14.75	23.02
0.925	73.98	10.56	15.47	62.43	15.33	22.24
0.950	73.95	11.27	14.78	62.48	15.46	22.06
0.975	73.83	11.96	14.21	62.50	15.86	21.65
1.000	73.63	12.74	13.62	63.36	15.92	20.72

Table 5. Contribution of each type of interaction in solutions of 4-tolyl-1,2,4-triazol-1-ium-4'-nitrophenacylid (TTNPY) in binary hydroxylic solvents mixtures.

x_1	Water + Ethanol			Water + Methanol		
	$C_1\pi^*$ (%)	$C_2\alpha$ (%)	$C_3\beta$ (%)	$C_1\pi^*$ (%)	$C_2\alpha$ (%)	$C_3\beta$ (%)
0.000	27.45	15.98	56.57	48.22	14.58	37.21
0.050	28.65	15.60	55.76	49.54	14.11	36.35
0.100	29.62	15.12	55.27	50.80	13.67	35.53
0.150	30.99	14.72	54.29	51.69	13.25	35.05
0.200	32.10	14.36	53.54	53.22	12.75	34.03
0.250	32.78	14.21	53.00	54.39	12.26	33.35
0.300	34.05	13.96	51.99	55.45	11.90	32.65
0.350	34.97	13.78	51.25	56.71	11.63	31.66
0.400	36.16	13.66	50.18	57.93	11.30	30.77
0.450	37.13	13.35	49.52	59.18	10.92	29.90
0.500	37.69	13.35	48.96	60.20	10.84	28.96
0.550	38.88	13.11	48.00	61.56	10.61	27.82
0.600	39.71	13.06	47.22	63.14	10.33	26.53
0.650	40.58	12.88	46.55	64.12	10.16	25.72
0.700	42.78	12.68	44.54	65.31	10.05	24.64
0.750	44.77	12.41	42.82	66.42	10.02	23.56
0.800	47.35	12.48	40.17	67.09	10.32	22.59
0.825	48.37	12.38	39.25	67.70	10.32	21.99
0.850	49.46	12.73	37.81	68.28	10.50	21.22
0.875	50.91	13.02	36.07	68.54	10.73	20.73
0.900	51.60	13.67	34.73	68.93	10.79	20.28
0.925	52.31	14.58	33.12	69.18	11.22	19.60
0.950	52.55	15.64	31.80	69.24	11.32	19.44
0.975	52.65	16.66	30.68	69.30	11.61	19.09
1.000	52.68	17.80	29.52	70.13	11.64	18.23

If the data from Tables 4 and 5 are plotted in bidimensional graphs versus the water molar concentration, one obtains Figures 3 and 4 for the two binary solvent mixtures: water + ethanol and water + methanol.

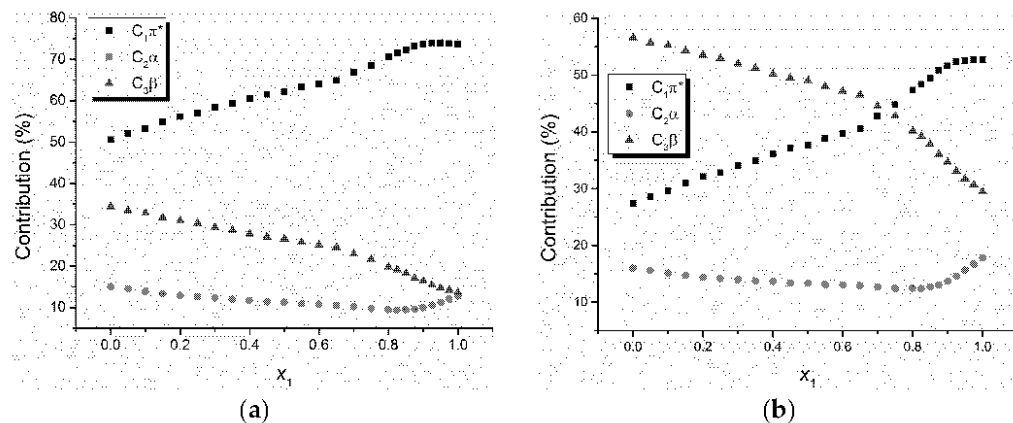


Figure 3. The contribution (percentage) to the spectral shift of universal and specific interactions for 4-tolyl-1,2,4-triazol-1-ium phenacylid (TTPY) (a) and 4-tolyl-1,2,4-triazol-1-ium-4'-nitro-phenacylid (TTNPY) (b) in binary solvent mixture water + ethanol.

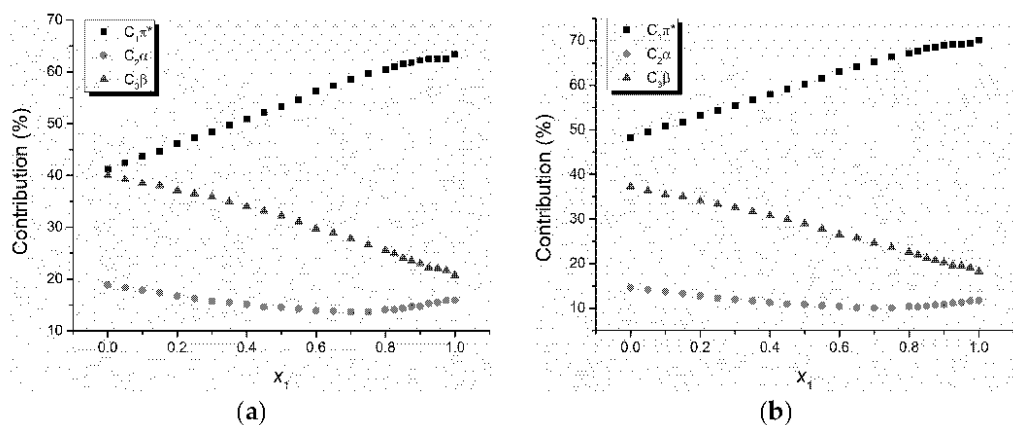


Figure 4. The contribution (percentage) to the spectral shift of universal and specific interactions for 4-tolyl-1,2,4-triazol-1-ium phenacylid (TTPY) (a) and 4-tolyl-1,2,4-triazol-1-ium-4'-nitro-phenacylid (TTNPY) (b) in binary solvent mixture water + methanol.

The universal interactions determine the highest shift of the visible electronic absorption band of the studied triazolium ylids in most of the studied solutions, except for the solution TTNPY + water + ethanol, where the specific interactions described by the term $C_3\beta$ are dominant for small values of the water content ($x_1 = 0-0.7$). The contribution of the universal interactions (described by the term $C_1\pi^*$ in relation (1)) increases with the water content in the binary solvent mixture (Figures 3 and 4). The specific interactions described by the term $C_2\alpha$ were the weakest. They contributed to the spectral shift of the visible electronic absorption band by a percent smaller than 20%. This observation could be explained by the fact that in all studied solutions, the ylid molecules (TTPY and TTNPY) formed complexes by hydrogen bonding. Though the probability of the hydrogen bonds in which the solvent receives protons from ylid (described by the term $C_3\beta$) is small (except for the solution TTNPY + water + ethanol for $x_1 = 0-0.7$), the contribution of these interactions to the total spectral shift is more important than the contribution of the specific interactions in which the ylid molecules (TTPY and TTNPY) receive protons. The contribution of the term $C_3\beta$ to the spectral shift of TTPY and TTNPY visible absorption bands decreased with the increase of the water content in the binary solvent mixture.

The decrease of the contribution of specific interactions to the total spectral shift at a high content of water in binary solvent mixture solutions of triazolium methylids has been explained by the presence of water complexes formed in these solutions [20].

The cell model of the binary solvent mixture solutions applied to the studied tolyl-triazol-1-ium phenacylids offers information about the difference between the potential energies in molecular pairs of the type ylid-water and ylid-alcohol. The dependences $\ln \frac{p_1}{1-p_1}$ vs. $\ln \frac{x_1}{1-x_1}$ are illustrated in Figures 5 and 6.

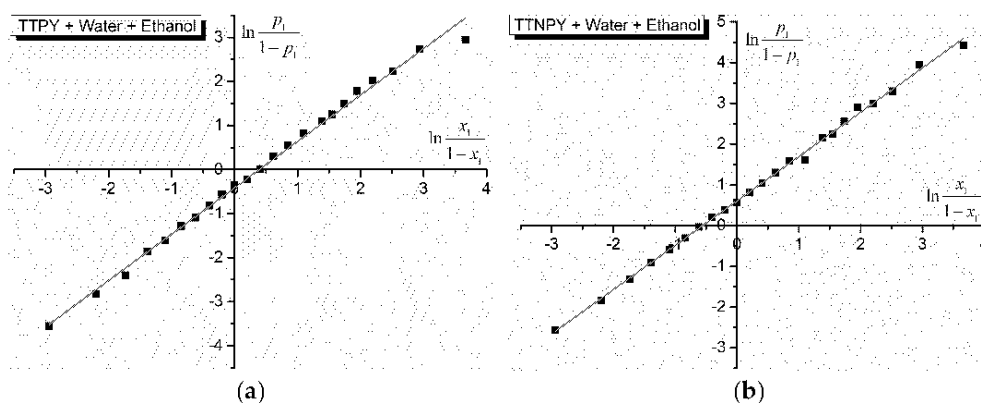


Figure 5. $\ln \frac{p_1}{1-p_1}$ vs. $\ln \frac{x_1}{1-x_1}$ for 4-tolyl-1,2,4-triazol-1-ium phenacylid (TTPY) (a) and 4-tolyl-1,2,4-triazol-1-ium-4'-nitro-phenacylid (TTNPY) (b) in binary solvent mixture water (1) + ethanol (2).

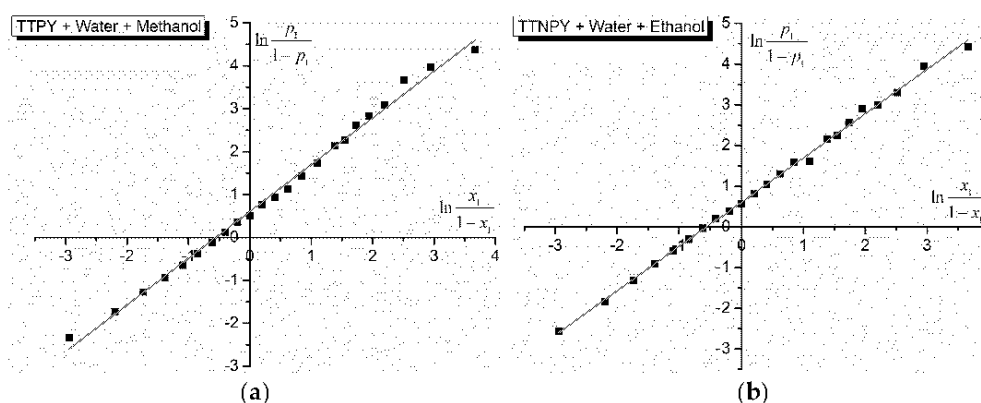


Figure 6. $\ln \frac{p_1}{1-p_1}$ vs. $\ln \frac{x_1}{1-x_1}$ for 4-tolyl-1,2,4-triazol-1-ium phenacylid (TTPY) (a) and 4-tolyl-1,2,4-triazol-1-ium-4'-nitro-phenacylid (TTNPY) (b) in binary solvent mixture water (1) + methanol (2).

The characteristics of the lines in Figures 5 and 6, obtained by using the application Linear Fit from OriginPro 9 software, are given in Table 6. The slopes of the lines (3) are near the unity, as the cell model of the binary solvent mixture solutions predicts. The cut at origin gives the strength of the hydrogen bonds in the studied solutions by the difference $w_2 - w_1$ between the formation energies of the complexes ylid (TTPY/TTNPY)-water and ylid (TTPY/TTNPY)-alcohol. In the last column of Table 6, this difference is expressed in kJ/mol. The values from Table 6 show weak differences between the formation energies of hydrogen bonds between TTPY/TTNPY and the hydroxylic components of the solution [11,17,25]. Similar results (of the same order of magnitude) were obtained for the binary hydroxylic solvent mixtures water + ethanol and water + methanol and different probes [15,17,22,38].

As can be seen from Figures 5 and 6 and Table 6, a good linear dependence exists between $\ln \frac{p_1}{1-p_1}$ and $\ln \frac{x_1}{1-x_1}$, demonstrating the applicability of the statistic model of binary solvent mixture solutions achieved with the studied triazolium ylids (TTPY and TTNPY)

and giving us the opportunity to evaluate the differences between the potential energies in molecular pairs realized by hydrogen bonds in the studied solutions (see Table 6). In the case of TTPY dissolved in water and ethanol, the difference $w_2 - w_1$ was negative, showing that $|w_2| > |w_1|$ (see Figure 6a). The hydrogen bond of TTPY with ethanol was stronger than that between TTPY and water molecules. For the other solutions, the differences $w_2 - w_1$ were positive, showing that the hydrogen bond TTPY–water was stronger than the hydrogen bond TTPY–methanol, and the hydrogen bond TTNPY–water was stronger than TTNPY–ethanol and TTNPY–methanol.

Table 6. Characteristics of the lines $\ln \frac{p_1}{1-p_1} = m \ln \frac{x_1}{1-x_1} + n$ for the studied binary solvent mixtures solutions.

Solution	m	Δm	n	Δn	R	$w_2 - w_1$ (kJ/mol)
TTPY + Water + Ethanol	1.0525	0.0164	−0.4166	0.0282	0.9947	-1.033 ± 0.070
TTNPY + Water + Ethanol	1.0881	0.0101	0.6034	0.0173	0.9981	1.496 ± 0.043
TTPY + Water + Methanol	1.0888	0.0162	0.6046	0.0278	0.9952	1.499 ± 0.069
TTNPY + Water + Methanol	1.0922	0.0166	0.5693	0.0285	0.9949	1.411 ± 0.071

The computed wavenumbers based on relation (1) and using the regression coefficients from Table 3 are plotted versus the corresponding experimental values in Figure 7. As is shown in Figure 7, the obtained curves reflect some changes in TTPY solutions by passing from the complexes formed in alcohol to the complexes formed in water molecules, when the water content increases.

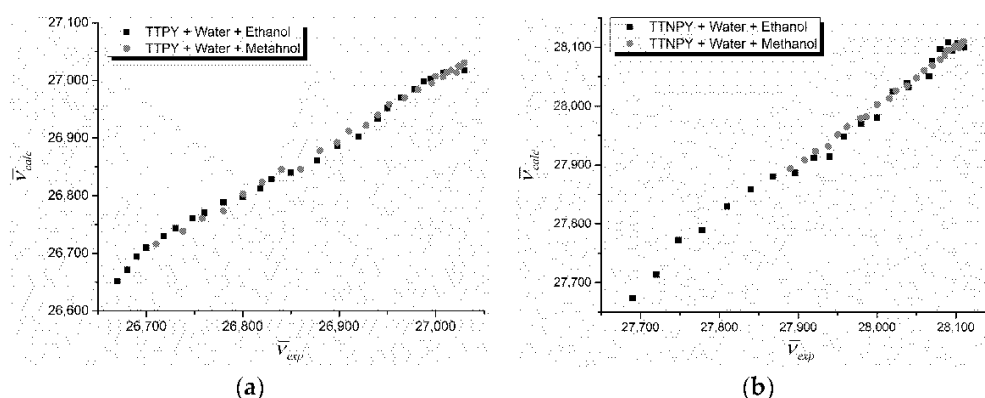


Figure 7. Computed wavenumber vs. experimental wavenumber for binary solvent mixture solutions of 4-tolyl-1,2,4-triazol-1-ium phenacylid (TTPY) (a) and 4-tolyl-1,2,4-triazol-1-ium-4'-nitro-phenacylid (TTNPY) (b).

In the studied solutions, the hydrogen bonds were very weak [12,17], and the thermal motion can change the nature of the complexes. At high water content, the complexes of the TTPY-water and TTNPY-water were dominant, and the water cages determined their relative stability [20].

The cell model of binary solvent mixture solution allows the estimation of the composition of TTPY and TTNPY, respectively (first shell). Figure 8 shows the dependence of the wavelength in the maximum of the electronic absorption band on the water content x_1 . Figure 9 shows the excess function $\delta_1 = p_1 - x_1$ of the water at the increase of its content. Except for the solution TTPY + water + ethanol, where the ethanol molecules are predominant in the first solvation shell of TTPY molecule, the water molecules predominate.

Figure 10 shows the dependence of $1/\Delta E_{CT}$ versus x_2/x_1 for TTPY and TTNPY in binary solvent mixtures water (1) + ethanol (2) (Figure 10a) and water (1) + methanol (2) (Figure 10b), respectively. The details of the linear fits (obtained by using the application Linear Fit from OriginPro 9 software) are given in Table 7. The very good linear dependence of $1/\Delta E_{CT}$ versus x_2/x_1 ($R > 0.99$, see Table 7) confirms that the hydrogen bonds were very

weak, having a negligible influence on the spectral shift of the visible electronic absorption band. The values obtained for the index of preferential solvation (Z) can be compared with the values of the intercept (n) in the Equation (3), given in Table 6. Thus, all of the values were of the same order of magnitude and, moreover, a very good quantitative agreement was observed for the case of the binary solvent mixture water + methanol.

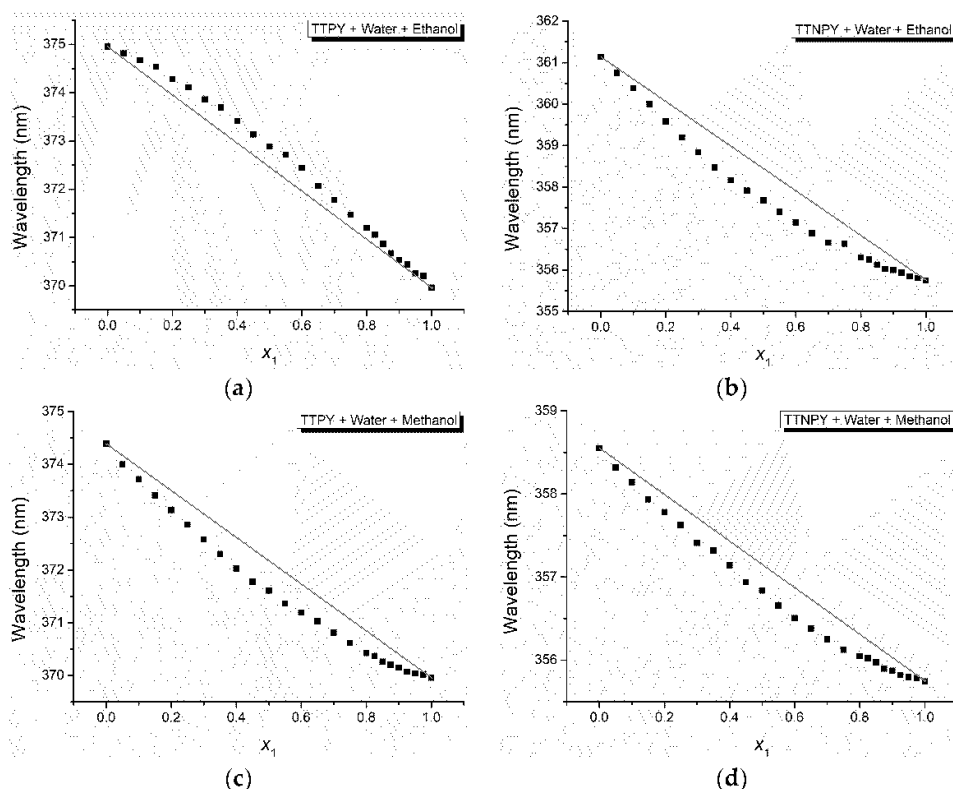


Figure 8. Wavelength in the maximum of the electronic absorption bands versus the water content for the investigated binary solvent mixture solutions of 4-tolyl-1,2,4-triazol-1-ium phenacylid (TTPY) (a,c) and 4-tolyl-1,2,4-triazol-1-ium-4'-nitro-phenacylid (TTNPY) (b,d).

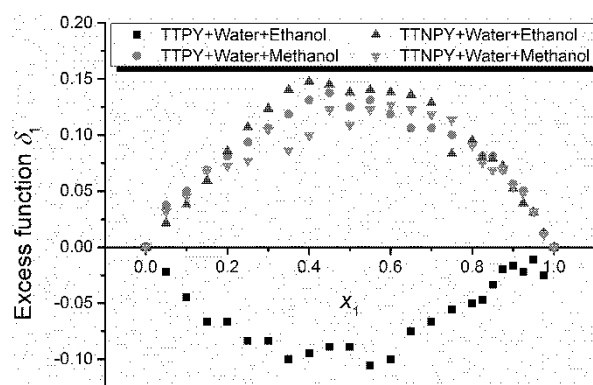


Figure 9. Excess function of the water molecules versus the water content in solution.

Suppan's model predicts the charge transfer energies with a high accuracy for the binary solvent mixture water + methanol, as can be observed in Figure 11, where the experimental versus calculated charge transfer energies are shown ($R > 0.99$ for both linear fits). In the case of the binary solvent mixture water + ethanol, Suppan's model predicts with accuracy the charge transfer energies for TTNPY, but fails in the case of TTPY (slope = 0.79).

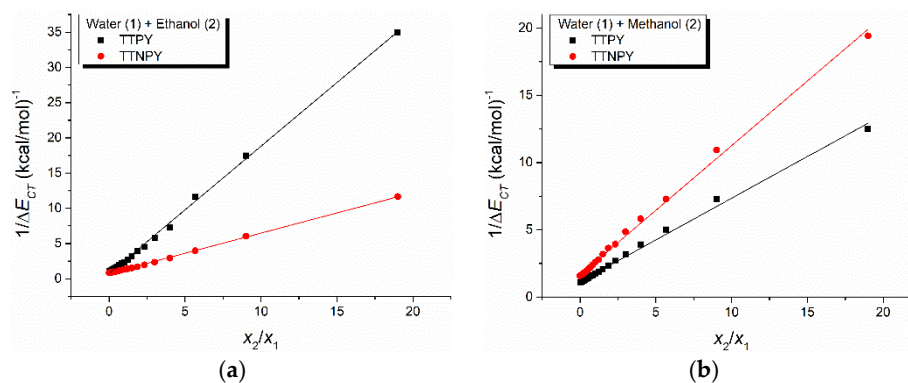


Figure 10. Inverse peak shift (measured against the peak corresponding to alcohols) of the 4-tolyl-1,2,4-triazol-1-ium phenacylid (TTPY) and 4-tolyl-1,2,4-triazol-1-ium-4'-nitro-phenacylid (TTNPY) absorption, respectively, versus the solvent bulk composition x_2/x_1 , for the binary solvent mixtures water (1) + ethanol (2) (a) and water (1) + methanol (2) (b).

Table 7. Results obtained through Suppan's model.

Solution	Intercept	Slope	Index of Preferential Solvation Z	R
TTPY + Water + Ethanol	0.7491 ± 0.0699	1.8064 ± 0.0151	-0.880	0.9984
TTNPY + Water + Ethanol	0.7538 ± 0.0176	0.5721 ± 0.0038	0.276	0.9990
TTPY + Water + Methanol	1.1490 ± 0.0438	0.6198 ± 0.0094	0.617	0.9947
TTNPY + Water + Methanol	1.6482 ± 0.0511	0.9609 ± 0.0110	0.540	0.9970

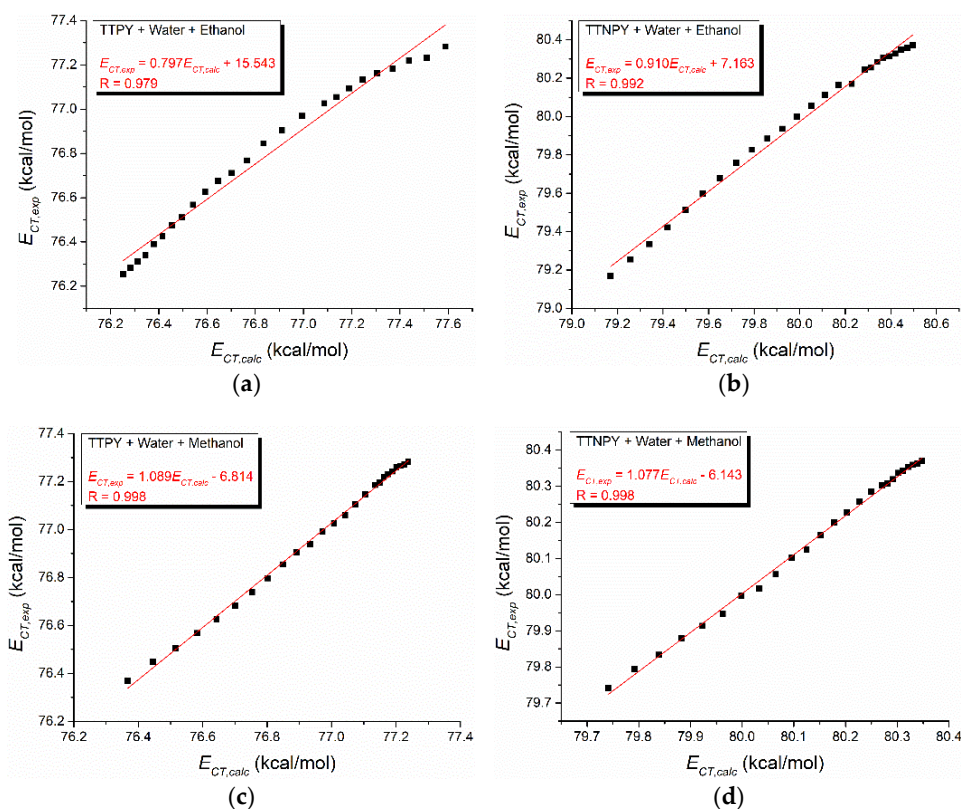


Figure 11. Experimental versus calculated charge transfer energies for 4-tolyl-1,2,4-triazol-1-ium phenacylid (TTPY) (a,c) and 4-tolyl-1,2,4-triazol-1-ium-4'-nitro-phenacylid (TTNPY) (b,d) in the binary solvent mixtures water + ethanol (a,b) and water + methanol (c,d).

For comparison between the two models (statistical cell model and Suppan), Figure 12 shows the local mole fractions calculated through the statistical cell model (p_2) and Suppan's model (y_2) as a function of the bulk mole fraction of ethanol and methanol, respectively. As can be observed, this figure emphasizes a very good agreement between the two models.

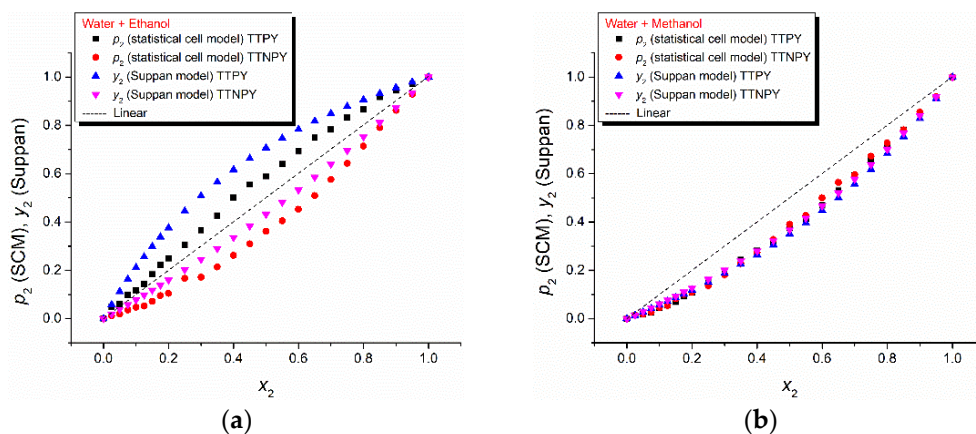


Figure 12. Local mole fractions calculated through statistical cell model (SCM) (p_2) and Suppan's model (y_2) as a function of bulk mole fraction of ethanol (a) and methanol (b), respectively.

4. Materials and Methods

The spectrally grade alcohols were purchased from Merck Company and the binary solvent mixtures were realized step by step with molar fractions of 0.05. Bi-distilled water was prepared in our labs. The weighing was repeated twice in order to assure a good precision, having in mind the very small quantities used for each experiment. The weighing was made with a balance having a precision of 0.005 g.

The ylids TTPY and TTNPY were prepared [1,2] in the Organic Chemistry Labs of Alexandru Ioan Cuza University and verified from the purity point of view by quantitative elemental analysis, Fourier transform infrared (FT-IR) spectroscopy, and ^1H nuclear magnetic resonance (NMR) spectroscopy. The salt method was used to prepare TTPY and TTNPY, the chemical reactions being schematically shown for TTPY in Figure 13; 0.05 mol of 1,2-diformylhydrazine mixed with 0.05 mol of *p*-Toluidine were refluxed for 8 h. Then, the mixture was kept in room temperature for 24 h. The obtained compound (*p*-Tolyl-1,2,4-triazol-1-ium) was dissolved in 50 mL of chloroform, while 0.05 mol of 2-Bromoacetophenone was dissolved in 50 mL of benzene. The two solutions were mixed, and potassium carbonate was added. The reaction was considered complete when the pH of the solution reached the value 8–8.5. The mixture was then kept at room temperature for 24 h. The white precipitate was filtered and then recrystallized from ethanol. TTNPY was obtained by the same procedure with one exception: 2-Bromo-4'-nitroacetophenone was used instead of 2-Bromoacetophenone. 1,2-diformylhydrazine, *p*-Toluidine, 2-Bromoacetophenone, and 2-Bromo-4'-nitroacetophenone were purchased from Sigma-Aldrich (now Merck).

To obtain the solutions of the two studied ylids, initially, two diluted solutions (10^{-4} mol/L concentration) were made: ylid + water and ylid + ethanol/ylid + methanol. Then, the two solutions were mixed in such a way that the molar fractions of the two solvents in the mixtures varied with a step of 0.05 (as it was made in the experiments for determining the KAT parameters, described in [20]).

The electronic absorption spectra were recorded with a Specord UV Vis Carl Zeiss Jena spectrophotometer with a data acquisition system, at a temperature $T = 295.15$ K. The wavenumber corresponding to the maximum of the electronic absorption band was determined by the first derivative method, after smoothing of the spectra.

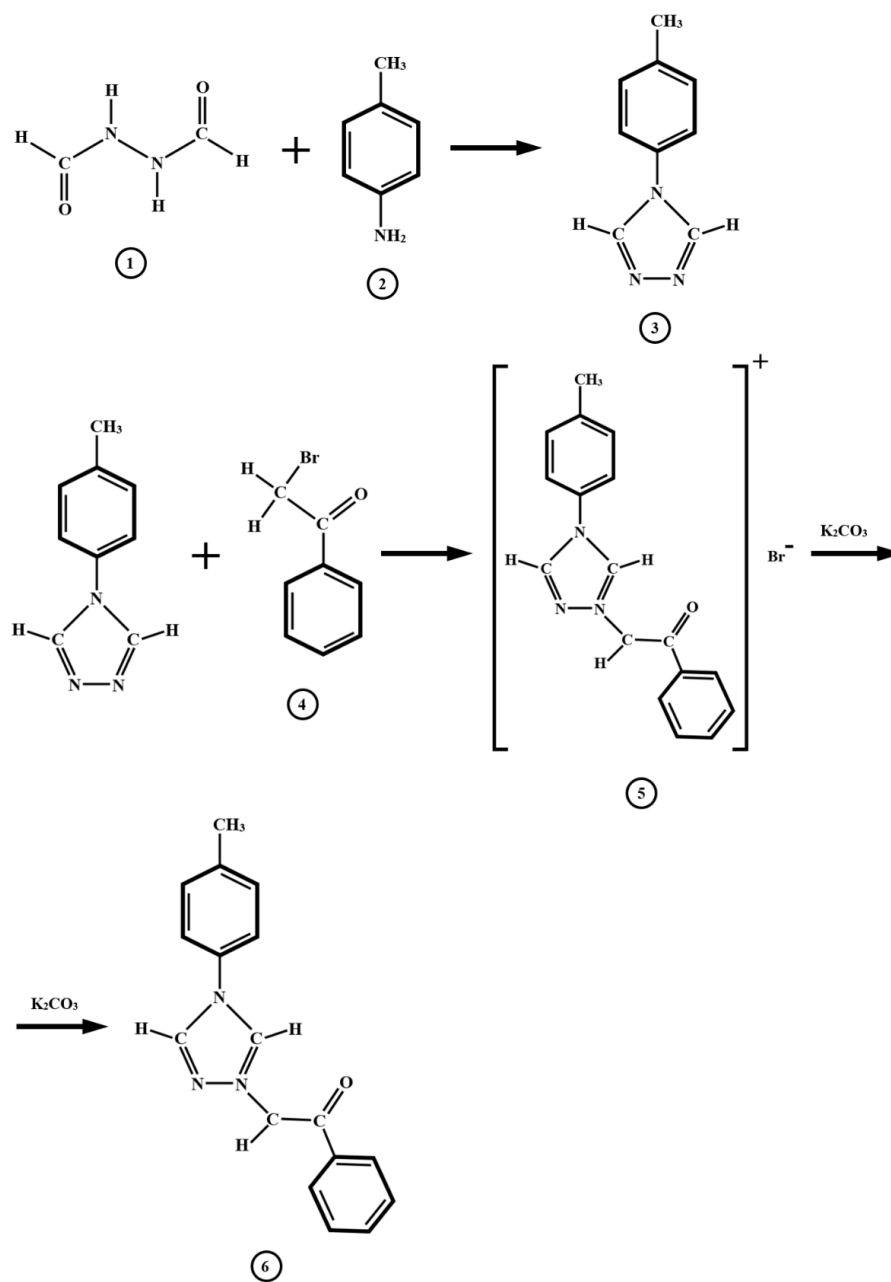


Figure 13. Schematic of the chemical reactions by which 4-tolyl-1,2,4-triazol-1-ium phenacylid (TTPY) was obtained (1—1,2-Diformylhydrazine, 2—*p*-Toluidine, 3—*p*-Tolyl-1,2,4-triazol-1-ium, 4—2-Bromoacetophenone, 5—TTPY salt, and 6—TTPY).

5. Conclusions

As basic compounds, the studied ylids participate in specific interactions of the hydrogen bond types, and the formed complexes are subjected to the global action of the binary hydroxylic solvent mixture.

The specific interactions in binary solvent mixtures of TTPY are enhanced by the presence of $-\text{NO}_2$ substituent. The delocalization of the electronic charge on the oxygen atoms facilitates the proton addition on the carbanion, increasing the contribution of the specific interactions to the total spectral shift of TTPY visible electronic absorption band.

The computed contribution of each type of interaction to the total shift of the ylid's electronic absorption band is estimated in this paper based on the KAT parameters of the binary hydroxylic solvent mixtures, and show the universal interaction important contribution to the spectral shift.

The difference $w_2 - w_1$ between the energies corresponding to the hydrogen bonds in molecular pairs of the types TTPY-water, TTPY-water, and ylid (TTPY/TTNPY)-alcohol (ethanol/methanol) is estimated here based on the statistical cell model of the binary solvent mixture solutions. The results reported in this paper are important, since cycloimmonium ylids, used in situ, are precursors in obtaining new heterocycle compounds in various domains.

For comparison, Suppan's model was approached to investigate the preferential solvation of solutes in the binary solvent mixtures. The obtained results are in very good agreement with those obtained through statistical cell model.

Author Contributions: Conceptualization, D.O.D. and D.-G.D.; methodology, D.O.D., D.-G.D., N.P.-M. and C.C.; software, D.-G.D., A.C.M. and A.G.-T.; validation, M.M.D.-O., N.P.-M., E.A. and C.C.; formal analysis, M.M.D.-O., E.A., A.C.M. and A.G.-T.; investigation, D.O.D., D.-G.D., N.P.-M. and C.C.; resources, D.-G.D., N.P.-M. and C.C.; data curation, D.O.D., D.-G.D., M.M.D.-O., E.A., A.G.-T. and C.C.; writing—original draft preparation, D.O.D. and D.-G.D.; writing—review and editing, D.O.D. and D.-G.D.; visualization, M.M.D.-O., A.C.M., E.A. and A.G.-T.; supervision, D.O.D.; project administration, D.O.D. and D.-G.D.; funding acquisition, D.-G.D., N.P.-M. and C.C. All authors have read and agreed to the published version of the manuscript.

Funding: This research received no external funding.

Institutional Review Board Statement: Not applicable.

Informed Consent Statement: Not applicable.

Data Availability Statement: The data presented in this study are available on request from the corresponding author.

Conflicts of Interest: The authors declare no conflict of interest.

Sample Availability: Not available.

References

- Petrovanu, M.; Luchian, C.; Surpateanu, G.; Barboiu, V. 1,2,4-Triazolium ylures I. Synthèse et stéréochimie des réactions de cycloaddition aux composés à liaison éthylenique active. *Rev. Roum. Chim.* **1979**, *24*, 733–744.
- Surpateanu, G.; Caea, N.; Sufletel, L.; Grandclaudon, P. Synthesis characterization of new azatriazolium ylids. *Rev. Roum. Chim.* **1995**, *40*, 133–136.
- Lars-Flörl, C. Triazole antifungal agents in invasive fungal infections. A comparative review. *Drugs* **2011**, *71*, 2405–2419. [CrossRef] [PubMed]
- Satish Kumar, S.; Kavitha, H.P. Synthesis and biological applications of triazole derivatives—A review. *Mini Rev. Org. Chem.* **2013**, *10*, 40–65. [CrossRef]
- Al-Omar, M.A.; Al-Abdullah, E.S.; Shehata, I.A.; Habib, E.E.; Ibrahim, T.M.; El-Emam, A.A. Synthesis, antimicrobial and anti-inflammatory activities of novel 5-(1-Adamantyl)-4-arylideneamino-3-mercapto-1,2,4-triazoles and related derivatives. *Molecules* **2010**, *15*, 2526–2550. [CrossRef]
- Chen, X.; Shi, Y.-M.; Huang, C.; Xia, S.; Yang, L.-J.; Yang, X.-D. Novel dibenzo[b,d]furan-1H-1,2,4-triazole derivatives: Synthesis and antitumor activity. *Anti-Cancer Agents Med. Chem.* **2016**, *16*, 377–386. [CrossRef] [PubMed]
- Shah, M.H.; Mhasalkar, M.Y.; Patki, V.M.; Deliwala, C.V.; Sheth, U.K. New 1,2,4(H)-triazole derivatives as diuretic agents. *J. Pharm. Sci.* **1969**, *58*, 1398–1401. [CrossRef]
- Alrawashdeh, M.S.M. Determination of antimicrobial activity of some 1,2,4-triazole derivatives. *Regul. Mech. Biosyst.* **2018**, *9*, 203–208. [CrossRef]
- Karczmarzyk, Z.; Swatko-Ossor, M.; Wysocki, W.; Drozd, M.; Ginalska, G.; Pachuta-Stec, A.; Pitucha, M. New applications of 1,2,4-triazole derivatives as antitubercular agents. Structure, in vitro screening and docking studies. *Molecules* **2020**, *25*, 6033. [CrossRef]
- Dorohoi, D.O.; Partenie, H. The spectroscopy of cycloimmonium ylides. *J. Mol. Struct.* **1993**, *293*, 129–132. [CrossRef]
- Dorohoi, D.O. Electronic spectroscopy of N-Ylid. *J. Mol. Struct.* **2004**, *704*, 31–43. [CrossRef]
- Dorohoi, D.O.; Dimitriu, D.G.; Dimitriu, M.; Closca, V. Specific interactions in N-ylid solutions, studied by nuclear magnetic resonance and electronic absorption spectroscopy. *J. Mol. Struct.* **2013**, *1044*, 79–86. [CrossRef]
- Melniciuc-Puica, N.; Barboiu, V.; Filoti, S.; Dorohoi, D.O. Reactivity of some 1 (N)-[(para-R₂)-phenacyl]-4(N)-[(para-R₁)-phenyl]-1,2,4-triazolium methylides by UV-VIS, IR and NMR spectra and molecular modeling. *Spectrosc. Lett.* **2004**, *37*, 457–467. [CrossRef]

14. Puica-Melniciuc, N.; Ivan, L.M.; Closca, V.; Dorohoi, D.O. Electro-optical and spectral comparative study of some triazolium methylids with biomedical applications. *Rev. Chim.* **2019**, *70*, 956–960. [CrossRef]
15. Closca, V.; Melniciuc-Puica, N.; Dorohoi, D.O. Specific interactions in hydroxyl ternary solutions of three carbanion mono-substituted 4'-tolyl-1,2,4-triazol-1-ium-4-R- phenacylids studied by visible electron spectra. *J. Mol. Liq.* **2014**, *200*, 431–438. [CrossRef]
16. Closca, V.; Puica Melniciuc, N.; Dorohoi, D.O.; Benchea, A.C. Intermolecular interactions in ternary solutions of some 1,2,4 triazolium ylids studied by spectral means. *Proc. SPIE* **2014**, *9286*, 92862T. [CrossRef]
17. Closca, V.; Puica Melniciuc, N.; Closca, M.; Avadanei, I.M.; Dorohoi, D.O. Spectral study of (4'-phenyl)-1,2,4-triazol-1-ium-phenacylid (PTPhY) in ternary solutions. *Ukr. J. Phys.* **2018**, *63*, 592–599. [CrossRef]
18. Kamlet, M.J.; Abboud, J.L.M.; Abraham, M.H.; Taft, R.W. Linear solvation energy relationships. 23. A comprehensive collection of the solvatochromic parameters, π^* , α , and β , and some methods for simplifying the generalized solvatochromic equation. *J. Org. Chem.* **1983**, *48*, 2877–2887. [CrossRef]
19. Reichardt, C. *Solvents and Solvent Effects in Organic Chemistry*, 3rd ed.; Wiley-VCH: Weinheim, Germany, 2003.
20. Buhvestov, U.; Rived, F.; Ràfols, C.; Bosch, E.; Rosés, M. Solute-solvent and solvent-solvent interactions in binary solvent mixtures. Part 7. Comparison of the enhancement of the water structure in alcohol-water mixtures measured by solvatochromic indicators. *J. Phys. Org. Chem.* **1998**, *11*, 185–192. [CrossRef]
21. Ivan, L.M.; Dimitriu, D.G.; Gritco-Todirascu, A.; Morosanu, A.C.; Dorohoi, D.O.; Cheptea, C. Excited state dipole moment of two pyridazinium-p-nitro-phenacylids estimated from solvatochromic study. *Spectrosc. Lett.* **2020**, *53*, 1–11. [CrossRef]
22. Dorohoi, D.O.; Creanga, D.E.; Dimitriu, D.G.; Morosanu, A.C.; Gritco-Todirascu, A.; Mariciuc, G.G.; Puica Melniciuc, N.; Ardelean, E.; Cheptea, C. Computational and spectral means for characterizing the intermolecular interactions in solutions and for estimating excited state dipole moment of solute. *Symmetry* **2020**, *12*, 1299. [CrossRef]
23. Dulcescu Oprea, M.M.; Melniciuc Puica, N.; Gritco-Todirascu, A.; Dorohoi, D.O. Spectral study of two carbanion monosubstituted 4'-phenyl-1,2,4-triazol-1-ium phenacylids in binary protic solvents. *Rev. Chim.* **2020**, *71*, 1–9. [CrossRef]
24. Pop, V.; Dorohoi, D.O.; Delibas, M. Consideration on the statistic model of the intermolecular interactions in ternary solutions. *An. Stiint. Univ. Al. I. Cuza, Iasi, s.Ib, Fizica* **1986**, *32*, 79–84.
25. Dorohoi, D.O.; Pop, V. Spectral shifts in the electronic absorption spectra of some cycloimmonium ylids in ternary solutions. *An. Stiint. Univ. Al. I. Cuza, Iasi, s.Ib, Fizica* **1987**, *33*, 78–85.
26. Dorohoi, D.O.; Avadanei, I.M.; Postolache, M. Characterization of the solvation spheres of some dipolar spectrally active molecules in binary solvents. *Optoelectron. Adv. Mater.* **2008**, *2*, 511–514.
27. Babusca, D.; Benchea, A.C.; Dimitriu, D.G.; Dorohoi, D.O. Solvatochromic characterization of Sudan derivatives in binary and ternary solutions. *Anal. Lett.* **2016**, *49*, 2615–2626. [CrossRef]
28. Avadanei, M.; Dorohoi, D.O. Interaction energy in pairs of pyridazinium ylids-solvent molecules estimated by spectral means within the cell ternary solution model. *Ukr. J. Phys.* **2012**, *57*, 118–122.
29. Sasirekha, V.; Vanelle, P.; Terme, T.; Ramakrishnan, V. Solvatochromism and preferential solvation of 1,4-dihydroxy-2,3-dimethyl-9,10 anthraquinone by UV-vis absorption and laser induced fluorescence measurements. *Spectrochim. Acta A* **2008**, *71*, 766–772. [CrossRef] [PubMed]
30. Suppan, P. Local polarity of solvent mixtures in the field of electronically excited molecules and exciplexes. *J. Chem. Soc. Faraday Trans.* **1987**, *83*, 495–509. [CrossRef]
31. Lerf, C.; Suppan, P. Hydrogen bonding and dielectric effects in solvatochromic shifts. *J. Chem. Soc. Faraday Trans.* **1992**, *88*, 963–969. [CrossRef]
32. Henseler, A.; von Raumer, M.; Suppan, P. Observation of dielectric enrichment upon the formation of benzophenone radical anion in a binary solvent mixture. *J. Chem. Soc. Faraday Trans.* **1996**, *92*, 391–393. [CrossRef]
33. Papadakis, R. Preferential solvation of a highly medium responsive Pentacyanoferrate(II) complex in binary solvent mixtures: Understanding the role of dielectric enrichment and the specificity of solute-solvent interactions. *J. Phys. Chem. B* **2016**, *120*, 9422–9433. [CrossRef] [PubMed]
34. Papadakis, R.; Deligkiozi, I.; Nowak, K.E. Study of the preferential solvation effects in binary solvent mixtures with the use of intensely solvatochromic azobenzene involving [2] rotaxane solutes. *J. Mol. Liq.* **2019**, *274*, 715–723. [CrossRef]
35. Malik, P.K.; Tripathy, M.; Kajjam, A.B.; Patel, S. Preferential solvation of *p*-nitroaniline in a binary mixture of chloroform and hydrogen bond acceptor solvents: The role of specific solute-solvent hydrogen bonding. *Phys. Chem. Chem. Phys.* **2020**, *22*, 3545–3562. [CrossRef]
36. Malik, P.K.; Tripathy, M.; Patel, S. D- π -A molecular probe to unveil the role of solute-solvent hydrogen bonding in solvatochromism, location specific preferential solvation and synergistic effect in binary mixtures. *ChemistrySelect* **2020**, *5*, 3551–3566. [CrossRef]
37. Van, S.-P.; Hammond, G.S. Amine quenching of aromatic fluorescence and fluorescent exciplexes. *J. Am. Chem. Soc.* **1978**, *100*, 3895–3902. [CrossRef]
38. Dulcescu-Oprea, M.M.; Morosanu, A.C.; Dimitriu, D.G.; Gritco-Todirascu, A.; Dorohoi, D.O.; Cheptea, C. Solvatochromic study of pyridinium acetyl benzoyl methylid (PABM) in ternary protic solutions. *J. Mol. Struct.* **2021**, *1227*, 129539. [CrossRef]

Article

Structural Insights of Three 2,4-Disubstituted Dihydropyrimidine-5-carbonitriles as Potential Dihydrofolate Reductase Inhibitors

Lama H. Al-Wahaibi ¹, Althaf Shaik ², Mohammed A. Elmorsy ³, Mohammed S. M. Abdelbaky ⁴, Santiago Garcia-Granda ⁴, Subbiah Thamotharan ⁵, Vijay Thiruvengatam ⁶ and Ali A. El-Emam ^{7,*}

¹ Department of Chemistry, College of Sciences, Princess Nourah bint Abdulrahman University, Riyadh 11671, Saudi Arabia; lhalwahaibi@pnu.edu.sa

² Discipline of Chemistry, Indian Institute of Technology, Gandhinagar 382355, India; althaf.shaik@iitgn.ac.in

³ Department of Pharmaceutical Organic Chemistry, Faculty of Pharmacy, Mansoura University, Mansoura 35516, Egypt; mwahhab95@gmail.com

⁴ Department of Physical and Analytical Chemistry, Faculty of Chemistry, Oviedo University-CINN, 33006 Oviedo, Spain; saidmohammed.uo@uniovi.es (M.S.M.A.); sgg@uniovi.es (S.G.-G.)

⁵ Biomolecular Crystallography Laboratory, Department of Bioinformatics, School of Chemical and Biotechnology, SASTRA Deemed University, Thanjavur 613401, India; thamu@sabt.sastra.edu

⁶ Discipline of Biological Engineering, Indian Institute of Technology Gandhinagar, Gujarat 382355, India; vijay@iitgn.ac.in

⁷ Department of Medicinal Chemistry, Faculty of Pharmacy, Mansoura University, Mansoura 35516, Egypt

* Correspondence: elemam@mans.edu.eg; Tel.: +20-50-2258087

Citation: Al-Wahaibi, L.H.; Shaik, A.; Elmorsy, M.A.; Abdelbaky, M.S.M.; Garcia-Granda, S.; Thamotharan, S.; Thiruvengatam, V.; El-Emam, A.A. Structural Insights of Three 2,4-Disubstituted Dihydropyrimidine-5-carbonitriles as Potential Dihydrofolate Reductase Inhibitors. *Molecules* **2021**, *26*, 3286. <https://doi.org/10.3390/molecules26113286>

Academic Editors: Rui Fausto, Sylvia Turrell and Gulce Ogruc Ildiz

Received: 6 May 2021

Accepted: 26 May 2021

Published: 29 May 2021

Publisher's Note: MDPI stays neutral with regard to jurisdictional claims in published maps and institutional affiliations.



Copyright: © 2021 by the authors. Licensee MDPI, Basel, Switzerland. This article is an open access article distributed under the terms and conditions of the Creative Commons Attribution (CC BY) license (<https://creativecommons.org/licenses/by/4.0/>).

Abstract: In this report, we describe the structural characterization of three 2,4-disubstituted-dihydropyrimidine-5-carbonitrile derivatives, namely 2-[[4-nitrophenyl)methyl]sulfanyl]-6-oxo-4-propyl-1,6-dihydropyrimidine-5-carbonitrile **1**, 4-(2-methylpropyl)-2-[[4-nitrophenyl)methyl]sulfanyl]-6-oxo-1,6-dihydropyrimidine-5-carbonitrile **2**, and 2-[(2-ethoxyethyl)sulfanyl]-6-oxo-4-phenyl-1,6-dihydropyrimidine-5-carbonitrile monohydrate **3**. An X-ray diffraction analysis revealed that these compounds were crystallized in the centrosymmetric space groups and adopt an L-shaped conformation. One of the compounds (**3**) crystallized with a water molecule. A cyclic motif ($R_2^2(8)$) mediated by N–H...O hydrogen bond was formed in compounds **1** and **2**, whereas the corresponding motif was not favorable, due to the water molecule, in compound **3**. The crystal packing of these compounds was analyzed based on energy frameworks performed at the B3LYP/6-31G(d,p) level of theory. Various inter-contacts were characterized using the Hirshfeld surface and its associated 2D-fingerprint plots. Furthermore, a molecular docking simulation was carried out to assess the inhibitory potential of the title compounds against the human dihydrofolate reductase (DHFR) enzyme.

Keywords: pyrimidine-5-carbonitriles; dihydrofolate reductase; crystal structure; DFT; Hirshfeld surface analysis

1. Introduction

Pyrimidine moiety was early discovered as an important scaffold in several chemotherapeutic agents [1]. The chemotherapeutic efficacy of pyrimidine-based drugs is attributed to their inhibitory effect on the biosynthesis of vital enzymes responsible for nucleic acids, such as thymidylate synthetase (TSase), thymidine phosphorylase (TPase), dihydrofolate reductase (DHFR), and reverse transcriptase (RTase). Several pyrimidine-based drugs are currently marketed as antineoplastic agents for the treatment of different human cancers [2–6]. Potent antiviral activities against human immunodeficiency viruses (HIV) [7–12], herpes simplex virus (HSV) [13], hepatitis B virus (HBV) [14], and SARS-CoV virus [15] have been reported for numerous substituted pyrimidine derivatives. In addition, pyrimidine-based dihydrofolate reductase (DHFR) inhibitors are currently used as clinically useful chemotherapeutic agents [16,17]. Trimethoprim, the prototype antibacterial

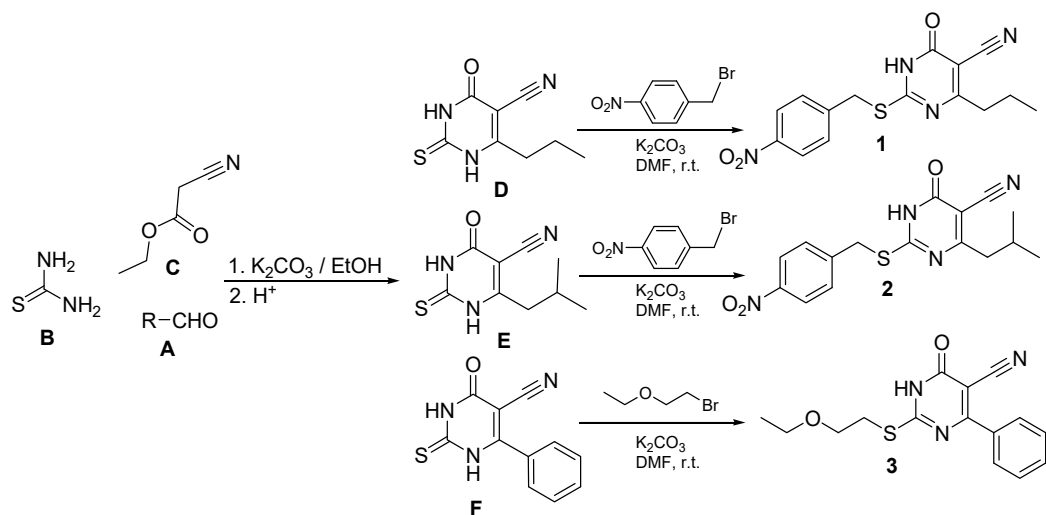
DHFR inhibitor was discovered to be a potent drug, mainly in the treatment of urinary tract infections [18]. The next generation of DHFR inhibitors was further developed as potent antibacterial drugs for the treatment of resistant respiratory tract infections [19–21]. Pyrimidine-based DHFR inhibitors are also employed as efficient antiprotozoal agents for the treatment of malaria [22,23], leishmaniasis [24], and trypanosomiasis [25]. In addition, several pyrimidine-5-carbonitrile derivatives were reported to display marked antimicrobial activities [26–32].

In the present investigation, we report an in-depth experimental and theoretical study of the structures of three 2,4-disubstituted dihydropyrimidine-5-carbonitrile derivatives in a trial to explore the mechanism of their antimicrobial activity.

2. Results and Discussion

2.1. Chemical Synthesis

The dihydropyrimidine-5-carbonitriles **1**, **2**, and **3** were synthesized via condensation of the corresponding aldehydes **A** with thiourea **B** and ethyl cyanoacetate **C**, in ethanol, in the presence of anhydrous potassium to yield the intermediate 6-substituted-2-thiouracil-5-carbonitriles **D** [31], **E** [32], and **F** [33]. Compounds **D** and **E** were reacted with 4-nitrobenzyl bromide and compound **F** with 1-bromo-2-ethoxyethane in the presence of anhydrous potassium carbonate to yield the target compounds **1**, **2**, and **3** (Scheme 1).



Scheme 1. Synthesis of compounds 1–3.

2.2. Crystal Structures

Single crystal X-ray diffraction was used to determine the crystal structures of compounds **1–3**. A summary of the crystallographic data and structure refinement parameters is listed in Table 1. The Oak Ridge Thermal Ellipsoid Plot (ORTEP) representation at 50% probability corresponding to the asymmetric units of **1**, **2**, and **3** is depicted in Figure 1. The bond lengths and bond angles of the three structures were comparable to the related reported structures [34–37].

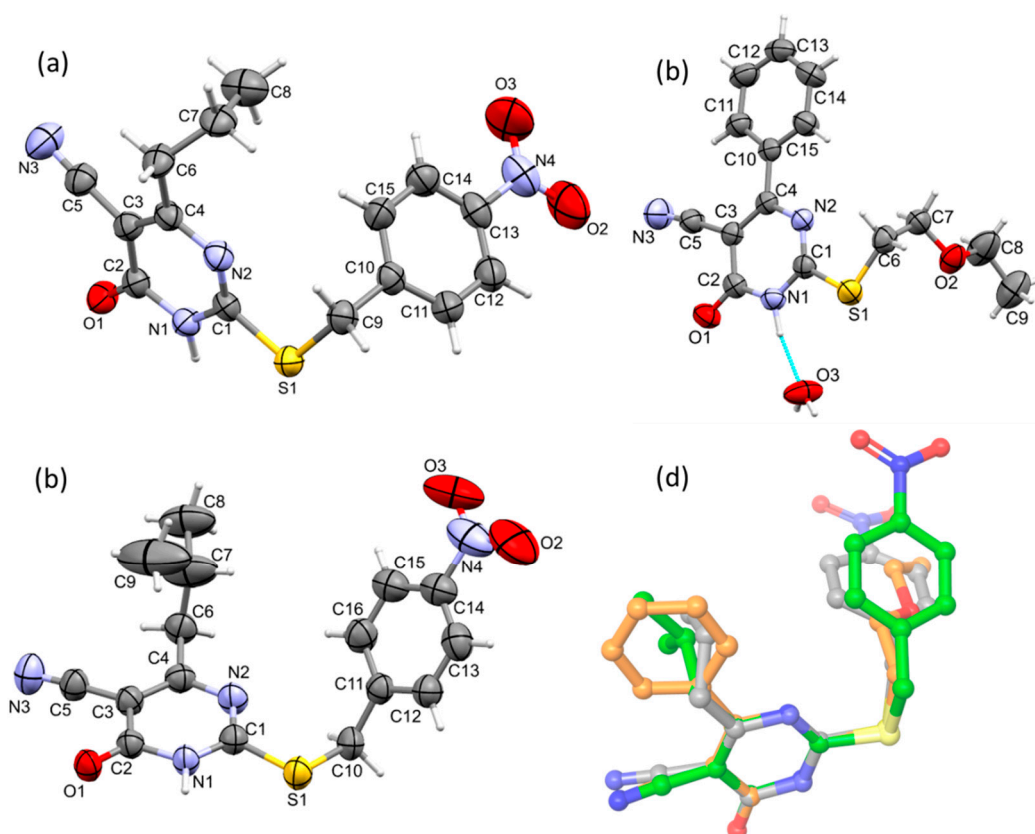


Figure 1. Thermal ellipsoid representation of compounds (a) **1**, (b) **2**, and (c) **3** at 50% probability level with atom numbering scheme is shown, and (d) structural superimposition of compounds **1** (grey), **2** (green), and **3** (orange). The water oxygen in compound **3** is not shown for clarity.

Table 1. Crystal data and structure refinement parameters of compounds **1–3**.

	Compound 1	Compound 2	Compound 3
Empirical formula	C ₁₅ H ₁₄ N ₄ O ₃ S	C ₁₆ H ₁₆ N ₄ O ₃ S	C ₁₅ H ₁₇ N ₃ O ₃ S
Formula weight	330.36	344.39	319.38
Temperature (K)		293 (2)	
Crystal system	Monoclinic	Monoclinic	Triclinic
Space group	<i>P</i> 2 ₁ / <i>n</i>	<i>C</i> 2/ <i>c</i>	<i>P</i> -1
<i>a</i> /Å	12.5792 (7)	18.3676 (7)	7.1456 (4)
<i>b</i> /Å	9.5493 (5)	5.7996 (2)	10.8642 (6)
<i>c</i> /Å	13.3158 (8)	31.8592 (12)	11.2566 (7)
α /°	90	90	104.672 (5)
β /°	106.432 (7)	95.343 (4)	108.159 (5)
γ /°	90	90	95.421 (5)
Volume/Å ³	1534.20 (16)	3379.0 (2)	788.84 (8)
<i>Z</i>	4	8	2
Calculated density (g/cm ³)	1.430	1.354	1.345
Absorption coefficient (mm ⁻¹)	2.068	1.899	1.968
<i>F</i> (000)	688	1440	336
Crystal size (mm ³)	0.16 × 0.12 × 0.08	0.16 × 0.05 × 0.05	0.26 × 0.14 × 0.10
Radiation		Cu K α (λ = 1.54184)	
2 θ range for data collection	8.5 to 151.4	5.6 to 151.4	8.6 to 151.1
Index ranges	−15 ≤ <i>h</i> ≤ 15, −11 ≤ <i>k</i> ≤ 11, −16 ≤ <i>l</i> ≤ 16	−22 ≤ <i>h</i> ≤ 22, −7 ≤ <i>k</i> ≤ 6, −39 ≤ <i>l</i> ≤ 40	−8 ≤ <i>h</i> ≤ 8, −13 ≤ <i>k</i> ≤ 13, −13 ≤ <i>l</i> ≤ 11
Reflections collected	15422	16836	12241

Table 1. Cont.

	Compound 1	Compound 2	Compound 3
Independent reflections	3163 [$R_{\text{int}} = 0.0971$, $R_{\text{sigma}} = 0.0654$]	3418 [$R_{\text{int}} = 0.1098$, $R_{\text{sigma}} = 0.0941$]	3220 [$R_{\text{int}} = 0.0442$, $R_{\text{sigma}} = 0.0377$]
Data/restraints/parameter	3163/0/213	3418/2/211	3220/2/212
Goodness-of-fit on F^2	1.030	0.998	1.035
Final R indices [$I > 2 \sigma(I)$]	$R_1 = 0.0569$, $wR_2 = 0.1209$	$R_1 = 0.0766$, $wR_2 = 0.1777$	$R_1 = 0.0432$, $wR_2 = 0.1040$
Final R indices (all data)	$R_1 = 0.1087$, $wR_2 = 0.1479$	$R_1 = 0.1565$, $wR_2 = 0.2358$	$R_1 = 0.0689$, $wR_2 = 0.1210$
Largest diff. peak and hole ($\text{e.}\text{\AA}^{-3}$)	0.20/−0.25	0.52/−0.36	0.16/−0.18
CCDC number	2063317	2063318	2063320

Full crystallographic data for compounds 1 (CCDC 2063317), 2 (CCDC 2063318) and 3 (CCDC 2063320) can be obtained free of charge from The Cambridge Crystallographic Data Centre at: www.ccdc.cam.ac.uk (Supplementary Materials).

Compound 1 crystallized in the monoclinic crystal system with the $P2_1/n$ space group. Figure 1a depicts the ORTEP diagram of compound 1. The asymmetric unit of compound 1 contains one molecule in an L-shape molecular conformation, where the angle between the 4-nitrobenzyl moiety and 1,6-dihydropyrimidine-5-carbonitrile (C9–S1–C1) was found to be 102.37° . The dihedral angle formed between the nitrobenzyl and pyrimidine ring is 87.90° .

To understand the crystal packing, we created an energy framework that combines pairwise intermolecular interaction energies with a graphical depiction of their magnitude [38]. The energy frameworks of 1 were projected onto the crystallographic ac plane, as shown in Figure 2a. As shown from this figure, the molecules of 1 are packed in a columnar fashion. The molecular packing was mainly stabilized by a pair of N1–H \cdots O1 (H \cdots O = 1.795 Å, N \cdots O = 2.800 (2) Å, \angle NHO = 174°) hydrogen bonds which form between the NH and carbonyl groups of two centrosymmetrically-related pyrimidine rings (Figure 2b). These hydrogen bonds led to a cyclic inversion dimer with a $R_2^2(8)$ graph-set motif. This hydrogen bond (represented as large cylindrical tubes) links the molecules in the layer with molecules in an adjacent layer. The total intermolecular interaction energy for this hydrogen bonded dimer is $-78.2 \text{ kJ mol}^{-1}$. In addition to this, a chalcogen bond of the type C1–S1 \cdots S1 is present, with the distance and angle 3.363 (2) Å and $166.2 (1)^\circ$, respectively (Figure 2b). The role of the chalcogen bond in this structure is similar to that of a N–H \cdots O hydrogen bond. One of the oxygens (O2 atom) of the nitro group makes a short N–O \cdots π (centroid of the pyrimidine ring) interaction with the distance of 3.033 (2) Å (Figure 2b). This interaction also bridges the adjacent ladders. The ladder-pattern is formed by weak van der Waals-type interactions.

Compound 2 crystallized in the monoclinic crystal system with the space group $C2/c$. The asymmetric unit contains one molecule, as shown in Figure 1b. The 4-nitrobenzyl moiety and 1,6-dihydropyrimidine-5-carbonitrile are positioned in an L-shaped structure similarly to compound 1. Molecules 2 are arranged as layers in the solid state, and these layers run parallel to the crystallographic a axis. Furthermore, the adjacent layers are interlinked by a short and directional C–H \cdots O interaction (involving H15 from nitrobenzyl and O3 of the nitro group), with H \cdots O = 2.35 Å and \angle CHO = 161° forming a double layer. Moreover, the adjacent layers are also connected by a C–S \cdots S chalcogen bond (S1 \cdots S1 = 3.444 (2) Å and \angle C1–S1 \cdots S1 = $162 (1)^\circ$).

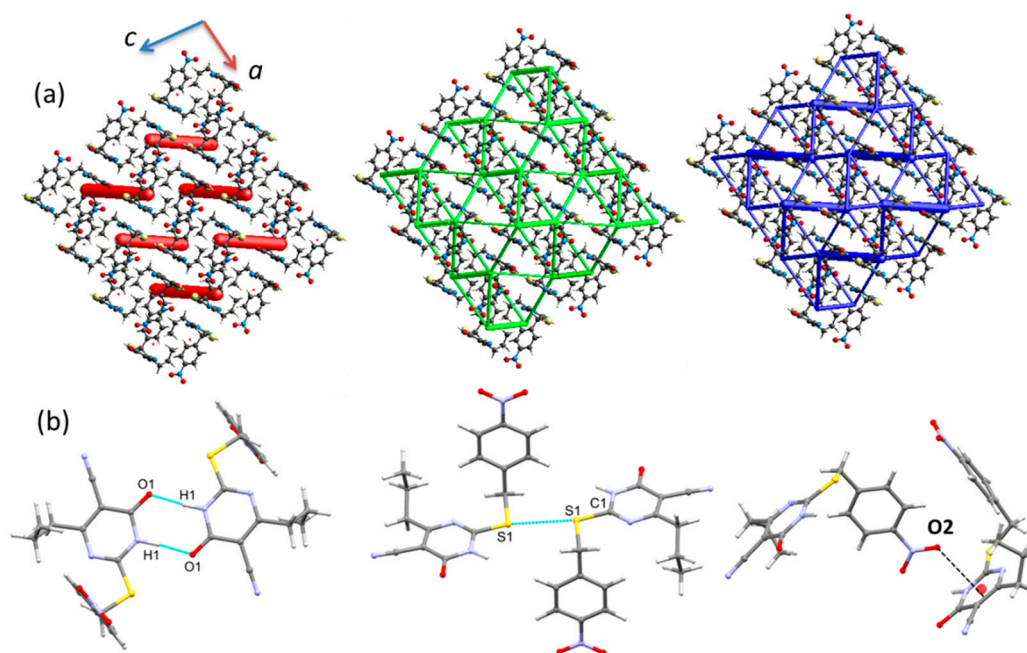


Figure 2. (a) Packing diagram of compound **1** viewed along the crystallographic *b*-axis with the incorporation of energy framework (electrostatic energy: red; dispersion energy: green; and net interaction energy: blue with the cylindrical size of 80; interaction energy for molecular pairs less than 15 kJ mol^{-1} has been omitted for clarity) and (b) molecular dimers formed in the crystal structure of **1**.

The adjacent double layers are further interconnected via cyclic N-H...O synthon (involving NH and C=O of pyrimidine ring and $R_2^2(8)$ graph-set motif) as observed in **1**. The N-H...O hydrogen bonding geometry ($\text{H}\cdots\text{O} = 1.79 \text{ \AA}$, $\text{N}\cdots\text{O} = 2.776(1) \text{ \AA}$ and $\angle\text{NHO} = 163^\circ$) is very similar to the structure of **1**. We also noted that the above mentioned C-H...O and N-H...O bonded motifs are connected alternately, leading to the formation of a chain (Figure 3a).

Though the molecular arrangement of **2** in solid-state is somewhat different from the crystal structure of **1**, these two structures show a different 3D-topology of the energy frameworks for electrostatic and net interaction energies (Figure 3b). However, the dispersion energy framework shows a similarity between compounds **1** and **2**. In the electrostatic energy framework, the large vertical cylindrical tubes correspond to cyclic N-H...O hydrogen bonds, and small horizontal tubes bridge the large cylindrical tubes. These horizontal tubes represent the intermolecular C-H...N interaction in which the nitrile N atom acts as an acceptor ($\text{C13-H13}\cdots\text{N3}$; $\text{H13}\cdots\text{N3} = 2.60 \text{ \AA}$ and $\angle\text{CHN} = 122^\circ$). Furthermore, the adjacent ladder-like topology is interconnected by small vertical cylindrical tubes that represent an intermolecular short and directional $\text{C15-H15}\cdots\text{O3}$ interaction. The chalcogen bond observed in this structure interlinks the large vertical cylindrical tubes diagonally in each ladder-like topology and is driven by the dispersion origin. The chalcogen bond and intermolecular C-H...N interaction combined to generate a supramolecular sheet, as shown in Figure 4.

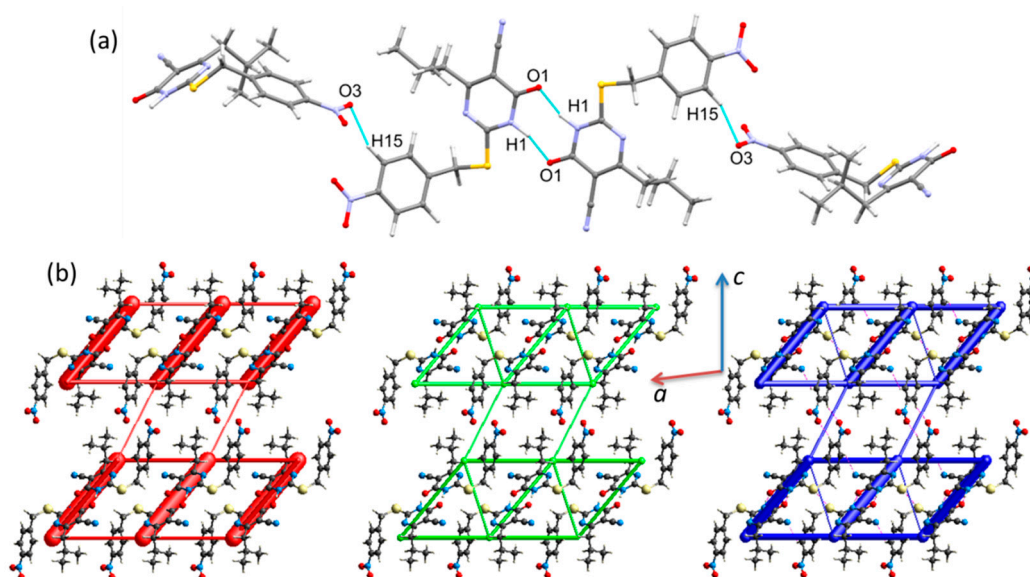


Figure 3. (a) Supramolecular chain built by intermolecular N/C–H...O hydrogen bonds, and (b) packing diagram of compound **2** viewed along the crystallographic *b*-axis with the incorporation of the energy framework (electrostatic energy: red; dispersion energy: green and net interaction energy: blue with the cylindrical size of 80; interaction energy for molecular pairs less than 10 kJ mol^{−1} has been omitted for clarity).

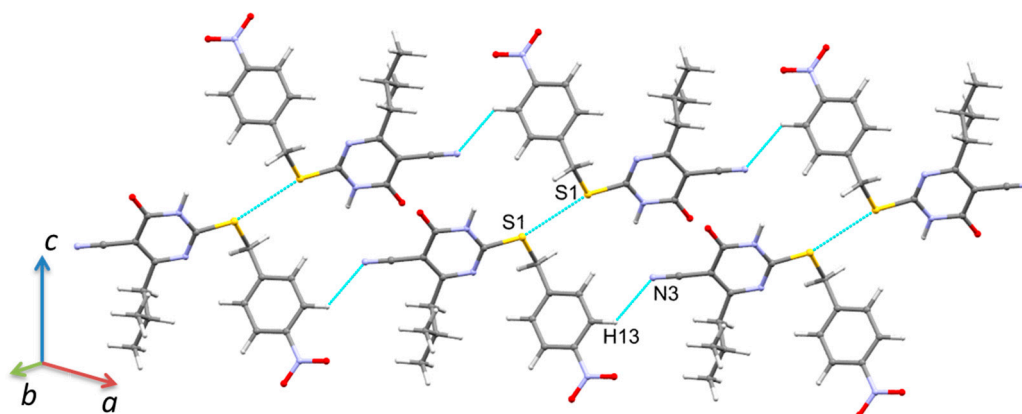


Figure 4. Supramolecular sheet built by intermolecular C–S...S chalcogen bond and C–H...N interaction in compound **2**.

Compound **3** crystallized as a monohydrated form in the triclinic crystal system with the space group *P*-1 (Figure 1c). The asymmetric unit contains one molecule of **3** and one water molecule. Unlike compounds **1** and **2**, compound **3** has a 2-ethoxyethyl group instead of a 4-nitrobenzyl moiety connected to the dihydropyrimidine ring via a thioether bridge. However, compound **3** maintains an L-shape with a bond angle of 101.56° (C8–S1–C12) between the 2-ethoxyethylthio group and the 1,6-dihydropyrimidine-5-carbonitrile. Furthermore, the 4-phenyl group is in the same plane of the 1,6-dihydropyrimidine ring, with a torsional angle of 178.18° (C6–C1–C7–C10). In the asymmetric unit of **3**, the pyrimidine ring NH is involved in an intermolecular N–H...O (N1 ... O3 = 2.710 Å) hydrogen bond with the water oxygen atom. Due to the presence of the crystallization water molecules in the crystal of **3**, a cyclic N–H...O bonded synthon, as observed in **1** and **2**, disappears.

The basic packing motif of **3** is the molecular stacking, which forms as a columnar fashion along the *ac* plane, and the water molecules sandwiched between adjacent columns. The molecular dimers formed in this structure are illustrated in Figure 5. The inversion-related molecules (1 − *x*, 1 − *y*, 1 − *z*) of **3** generate molecular stacking, and the centroid-to-centroid distance between the phenyl and pyrimidine rings is 3.588 (2) Å (Figure 5a). Different inversion-related molecules (2 − *x*, 1 − *y*, 1 − *z*) of **3** also produce a molecular

stacking, and the centroid-to-centroid separation of phenyl and pyrimidine rings is 3.638 (2) Å. This molecular stacking is further stabilized by the intermolecular C–H⋯N interaction, in which nitrile N atom acts as an acceptor (Figure 5b).

The water molecule is involved in three intermolecular interactions, of which two are O–H⋯O type hydrogen bonds and the remaining one is the N–H⋯O type hydrogen bond (H1⋯O3 = 1.72 Å, N1⋯O3 = 2.709 (2) Å and \angle NHO = 167°; symmetry operation: $-x + 1, -y + 1, -z + 2$). In the O–H⋯O hydrogen bonds (H1w⋯O1 = 1.83 Å, O3⋯O1 = 2.766 (2) Å and \angle OHO = 157°; symmetry operation: $-x + 1, -y + 1, -z + 2$ and H2w⋯O2 = 1.86 Å, O3⋯O2 = 2.832 (2) Å and \angle OHO = 169°; symmetry operation: $-x + 1, -y + 2, -z + 2$) oxygens of carbonyl and ether moieties are involved as acceptors and water acts as a donor. As shown in Figure 5c, the neighboring molecules of **3** are interlinked by two water molecules, forming alternate $R^4_4(12)$ and $R^4_4(18)$ rings.

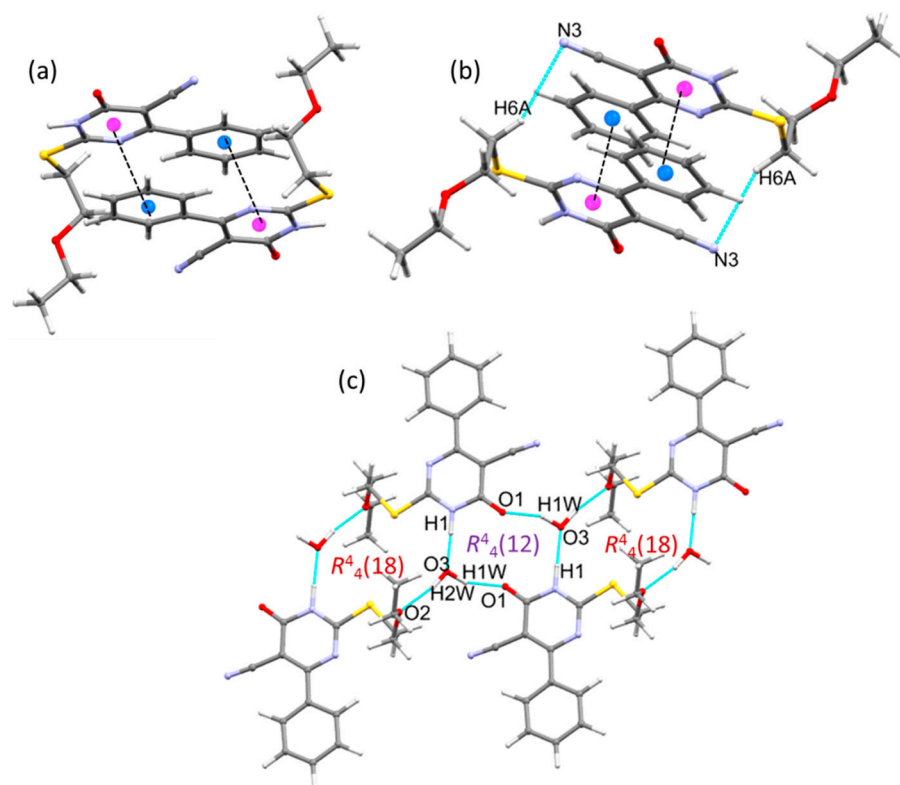


Figure 5. Different dimeric motifs formed by (a) π -stacking interaction, (b) π -stacking and C–H⋯N interactions, and (c) N–H⋯O and O–H⋯O hydrogen bonds in the crystal structure of compound **3**.

The energy framework of the crystal structure **3** viewed down the b axis is depicted in Figure 6. As can be seen from this figure, the crystal packing of compound **3** is predominantly dispersive in nature. The zigzag chains with small cylindrical tubes (electrostatic energy component) run parallel to the crystallographic a axis. The adjacent zigzag chains are further interconnected by small vertical tubes. These vertical tubes correspond to intermolecular N–H⋯O and O–H⋯O hydrogen bonds. The horizontal tubes represent the π -stacking interaction and C–H⋯N interaction. Overall, the energy framework of the crystal packing analysis suggests that compounds **1** and **2** display a similar 3D topology of the energy framework, whereas compound **3** shows a different framework compared to the other two compounds. These features suggest that compound **3** may possess different mechanical properties compared to the other two compounds.

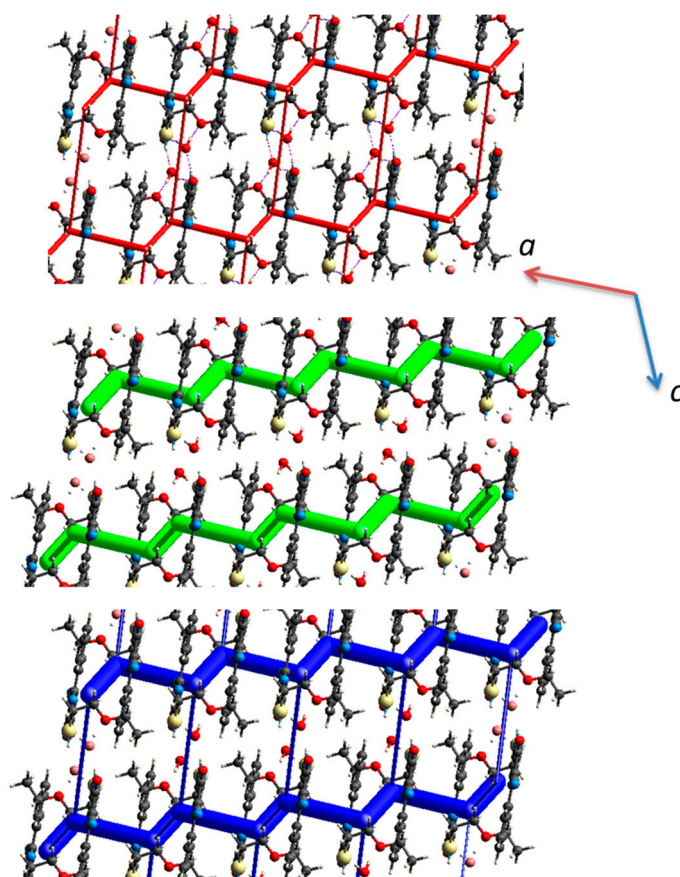


Figure 6. Packing diagram of compound **3** viewed along the crystallographic *b*-axis with the incorporation of the energy framework (electrostatic energy: red; dispersion energy: green; and net interaction energy: blue with the cylindrical size of 80; interaction energy for molecular pairs less than 10 kJ mol^{-1} has been omitted for clarity).

2.3. Hirshfeld Surface and 2D Fingerprint Plot Analysis

The Hirshfeld surfaces (HS) of the three dihydropyrimidine derivatives are represented in Figure 7. In compound **1**, the most prominent features are the deep red spots on the HS due to the cyclic $\text{N-H}\cdots\text{O}$ hydrogen bonds, while a $\text{C-S}\cdots\text{S}$ type chalcogen bond shows a relatively less intense red spot. In compound **2**, in addition to the above two interactions in **1**, there is a $\text{C-H}\cdots\text{O}$ interaction in which the nitro oxygen is involved as an acceptor, showing red spots on the HS. Due to the presence of the crystallization water molecule in the crystal of **3**, a cyclic $\text{N-H}\cdots\text{O}$ synthon has disappeared. However, the water molecule makes three hydrogen bonds, including two $\text{Ow-H}\cdots\text{O}$ hydrogen bonds with the carbonyl oxygen of pyrimidine and ester oxygen atoms, and the $\text{N-H}\cdots\text{Ow}$ hydrogen bond with the amine group of the pyrimidine ring. These three intermolecular interactions are shown as intense red areas on the HS.

The shape index of compounds **1** and **2** showed no sign of complementary blue and red triangles on the HS, indicating the absence of $\pi\cdots\pi$ interactions in these two compounds. On the other hand, compound **3**, having a phenyl ring at position 4, showed complementary blue and red triangles (at the phenyl ring and dihydropyrimidine rings) on the shape index mapped over the Hirshfeld surface. Furthermore, the curvedness of compound **3** showed a flat region in the same area, confirming the presence of a weak $\pi\cdots\pi$ stacking.

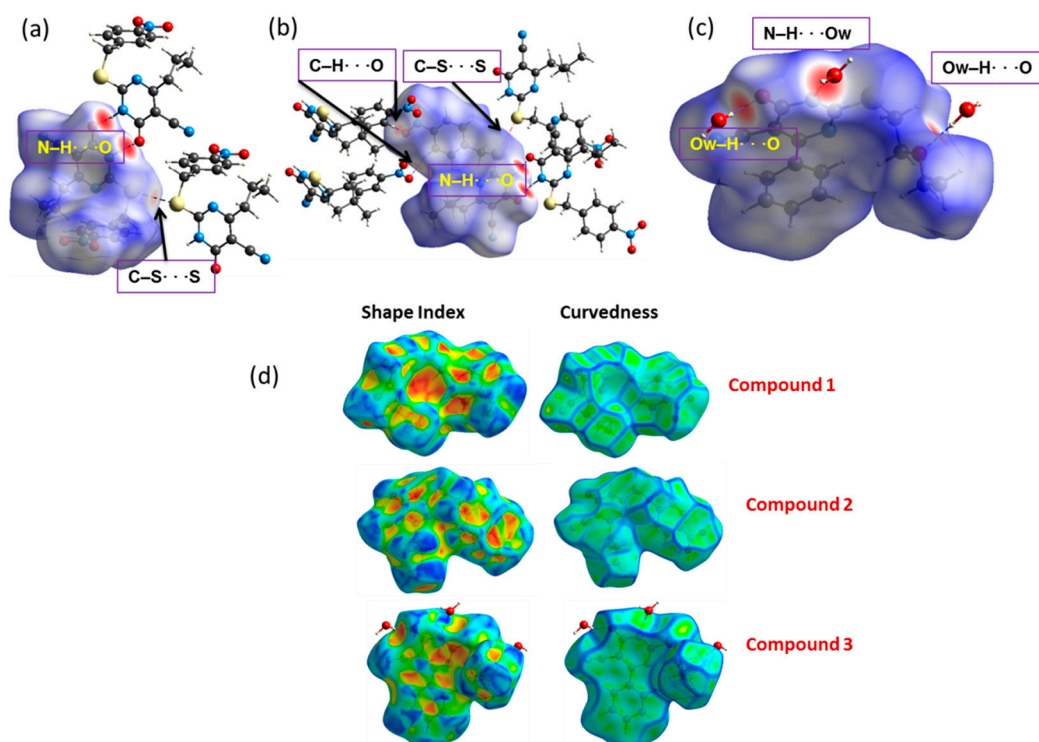


Figure 7. Hirshfeld surface of compounds 1 (a), 2 (b), and 3 (c) mapped with d_{norm} , and (d) shape index, and curvedness.

The main intermolecular interactions influencing the molecular packing of compounds 1–3 were studied using the 2D fingerprint plots. The 2D fingerprint plots of the compounds are shown in Figure 8.

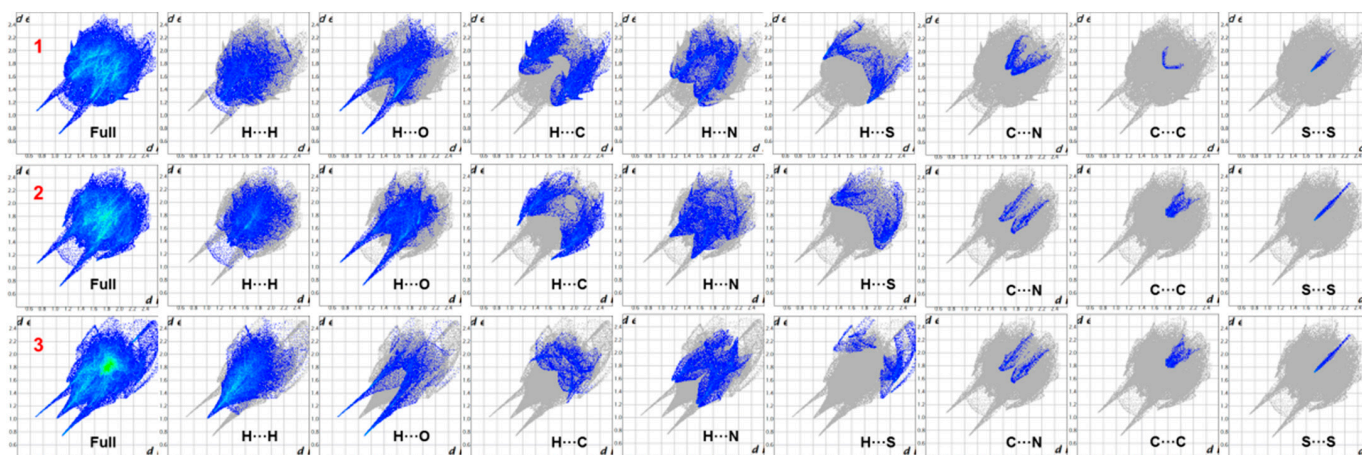


Figure 8. The 2D fingerprint plots for different inter-contacts obtained from structures 1, 2, and 3.

It is noticeable that the $\text{O}\cdots\text{H}$, $\text{N}\cdots\text{H}$, $\text{C}\cdots\text{H}$, and $\text{S}\cdots\text{H}$ contacts play a significant role in crystal packing [39–42]. The $\text{O}\cdots\text{H}/\text{H}\cdots\text{O}$ contacts are represented by a pair of sharp spikes in all three compounds, and these contacts are symmetrical in 1–2 with a $d_i + d_e$ distance of ~ 1.8 Å. In contrast, the corresponding contacts are not symmetrical in the 2D-FP due to the presence of a water molecule in compound 3. The distribution of $\text{H}\cdots\text{H}$ contacts markedly varied between compounds 1–2 and 3. In the latter compound, a single spike with the shortest contact is located at 2.0 Å. We also noted that there is a considerable difference in the contact distribution pattern of $\text{C}\cdots\text{H}/\text{H}\cdots\text{C}$ interactions in these compounds. The shortest contact of these interactions is located at ~ 2.8 , 2.7, and 3.0 Å in compounds 1, 2,

and **3**, respectively, suggesting its strength. The strength of this interaction is nearly equal in **1** and **2**, whereas it is weak in nature in **3**.

Similarly, the distribution pattern of N \cdots H/H \cdots N interactions also looks different in these compounds, with the closest contact separation of \sim 2.7, 2.6, and 2.8 Å in compounds **1**, **2**, and **3**, respectively. It is important to point out that the contribution (0.7–0.9% to the total HS area) of the chalcogen contact (S \cdots S) is nearly the same in all three compounds. However, there is a remarkable variation in the closest contact distance. The shortest S \cdots S contact is at 3.4 Å in **1** and **2**, and the corresponding contact is located beyond 3.4 Å in **3**, which indicates that the chalcogen bond plays a significant role in the stabilization of the crystal structures of **1** and **2**, rather than the structure of **3**.

The relative contribution of various intermolecular interactions in the title dihydropyrimidine derivatives was also obtained from 2D fingerprint plots. In compound **1**, the most important contribution towards crystal packing is from the O \cdots H (25.4%), C \cdots H (19.1%), N \cdots H (13.5%), and S \cdots H (6.6%) contacts. The O \cdots H/H \cdots O showed a dominant role in the overall crystal packing of compound **1** (Figure 9). Compound **2** also showed similar contributions for some of the inter-contacts as compound **1**. The replacement of propyl group with an isobutyl group at position 4 of the dihydropyrimidine ring led to increasing the H \cdots H (25.8%) and O \cdots H (27.9%) and decreasing the H \cdots C (16.7%) contacts compared to compound **1**. Additionally, the nitro group in compound **2** also contributed towards the increase in O \cdots H/H \cdots O contacts in the whole system (Figure 7). Compound **3** has a maximum contribution from H \cdots H (44.5%), followed by N \cdots H (13.8%), O \cdots H (13.4%), and S \cdots H contacts (5.6%). On the other hand, the substitution of the phenyl ring at position 4 of the dihydropyrimidine ring led to a significant increase in the C \cdots C (9.7%) contacts, confirming the $\pi \cdots \pi$ interaction in this structure (Figure 9).

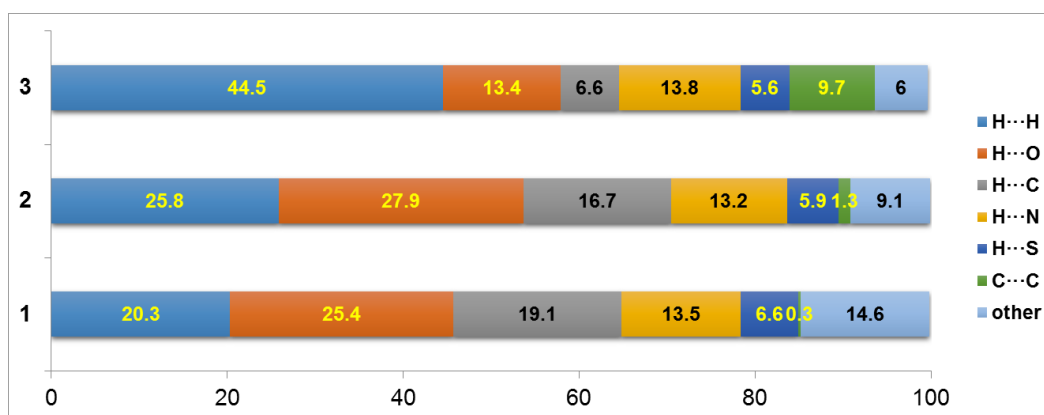


Figure 9. Relative contribution of various intermolecular interactions in the crystal packing of compounds **1**, **2**, and **3**.

2.4. Molecular Docking Studies as Human Dihydrofolate Reductase (hDHFR) Inhibitors

Molecular docking studies were performed to predict the molecular interaction between the receptor and compounds **1**, **2**, and **3**, and possible binding poses and binding energies. The crystal structures of compounds **1**, **2**, and **3** prepared from LigPrep [43] were subjected to rigid docking against hDHFR using Glide docking, followed by an induced fit docking protocol. Amino acid residues Ile-7, Leu-22, Phe-31, Phe-34, Arg-70, and Val-115 are essential for the activity of hDHFR and DHFR inhibition studies [44]. Our docking results (Table 2) identified compound **2** as a top binding ligand with a docking score of -8.58 kcal/mol (Figure 10). The nitro group formed a $\pi \cdots$ cation interaction with key residue Phe34, present in the alpha helix. Importantly, the nitrile group and 1,6-dihydropyrimidine enhance the binding energy with several water-mediated hydrogen bonding interactions with Asn64 and Ser59. Compound **1** showed a docking score of -8.34 kcal/mol, it formed key interactions with essential residues Phe34, Val115, and Phe34 in the active site. The 1,6-dihydropyrimidine ring formed a hydrogen bonding

interaction with Val115 and $\pi \dots \pi$ interaction with Phe34 residues. Unlike compound 2, the nitro group of compound 1 formed a $\pi \dots$ cation interaction with the Phe31 residue. Additionally, the nitro and nitrile groups enhanced the binding affinity with hDHFR via several water-mediated interactions with Val8, Gln35, and Asp64. Compound 3 showed a docking score of -7.34 kcal/mol, with hydrogen bonding interactions with Arg70 and Gln35 residues in the active site. The oxygen of the carbonyl group formed a hydrogen bond with residue Gln35 and the nitrile group formed an interaction with Arg70. Furthermore, compound 3 and hDHFR complex were stabilized by water-mediated hydrogen-bonding interactions with Asn64 (Figure 11).

Table 2. The docking scores of compounds 1, 2, and 3 against hDHFR after IFD.

Compound	Docking Score	Glide Energy	No. of Interactions	No. of H-Bonding Residues	Interacting Residues
1	-8.53 kcal/mol	-93.57	1	0	Phe34 (pi.cation) Interaction with Gln35, Asn64, and Ser59 via water
2	-8.34 kcal/mol	-84.82	1	1	H-bond: Val115, Phe34 (pi \dots pi), Phe31 (pi \dots cation) Interaction with Gln35, Asn64, and Val8 via water
3	-7.34 kcal/mol	-75.03	2	2	H-bond: Arg 70, and Gln35; water-mediated interactions with Asn4

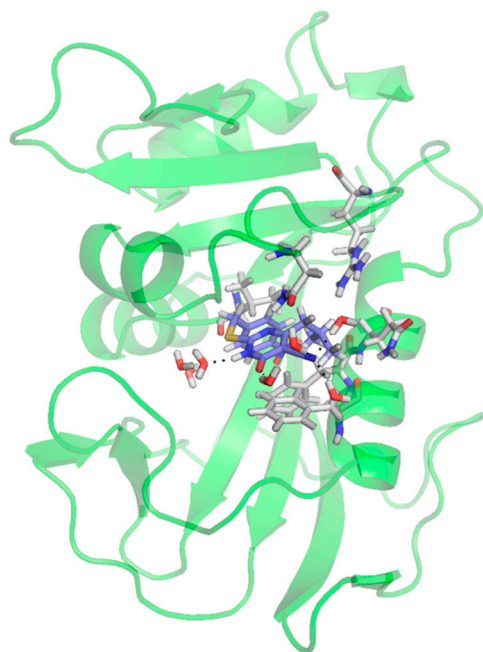


Figure 10. Binding pose of compound 2 (blue) in the active site of hDHFR, with a docking score of -8.58 kcal/mol (hDHFR represented as an illustration in a green color; interacting residues and ligands are represented in a tube model).

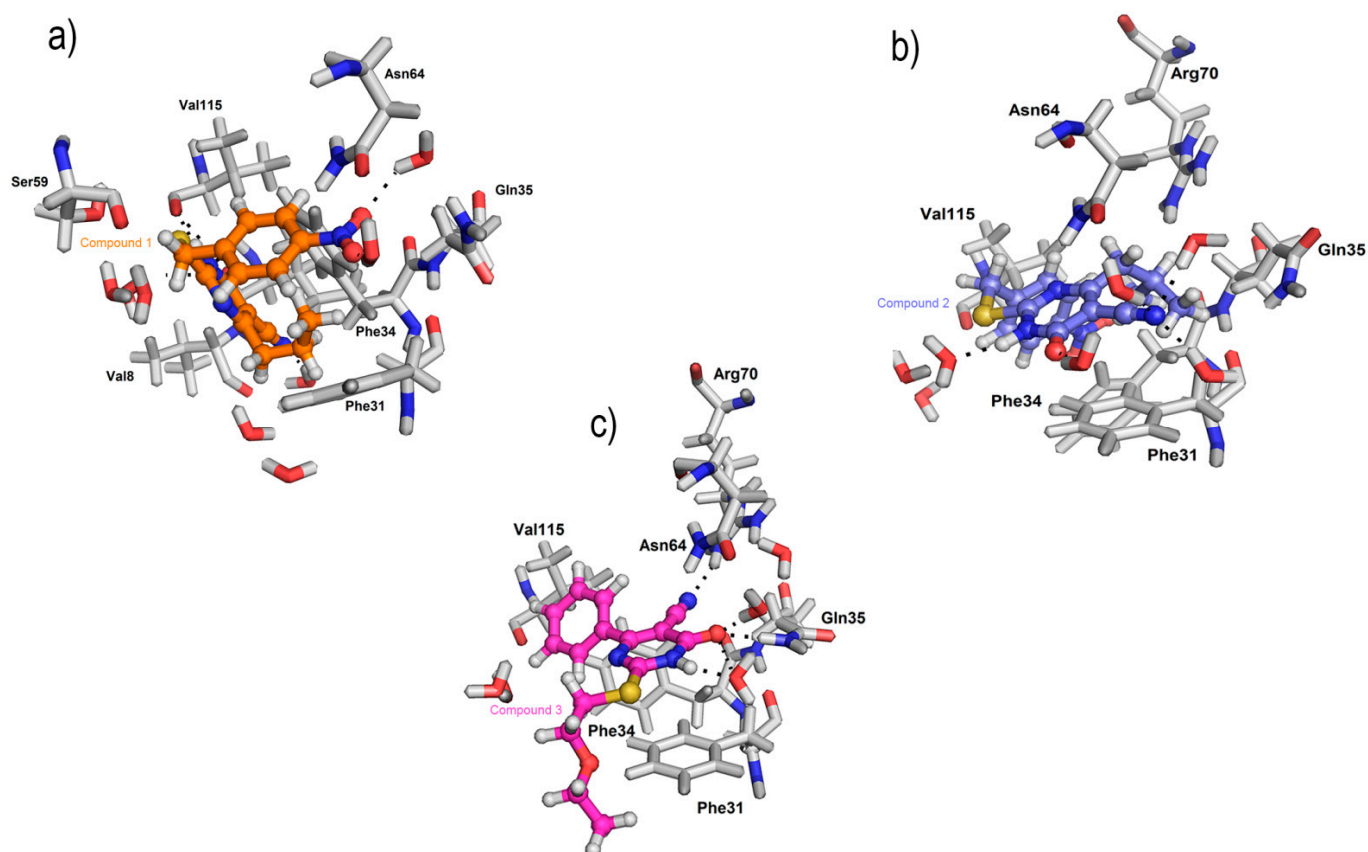


Figure 11. Binding poses of (a) compounds 1 (orange), (b) 2 (blue), and (c) 3 (magenta) in the active site of hDHFR (active site residues and water molecules are represented as tubes and ligands in a ball and stick model).

3. Materials and Methods

3.1. Synthesis and Crystallization

Compounds 1, 2, and 3 were prepared following the reaction sequences in Scheme 1. The pure single crystals were obtained by slow evaporation of EtOH/CHCl₃ (1:2, *v/v*) solution at room temperature to yield the compounds as colorless transparent prism crystals.

2-[[[4-Nitrophenyl)methyl]sulfanyl]-6-oxo-4-propyl-1,6-dihydropyrimidine-5-carbonitrile 1 [31]: Yield: 92%; M.p. 210–212 °C (EtOH); Mol. Formula (Mol. wt.): C₁₅H₁₄N₄O₃S (330.36).

4-(2-Methylpropyl)-2-[[[4-nitrophenyl)methyl]sulfanyl]-6-oxo-1,6-dihydropyrimidine-5-carbonitrile 2 [32]: Yield: 90%; M.p. 217–219 °C (EtOH/H₂O); Mol. Formula (Mol. wt.): C₁₆H₁₆N₄O₃S (344.39).

2-[[[2-Ethoxyethyl)sulfanyl]-6-oxo-4-phenyl-1,6-dihydropyrimidine-5-carbonitrile monohydrate 3 [30]: Yield: 42%; M.p. 161–163 °C (EtOH); Mol. Formula (Mol. wt.): C₁₅H₁₅N₃O₂S (301.36).

3.2. Single Crystal X-ray Diffraction Determination

Single crystals of compounds 1–3 were used to measure the X-ray diffraction at room temperature (293 K) on a Xcalibur, Ruby, Gemini diffractometer (Agilent Technologies, Inc., Santa Clara, CA, USA) using a single wavelength X-ray source (Cu K α radiation: $\lambda = 1.54184$ Å). Pre-experiment, data collection, data reduction, and analytical absorption correction were performed with the program suite *CrysAlisPro* (Rigaku Oxford Diffraction) [45]. The structures were solved with the Olex2 program [46], and the refinement was performed with the *SHELXL 2018/3* program [47]. In all three structures, the position of the NH atoms was located from a difference Fourier map, and in compound 3, the positions of water H atoms were also located from a difference map. In compound 2, EADP constraints were applied to atoms C7, C8, C14, and C15 and DFIX restraints were applied to C7–C8/C7–C9 bonds with 2.0 Å. Furthermore, SIMU restraints were applied to make

the atomic displacement parameter (ADP) values for these atoms more reasonable. In compound **3**, the O–H distances were restrained to 0.90 (2) Å during the final refinement. In all three structures, H atoms bound to C atoms were placed in geometrically idealized positions (C–H = 0.93–0.98 Å) and were constrained to ride on their parent atoms with $U_{\text{iso}}(\text{H}) = 1.2U_{\text{eq}}(\text{C})$. The positions of methyl H atoms were placed in calculated positions (C–H = 0.96 Å), but were allowed to rotate about the C–C bonds and constrained to ride on their parent atoms with $U_{\text{iso}}(\text{H}) = 1.5U_{\text{eq}}(\text{C})$.

3.3. Computational Details

3.3.1. Hirshfeld Surface Analysis

Hirshfeld surface and 2D fingerprint plots were generated using CrystalExplorer3.1 [42]. The Crystallographic Information Files (cif files) of compounds **1**, **2**, and **3** were used as input files to visualize HS and 2D fingerprint plots. The normalized contact distance (d_{norm}), mapped throughout the surface, is defined as:

$$d_{\text{norm}} = \frac{d_i - r_i^{\text{vdW}}}{r_i^{\text{vdW}}} + \frac{d_e - r_e^{\text{vdW}}}{r_e^{\text{vdW}}}$$

where d_e and d_i represent the distances from a point on the surface to the nearest nucleus outside and inside the surface, respectively, and r^{vdW} corresponds to the van der Waals (vdW) radii of the atoms involved. The red-white-blue colors on the d_{norm} surface indicate the interatomic distances are shorter than vdW (red), equal to vdW (white), and longer than vdW (blue) [39]. Shape index and curvedness were generated to study $\pi \cdots \pi$ interaction in the current derivatives. Complimentary blue and red triangle on the shape index and green flat areas on the curvedness are distinctive features of $\pi \cdots \pi$ stacking [40]. Furthermore, 2D-fingerprint plots were used to compare the relative contribution of various non-covalent contacts present in the molecular packing of the dihydropyrimidine derivatives [40,41]. Furthermore, the energy frameworks for compounds **1–3** were generated with a B3LYP/6-31G(d,p) level of approximation using the CrystalExplorer-17.5 program [48].

3.3.2. Molecular Docking Studies

Protein Preparation and Grid Generation

The 3D structure coordinates of human dihydrofolate reductase (hDHFR) were retrieved from RCSB (PDB ID: 1drf) [49], and refined using a protein preparation module in Schrödinger suite [50]. In protein preparation, hydrogen atoms were added, water beyond 5 Å was removed, added missing side chain using prime, assigned pH 7.0 ± 1, followed by structure optimization and minimization steps. After the protein preparation, the resulting structure was subjected to a grid generation protocol. Receptor grid was generated on the folic acid binding site using Schrodinger suite to dock small molecules of interest.

Ligand Preparation

Structures of compounds **1–3**, along with cocrystallized ligand (folic acid), were imported into the Maestro suite for docking calculation. These ligands were subjected to ligand preparation using LigPrep module [51]. Possible ring conformations, ionization states, and tautomers were generated using the Maestro suite.

4. Conclusions

The crystal structures of three 2,4-disubstituted-dihydropyrimidine-5-carbonitrile derivatives were determined at the room temperature. The structural analysis revealed that compounds **1** and **2** are primarily stabilized by a N–H \cdots O hydrogen bond and C–S \cdots S chalcogen bond. In compound **2**, a short intermolecular C–H \cdots O interaction and C–H \cdots N interaction provided additional stabilization. The N–H \cdots O hydrogen bond forms an $R^2_2(8)$ cyclic synthon in both compounds **1** and **2**. Due to the presence of a water molecule in compound **3**, the cyclic synthon disappears, and the water molecule participates in

N–H...O and O–H...O hydrogen bonds. In addition, C–H...O and C–H...N interactions are additionally stabilized in compound **3**. The Hirshfeld analysis revealed variations in different inter-contacts due to the presence of substituents in these compounds. The shape index plot confirmed the π -stacking interaction in compound **3**. The energy framework analysis showed that these compounds adopt distinct 3D-energy topologies. However, the dispersion energy framework showed a similar feature in compounds **1** and **2**. Molecular docking analysis indicated that these three compounds showed an inhibitory potential against the human DHFR enzyme.

Supplementary Materials: The Checkcif report of compounds **1–3** are available online.

Author Contributions: Conceptualization, A.A.E.-E.; methodology, L.H.A.-W., A.S., M.S.M.A. and M.A.E.; software, V.T., S.T. and M.S.M.A.; validation, L.H.A.-W., M.A.E. and S.T.; formal analysis, V.T., S.T. and M.S.M.A.; investigation, S.G.-G., V.T., A.S. and M.A.E.; data curation, S.G.-G. and S.T.; writing—original draft preparation, A.A.E.-E.; writing—review and editing, A.A.E.-E., V.T. and S.T.; supervision, L.H.A.-W. and A.A.E.-E.; project administration, A.A.E.-E.; funding acquisition, L.H.A.-W. All authors have read and agreed to the published version of the manuscript.

Funding: This research was funded by the Deanship of Scientific Research at Princess Nourah bint Abdulrahman University through the Fast-track Research Funding Program.

Institutional Review Board Statement: Not applicable.

Informed Consent Statement: Not applicable.

Data Availability Statement: Not applicable.

Acknowledgments: The DST-FIST for Schrodinger facility offered by the Indian institute of Technology Gandhinagar, India, is greatly appreciated.

Conflicts of Interest: The authors declare no conflict of interest.

Sample Availability: Samples of compounds **1**, **2** and **3** are available from the corresponding author.

References

- Kumar, S.; Narasimhan, B. Therapeutic potential of heterocyclic pyrimidine scaffolds. *Chem. Cent. J.* **2018**, *12*, 38. [CrossRef] [PubMed]
- Klein, R.S.; Lenzi, M.; Lim, T.H.; Hotchkiss, K.A.; Wilson, P.; Schwartz, E.L. Novel 6-substituted uracil analogs as inhibitors of the angiogenic actions of thymidine phosphorylase. *Biochem. Pharmacol.* **2001**, *62*, 1257–1263. [CrossRef]
- Matsushita, S.; Nitanda, T.; Furukawa, T.; Sumizawa, T.; Tani, A.; Nishimoto, K.; Akiba, S.; Miyadera, K.; Fukushima, M.; Yamada, Y.; et al. The effect of a thymidine phosphorylase inhibitor on angiogenesis and apoptosis in tumors. *Cancer Res.* **1999**, *59*, 1911–1916. [PubMed]
- Boisdron-Celle, M.; Remaud, G.; Traore, S.; Poirier, A.L.; Gamelin, L.; Morel, A.; Gamelin, E. 5-Fluorouracil-related severe toxicity: A comparison of different methods for the pretherapeutic detection of dihydropyrimidine dehydrogenase deficiency. *Cancer Lett.* **2007**, *249*, 271–282. [CrossRef]
- Cole, C.; Reigan, P.; Gbaj, A.; Edwards, P.N.; Douglas, K.T.; Stratford, I.J.; Freeman, S.; Jaffar, M. Potent tumor-selective nitroimidazolymethyluracil prodrug derivatives: Inhibitors of the angiogenic enzyme thymidine phosphorylase. *J. Med. Chem.* **2003**, *46*, 207–209. [CrossRef]
- Pedikian, A.Y.; Stroihein, J.; Karlin, D.; Bodey, G.P. A comparative study of oral tegafur and intravenous 5-fluorouracil in patients with metastatic colorectal cancers. *Am. J. Clin. Oncol.* **1983**, *6*, 181–186. [CrossRef]
- De Corte, B.L. From 4,5,6,7-tetrahydro-5-methylimidazo[4,5,1-jk](1,4)-benzodiazepin-2(1H)-one (TIBO) to etravirine (TMC125): Fifteen years of research on non-nucleoside inhibitors of HIV-1 reverse transcriptase. *J. Med. Chem.* **2005**, *48*, 1689–1696. [CrossRef]
- Andries, K.; Azijn, H.; Thielemans, T.; Ludovici, D.; Kukla, M.; Heeres, J.; Janssen, P.; De Corte, B.; Vingerhoets, J.; Pauwels, R.; et al. TMC125, a novel next-generation nonnucleoside reverse transcriptase inhibitor active against nonnucleoside reverse transcriptase inhibitor-resistant human immunodeficiency virus type 1. *Antimicrob. Agents Chemother.* **2004**, *48*, 4680–4686. [CrossRef]
- Ji, L.; Chen, F.-E.; De Clercq, E.; Balzarini, J.; Pannecouque, C. Synthesis and anti-HIV-1 activity evaluation of 5-alkyl-2-alkylthio-6-(arylcabonyl or alpha-cyanoarylmethyl)-3,4-dihydropyrimidin-4(3H)-ones as novel non-nucleoside HIV-1 reverse transcriptase inhibitors. *J. Med. Chem.* **2007**, *50*, 1778–1786. [CrossRef]
- Mai, A.; Artico, M.; Rotili, D.; Tarantino, D.; Clotet-Codina, I.; Armand-Ugón, M.; Ragno, R.; Simeoni, S.; Sbardella, G.; Nawrozkij, M.B.; et al. Synthesis and biological properties of novel 2-aminopyrimidin-4(3H)-ones highly potent against HIV-1 mutant strains. *J. Med. Chem.* **2007**, *50*, 5412–5424. [CrossRef]

11. Mai, A.; Artico, M.; Ragno, R.; Sbardella, G.; Massa, S.; Musiu, C.; Mura, M.; Marturana, F.; Cadeddu, A.; Maga, G.; et al. 5-Alkyl-2-alkylamino-6-(2,6-difluorophenylalkyl)-3,4-dihydropyrimidin-4(3H)-ones, a new series of potent, broad-spectrum non-nucleoside reverse transcriptase inhibitors belonging to the DABO family. *Bioorg. Med. Chem.* **2005**, *13*, 2065–2077. [CrossRef]
12. Yang, S.; Chen, F.E.; De Clercq, E. Dihydro-alkoxyl-benzyl-oxopyrimidine derivatives (DABOs) as non-nucleoside reverse transcriptase inhibitors: An update review (2001–2011). *Curr. Med. Chem.* **2012**, *19*, 152–162. [CrossRef]
13. Gauni, K.K.; Kohlhage, H. In vitro and in vivo virostatic properties of alkylated pyrimidines against DNA and RNA viruses. *Chemotherapy* **1969**, *14*, 158–169. [CrossRef]
14. Semaine, W.; Johar, M.; Tyrrell, D.L.; Kumar, R.; Agrawal, B. Inhibition of hepatitis B virus (HBV) replication by pyrimidines bearing an acyclic moiety: Effect on wild-type and mutant HBV. *J. Med. Chem.* **2006**, *49*, 2049–2054. [CrossRef]
15. Ramajayam, R.; Tan, K.P.; Liu, H.G.; Liang, P.H. Synthesis, docking studies, and evaluation of pyrimidines as inhibitors of SARS-CoV 3CL protease. *Bioorg. Med. Chem. Lett.* **2010**, *20*, 3569–3572. [CrossRef] [PubMed]
16. Schweitzer, B.I.; Dicker, A.P.; Bertino, J.R. Dihydrofolate reductase as a therapeutic target. *FASEB J.* **1990**, *4*, 2441–2452. [CrossRef] [PubMed]
17. Kompis, I.M.; Islam, K.; Then, R.L. DNA and RNA synthesis: Antifolates. *Chem. Rev.* **2005**, *105*, 593–620. [CrossRef]
18. Amyes, S.G. Comparative antibacterial spectrum of trimethoprim and brodimoprim. *J. Chemother.* **1993**, *5*, 417–421. [CrossRef] [PubMed]
19. Sincak, C.A. Iclaprim, a novel diaminopyrimidine for the treatment of resistant Gram-positive infections. *Ann. Pharmacother.* **2009**, *43*, 1107–1114. [CrossRef]
20. Locher, H.H.; Schlunegger, H.; Hartman, P.G.; Anghern, P.; Then, R.L. Antibacterial activities of epiroprim, a new dihydrofolate reductase inhibitor, alone and in combination with dapsone. *Antimicrob. Agents Chemother.* **1996**, *40*, 1376–1381. [CrossRef]
21. Walzer, P.D.; Kim, C.K.; Foy, J.M.; Linke, M.J.; Cushion, M.T. Inhibitors of folic acid synthesis in the treatment of experimental *Pneumocystis carinii* pneumonia. *Antimicrob. Agents Chemother.* **1988**, *32*, 96–103. [CrossRef]
22. Cowman, A.F.; Morry, M.J.; Biggs, B.A.; Cross, G.A.; Foote, S.J. Amino acid changes linked to pyrimethamine resistance in the dihydrofolate reductase-thymidylate synthase gene of *Plasmodium falciparum*. *Proc. Natl. Acad. Sci. USA* **1988**, *85*, 9109–9113. [CrossRef] [PubMed]
23. Bunyarataphan, S.; Leartsakulpanich, U.; Taweechai, S.; Tarnchompoo, B.; Kamchonwongpaisan, S.; Yuthavong, Y. Evaluation of the activities of pyrimethamine analogs against *Plasmodium vivax* and *Plasmodium falciparum* dihydrofolate reductase-thymidylate synthase using in vitro enzyme inhibition and bacterial complementation assays. *Antimicrob. Agents Chemother.* **2006**, *50*, 3631–3637. [CrossRef] [PubMed]
24. Suryawanshi, S.N.; Bhat, B.A.; Pandey, S.; Chandra, N.; Gupta, S. Chemotherapy of leishmaniasis. Part VII: Synthesis and bioevaluation of substituted terpenyl pyrimidines. *Eur. J. Med. Chem.* **2007**, *42*, 1211–1217. [CrossRef] [PubMed]
25. Mc Carthy, O.K.; Schipani, A.; Buendia, A.M.; Ruiz-Perez, L.M.; Kaiser, M.; Brun, R.; Pacanowska, D.G.; Gilbert, I.H. Design, synthesis and evaluation of novel uracil amino acid conjugates for the inhibition of *Trypanosoma cruzi* dUTPase. *Bioorg. Med. Chem. Lett.* **2006**, *16*, 3809–3812. [CrossRef] [PubMed]
26. Deshmukh, M.B.; Salunkhe, S.M.; Patil, D.R.; Anbhule, P.V. A novel and efficient one step synthesis of 2-amino-5-cyano-6-hydroxy-4-aryl pyrimidines and their anti-bacterial activity. *Eur. J. Med. Chem.* **2009**, *44*, 2651–2654. [CrossRef] [PubMed]
27. Agarwal, N.; Srivastava, P.; Raghuvanshi, S.K.; Upadhyay, D.N.; Sinha, S.; Shukla, P.K.; Ji Ram, V. Chloropyrimidines as a new class of antimicrobial agents. *Bioorg. Med. Chem.* **2002**, *10*, 869–874. [CrossRef]
28. Agarwal, N.; Raghuvanshi, S.K.; Upadhyay, D.N.; Shukla, P.K.; Ram, V.J. Suitably functionalised pyrimidines as potential antimycotic agents. *Bioorg. Med. Chem. Lett.* **2000**, *10*, 703–706. [CrossRef]
29. Taher, A.T.; Abou-Seri, S.M. Synthesis and bioactivity evaluation of new 6-aryl-5-cyano thiouracils as potential antimicrobial and anticancer agents. *Molecules* **2012**, *17*, 9868–9886. [CrossRef]
30. Al-Abdullah, E.S.; Al-Obaid, A.-R.M.; Al-Deeb, O.A.; Habib, E.E.; El-Emam, A.A. Synthesis of novel 6-phenyl-2,4-disubstituted pyrimidine-5-carbonitriles as potential antimicrobial agents. *Eur. J. Med. Chem.* **2011**, *46*, 4642–4647. [CrossRef]
31. Al-Abdullah, E.S.; Al-Turkistani, A.A.; Al-Deeb, O.A.; El-Brollosy, N.R.; Habib, E.E.; El-Emam, A.A. Pyrimidine-5-carbonitriles II: Synthesis and antimicrobial activity of novel 6-alkyl-2,4-disubstituted pyrimidine-5-carbonitriles. *Drug Res.* **2014**, *64*, 31–39. [CrossRef]
32. Al-Deeb, O.A.; Al-Turkistani, A.A.; Al-Abdullah, E.A.; El-Brollosy, N.R.; Habib, E.E.; El-Emam, A.A. Pyrimidine-5-carbonitriles—Part III: Synthesis and antimicrobial activity of novel 6-(2-substituted propyl)-2,4-disubstituted pyrimidine-5-carbonitriles. *Heterocycl. Commun.* **2013**, *19*, 411–419. [CrossRef]
33. Kambe, S.; Saito, K.; Kishi, H. A one-step synthesis of 4-oxo-2-thioxopyrimidine derivatives by ternary condensation of ethyl cyanoacetate, aldehydes, and thiourea. *Synthesis* **1979**, 287–289. [CrossRef]
34. El-Emam, A.A.; Demirtaş, G.; Dege, N.; Al-Deeb, O.A.; El-Brollosy, N.R. 2-[(2-Methoxyethyl)sulfanyl]-4-(2-methyl-propyl)-6-oxo-1,6-dihydropyrimidine-5-carbonitrile. *Acta Crystallogr.* **2012**, *E68*, o1379. [CrossRef]
35. Al-Tamimi, A.-M.S.; Ghabbour, H.A.; El-Emam, A.A. Crystal structure of 6-oxo-4-propyl-2-(propylthio)-1,6-dihydropyrimidine-5-carbonitrile, C₁₁H₁₅N₃OS. *Z. Kristallogr. NCS* **2016**, *231*, 583–585. [CrossRef]
36. Sert, Y.; El-Emam, A.A.; Al-Deeb, O.A.; Al-Turkistani, A.A.; Uzun, F.; Cırak, C. The biomolecule, 2-[(2-methoxy)sulfanyl]-4-(2-methylpropyl)-6-oxo-1,6-dihydropyrimidine-5-carbonitrile: FT-IR, Laser Raman spectra and DFT. *Spectrochim. Acta A Mol. Biomol. Spectrosc.* **2014**, *126*, 86–97. [CrossRef] [PubMed]

37. Sert, Y.; Al-Turkistani, A.A.; Al-Deeb, O.A.; El-Emam, A.A.; Ucun, F.; Çırak, Ç. Experimental FT-IR, Laser-Raman and DFT spectroscopic analysis of a potential chemotherapeutic agent 6-(2-methylpropyl)-4-oxo-2-sulfanylidene-1,2,3,4-tetrahydropyrimidine-5-carbonitrile. *Spectrochim. Acta A Mol. Biomol. Spectrosc.* **2014**, *120*, 97–105. [CrossRef] [PubMed]
38. Turner, M.J.; Thomas, S.P.; Shi, M.W.; Jayatilaka, D.; Spackman, M.A. Energy frameworks: Insights into interaction anisotropy and the mechanical properties of molecular crystals. *Chem. Commun.* **2015**, *51*, 3735–3738. [CrossRef]
39. Spackman, M.A.; Jayatilaka, D. Hirshfeld surface analysis. *CrystEngComm* **2009**, *11*, 19–32. [CrossRef]
40. McKinnon, J.J.; Jayatilaka, D.; Spackman, M.A. Towards quantitative analysis of intermolecular interactions with Hirshfeld surfaces. *Chem. Commun.* **2007**, 3814–3816. [CrossRef] [PubMed]
41. McKinnon, J.J.; Fabbiani, F.P.A.; Spackman, M.A. Comparison of polymorphic molecular crystal structures through Hirshfeld surface analysis. *Cryst. Growth Des.* **2007**, *7*, 755–769. [CrossRef]
42. Spackman, M.A.; McKinnon, J.J. Fingerprinting intermolecular interactions in molecular crystals. *CrystEngComm* **2002**, *4*, 378–392. [CrossRef]
43. *LigPrep*; v2.5; Schrödinger Inc.: Portland, OR, USA, 2011.
44. Volpato, J.P.; Yachnin, B.J.; Blanchet, J.; Guerrero, V.; Poulin, L.; Fossati, E.; Berghuis, A.M.; Pelletier, J.N. Multiple conformers in active site of human dihydrofolate reductase F31R/Q35E double mutant suggest structural basis for methotrexate resistance. *J. Biol. Chem.* **2009**, *284*, 20079–20089. [CrossRef] [PubMed]
45. Clark, R.C.; Reid, J.S. The analytical calculation of absorption in multifaceted crystals. *Acta Cryst. A* **1995**, *51*, 887–897. [CrossRef]
46. Dolomanov, O.V.; Bourhis, L.J.; Gildea, R.J.; Howard, J.A.K.; Puschmann, H. A complete structure solution, refinement and analysis program. *J. Appl. Cryst.* **2009**, *42*, 339–341. [CrossRef]
47. Sheldrick, G.M. Crystal structure refinement with SHELXL. *Acta Cryst. C* **2015**, *71*, 3–8. [CrossRef]
48. Turner, M.J.; McKinnon, J.J.; Wolff, S.K.; Grimwood, D.J.; Spackman, P.R.; Jayatilaka, D.; Spackman, M.A. *CrystalExplorer17*; University of Western Australia: Perth, Australia, 2017.
49. Oefner, C.; D’Arcy, A.; Winkler, F.K. Crystal structure of human dihydrofolate reductase complexed with folate. *Eur. J. Biochem.* **1988**, *174*, 377–385. [CrossRef]
50. Sastry, G.M.; Adzhigirey, M.; Day, T.; Annabhimoju, R.; Sherman, W. Protein and ligand preparation: Parameters, protocols, and influence on virtual screening enrichments. *J. Comput. Aid. Mol. Des.* **2013**, *27*, 221–234. [CrossRef]
51. Halgren, T.A.; Murphy, R.B.; Friesner, R.A.; Beard, H.S.; Frye, L.L.; Pollard, W.T.; Banks, J.L. Glide: A new approach for rapid, accurate docking and scoring. 2. Enrichment factors in database screening. *J. Med. Chem.* **2004**, *47*, 1750–1759. [CrossRef]

Article

Spectroscopic Study of the Molecular Structure of the New Hybrid with a Potential Two-Way Antibacterial Effect

Dorota Kowalczyk ^{1,*}, Agata Gładysz ¹, Monika Pitucha ², Daniel M. Kamiński ³, Agnieszka Barańska ⁴ and Bartłomiej Drop ⁴

¹ Department of Medicinal Chemistry, Faculty of Pharmacy, Medical University, Jaczewskiego 4, 20-090 Lublin, Poland; agata.gladysz@umlub.pl

² Independent Radiopharmacy Unit, Faculty of Pharmacy, Medical University, Chodzki 4A, 20-093 Lublin, Poland; monika.pitucha@umlub.pl

³ Department of Chemistry, University of Life Sciences in Lublin, Akademicka 15, 20-950 Lublin, Poland; daniel.kaminski@poczta.umcs.lublin.pl

⁴ Department of Informatics and Medical Statistics, Medical University, Jaczewskiego 4, 20-090 Lublin, Poland; agnieszkabaranska@umlub.pl (A.B.); bartlomiej.drop@umlub.pl (B.D.)

* Correspondence: dorota.kowalczyk@umlub.pl; Tel.: +48-81-448-7388

Abstract: Bacterial strains become resistant to almost all classes of antibiotics, which makes it necessary to look for new substitutes. The non-absorbable ciprofloxacin–biguanide bismuth complex, used locally, may be a good alternative to a conventional therapy. The purpose of this study was to study the structure of the proposed ciprofloxacin (CIP)–bismuth(III)—chlorhexidine (CHX) composite (CIP–Bi–CHX). The spectroscopic techniques such as UV–VIS (ultraviolet–visible) spectroscopy, FTIR (Fourier–transform infrared) spectroscopy and NMR (Nuclear Magnetic Resonance) spectroscopy were used for structure characterization of the hybrid compound. The performed analysis confirmed the presence of the two active components—CIP and CHX and revealed the possible coordination sites of the ligands with bismuth ion in the metallo–organic structure. Spectroscopic study showed that the complexation between Bi(III) and CIP occurs through the carboxylate and ketone groups of the quinolone ring, while CHX combines with the central ion via the biguanide moieties.

Keywords: ciprofloxacin–biguanide bismuth complex; metallo–organic compound; structure characterization; spectroscopic study; FTIR; NMR

Citation: Kowalczyk, D.; Gładysz, A.; Pitucha, M.; Kamiński, D.M.; Barańska, A.; Drop, B. Spectroscopic Study of the Molecular Structure of the New Hybrid with a Potential Two-Way Antibacterial Effect.

Molecules **2021**, *26*, 1442. <https://doi.org/10.3390/molecules26051442>

Academic Editors: Rui Fausto, Sylvia Turrell and Gulce Ogruc Ildiz

Received: 27 January 2021

Accepted: 1 March 2021

Published: 7 March 2021

Publisher's Note: MDPI stays neutral with regard to jurisdictional claims in published maps and institutional affiliations.



Copyright: © 2021 by the authors. Licensee MDPI, Basel, Switzerland. This article is an open access article distributed under the terms and conditions of the Creative Commons Attribution (CC BY) license (<https://creativecommons.org/licenses/by/4.0/>).

1. Introduction

Bacterial resistance to antimicrobial drugs might become one of the biggest threats to human health in the 21st century. The rapid global spread of Gram-positive and Gram-negative bacterial pathogens, that are resistant to currently available antimicrobial therapies marks the onset of a major global health crisis. Clinicians are forced to improve medical practices and procedures to combat the spread of antibiotic resistance, which is not easy at a time when access to antibiotics and chemotherapeutic agents is common [1–3]. The problem of the spread of bacterial resistance is also associated with the production and the antibiotic production wastewater, as well as with the wide application, excretion and penetration into the aquatic environment [4,5].

One way to solve this problem is to develop new antibiotics or new drug classes that delay the evolution of drug resistance. In recent years, the number of studies looking for new compounds with antibacterial properties has increased significantly. To this end, new molecules are synthesized in the hope of their potential antibacterial activity, compounds and substances naturally occurring in the environment are tested, or compounds with proven antimicrobial activity are combined to form hybrids, composites, or complexes [6]. Scientists make attempts to create drug complexes with metal ions [7–9], combine drugs with different range of activity [10], incorporate substances naturally occurring in the

environment into the polymer matrix [11,12]. It is possible that combining two therapeutic agents may enhance their antibacterial properties or even give a new mechanism of antibacterial action to the resulting hybrid. Interactions between different components are governed by a variety of chemical bonds. The study of their properties can be a valuable tool to understand the influence of interactions between components on their properties [13]. The interesting approach is the development of new dual acting antibacterial combinations or compounds by the simultaneous administration of two different antimicrobial agents, or by combining two molecules of different antibiotics together through a chemical reaction to obtain a single molecule named a hybrid [10,14]. The advantage of this approach is the development of compounds that possess often better biological activity or even more, that may be active to microorganisms that are resistant to both antibiotics.

Structure information of newly synthesized composites is important not only for the synthesis verification and determination of the structure–activity relationship (SAR), but also the entire development and registration process [15,16].

Nuclear magnetic resonance (NMR) spectroscopy and Fourier transform infrared spectroscopy (FTIR) are the commonly used methods for the confirmation of synthesis and structural characterization of a novel chemical framework [17–33]. The spectroscopic studies were used: (i) For the characterization of metal-complexes [17–22,24,32,33] such as metalloantibiotics [21,22], including metalofluoroquinolones [18,19,22,26,33] and metal complexes with chlorhexidine [20,24], (ii) for the analysis of the decomposition of metal-complexes [20], (iii) for the characterization of inclusion compounds [25], composites/mineral composites [27,28,31,32] and (iv) for the examination of interactions between the components [23]. Infrared (IR) spectroscopic method, especially the Attenuated Total Reflectance (ATR) technique and NMR spectroscopic measurements were often applied to confirm the coordination of the ligands to metal ions and to find out the possible coordination sites in the metallo-organic structures [17]. The NMR spectroscopic measurements and FTIR studies were also proposed for the confirmation of synthesis hybrids [30].

This article is intended to demonstrate the application of spectroscopic techniques (particularly ATR-FTIR and NMR) for the structure characterization of the new metal-drug composite that is targeted at the local treatment of wounds.

2. Results and Discussion

Based on the knowledge that the ligands in metal complexes can be the ions or neutral molecules containing the atoms with free electron pairs (in particular N, O, halogens) such as carboxylate [19], triethylenetetramine, bipyridine [18,19], biguanide [20,29], the new composites (hybrids) were synthesized by covalently combining fluoroquinolone antibiotics and the biguanide derivatives with metal ion.

We present the spectroscopic structure characterization of the selected hybrid containing ciprofloxacin (CIP, fluoroquinolone antibiotic, DNA gyrase inhibitor) and chlorhexidine (CHX, biguanide derivative, antiseptic, agent disrupting the cell membrane function) as ligands. The prepared dual acting hybrid with antibacterial and potentially anti-inflammatory properties are dedicated for the local treatment of wounds. Our previous research has shown that the ciprofloxacin -bismuth complex exhibits high anti-bacterial activity and a broad spectrum of activity [33].

Taking into account of the synthesis conditions, CIP and CHX ligands were bonded to bismuth atom in a molar ratio of 1: 1: 1. Thus, the following compositions of prepared hybrid were considered:

- (a) Bi(CHX)₂NH₃: C(35.45%) H(4.46%) Bi(28.03%) Cl(9.51%) N(22.55%),
- (b) Bi(CIP)(2NH₃)₂Cl: C(31.69%) H(3.60%) Bi(32.44%) Cl(11.01%) F(2.95%) N(10.87%) O(7.45%),
- (c) Bi(CIP)(CHX): C(44.92%) H(4.35%) Bi(20.04%) Cl(6.80%) F(1.82%) N(17.46%) O(4.60%),
- (d) Bi(CIP)(CHX)₂Cl: C(41.99%) H(4.25%) Bi(18.73%) Cl(12.71%) F(1.70%) N(16.32%) O(4.30%).

The results of elemental analysis (Table 1) showed that the structure of the composite [Bi(CIP)(CHX)2Cl] is the most probable—the T-Student test showed no significant differences between the values found and the values calculated ($P(0.12-0.95) > 0.05$). Results also revealed that the reaction of CIP and CHX with bismuth salt in molar ratio of 1:1:1 gives the mixed ligand complex with stoichiometric 1:1:1. The obtained bismuth complexes are very slightly soluble in common organic solvents. Thus, the studies of electrolytic behavior of metal complex solutions, providing the insights into their nature and composition, were not successful. The melting point of the CIP-Bi-CHX composite was found to be 294.7 °C, while the melting points of the ligands, CIP and CHX, and their physical mixture, CIP + CHX, were found to be 255 °C, 134 °C and 225.7 °C, respectively.

Table 1. Percentage of elements in the CIP-Bi-CHX hybrid.

Parameter	C	H	N	Cl
Found value, % (n = 6)	41.72	5.09	15.68	13.64
Minimum	37.16	4.56	15.12	12.67
Maximum	46.85	5.69	16.06	14.72
Variance	12.9246	0.1763	0.1285	0.5036
Standard deviation	3.5951	0.4199	0.3585	0.7096
Relative standard deviation, %	8.62	8.25	2.29	5.20
Calculated value, %	41.99	4.25	16.32	12.71
T-Student test, P = 95%	t = -0.07 P = 0.9466	1.85 0.1232	-1.65 0.1601	1.21 0.2800

Figure 1 shows the structure of the CIP-Bi-CHX composite, which was suggested from the above analysis. Similar structures have been proposed for antibiotic-based complexes [18,19,21], including quinolone complexes with the participation of bipyridine [18,19].

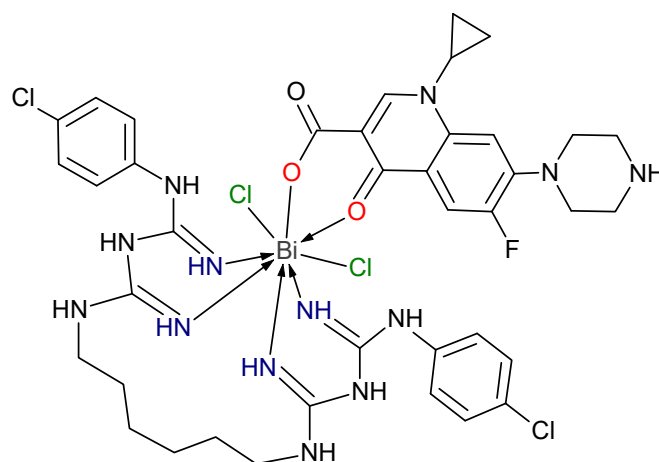


Figure 1. The probable structure of metal complex (generated by ACD ChemSketch Freeware).

2.1. UV-VIS Analysis

Chlorhexidine acetate shows absorption bands in the ultraviolet (UV) range at 208 nm and 259 nm. The spectrum of ciprofloxacin has a strong absorption band at 277.0 nm and two much weaker bands near 315.0 nm and 328.0 nm (Figure 2). The spectrum of the complex in the UV region shows the same characteristic bands as the spectra of the ligands, but the complex formation influences changes in the shape of the bands and their shifts. In the visible (VIS) region, the composite shows no absorption bands. Upon complexation with Bi(III), the bands of CIP in the region from 310 nm to 340 nm were modified and the major absorption band of CIP at 277.0 nm was shifted slightly to 272 nm and widened by overlapping with the main band of CHX. The observed changes suggest the formation of

a six-member ring (complexation between Bi(III) and CIP via the carboxylate and ketone group) which disturb the conjugation system of the ciprofloxacin structure [23,33].

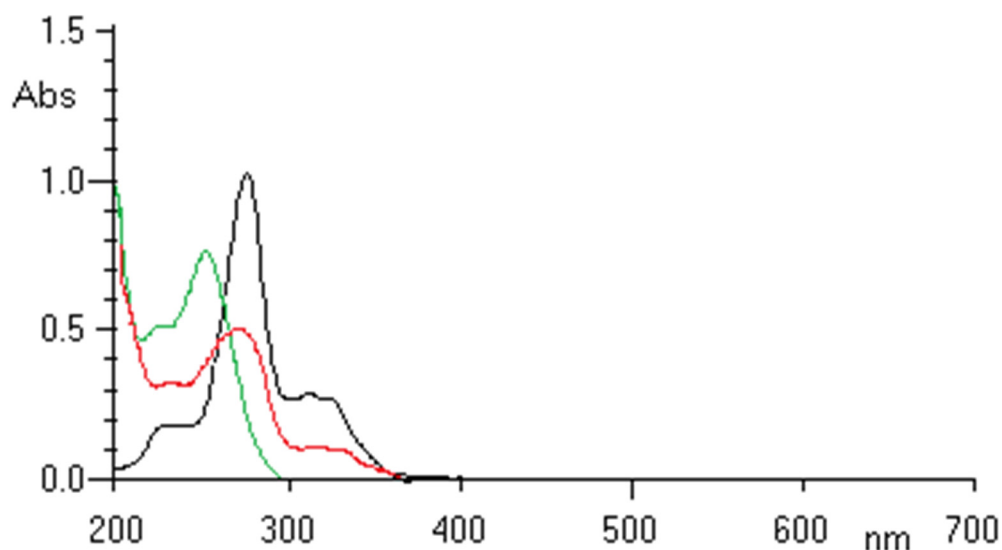


Figure 2. UV-VIS absorption spectra of ciprofloxacin (back line), chlorhexidine (green line) and ciprofloxacin-Bi-chlorhexidine composite (red line).

2.2. FTIR Analysis

A FTIR analysis was conducted for active substances (ligands) used for the synthesis of the hybrid—ciprofloxacin hydrochloride (CIP-HCl), chlorhexidine acetate (CHX-acetate), their physical mixture (CIP-HCl + CHX-acetate) (Figure 3) as well as the CIP-Bi-CHX composite, taking into account two methods of its synthesis and two synthesis stages: (i) The formation of simple complex (CIP-Bi or CHX-Bi), (ii) the formation of mixed ligand complex (CIP-Bi-CHX) (Figure 4). The recorded spectra were subjected to a comparative analysis which demonstrated the presence of vibrational bands characteristic for the functional groups occurring in the analyzed molecules (Tables 2 and 3). The absorption bands obtained for CHX-acetate and CIP-HCl (Tables 2 and 3) are in good agreement with previous literature [20,24,25,27,28] and [22,26,34], respectively.

The spectrum of the physical mixture of CIP and CHX salts is characterized by higher intensity when compared to individual substances with minor band shifts of functional groups, which can result from the intermolecular interactions of the said substances in the mixture (Figure 3, Table 2).

The IR spectrum of the ciprofloxacin-bismuth(III) complex shows changes suggesting the formation of a complex salt within the carboxyl and ketone groups in relation to the ligand, i.e., ciprofloxacin hydrochloride. The carboxyl group (COOH) in the CIP HCl molecule undergoes deprotonation, due to the substitution of hydrogen by the bismuth(III) ion, which results in the formation of an ionised carboxylate group (COO⁻) in the CIP-Bi molecule. As a consequence, the stretching vibration band of the hydroxyl group (ν OH) disappears at 3528 cm⁻¹, whereas the stretching vibration band of the carbonyl group (ν C=O) in the carboxyl group undergoes a significant shift towards lower frequencies to 1702 cm⁻¹. An intensive stretching vibration band appears at 1575 cm⁻¹, characteristic of the carbonyl group in the carboxylate group (a change of the COOH group in the CIP molecule into COO⁻ in the CIP-Bi molecule). A shift towards lower frequencies also occurs in the carbonyl spectrum of the ketone group—from 1623 cm⁻¹ in the CIP molecule to 1614 cm⁻¹ in the CIP-Bi molecule—due to the formation of a coordinate bond between C=O and the bismuth ion. In addition, the IR spectrum of the CIP-Bi complex shows changes allowing the conclusion that the ciprofloxacin in the complex is a base rather than a hydrochloride. The asymmetric and symmetric stretching vibration bands of the ionised secondary amino group (ν as/s >NH₂⁺) in the range of 2688–2465 cm⁻¹ present in the CIP-

HCl molecule disappear in the spectrum of the complex and the stretching vibration bands of the non-ionised secondary amino group (ν as/s $>NH$) appear at about $3400\text{--}3200\text{ cm}^{-1}$, which are significantly extended probably due to the formation of hydrogen bonds (the associated amino group) and/or the effect of molecular configuration in crystal.

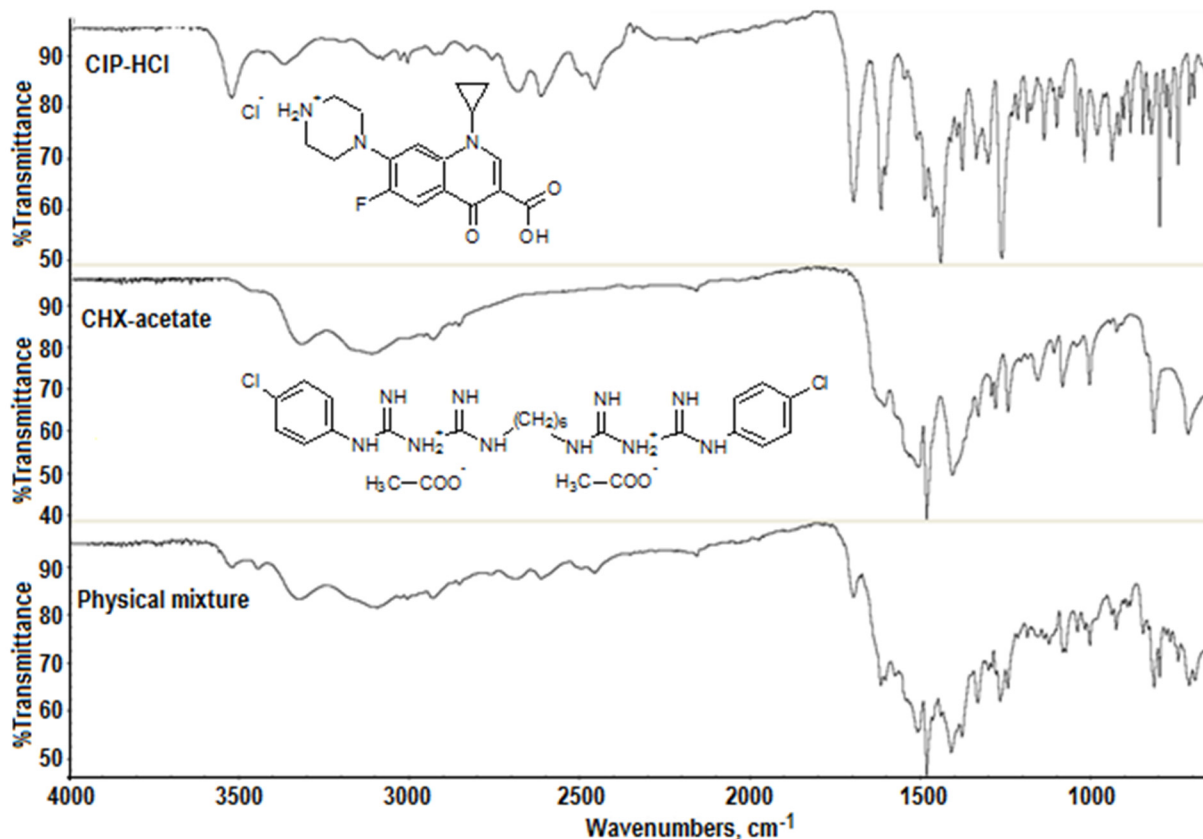


Figure 3. FT-IR spectra registered for CIP-HCl, CHX-acetate and their physical mixture ($\nu_{\max}/\text{cm}^{-1}$).

The changes observed in the IR spectrum of the complex of chlorhexidine with the bismuth(III) ion, with regard to the CHX-acetate ligand, indicate the coordination of CHX to the Bi(III) ion by the nitrogen atoms of amino groups (--C=NH). In the spectrum of the CHX-Bi complex, the stretching vibration bands at 3195 cm^{-1} and 1625 cm^{-1} corresponding to the =NH and C=N groups, respectively, and the bending vibration band at 1520 cm^{-1} corresponding to the secondary amino groups (=NH), show a positive shift and significant intensification. Although it is also possible for the nitrogen to coordinate amino groups, numerous studies of the complex compounds of biguanides emphasize the precedence of the formation of complexes with metals by nitrogen from imino groups, probably due to an increase in stability via coupling π [29].

In the CIP-Bi-CHX hybrid, which can be considered as two metal-complexes, CIP-Bi and CHX-Bi, ciprofloxacin is present as a deprotonated anion. The COOH group in the CIP molecule undergoes deprotonation and forms a salt with bismuth(III) (bismuth carboxylate), stabilized with a coordinate bond originating from the oxygen of the ketone group adjacent to the said carboxyl group. The assumed concept of the bond between Bi(III) and the CIP molecule in the composite is confirmed by the changes observable during the analysis of the spectrum (Figure 4A):

- The disappearance of the stretching vibration band of the OH group at 3528 cm^{-1} ;
- The disappearance of the stretching vibration band of C=O in the COOH group at 1702 cm^{-1} , and the appearance of the stretching vibration band of C=O in the COO^- group at 1580 cm^{-1} ;

- The shift and significant intensification of the stretching vibration band of the ketone group $>C=O$ at 1621 cm^{-1} due to interference with the $\nu\text{ C=N}$ band of chlorhexidine.

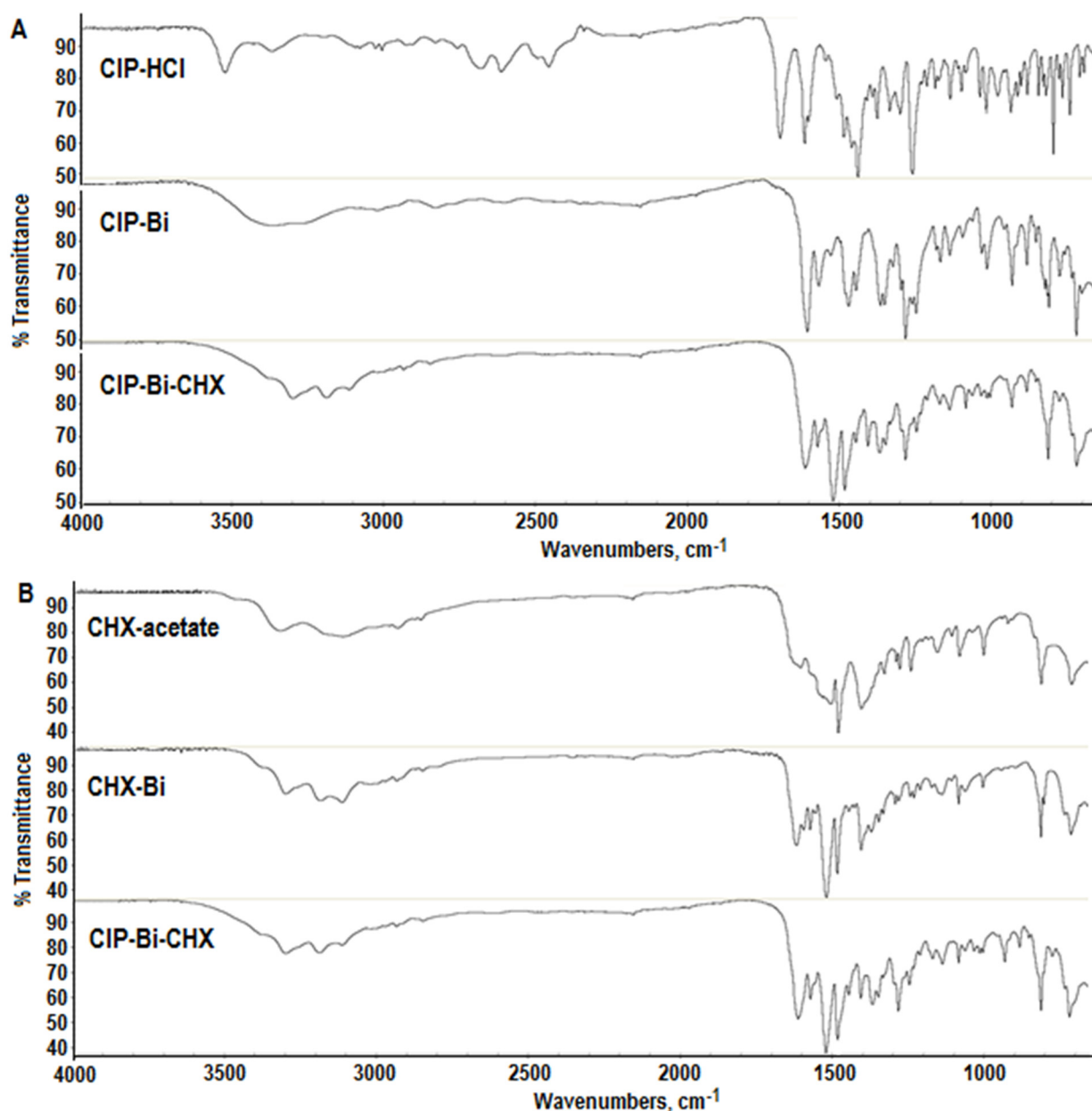


Figure 4. FTIR spectra obtained in the subsequent stages of the hybrid synthesis for method 1 (A) and method 2 (B).

The metallic coordination center of the analyzed composite also contains chlorhexidine, which is coordinated to the Bi(III) ion through the nitrogen atoms of imino groups ($-C=NH$). The assumed hypothesis is confirmed by the following changes observable during the analysis of spectrum (Figure 4B):

- A positive shift (towards higher frequencies) from 3178 cm^{-1} in the CHX molecule to 3196 cm^{-1} in the composite molecule and an intensification of the stretching vibration band of the $=NH$ group;
- A positive shift from 1611 cm^{-1} in the CHX molecule to 1621 cm^{-1} in the composite molecule, and a significant intensification of the stretching vibration band of the $C=N$ group, probably indicating a loosening of the bond due to its coordination to the metal ion [29];

- A positive shift from 1515 cm^{-1} in the CHX molecule to 1520 cm^{-1} in the composite molecule, and a significant intensification of the stretching vibration band of the N=H group.

Table 2. The characteristic vibration bands registered for CIP-HCl, CHX-acetate and their physical mixture ($\nu_{\text{max}}/\text{cm}^{-1}$).

Main Bands of Vibrations of Functional Groups	CIP-HCl	CHX-Acetate	Physical Mixture CIP-HCl + CHX-Acetate
CIP-HCl			
ν as/s (O-H in COOH)	3528m, 3375w		3525w
ν as/s (C-H in Ar)	3085w		about 3044w
ν as/s (C-H in CH_2 -cyclopropane)	3013w		3038w
ν as/s (C-H alk)	2937w		2939w
ν as/s ($>\text{NH}_2^+$)	2688m		2693m
ν (C=O; COOH)	1702s		1704 m
ν (C=O; ketone)	1623s		1623s
ν (C=C in Ar) + δ (NH)	1552–1445s		about 1495s
ν as/s (C-O)	1267s		1273 s
CHX-acetate			
ν (-NH) Alk-NH-Ar/(Alk) ₂ NH		3324m	3329m
ν (=NH)		3178m	about 3180m
ν as/s ($>\text{NH}_2^+$)		3115m	3101m
ν (C=N)		1611s	1608s
ν as/s (COO ⁻ in acetate)		1536m	1538m
δ (NH)		1515s	1516s
ν (C=C) in Ar		1488s	1492s
ν (C-N)		1249m	1250m

Vibration type: ν —stretching vibration (as-asymmetric, s-symmetric vibration), δ —deformation vibration. Vibration intensity: vs—very strong, s—strong, m—moderate, w—weak; Ar—aryl, Alk—alkyl, aliph—aliphatic.

Table 3. The structural and spectral parameters of the parent forms of ligands: CIP-HCl, CHX-acetate, their complexes with bismuth(III): CIP-Bi, CHX-Bi and CIP-Bi-CHX hybrid ($\nu_{\text{max}}/\text{cm}^{-1}$).

Main Bands of Vibrations of Functional Groups	CIP-HCl	CIP-Bi Complex	CHX-Acetate	CHX-Bi Complex	CIP-Bi-CHX Hybrid
CIP-HCl					
ν (O-H in COOH)	3528m, 3375w	No peak			No peak
ν as/s ($>\text{NH}$)	-	3362m			3383m
ν as/s (C-H in Ar)	3085w	about 3100w			No detected *
ν as/s (C-H in CH_2)	3013w	3026w			No detected *
ν as/s (C-H in CH_3)	2937w	2838w			2936w
ν as/s ($>\text{NH}_2^+$)	2688m	No peak			No peak
ν (C=O; COOH)	1702s	No peak			No peak
ν (C=O; ketone)	1623s	1614s			1621vs (int.)
ν as/s (COO ⁻)	-	1575s			1580s
ν (C=C in Ar) + δ (NH)	1552–1445s	1533–1454s			1491s
ν as/s (C-O)	1267s	1291s			1291s
CHX-acetate					
ν (-NH)			3324m	3307s	3307s
Alk-NH-Ar/(Alk) ₂ NH					
ν (=NH)			3178m	3195s	3196s
ν as/s ($>\text{NH}_2^+$)			3115m	3120s	3117m
ν (C=N)			1611m	1625vs	1621vs (int.)
ν as/s (COO ⁻ in acetate)			1536m	No peak	No peak
δ (NH)			1515s	1520vs	1520vs
ν (C=C) in Ar			1488s	1492s	1491s
ν (C-N)			1249m	No detected *	No detected *

Vibration type: ν —stretching vibration (as-asymmetric, s-symmetric vibration), δ —deformation vibration. Vibration intensity: vs—very strong, s—strong, m—moderate, w—weak. Abbreviations: int.—intensification of intensity as a result of overlapping; Ar—aryl, Alk—alkyl, aliph—aliphatic; *—hard-to-detect peak.

In addition, the IR spectrum of the composite shows changes leading to the conclusion that ciprofloxacin and chlorhexidine are present in the composite in a non-ionised form. The asymmetric and symmetric stretching vibration bands of the ionised secondary amino group (ν as/s $>\text{NH}_2^+$) in the range 2688–2465 cm^{-1} , present in the CIP HCl molecule, disappear in the composite, as does the stretching vibration band of the acetate group (ν as/s COO⁻) present in the CHX acetate molecule at about 1536 cm^{-1} (Table 3).

2.3. $^1\text{H-NMR}$ and $^{13}\text{C-NMR}$ Analyses

The NMR spectra of the CIP-Bi-CHX composite (Figures 5 and 6) indicate the presence of ciprofloxacin and chlorhexidine (Figure 7), as they contain signals characteristic of those substances (Tables 4 and 5). The obtained $^1\text{H-NMR}$ (Table 4) and $^{13}\text{C-NMR}$ (Table 5) signals are in agreement with the spectral database for organic compounds [35] and available literature [36–40] for CHX-acetate and CIP-HCl, respectively. A comparative analysis of the NMR spectra also indicates the CIP and CHX bonding through the bismuth atom, owing to the appearance of significant changes in the composite spectrum, in relation to the same signals in the spectra of the parent substances. The changes involve:

- Differences in the multiplicity of the band;
- Differences in the band intensity (mainly signal reduction);
- Band broadening;
- Significant band shifts;
- Bands disappearance.

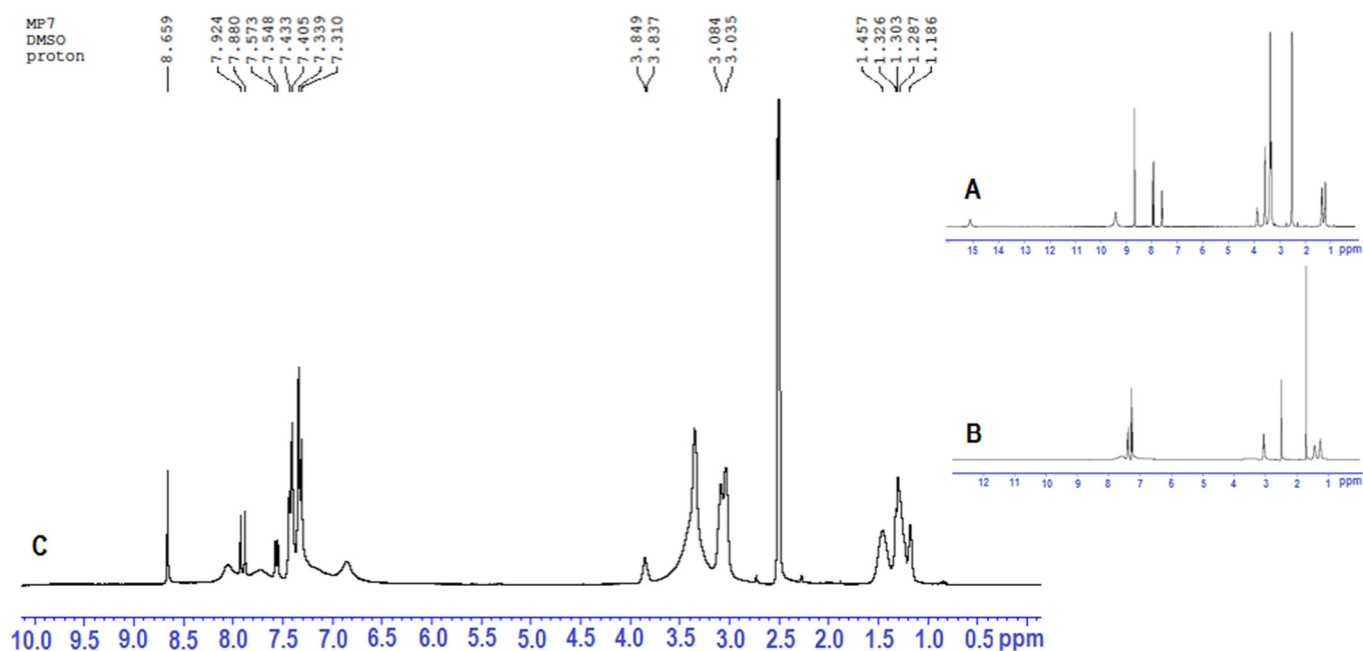


Figure 5. The $^1\text{H-NMR}$ spectra of the parent forms of ligands: CIP-HCl (A), CHX-acetate (B) and the tested CIP-Bi-CHX composite (C).

These changes indicate a strong interference into the molecules of the parent substances, with the possibility of forming a hybrid structure—forming covalent and coordinate bonds.

The $^1\text{H-NMR}$ spectrum of the composite show proton bands characteristic of ciprofloxacin at 1.19, 1.30–1.33, 3.84–3.85, and 7.55–8.66 ppm. When compared to the CIP, the CIP-Bi-CHX composite shows changes in the chemical shifts ($\Delta 0.025$ – 0.054 ppm) of the aromatic hydrogen atoms towards lower values in the quinolin-4-one ring, probably caused by the coordination of the Bi(III) ion by the oxygen atom of the 4-ketone group, and the formation of a covalent bond with the 3-carboxyl group, which is confirmed by the disappearance of the carboxyl group hydrogen signal at 15.14 ppm, due to the substitution of the carboxyl group proton with the bismuth atom. The similar changes in chemical shifts have been seen previously with the mixed ligand metal complexes [32]. The $^1\text{H-NMR}$ spectrum of the composite shows the disappearance of the proton band of the $>\text{NH}_2^+$ group in the piperazinium ring, which is present in the CIP-HCl molecule [39]. This fact supports the assumption that CIP is present in the composite in its non-ionised form.

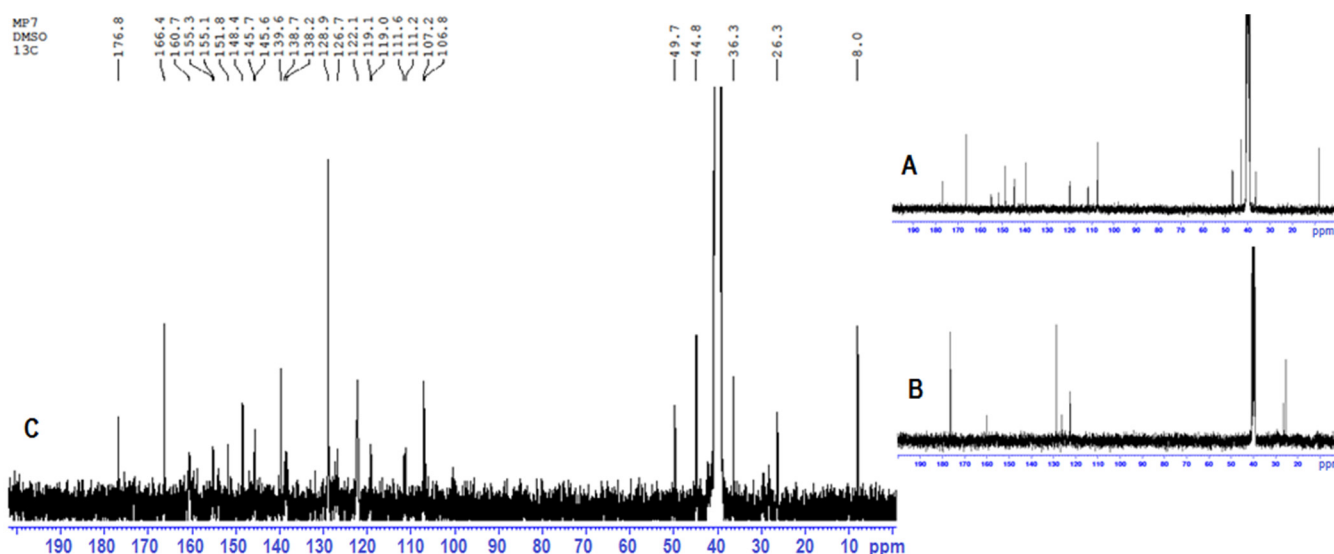


Figure 6. The ^{13}C -NMR spectra of the parent forms of ligands: CIP-HCl (A) and CHX-acetate (B) and the tested CIP-Bi-CHX composite (C).

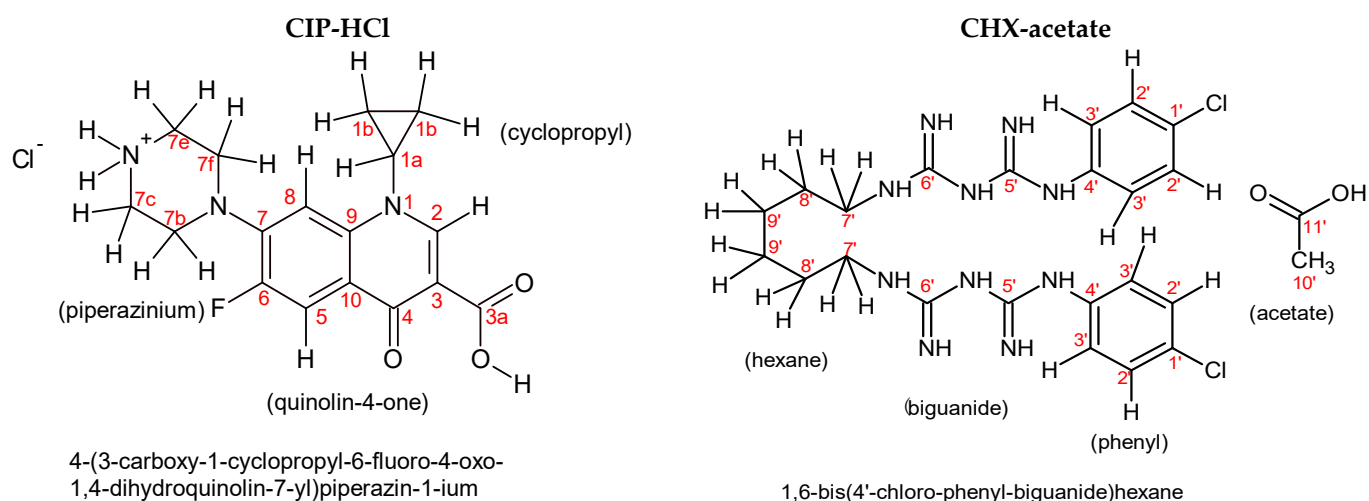


Figure 7. Structural formulas of CIP-HCl and CHX-acetate (generated by ACD ChemSketch Freeware).

The ^1H -NMR spectrum of the composite also shows the presence of proton bands characteristic of chlorhexidine at 1.29, 1.46, 3.04–3.08, 7.31–7.43 ppm, which underwent critical shifts after the incorporation of CHX into the composite structure. The changes particularly involve multiplicity and chemical shifts ($\Delta 0.015$ – 0.052 ppm) in the aromatic hydrogen atoms in the CHX phenyl rings towards higher shift values, and which are, with a high probability, the consequence of Bi(III) ion coordination to the nitrogen atoms of the biguanide groups directly connected with the aryl centers of the CHX molecule. In addition, the ^1H -NMR spectrum of the composite shows the disappearance of the signal of the $-\text{CH}_3$ group of the acetate molecule, which suggests that CHX is present in the composite in its non-ionised form.

Changes in the ^{13}C -NMR spectra of the composite, in relation to the spectra of the non-bonded substances, involve band shifts and band disappearances, and are observed in similar areas, as in the ^1H -NMR spectra. When compared to CIP, the CIP-Bi-CHX composite indicates significant changes in the chemical shifts in the aromatic carbon atoms in the quinolin-4-one ring. The observed behaviour of the carbon signals might be caused by the inductive effect due to the participation of the 4-ketone group and 3-carboxyl group in the complexation of the Bi(III) ion (Scheme 1) with the formation of a six-membered ring [23].

The conclusion arrived at on the basis of the NMR analysis, stating that the coordination of metal ions with fluoroquinolones through the carboxyl and carbonyl group, occurring at positions 3 and 4 of the quinolin-4-one, respectively, is consistent with the available literature [23,41–43], as well as with the data obtained by interpreting the FTIR spectra.

Table 4. The values of chemical shifts for the hydrogen atoms of the parent forms of ligands: CIP-HCl and CHX-acetate, and the studied CIP-Bi-CHX composite. (+)—change in chemical shift towards higher ppm values; (—)—change in chemical shift towards lower ppm values; *—signal difficult to detect due to its low resolution.

H-Atom	Chemical Shifts for the Hydrogen Atoms (δ , ppm)			Change in Chemical Shift ($\Delta\delta$, ppm)
	CIP-HCl	CHX-Acetate	CIP-Bi-CHX Composite	CIP-Bi-CHX Composite
1b (CIP, <i>cis</i> CH ₂ cyclopropyl)	1.194 1.203		1.186	$\Delta 0.008$ (—)
9' (CHX, CH ₂ hexane)		1.263	1.287	$\Delta 0.024$ (+)
1b (CIP, <i>trans</i> CH ₂ cyclopropyl)	1.317 1.337		1.303 1.326	$\Delta 0.014$ (—)
8' (CHX, CH ₂ hexane)		1.444	1.457	$\Delta 0.013$ (+)
10' (CHX, CH ₃ acetate)		1.715		No peak
7' (CHX, CH ₂ hexane)		3.041 3.064 3.086	3.035 3.084	$\Delta 0.006$ (—)
7 (CIP, CH ₂ piperazinium)	3.568		No detected *	No detected *
1a (CIP, CH cyclopropyl)	3.854 3.866 3.878		3.837 3.849	$\Delta 0.017$ (—)
2' (CHX, CH phenyl)		7.258 7.281 7.288	7.310 7.339	$\Delta 0.052$ (+)
3' (CHX, CH phenyl)		7.390	7.405 7.433	$\Delta 0.015$ (+)
8 (CIP, CH quinolin-4-one)	7.600 7.625		7.548 7.573	$\Delta 0.052$ (—)
5 (CIP, CH quinolin-4-one)	7.934 7.977		7.880 7.924	$\Delta 0.054$ (—)
2 (CIP, CH quinolin-4-one)	8.684		8.659	$\Delta 0.025$ (—)
>NH ₂ ⁺ (CIP piperazinium)	9.432			No peak
3a (CIP, COOH)	15.141			No peak

Significant changes of the bands of hydrogen and carbon atoms in the piperazine ring of the composite might suggest that nitrogen atoms in this region are coordination locations [40,44], which is, however, unlikely, due to important evidence indicating the coordination of the Bi(III) ion with the COOH and C=O groups. In addition, the capability of forming a complex both by the COOH and C=O groups and the N-H group of piperidine [44] should also be rejected due to the ligand proportions in the composite (1:1:1, respectively for CIP, Bi and CHX). Therefore, the modifications of resonance corresponding to both the hydrogen and the carbon atoms in the piperazine ring after the incorporation of CIP into the composite might involve the deprotonation of the nitrogen atom, as well as intramolecular forces with other atoms of composite in the spatial configuration of its molecule and the interactions resulting from the configuration of the composite molecules in crystal, e.g., the interaction N-H ... O(N), C-H ... O(N), C-H (N-H) ... π (aromatic system) [44–46].

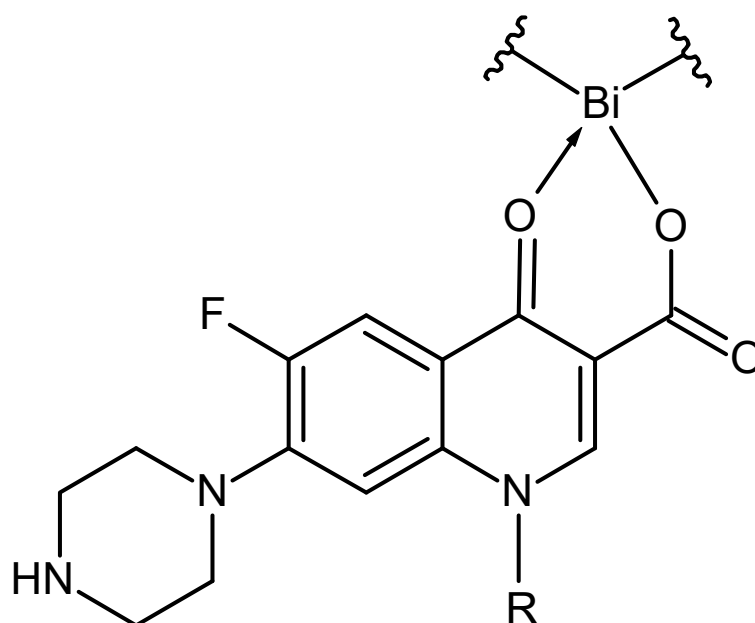
In comparing the ¹³C-NMR spectrum of the composite and CHX, the greatest changes in chemical shifts can be observed for the carbon atoms of the aromatic area, and mainly in the biguanide group (bonded with the C4' carbon of the aromatic area); the signal of the imine C6' carbon (C=NH) atom moves towards higher shift values, from 160.07 to 160.74 ppm, and the signals of C5' and C4' carbon atoms are not visible in the spectrum due to their low intensity. The said modifications might be the result of coordination

of the Bi(III) ion with the nitrogen atoms of the imine groups (C=NH) of the biguanide groups (NH-C(=NH)-NH-C(=NH)-NH) of the CHX molecule (Scheme 2), as indicated by the available papers [47].

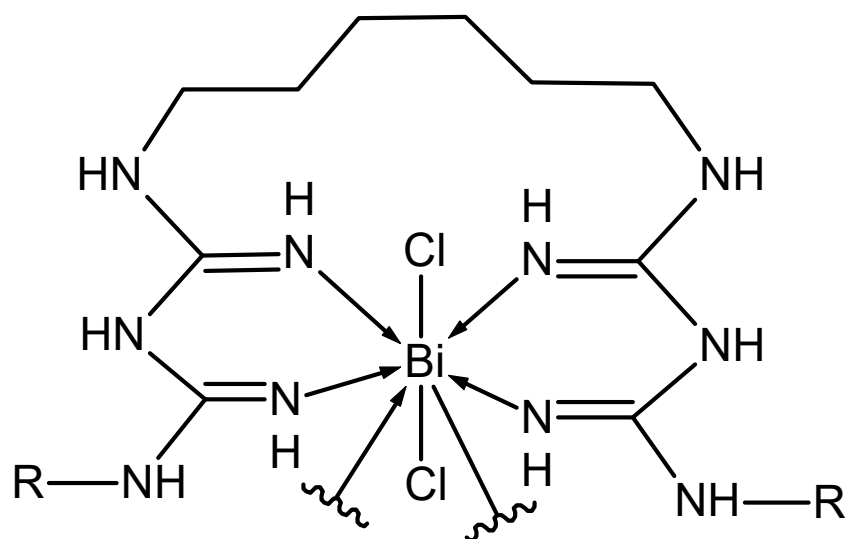
Furthermore, the ^{13}C -NMR spectrum of the composite reveals the disappearance of the signals of the CH_3 and COOH groups, which are present in the acetate group, indicating the deionisation of the CHX molecule in the composite.

Table 5. Values of chemical shifts for the carbon atoms of ligands: CIP-HCl and CHX-acetate and the studied CIP-Bi-CHX composite. (+)—change in chemical shift towards higher ppm values; (—)—change in chemical shift towards lower ppm values.

C—Atom	Chemical Shifts for the Carbon Atoms (δ , ppm)			Change in Chemical Shift ($\Delta\delta$, ppm)
	CIP-HCl	CHX-Acetate	CIP-Bi-CHX Composite	CIP-Bi-CHX Composite
1b (CIP, CH_2 cyclopropyl)	8.091		8.048	$\Delta 0.043$ (—)
10' (CHX, CH_3 acetate)		25.286		No peak
9' (CHX, CH_2 hexane)		26.365	26.391	$\Delta 0.026$ (+)
1a (CIP, CH cyclopropyl)	36.465		36.369	$\Delta 0.096$ (—)
7c/7e (CIP, CH_2 piperazinium)	42.950		44.887	$\Delta 1.937$ (+)
7b/7f (CIP, CH_2 piperazinium)	46.776 46.838		49.790	$\Delta 2.952$ (+)
8 (CIP, CH quinolin-4-one)	107.288		106.814	$\Delta 0.474$ (—)
3 (CIP, =C< quinolin-4-one)	107.411		107.234	$\Delta 0.177$ (—)
5 (CIP, CH quinolin-4-one)	111.501 111.808		111.298 111.610	$\Delta 0.203$ (—)
9 (CIP, =C< quinolin-4-one)	119.763 119.867		119.079 119.181	$\Delta 0.684$ (—)
3' (CHX, CH phenyl)		122.467	122.159	$\Delta 0.308$ (—)
1' (CHX, C-Cl phenyl)		126.180	126.732	$\Delta 0.552$ (+)
2' (CHX, CH phenyl)		128.689	128.928	$\Delta 0.239$ (+)
10 (CIP, =C< quinolin-4-one)	139.554		138.282 138.755 139.661	$\Delta 0.799$ (—)
7 (CIP, =C< quinolin-4-one)	144.537 144.675		145.641 145.774	$\Delta 1.104$ (+)
2 (CIP, CH quinolin-4-one)	148.697		148.483	$\Delta 0.214$ (—)
6 (CIP, C-F quinolin-4-one)	151.697 155.005		151.815 155.127 155.375	$\Delta 0.118$ (+) $\Delta 0.122$ (+)
6' (CHX, biguanide)		160.072	160.741	$\Delta 0.669$ (+)
3a (CIP, COOH)	166.334		166.454	$\Delta 0.120$ (+)
11' (CHX, COOH acetate)		176.391		No peak
4 (CIP, C=O)	176.839 176.872		176.811	$\Delta 0.028$ (—)



Scheme 1. Six-membered ring formed probably by complexation of ciprofloxacin.



Scheme 2. The suggested complexation of chlorhexidine.

2.4. X-ray Diffraction

The determination of X-ray crystal structures of the complexes was impossible because the efforts to obtain the suitable crystal were not successful. Thus, the X-ray powder diffraction measurements were performed for the phase identification of a crystalline material. Figure 8 shows powder diffraction data for the main product CIP-Bi-CHX and substrates used in synthesis. It can be seen that the main compound contains impurities of CHX-acetate, CIP-HCl, and Bi-citrate. The new phase of CIP-Bi-CHX can be characterized by weak reflections indicated by red vertical lines. The synthesized material has also amorphous content characterized by a broad background peak around 30°.

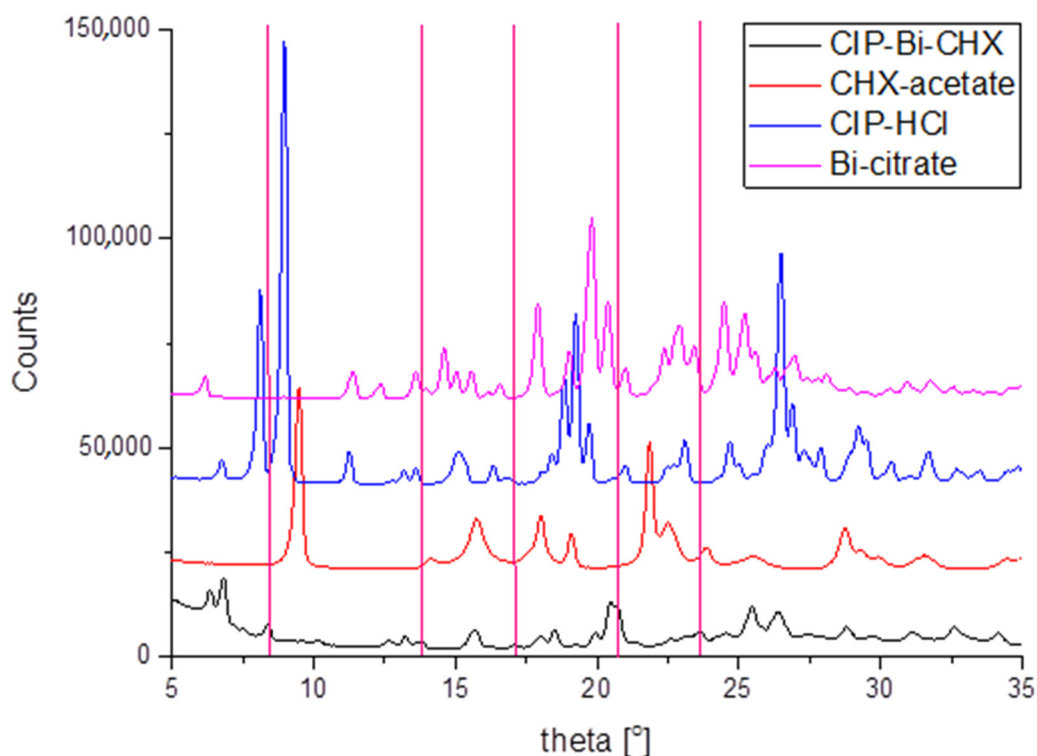


Figure 8. Diffraction patterns of CIP-Bi-CHX composite and the parent forms of ligands: Bi-citrate, CIP-HCl, CHX-acetate. For clarity presented patterns are shifted of 20,000 counts. The red vertical lines indicate a new phase of CIP-Bi-CHX.

3. Materials and Methods

Ciprofloxacin (CIP) hydrochloride, chlorhexidine (CHX) diacetate, and bismuth(III) citrate (Bi) were obtained from Sigma-Aldrich Co. Ethanol, 35–38% hydrochloric acid, citric acid, and other reagents and solvents of analytical grade were acquired from Avantor Performance Materials Poland S.A. The water used in the experiments was double-distilled.

3.1. General Methods

^1H and ^{13}C -NMR spectra were recorded on a Bruker Avance 300 spectrometer (Bruker BioSpin GmbH, Rheinstetten, Germany). The compounds (20 mg) were dissolved in DMSO- d_6 (0.6 mL). In the case of sample slightly dissolved, the supernatant was decanted. Chemical shifts were reported in parts per million (ppm, Δ scale) relative either to internal standard (TMS) or residual solvent peak. The number of scans used for registration was variable depending on weight of substance and quality of the signal (i.e., signal to noise). In the case of ^{13}C -NMR it was 8000 scans.

FTIR (Fourier transform infrared spectroscopy) analysis was performed on a Thermo Scientific Nicolet 6700A spectrometer (Waltham, MA, USA) equipped with a deuterated triglycine sulfate detector (DTGS/KBr) and a versatile Attenuated Total Reflectance (ATR) sampling accessory with the diamond crystal plate. The FTIR spectra averaged over 32 scans were recorded in the spectral range of 600–4000 cm^{-1} at spectral resolution of 4 cm^{-1} using OMNIC 8.1 computer software (Thermo Fisher Scientific Inc., Waltham, MA, USA). The FTIR spectra were collected in the same way using the same pressure. The spectral intensities were compared in an absorbance mode by overlaying the spectra and measuring the absorbance values at a particular wavelength.

The absorption spectral measurements were carried out on a UV-Vis Hitachi U-2001 spectrophotometer (Hitachi Instrument Inc., Tokyo, Japan) controlled by UV Solutions software using 1 cm matched quartz cells. The examined solutions were prepared in dilute hydrochloric acid at the concentration of 10 $\mu\text{g}/\text{mL}$. The ultraviolet spectra were recorded in the range 200–700 nm.

The powder X-ray diffraction measurements were conducted on an Empyrean, PANalytical diffractometer using Cu anode which produced CuK α radiation ($\lambda = 0.15406$ nm). The measurements were performed in the 2θ angle range from 20° to 90° . The radiation source was equipped with a mirror to cut-off the CuK β radiation. The input slit was $\frac{1}{2}$ mm and both detector and source were equipped with soller slits. The signals were recorded using a PixelX detector.

The elemental analyses were performed using a Perkin Elmer 2400 CHNS/O elemental analyzer. The chlorine was determined by the Schöniger procedure.

Melting points were recorded on a MP90 Melting Point System (Mettler-Toledo International Inc., Greifensee, Switzerland).

3.2. Preparation of the CIP-Bi-CHX Composite

The ciprofloxacin-bismuth-chlorhexidine (CIP-Bi-CHX) composite was synthesized according to the patent procedure no 235823 [48] by dissolving bismuth(III) salt in dilute hydrochloric acid, then mixing with chlorhexidine and ciprofloxacin in the ratio 1:1:1. The substances were added sequentially: first—CIP, later—CHX (method 1) or first—CHX, later—CIP (method 2). The syntheses were carried out with stirring at 40°C for 15 min. Next the reaction medium was basified to precipitation with dilute ammonium hydroxide and allowed to stand at room temperature for 12 h. The pale yellowish precipitate was filtered, washed with water-ethanol (1:1 *v/v*) solution and dried in a desiccator under vacuum. Bi(CIP)(CHX) $_2$ Cl, molecular formula: $\text{C}_{39}\text{H}_{47}\text{BiCl}_4\text{FN}_{13}\text{O}_3$, formula weight: 1115.67 g/mol, composition: C(41.99%) H(4.25%) Bi(18.73%) Cl(12.71%) F(1.70%) N(16.32%) O(4.30%).

4. Conclusions

The detailed spectroscopic characterization of the molecular structure of the new hybrid confirmed the presence of ciprofloxacin and chlorhexidine and revealed the possible coordination sites. Special attention was given to the interactions between the functional groups of the ligands and the bismuth ion in the relation to the parent forms of complexing agents. Based on the commonly used spectroscopic techniques and the literature data, the probable structure of the synthesized composite has been suggested. The applicability of the composite, the properties and healing advantages will be presented in subsequent papers.

It should also be emphasized that the conducted analyses have also shown the special role of spectroscopic techniques in the evaluation of the molecular structure of new compounds being potential drug candidates.

5. Patents

Results from the work reported in this manuscript are two patents [48,49].

Author Contributions: Conceptualization, methodology, writing—original draft preparation, D.K.; investigation (preparation of samples), writing—original draft preparation (introduction section), A.G.; methodology (NMR analysis), D.K., M.P.; methodology (XRD analysis), D.M.K.; writing review (linguistic verification), A.B.; funding acquisition, B.D. All authors have read and agreed to the published version of the manuscript.

Funding: This research received no external funding.

Institutional Review Board Statement: Not applicable.

Informed Consent Statement: Not applicable.

Data Availability Statement: The data presented in this study are available in this article.

Acknowledgments: The authors would like to thank to Matosiuk from Department of Synthesis and Chemical Technology of Pharmaceutical Substances with Computer Modeling Laboratory, Medical University of Lublin, for making it possible to perform the elemental analysis and NMR spectra recording.

Conflicts of Interest: The authors declare no conflict of interest.

Sample Availability: Not available.

References

1. Prestinaci, F.; Pezzotti, P.; Pantosti, A. Antimicrobial resistance: A global multifaceted phenomenon. *Pathog. Glob. Health* **2015**, *109*, 309–318. [CrossRef]
2. Aslam, B.; Wang, W.; Arshad, M.I.; Khurshid, M.; Muzammil, S.; Rasool, M.H.; Nisar, M.A.; Alvi, R.F.; Aslam, M.A.; Qamar, M.U.; et al. Antibiotic resistance: A rundown of a global crisis. *Infect. Drug Resist.* **2018**, *11*, 1645–1658. [CrossRef]
3. Lee Ventola, C. The Antibiotic Resistance Crisis, Part 1: Causes and Threats. *P&T* **2015**, *40*, 277–283.
4. Burke, V.; Richter, D.; Greskowiak, J.; Mehrtens, A.; Schulz, L.; Massmann, G. Occurrence of Antibiotics in Surface and Groundwater of a Drinking Water Catchment Area in Germany. *Water Environ. Res.* **2016**, *88*, 652–659. [CrossRef]
5. Haddad, T.; Baginska, E.; Kümmerer, K. Transformation products of antibiotic and cytostatic drugs in the aquatic cycle that result from effluent treatment and abiotic/biotic reactions in the environment: An increasing challenge calling for higher emphasis on measures at the beginning of the pipe. *Water Res.* **2015**, *72*, 75–126. [CrossRef] [PubMed]
6. Domalaon, R.; Idowu, T.; Zhanel, G.G.; Schweizer, F. Antibiotic Hybrids: The Next Generation of Agents and Adjuvants against Gram-Negative Pathogens? *Clin. Microbiol. Rev.* **2018**, *31*, 1–45. [CrossRef]
7. Keter, F.K.; Darkwa, J. Perspective: The potential of pyrazole-based compounds in medicine. *Biometals* **2012**, *25*, 9–21. [CrossRef] [PubMed]
8. Chen, F.; Moat, J.; McFeely, D.; Clarkson, G.; Hands-Portman, I.J.; Furner-Pardoe, J.P.; Harrison, F.; Dowson, C.G.; Sadler, P.J. Biguanide Iridium(III) Complexes with Potent Antimicrobial Activity. *J. Med. Chem.* **2018**, *61*, 7330–7344. [CrossRef] [PubMed]
9. Prakash, A.; Singh, B.K.; Bhojak, N.; Adhikari, D. Synthesis and characterization of bioactive zinc(II) and cadmium(II) complexes with new Schiff bases derived from 4-nitrobenzaldehyde and acetophenone with ethylenediamine. *Spectrochim. Acta A* **2010**, *76*, 356–362. [CrossRef] [PubMed]
10. Pokrovskaya, V.; Baasov, T. Dual-acting hybrid antibiotics: A promising strategy to combat bacterial resistance. *Expert Opin. Drug Discov.* **2010**, *5*, 883–902. [CrossRef] [PubMed]
11. Altiok, D.; Altiok, E.; Tihminlioglu, F. Physical, antibacterial and antioxidant properties of chitosan films incorporated with thyme oil for potential wound healing applications. *J. Mater. Sci. Mater. Med.* **2010**, *21*, 2227–2236. [CrossRef]
12. Xu, F.; Weng, B.; Gilkerson, R.; Materon, L.A.; Lozano, K. Development of tannic acid/chitosan/pullulan composite nanofibers from aqueous solution for potential applications as wound dressing. *Carbohydr. Polym.* **2015**, *115*, 16–24. [CrossRef]
13. Branca, C.; D'Angelo, G.; Crupi, C.; Khouzami, K.; Rifici, S.; Ruello, G.; Wanderlingh, W. Role of the OH and NH vibrational groups in polysaccharide-nanocomposite interactions: A FTIR-ATR study on chitosan and chitosan/clay films. *Polymer* **2016**, *99*, 614–622. [CrossRef]
14. Gordeev, M.F.; Hackbarth, C.; Barbachyn, M.R.; Banitt, S.; Gage, J.R.; Luehr, G.W.; Gomez, M.; Trias, J.; Morin, S.E.; Zurenko, G.E.; et al. Novel Oxazolidinone–Quinolone Hybrid Antimicrobials. *Bioorg. Med. Chem. Lett.* **2003**, *13*, 4213–4216. [CrossRef]
15. Singh, S.; Roy, R. The Application of Absolute Quantitative ¹H-NMR Spectroscopy in Drug Discovery and Development. *Expert Opin. Drug Discov.* **2016**, *11*, 695–706. [CrossRef] [PubMed]
16. Wan, H.; Tian, Y.; Jiang, H.; Zhang, X.; Ju, X. A NMR-based drug screening strategy for discovering active substances from herbal medicines: Using Radix Polygoni Multiflori as example. *J. Ethnopharmacol.* **2020**, *254*, 112712. [CrossRef]
17. Fiori-Duarte, A.T.; de Paiva, R.; Manzano, C.M.; Lustri, W.R.; Corbi, P.P. Silver(I) and gold(I) complexes with sulfasalazine: Spectroscopic characterization, theoretical studies and antiproliferative activities over Gram-positive and Gram-negative bacterial strains. *J. Mol. Struct.* **2020**, *1214*, 128158. [CrossRef]
18. Wallis, S.C.; Gahan, L.R.; Charles, B.G.; Hambley, T.W.; Duckworth, P.A. Copper(II) Complexes of the Fluoroquinolone Antimicrobial Ciprofloxacin. Synthesis, X-Ray Structural Characterization, and Potentiometric Study. *J. Inorg. Biochem.* **1996**, *62*, 1–16. [CrossRef]
19. Debnath, A.; Hussain, F.; Masram, D.T. Synthesis, Characterization, and Antifungal Studies of Cr(III) Complex of Norfloxacin and Bipyridyl Ligand. *Bioinorg. Chem. Appl.* **2014**, 457478. [CrossRef] [PubMed]
20. Badea, M.; Olar, R.; Ilis, M.; Georgescu, R.; Calinescu, M. Synthesis, characterization, and thermal decomposition of new copper (II) complex compounds with chlorhexidine. *J. Therm. Anal. Calorim.* **2013**, *111*, 1763–1770. [CrossRef]
21. Abdulghani, A.J.; Jasim, H.H.; Hassan, A.S. Determination of β -lactam Antibiotics in Pharmaceutical Preparations by UV-visible Spectrophotometry Atomic Absorption and High Performance Liquid Chromatography. *Pak. J. Chem.* **2012**, *2*, 150–160. [CrossRef]
22. Shaikh, A.R.; Giridhar, R.; Megraud, F.; Yadav, M.R. Metalloantibiotics: Synthesis, characterization and antimicrobial evaluation of bismuth-fluoroquinolone complexes against Helicobacter pylori. *Acta Pharm.* **2009**, *59*, 259–271. [CrossRef]
23. Ma, X.; Li, L.; Xu, C.; Wei, H.; Wang, X.; Yang, X. Spectroscopy and Speciation Studies on the Interactions of Aluminum (III) with Ciprofloxacin and β -Nicotinamide Adenine Dinucleotide Phosphate in Aqueous Solutions. *Molecules* **2012**, *17*, 9379–9396. [CrossRef] [PubMed]
24. Călinescu, M.; Negreanu-Pîrjol, T.; Georgescu, R.; Călinescu, O. Synthesis and characterization of new copper(II) complex compounds with chlorhexidine. *Part I Cent. Eur. J. Chem.* **2010**, *8*, 543–549. [CrossRef]

25. Cortes, M.E.; Sinisterra, R.D.; Avilacampos, M.J.; Tortamano, N.; Rocha, R.G. The Chlorhexidine: β -Cyclodextrin Inclusion Compound: Preparation, Characterization and Microbiological Evaluation. *J. Incl. Phenom. Macrocycl. Chem.* **2001**, *40*, 297–302. [CrossRef]
26. Sadeek, S.A.; El-Attar, M.S.; Abd-El-Hamid, S.M. Synthesis, characterization and antibacterial activity of some new transition metal complexes with ciprofloxacin-imine. *Bull. Chem. Soc. Ethiop.* **2015**, *29*, 259–274. [CrossRef]
27. Samlíková, M.; Holešová, S.; Hundáková, M.; Pazdziora, E.; Jankovič, L.; Valášková, M. Preparation of antibacterial chlorhexidine/vermiculite and release study. *Int. J. Miner. Process.* **2017**, *159*, 1–6. [CrossRef]
28. Holesová, S.; Valášková, M.; Hlavác, D.; Madejová, J.; Samlíková, M.; Tokarsky, J.; Pazdziora, E. Antibacterial kaolinite/urea/chlorhexidine nanocomposites: Experiment and molecular modelling. *Appl. Surf. Sci.* **2014**, *305*, 783–791. [CrossRef]
29. Zhu, M.; Lu, L.; Yanga, P.; Jin, X. Bis(1,1-dimethylbiguanido)copper(II) octahydrate. *Acta Cryst.* **2002**, *E58*, m217–m219. [CrossRef]
30. Dinari, M.; Gharahi, F.; Asadi, P. Synthesis, spectroscopic characterization, antimicrobial evaluation and molecular docking study of novel triazine-quinazolinone based hybrids. *J. Mol. Struct.* **2018**, *1156*, 43–50. [CrossRef]
31. Azhara, F.F.; Olad, A.; Salehi, R. Fabrication and characterization of chitosan–gelatin/nanohydroxyapatite–polyaniline composite with potential application in tissue engineering scaffolds. *Des. Monom. Polym.* **2014**, *17*, 654–667. [CrossRef]
32. Elshafie, H.S.; Sadeek, S.A.; Camele, I.; Mohamed, A.A. Biological and Spectroscopic Investigations of New Tenoxicam and 1.10-Phenthroline Metal Complexes. *Molecules* **2020**, *25*, 1027. [CrossRef] [PubMed]
33. Kowalczyk, D.; Miazga-Karska, M.; Gładysz, A.; Warda, P.; Baranska, A.; Drop, B. Characterization of Ciprofloxacin-Bismuth-Loaded Antibacterial Wound Dressing. *Molecules* **2020**, *25*, 5096. [CrossRef] [PubMed]
34. Doroffev, V.L. Infrared spectra and the structure of drugs of the fluoroquinolone group. *Pharm. Chem. J.* **2004**, *38*, 693–697. [CrossRef]
35. Spectral Database for Organic Compounds SDBS. Available online: https://sdb.sdb.aist.go.jp/sdb/cgi-bin/direct_frame_top.cgi (accessed on 6 March 2021).
36. Zieba, A.; Maslankiewicz, A.; Sitkowski, J. Spectral Assignments and Reference Data. ^1H , ^{13}C and ^{15}N NMR spectra of ciprofloxacin. *Magn. Reson. Chem.* **2004**, *42*, 903–904. [CrossRef] [PubMed]
37. Parwe, S.P.; Chaudhari, P.N.; Mohite, K.K.; Selukar, B.S.; Nande, S.S.; Garnaik, B. Synthesis of ciprofloxacin-conjugated poly(L-lactic acid) polymer for nanofiber fabrication and antibacterial evaluation. *Int. J. Nanomed.* **2014**, *9*, 1463–1477. [CrossRef]
38. Rabbani, M.G.; Islam, R.; Ahmad, M.; Hossion, A.M.L. Synthesis of some NH-Derivatives of ciprofloxacin as antibacterial and antifungal agents. *Bangladesh J. Pharmacol.* **2011**, *6*, 8–13. [CrossRef]
39. Jadrijevic-Mladar, T. Effects of substituents on the NMR features of basic bicyclic ring systems of fluoroquinolone antibiotics and the relationships between NMR chemical shifts, molecular descriptors and drug-likeness parameters. *Acta Pharm.* **2010**, *60*, 237–254. [CrossRef]
40. Rusu, A.; Hancu, G.; Tóth, G.; Toma, F.; Mare, A.D.; Man, A.; Velescu, B.S.; Uivarosi, V. Synthesis, characterization and microbiological activity evaluation of two silver complexes with norfloxacin. *Farmacia* **2016**, *64*, 922–932.
41. Chattah, A.K.; Linck, Y.G.; Monti, G.A.; Levstein, P.R.; Breda, S.A.; Manzo, R.H.; Olivera, M.E. NMR and IR characterization of the aluminium complexes of norfloxacin and ciprofloxacin fluoroquinolones. *Magn. Reson. Chem.* **2007**, *45*, 850–859. [CrossRef] [PubMed]
42. Urbaniak, B.; Kokot, Z.J. Spectroscopic investigations of fluoroquinolones metal ion complexes. *Acta Pol. Pharm.* **2013**, *70*, 621–629. [PubMed]
43. Uivarosi, V. Metal Complexes of Quinolone Antibiotics and Their Applications: An Update. *Molecules* **2013**, *18*, 11153–11197. [CrossRef]
44. Pansuriya, P.R.; Patel, M.N. Iron(III) complexes: Preparation, characterization, antibacterial activity and DNA-binding Enzyme. *Inhib. Med. Chem.* **2008**, *23*, 230–239. [CrossRef] [PubMed]
45. Poppler, A.C.; Corlett, E.K.; Pearce, H.; Seymour, M.P.; Reid, M.; Montgomery, M.G.; Brown, S.P. Single-crystal X-ray diffraction and NMR crystallography of a 1:1 cocrystal of dithianon and pyrimethanil. *Acta Cryst.* **2017**, *C73*, 149–156. [CrossRef] [PubMed]
46. Linck, Y.G.; Chattah, A.K.; Graf, R.; Romanuk, C.B.; Olivera, M.E.; Manzo, R.H.; Monti, G.A.; Spiess, H.W. Multinuclear solid state NMR investigation of two polymorphic forms of Ciprofloxacin-saccharinate. *Phys. Chem. Chem. Phys.* **2011**, *13*, 6590–6596. [CrossRef] [PubMed]
47. Al-Abdali, B.I.; Shakir, I.M.A.; Nafea, H.M. Synthesis and Spectroscopic Studies of Some transition metal Complexes with Mixed ligand of Metformin and Cysteine. *Iraqi J. Sci.* **2015**, *56*, 3036–3047.
48. Kowalczyk, D.; Gładysz, A.; Pietraś, R.; Ginalska, G.; Miazga-Karska, M.; Rajtar, B. Antimicrobial Composite for the Prevention or Treatment, Especially of Local Infections, and the Method of Its Preparation. Poland Patent No. 235823, 17 November 2020.
49. Kowalczyk, D.; Gładysz, R.; Ginalska, G.; Miazga-Karska, M.; Rajtar, B.; Polz-Dacewicz, M.; Pietraś, R. Medical Use of an Antibacterial Composite in Dressing Materials, Especially for the Prevention or Treatment of Local Infections. Poland Patent No. 235824, 17 November 2020.

MDPI AG
Grosspeteranlage 5
4052 Basel
Switzerland
Tel.: +41 61 683 77 34

Molecules Editorial Office
E-mail: molecules@mdpi.com
www.mdpi.com/journal/molecules



Disclaimer/Publisher's Note: The title and front matter of this reprint are at the discretion of the . The publisher is not responsible for their content or any associated concerns. The statements, opinions and data contained in all individual articles are solely those of the individual Editors and contributors and not of MDPI. MDPI disclaims responsibility for any injury to people or property resulting from any ideas, methods, instructions or products referred to in the content.



Academic Open
Access Publishing

mdpi.com

ISBN 978-3-7258-1851-8